On outflow mechanisms in galaxies

Ulrich Philipp Steinwandel

München 2020

On outflow mechanisms in galaxies

Ulrich Philipp Steinwandel

Dissertation
an der Fakultät für Physik
der Ludwig–Maximilians–Universität
München

vorgelegt von
Ulrich Philipp Steinwandel
aus Ostfildern-Ruit

München, den 05.08.2020

Erstgutachter: Dr. Benjamin P. Moster
Zweitgutachter: Prof. Dr. Harald Lesch
Tag der mündlichen Prüfung: 07.10.2020

Contents

Zusammenfassung

In dieser Arbeit untersuche ich den Ursprung galaktischer Ausströmungen, die durch verschiedene Rückkopplungsprozesse angetrieben werden. Dazu betrachte ich nicht nur allgemein akzeptierte Rückkopplungsprozesse wie Supernovae, sondern entwickle auch einen auf Magnetfeldern basierenden Ausströmkanal. Somit trägt diese Doktorarbeit grundlegend zum Verständnis von galaktischen Winden bei. Um ein tieferes Verständnis der bereits erwähnten Ausström-Prozesse zu erlangen, verwende ich numerische (magneto-) hydrodynamische Simulationen von schweren, milchstraßenähnlichen Galaxien bis hin zu kleinskaligen Supernova-Überresten. Ich nutze meine Milchstraßenmodelle, um einen Prozess zu beschreiben auf dessen Grundlage es möglich ist, galaktische Winde mithilfe des magnetischen Drucks in massiven Galaxien anzutreiben. Dieser Prozess hat das Potentzial stark zum Baryonen-Zyklus von Galaxien unterschiedlicher Größe beizutragen. Das Magnetfeld in diesen Simulationen zeigt die Struktur eines voll entwickelten α^2-Ω Dynamos. Basierend auf den Ergebnissen meiner numerischen Simulationen konnte ich die Details des Startprozesses eines magnetischen Windes in Balken-Spiral-Galaxien ableiten. Dieser Prozess wird durch die Parker-Instabilität, in Kombination mit adiabatischer Kompression und einem radialen Einströmdynamo aus einem bereits gesättigten Magnetfeld ausgelöst. Das Magnetfeld wurde hierbei durch den α^2-Ω Dynamo verstärkt. Das Prinzip des radialen Einströmdynamos als Ursprung eines Wind Prozesses ist völlig neu, und ich konnte eine analytische Beschreibung für die Ausströmraten ableiten, die mit diesem radialen Einströmdynamo erzielt werden können. Darüber hinaus ist dieser Prozess interessant, da er niedrige Massenauströmraten für den Wind erzeugt, was typischerweise in Galaxien bei hoher und niedriger Rotverschiebung beobachtet wird.

Darüber hinaus untersuche ich im zweiten Teil der Arbeit den wichtigsten Rückkopplungsmechanismus in Zwerggalaxien, Supernovae. In einer detaillierten Studie mit über 120 Simulationen isolierter Supernova-Überreste habe ich Auflösungsanforderungen für die Sedov-Taylor-Phase und die korrekte Modellierung der heißen Phase und der Impulsinjektion auf Skalen einer globalen Galaxiensimulation abgeleitet. Diese Art von Simulationen löst den Übergang von sehr heißem Gas ($\sim 10^6$ K) zu sehr kaltem Gas (unter 10 K) korrekt auf. Diese Studie wird mit der nächsten Iteration unseres Codes Gadget durchgeführt, die ein stark verbessertes Verhalten beim lösen der hydrodynamischen Gleichungen aufweist. Die neue Method trägt hierbei den englischen Namen Meshless Finite Mass (MFM). Diese Methode wurde vor der Supernova-Überrest Evolutionsstudie ausgiebig getestet. Die Kombination der neuen Methode zur Behandlung hydrodynamischer Strömungen und das aufgelöste Rückkopplungsschema für Supernovae in galaktischen Simulationen ermöglicht es uns, die nächste Generation von Galaxienentstehungs-Simulationen mit einer Teilchenauflösung im Bereich einiger weniger Sonnenmassen und einer räumlicher Auflösung von weniger als einem parsec durchzuführen. Wir haben isolierte Zwerggalaxiensimulationen und Galaxienverschmelzungs-Simulationen durchgeführt, um die Konsistenz des neuen Modells nachzuweisen. Darüber hinaus, habe ich das Modell verwendet, um die Auswirkung von sogenannten Wander-Sternen auf galaktische Winde zu untersuchen und konnte zeigen, dass der Effekt gering ist.

Abstract

In this thesis I investigate the origin of galactic outflow channels, driven by various feedback processes. To do so, I not only look at commonly accepted feedback processes like the feedback of supernovae but also develop an outflow mechanism based on magnetic fields. Thus, this thesis fundamentally contributes to the understanding of how galaxies can drive outflows from dwarf galaxies to Milky Way-like galaxies in our Universe. To achieve a deeper understanding of the already mentioned outflow processes I employ numerical (magneto-) hydrodynamical simulations from large Milky Way-like galaxies to small isolated SN-remnants. I use my Milky Way models to describe a process that drives outflows with the magnetic pressure in massive galaxies. This has the potential to contribute to the galactic baryon cycle. In these simulations I find a fully developed α^2-Ω dynamo. Based on the results of my numerical simulations I have been able to derive the details of the launching process of a magnetic tower outflow in barred spiral galaxies, that is driven by mass-inflow over a bar. This process is triggered by the Parker-Instability in combination with adiabatic compression and an acting radial inflow dynamo from an already saturated magnetic field, that is amplified by the α^2-Ω dynamo. The principle of the radial inflow dynamo as the origin of an outflow driving process is completely new and I was able to derive an analytic prescription for the outflow rates that can be obtained from this radial inflow dynamo. Furthermore, this process is interesting as it intrinsically produces very low mass loading factors for the outflow, which is typically observed at high and low redshift. This fact makes the process very attractive, and it could be established as an important outflow process over a wide range of redshifts, for all galaxies, that can trigger mass inflow over a non-axis symmetric instability. Moreover, in the second part of the thesis I investigate the most important feedback mechanism in dwarf galaxies, the feedback of supernovae. In a detailed study of over 120 simulations of isolated supernova remnants, I derived resolution requirements for resolving the Sedov-Taylor phase and properly modelling the hot phase and momentum injection by supernovae on scales of a global galaxy simulation. This kind of simulations properly resolve the transition from the very hot gas ($\sim 10^6$ K) to the very cold gas (below 10 K). This study is carried out with the next iteration of our code GADGET, that shows heavily improved behaviour in capturing the fluid flow by using a method that is called Meshless Finite Mass (MFM). This method has been extensively tested prior to the supernova-remnant evolution study. The combination of the new method for treating hydrodynamic flows and the resolved feedback scheme for supernovae in galactic simulations enables us to run the next generation of galaxy formation and evolution simulations with solar mass particle and sub-parsec spatial resolution. We have carried out isolated dwarf galaxy simulations, and galaxy merger simulations to gauge the consistency of the new model. I used the model to investigate the effect of runway stars on the galactic outflow history and was able to show that the effect of runways stars is most likely overestimated in recent outflow studies of Milky Way-like galaxy simulations. This model will be the foundation for the next generation of high resolution cosmological galaxy formation zoom-in simulations at high and low redshift.

Chapter 1

Introduction to galaxy formation and evolution

Within the class of nowadays established mathematical and physical sciences astronomy and astrophysics belong to the oldest. Already numerous philosophers and mathematicians in ancient Greece tried to explain the movement of the planets and stars to understand their cosmic origin. Thales of Milet was one of the first astronomers who reported stellar constellations and who successfully predicted a solar eclipse. Although, the ancient philosophers and mathematicians were able to accurately describe the movement of stars and planets on the night sky, they were not yet ready to give up on the thought that the Earth has to have a distinguished place within the Universe and that all other objects within the Universe are moving around the Earth. This fact has only been changed once Nicolaus Copernicus established the heliocentric picture with the sun in the centre of the solar system which was heavily supported by observations of Galileo Galilei, Tycho Brahe and later Johannes Kepler. The theoretical starting point of modern astrophysics has been set by Isaac Newton who for the first time worked out a self-consistent theory for gravitation that has been extremely successful in predicting the movements of stars and planets ever since. These laws of physics derived by Isaac Newton with further modifications by Joseph-Louis Lagrange, Edward-John Routh, William Rowan Hamilton and Carl Gustav Jacobi, together with the theory of electromagnetism by James Clerk Maxwell and the theory of thermodynamics with major contributions of James Clerk Maxwell, Ludwig Boltzmann, Max Planck, Rudolf Clausius and Josiah Willard Gibbs have been a description of modern physics around 1900 which was thought to be complete. Then came Albert Einstein. He pointed out several remarkable things during his lifetime like the details of Brownian-motion or the theory of the photo-electric-effect. However, his biggest contribution are special and general relativity which is still the foundation of modern cosmology which is the building-block for galaxy formation theory. Together with the theory of Quantum Mechanics with major contributions of Erwin Schrödinger, Werner Heisenberg and Niels Bohr, special and general relativity remain the building blocks of modern day physics to this day.

1.1 The standard model of cosmology and galaxy formation

The starting point for the standard model of cosmology is Einstein's theory of gravitation, general relativity. In 1905 the general understanding of physics was that the subject is complete and there is nothing left to discover, despite the fact that the well working theories of Newtonian mechanics and Maxwell's Electromagnetism could not be combined and the astonishing fact that despite the failed Michelson-Morely experiment, physicists were still clinging on to the Aether-theory to explain light propagation at a fixed speed c which yields one reference frame in Newtonian mechanics. Thus the Aether was introduced as a carrier medium for Maxwellian physics to explain the mismatch in the different reference frames of Newtonian mechanics and Maxwellian electrodynamics. However, in 1905 Albert Einstein showed that the movement of charged bodies can be explained when one replaces the Galilean coordinate transformation in Newtonian mechanics with the Lorentz-transformation which lead to the formulation of special relativity which is valid in flat space-times. It took until 1916 until the theory could be combined with gravity, yielding general relativity, that connects the four-dimensional space-time structure with fundamental physical processes in Einstein's field equations given via:

$$R_{\mu\nu} - \frac{1}{2} R g_{\mu\nu} + \Lambda g_{\mu\nu} = \frac{8\pi G}{c^4} T_{\mu\nu}, \tag{1.1}$$

in Einstein's sum convention and directly with cosmological constant Λ. $R_{\mu\nu}$ is the second order Ricci-tensor which is a contraction over the first and third indices of the fourth order Riemann-tensor $R_{\alpha\mu\beta\nu}$ via $g^{\alpha\beta} R_{\alpha\mu\beta\nu} = R_{\mu\nu}$. The second order tensor $g_{\mu\nu}$ is the so called metric tensor and R is the Ricci-scalar which gives the curvature [1]. G is the Newtonian gravity constant and c the speed of light. The second order tensor $T_{\mu\nu}$ is the energy-momentum tensor, which exact structure depends on the completeness of the underlying Lagrangian (e.g. for electromagnetism this is the electromagnetic field tensor in co-variant form). We want to highlight one important difference of this equations if they are compared for example to the equations of electromagnetism. Einstein's field equations are based on second derivatives while electromagnetism is based on first derivatives. Due to this non-linear nature of the equations, inhomogenities and anisotropies can lead to an effective contribution to the energy-momentum tensor on the right hand side. This is called back-reaction problem and might contribute to what is typically referred to as dark energy[2]. Generally, these equations have tons of solutions and finding them is not at all straightforward. Despite the fact that the equations are complicated one might start with an Ansatz for a line-element that looks similar like this:

$$ds^2 = -c^2 A(r) dt^2 + B(r) dr^2 + r^2 d\Omega^2, \tag{1.2}$$

with $d\Omega^2 = d\theta^2 + \sin^2(\theta) d\varphi^2$. Inserting this in the field equations and solving for $A(r)$ and $B(r)$ would yield the famous Schwarzschild-metric with $A(r) = B^{-1}(r)$. However, we need to find a metric that solves the field equations under the assumption of the so-called cosmological principle that can be described following Newton by:

- Apart from local irregularities the Universe shows the same behaviour from every point for every observer.

This implies that the Universe is homogeneous and isotropic. Furthermore, an addition of Weyls postulate (e.g. Weyl, 2009, in re-publication) is usually applied alongside with the cosmological principle:

- In a cosmological model the world lines that are the source of the gravitational field, form time like geodesic lines.

Therefore, we have to find a line-element ds that fulfils homogeneity and isotropy, which is given by the Friedmann-Lemaitre-Robertson-Walker (FLRW) metric:

$$ds^2 = c^2 dt^2 - a^2(t) \left[\frac{dr^2}{1 - kr^2} + r^2 d\Omega^2 \right]. \tag{1.3}$$

[1] In two dimensional flat coordinates this is the inverted radius of a circle.

[2] I would love the go in further detail on the mathematical details and the implications for physics derived from the equations, but I have to restrict myself to cosmology now.

In this context k is the absolute value of the curvature and $k = 0, \pm 1$ gives the general shape of the Universe, where $k = 0$ is a flat space time, $k = -1$ is a saddle-shaped space time and $k = +1$ is a convex-shaped space-time. The factor $a(t)$ is the scale-factor of the considered Universe. This results in the so called Friedmann equations when accounting for an ideal fluid, of the form:

$$\frac{\dot{a}^2}{a^2} + \frac{kc^2}{a^2} = \frac{8\pi G}{3}\rho + \frac{\Lambda c^2}{3}, \tag{1.4}$$

$$\frac{\ddot{a}}{a} = \frac{4\pi G}{3}\left(\rho + \frac{3p}{c^2}\right) + \frac{\Lambda c^2}{3}. \tag{1.5}$$

With pressure p and density ρ. The structure of those depends on the exact structure of the energy-momentum tensor, that usually accounts for contributions of baryonic matter (e.g. hydrodynamical modes), dark matter and radiation. To understand these equations in greater detail we will re-write them now in terms of the different matter contributions in the Universe, that are usually given via $\Omega_\mathrm{m} = \Omega_\mathrm{b} + \Omega_\mathrm{dm}$, Ω_r, Ω_Λ and Ω_k. Hereby, Ω_m is the matter density that consists out of baryons given via Ω_b and dark matter described by Ω_dm, Ω_r is the contribution of radiation, Ω_Λ is the contribution due to the cosmological constant[3] that is usually interpret as dark energy which is driving the expansion of the Universe and Ω_k which is the contribution of the curvature k of the underlying space-time. Now we can re-write the Friedman-equations, together with the definition of the Hubble-constant $H(t)$ given via $H(t)^2 = \dot{a(t)}^2/a(t)^2$ and find:

$$\frac{H}{H_0} = \sqrt{\Omega_\mathrm{m} a^{-3} + \Omega_\mathrm{r} a^{-4} + \Omega_\mathrm{k} a^{-2} + \Omega_\Lambda a^{-3(1+w)}}. \tag{1.6}$$

The different Ω add up to 1. In our universe the parameter w is 1 and we obtain:

$$\frac{H}{H_0} = \sqrt{\Omega_\mathrm{m} a^{-3} + \Omega_\mathrm{r} a^{-4} + \Omega_\mathrm{k} a^{-2} + \Omega_\Lambda}. \tag{1.7}$$

In this general form this equations are often simply solved numerically. Nevertheless, one can determine the solutions for Universes in which matter, radiation, dark energy or the curvature are dominating. The solution can be obtained by rearranging equation 1.7, separating variables and integrating:

$$H_0 t = \int_0^a \frac{da'}{\sqrt{\Omega_\mathrm{r} a'^{-2} + \Omega_\mathrm{m} a'^{-1} + \Omega_\mathrm{k} + \Omega_\Lambda a'^2}}. \tag{1.8}$$

An initial understanding of what this means for the evolution of the Universe can then be obtained by assuming that one component dominates over all the others. First, we assume that $\Omega_\mathrm{m} = \Omega_\mathrm{k} = \Omega_\Lambda = 0$. This leaves us with the following integration:

$$H_0 t = \int_0^a \frac{da'}{\sqrt{\Omega_\mathrm{r} a'^{-2}}}. \tag{1.9}$$

which can easily be solved and one finds:

$$a(t) = \sqrt{2tH_0\Omega_\mathrm{r}}, \tag{1.10}$$

[3]This is the vacuum energy density in the limit of general relativity. On a side note this is 123 orders of magnitude different from the vacuum energy density that is derived from Quantum Mechanics. This is a problem, which has to this day no clear solution and different mechanisms for solving this issue have been proposed (see e.g. String Theory, modifications of general relativity, fluctuating quantum fields, light front quantisation).

for a radiation dominated Universe, which we assume was an accurate condition in the early Universe, due to the scaling of Ω_r with the scale-factor a. Second, we assume $\Omega_r = \Omega_k = \Omega_\Lambda = 0$ and we find the results for a matter dominated Universe by integrating:

$$a(t) = \left(\frac{3}{2} t H_0 \Omega_m\right)^{2/3}. \tag{1.11}$$

Third, we consider a Universe with $\Omega_m = \Omega_R = \Omega_\Lambda = 0$, the case of a dominating energy-density of the curvature. This is typically not done in the standard literature as our Universe seems to have negligible contribution of curvature and is almost flat, further the integration is trivial and one finds:

$$a(t) = t H_0 \sqrt{\Omega_k}. \tag{1.12}$$

Finally, one can assume $\Omega_r = \Omega_m = \Omega_k = 0$ and derive the time-dependent scale factor $a(t)$ for a universe dominated by the cosmological constant (vacuum energy density). This integration is a bit more tricky compared to the ones we already carried out[4]. We start again with equation 1.7 and let the terms above vanish. However, this time we will not integrate from time zero but a certain transition time t_i after which the cosmological constant becomes dominant. This gives us the following expression for a(t):

$$a(t) = (t - t_i) H_0 \sqrt{\Omega_\Lambda} = \ln(a)|_{a_i}^{a}. \tag{1.13}$$

Solving for $a(t)$ gives:

$$a(t) = a_i \exp(t - t_i) H_0 \sqrt{\Omega_\Lambda}. \tag{1.14}$$

From all these single solutions, this is the only one that results in exponential growth of the scale factor with time. While the Unviverse is not observed to expand exponentially, it is observed to expand accelerated (Riess et al., 2001). Therefore, it is fair to conclude that the cosmological constant is dominating the matter density in our Universe. This is typically rendered as dark energy in the Standard Model of cosmology, the ΛCDM model. However, this actually depends on were we place Λ in Einstein's field equations (equation 1.1). The typical consensus today assumes that it is on the left hand side, where it would represent the vacuum energy density (Icke, 2016). One could be as brave as writing Λ on the right hand side, which would not change the mathematical consistency but the physical interpretation. If Λ is on the right hand side it implies that the energy density of the vacuum is directly related to the fundamental physics on these scales and the energy density of the vacuum would be closely related to presence of particles rather than a consequence of the geometry of space-time (see Icke, 2016, for an interesting discussion). Regardless, on which side of the field equations we put Λ, the observed accelerated expansion tells us that we need to include it in a Standard-Model for cosmology. Now the only thing we have to understand is where the CDM part comes from. CDM stands for cold dark matter and to this day it is not completely clear what this means. Observational, there are several indicators for the existence of dark matter. We will first look into the evidence that we have for the presence for dark matter and then we will discuss why it has to be cold.

Oort (1932) investigated the density and velocity structure of stellar populations alongside the vertical direction of the Milky Way. From this he estimated a mass that was about a factor of 2.5 higher than the value that was observed to this point in time in the solar neighbourhood. Therefore, he concluded that there must be some kind of not visible mass that accounts for this. While it has been shown later that this discrepancy can be explained by dust and cold gas a controversy was born that lasts until this day.

[4]The bounds of the integral are non-trivial

One year later Zwicky (1933) found, while investigating the rotational velocities of galaxies in the Coma-cluster, that the gravitational potential of the stellar mass could not account for the high observed rotational velocities of around 7500 km s^{-1}. He came to the conclusion that the cluster must be 400 times more massive than the stellar mass can account for to explain this.
One of the strongest indicators for dark matter are the rotation curves of spiral galaxies. Rubin and Ford (1970) observed the rotational velocities of spiral galaxies. Surprisingly they found that the velocities seem to be rather constant with increasing radius, and not, as expected from keplerian rotation, declining. This suggests that there must be more mass on larger scales than expected by only considering the enclosed observable baryon mass.
Other strong evidence comes from gravitational lensing which for example indicates that the mass of the Bullet-cluster must be higher than the observable mass based on the reflection angle of the light due to the gravitational potential of the cluster (Clowe et al., 2006).
All this observational evidence gives a strong claim to further investigate the ΛCDM model in greater detail. Subsequent large scale observational projects have made it their main goal to do so and the most striking scientific evidence for the ΛCDM-model is given by the cosmic microwave background (CMB). The CMB shows a black-body spectrum that perfectly fits the theory at 2.7 K, with tiny temperature fluctuations of the order of 10^{-6} K that show a specific anisotropy on angular scales which can be perfectly described by the six parameter fit of the ΛCDM-Standard Model, which is the biggest success of the model. In Figure 1.1 we show the temperature fluctuations as measured by the initial detection from Penzias and Wilson (1965), COBE (Smoot et al., 1992), WMAP (Komatsu et al., 2011; Spergel et al., 2007) and PLANCK (Planck Collaboration et al., 2016) missions, which shows the clear improvement of the measurements over the years. We show the resulting anisotropy spectrum of the CMB as measured by the Planck Collaboration et al. (2016) in Figure 1.2. The position, the height and the width of the different peaks in the angular anisotropy powerspectrum has important physical implications. First, we note that the angular scale is decreasing with increasing numerical value. Thus the large scales are given by the left hand side of the plot. The plateau on the left hand side is a combination of the initial conditions of the Universe and the integrated Sachs-Wolfe effect (ISW, Sachs and Wolfe, 1967), which is given as redshifted CMB photons due to density fluctuations. The effect dominates on angular scales larger than 2°. In linear perturbation theory the effect is not present and only occurs due to non-linear behaviour when the Universe transits from the radiation to the matter dominated era and from the matter dominated era to the dark-energy dominated era. In the former case the effect is is labelled as early ISW and in the latter case as late ISW. The early ISW is then placed at a few tens on the angular degree scale while the late ISW is set on the degree scale. There is secondary effect that acts similar in the physical behaviour which is the Rees-Sciama-effect (Rees and Sciama, 1968) that occurs due to non-linear structure formation in the early Universe. This plateau is followed by several peaks when we move to smaller and smaller scales caused by interactions of the tightly coupled photon-matter fluid in the early Universe. The gravitational potential of the dark matter attracts the baryons and leads to collapse of structure in the early Universe. However, as the radiation is tightly coupled to the baryons this leads to a response of the photons generating an excess in outward pressure, counter-balancing the effects of gravity. The interplay of these forces generates acoustic oscillations in the matter density. As soon as the photons decouple from the residual baryons, they escape but the baryons stay in place. The exact position, width and height of this resulting baryon-acoustic (BAO) oscillations give us information on the matter content in the Universe. The first peak has two important physical implications. The position of the peak holds the information of the curvature of the Universe and the shape of the peak is set by the baryon content. The peak essentially shows us that our Universe is flat. The second peak results due to inflationary soundwaves and holds evidence on the baryon content which is consistent with the expectations from primordial nucleosynthesis. The third

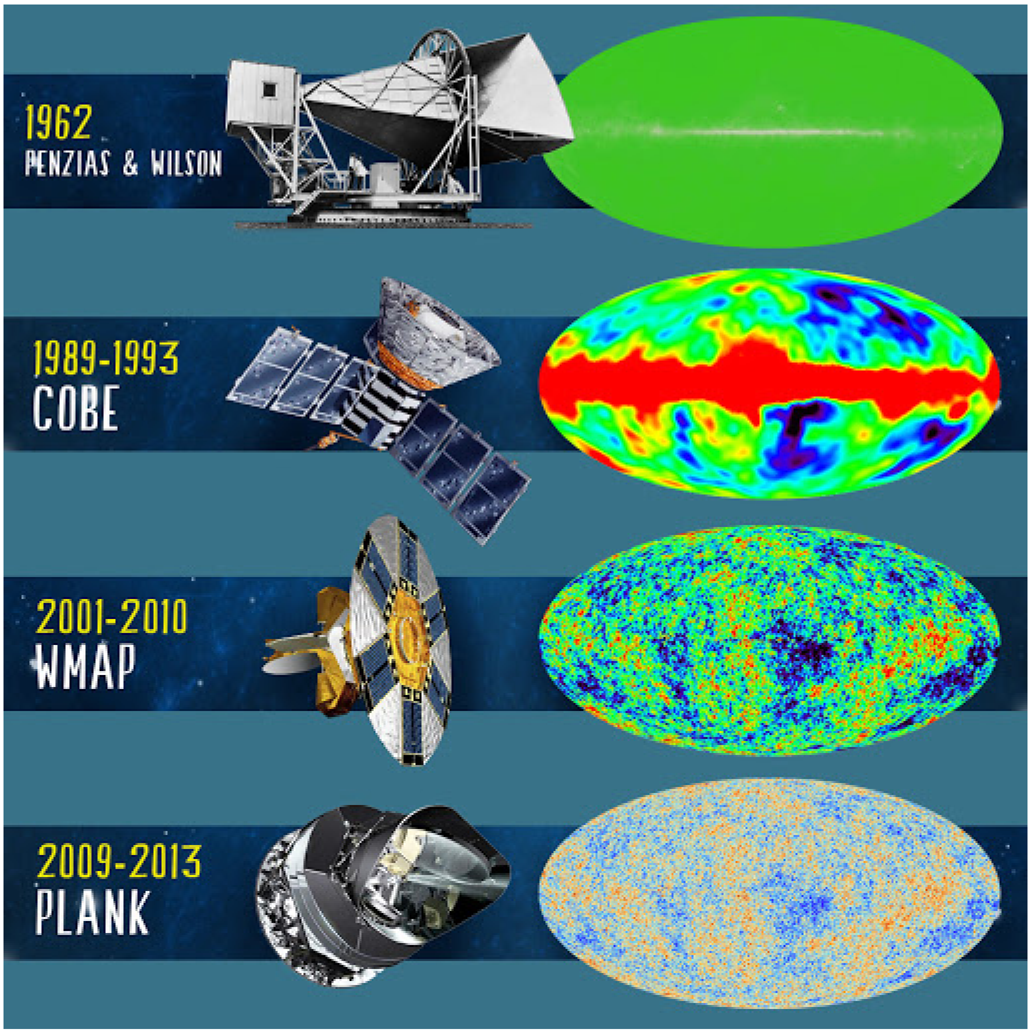

Figure 1.1: We show the temperature fluctuations as measured in the initial study of the CMB by Penzias and Wilson (1965) and compare with the results from the COBE, WMPA and Planck collaborations that show the amazing increase in angular resolution over the years. The figure has been taken from `http://marsatschool.ethz.ch/mission/1/img/cosmic-microwave-background.jpg`

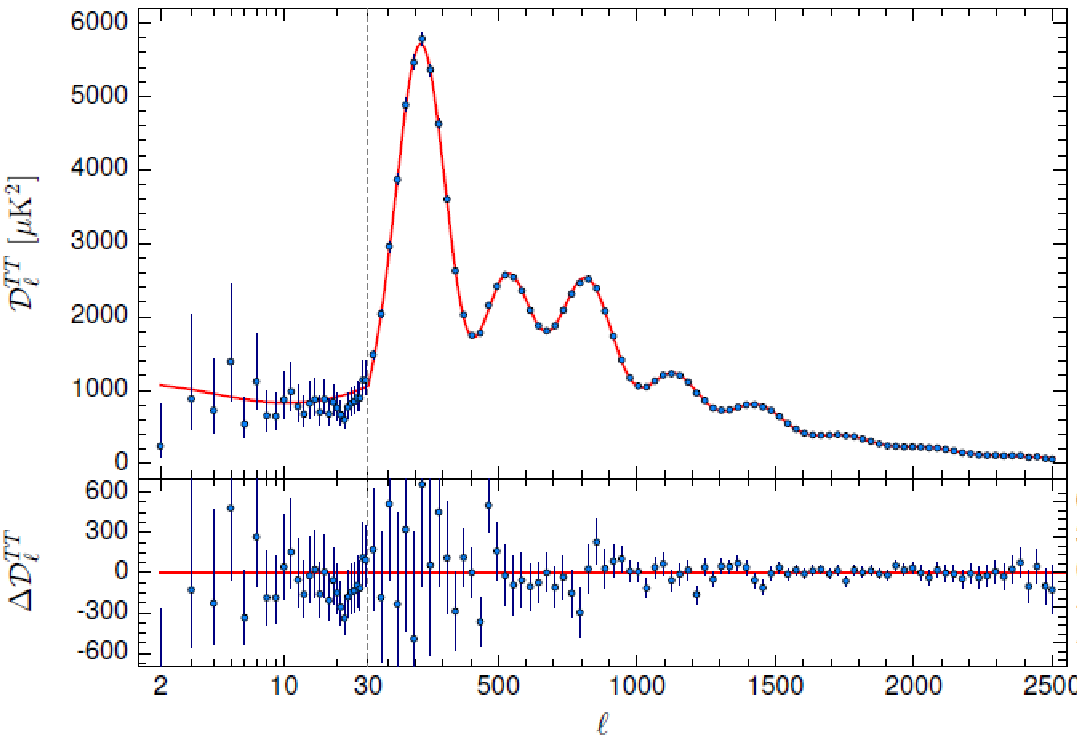

Figure 1.2: Temperature anisotrpoy powerspectrum as observed by the Planck satellite taken from the Planck Collaboration et al. (2016) data release. The upper panel shows the best fit model to the ΛCDM framework and the lower panel the residuals of this fit.

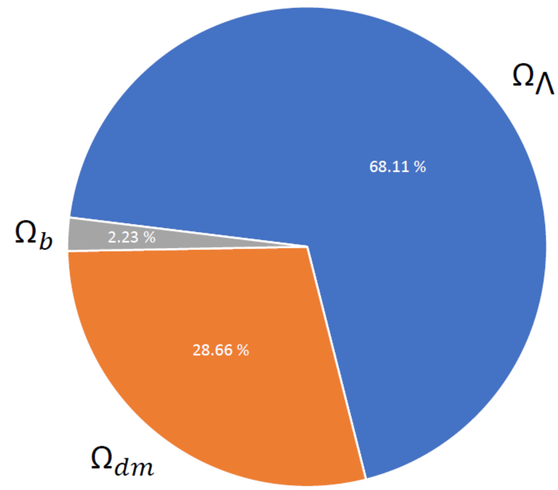

Figure 1.3: We illustrate the composition of the Universe in the percentage of baryons (grey), dark matter (orange) and dark energy (blue), with the values obtained from Planck Collaboration et al. (2016).

peak is driven by radiation support in the early Universe and can be used to deduce the dark matter content of our Universe. Finally, on the right hand side of Figure 1.2 we can see a dampening of the power-spectrum. The photons diffuse and drag the baryons along to generate the acoustic oscillations as they move from the hot regions to the cold regions. Essentially, this leads to an reduction in the temperature gradients between hot and cold regions suppressing the temperature anisotropy on smaller scales. This process is called diffusion damping or Silk-damping (Silk, 1968). Bringing the evidence from the CMB together, one can derive the composition of our Universe today, which is illustrated in Figure 1.3. The overwhelming evidence that is put forward by the COBE, WMAP and PLANCK missions renders the ΛCDM-modell one of the biggest success-stories of modern day astrophysics and it is especially successful in explaining the Universe on the largest scales. Furthermore, it is possible to gauge the consistency of the model via direct numerical simulations of structure formation. The idea is that the large scale clustering of galaxies as it is observed can directly be simulated in the ΛCDM framework which yields very good agreement of the two. This has been done for the first time in a large cosmological box in the Millennium simulation Springel et al. (2005b). We show the structure of the dark matter density obtained by the simulation in Figure 1.4. In Figure 1.5 we show the direct comparison of the clustering in the simulation with the observed galaxy clustering in the local redshift Universe from the CfA2 survey (Geller and Huchra, 1989).

Despite the success of the model in connecting theory, direct numerical simulations and observations, the model had to face several problems over the years. While most of them could be resolved by now a few remain. One of the first problems that had to be solved is the so called missing satellites problem pointed out by several authors (Kauffmann et al., 1993; Klypin et al., 1999; Moore et al., 1999). The problem manifests in the following manner. While numerical simulations in the ΛCDM framework find good agreement in the number density of massive galaxies, they over predicted the number of dwarf-satellite galaxies. Another problem of the same kind is the too-big-too-fail problem (Boylan-Kolchin et al., 2011, 2012; Garrison-Kimmel et al., 2014), which states that given the observed mass

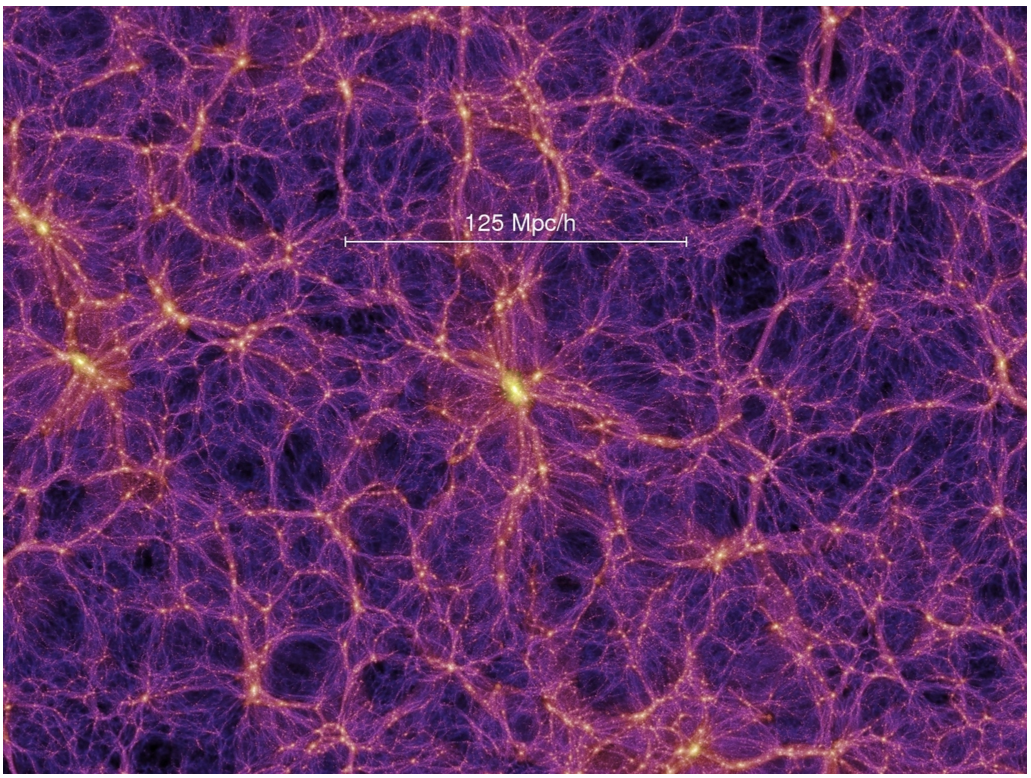

Figure 1.4: Dark matter structure as it is obtained by direct numerical simulation with the fluctuations at the formation of the CMB at 380,000 years for an initial condition. The large scale clustering shows similar structure to the observed one. The Figure has been taken from: `https://wwwmpa.mpa-garching.mpg.de/galform/virgo/millennium/seqD_063a_half.jpg`.

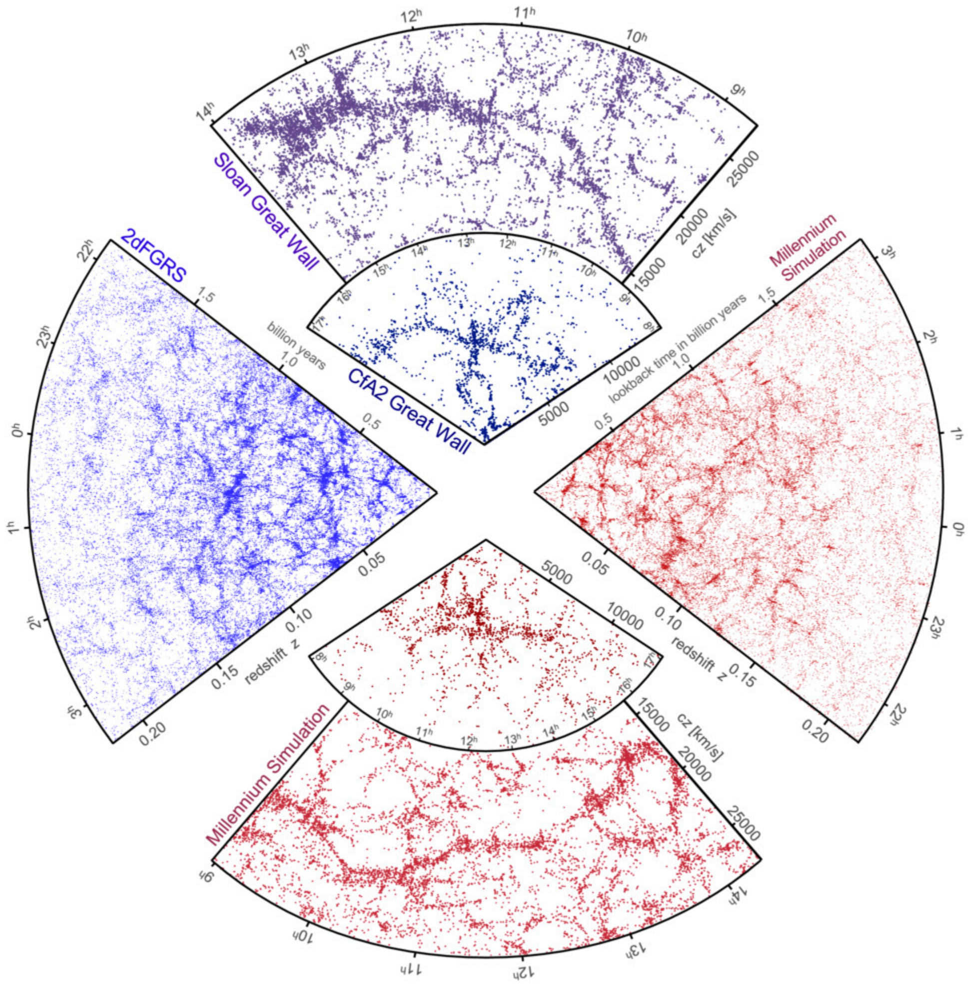

Figure 1.5: Comparison between the simulated galaxy clustering from the Millennium simulation and the observed clustering from the CfA2 redshift survey. In general one can find remarkable agreement between the simulated structure within the ΛCDM framework and the observed clustering. The figure has been taken from: `https://www.h-its.org/de/wp-content/uploads/sites/2/2014/10/pie_millennium_walls.jpg`

function there should be much more intermediate mass systems in the local group. Moreover, Moore (1994) and Navarro et al. (1996) pointed out that the dark matter distribution of observed low mass galaxies differs from the results of N-body simulations. Typically, these phenomena can be explained by including proper feedback channels in the simulations that drive galactic outflows. However, there are different approaches that suggest warm or fuzzy dark matter to resolve these problems or even remove dark matter completely out of the modelling of dwarf galaxies (Milgrom, 1983, e.g.) just to re-introduce it on galaxy cluster scales in the form of hot dark matter.
The biggest problem for the ΛCDM framework to this day is the fact that it is completely unclear what dark matter is. A lot of candidates have been discussed over the years, ranging from a baryon origin like the brown dwarf population or large cold gas reservoirs to other Massive Compact Halo Objects (MACHOs) that are located in the halos of galaxies over neutrinos to axions that are needed in Quantum Chromodynamics to tackle the problem of the electric dipole moment of the neutron.
Finally, we briefly discuss why dark matter has to be cold. For this let us briefly assume that dark matter is warm or even hot. The idea behind this is to solve issues like the missing satellites problem not by galactic feedback mechanisms, but by preventing the hierarchical clustering. The idea of cold dark matter is that it consists out of slowly moving, massive particles with an energy above 100 GeV. As these particles are slow and massive and only interact via gravity with the baryons they are more less fixed in space and the initial dark matter density fluctuations generate the seeds for the baryon structure collapse. Because they are slow, hierarchical clustering is possible on all scales. This would be different in warm or even hot dark matter scenarios where clustering on smaller scales would be prevented as the particles are less massive and move at higher velocities. However, the warmer the dark matter is, the larger are the structures that are being prevented from forming and therefore this gives an upper limit of around 2 keV for the mass of the warm dark matter particle, which can for example be constrained by the abundances of high redshift galaxies in the Hubble Frontier Fields (HFF) survey (Menci et al., 2016).

1.2 Our current understanding of galaxy formation

Despite the fact that the ΛCDM framework has some issues it is still the best working model for galaxy formation theory and enormous progress in the field of galaxy formation has been made since the 1970's and in principle our current understanding of galaxy formation is quite good. The basic idea of structure formation in this framework is that structures grow by gravitational instabilities in regions of slight over-densities. The growth of structure by gravitational collapse has been pointed out for the first time by Jeans (1902) who was able to show that modes can grow if the gravitational attraction is larger than the thermal support of the gas. Gamow and Teller (1939) and Lifshitz (1946) were able to show that this theory for gravitational collapsing modes can be extended towards expanding space-time, yielding a power-law like structure for the growth of initial perturbations. In the first models for structure formation it was still unclear how the initial conditions for structure formation can be obtained and one simply assumed that there were two different contributions from baryons and from photons. Now, one can assume that the perturbations are either adiabatic or isothermal. If they are adiabatic this means that perturbations of the matter and the radiation field are tightly coupled and initially grow at the same rate. Therefore, one can go ahead and assume that a one-fluid approach is valid on the time-scale on which radiation and baryons stay tightly coupled. In this regime the Jeans mass is quite large (up to 10^14 $M_\odot$) and structure formation is suppressed during this period. However, this changes as soon as the photon-field decouples from the baryon matter (at recombination). At recombination small-scale fluctuations are damped (Silk-dampening) as photons start to diffuse. This results in a

major drop of the Jeans mass to around 10^6 $M_\odot$ and structures above this threshold start to undergo gravitational collapse. However, at recombination most of the perturbations on galaxy-scales have already vanished, which implies that there must be hierarchical formation scenario from the top down, where larger structures start collapse and fragment to form smaller structures (Zel'Dovich, 1970).
The situation for isothermal initial conditions is different. In this scenario the spatial fluctuations of the ratio between baryons and photons stays constant and the background temperature (and pressure) remains fixed. Small-scale structure survives in this scenario until after the era of recombination as there are no acoustic modes that would be dampened out by Silk-dampening. Thus structures would form from the bottom up by hierarchical clustering of smaller structures (Peebles, 1965).
This was the situation in the early 1970's and the linear regime of structure growth was already established very well by major contributions of only a few groups (Lifshitz, 1946; Peebles and Yu, 1970; Sato et al., 1971; Silk, 1968; Weinberg, 1971). The general assumption was hereby that the structure that can be observed today in the Universe can be obtained from finite scale perturbations that are set by the Big-Bang itself. Harrison (1970a) and Zeldovich (1972) pointed out that that there is exactly one normalisation of the amplitude that is set by the Big Bang that is consistent with the observed galaxy formation structure, which is given by fluctuations of the Newtonian potential of the order of 10^{-4}. Quickly after the theory of inflation was established, several authors (Bardeen et al., 1983; Guth and Pi, 1982; Hawking, 1982; Starobinsky, 1982) pointed out that the density fluctuations that can be obtained during inflation have the predicted shape of the fluctuations suggested by Harrison (1970a) and Zeldovich (1972). Furthermore, the fluctuations obtained from inflation typically have the form of a Gaussian random field and are of adiabatic nature. With the advancements of the COBE, WMAP and PLANCK missions it became possible to test the theory of the Harrison-Zeldovich-like fluctuations and it turns out that the initial density fluctuations that are established after the formation of the CMB 380,000 years after the Big Bang are Gaussian and follow the Harrison-Zeldovich-spectrum.
Now that the linear regime is established we have to make the transition to the non-linear regime. The first attempt to do so has been made by Zel'Dovich (1970) who suggested an analytical prescription for non-linear growth of structure by investigating the one-dimensional collapse of an initial density perturbation. To this day this scenario is used as a hydrodynamical test case for verifying structure growth in numerical astrophysics. This has been followed up by Gunn and Gott (1972) who derived the spherical growth, turn-over, collapse and finally the virialisation of structure obtained by an initial perturbation of the density field. The intriguing result of this calculation is that they obtained an equilibrium condition of roughly half the size of the turn-over radius of the halo. Press and Schechter (1974) further developed this model by accounting for a Gaussian initial density field, which allowed them to directly derive the halo mass function from hierarchical clustering.
Another important attempt for non-linear structure growth was already made early on by Hoyle (1949) who suggested that perturbations can obtain angular momentum by interaction over tidal torques with neighbouring perturbations. This was later confirmed by numerical simulations (Efstathiou and Jones, 1979; Peebles, 1971).
As we already pointed out above indicators fro dark matter where present quite early on (e.g Oort, 1932; Zwicky, 1933) but it took until 40 years later when Ostriker et al. (1974) and Einasto et al. (1974) took a closer look again into the analysis of Zwicky (1933) and pointed out that the motion of the Milk Way satellites could only be explained if the neighbouring halos contained much more mass then the observable stellar mass. This was evermore supported by the observational evidence for flat rotation curves that was brought forward. Furthermore, several authors started speculating what exactly could be the origin of this additional mass component, ranging from brown dwarfs, white dwarfs and black holes (Carr et al., 1984; White, 1978) to elementary particles like the massive neutrino population (Cowsik and McClelland, 1972; Gershtein and Zel'dovich, 1966). Neutrinos came into play due to the

findings of particle physics. The first neutrino that was massive enough to account for a dark matter contribution was detected by Lyubimov et al. (1980) and Reines et al. (1980) with a mass around 30 eV and several authors started to investigate structure formation with neutrinos (e.g. Bond et al., 1980; Klinkhamer and Norman, 1981; Sato and Takahara, 1980; Schramm and Steigman, 1981). The idea of structure formation with neutrinos is that they decouple quickly, while they are still relativistic before recombination. As they are then very similar to the abundance of CMB-photons one can estimate that they became non-relativistic when the Unis-verse transits from the radiation to the matter dominated era. This would imply Mpc-scale structure in Zeldovich-Pancake from that would need to further fragment to smaller and smaller structures. This is not only inconsistent with observations, it was also pointed out by Tremaine and Gunn (1979) that 30 eV neutrinos in a structure formation context are in conflict with the Pauli-exclusion principle. Moreover, White et al. (1984) pointed out in numerical simulations that a Universe that is dominated by neutrinos (i.e. hot dark matter) would show much stronger galaxy clustering than what we currently observe. Therefore, the term of Weakly Interacting Massive Particle (WIMP) was established and as we pointed out above it is not clear to this day what a WIMP is. Despite this fact, the CMB provides good evidence for the presence of such a particle, as models for primordial nucleosynthesis provide not enough baryon matter to account for the preferred flat universe that is obtained out of inflation. Furthermore, the upper limit of the CMB anisotropy rules out baryon-only models for structure formation.

Quite early on (in the 1930's) it was clear that there are more less two types of galaxies that are the end-product of the structure formation process obtained by the initial conditions we discussed thus far, ellipticals and spirals. However, the first monolithic collapse model has been established somewhat later by Eggen et al. (1962). They speculated that ellipticals and spirals only differ by how efficient star formation occurs during the collapse. Thus if a gas cloud collapses and undergoes runaway star formation it becomes and elliptical. If the star formation process is suppressed it becomes a spiral. The later can for example be established by shocks and radiative cooling which will reduce the clouds size until it becomes supported by angular momentum. This picture can be further developed by assuming that ellipticals are the results of the largest density perturbation as the star formation efficiency scale with ρ^2. This was pointed out by Gott and Thuan (1976) who suggested that ellipticals are the end products of the strongest density perturbations while spirals originate from the weakest density perturbations. Already in the first numerical simulations of the formation process of galaxies Larson (1974, 1975, 1976) it was pointed out that feedback processes have to play a major role in the formation of galaxies. Toomre and Toomre (1972) carried out the first simulations of a galaxy merger suggesting that structures that are observed in galaxies might be explained by tidal interactions and they concluded that almost all ellipticals are formed in major mergers of disc galaxies. It could be shown that the surface brightness profiles obtained from merger simulations is consistent with observed ellipticals (White, 1978). However, it was shown by Ostriker (1980) that the velocity dispersion's in massive ellipticals are way too high to be explained by major mergers of present day galaxies.

There is striking observational evidence that there are basically no galaxies with stellar masses that are larger than 10^{12} $M_\odot$. In the pure baryon picture this could simply be explained because Silk-dampening would force an upper limit on galaxy mass. However, if dark matter is dominating this does not matter as the baryons collapse in the dark matter potential later on. Also from Press-Schechter formalism we expect higher mass objects. Silk (1977), Rees and Ostriker (1977) and Binney (1977) put the conclusion forward that radiative cooling sets an upper mass limit, because the collapse is only effective where the cooling time is shorter than the collapse time.

Today we assume that galaxies from in a two stage process following White and Rees (1978) who propose that dark matter structures collapse first via hierarchical clustering, before the baryons fall into the dark matter potential and from galaxies. The galaxy mass function can then be computed

Figure 1.6: The poster child galaxy for outflow activity, M 82. We show the galaxy as seen by the Hubble space telescope in the optical bands. The red colour that indicates the out flowing gas, comes from H-α emission. The picture has been taken from `https://de.wikipedia.org/wiki/Messier_82` on the 23.07.2020 at 10:48 pm.

by applying the Press-Schechter theory and accounting for low galaxy formation efficiency due to feedback processes in the proto-galactic haloes. In today's galaxy formation and evolution simulations these feedback processes are vastly important to obtain the observed galaxy population consisting of ellipticals and spirals. One of the most important results of the past decade was the realisation by Moster et al. (2010b) and Behroozi et al. (2010) who pointed out that many state-of-the-art galaxy formation models tend to overproduce stars, hinting towards a more complete theory for quenching star formation in galaxies, which could for example be resolved by feedback and the build-up of galactic winds.

1.3 Galaxy Outflows

Outflows are widely observed features in all kinds of galaxies. Still, it remains unclear how exactly galaxies drive their outflows, which is a problem that is historically tightly coupled to galaxy formation and evolution. The story of galactic winds starts early on and it starts with M 82. We show a picture of M 82 in Figure 1.6. The composite colour in red shows the H-α emission from the out flowing none-star forming gas. Lynds and Sandage (1963) and Burbidge et al. (1964) where the first ones to report on explosions inside of M 82 and excess energy leaving the system. Burbidge et al. (1964) even state:

- The activity in M 82 is yet another manifestation of the generation of vast fluxes of energy by processes which are not yet properly understood.

This raises two questions. The first one is, what are the origins of these outflows and excess energy losses and what is our current understanding of them today. Although the first quasar was observed in

Schmidt (1963) it was not at all clear what kind of object this could be. The lack of knowledge on this part inspired people to speculate on the origin of these objects Hoyle and Ellis (1963) but no conclusive answer could be obtained. As the 1960s progressed the community obtained a deeper understanding of what was going on in M 82. The first important realisation from the work that has been carried out thus far was that there seems to be a resemblance of the optical and the radio features of M 82 and the Crab nebula. Today, we know the origin of the Crab nebular very well and we know that it is the result of the supernova SN 1054. From this one can drive the conclusion that the wind in M 82 is driven by nuclear star clusters in the centre of the system. On the other hand Lynden-Bell (1969) showed that black holes are the origin of quasars and the strong observed radio emission. The observations of M 82 are really groundbreaking in that regard, as galaxy outflows have not been established a research topic by that time. This is entirely different at the present day where we know from the combined efforts of observations, theoretical modelling and numerical simulations that the understanding of the feedback cycle that drives galactic winds is essential in the understanding of how galaxies form in the Universe. In principle there are two energy sources that are established nowadays that can explain the origin of galactic winds. The first is stellar feedback, the second is the feedback of active galactic nuclei (AGN). In terms of stellar feedback there are several processes that can play a major role in setting outflow rates in galaxies, with the most energetic ones being the Core Collapse SNe. However, the exact wind-driving process in a starburst galaxy is unknown to this day, but it can be divided in different time spans in which different components dominate to the wind driving process. In early stages of the star cluster, the wind driving mechanism is dominated by stellar winds, from massive O/B -stars (below 3 Myr), until they move away from the main-sequence and become Wolf-Rayert (WR) stars with even higher mass loss rates (up to 10 Myr). From that point on the environment is dominated by frequent core collapse supernova explosions. While this picture is valid in the Milky Way (MW) and other nearby galaxies, the importance of stellar winds is probably not present in lower metallicity systems as stellar winds are driven by line-emission in massive O and B stars which significantly decreases in low metallicity stars. From numerical modelling (Leitherer et al., 1999) we know quite well that the outflow rate, the energy and momentum loss, scale linear with the star formation rate, which is a rather strong correlation for astrophysical environments.

The second well established candidate for the origin of a galactic wind is the feedback of black holes. The energy loading $\dot{E}$ of an accreting black hole is directly proportional to the mass accretion rate $M_{\rm acc}$ via :

$$\dot{E} \propto 10^{11} \frac{\epsilon}{0.01} \dot{M}_{\rm acc} L_{\odot}. \tag{1.15}$$

The crucial parameter in this model is the parameter ϵ which describes how efficiently the energy couples to the surrounding medium which depends not only on the properties if the black hole (e.g. its spin or electric charge) but also on the thermal properties of the environment. Typical values for ϵ are around 0.4 (e.g. Krolik, 1999) and typical accretion rates range form 0.001 $M_{\odot}$ yr^{-1} to 100 $M_{\odot}$ yr^{-1}. The energy that is deposited by black holes can be deposited in the ambient environment of the black hole and a good fraction of it can be used for launching a galactic wind. In the case of a very luminous AGN, one can assume that radiation plays the most important role. The ambient gas can strongly be influenced by radiation emitted from a luminous AGN via electron scattering, radiation pressure on dust, photoionisation or atomic line emission from metals. While the latter is expected to play a role in broad absorption line quasars (Crenshaw et al., 2003) it is typically subdominant compared to radiation pressure on the dust. Another option for AGN providing the energy to launch a galactic outflow is so called runaway heating. Krolik et al. (1981) report that gas above a temperature of $3.1 \cdot 10^4$ K can be heated very efficiently by thermalising energy from radiation of the AGN. This quickly establishes

super-heated gas that is kept at around 10^6 K by the interaction between cooling by Compton-scattering and heating by inverse Compton-scattering. This gas has very high sound speed that is larger than the rotation velocity of the galaxy and can easily become unbound and leave the galaxy as a superwind.
A superwind can also be established by stellar feedback in a so-called superbubble. The idea is, that frequent supernovae explode in the very low density bubble of predecessor supernova, which completely overpressurises the bubble, which can effectively not cool. An isolated supernova generates momentum in the Sedov-Taylor (ST) phase until cooling becomes dominating and the swept-up mass starts to cool and forms a thin shell. The dynamics of this shell is then supported by the hot bubble interior until the bubble starts to cool and reaches pressure equilibrium with the shell. However, if the bubble is constantly heated this never happens and the shell is pushed forward while more and more material from inside the bubble catches up, making the shell more an more massive. As soon as this bubble reaches the edge of the galactic disc it transits into the low density CGM regime where it can freely expand towards higher velocities, launching an outflow.
The central aspect of my PhD-thesis is to understand how exactly outflows work and investigate both, conventional outflow mechanisms based on some thermal pressure support, but also unconventional outflow mechanisms that are driven by non-thermal pressure components like for example magnetic field. A good starting point for a detailed investigation of these process is therefore hydrodynamics and magnetohydrodynamics.

Chapter 2

Fundamentals of Fluid Dynamics

In this chapter we discuss the equations of hydrodynamics and magneto hydrodynamics. The discussion of the fundamentals of hydrodynamics will be worked out following Landau and Lifshitz (1959). For the details of the equations of magneto hydrodynamics we will follow Schnack (2009). Thus for a more comprehensive introduction we point the reader to the latter references as we will only introduce the basic equations in this brief discussion. However, hydrodynamics in general is a rich topic and it is no coincidence that Landaus book number five in his essentials of theoretical physics is the longest (if one excludes the statistical mechanic books). It is a beautiful theory that is actually relatively close to quantum mechanics (the Madelung transformation of the Schrödinger equation yields a form that is similar to the basic equations of hydrodynamics) and it can be straightforward extended to the limit of special and general relativity. Further, the equations of magneto hydrodynamics are a direct consequence of Maxwell's equations of electrodynamics which directly shows that magneto hydrodynamics can be extend to relativistic flows.

2.1 Hydrodynamics

Classic hydrodynamics can be formulated in two different pictures:

- Euler formulation: Spatially fixed reference frame.
- Lagrange formulation: Co-moving reference frame[1].

From a physical point of view both of these pictures are completely identical and they are related via the Lagrange derivative:

$$\frac{\mathrm{d}}{\mathrm{d}t} = \frac{\partial}{\partial t} + \mathbf{v} \cdot \nabla \tag{2.1}$$

We take a slightly different approach in deriving the equations of hydrodynamics than it is done in most text books. Before we look at any equation we first ask the question what are the central quantities of fluid dynamics. The central quantities of hydrodynamics are density ρ, velocity $\mathbf{v}$, pressure P, specific internal energy u and entropy S. As the velocity has three spatial directions we find that there are seven fundamental quantities that are needed to describe a fluid flow[2].

[1] Later, when we discuss numerical methods we will see that these two pictures can be correlated with the Ansatz of a grid code (Euler) and a particle code (Lagrange)

[2] We will see in the following why I think it is important to point out that there are seven central quantities. The entropy is usually neglected and we will see why. However, for the transition from Eulerian hydrodynamics to the Navier-Stokes picture it is crucial if one forgets about the entropy.

2.1.1 The continuity equation

A good point of entrance for the derivations of the equations of hydrodynamics is the continuity equation. It can be straightforward derived in the Eulerian view of hydrodynamics. In this picture, the mass within the volume V can change due to a mass flux over the surface A. By applying the integral theorem of Gauss we quickly find the continuity equation:

$$\frac{\partial \rho}{\partial t} + \nabla \cdot (\rho \mathbf{v}) = 0. \tag{2.2}$$

This can be transformed into the Lagrange formulation by applying the Lagrange derivative (2.1):

$$\frac{\mathrm{d}\rho}{\mathrm{d}t} + \rho(\nabla \cdot \mathbf{v}) = 0. \tag{2.3}$$

2.1.2 The Euler equations

The equations of motion of ideal hydrodynamics are called Euler-equations and can be derived from Newtons second law. One can express the linear momentum $\mathbf{p}(t)$ for an arbitrary time dependant volume $V(t)$ via:

$$\mathbf{p}(t) = \int_{\mathrm{V(t)}} \rho(\mathbf{r},t)\mathbf{v}(\mathbf{r},t)\mathrm{d}\mathbf{r}. \tag{2.4}$$

Newton second law states that the time derivative of the linear momentum yields the force field and one obtains:

$$\mathbf{F} = \frac{\mathrm{d}\mathbf{p}}{\mathrm{d}t} = \frac{\mathrm{d}}{\mathrm{dt}} \int_{\mathrm{V(t)}} \rho(\mathbf{r},t)\mathbf{v}(\mathbf{r},t)\mathrm{d}\mathbf{r}. \tag{2.5}$$

The mathematical issue by the evaluation of this integral equation is the fact that we cannot exchange the time derivative with the integral as $V(t)$ depends on the time as well. We note that this would be trivial for a static volume. This can be resolved by applying the Reynolds transport theorem (RTT) which is three dimensional generalisation of the Leibniz integral theorem that states how to evaluate an integral if the boundaries depend on the variable that is supposed to be integrated. The RTT states for an arbitrary field α[3]:

$$\frac{\mathrm{d}}{\mathrm{d}t} \int_{\mathrm{V(t)}} \alpha(\mathbf{r},t)\mathrm{d}\mathbf{r} = \int_{\mathrm{V}} \left[\frac{\partial \alpha}{\partial t} + \nabla \cdot (\alpha \mathbf{v})\right]\mathrm{d}\mathbf{r} = \int_{\mathrm{V}} \left[\frac{\partial \alpha}{\partial t} + \nabla\beta + \alpha(\nabla \cdot \mathbf{v})\right]\mathrm{d}\mathbf{r} \tag{2.6}$$

This theorem states the local time variation of α (first term on the right hand side of equation 2.6), the spatial movement of β within $V(t)$ (second term on the right hand side of equation 2.6) as well as the rate of the change of the volume element d$\mathbf{r}$ with α (third term on the right hand side of equation 2.6). We use the RTT on equation 2.5 and reduce the resulting expression:

$$\mathbf{F} = \frac{\mathrm{d}}{\mathrm{d}t} \int_{\mathrm{V(t)}} \rho \mathbf{v} \mathrm{d}\mathbf{r} = \int_{\mathrm{V}} \rho \frac{\mathrm{d}\mathbf{v}}{\mathrm{d}t} \mathrm{d}\mathbf{r}. \tag{2.7}$$

[3] Strictly speaking this tells us how to partially integrate an expression if the boundaries depend on the differential in the integral

Under the assumption that there are no particle interactions, we can assume that the force **F** acts as surface tension across the boundary ∂V of V and we find **F**:

$$\mathbf{F} = \int_{\partial \mathrm{V}} \mathrm{d}\mathbf{F}, \tag{2.8}$$

d**F** acts only alongside the surface normal vector with:

$$\mathrm{d}\mathbf{F} = -p\mathbf{n}dA, \tag{2.9}$$

This yields $\mathbf{F}(t)$ through integration over the surface ∂V of V:

$$\mathbf{F}(t) = -\int_{\partial \mathrm{V}} p(\mathbf{r}, t)\mathbf{n}da = -\int_{\mathrm{V}} \nabla p \mathrm{d}\mathbf{r}. \tag{2.10}$$

We find:

$$\rho \frac{\mathrm{d}\mathbf{v}}{\mathrm{d}t} = \rho \left[\frac{\partial \mathbf{v}}{\partial t} + (\mathbf{v} \cdot \nabla)\mathbf{v} \right] = -\nabla p. \tag{2.11}$$

If there is an acting external conservative force field (e.g. gravity) we find an additional force term via the negative gradient of the potential Φ of this force field:

$$\rho \frac{\mathrm{d}\mathbf{v}}{\mathrm{d}t} = \rho \left[\frac{\partial \mathbf{v}}{\partial t} + (\mathbf{v} \cdot \nabla)\mathbf{v} \right] = -\nabla p - \nabla \Phi \tag{2.12}$$

In this form the Euler equations yield the equations of motion for ideal hydrodynamics. One can introduce a friction term and carry out the same calculation again, which will result in the Navier-Stokes-equations for non-ideal fluids. However, the calculation is somewhat more tedious and we only report the result for an in-compressible fluid:

$$\rho \frac{\mathrm{d}\mathbf{v}}{\mathrm{d}t} = \rho \left[\frac{\partial \mathbf{v}}{\partial t} + (\mathbf{v} \cdot \nabla)\mathbf{v} \right] = -\nabla p - \nabla \Phi + \nu \nabla^2 \mathbf{v}. \tag{2.13}$$

2.1.3 Equations for the internal energy

One can obtain an equation for the internal energy U with a similar approach as for the Euler equations:

$$U(t) = \int_{\mathrm{V(t)}} \rho(\mathbf{r}, t) u(\mathbf{r}, t) \mathrm{d}\mathbf{r}, \tag{2.14}$$

with the specific internal energy u. We can express the rate of change of the internal energy U via the first law of thermodynamics:

$$\frac{\mathrm{d}U}{\mathrm{d}t} = \dot{W} + \dot{Q}, \tag{2.15}$$

where $\dot{W}$ dis the work on the system and $\dot{Q}$ is rate of change of the heat in the system. For $\dot{W}$ and $\dot{Q}$ we find:

$$\dot{W} = \int_{\partial \mathrm{V}} \mathbf{n}\mathbf{v}da = \int_{\partial \mathrm{V}} \mathbf{n} \cdot (\Sigma \cdot \mathbf{v})da = \int_{\mathrm{V}} \nabla \cdot (\Sigma \cdot \mathbf{v}) \mathrm{d}\mathbf{r}, \tag{2.16}$$

$$\dot{Q} = -\int_{\partial V} \mathbf{q} \cdot \mathbf{n} da = -\int_{V} \nabla \cdot \mathbf{q} \mathrm{d}\mathbf{r}, \tag{2.17}$$

with the stress tensor Σ of hydrodynamics. Now we find an equation for the specific internal energy u by applying the time derivation operator on U:

$$\rho \frac{\mathrm{d}u}{\mathrm{d}t} = \nabla \cdot (\Sigma \cdot \mathbf{v}) - \nabla \cdot \mathbf{q} \tag{2.18}$$

We treat this equation in operator split fashion, with $\Sigma = -p\mathbf{1} + \Sigma'$, where Σ' describes the shear and stress flows in the fluid that can be neglected in ideal hydrodynamics, as well as the heat flux (thermal conductivity) $\nabla \cdot \mathbf{q}$[4]. Thus we find for the specific internal energy:

$$\rho \frac{\mathrm{d}u}{\mathrm{d}t} = -p(\nabla \cdot \mathbf{v}) \tag{2.19}$$

In the Euler picture of hydrodynamics this yields:

$$\frac{\partial u}{\partial t} + (\mathbf{v} \cdot \nabla) u = -\frac{p}{\rho} \nabla \cdot \mathbf{v}. \tag{2.20}$$

In a reversible system we have a trivial equation for the specific entropy of an ideal fluid[5]:

$$\frac{ds}{\mathrm{d}t} = 0 \tag{2.21}$$

Thus we find six equations for seven quantities. Here we see the purpose of acknowledging the entropy as one of them. As equation 2.21 is trivial it is usually neglected, but I find it essential to point it out as it becomes crystal clear that there is an equation of state missing in the current description, that can for example be provided as the entropy function $A(s)$:

$$P = A(s)\rho^{\gamma}, \tag{2.22}$$

with the adiabatic coefficient γ. We directly see that we can formulate the internal energy with the entropy function $A(s)$:

$$\frac{dA}{dt} = \frac{\gamma - 1}{\rho^{\gamma-1}} \left(\frac{\mathrm{d}u}{\mathrm{d}t} - \frac{p}{\rho^2} \frac{\mathrm{d}\rho}{\mathrm{d}t} \right), \tag{2.23}$$

which is often used in numerical fluid dynamics.

2.2 Magneto Hydrodynamics

The fundamentals of magnetohydrodynamics are given via the Maxwell-equations, which describe a unified theory for electromagnetism that can be written in a very compact form as four partial differential equations, two material equations and a continuity equation that follows from charge conservation (in hydrodynamics it follows from mass conservation). Typically, only the first four equations are displayed. However, this is equally confusing as writing down the equations of hydrodynamics without the equation for the entropy. The first four equations are the most important ones and all physical

[4]This simply means that Σ has no off-diagonal elements.

[5]That is actually interesting because the vanishing change of entropy makes it impossible for an ideal fluid to mix, which is a huge limitation in the cope of an ideal fluid

conclusion can be derived from them, but they do not represent the full physics system without the material equations. This is given via:

$$\nabla \cdot \mathbf{E} = 4\pi\rho \tag{2.24}$$

$$\nabla \cdot \mathbf{B} = 0 \tag{2.25}$$

$$\nabla \times \mathbf{E} = -\frac{1}{c}\frac{\partial \mathbf{B}}{\partial t} \tag{2.26}$$

$$\nabla \times \mathbf{B} = \frac{1}{c}\frac{\partial \mathbf{E}}{\partial t} + \frac{4\pi}{c}\mathbf{j} \tag{2.27}$$

$$\mathbf{D} = \mathbf{E} + 4\pi\mathbf{P} \tag{2.28}$$

$$\mathbf{H} = \mathbf{B} - 4\pi\mathbf{M} \tag{2.29}$$

Where c is the speed of light, $\mathbf{P}$ is the Polarisation and $\mathbf{M}$ the magnetisation of the material[6].Finally, we can derive a continuity equation from equation 2.24 and equation 2.27:

$$\frac{\partial \rho}{\partial t} + \nabla \cdot \mathbf{j} = 0. \tag{2.30}$$

2.2.1 The equations of motion of ideal MHD

In the following we will derive the equations of motion of ideal MHD. Similar to the hydrodynamics case, this can be derived from Newtons second law by using the Lorentz-force:

$$\mathbf{F}_{\mathrm{L}} = q(\mathbf{E} + \mathbf{v} \times \mathbf{B}), \tag{2.31}$$

with the charge q. First, we want to note, why it is called magnetohydrodynamics and not electro-magneto-hydrodynamics. In every plasma there are so called displacement currents, that lead to zero net electric field in the plasma. This displacement currents induce the magnetic field, which remains as a residual. This implies that we look at an astrophysical plasma with infinite conductivity. Thus in the MHD limit the two dominating components are the thermal pressure and the magnetic pressure of a system. The equation of motion of MHD can then be written as:

$$\rho\frac{\mathrm{d}\mathbf{v}}{\mathrm{d}t} = -\nabla p + \mathbf{j} \times \mathbf{B} + \rho\mathbf{g}, \tag{2.32}$$

in the Lagrange formulation or as:

$$\rho\left(\frac{\partial \mathbf{v}}{\partial t} + \mathbf{v} \cdot \nabla\mathbf{v}\right) = -\nabla p + \mathbf{j} \times \mathbf{B} + \rho\mathbf{g}, \tag{2.33}$$

in the Euler formulation. This time we directly consider gravity $\mathbf{g}$, where $\mathbf{g} = -\nabla\Phi$.

2.2.2 Induction equation

In MHD it is not only interesting how the magnetic field alters the equations of motion, but also how the magnetic field itself evolves with time. The magnetic field evolution can be derived from Amperes law:

$$\frac{\partial \mathbf{B}}{\partial t} = -c(\nabla \times \mathbf{E}). \tag{2.34}$$

[6]We note that $\mathbf{P}$ and $\mathbf{M}$ are zero in the vacuum (at least to first order, there is always some regime where this is not valid). So in astrophysical MHD it is justified to only write down the first 4 equations.

This can be combined with Ohm's law $\mathbf{j} = \sigma\mathbf{E}$ of electrodynamics modified for the plasma physics regime in which we apply it:

$$\mathbf{j} = \sigma\left(\mathbf{E} + \frac{\mathbf{v}}{c} \times \mathbf{B}\right). \tag{2.35}$$

We now insert the electric field of equation 2.35 in 2.34 we obtain:

$$\frac{\partial \mathbf{B}}{\partial t} = -c\nabla \times \left(\frac{\mathbf{j}}{\sigma} - \frac{\mathbf{v}}{c} \times \mathbf{B}\right). \tag{2.36}$$

We now use equation 2.27 and assume that the magnetic field is dominating ($1/c\partial\mathbf{E}/\partial t \approx 0$). We further use 2.25 and obtain the induction equation in the Eulerian picture of magnetohydrodynamics:

$$\frac{\partial \mathbf{B}}{\partial t} = \nabla \times (\mathbf{v} \times \mathbf{B}) + \eta\nabla^2\mathbf{B} \tag{2.37}$$

$$= (\mathbf{B} \cdot \nabla)\mathbf{v} - \mathbf{B}(\nabla \cdot \mathbf{v}) - (\mathbf{v} \cdot \nabla)\mathbf{B} + \eta\nabla^2\mathbf{B}, \tag{2.38}$$

where $\eta = c^2/4\pi\sigma$ is the magnetic resistivity and σ the electric conductivity. In ideal MHD σ is infinite and η is zero and one finds the induction equation of ideal MHD in the Lagrangian limit:

$$\frac{\mathrm{d}\mathbf{B}}{\mathrm{d}t} = (\mathbf{B} \cdot \nabla)\mathbf{v} - \mathbf{B}(\nabla \cdot \mathbf{v}). \tag{2.39}$$

2.2.3 Energetics of ideal MHD

Finally, we have to correct the total specific energy e of the system for the presence of the magnetic field.

$$e = \frac{1}{2}v^2 + u + \frac{B^2}{8\pi\rho}. \tag{2.40}$$

With this we find the time evolution of the specific internal energy:

$$\frac{\mathrm{d}u}{\mathrm{d}t} = \frac{\mathrm{d}e}{\mathrm{d}t} - \mathbf{v} \cdot \frac{\mathrm{d}\mathbf{v}}{\mathrm{d}t}\left(\frac{B^2}{8\pi\rho}\right) = -\frac{P}{\rho}\nabla \cdot \mathbf{v}. \tag{2.41}$$

2.3 Turbulence

2.3.1 Statistical ensemble average

Hydrodynamic turbulence is complicated and from my personal point of view the only statement the can be made on turbulence is that there are different states of NOT understanding turbulence. The longer I think about turbulence the more I think that I do not understand it. However, one might make the not completely pointless attempt of starting with the statistical description of turbulence where one might consider the Navier-Stokes equations in their in compressible form:

$$\frac{\partial \mathbf{v}}{\partial t} + \mathbf{v} \cdot \nabla\mathbf{v} = -\frac{1}{\rho}\nabla p + \nu\nabla^2\mathbf{v}, \tag{2.42}$$

$$\nabla \cdot \mathbf{v} = 0. \tag{2.43}$$

This equation will now be Reynolds decomposed where one assumes that the velocity field $\mathbf{v}$ and the pressure scalar p consist out of an ensemble average and a part that shows statistical fluctuations:

$$\mathbf{v}(\mathbf{r},t) = \overline{\mathbf{v}}(\mathbf{r},t) + \mathbf{v}'(\mathbf{r},t), \tag{2.44}$$
$$p(\mathbf{r},t) = \overline{p} + p'(\mathbf{r},t). \tag{2.45}$$

The averages $\overline{\mathbf{v}}$ and $\overline{p}$ can be computed as:

$$\overline{\mathbf{v}}(\mathbf{r},t) = \langle \mathbf{v} \rangle = \frac{1}{T}\int_{-T/2}^{T/2} \mathbf{v}(\mathbf{r},t+t')dt', \tag{2.46}$$
$$\overline{p}(\mathbf{r},t) = \langle p \rangle = \frac{1}{T}\int_{-T/2}^{T/2} p(\mathbf{r},t+t')dt'. \tag{2.47}$$

T is the time over which we average those quantities. Thus the mean values of the fluctuation vanish. Now we can write down an equation for the time evolution of the fluctuations:

$$\frac{\partial \mathbf{v}'}{\partial t} + \nabla\cdot(\overline{\mathbf{v}}\mathbf{v}' + \mathbf{v}'\overline{\mathbf{v}}) + \nabla\cdot[\mathbf{v}'\mathbf{v}' - \langle \mathbf{v}'\mathbf{v}'\rangle] = -\frac{1}{\rho}\nabla p' + \nu\nabla^2\mathbf{v}'. \tag{2.48}$$

This is the very basic idea behind turbulence from a statistical point of view. We note that every term of equation 2.48 vanishes in time average.

2.3.2 The Kolmogorov energy cascade

A central theory for turbulence is given by (Kolmogorov, 1941), who introduced a turbulent energy cascade in the so called Kolmogorov equations under the assumption of homogeneity, isotropy and incompressibility of a fluid. Kinetic energy is injected on the large scales (small k-values), for example by fluid instabilities or supernova shocks. The non-linear term in the Navier-Stokes equations $\mathbf{v}\cdot\nabla\mathbf{v}$ is transporting the energy to smaller and smaller scales (large k-values) where they are dissipated by the resistivity term. This is called the turbulent energy cascade.
The size of some initial vortex is cut in half at the rate $\mathbf{v}\cdot\nabla \approx \widetilde{kv}$, which is the so called eddy turnover rate with a scale time that is called eddy turnover time.
Thus, one can express the kinetic energy in the wave number interval $[k,\, k+\mathrm{d}k]$ as $\rho I(k)\mathrm{d}k$, with $I(k)$ as the wave number spectrum (Kolmogorov spectrum) of the velocities:

$$\frac{\rho v^2}{2} = \frac{\rho}{2}\int I(k)\mathrm{d}k. \tag{2.49}$$

Vortices of order $\mathrm{d}k \propto k$ result in velocities v_k with:

$$v_k^2 = I(k)\mathrm{d}k. \tag{2.50}$$

One assumes that the energy of a strongly spatially distributed vortex given with the energy bandwidth $\varepsilon^{\frac{3}{2}}k$ and $\varepsilon^{\frac{1}{2}}k$ decays towards smaller vortices with energy bandwidth $\varepsilon^{\frac{1}{2}}k$ and $\varepsilon^{-\frac{1}{2}}k$ and the energy alongside the rate νk^2 dissipates. Thus one obtains a rate equation for $kI(k)$ which is given by (Kulsrud, 2005):

$$\frac{\partial(kI)}{\partial t} = \varepsilon k v_{\varepsilon k}[\varepsilon k I(\varepsilon k)] - k v_k[kI(k)] - k\nu I(k) \tag{2.51}$$
$$= -\frac{\partial}{\partial \ln k}\left(k\sqrt{kI}kI\right) - k^3\nu I. \tag{2.52}$$

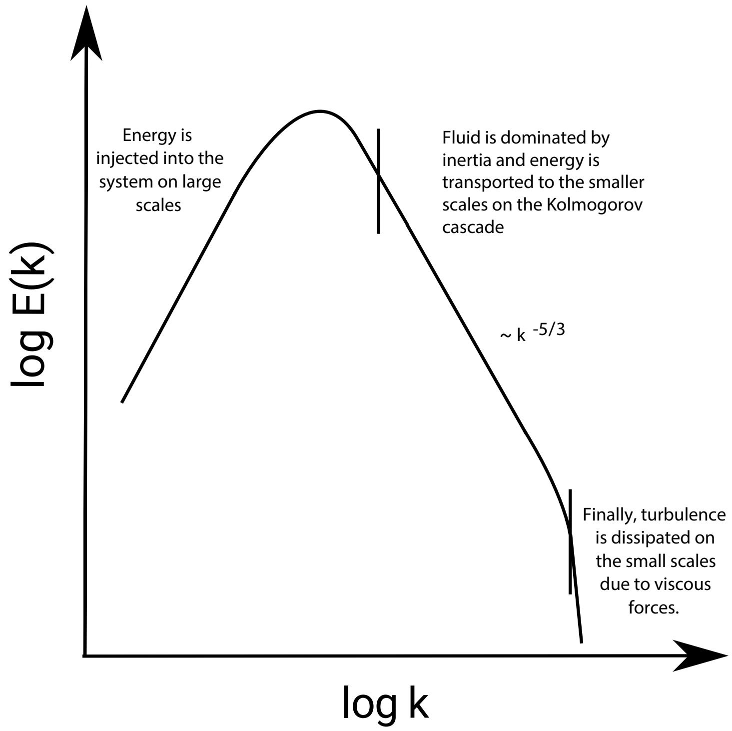

Figure 2.1: Schematic sketch of the Kolmogorov turbulence spectrum. The spectrum can be subdivided in three different ranges. First, energy is brought in the system at large scales. Second, it will be transported to the small scales on the Kolmogorov-cascade due to the moment of inertia of the fluid. Finally, energy is dissipated at the smallest scales due to the viscous behaviour of the fluid. Numerical simulations are partially so tricky, because they are generally not able to capture the dissipation scale of turbulence.

This is obtained with $\varepsilon = 1$ and the logarithmic derivative $\mathrm{d}/\mathrm{d}\ln k$. Now we use $y = k^{\frac{5}{2}} I^{\frac{3}{2}}$ and insert equation 2.52):

$$y^{\frac{1}{3}} = \left(k^{\frac{5}{2}} I^{\frac{3}{2}}\right)^{\frac{1}{3}} = \alpha - \frac{\nu k^{\frac{4}{3}}}{4}, \tag{2.53}$$

with $\alpha = k_0^{\frac{1}{3}} v_0$, by dropping the viscous term and with the boundary condition $k = k_0 = 2\pi/L$. This gives the Kolmogorov energy spectrum:

$$I(k) = \frac{k_0^{\frac{2}{3}} v_0^2}{k^{\frac{5}{3}}} \left[1 - \left(\frac{k}{k_0}\right)^{\frac{4}{3}} \frac{1}{4R}\right]^2, \tag{2.54}$$

with $R = v_0/k_0\nu = 1/2\pi \cdot \mathrm{Re}$. Re is the Reynolds number. For $k << k_{\max}$ equation 2.54 is reduced to:

$$I(k) = k_0^{\frac{2}{3}} v_0^2 k^{-\frac{5}{3}}. \tag{2.55}$$

We show a typical Kolmogorov spectrum in Figure 2.1. However, Kolmogorov turbulence is only valid in the sub-sonic regime. For super sonic regimes one finds the Burgers spectrum (e.g. Kulsrud, 2005):

$$I(k) \propto k^{-2}. \tag{2.56}$$

In the presence of magnetic fields it is possible to grow magnetic fields on the smallest eddy turn over time with a small scale turbulent dynamo. However, this is only valid as long as the magnetic energy in the smallest eddy is smaller than the turbulent energy in the smallest eddy. This energy is then transported from the smallest eddies to the largest scales via an inverse turbulence cascade following the spectrum given in Kazantsev (1968), which we will discuss in detail in the next chapter.

$$I(k) \propto k^{\frac{3}{2}}. \tag{2.57}$$

In the presence of strong magnetic fields MHD-turbulence is suppressed and one finds as spectrum with a different scaling following (Kraichnan, 1965):

$$I(k) \propto k^{-\frac{3}{2}}. \tag{2.58}$$

Chapter 3

Magnetic fields in the Universe

Regarding magnetic fields in the Universe there are three open questions that could not yet finally be answered. The first question is where exactly they come from. The second is how did they get amplified to the values that are observed today. The third is, are they dynamically important for galaxy formation and evolution. In this chapter we will try to shed light on these three question. We will start with an observational overview of magnetic fields and discuss the recent finding of different groups and present their conclusions in a galactic context. In a next step we will then discuss the theoretical point of view by explaining theories that tell us how magnetic fields could be generated in the early Universe and subsequently be amplified during large scale structure and later galaxy formation processes. The observational part of this chapter will be derived following the excellent review of Beck (2015). The theoretical part will be mainly influenced by the book of Kulsrud (2005) and the review article of Kulsrud and Zweibel (2008).

3.1 Observing magnetic fields in galaxies

There are several observational methods which can be utilised to constrain magnetic fields in galaxies and galaxy clusters. Generally, the magnetic field in galaxies consists out of a regular component and a turbulent component. The regular magnetic field component shows hereby a well defined structural form in the telescope beam, whereas the turbulent field changes its orientation within the telescope beam. However, even modern radio-polarisation observations do typically not have high enough resolution to determine the origin of the turbulent field component and one can only speculate whether the turbulent field comes from small-scale turbulent motions or is driven by turbulent (accretion) flows.

3.1.1 Dust Polarisation

One of the most important mechanisms to determine the magnetic field of a galaxy is the polarisation introduced by elongated dust grains. The idea is that elongated dust grains can align with the galactic magnetic field by paramagnetic alignment processes which is known as the Davis-Greenstein-effect (Davis and Greenstein, 1951) or by radiation torque (Hoang and Lazarian, 2008, 2014). Thus, dust grains along the line-of-sight between the observer and a star align their major axis alongside the magnetic field, which results in different polarisation of the electric field alongside the major and minor axis of the dust grain. While it is poorly understood how exactly the dust grains align with the magnetic field, the process can be used to re-construct the magnetic field from optical and infrared wavelengths as well as from diffuse star light as the polarisation p along the distance L along the line-of-sight is

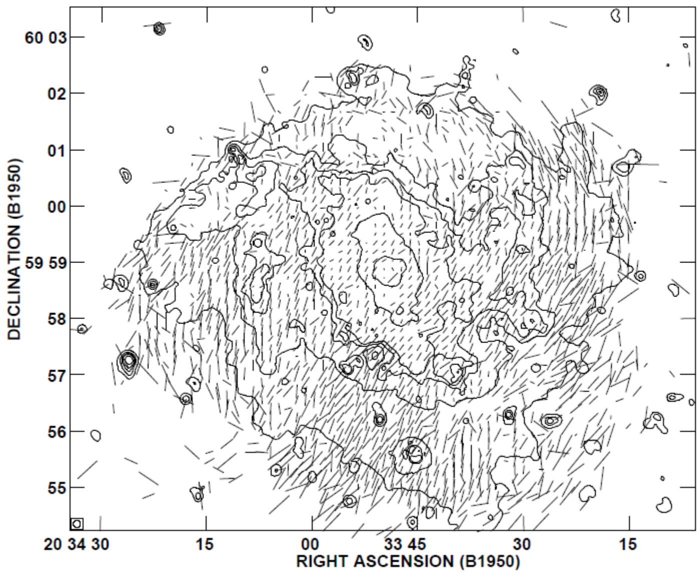

Figure 3.1: Magnetic field structure of the galaxy NGC 6946 as obtained from star light polarisation. The contour lines show the optical emission and the vectors the direction of the electric field polarisation from which the magnetic field structure can be obtained. The Figure is taken from Fendt et al. (1998).

given via (Ellis and Axon, 1978):

$$p = B_{\mathrm{tot},\perp} L, \tag{3.1}$$

where $B_{\mathrm{tot},\perp}$ is the magnetic field component perpendicular to the line-of-sight. The polarisation of diffuse starlight carries the information of the orientation of the large scale magnetic field structures which cannot only be applied to the Milky Way but also to other nearby galaxies like M 51 or NGC 6946. An example of how the magnetic field structure looks like that is obtained from the diffuse star light is shown in Figure 3.1 for NGC 6946.

The big issue in using the starlight polarisation is that there is a lot of background polarisation due to various scattering processes, that do not originate from the magnetic field structure and in practice it is very hard to subtract the background of other polarisation sources from the contribution of the magnetic field. This is different when one uses infrared or sub-millimetre wavelengths where there is mostly no contribution from scattering processes and the magnetic field will lead to linear polarised electric waves. The total magnetic field component can then be determined by assuming equipartition between magnetic field energy density and turbulent energy density (Chandrasekhar and Fermi, 1953):

$$B_{\mathrm{tot},\perp} = \left(\frac{4}{3}\pi\rho\right)^{1/2} \frac{v_{\mathrm{turb}}}{\sigma}. \tag{3.2}$$

This yields a value of around 7 μG in the Milky Way.

3.1.2 Zeeman and Goldreich-Kylafis effect

Most direct, magnetic fields can be observed via the Zeeman-Effect (Zeeman, 1897), which describes the energy-degeneracy of atomic energy levels in an external (static) magnetic field due to the coupling of an electrons spin to its angular momentum that introduces a dipole moment. If the magnetic field is weak (which it will be in galaxies) the correction for the discrete energy levels of atoms can be derived from quantum mechanical linear perturbation theory which gives:

$$E_{\mathrm{Z}}^{(1)} = \mu_{\mathrm{B}} g_{\mathrm{j}} B m_j, \tag{3.3}$$

where μ_{B} is Bohr's Magneton, g_{j} is the Landé factor and m_j is the electron spin quantum number. This directly implies that there is an offset energy from certain line-transitions that can be measured and one can determine the magnetic field strength based on this offset energy. For the HI-line this results in a frequency shift of roughly 2.8 MHz/G which can be measured if the magnetic field is parallel to the line-of-sight and results in two circularly polarised, shifted components with fluctuating sign. The effect is typically larger for molecules like OH (Heiles and Crutcher, 2005). If the magnetic field is perpendicular to the line-of-sight, there are two additional lines as well, but this time the components are linear polarised. However, these lines remain unresolved in practice, even for observations within the Milky Way as long as the there is symmetric behaviour. Under extreme velocity gradients one would get a contribution to the polarisation from these lines as well, which is known as the Goldreich-Kylafis effect (Goldreich and Kylafis, 1981). The Zeeman and the Goldreich-Kylafis-effect can only be used in very close by objects to determine the magnetic field strength.

3.1.3 Total radio synchrotron emission

The radio continuum is one of the most powerful tools to observe galactic magnetic fields. It is a mix of a thermal component and a non-thermal component, given as synchrotron emission. At large wavelengths the spectrum is dominated by the emission of synchrotron radiation and the thermal contribution can be neglected. This changes in star forming regions where absorption might be important and reduces the synchrotron emission. The basic idea is to distinguish between these components by mapping their intensity with a power-law via $I_{\mathrm{synchrotron}} \propto \nu^{-\alpha}$ with different spectral indices α for thermal ($\alpha = 0.1$ in optically thin approximation) and non-thermal component ($\alpha \approx 0.8$). While this a good approximation for many cases it does not account for the fact that the synchrotron emission also depends on the population of cosmic rays (CRs), that diffuse from the spiral arms to the inter arm regions, which leads to a smaller α in the spiral arms than in the inter arm regions and one can follow (Tabatabaei et al., 2007) for a proper correction. They use H-α as a mask for radio emission that was rectified for extinction. By measuring the radio synchrotron emission we get the CR (electron) number density n_{CR} with some given specific energy E and the magnetic field $B_{\mathrm{tot},\perp}$ perpendicular to the line-of-sight, which yields: $\nu \approx 16\mathrm{MHz} E^2 B_{\mathrm{tot},\perp}$. Now, we assume equipartition between the energy densities of cosmic rays and the magnetic field and we can find the perpendicular magnetic field component $B_{\mathrm{tot},\perp}$ via (Arbutina et al., 2012; Beck, 2005):

$$B_{\mathrm{tot},\perp} \propto \left(\frac{I_{\mathrm{synchrotron}}(K_0 + 1)}{L}\right)^{1/(3+\alpha)}. \tag{3.4}$$

K_0 describes the fraction between the number densities of cosmic ray protons to cosmic ray electrons with $K_0 = 100$ in the disc and $K_0 = 0$ close to high energetic jets (Bell, 1978). L is the path length. Both of these parameters are relatively uncertain. Further, the equipartition argument breaks down at scales smaller than 1 kpc (Beck, 2015) and the method overestimates the magnetic field due to the non-linear behaviour of equation 3.4 as long as cosmic ray loss is small. If cosmic ray losses are high the method underestimates the field strength (Beck, 2015). In Figure 3.2 we show the galaxies NGC 1097 (top) and M 31 (bottom) in the total radio synchrotron continuum.

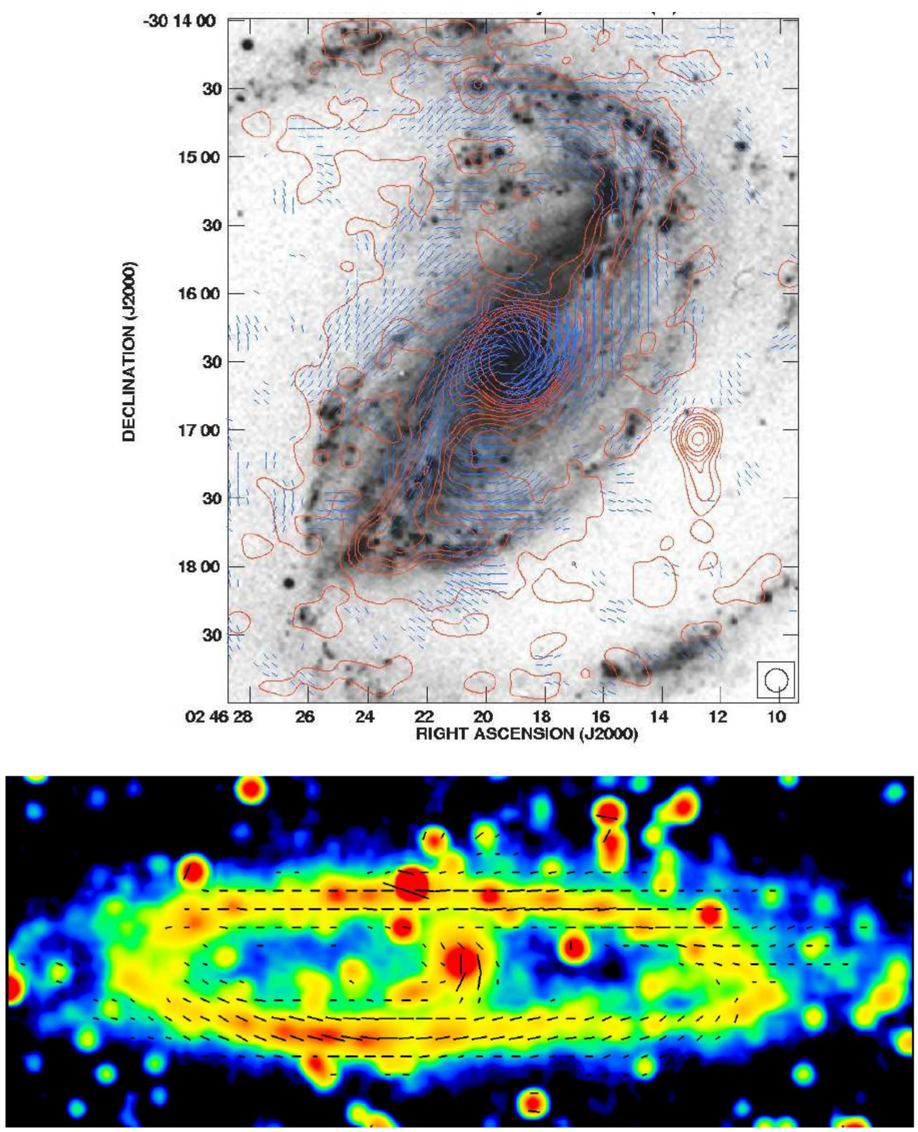

Figure 3.2: We show two examples for measurements of the total radio synchrotron emission in nearby galaxies, for NGC 1097 (top) and M 31 (bottom). The picture of NGC 1097 is taken from Beck (2005) and has been observed with the Very Large Array (VLA) in New Mexico at 6 cm wavelength. The picture of M 31 is taken from Beck (2015). The colour shows the radio emission. The vectors show the magnetic field direction in both pictures.

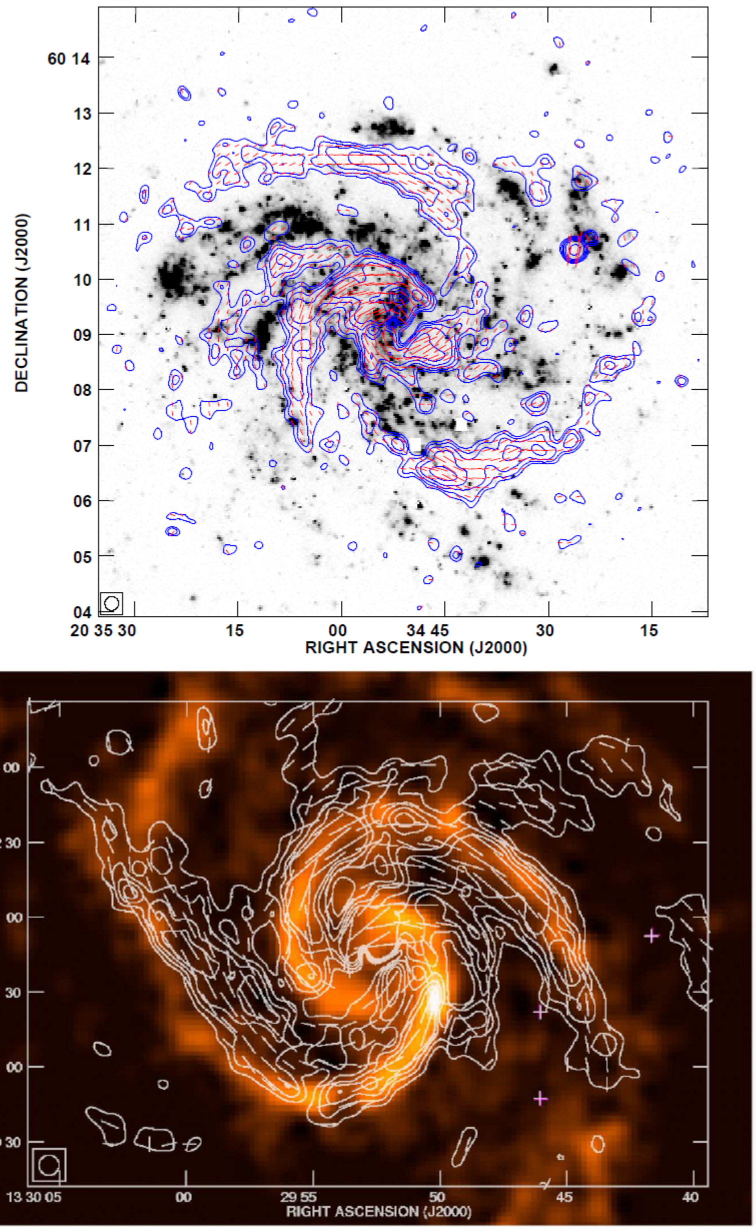

Figure 3.3: We show two examples for measurements of the polarised radio synchrotron emission in the galaxy NGC 6946 (top) and M 51 (bottom). NGC 6946 is shown with the vectors of the magnetic field and with the radio emission in the contour lines, overlaid on an H-α. The same is valid for M 51, the background colour however, comes from the emission of CO. Both pictures have been extracted from Beck (2015).

3.1.4 Polarised radio synchrotron emission

Another option to constrain magnetic fields in spiral galaxies is to use the linear polarised synchrotron emission from CR-electrons which are a tracer for the ordered field component. On the other hand unpolarised synchrotron emission indicates isotropic turbulent or tangled magnetic fields, which have most likely been generated by turbulent flows. The amount of linear polarisation is given via:

$$p_0 = \frac{1+\alpha}{\frac{5}{3}+\alpha}. \tag{3.5}$$

As discussed above the value for α is around 0.8 in spiral galaxies which leads to roughly 72 per cent polarisation fraction. In practice the degree of linear polarisation is lower, as there is contamination by thermal emission and depending on the exact wavelength at which the observation takes place, also Faraday-depolarisation. Further, there is some degree of intrinsic beam depolarisation. For an isotropic turbulent field with a specific length scale d on which the turbulent structure is correlated and coherent Sokoloff et al. (1998) propose the correction:

$$p = \frac{p_0}{\sqrt{N}}, \tag{3.6}$$

with $N \approx D^2 Lf/d^3$, which is the number of cells that emit synchrotron radiation within the telescope beam, with the path length L, the distance to the object D and the filling factor f of the cells emitting synchrotron radiation. This leads to values for the linear polarisation between 1 and 5 per cent. The magnetic field can then again be estimated from an equipartition argument between CR and magnetic field energy density following Sokoloff et al. (1998). In Figure 3.3 we show two examples of magnetic field maps obtained from polarised radio synchrotron emission in the galaxies NGC 6946 and M 51.

3.1.5 Faraday rotation

The Faraday effect generates some intrinsic rotation of the plane of the polarisation of an electromagnetic wave while propagating through a magnetised carrier medium. This effect can play a major role to observationally constrain the magnetic field of the carrier medium as the amount of rotation of the polarisation plane depends on the strength of its magnetic field. Strictly, the Faraday rotation measure is defined as the slope of the variation of the polarisation angle χ obtained from observations, which scales with the wavelength squared in the observed waveband:

$$\chi = \chi_0 + \mathrm{RM}\lambda^2. \tag{3.7}$$

This gives a constant if RM scales with λ^2 but has to be corrected in all other cases where RM does not scale with λ^2 by the so called Faraday-depth, which yields for RM (Burn, 1966):

$$\mathrm{RM} = \frac{e^3}{2\pi m^2 c^4} \int_0^l n_\mathrm{e} B_\| dl, \tag{3.8}$$

in CGS-units. In practice the situation is even more complicated as it is hard to distinguish the contribution from different sources in the integral from equation 3.8. However, the method can be improved by so called Faraday synthesis modelling by evaluating the RM signal in Fourier space and constraining the Stokes Q and U parameters. This is necessary in situations where one does not have the full information over a wide wavelength spectrum. By doing this one can determine the three dimensional magnetic field and distinguish between regular fields, turbulent fields and field reversals

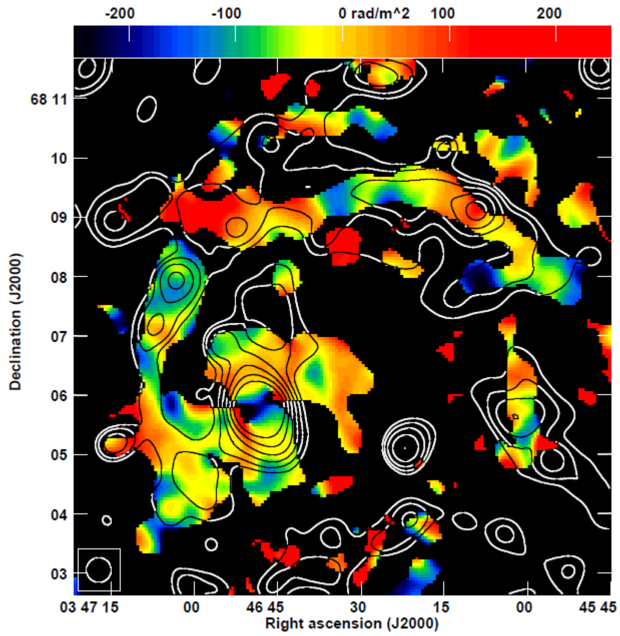

Figure 3.4: Faraday rotation map of the galaxy IC 342 takne from Beck (2015), measured between 3.5 and 6 cm with the VLA.

(Beck et al., 2012; Bell et al., 2011; Frick et al., 2011), that are typically seen as indicators for ongoing dynamo action. Moreover, even the helicity structure of the large scale field as shown in Brandenburg and Stepanov (2014) or Horellou and Fletcher (2014) can be obtained with this method. The parallel field component can then be determined by also measuring the thermal dispersion DM of the electron density given by:

$$\mathrm{DM} \propto \int_0^l n_\mathrm{e} dl. \tag{3.9}$$

yielding the parallel component of the magnetic field via:

$$B_{||} \propto \frac{\mathrm{RM}}{\mathrm{DM}}. \tag{3.10}$$

We show an example for the magnetic field structure obtained by Faraday rotation measurements in Figure 3.4.

3.1.6 Beyond state of the art measurements: Velocity gradients

Although the success of the methods we discussed so far to constrain magnetic fields is undoubtedly present, there are newer methods that are very successful in constraining the magnetic fields on the scales of the ISM, using HI observations. Popular methods are the approaches that are put forward in HI fibres, using the Rolling Hough transform (RTH, e.g. Clark et al., 2014) or the velocity gradient method (González-Casanova and Lazarian, 2017; Yuen and Lazarian, 2017). We will briefly focus on the latter one, as it has recently been applied to constrain the magnetic field in galaxies and galaxy clusters (e.g. Hu et al., 2020; Yuen et al., 2019), while the former one is mostly applied on ISM scales thus far. The idea behind constraining magnetic fields with velocity gradients is the following. Several

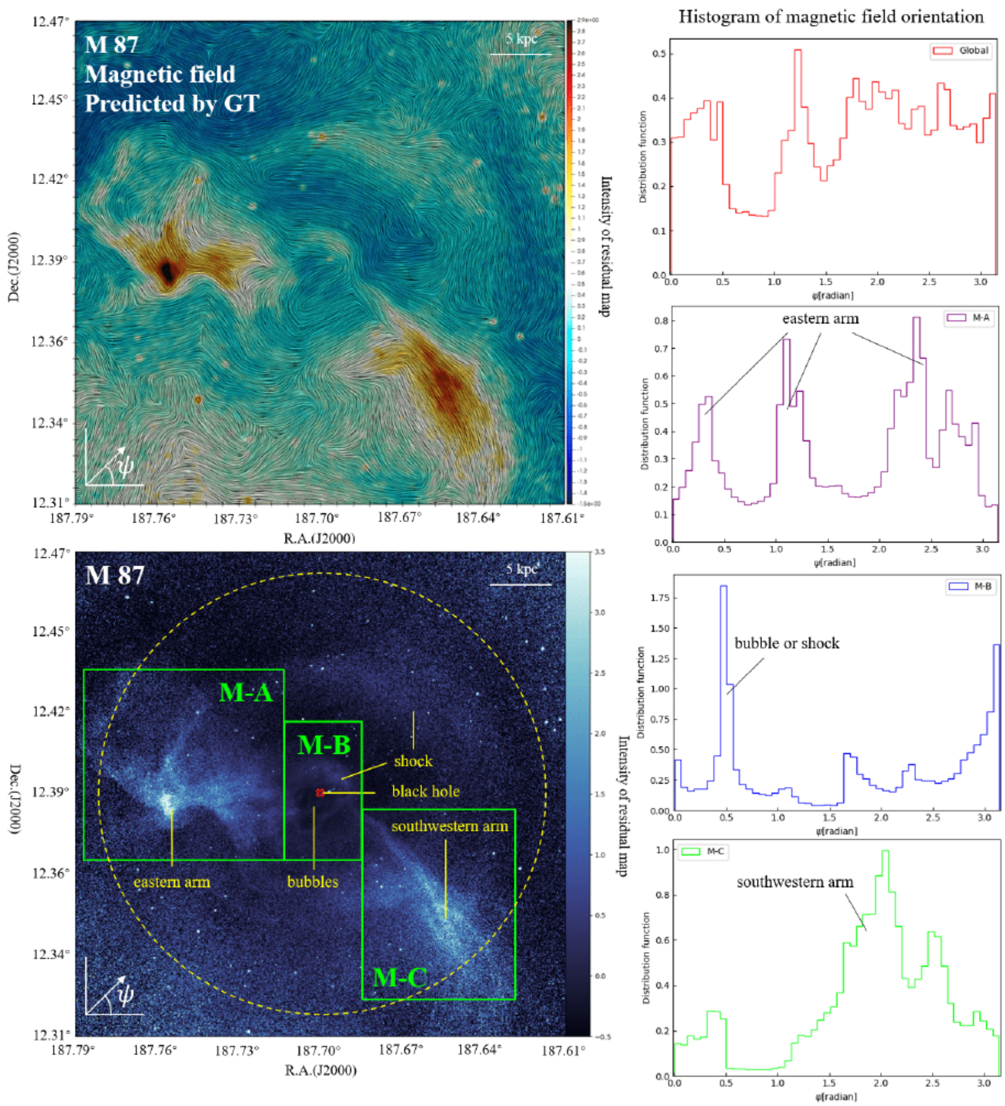

Figure 3.5: We show the velocity gradient predicted magnetic field for the galaxy M 87 (top left) in comparison to the residual image, where different sub-regions are identified. On the right hand side we show the distribution of the magnetic field orientation φ for the total signal (top) and for the sub-regions (three bottom panels). The figure has been taken from Hu et al. (2020).

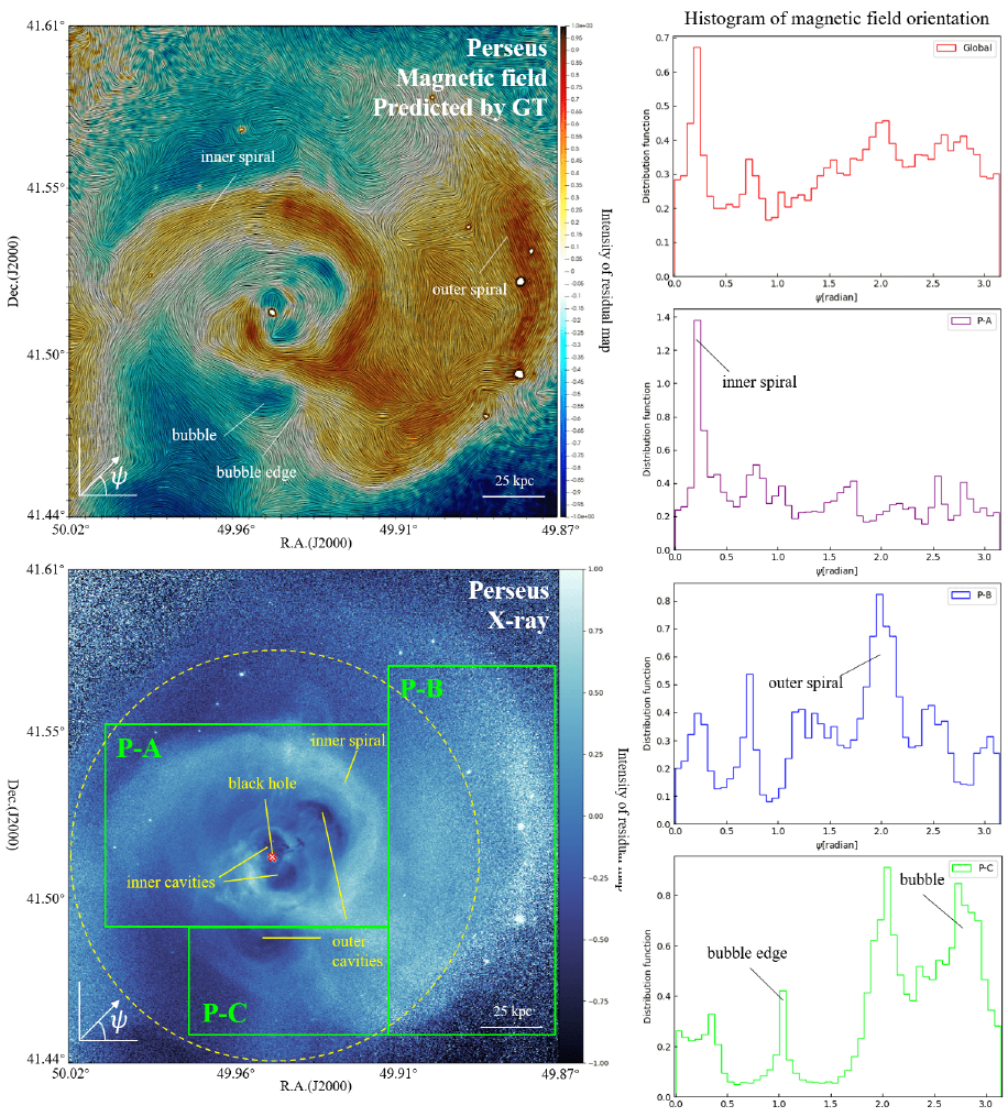

Figure 3.6: We show the velocity gradient predicted magnetic field for the Perseus galaxy cluster (top left) in comparison to the residual X-ray image, where different sub-regions are identified. On the right hand side we show the distribution of the magnetic field orientation φ for the total signal (top) and for the sub-regions (three bottom panels). The figure has been taken from Hu et al. (2020).

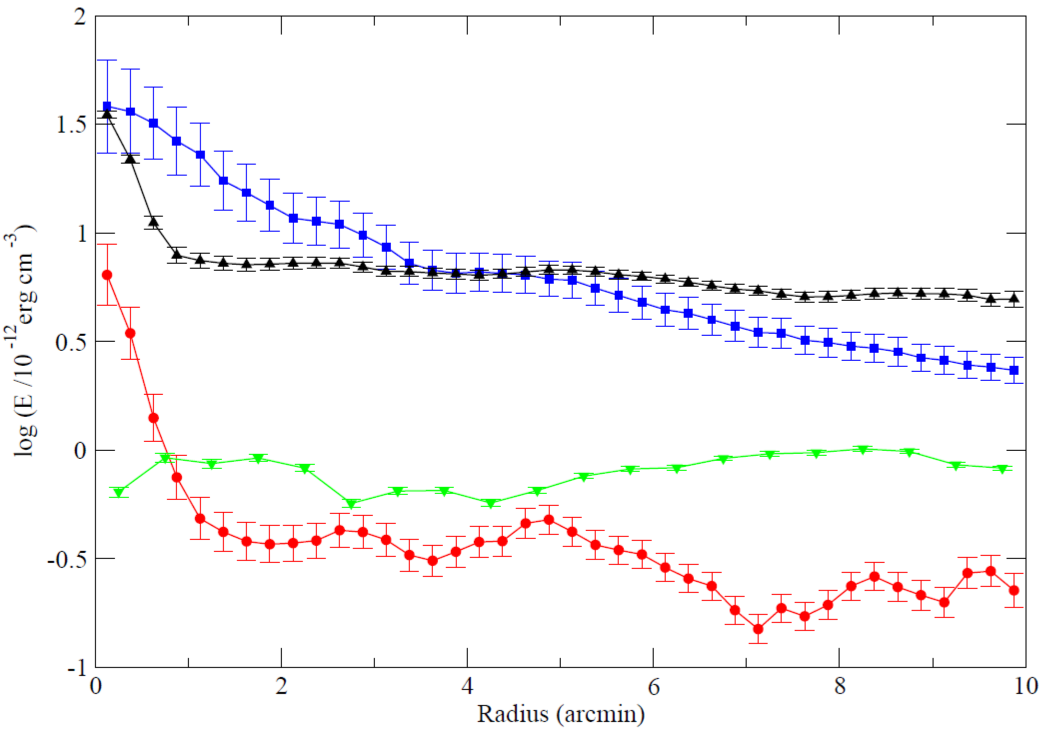

Figure 3.7: we show the energy densities of different ISM-components in the galaxy IC 342 for total magnetic field (black), turbulent pressure (bue), ordered field (green) and thermal pressure (red). This shows that magnetic fields are dynamically important for the evolution of a galaxy. The Figure has been taken from Beck (2015).

authors have pointed out rotation of turbulent eddies due to the presence of a magnetic field (Cho et al., 2002; Cho and Vishniac, 2000; Goldreich and Sridhar, 1995; Lazarian and Vishniac, 1999). The eddies show the largest gradient on the velocity alongside their major axis in the case that the eddy is elongated[1]. Usually, the magnetic field is perpendicular to the major axis of the eddy[2]. From this, one can then determine the magnetic field direction from Doppler-shifted line emission over determining the normalised and non-normalised centeroids $C(\mathbf{x})$ and $S(\mathbf{x})$ along the line-of-sight. This yields a very good estimate of the magnetic field structure, as the directions of the magnetic field vectors can be very well determined from the velocity gradient. We show an application on galaxy and galaxy-cluster scales in Figure 3.5 for M 87 and in Figure 3.6 for the Perseus galaxy cluster, from the very recent work of Hu et al. (2020), who determined the magnetic field structure with velocity gradients in clusters and massive galaxies for the first time.

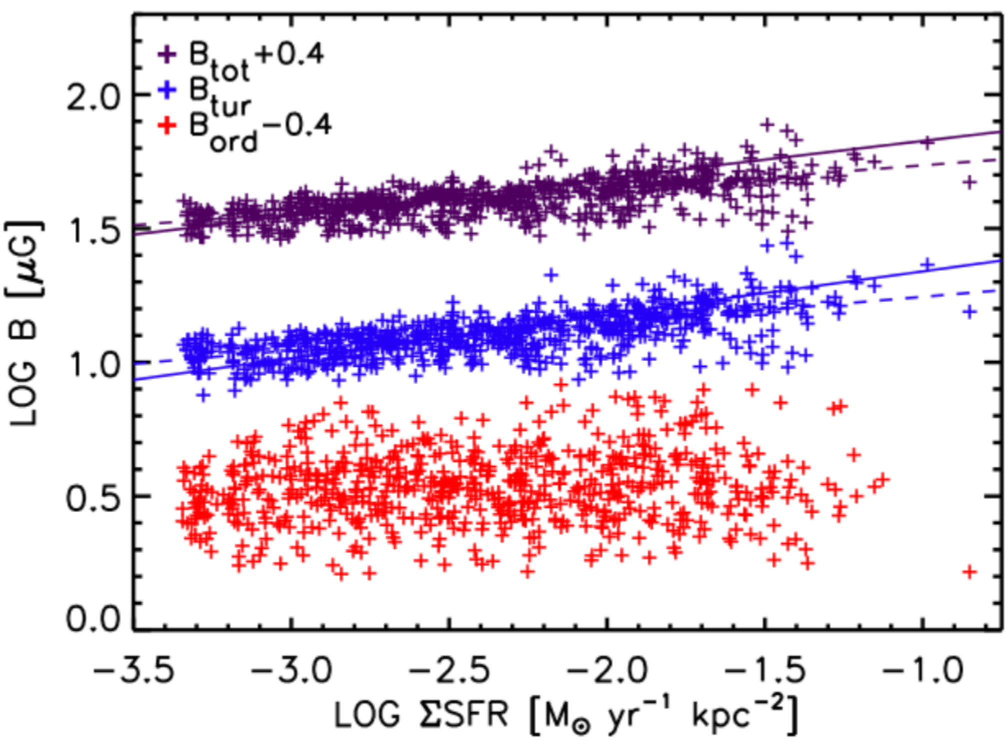

Figure 3.8: We show the correlation between magnetic field strength and star formation rate density. Typically, one finds a slight increase of the magnetic field strength and the star formation rate density with $B \propto \Sigma_{\rm sfr}^{0.3}$ to $B \propto \Sigma_{\rm sfr}^{0.45}$ depending on the gas composition. The Figure has been taken from Tabatabaei et al. (2013).

3.1.7 Properties of observed magnetic fields

The properties of magnetic fields, observed by the presented methods can be reduced to the field strength, energy densities and correlation with the star formation rate. Generally, magnetic field strengths are observed to be in the regime a few μG. However, depending on the exact environment this might differ. Regular spiral galaxies show total mean field strengths from 9 μG to 17 μG (Fletcher, 2010; Niklas et al., 1995). The field strength in the spiral arms of star forming galaxies like M 51 is typically higher and can reach values up to 50 μG (Beck, 2015). Even higher magnetic field strengths can be found in interacting galaxies (Chyży and Beck, 2004), starburst galaxies like M 82 (Adebahr et al., 2013), nuclear starburst environments (Heesen et al., 2011) and in barred spiral galaxies (Beck, 2011). Galaxies in these extreme regimes often show signs of strong losses due to CRs (Beck, 2015), which makes it extremely difficult to accurately determine the field strength from equipartition of CRs and magnetic field energy density. While this leads to higher field strengths than in typical spiral galaxies, one needs to keep in mind that the already high values are still under predicted. Evidence for this is provided by OH-megamaser measurements of starburst galaxies (Robishaw et al., 2008) which predict values of up to 18 mG. Further evidence for fields far beyond typical equipartition field values comes from observations of the galactic centre where one can also find field strengths above 1 mG (Yusef-Zadeh et al., 1996). This observational results already indicate that field strengths can be much larger than the equipartition value and we will provide a theoretical solution for this problem for barred galaxies in section 3.3.4 and provide an outlook towards a solution for starburst galaxies in section 10.4.

We show the energy-densities for the galaxy IC 342 in Figure 3.7 which demonstrates the dynamical importance of magnetic fields at least in some galaxies. The black line is the total magnetic energy density as the function of the radius. The blue line is the turbulent energy density. As the total magnetic field is derived from CR-energy density equipartition, the CR pressure is of the same order of magnitude as those components as well. The green line shows the ordered magnetic field component and the red line the thermal energy density. From this Figure it is instantly clear that magnetic fields (and cosmic rays) are in the same order of magnitude than the turbulent pressure of the galaxy. This is an extremely important realisation, because it means that most numerical calculations to this day neglect two massively dynamical important components of the ISM. Furthermore, similar results are reported for the MW (Cox, 2005).

Moreover, one can investigate the correlation of the magnetic field with the star formation rate of the galaxy. Several studies report similar results (Niklas and Beck, 1997; Schleicher and Beck, 2013; Tabatabaei et al., 2013) and find that overall the magnetic field shows a slight increase with increasing star formation rate density. Theoretically, this results is not really surprising as this is a direct consequence of the Schmidt-Kennicutt relation and adiabatic compression in the flux-freezing limit (e.g. Steinwandel et al., 2020a, for a more detailed discussion). The relation is shown Figure 3.8. Despite the fact that this relation is observed in a large sample of galaxies, it seems not to be valid on smaller scales and Tabatabaei et al. (2018) find an anti-correlation of the magnetic field with the star formation rate density on the molecular cloud scale.

[1] It most likely will be stretched by turbulence

[2] This is ab initio not clear, especially in the turbulence picture. But one might argue in the following manner. The eddy works against the velocity gradient in the eddy to reduce it. Therefore, there must be some net flow in the eddy alongside the gradient. However, this net flow would directly establish a magnetic field perpendicular to the gradient, hence giving us some information of the intrinsic magnetic field structure.

3.2 Seed Fields

We start the discussion of the origin of magnetic fields with magnetic seed field generation. Biermann (1950) suggested a battery process, which we will discuss in depth as it is the most popular process to obtain magnetic seed fields. However, as there are many more we will also mention the processes described in Harrison (1970b), Gnedin et al. (2000), Matarrese et al. (2005), Demozzi et al. (2009), but also the slightly alternative approach given in Rees (1987, 1994, 2005, 2006).

3.2.1 Biermann-Battery

The most common and the most straightforward explanation for magnetic seed fields is the theory that has been developed by Biermann (1950). The processes can be derived by a more accurate prescription of the right hand side of the induction equation. In the following form:

$$\frac{\partial \mathbf{B}}{\partial t} = \nabla \times (\mathbf{v} \times \mathbf{B}) + \eta \nabla^2 \mathbf{B}. \tag{3.11}$$

the induction equation is lacking a source term. Thus for a zero initial magnetic field the magnetic field will be zero forever. Theoretically, we are done here and everything works out quite well because there will never be a magnetic field. However, not only galaxy observations but also everyday observations show that there is a magnetic field. Thus we have to explain where it comes from. The starting point for this is a generalisation of Ohm's law where we only drop the electron ion friction term but keep the others (Spitzer, 1962):

$$nm\left(\frac{\partial \mathbf{v}}{\partial t} + \mathbf{v}\cdot\nabla\mathbf{v}\right) = ne\left(\mathbf{E} + \frac{\mathbf{v}\times\mathbf{B}}{c}\right) - \nabla p - \nu m(\mathbf{v} - \mathbf{v}_{\mathrm{i}}). \tag{3.12}$$

With the electron number density n and the velocity $\mathbf{v}_i$ of the ions. This can be simplified by assuming that the electron mass on the left hand side of equation (3.12) is much smaller than the mass of the ions. The last term is just $\eta\mathbf{j}$ from equation 2.35. Typically, one would now assume that $r_{\mathrm{g}} = \frac{mv_\perp}{eB}$ is small and argue that ∇p is zero. However, for a vanishing magnetic field the gyro radius is large and the assumption cannot be made and we find:

$$\mathbf{E} + \frac{\mathbf{v}\times\mathbf{B}}{c} = -\frac{\nabla p}{ne}. \tag{3.13}$$

Now, to understand how the Biermann-battery works, one has to understand how the term ∇p acts on the electrons. Any sink of ∇p leads to a force on the electrons that makes them move away from this sink, resulting in a charge imbalance (electric field) to counter act the movement of the electrons ($\mathbf{E} = \nabla p / -ne$). If n is constant in space and time, everything is fine and this electric field remains curl-free. However, if n varies spatially then this is different and the resulting electric field will be not curl-free. A none curl-free magnetic field introduces a magnetic field. By calculating the curl of equation 3.13 and if we simultaneously insert equation 2.26 we find:

$$\frac{\partial \mathbf{B}}{\partial t} = \nabla \times (\mathbf{v} \times \mathbf{B}) + \nabla \times \left(\frac{c\nabla p}{ne}\right) \tag{3.14}$$

$$= \nabla \times (\mathbf{v} \times \mathbf{B}) - c\frac{\nabla n \times \nabla p}{n^2 e}. \tag{3.15}$$

Thus whenever a system has misaligned pressure and density gradients (i.e shocks) then it has the potential to grow a tiny magnetic field by assuming that potential energy is transferred in magnetic field energy on the free-fall time scale of the halo. This magnetic field then can be estimated to be below 10^{-20} G. Finally, it is interesting to point out that a similar equation like equation 3.15 can be derived for the vorticity ω of a fluid and one can directly conclude that with growing vorticity (i.e. the collapse of a proto-halo) the magnetic field grows.

3.2.2 Harrison Process

Harrison (1970b) suggests that magnetic fields can be generated in the radiation dominated era of the Universe in rotating proto-halos with rotation velocity $\omega \propto r^{-2}$ for the gas and $\omega_\gamma \propto r^{-1}$ for the photon field. The rotating domain expands and the gas spins down faster than the photons. Now, one has to compute the interactions caused by this effect. In general, the Thompson cross section is much smaller for ions than for electrons. Thus the electrons are tightly coupled to the photons and build a negative charged electron-photon gas that is fully decoupled from the ions in the rotating structure. This difference in the movement between electrons and ions generates an electric field which is curled under rotation and induces a magnetic field of the order:

$$\mathbf{B} = -2(m_H c)\omega, \tag{3.16}$$

which yields a tiny magnetic seed of maximum 10^{-16} G in the non-relativistic limit. A similar process as the Harrison-process is described in Matarrese et al. (2005) based on density perturbations, yielding tiny seed field below 10^{-23} G. Further, there is the possibility that tiny seed field could be introduced during inflation (e.g. Demozzi et al., 2009) or could be generated in SN-shocks Rees (1987, 1994, 2005, 2006).

3.3 Amplification processes

3.3.1 Adiabatic compression

Accretion of baryon matter in proto-galactic halos can lead to an increase of the baryon matter density in the proto-halo. In this collapse scenario, the weak magnetic seed fields are closely correlated with the velocity distribution of the halo. The collapse of the gas brings magnetic field lines closer together and the magnetic field strength increases. We follow Kulsrud (2005) to describe this in more detail and derive the increase of the magnetic field in the proto-halo. One may start by combining equation 2.3 and the induction equation 2.39:

$$\frac{\mathrm{d}\mathbf{B}}{\mathrm{d}t} - \frac{\mathbf{B}}{\rho}\frac{\mathrm{d}\rho}{\mathrm{d}t} = (\mathbf{B}\cdot\nabla)\mathbf{v}. \tag{3.17}$$

The chain rule used on $(\mathbf{B}/\rho)$ yields:

$$\frac{\mathrm{d}}{\mathrm{d}t}\left(\frac{\mathbf{B}}{\rho}\right) = \frac{1}{\rho}\frac{\mathrm{d}\mathbf{B}}{\mathrm{d}t} - \frac{\mathbf{B}}{\rho^2}\frac{\mathrm{d}\rho}{\mathrm{d}t} \tag{3.18}$$

Multiplying equation 3.17 with $1/\rho$ and using this expression in equation 3.18 one obtains an expression for the time variation of the magnetic field caused by the increase of the density.

$$\frac{\mathrm{d}}{\mathrm{d}t}\left(\frac{\mathbf{B}}{\rho}\right) = \frac{1}{\rho}\nabla(\mathbf{B}\cdot\mathbf{v}). \tag{3.19}$$

The exact process depends now on the direction of the magnetic field. If the collapse is perpendicular to the field we get $\mathbf{B} \perp \mathbf{v}$. Thus the right hand side of equation 3.19 vanishes and $(\mathbf{B}/\rho) = \text{const.}$. The magnetic field increases with the density.
If the collapse is parallel to the magnetic field this means we get the divergence of the velocity field via $\nabla \cdot \mathbf{v} = \mathrm{d}\mathbf{v}/\mathrm{d}\mathbf{r}$ and find:

$$\frac{\mathrm{d}}{\mathrm{d}t}\left(\frac{\mathbf{B}}{\rho}\right) = -\frac{1}{\rho}\frac{\mathbf{B}}{\rho}\frac{\mathrm{d}\rho}{\mathrm{d}t}, \tag{3.20}$$

with $\frac{\mathrm{d}}{\mathrm{d}t}\ln\rho = \frac{1}{\rho}\frac{\mathrm{d}\rho}{\mathrm{d}t}$ one obtains:

$$\frac{\mathrm{d}}{\mathrm{d}t}\ln\left(\frac{\mathbf{B}}{\rho}\right) = -\frac{\mathrm{d}}{\mathrm{d}t}\ln\rho, \tag{3.21}$$

and the magnetic field remains constant under parallel collapse.

3.3.2 The Mean-Field or α-Ω dynamo

Larmor (1919) pointed out that strong magnetic fields could be obtained in a dynamo process in stellar bodies and first attempts for cosmic magnetic field amplification were made considering axis-symmetric velocities by splitting the field in its poloidal and toroidal components. It is straightforward to see that toroidal fields can be generated from a poloidal field by differential rotation (e.g. Kulsrud, 2005). However, rotation alone will not amplify the toroidal component of the field. Therefore, it is impossible to amplify a weak axis-symmetric magnetic field by pure axis-symmetric motions[3] (see Cowling, 1934) to a substantial field strength.
Parker (1955) pointed out that one could generate a significant poloidal field from an initial toroidal field by introducing rising convection cells[4] that are twisted by the Coriolis force of a rotating body when combined with differential rotation. This distortion of the poloidal component would inflict growth in the toroidal component and one obtains exponential growth of the form $e^{\gamma t}$. The Parker (1955) dynamo model can be generalised in the mean field dynamo approximation of Steenbeck et al. (1966), where turbulent motions are treated by the kinetic helicity, quantified by $\alpha = -\tau/3 < \mathbf{v} \cdot \nabla \times \mathbf{v} >$. Their mixing can be quantified with the turbulent resistivity $\beta = \tau/2 < \mathbf{v} \cdot \mathbf{v} >$. Introducing fluctuations of velocity and magnetic field of the form $\mathbf{w} = \mathbf{w^0} + \mathbf{w}'$, where $\mathbf{w}$ is an arbitrary vector quantity yields the dynamo equation in thin disc approximation in cylindrical coordinates, after dropping all non-linear terms:

$$\frac{\partial B_r}{\partial t} = -\frac{\partial}{\partial z}\left(\alpha B_\phi\right) + \beta\frac{\partial^2 B_r}{\partial z^2}, \tag{3.22}$$

$$\frac{\partial B_\phi}{\partial t} = -\Omega B_r + \beta\frac{\partial^2 B_\phi}{\partial z^2} \tag{3.23}$$

[3] This gives a linear growth and one can easily show that one would need order of 10^{14} rotations of the Milky Way to reach this field strength while it could have only rotated 50 times even if it formed with today's properties at redshift 20.

[4] In disc galaxies rising convection cells could be interpret as SN-remnants that experience backward motion due to the Coriolis force.

This can be solved as an Eigenvalue problem with boundary conditions of a thin disc with scale height h where B_r and B_ϕ vanish at $\pm h$ (only valid if β is large) in reduced coordinates yielding:

$$\gamma' B'_r = -\frac{\partial(z' B'_\varphi)}{\partial z'} + \frac{\partial^2 B'_r}{\partial z'^2}, \tag{3.24}$$

$$\gamma' B'_\varphi = D B'_r + \frac{\partial^2 B'_\varphi}{\partial z'^2}, \tag{3.25}$$

with $z' = z/h$, $t' = \beta t/h^2$, $\gamma' = \gamma h^2/\beta$, $B_\varphi = B'_\varphi(\beta/h\alpha_0)$, $B_r = B'_r(\beta/h\alpha_0)$, $\alpha_0 = \alpha h/z$ and the dimensionless dynamo number $D = -\Omega\alpha_0 h^3/\beta^2$. The solution shows exponential growth for $D < D_{\rm crit}$ where $D_{\rm crit}$ is smaller than -4 for dipol modes and smaller than -13 for quadrupol modes on the time scale h^2/β. The growth is then mostly dependent on the disc scale height h and a good estimate for β. Parker (1979) and Ruzmaikin et al. (1988a) give an estimate of 0.5 Gyr for a turbulent velocity of 10 km s^{-1}, SN-injection radius of 100 pc and a disc scale height of 300 pc, which is reasonable for the Milky Way at redshift zero. On this time scale one can amplify a field of 10^{-14} G to 10^{-6} over the lifetime of the galactic disc of 6 Gyr assuming that the MW did not experience a merger since redshift one (Jeremiah P. Ostriker, private communication).
However, this picture is flawed. We already discussed in 3.2.1 that there are good arguments to assume that primordial seed fields are much lower than 10^{-14} G. Thus it is obvious that the α-Ω dynamo has a time scale problem. Furthermore, the magnetic field structure of the Galaxy is observed to be quadrupolar but the α-Ω dynamo favours a dipol structure. It is very hard to explain why the leading dipol mode has vanished. Finally, we note that the boundary conditions for the dynamo equations are problematic as well. In ideal MHD the field is locked to the fluid. Thus, to remove magnetic field at the edges, interstellar matter has to be removed from the galaxy for each cycle of exponential growth, which leads to problems in both the enrichment history of the halo and its energetics (see Kulsrud and Zweibel, 2008, in their chapter 9). However, the time scale problem in combination with the reality of small seed fields from cosmology is the biggest problem and it heavily depends on the estimate of β although we acknowledge that this could still be resolved with a better estimate for β (e.g. Brandenburg et al., 1995; Poezd et al., 1993) or a modified dynamo model based on super bubbles (Ferriere, 1992a,b, 1993a,b, 1996; Ferrière, 1998; Ferrière and Schmitt, 2000).

3.3.3 Small scale turbulent dynamo

It has been pointed out that the magnetic field could be generated during the formation process (Kulsrud et al., 1997; Pudritz and Silk, 1989) of galaxies and galaxy clusters due to strong turbulence driven by shocks in the high redshift ISM and ICM of these objects. These shocks lead to miss aligned pressure and density gradients and induce a magnetic field. This leads to a magnetic field growth proportional to the eddy-turnover time of the smallest eddies.
This process has been studied extensively in theory (Boldyrev and Cattaneo, 2004; Kazantsev, 1968; Kraichnan and Nagarajan, 1967; Kulsrud and Anderson, 1992; Subramanian and Barrow, 2002) and is well understood. Mathematically, the idea is to derive the distribution of the power in the magnetic field under the assumption that velocity and magnetic field can be Fourier decomposed. The turbulent velocities are supposed to be random. Then the magnetic power spectrum $P_{\rm M}(k)$ is given as the ensemble average of the magnetic energy density:

$$E_{\rm mag} = \frac{< \mathbf{B}^2 >}{8\pi} = \int P_{\rm M}(k) dk. \tag{3.26}$$

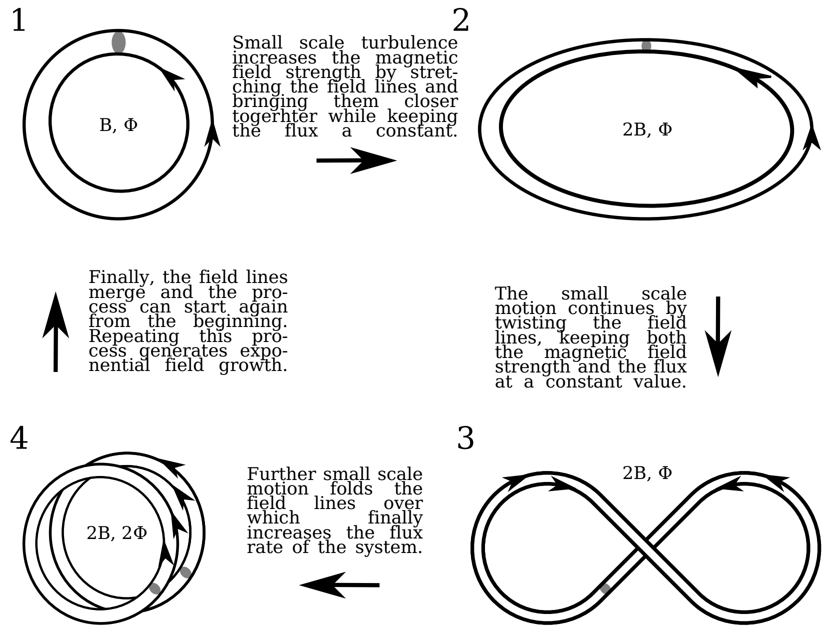

Figure 3.9: Schematical sketch of the stretching twisting and folding of magnetic field lines in the small scale turbulent dynamo. In this picture the field strength is increased by stretching a field line at constant magnetic flux. Small scale turbulent motion then twist and fold the field line which also increases the magnetic flux. Subsequent stretch twist and fold events then lead to exponential growth of the field.

The evolution of $P_{\mathrm{M}}(k)$ is given as (e.g. Kulsrud and Zweibel, 2008):

$$\frac{\partial P_{\mathrm{M}}(k)}{\partial t} = \int K(k,k_0)M(k_0)dk_0 - 2\beta k^2 P_{\mathrm{M}}(k), \tag{3.27}$$

with the structure function K and the turbulent resistivity β. Combining equations 3.26 and 3.27 one can find:

$$\frac{dE_{\mathrm{mag}}}{dt} = 2\gamma E_{\mathrm{mag}}. \tag{3.28}$$

This directly implies that the magnetic field strength doubles with every eddy turn. We show this process schematically in Figure 3.9. The growth rate is then directly given as the smallest eddy turn over time (in the Kolmogorov limit for turbulence) and is transported via an inverse turbulence cascade to the larger scales. In the kinematic regime the evolution of $P_{\mathrm{M}}(k)$ is given via:

$$\frac{\partial P_{\mathrm{M}}(k)}{\partial k} = \frac{\gamma}{5}\left(k^2\frac{\partial^2 P_{\mathrm{M}}(k)}{\partial k^2} - 2k\frac{\partial P_{\mathrm{M}}(k)}{\partial k} + 6P_{\mathrm{M}}(k)\right) - 2k^2\lambda_{\mathrm{res}}P_{\mathrm{M}}(k), \tag{3.29}$$

with the resistivity λ_{res}. This can be solved in Fourier space and one obtains:

$$P_M(k,t) \propto e^{3/4\gamma t}k^{3/2}, \tag{3.30}$$

yielding exponential growth of Kazantsev-like modes with $k^{3/2}$. Easy estimates show that this dynamo has eddy turn over times that are smaller by a factor of 100 compared to the free-fall time of protogalactic halo. While this can easily lead to field strengths that are observed in today's spiral galaxies by a factor of 1000 the dynamo saturates when equipartition of the magnetic energy and the turbulent velocity of the smallest eddy is reached. This gives rise to field strengths in the order of a few μG. Therefore, the small-scale turbulent dynamo amplifies the field early on and the α-Ω dynamo orders the already saturated field on the larger scales in an combined α^2-Ω dynamo.

3.3.4 Driving outflow with the radial inflow dynamo

We propose how such a field, obtained by the α^2-Ω dynamo can drive an outflow induced by a non axis-symmetric gravitational instability (e.g. bar, spiral arm, warp etc.). Every axis-symmetric instability transports mass inwards and angular momentum outwards. In the specific case of a bar this leads to a gas response that is quicker than the outside co-rotation of the bar like mode with the rotation frequency of the bar Ω_p equal to the rotation frequency of the galaxy. We can now derive the magnetic field evolution via the induction equation where we directly drop the diffusion term:

$$\frac{\partial \mathbf{B}}{\partial t} = \nabla \times (\mathbf{v} \times \mathbf{B}), \tag{3.31}$$

which gives us for the toroidal field component in thin disc approximation:

$$\frac{\partial B_\varphi}{\partial t} = \frac{\partial v_r B_\varphi}{\partial r} + B_r r \frac{d\Omega}{dr}. \tag{3.32}$$

For a fully developed bar like mode we assume that all the magnetic field lines are already perfectly aligned with the bar. This only allows mass flux alongside the radial direction because the mass flux alongside the field lines is force free in ideal MHD. Thus B_r remains roughly constant as the bar transports angular momentum outwards and mass inwards. We can then solve equation 3.32 by integrating for fixed B_r and we find:

$$B_\varphi = \left[B_{\varphi,0}(r_0) + \tau B_r r \frac{d\Omega}{dr} \right] e^{t/\tau} - \tau B_r r \frac{d\Omega}{dr}, \tag{3.33}$$

with the amplification time scale $\tau = -(\partial v_r / \partial r)^{-1}$. Typically, the time scale of such a process is of order of 0.1 Gyr. If we now assume that the bar formation process takes 0.5 Gyr, which is not a bad estimate given our simulation results which we discuss in chapter 7 and chapter 8. We obtain magnetic field growth of the toroidal component by factor of 150 in the centre of the galaxy. If we assume a typical field strength of an already saturated field between 1 μG and 10 μG, obtained by the α^2-Ω dynamo we obtain a central toroidal field of between 100 μG and 1000 μG, which is in accordance with observations of the galactic centre (e.g. Yusef-Zadeh et al., 1996). Now we can even derive the outflow rate of the galaxy given the assumed thin disc approximation. As we pointed out in section 3.3.2 the thin disc approximation has to fulfil the boundary conditions of B_r=$\mathrm{B}_\varphi = 0$ at the edges of the disc. While this is a big issue in the prescription of the α-Ω dynamo as it would imply large outflow rates to actually obey this boundary condition, we can use it to calculate the outflow rate that one obtains due to our radial inflow dynamo. If we assume that the field grows by a factor of 100, we can directly calculate the mass that moves out of the disc towards to CGM. We assume that the disc had a mass of $M_\mathrm{disc,1}$ before the radial inflow dynamo process started and has the mass $M_\mathrm{disc,2}$ after the process is suppressed again. The following conditions is then valid:

$$M_\mathrm{disc,2} = M_\mathrm{disc,1} \cdot \left(\frac{B_2}{B_1} \right)^{-1/3}. \tag{3.34}$$

We find that the central region can lose up to a fifth of its total mass due to this process, which results in an outflow rate of the order of 0.1 $\mathrm{M}_\odot\ \mathrm{yr}^{-1}$.

Chapter 4

The physics of the Interstellar medium

In this chapter we present a compact description of the Interstellar medium (ISM). The ISM is one of the most fascinating and complicated mysteries in modern day astrophysics and there are many unsolved problems that happen on ISM scales, with the most popular ones being star formation, how the feedback of stars couples to the ambient ISM and how the turbulent structure is obtained. However, to properly understand how these problems are connected and how they can be progressed, one has to understand gas dynamics in the ISM and its interaction with the stellar components of galaxies. This exchange is dominated by the heating and cooling processes in the ISM. We will give an overview on the most important cooling and heating processes, describe their interaction with dust and radiation, derive a basic understanding how turbulence in the ISM is generated and discuss the implications for molecular cloud formation, star and star cluster formation. This picture that is drawn here is heavily influenced by the review of Klessen and Glover (2016) and the discussions with my co-supervisor Thorsten Naab, which heavily shaped my own picture of the ISM.

4.1 Composition of the ISM

4.1.1 The gas component

The vast majority of the gas in the Milky Way consists out of hydrogen (roughly 72 per cent) and helium (roughly 28 per cent). The residual 2 per cent are other species like metals and higher order molecules. It is interesting to point out that while the majority of the volume in the ISM is dominated by hot ionised gas, it only contributes up to a maximum of 25 per cent of the total gas mass which is estimated to be around 10^{10} $M_{\odot}$ (e.g. Kalberla and Kerp, 2009) in the Milky Way. While the volume is dominated by hot, ionised gas, the majority of the mass in the ISM is located in the cold gas in the form of atomic hydrogen and helium or molecular hydrogen. This phase only fills a few per cent of the total ISM volume.

Historically, the ISM is subdivided in different phases. The first theoretical model for the ISM is given by Field et al. (1969) who derived that there is a pressure regime for which one can find two solutions that are thermally stable, a warm diffuse phase at roughly 10^4 K, known as the warm neutral medium (WNM) and a cold phase at roughly 100 K, known as the cold neutral medium (CNM). This model implies that a tracer particle with a given temperature density pair will either move towards the WNM or the CNM, by heating up or cooling down. However, McKee and Ostriker (1977) point out the SN play a crucial role in heating gas from the CNM and the WNM. In their picture, SNe heat and ionise gas in bubbles to temperatures of around 10^6 K. Due to the long cooling times at 10^6 K

one obtains a stable third phase which is known as the hot ionised medium (HIM), hwich is typically believed to be stabilised by thermal conduction. This model has proven to be very successful, but there is overwhelming observational evidence for at least one more phase in the ISM. This evidence comes from the synchrotron emission, the free-free emission (Hoyle and Ellis, 1963), radio signals from pulsars and optical emission produced by species like O^+ (Mierkiewicz et al., 2006; Reynolds et al., 1973), indicating the existence of the so called warm ionised medium (WIM), with a significant scale-height above the mid plane. This phase contains roughly 90 per cent of the total ionised gas in the galaxy.
One could now also further distinguish the cold phase in CNM and the cold molecular medium (CMM), which is mostly found in dense molecular clouds with a scale length of the order of 10 pc and densities above 10^5 particles per cubic centimetre.
However, this picture neglects the fact that the ISM shows a highly turbulent structure that is driven by various physical processes, including but not restricted to the feedback of SNe, stellar winds and cosmic accretion to the disc. This shows that in reality the situation might be more complex than just generalising different pressure regimes based on temperature and density. Moreover, the exact properties depend on the exact amount of metals in the ambient ISM, which mostly impact the high temperature cooling of the gas as metal line cooling is the dominant cooling process in this regime. However, also the low temperature cooling down to 1000 K is dominated by metal species, mainly C^+.

4.1.2 The importance of dust

Observations indicate that there must be an additional component of the ISM, that is usually referred to as dust, which shows the nature of absorbing and re-emitting star light in various frequency bands. The exact broadening of these absorption features along the extinction curve can tell us about the detailed composition of the dust in the ISM. Typically, these features are observed to be very brought, which indicates that they cannot originate from the small atoms or molecules (e.g. Klessen and Glover, 2016). Further, observations of the abundance of metals in the local ISM show that there is much less carbon, silicon and iron as one would expect from the solar abundance of metals. To obtain the physical structure of the dust particles one has to explain the structure of the dust-extinction curve, related to these particles. The idea is the following. Dust grains only absorb photons with a wavelength that is smaller than the dust grain. The absorption is much stronger in the UV, compared to the optical and the infrared wavelengths. We can learn two things from this. The first one is that there mus be more small grains than large grains in the ISM. The second point is that (surprisingly) the small grains dominate the absorption, which is related to them being more abundant. Furthermore, it is also possible to relate the absorption features at specific wavelengths to the type of grain. The two most observed dust species are carbon based dust grains with an absorption feature at around 217.5 nm and amorphous silicates with absorption features around 9.7 μm and 18 μm. It is interesting to point out that the grain size distribution has been determined quite early on by Mathis et al. (1977) and follows a steep power-law decline from small to big grains given via:

$$N(a)da \propto a^{-3.5}da, \tag{4.1}$$

where a is the size of the dust grain that has typically a size of 50 nm to 0.25 μm. In total the dust mass in the local ISM can be constrained to roughly 1 per cent of the total mass of the ISM. While this seems negligible, dust can majorly impact the cooling curve and the formation of molecules as it can act as a catalyst for example in the formation of molecular hydrogen (Klessen and Glover, 2016).

4.1.3 The Interstellar Radiation Field

The exact thermal state of the gas/metal/dust composition in the ISM is determined by the Interstellar Radiation field (ISRF) which is set by six different components, at least in solar neighbourhood conditions. First, galactic synchrotron emission that comes from relativistic electrons. Second, the CMB. Third, Infrared and Far-infrared emission form dust heated by stars. Fourth, bound-bound, bound-free and free-free emission from the 10^4 K fully ionised component of the ISM, Fifth, light from stars. Sixth, X-ray emission from the hot phase of the ISM. If one considers the energy density of each component one can see that the most dominant component is star light at a combined energy density of 10^{-12} erg cm^{-3}, followed by dust emission at $5 \cdot 10^{-13}$ erg cm^{-3} and the contribution of the CMB at $4.9 \cdot 10^{-13}$ (Draine, 2011). The other components are sub-dominant with at least two orders of magnitude lower energy density. Thus we will only discuss the contribution of the dominating components.

The radiation from stars

The stellar body of a galaxy emits energy mostly in the near infrared, the optical wavelengths and the near UV. As the photons that are emitted from stars travel through the cold ISM, photons above 13.6 eV tend to ionise hydrogen in the ISM. Thus photons with an energy greater than 13.6 eV cannot move far into regions of cold neutral hydrogen. Under solar neighbourhood conditions one can assume that ISRF consists out of three different diluted black body spectra. Mathis et al. (1983) point out that above 245 nm the ISRF can be descried by the following spectrum:

$$\nu u_\nu = \frac{8\pi h \nu^4}{c^3} \frac{W_i}{e^{h\nu/k_{\rm B}T_i} - 1}, \tag{4.2}$$

with the dilution coefficients W_i and T_i for different regimes. For wavelengths below 245 nm Habing (1968) gives a good estimate for the ISRF at 100 nm with $\nu u_\nu \approx 4 \cdot 10^{-14}$ erg cm^{-3}. This can be also presented in terms of a photon energy of 12.4 eV slightly below the ionisation value for hydrogen. This value can be used as reference value via $\chi = \nu u_\nu / (4 \cdot 10^{-14}$ erg cm$^{-3})$. Another estimate can be made based on Habing (1968) for radiation between 6 eV and 13.6 eV, usually defined as G_0 given by:

$$G_0 = \frac{u(6 - 13.6\text{eV})}{5.29 \cdot 10^{-14}\ \text{erg cm}^{-3}}. \tag{4.3}$$

The later is the appropriate parameter to determine the photo-electric heating rate which we will use later on in section 5.8 to compute the photoelectric heating rate in our simulations.

Infrared emission from dust grains

At larger wave lengths between 5μm and 600μm the spectrum of the ISRF is dominated by the re-emission of infrared radiation from dust grains. The majority of the energy density from this component is emitted in the near and mid infrared and follows a slightly modified black body spectrum (Klessen and Glover, 2016):

$$J_\nu = B_\nu(T_0) \left(\frac{\nu}{\nu_0} \right)^\beta, \tag{4.4}$$

with J_ν as the mean of the specific intensity of the system in the infrared, B_ν the typical black body spectrum, T_0 the dust temperature (roughly 20 K in the MW) and β as the spectral index (roughly 1,7,

Planck Collaboration et al., 2014). It is not clear whether β depends on the dust temperature or not. Some studies indicate an anti correlation, while thePlanck Collaboration et al. (2014) finds a weak correlation between β and the dust temperature.
Dust emission that is not observed in the near and mid infrared is usually coming from polycyclic aromatic hydrocarbons (PAHs) with peak wavelengths between 3.3 and 12.7 μm, which absorb radiation and re-emit in the infrared due to fluorescence.

Emission from the CMB

At even larger wavelengths between 600 μm and 30 cm the CMB is dominating the energy density distribution. As we described in chapter 1 the CMB is a picture perfect black body spectrum at 2.75 K. While the CMB energy does not couple very efficiently to the MW-ISM, at higher redshift the contribution is assumed to be much stronger as the energy density of the CMB grows with $(1+z)^4$ which makes a substantial contribution at higher redhsifts. As the CMB regulates the temperature floor of the ISM it could potentially affect star formation in the first galaxies and contribute to the shape of the initial mass function (IMF) (Klessen and Glover, 2016).

4.1.4 Cosmic rays

Last but not least, the ISM is the host for cosmic rays in a relatively wide energy range from a few MeV up to TeV. Cosmic rays are usually classified as relativistic protons or electrons. A small fraction of the ions can also contribute to this population. They are expected to be dynamically important for all processes in the ISM, as they have an energy density of roughly 2 eV cm^{-3} which is comparable to the thermal energy density under solar neighbourhood conditions. As they tightly couple to the magnetic field, one would expect that they also homogeneously scatter within the ISM. The cosmic ray spectrum in the ISM shows a strong decline with increasing energy, with the majority of the cosmic rays that contribute to heating, coming from the low energy end of the spectrum.

4.2 Heating and cooling of the ISM

4.2.1 Radiative cooling: How does it work?

Two level system

The basics of radiative cooling can be straightforward understood by considering the simple two level system with two energy states, the ground state E_0 and the first excited state E_1. To first order the transitions between these two states can be described by the Einstein coefficients $A_{1,0}$, for spontaneous emission of a photon, $B_{1,0}$ for stimulated emission of a photon and B_{01} for absorption of a photon. We can then assume that the total number of atoms n_{tot} in the system is the sum of the atoms that are excited n_1 and that are in the ground state n_0. From this, one can write down simple rate equations by also considering the collisional excitation rate $C_{0,1}$ and the collisional de-excitation rate $C_{1,0}$ and we find:

$$\frac{dn_1}{dt} = C_{0,1}n_0 - C_{1,0}n_1 - A_{1,0}n_1 - B_{1,0}I_{1,0}n_1 + B_{0,1}I_{1,0}n_0, \tag{4.5}$$

$$\frac{dn_1}{dt} = -C_{0,1}n_0 + C_{1,0}n_1 + A_{1,0}n_1 + B_{1,0}I_{1,0}n_1 - B_{0,1}I_{1,0}n_0, \tag{4.6}$$

with $I_{1,0}$ as the interstellar photon field. The energy gap $E_{1,0}$ is then resonant at a given frequency $\nu_{1,0} = E_{1,0}/h$, where h is Plancks quantum of action. These actions occur on time scales that are much smaller than a second and thus we can assume that there is an equilibrium condition that yields $dn_1/dt = dn_0/dt = 0$ and one finds:

$$(C_{0,1} + B_{0,1} I_{1,0}) n_0 = (C_{1,0} + A_{1,0} + B_{1,0} I_{1,0}) n_1. \tag{4.7}$$

In optically thin approximation one could even neglect the radiation field $I_{1,0}$ and one obtains:

$$C_{0,1} n_0 = (C_{1,0} + A_{1,0}) n_1. \tag{4.8}$$

This directly gives the fraction of excited to de-excited atoms in the ISM. $C_{0,1}$ describes physical processes that cause a transition from level 0 to level 1. Usually, this transitions are triggered by the following species: H, H_2, H^+, He and free electrons. Thus $C_{0,1}$ is the sum of the excitation rates of the single species.

In local thermal equilibrium (LTE) we know that energy states will be populated via the Boltzmann-distribution, which gives us:

$$\frac{n_1}{n_0} = \frac{g_1}{g_0} e^{-E_{1,0}/k_B T}, \tag{4.9}$$

with g_0 and g_1 as the statistical weights for different species. This equation can directly be correlated with the excitation and de-excitation coefficients $C_{0,1}$ and $C_{1,0}$ via the principle of detailed balance that states that $C_{0,1} n_0 = C_{1,0} n_1$. We find the following result for a system in thermal equilibrium.

$$\frac{n_1}{n_0} = \frac{g_1}{g_0} \frac{e^{-E_{1,0}/k_B T}}{1 + A_{1,0}/C_{1,0}}. \tag{4.10}$$

From this equation we can directly see, that as long as we are in the collision regime we obtain Boltzmanian behaviour of the system and only as radiation dominates the de-excitation process the distribution is altered. In other words, for a system dominated by collisions we obtain the LTE configuration. If radiation is strong however, the system is de-excited by emission of photons and collisional de-excitation is sub-dominant.

Now it depends on the contribution of different species to $C_{1,0}$. We directly consider the most general case in which there are various contributions from various species. In this case one can define a critical density n_{crit} via $A_{1,0}/C_{1,0} = n_{\mathrm{crit}}/n$, with n_{crit} as fractional contribution of different species given by:

$$n_{\mathrm{crit}} = \left[\sum_i \frac{x_i}{n_{i,\mathrm{crit}}} \right]. \tag{4.11}$$

x_i is the fractional abundance of each species and we can re-formulate equation 4.10 and we get:

$$\frac{n_1}{n_0} = \frac{g_1}{g_0} \frac{e^{-E_{1,0}/k_B T}}{1 + n_{\mathrm{crit}}/n}. \tag{4.12}$$

Finally, we can re-write equation 4.12 by using $n_{\mathrm{tot}} = n_0 + n_1$ and re-arrange to find:

$$\frac{n_1}{n_{\mathrm{tot}}} = \frac{g_1}{g_0} \frac{e^{-E_{1,0}/k_B T}}{1 + n_{\mathrm{crit}}/n + (g_1/g_0) e^{-E_{1,0}/k_B T}}. \tag{4.13}$$

This has some important implications as we can now directly derive the radiative cooling rate from this, which is simply given by $\Lambda_{1,0} = A_{1,0}E_{1,0}n_1$ leading to:

$$\Lambda_{1,0} = A_{1,0}E_{1,0}n_{\text{tot}}\frac{g_1}{g_0}\frac{e^{-E_{1,0}/k_{\text{B}}T}}{1+n_{\text{crit}}/n+(g_1/g_0)e^{-E_{1,0}/k_{\text{B}}T}}. \tag{4.14}$$

Using this we can look at two regimes for $n \rightarrow 0$ and $n >> n_{\text{crit}}$. In the first case we find that the cooling rate scales with n^2 which implies that cooling is a strong function of density. In the second regime (this is often called the LTE-regime), we only find a scaling of the cooling rate with n. An interesting side note is that, while the first regime is dependent on the collisional excitation rate the second is only dependent on temperature.
However, this calculation neglects the effects of absorption and stimulated emission and thus the situation changes once the radiation field becomes stronger. Further we did not discuss the effect of multi-level atomic systems that can largely influence the cooling rate. A detailed description for the optically thick limit is given via the Sobolev-approximation (Sobolev, 1957). The multi-level system on the other hand is an extension of the two-level atom in which one can find the cooling rate of the total system via:

$$\Lambda = \frac{\Lambda_{\text{let}}}{1+n_{\text{crit,eff}}/n}, \tag{4.15}$$

which is a good approximation for low and high densities compared to $n_{\text{crit,eff}}$ following Klessen and Glover (2016).

Dipole allowed line transition cooling

Above 10^4 K in the hot ionised medium, cooling via dipole allowed line transitions is the most prominent cooling process. This originates from different atoms and ions in the ambient ISM. Close to 10^4 K the most important coolant is atomic hydrogen due to resonance cooling of its Lyman series with a cooling rate that different authors have pointed out thus far (Black, 1981; Cen, 1992):

$$\Lambda_H = 7.5 \cdot 10^{-19}\frac{1}{1+(T/10^5)^{\frac{1}{2}}}e^{\frac{-118348}{T}}n_e n_H, \tag{4.16}$$

where n_e is the electron number density and n_H is the proton number density[1]. At around $3 \cdot 10^4$ K hydrogen line cooling starts to become sub-dominant and metal line cooling takes over, mainly via the species C, O, Ne and Fe. In collisional ionisation equilibrium the cooling function is only a function of density, temperature and metallicity of the gas composition. It is quite obvious, that this will mostly not apply to the ISM and modelling cooling in the ISM is more complicated than just deriving cooling rates from density temperature pairs, like it is often done in simulations of galaxy formation and evolution to this day. Just consider an H-II region around an massive O-star, it is straightforward to recognise that this system is driven by ionisation due to photoionisation rather than collisions. On the other hand if you consider strong shocks (due to accretion or SNe) the gas is heated so quickly that it cannot react fast enough to be in collisional ionisation equilibrium. Such non-equilibrium effects are the key in determining the cooling curve already around 10^4 K and there are two approaches of how that can be handled. The first is to tabulate cooling rates dependent on the environment and while this is fast it obviously does not give the physical system time to react on the perturbation and just reacts based

[1]The number that seems arbitrary in the exponent is in fact the Rydberg energy.

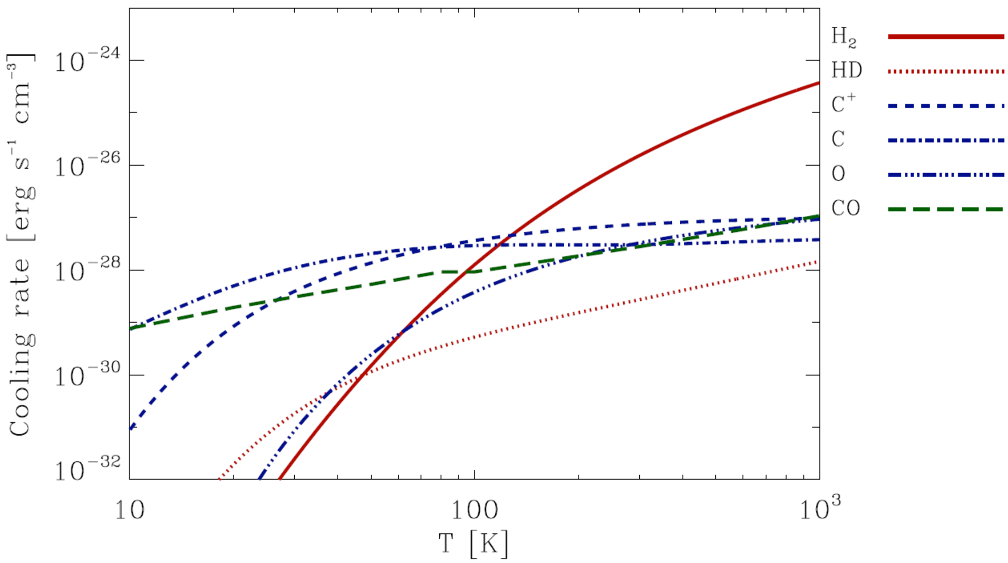

Figure 4.1: We display the most important coolants at low temperatures, below 1000 K. Above 100 K, H_2 is the most importatn cooling, but it quickly drops below 100 K, as it becomes impossible to excite the $J = 2$ rotaionla modes and the $J = 0$ and $J = 1$ modes are forbidden due to the para/ortho configurations of molecular hydrogen and C, C^+ and O become the most important coolants. The Figure has been taken from Klessen and Glover (2016).

on pre-tabulated values that ignore the detailed structure of the environment. Nevertheless, a lot of groups follow this approach (Gnat and Sternberg, 2007; Gnedin and Hollon, 2012; Wiersma et al., 2009). The more accurate approach is to actually calculate the non-equilibrium cooling rates which is more expensive but the only chance to capture the ISM in a full galaxy simulation (e.g. Hu et al., 2016; Richings et al., 2014; Steinwandel et al., 2020b).

Fine structure line cooling

The crucial part in cooling happens in the regime below 10^4 K where gas densities become high and temperatures are low. In this regime metal line cooling of forbidden fine structure and hyper fine structure lines is dominating the cooling. Fine structure lines in atoms appear due the spin-orbit coupling of the electrons angular momentum of the orbit and its spin. The electron can now induce two different magnetic moments, one due to the movement of the electron around the nucleus and another due to the spin of the electron. These moments can either align or miss-align. In the first case, the energy level is slightly increased, in the latter case it is reduced. However, this is only valid for atoms with a non zero angular momentum of the electrons orbit and non zero spin in the ground state, in the outer electron shell. This directly tells us why hydrogen becomes less important below 10^4 K as it has no fine structure lines with electron spin S=1/2, but angular momentum L=0. Carbon on the other hand, as one (or the most) important coolant below 10^4 K has S=1 and L=1 and is thus fine-structure degenerated and cooling can become effective for carbon, down to very low temperatures around 20 K.

Molecular cooling

Cooling due to molecules is most effective below 1000 K and thus helps in establishing the cold phase of the ISM. Straightforward, one would assume that this is driven by molecular hydrogen as it is the most abundant molecule in the ISM. While this is true at higher temperatures between 100 K and 1000 K, the situation is different at temperatures below 100 K where the H_2 cooling rate drops significantly, compared to other major coolants like carbon or oxygen. However, one can explain this by considering that molecular hydrogen has two distinguished states. The rotational energy states, given by the quantum number J of molecular hydrogen, differ depending on the spin of the two protons that form the H_2 molecule. If the spins have different sign, the resulting nuclear spin I is zero. This is often referred to para-hydrogen. If the spins are aligned one obtains ortho-hydrogen. For the para state the Pauli-exclusion principle requires that J is even (J=0). Vice versa, it requires for the ortho-state that J is odd ($J = 1$). To trigger a transition from the ortho to the para or the para to the ortho state enforces a change of the nuclear spin I. While this is not impossible, it is extremely unlikely. As these transitions are so unlikely to occur, the most commonly excited state of molecular hydrogen is the rotational state with $J = 2$. However, these rotational states have large energy gaps for excitation with the $J = 2$ state corresponding to roughly 500 K. This explains why H_2 cooling is dominating at around 1000 K, where the $J = 2$ state can easily be excited, but it is so inefficient below 100 K as the $J = 0$ and $J = 1$ states are so rare and the $J = 2$ state can not be excited anymore. We show this in Figure 4.1 where we show the cooling rate of different atomic and molecular species as a function of the temperature. One can easily see that H_2 is dominating above 100 K but falling exponentially below 100 K in terms of the cooling rate. In this regime carbon, oxygen, CO and even hydrogen deuteride (HD) are more important coolants. Further, we have to mention that the H_2 cooling rate drops significantly with abundance of H_2 and is under real ISM conditions in the solar neighbourhood usually sub-dominant, especially below 100 K.

The situation for HD is different compared to H_2. This is because HD does not show any para or ortho configuration and transitions between the $J = 0$ and $J = 1$ level are easy to excite. Further, the energy gap between the rotational levels are smaller for HD compared to H_2. While the abundance of deuterium is relatively low, the abundance of HD can be majorly increased in cold gas which is not fully molecular yet, by chemical fractionation where ionised deuterium captures an H_2 molecule. This reaction is exothermic and can thus occur at any given temperature. The back reaction, however, that would destroy HD again is endothermic and becomes less likely the lower the temperature gets. Thus HD can contribute significantly to the cooling channel. The limit for this is obviously the initial deuterium abundance and therefore HD is only more effective than H_2 in terms of cooling below 50 K, if it was initially overabundant.

Another important molecule which can act as a coolant is CO, where it is mostly important at very low gas temperatures below 20 K. The cooling rate is comparable to C^+ in this low temperature regime which we can see clearly in Figure 4.1. Further, the higher rotational transitions for CO become quickly optically thick (self-shielded) which reduces its capability as a coolant.

Other molecules that are important for the cooling in the ISM are H_2O, HCN and N_2H^+. While they are sub-dominant compared to CO, H_2O can become the dominant coolant in warm molecular outflows (Nisini et al., 2010).

Dust cooling

We already saw that, it is very difficult to cool below 100 K and this is only possible by considering atomic line transitions of metals, fine structure line cooling and rotational and vibrational transitions

of molecules. For example, cooling via CO is efficient while the densities are not too high because specifically CO becomes strongly self-shielded at a density at around 2000 cm^{-3} for $J = 0$ and $J = 1$, while the $J = 2$ mode only becomes self shielded at around 20000 cm^{-3}. Self shielding is the process of selective photodissociation mostly in the far UV with a wavelength around 100 nm. Still, this raises the question how cooling works at very low temperatures when the gas becomes optically thick. Imagine a spherical cold collapsing cloud at around 20 K at low redshift where we have a metal mix comparable to the solar neighbourhood. This collapsing cloud converts gravitational potential energy in heat, which will counterbalance the collapse. To further collapse, fragment and finally form stars, this cloud has to radiate the heat away. Every system that is not in thermal equilibrium will undergo an energy flow to establish thermal equilibrium[2]. Thus, if dust and gas have different temperatures there will be an energy flow between gas and dust and the gas can loose energy via collisions. Further, dust can absorb UV-photons and re-emit them in the infrared, for which the dense clouds are typically optically thin. Dust cooling is therefore the dominant cooling process in dense regions.
While this argumentation works perfectly at low redshift, where SNe already established a good metal mix, that accounts for a reasonably high dust-to-gas ratio, the situation at very high redshift is more complicated as there are no metals to cool primordial molecular clouds. Lets assume the same cloud we assumed above at redhsift 6. The situation is completely different. First, the CMB-temperature at $z = 6$ is roughly at 19 K which basically set the cooling floor. This cloud can basically not cool, fragment and form stars. While cooling below 100 K can be established by molecules, cooling below 20 K is really difficult as there are no metals and dust and the CMB sets the pressure floor. To this day this is one of the most complicated problems in POP-III star formation as the primordial gas composition is very inefficient in cooling the gas below 20 K, which is directly linked to the strongly top heavy Initial Mass Function (IMF) of the first stars. This would then directly explain why one assumes that POP-III stars are so heavy, which is because the Jeans masses are higher at higher temperatures, favouring the collapse of larger gas structures, where fragmentation is prevented by the pressure floor of the CMB.

4.2.2 Heating processes in the ISM

The relevant heating processes in the ISM are much more straightforward to discuss than the cooling processes. The heating rate is typically denoted as Γ and the most important heating process in the ISM is photoelectric heating[3]. The idea is that a dust grain collides with a photon that has high enough energy to eject an electron from the outer shell of the dust grain. The residual energy of the photon that remains after the electron is detached can be converted in kinetic energy of the electron that quickly thermalises via collisions and gives back heat to the ambient ISM. The photo electric heating rate is typically given by Bakes and Tielens (1994):

$$\Gamma_{\rm pe} = 1.3 \cdot 10^{-24} \epsilon G_0 n \mathrm{ergs^{-1} cm^{-3}}. \tag{4.17}$$

G_0 is the ISRF. The parameter ϵ denotes the efficiency of the process given by:

$$\epsilon = \frac{0.049}{1 + (\psi/1925)^{0.73}} + \frac{0.037(T/10000)^{0.7}}{1 + (\psi/5000)}, \tag{4.18}$$

with $\psi = G_0 T^{1/2}$.
Another important heating source in the ISM is the UV-radiation of stars. The most important heating process of UV photons in the ISM is the so called UV-pumping of the H_2 molecule. In this scenario, an

[2] This is nothing else than the principle of least action
[3] Actually it is SN-feedback, but we discuss the fundamentals of radiative heating.

UV-photon is absorbed by a H_2 molecule which transits into an excited electric state. In the low density gas, this is not a very effective heating process, as the molecule quickly decays back to the ground state, by emitting a series of infrared photons. In the dense gas the situation is different, as the excited hydrogen molecule is more likely to be de-excited by a series of collisions that occur on a shorter time scale than the radiative transitions in very dense gas above 10^4 cm^{-3}. This process introduces around 2 eV in the ambient ISM. The other process that is important for heating in the ISM due to UV radiation is photodissociation of H_2, where the molecule is split apart by the interaction with an UV-photon, which typically results in higher velocities of the split apart single atoms. Those atoms are thermalising in the nearby ISM, with a net heating rate of 0.2 eV per photodissociation process.
Moreover, there is heating by cosmic rays, which is a very important source of heating in the dense gas, where self-shielding is already important. As cosmic rays are high energetic electrons or protons, they can heat the surrounding ISM by collisions. The energy loss of the cosmic rays due to a collision with hydrogen or helium atoms typically leads to full ionisation of the atoms. However, the energy carried by a cosmic ray is much larger than the energy needed for ionisation and the rest frame energy is converted into kinetic energy of the hydrogen atom or electron, thermalising and heating the nearby medium. In this process, typically order of 10 eV are brought into the ISM. Subsequent collisions of the excited hydrogen atoms and electrons can trigger more ionisation events. The cosmic ray ionisation heating can be described like (Glover et al., 2010; Krumholz et al., 2011):

$$\Gamma_{\rm cr} \approx 3.2 \cdot 10^{-28} (\zeta_{\rm H}/10^{-17} s^{-1}) n \text{ erg cm}^{-3} \text{ s}^{-1}, \tag{4.19}$$

with the cosmic ray ionisation rate $\zeta_{\rm H}$ of hydrogen.
Furthermore, X-ray radiation can play an important role in heating the ISM. The process is similar compared to heating by cosmic rays with one important difference. Cosmic rays are a very effective source of heating in the dense gas, where X-rays tend to be absorbed because they have a relatively short mean free path when the density is high and the gas is optically thick. In the lower density diffuse ISM, where the mean free path is longer the situation is different (Wolfire et al., 1995). X-rays are very energetic and can ionise hydrogen and helium easily with the excess energy being deposited in kinetic energy of the atoms and the now free electrons. This atoms and electrons can cause further ionisation events and effectively contribute to heating in the ISM.
Often neglected is the heating contribution by chemical reactions. Specifically the formation process of H_2 can release a high amount of energy into the ambient medium, as it is a strongly exothermic reaction. In lower density environments this is not effective for two reasons. The first is the low rate at which molecular hydrogen forms and the second is that a lot of the energy that is released in the formation process will naturally be stored in rotational or vibrational modes of the formed molecule, which will be released in a series of photons that radiate away the energy. In higher density environments, where the system is dominated by collisions, the energy stored in rotational and vibrational modes can be released via collsional de-excitation, heating the environment. The heating rate for H_2 depends on the H_2 formation rate given via (Jura, 1975):

$$R_{\rm H2} \approx 3 \cdot 10^{-17} n n_{\rm H} \text{ erg cm}^{-3} \text{ s}^{-1}, \tag{4.20}$$

which leads to the heating rate:

$$\Gamma_{\rm H2} \approx 2 \cdot 10^{-28} \epsilon_{\rm H2} n n_{\rm H} \text{ erg cm}^{-3} \text{ s}^{-1}, \tag{4.21}$$

where $\epsilon_{\rm H2}$ describes how efficient this heating process is.
Finally, heating can be initialised by dynamical processes in the ISM. Two main sources of heating can

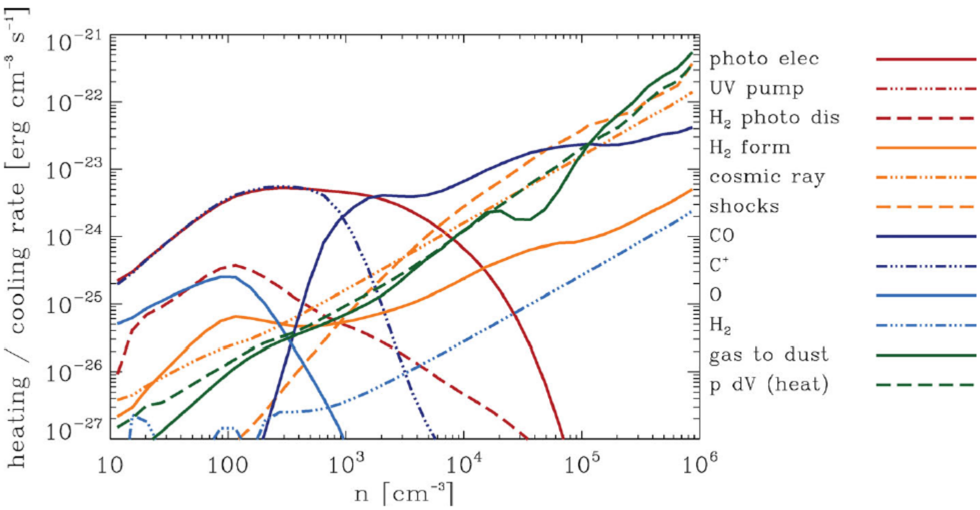

Figure 4.2: We show the cooling and heating rates for various processes as a function of the hydrogen number density. The Figure has been taken from Glover and Clark (2012).

be introduced by collapsing clouds due to adiabatic heating (usually referred to as PdV heating) or the energy cascade introduced by turbulence that decays and transports energy from the large scales to the small scales. The first process is very effective in dense cloud cores where it can be as least as effective as the heating by cosmic rays (Klessen and Glover, 2016). Turbulent heating can also be of similar significance as cosmic ray heating, with a heating rate given via (Pan and Padoan, 2009):

$$\Gamma_{\rm turb} \approx 3 \cdot 10^{-27} \left(\frac{L}{1\rm pc}\right) n \ {\rm erg\ cm^{-3} s^{-1}} \tag{4.22}$$

The main cooling and heating processes in the ISM are summarised in Figure 4.2, where the cooling and heating rates for different processes are displayed as a function of the hydrogen number density (see Glover and Clark, 2012, for details).

4.3 The formation of molecular Clouds

4.3.1 Molecule formation in the ISM

The formation of a molecular cloud in a galaxy undoubtedly involves the transition from atomic gas to molecular gas, hence the term molecular cloud. Specifically, this implies that most of the atomic hydrogen has to be converted in molecular hydrogen at some point of the formation process of a molecular cloud, which is triggered by chemical reactions. Molecular hydrogen can be formed via the following reaction:

$$\rm H + H \rightarrow H_2 + \gamma, \tag{4.23}$$

which is a relatively ineffective process with a low rate coefficient. Surprisingly, H_2 can be formed in partially ionised gas, if a hydrogen atom captures an electron which charge attracts another hydrogen atom, via the following reaction chain:

$$\rm H + e^- \rightarrow H^- + \gamma \tag{4.24}$$

$$\rm H^- + H \rightarrow H_2 + e^-. \tag{4.25}$$

In principle this reaction is supported by e^-, which acts as catalyst. Similarly one can form H_2 by the support of H^+ in the reaction chain:

$$H + H^+ \rightarrow H_2^+ + \gamma \tag{4.26}$$
$$H_2^+ + H \rightarrow H_2 + H^+. \tag{4.27}$$

Tegmark et al. (1997) point out that the fractional abundance of molecular hydrogen that can be obtained by this channels cannot exceed 10^{-2} and Glover (2003) state that the situation is even worse in reality as the ISRF lead to photodeattachment of H^- and photodissociation of H_2^+. However, the channel is massively important for primordial cooling channels. Still, the question remains how the massive amounts of H_2 that are observed in the galactic mid plane can be obtained when objectively all formation channels are inefficient. The answer is that reaction 4.23 can be supported by dust grains capturing a hydrogen atom and initialising the reaction as a catalyst (e.g. Gould and Salpeter, 1963), with the formation rate given in Jura (1975) (see equation 4.20), which leads to a formation time scale:

$$t_{\mathrm{H2,form}} = \frac{n_{\mathrm{H}}}{R_{\mathrm{H2}}} \approx 10^9 \mathrm{yr}\, n^{-1}. \tag{4.28}$$

This shows that the higher the density, the shorter is the timescale for H_2 formation.
Obviously, the formed H_2 can be destroyed, either by collisions or more importantly via spontaneous radiative photodissociation (Stecher and Williams, 1967; van Dishoeck, 1987). In this two stage process the H_2 molecule absorbs a photon with a larger energy than 11.2 eV, which results in an electronic excitation of the molecule. Now, the molecule de-excites back to the ground state and there are two possibilities how this can happen. If a rotational mode was excited by the photon, it just spins down by emitting a series of photons. In a vibrational mode, the molecule transits back over the vibrational continuum, which leads to de-attachment of the bounding hydrogen atoms. The UV-absorption lines that originate form this process are known as Lyman-Werner photons. This process is dependent on the self-shielding of H_2. In high density regions the Lyman-Werner photons are mostly absorbed by H_2 further outside in the region, shielding the inner region against the Lyman-Werner photons[4]
The other important transition from atomic to molecular gas is the formation of carbon monoxide (CO). Observationally, CO is an important tracer for molecular hydrogen as H_2 is not detectable in the cold gas (forbidden para-ortho transitions). The formation process of CO in the ISM is driven by the following reactions. First C^+ needs to recombine with electrons to form C:

$$C^+ + e^- \Longleftrightarrow C + \gamma. \tag{4.29}$$

C can be destroyed, again by photodissociation. We indicated that this reaction can be driven in both directions but there will be an equilibrium eventually. While this process is relatively easy and happens naturally, as the temperature of the ISM decreases, the formation of CO is more complicated. A good starting point is the following reaction:

$$C + OH \rightarrow CO + H. \tag{4.30}$$

This reaction has basically a zero activation energy and thus CO formation remains efficient even at very low temperatures when most of the carbon is already recombined and there is only little C^+.

[4]The principle is the same like the saying of the Stark family in Game of Thrones: The lone Wolf dies, but the pack survives.

Nevertheless, it is also possible to form CO over the ionised form of carbon following the reaction chain:

$$C^+ + OH \rightarrow CO^+ + H, \tag{4.31}$$
$$CO^+ + H \rightarrow CO + H^+, \tag{4.32}$$

in a direct channel. Further, it is possible tho obtain CO over some HCO^+ reactions:

$$CO^+ + H_2 \rightarrow HCO^+ + H, HCO^+ + e^- \rightarrow CO + H. \tag{4.33}$$

From this one can directly understand that OH is of paramount importance for the formation of CO. However, forming OH is not trivial. The most intuitive way to initialise this reaction is to have oxygen react with H_2:

$$O + H_2 \rightarrow OH + H. \tag{4.34}$$

As this reaction has an relatively high activation energy of order 0.26 eV, it is favoured in the warm diffuse ISM but not in the cold neutral medium in which molecular clouds form. Another channel for CO formation is initialised by H_3^+:

$$O + H_3^+ \rightarrow OH^+ + H_2. \tag{4.35}$$

These OH^+ molecules quickly react further in the following reaction chain:

$$OH^+ + H_2 \rightarrow H_2O^+; \tag{4.36}$$
$$H_2O^+ + H_2 \rightarrow H_3O + H. \tag{4.37}$$

This reaction has several by-products as the reaction efficiency for H_2 reacting with H_2^+ is fairly low. The by-products have channels that are important for CO formation as well, based on H_2O (water) and OH (Jensen et al., 2000):

$$H_3O + e^- \rightarrow H_2O + H, \tag{4.38}$$
$$H_3O + e^- \rightarrow OH + H_2, \tag{4.39}$$
$$H_3O + e^- \rightarrow OH + H + H, \tag{4.40}$$
$$H_3O + e^- \rightarrow O + H_2 + H. \tag{4.41}$$

Another way to form OH is given by cosmic ray ionisation of O^+, that can react to OH in the following manner:

$$O^+ + H_2 \rightarrow OH^+ + H. \tag{4.42}$$

The bottleneck in all these channels is the formation of OH^+. Once this is established the rest falls into place rather quickly (Klessen and Glover, 2016).
CO can also be formed via simple hydrocarbons that should be present in the evolved ISM of galaxies like the Milky Way, specifically CH, CH_2 and CH^+. The latter can trivially be formed by two different reactions:

$$C^+ + H_2 \rightarrow CH^+ + H, \tag{4.43}$$
$$C^+ + H \rightarrow CH^+ + \gamma. \tag{4.44}$$

Interestingly enough both of these reactions are slow. The first one suffers from a high activation energy of roughly 0.4 eV. The second one is slow because radiative association of species is relatively unlikely. Even together these reactions have so low reaction rates in the cold neutral and diffuse atomic medium that it is not possible to explain the amount of observed CH, suggesting that other processes dominate its formation (Godard et al., 2009; Sheffer et al., 2008). Therefore, in ionised gas this reaction is dominating:

$$C^+ + H_2 \rightarrow CH_2^+ + \gamma, \tag{4.45}$$

which is also a radiative association process, but with a higher rate coefficient (McElroy et al., 2013). CH^+, once present can react very fast with molecular hydrogen in the reactions:

$$CH^+ + H_2 \rightarrow CH_2^+ + H, \tag{4.46}$$
$$CH_2^+ + H_2 \rightarrow CH_3^+ + H \tag{4.47}$$
$$CH_3^+ + H_2 \rightarrow CH_5^+ + \gamma, \tag{4.48}$$

where the latter is very unlikely but still possible. Due to this fact most of the CH_3^+ will recombine with electrons instead:

$$CH_3^+ + e^- \rightarrow CH + H_2, \tag{4.49}$$
$$CH_3^+ + e^- \rightarrow CH + H + H, \tag{4.50}$$
$$CH_3^+ + e^- \rightarrow CH_2 + H. \tag{4.51}$$
$$\tag{4.52}$$

These hydrocarbons quickly react to CO:

$$CH + O \rightarrow CO + H, \tag{4.53}$$
$$CH_2 + O \rightarrow CO + H_2, \tag{4.54}$$
$$CH_2 + O \rightarrow CO + H + H. \tag{4.55}$$
$$\tag{4.56}$$

The CO formed via these channels can either be destructed by photodissociation or by chemical reactions with single ionised helium to neutral helium, ionised carbon and ionised oxygen.
In summary, this gives us two formation channels for molecular hydrogen, dust catalysed or H^- catalysed and two larger formation channels for CO over OH and various hydrocarbons. However, one could also specify more formation channels for CO by considering the various formation channels for OH. Nowadays, these chemical reactions can be modelled in chemical reaction networks in galaxy wide simulations by directly solving the non-equilibrium rate equations for different species alongside with all the necessary and complicated photo-chemistry. For the numerical details we refer to the excellent papers of Simon Glover (e.g. Glover, 2003; Glover and Clark, 2012; Glover and Mac Low, 2007a,b) who is the expert in chemical modelling in simulations of star and galaxy formation.
This transition from atomic to molecular gas is then strongly driven by the column density of the ambient medium. In this context not only the self-shielding mechanism of H_2 is important but also the shielding process by dust which supports the formation of molecular hydrogen and CO. If the column density is low the photodissociation rates of H_2 and CO are high due to the effective coupling to the ISRF. In high column density regions this is hindered by self-shielding and shielding by dust. These high column density regions have a large visual extinction, which depends not only on the

ISRF, but also on the coupling of the shielding to the photon field and the volume that is occupied by the gas. While the latter two show only linear dependence on the visual extinction the first one is actually exponentially dependent and thus dominating the visual extinction. In giant molecular clouds (GMCs) the gas transients from atomic hydrogen to the molecular hydrogen phase at a visual extinction of around $A_\mathrm{v} \approx 0.1-0.2$ (Krumholz et al., 2008), while the transition from ionised carbon to CO happens at higher visual extinction of $\mathrm{A_v} \approx 1$ (Wolfire et al., 2010). For solar neighbourhood conditions the resulting hydrogen column densities that have to be reached are $2 \cdot 10^{20}$ cm^{-2} for H to transient to H_2 and $2 \cdot 10^{21}$ cm^{-2} for carbon to transient to CO. This picture changes drastically under high redhshift conditions or in low metallicity galaxies, where higher column densities are required to trigger the transition. While the densities are generally higher at high redshift, this is less of a problem for high redshift galaxies but more of a problem for low redshift dwarfs with the important observational conclusion that they do not contain a lot of fractional mass in the molecular phase (Leroy et al., 2005).

The gas temperature is also affected by the increase of the visual extinction in the regions of interest. The higher the visual extinction coefficient, the lower the gas temperature gets, as photoelectric heating becomes very inefficient. One can immediately realise why this is extremely important for the formation of molecular clouds by considering the Jeans mass which gives the critical threshold for gravitational collapse:

$$M_\mathrm{J} \approx 60 M_\odot \mu^{-2} T^{3/2} n^{-1/2}, \tag{4.57}$$

with the mean mass per particle μ and the total number density n. The Jeans mass can now decrease almost by a factor of 40 due to two effects. First, the mean particle mass is increased in the transition from atomic to molecular gas by around a factor of 2.5 Second, the temperature drops by a factor of 6. Combined this significantly reduces the Jeans mass and supports the formation of molecular clouds. Furthermore, the drop in temperature reduces the sound speed c_s by a factor of $\sqrt{6}$ which increases the Machnumber and interstellar turbulence can engage more strongly on the ISM by forming high density regions. This will subsequently have an effect on the local star formation rate and consequently one would assume that there is an observed correlation between visual extinction, not only with the column density of H_2 but also with the star formation rate density. The former can be assumed to be driven by molecular cooling and one typically puts the conclusion forward that gas of order 10 K is star forming (Bergin and Tafalla, 2007) which can exclusively reached by molecular cooling, indirectly suggesting that star formation takes place exclusively in molecular gas. However, other groups (e.g. Glover and Clark, 2012; Krumholz, 2012) put the idea forward that the star formation rate is insensitive to whether the gas is in the atomic or the molecular state and undermine their claims with detailed numerical simulations. However, it is interesting to point out that star formation seems to be highly correlated with molecular gas in observations and is observed to take place in regions of high H_2 column density above $7.5 \cdot 10^{21}$ cm^{-2} (Klessen and Glover, 2016).

Finally, we briefly discuss the current understanding of how molecular clouds form in galaxies. The formation of molecular clouds are highly connected to the formation process of galaxies. While gas is falling onto dark matter potentials it first gets compressed, cools down, gets shocked and heated again before it starts to cool down and settle in the centre of the dark matter potential. While the density of the gas increases it enables the transition to molecular gas and finally molecular clouds can form in high column density, shielded regions of the ISM. Therefore, molecular clouds always form when the latter condition is fulfilled. Now one has to understand which physical processes drive the gas in dense regions and keep it there.

One of the first models for the formation of molecular clouds is the model proposed by Oort (1954) the so called coagulation model. The model has been further developed by different authors (Field,

1965; Kwan, 1979; Tasker and Tan, 2009; Tomisaka, 1984). The idea behind this model is to assume that the ISM is subdivided in groups of smaller clouds of cold atomic gas that just cools down from the warm gas reservoir of the galaxy by the thermal instability (Field, 1965). These clouds start to collide and form larger and larger clouds, until the cloud is able to shield itself against the ISRF, transients from atomic to molecular gas and initiates star formation. The shielded clouds can undergo further collisions until the stellar feedback from the first massive star population (e.g. radiation, SNe...) destroys the cloud. This model has the big advantage that the stochastic process of colliding clouds directly establishes a power-law mass function which is observed (e.g. Alves et al., 2006). Further, the model naturally explains why there is more gas in the molecular state in spiral arms. Furthermore, the angular momentum transport during cloud-cloud collisions can explain why there are clouds rotating in different directions compared to the angular rotation of the gas in the disc (e.g. Dobbs, 2008; Imara and Blitz, 2011; Phillips, 1999; Tasker and Tan, 2009).
The model has the same flaw like the similar models that have been brought forward by a number of authors in the theory of planet formation. While it is easy to build smaller clouds by collisions, collisions between larger clouds could might as well disrupt them again. Furthermore, the time scale to accumulate a cloud with a mass above 10^5 $M_\odot$ is above 100 Myr which is factor of 10 larger than the expected lifetime of a molecular cloud (Klessen and Glover, 2016). On top of this, it seems highly unrealistic that the ISM is structured like the coagulation model suggests, as this requires confined isolated high density clouds which are driven by cloud-cloud collisions and their size is limited to the high density region within the cloud. However, as we pointed out above, they are called molecular clouds for a reason and observationally it makes more sense to define a molecular cloud as the regions where the CO emission is located. Thus the border of the cloud is not given by a density drop but rather by a change of the chemical state of the ambient gas from molecular to atomic (e.g. Motte et al., 2014; Wannier et al., 1983).

As there are some problems with the coagulation model one has to further develop a theory of molecular cloud formation. A promising approach is the so called converging/colliding flow model where one assumes that molecular clouds form in over dense post-shock regions where lower density gas structures collide[5] and fall victim to rapid cooling of thermally unstable gas, quickly forming a cold, dense region with $n \approx 100\,\mathrm{cm}^{-3}$ (e.g. Heitsch and Hartmann, 2008; Hennebelle and Pérault, 1999, 2000; Koyama and Inutsuka, 2002). There are several physical processes that can drive the converging flow in the gas. The most prominent process is gravo-turbulent motion followed by instabilities introduced by the Parker-Instability in spiral galaxies (Parker, 1966). Another option to achieve converging flows in the gas is to generate ISM turbulence by feedback processes in the ISM (mostly SN-feedback). We show the highly turbulent structure of a molecular cloud complex that was supposedly formed by a similar process in Figure 4.3 where we display the Orion molecular cloud complex.

4.4 Star formation and star clusters

4.4.1 The structure of cloud cores

The dense molecular cloud cores that can be formed by such molecular cloud formation channels are the spatial regions of active star formation. To understand how star formation takes place in molecular cloud cores, one has to understand their detail internal structure. The overall cloud follows a mass spectrum of the form of a single power-law. However, extending the mass spectrum to smaller and

[5]This is not so different from galaxy formation models that are based on the controversial idea of cold streams via a process that is usually referred to as Dekel-Birnboim accretion of cold filaments(e.g. Dekel et al., 2009).

Figure 4.3: The Orion molecular cloud complex of two colliding, star forming molecular clouds that are disrupted by the feedback of SNe which established a prominent ring around the complex that is very well visible due to Hα emission. Taken from `https://apod.nasa.gov/apod/image/1010/Orion2010_andreo2000.jpg` at the 30.07.2020.

smaller scales shows that the mass spectrum of pre-stellar cores is more similar to the structure of the IMF (e.g. Johnstone et al., 2001; Lada et al., 2008; Motte et al., 1998; Testi and Sargent, 1998). This would imply that the IMF is a direct result of the structure that is obtained by fragmenting molecular clouds. The density structure of the cloud is similar to a Bonnor-Ebert sphere (Bonnor, 1956; Ebert, 1955) with a flattened core around 10^6 cm^{-3}. The gas motion inside molecular clouds is typically dominated by supersonic turbulence, while the velocities inside fragmented cloud cores are usually subsonic with typical inflow velocities of order 0.1 km s^{-1} on a spatial scale of 0.05 pc. However, in practice the numerical modelling on this part is insufficient to this day and one needs full radiative transfer and magnetic fields in the cloud cores to accurately model them. The temperature structure of clouds cores show only a very weak radial dependence when compared to the rest of the galaxy, with central values ranging from 8 – 12 K and outside temperature of 15 – 20 K. Typically, there is a ring like emission of carbon molecules but nitrogen based molecules show more resemblance with the local dust emission which can indicate that the nitrogen species are still in the gas phase while carbon is condensed out on dust grains (e.g. Lada and Lada, 2003). Finally, magnetic fields can also play a crucial role in molecular cloud cores. There is a famous bi-modality for whether magnetic fields stabilise cloud cores or trigger their collapse, based on the mass to flux ratio. A cloud becomes supercritical when this ratio is larger than some threshold. On the other hand however, if the mass to flux ratio is subcritical the core is stabilised by magnetic fields. In other words if the mass is low enough to be stabilised by the current magnetic flux the core is stable (e.g. Spitzer, 1978). While for galaxies mainly irrelevant, for molecular clouds and cloud cores effects of non-ideal MHD, like ohmic resistivity, hall effect and ambipolar diffusion can be of relevance as the magnetic field strength can easily exceed the μG regime (e.g. Wurster et al., 2019).

4.4.2 Stars and star clusters: A look from statistics

Not only the detailed formation process of stars is important, but also the statistical implications of star formation, timescales and the spatial properties play a crucial role. Typically, the star formation time scale can be related to the collapse time scale of a molecular cloud, which is of the order of a Myr. Hereby it is interesting to point out, that the cloud structure is tightly coupled to the structure of the resulting star cluster. High density, high mass clouds have a higher star formation efficiency than low density, low mass clouds which further shapes the structure of the star cluster leading to a population of more massive stars in the former with up to a few 100 members and less massive stars in the latter case with around 10 members. The formation of dense nuclear star clusters or globular cluster systems is rare and it is hard to actually form a star clusters with more than 1000 stellar bodies.
Stellar mass is the most important driver of stellar evolution as the stars luminosity increases with a strong power-law exponent of 3.5 with the stellar mass. Stars produce energy by nuclear fusion of hydrogen to helium as long as they are on the main-sequence. The rate at which they burn hydrogen and convert it to helium determines their exact place on the main-sequence. However, determining the distribution function for these stars is a tricky task. Typically, one can assume that the IMF has the form of a power-law:

$$\frac{dN}{dM} \propto M^{-\alpha}, \tag{4.58}$$

where α is the power-law exponent that was derived empirically for the first time by Salpeter (1955) for stars above 1 $M_\odot$ yielding $\alpha = 2.35$. However, this can be improved and extended for lower mass stars as well, as carried out by Kroupa (2001) who used the idea of a broken power-law to describe the shape of the IMF. Another approach has been taken by Chabrier (2003) who suggests a log-normal distribution with a power-law scaling. In practice the three distributions do not differ strongly which we show in Figure 4.4

4.4.3 The role of turbulence: Formation of low mass stars

Theoretically, low mass star formation is better understood than high mass star formation. This is highly related to the fact that there are many more low mass stars than high mass stars. In the 1980's it was an established picture that low mass stars form in clouds which are magnetically sub critical (Shu et al., 1987) while being balanced by ambipolar diffusion (e.g. Mouschovias, 1976) which is regulating the magnetic flux until a mass to flux ratio is established which enables collapse. However, this only works if the timescale for ambipolar diffusion is much longer than the dynamical time of the system. This is not what is observed, where timescales of the same order of magnitude are typically obtained. Furthermore, numerical investigations suggest that this can be even more crucial as several groups indicate that the ambipolar diffusion timescale is much shorter than the dynamical time (e.g. Fatuzzo and Adams, 2002; Heitsch et al., 2004; Li and Nakamura, 2004). The fact that ambipolar diffusion seems to be a very efficient process in the ISM makes this whole model tumble and the today state-of-the-art view on low mass star formation is that it is triggered via fragmentation due to supersonic turbulence (e.g. Mac Low and Klessen, 2004; McKee and Ostriker, 2007; Offner et al., 2014). On the larger molecular cloud scale, turbulence can prevent the collapse of the cloud, but on smaller scales, turbulence is very effective in generating high density regions that can locally collapse and trigger the formation of star clusters. We illustrate this process in Figure 4.5 which we took from Klessen (2011). In this picture turbulence is generating a hierarchy of clumps in a molecular cloud that can locally collapse. The clumps collapse to star forming regions while the whole molecular cloud is collapsing. In very dense regions these clumps can merge to structures that contain several proto-stars

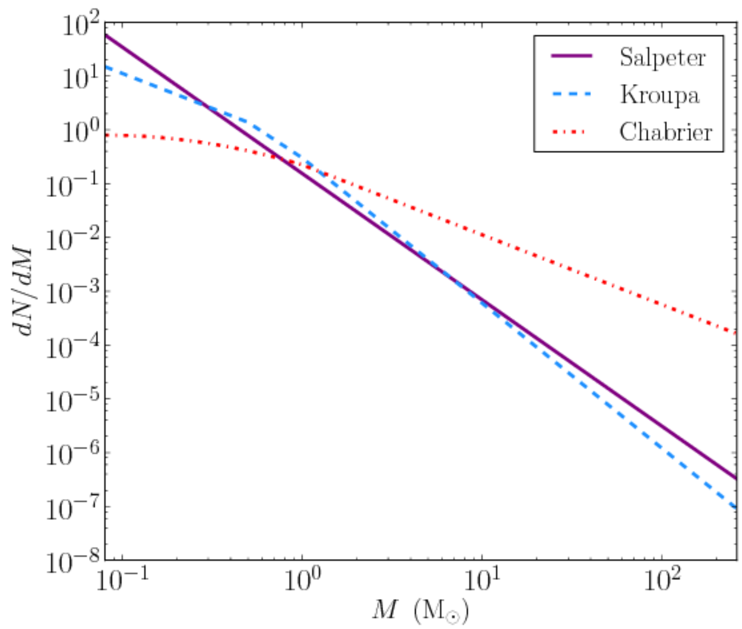

Figure 4.4: We show the three most commonly used initial mass functions following Salpeter (1955), Kroupa (2001) and Chabrier (2003).

which will go on to form the first small star clusters. In this small star clusters there is competition of the stars for the gas mass in the clump to become more massive. Furthermore, the mass growth of the star cluster is regulated by direct N-body scattering of the cluster members, which can lead to the ejection of low mass stars from the clusters and circumvent the accretion process. Finally, the clump is disrupted by the photoionising feedback of the first main-sequence stars that form in the cluster, which can establish an extended HII-region of ionised hydrogen around the star cluster which itself is then mainly cleared of ambient gas. In Figure 4.6 we show a star cluster that could have been obtained in a similar process.

4.4.4 The IMF from first principles

Even after all these years, the theoretical origin of the IMF remains unclear. However, the community has made significant progress over the past years to get a good theoretical understanding of possible physical processes for the origin of the IMF. Klessen and Glover (2016) report three main ideas that lead to a theoretical determination of the IMF from straightforward statistical processes, namely the core accretion model, the collective model and a model that accounts for the thermodynamical behaviour of the gas. In the core accretion model one simply assumes that there is a one-to-one correlation between the mass distribution of cores in molecular clouds and the IMF. While these typically yield a factor of around three difference in normalisation, this could be explained by feedback of stars in the clumps that makes star formation less efficient compared to clump formation (e.g. Matzner and McKee, 2000). This yields a peak at the Jeans length combined with a power-law.
The collective model makes use of the observational evidence that most stars form in clusters, rather than as isolated objects. While the peak is again settled via the Jeans mass, the tail is established by interactions of proto-stars and not by further fragmentation of clumps. The third approach is based on

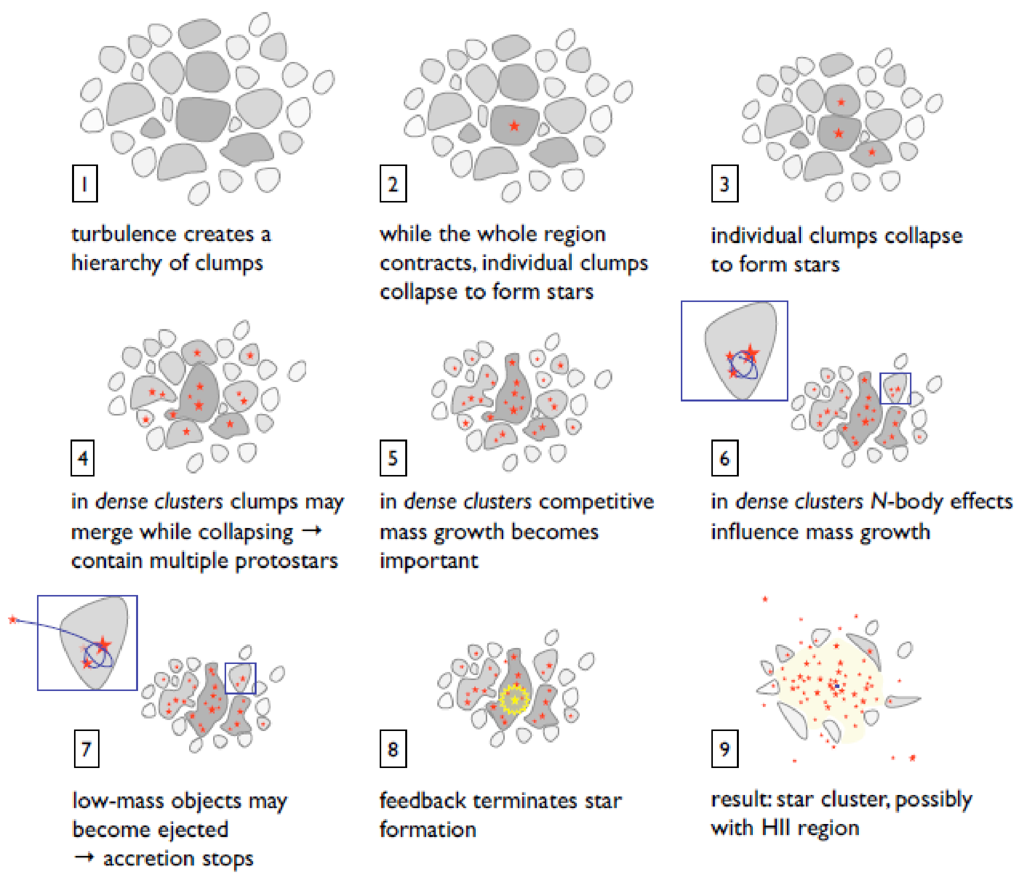

Figure 4.5: Schematic sketch of the formation process of star cluster in dense molecular clouds cores. The figure has been taken from Klessen (2011).

Figure 4.6: Typical picture of a star cluster that can be formed via cloud fragmentation due to supersonic turbulence in the dense cores of molecular clouds, taken from https://apod.nasa.gov/apod/image/1810/NGC1898_Hubble_2913.jpg, at 30.07.2020.

the fragmentation properties of compressed gas and accounts for the fact that not all of the gas falls victim to fragmentation as the clumps collapse.

The IMF derived from statistical physics

Interestingly enough, it is possible to achieve some understanding about the IMF from purely applying statistical mechanics. The basic idea is to define a dimensionless mass m in units of the solar mass with:

$$m = \prod_{i=1}^{N} x_i, \tag{4.59}$$

and transfer that into log space via:

$$\ln m = \sum_{i}^{N} \ln x_i + \text{constant}. \tag{4.60}$$

The constant term on the right hand side of 4.60 is based on all physical constants that play a role like k_B or G. Now, we transform into normalised variables

$$\xi_i = \ln x_i + \langle x_i \rangle = \ln\left(\frac{x_i}{\overline{x}_i}\right). \tag{4.61}$$

We can straightforward solve for the mean and the second moment σ via:

$$\overline{x}_i = \int_{-\infty}^{\infty} \ln x_i f_i(\ln x_i) d\ln x_i. \tag{4.62}$$

and

$$\sigma_i^2 = \int_{\infty}^{\infty} \xi_i^2 f_i(\xi_i) d\xi_i, \tag{4.63}$$

with the distribution function f_i. One can further introduce the canonical variables $\Xi = \sum_i \xi_i$ and $\Sigma^2 = \sum_i \sigma^2$. By doing so, one obtains a Gaussian distribution function for f with:

$$f(\Xi) = \frac{1}{\sqrt{2\pi\Sigma^2}} \exp\left(-\frac{1}{2}\frac{\Xi^2}{\Sigma^2}\right). \tag{4.64}$$

And we find the mass function $\ln m = \ln m_0 + \Xi$ which yields:

$$\ln f(\ln m) = A - \frac{1}{2\Sigma^2}\left(\frac{m}{m_0}\right)^2. \tag{4.65}$$

This directly gives the log-normal distribution of the IMF, which is consistent with several stellar systems close to the sun (Miller and Scalo, 1979).

The IMF from variable accretion rates

To first order, obtaining a log-normal distribution for the IMF is already good. Nevertheless, the power-law tail can not be obtained with the modelling presented thus far. One can therefore account for stellar growth with a simple accretion model (e.g. Maschberger, 2013), where the mass of a single star changes via:

$$dm = m^{\alpha} A dt. \tag{4.66}$$

In this context A and α are constants, that are accounting for the physical properties of the accretion model. A classic choice would hereby be the Bondi-Hoyle-Lyttleton (BHL) accretion model with $A = 2\pi G^2 \rho/(v^2 + c_s^2)^{3/2}$ and $\alpha = 2$ (Bondi, 1952; Hoyle and Lyttleton, 1939). While A varies with more detailed accretion models[6] that can for example be obtained by direct numerical simulations. However, the parameter α is always close to two. One can assume now that the accretion rate changes via some mean growth rate and some fluctuations around the mean value of accretion:

$$dm = m^{\alpha} A dt + B dW, \tag{4.67}$$

where BdW gives the accretion rate fluctuation around its mean Adt. The idea is to make the model complex enough to account for mass loss of the star for example due to proto-stellar outflows[7]. Despite this higher complexity, one has to limit the term BdW to not over estimate the outflow rate which would yield negative masses for the stars. Finally, one can integrate equation 4.67 and obtains:

$$m(t) = \left[(1-\alpha) \left(\frac{m_0^{1-\alpha}}{1-\alpha} + At + BW(t) \right) \right]^{1/(1-\alpha)}. \tag{4.68}$$

From this, one can obtain a probability distribution function, that gives a log normal distribution for low mass stars with an extended power-law tail towards high mass stars:

$$f(m,t) = \frac{1}{2\pi^{1/2} m B t^{1/2}} \exp\left(-\frac{1}{2B^2 t} (\log m - \log m_0 - At)^2 \right). \tag{4.69}$$

The IMF set by turbulence

A working IMF model can also be obtained from the theory of turbulence by computing the density probability distribution function (PDF) from which the clump mass function is obtained. Via clump collapse and re-mapping this gives a model for the IMF. Thus a good starting point for this model is to come up with the PDF, established by supersonic turbulence. The shape of the PDF is driven by the compressive modes in the ISM. This compressive modes drive the ISM locally in converging flows where the density can easily increase. The exact structure of the compressive modes depends highly on Mach number, magnetic field and the thermal gas properties. The resulting PDF is typically isothermal with a Gaussian shape:

$$PDF(s) = \frac{1}{\sqrt{2\pi\sigma_s}} e^{\frac{-(s-s_0)^2}{2\sigma_s}}. \tag{4.70}$$

[6] BHL-accretion is spherical, which is probably a good approximation in the first stages of proto-star accretion. In the later stages it can in principle not be a good approximation as angular momentum forces the gas around the proto-star in a disc, establishing a thin plane that is settling the accretion rate (e.g. Shakura and Sunyaev, 1973).

[7] Actually, this is an important feedback process even in galaxy scale simulations because it enables feedback on the free-fall time scale that can last up to Myr timescales, before photoionising feedback disrupts the cloud core and stops star formation. This fact is completely ignored by all galaxy formation simulations and it would be interesting to study this further.

The parameter σ_s can directly be related to Mach number and plasma $\beta = c_s^2/(B^2/8\pi\rho)$:

$$\sigma_s = \ln\left(1 + b^2\mathcal{M}\frac{\beta}{\beta+1}\right). \tag{4.71}$$

The Gaussian shape of the IMF can be altered by non-isothermal gas (adiabatic index $\gamma \neq 1$). For $\gamma > 1$ one finds an extended tail towards lower densities and for $\gamma < 1$ an extended tail towards higher densities. Furthermore, the same effect can be observed for self-gravitating fluids, where the dense regions can undergo gravitational collapse which establishes a tail at higher densities.
From this PDF we have to find the clump mass function (CMF). The most common assumption is hereby, that the CMF directly follows shock-compressed supersonic gas. From the jump conditions of the shock, one finds the density contrast generated by turbulence (Elmegreen, 1993; Padoan and Nordlund, 2002; Padoan et al., 1997), which provides the clump mass. Another straightforward formalism to achieve this, is to adapt the fluctuation growth from galaxy formation via the Press-Schechter formalism (Press and Schechter, 1974) and several authors have extended this formalism to clump growth (Hennebelle and Chabrier, 2008, 2013; Hennebelle and Ciardi, 2009; Inutsuka, 2001)
The next step is, to determine the amount of clumps that undergo gravitational collapse which is typically done by some Jeans-mass approximation (Jeans, 1902) and clumps with masses above the Jeans threshold undergo collapse. The issue with this is the following. Both methods (turbulent compression and extended Press-Schechter) for getting the CMF are based on establishing the mass hierarchy of the clumps. This does not account for the density or the thermal properties which are essential for the Jeans mass calculation. This can be solved numerically by assuming reasonable cloud temperatures and drawing random numbers from the PDF.
Now, that we have the collapsing and star forming clumps we just have to re-map its mass distribution to the IMF, where usually a constant efficiency of around 30 per cent is taken into account.

4.4.5 High mass star formation

In the last section of this chapter we briefly want to highlight the problems in the theory of massive star formation. While it is well established that the feedback from massive stars has a huge impact on driving the baryon cycle in galaxies it is hard to develop a conclusive theory of their formation because this happens on the time scale of 100,000 years. The regions of high mass star formation are typically more extreme by a factor of 10 in terms of clump mass and clump size compared to low mass star forming regions (Krumholz, 2014). The massive stellar bodies are normally members of star clusters which complicates the theory on the formation process as they could be heavily engaged in N-body scattering processes. Another complication is the short Kelvin-Helmholtz time scale for massive stars which means that they are still actively accreting material when they start hydrogen burning in their centres and this has to be taken into account together with the strong photoionising feedback that takes place, once these stars reach the main-sequence (Keto, 2002, 2003, 2007; Peters et al., 2010a,b). Today there are two established mechanisms for high mass star formation. The first is that massive stars are always formed in stellar clusters as remnants of colliding low mass proto-stars in dense nuclear star clusters. This seems to be rather unlikely though, because the star clusters density must be extremely high to be dominated by direct N-body scattering (Baumgardt and Klessen, 2011; Portegies Zwart et al., 2010). The other approach is that the formation process is the same as for low mass stars where they start collapse and form an accretion disc, where the radiation can escape easily in the northern and southern poles of the stars perpendicular to the accretion disc. The other problem of massive star formation is the observed upper mass limit of around 150 $M_\odot$ which could be resolved by feedback of ionising radiation or fragmentation of accretion discs early on.

Chapter 5

Numerical Methods

In this chapter we discuss the numerical methods that are currently used to tackle state-of-the-art challenges in the field of galaxy formation and evolution. We start this chapter with a general note. While there is a consensus within the community how to deal with gravitational N-body calculations, the computation of hydrodynamical flows is more tedious and different groups use different approaches that have different advantages and disadvantages and one should consider the problem at hand before choosing the method to solve for hydrodynamical flows. However, in practise this is often not the case and the choice for the hydro-solver is more made by a day-by-day working experience with a certain code.

Thus, this brief introduction of this numerical methods chapter is a brief warning to the reader. The research work presented later in this thesis uses a wide variety of methods for computing the fluid fluxes within a simulation framework that is more driven by a setup choice and the advantages of each numerical scheme towards solving that numerical setup with the highest possible accuracy (convergence). During the course of this thesis we will use four different but highly related methods for solving hydrodynamical fluxes. The classic Smoothed Particle Hydrodynamics (SPH) method, first in its density entropy formulation, second in its pressure-energy formulation. As a central part of this thesis is to further improve the numerical treatment of the Euler-equations we present and use the new meshless finite mass (MFM) and meshless finite volume (MFV) methods and implement them into our working version of Gadget following the implementation of Hopkins (2015) in the code Gizmo. These methods use a SPH-density interpolation but solve for the fluid fluxes with a Riemann-solver which makes them generally more robust towards various numerical instabilities.

5.1 N-Body methods

5.1.1 Direct Summation

The simplest method for obtaining orbits of a gravitational N-body system is the method of direct summation. This method evaluates the gravitationel potential $\Phi(\mathbf{r})$ of a cloud of point masses by summing over the masses of the individual points. This potential represents the correct Newtonian gravitational potential from which one can obtain the acceleration on each particle in the simulation domain. This can be integrated to compute the update velocities and positions after the timestep Δt using the numerical integrator of choice (see 5.6 for a detailed discussion on the best choice). The potential is calculated in the following manner (Dolag et al., 2008; Springel, 2010):

$$\Phi(\mathbf{r}) = -G \sum_i \frac{m_i}{(|\mathbf{r}_j - \mathbf{r}_i|^2 + \varepsilon^2)^{\frac{1}{2}}}. \tag{5.1}$$

The factor ε is known to be the gravitational softening. It is introduced for two different reasons. The first (and the major) one is to ensure numerical stability of the scheme. Let us imagine two particles at exactly the same spatial point r_i. Thus $\mathrm{r}_i = \mathrm{r}_j$ in equation 5.1, resulting in a zero denominator. This results in a infinite acceleration, resulting in a infinite change of velocity over the time step Δt, subsequently resulting in a infinite change of the position vector. This renders the system numerically unstable as we could easily construct arbitrary orbits for an N-body system fulfilling these conditions. By introducing a small offset (softening) of the potential with a (small) finite value we elegantly circumvent this complication introduced by the nature of Newtons second law for gravitational N-body interactions. The softening then acts as a maximum value for the acceleration that a particle in the N-body system can experience. While this is a useful numerical trick it also has a physical motivation coming from the systems we try to model throughout this thesis, namely galaxies that are collisionless N-body systems (to first order). In this framework the softening ensures the collisionless nature of the system by preventing that particles can come each other close enough that the approximation of a collisionless systems breaks down by giving the point masses a physical size of ε. In practice the choice of ε for a certain simulation is a tedious task as it depends not only on the system size but also on the resolution (spatial and mass) of a certain simulation and there is no clear consensus in the community how to appropriately set the softening for a simulation. However, there is a rule of thumb which is given by the mean particle spacing in the simulation. The softening should always be smaller than the mean particle spacing, by roughly a factor of 10 to 100. But this depends again on the dynamic range of the system. The softening is typically constant in a simulation which introduces several problems. For example in a cosmological volume simulation the voids are under resolved compared to the filaments, and cluster environments but still the same softening is applied despite the fact that the mean particle spacing is orders of magnitude different between those environments. Thus many groups suggested to make the softening a function of the spatial region, as $\varepsilon = \varepsilon(\mathbf{r})$. However, this immediately introduces numerical issues as we break the symmetry of equation 5.1, resulting in energy conservation issues of the scheme. While it is possible to correct for this, it remains tricky as the correction terms act highly non-linear.

While this formulation of the Newtonian potential is the most accurate representation of the Newtonian potential it comes at the numerical disadvantage of $O(N^2)$ computational operations. Thus one has to raise the question if it is possible to optimise the force calculation.

5.1.2 Tree-Code and Peano-Hilbert-Curves

The answer to this question is provided by the so called Tree-code (Barnes and Hut, 1986) that evaluates gravitational forces by subdividing the simulation domain in a tree like structure and evaluating the multipole moments of the separate leaves of the tree. Most codes hereby only use the monopole moment for the force evaluation to save computational cost. Overall the method reduces the computational cost from $O(N^2)$ to $O(N\log(N))$.

The idea of the method is to group force calculations of particles with a large distance from the point $\mathbf{r}$ together and perform a multipole expansion that is cut after the monopole moment. The tree is initialised as a hierarchical oct-tree (in three dimensions) or a quad-tree in two dimensions. We visualise the quad-tree in Figure 5.1.

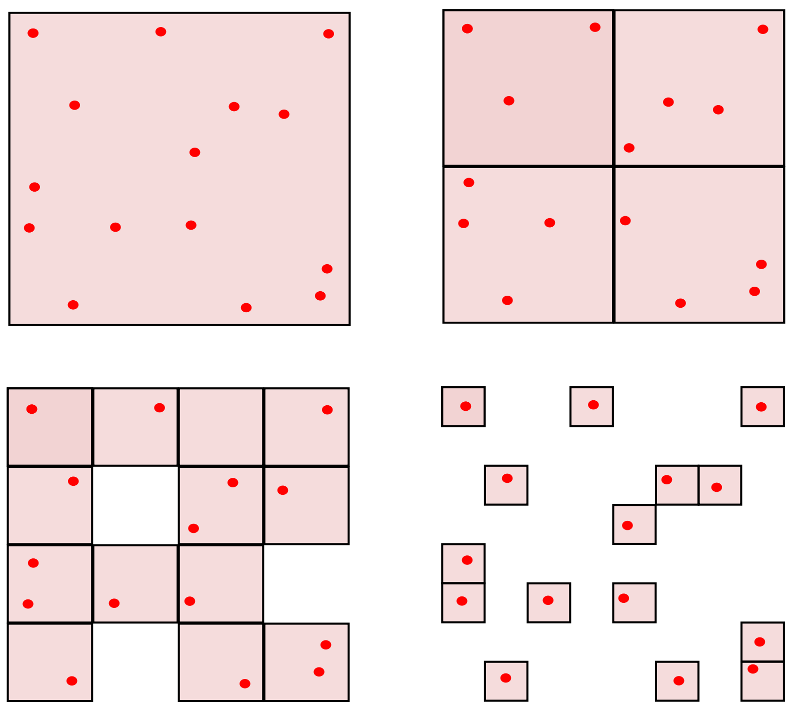

Figure 5.1: We show a schematic sketch of how a hierarchical quad-tree can be realised in two dimensions. We construct sub volumes around the particle distribution and reject all the empty leaves, leaving us only with the relevant leaves for the particular distribution of particles. A similar Figure can be found in Springel et al. (2001b).

Hereby, the simulation domain is split into cubes (squares in two dimensions) by subdividing the edges of the cubic (squared) form of the simulation domain at the midpoints of their edges. This procedure is repeated until only one particle (or none particle) is left within on the sub domains. The actual force calculation is then initialised from the root of the tree. For each domain we calculate the centre of mass. If the position **r** for which we want to calculate the force via the tree is far away from the root node we compute the monopole moment. Thus all the particles in the root node contribute to the force calculation with the monopole moment. On the other hand if the we are close to the point **r** at which we want to calculate the force we evaluate the monopole moments of the children of the respective root node and the procedure continues, controlled by the following criterion:

$$\theta = \frac{s}{r}, \tag{5.2}$$

where s denotes the size of the internal node and d the distance from **r** to the centre of mass of the respective node. If we assume that only the monopole moment is taken into account we can reformulate by assuming the mass within a node at distance r and correcting for the side-length of the respective node. We obtain:

$$\frac{GM}{r^2}\left(\frac{l}{r}\right)^2 \leq \alpha \mathbf{a}, \tag{5.3}$$

where M is the enclosed mass, l is the side length of the cell and r is the distance from the point at which we want to derive the force. This is controlled by a small quality factor α and the respective acceleration **a**. As long as the above criterion is met there will be no new root openings. Now, let us assume that the quality factor α is set to zero. If this is the case the opening criterion is always violated and forces are computed by summing over the monopole moments of each sub-division. However, this means nothing else than calculating the direct sum.

While tree codes are extremely efficient in calculating gravitational forces for arbitrary particle configurations they can suffer from numerical artefacts (force errors) when the distance to the nearest particle within one node becomes very small. In this case the opening criterion of equation 5.3 might be valid but we would prefer to compute the force in a more accurate fashion by adding the multipole moments of the sub nodes. To initiate that one can implement a second safety criterion to ensure the more accurate force calculation in these scenarios, given as:

$$|r_k - c_k| \leq 0.6l, \tag{5.4}$$

with r_k as the particle coordinate and c_k as the centre of the respective node. This requires that the particle lies outside the respective node of size l by a 20 per cent margin. Taken all these advantages into account the advancement of the Tree-code compared to the more accurate method of direct summation is obvious. However, in practice one has to take the fact into account that astrophysical simulations will always run on multiple computational cores and or nodes. To optimise the computational cost in this regard one has not only to build this tree, it has to be built in an efficient and clever way to avoid memory overhead by communicating particles from one CPU to the other all the time and to safe computational cost. A popular choice for realising this in practice is to order the particles on a so called Peano-Hilbert curve which is the geometric analogue to a Tree-code realisation. The idea is hereby to order particles on this Peano-Hilbert structure while building the tree and order the particles to the various CPUs by cropping the constructed Peano-Hilbert curve. This ensures that particles that are close in space are likely to be on the same CPU which reduces the communication cost between processors in a very efficient manner. We show the structure of the Peano-Hilbert curve in Figure 5.2 and the resemblance between the Tree-code and the Peano-Hilbert curves in Figure 5.3.

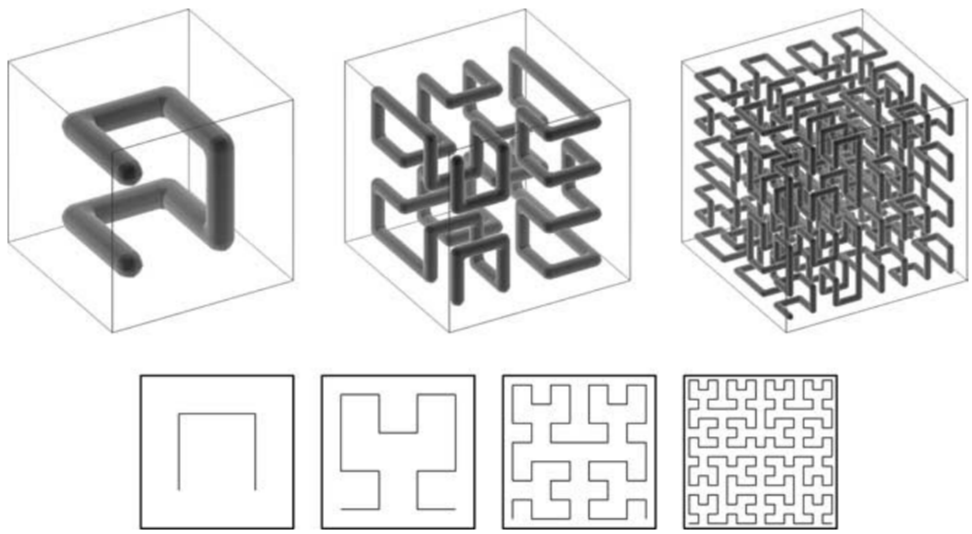

Figure 5.2: We show the structure of a Peano-Hilbert curve in two dimensions. The Figure has been taken from Springel (2005).

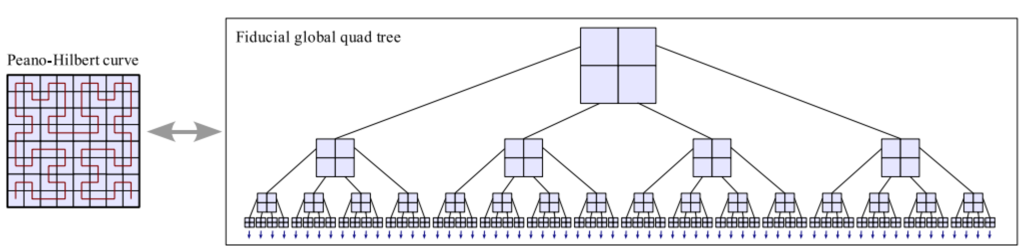

Figure 5.3: This Figure shows how the Peano-Hilbert curves are related to the three dimensional structure of a tree adn was taken from Springel (2005).

5.1.3 Tree-Particle-Mesh-Code

Another method for calculating the gravitational potential can be realised using the particle mesh method. The idea hereby is to use the advantages of the Fast Fourier Transformation (FFT). In this case one can calculate the gravitational potential of an arbitrary particle distribution at distance $\mathbf{r}$ by generating a mesh, binning the data to this mesh using either the nearest grid point (NGP), the cloud in cell (CSC) or the triangular shaped cloud (TSC) method to calculate the density distribution on the right hand side of the Poisson equation. The Poisson equation can then be solved by calculating the Greens-function of the distribution. In real space one would have to solve the convolution integral of the Poisson equation to obtain the potential. However, a convolution integral in Fourier space is reduced to a simple multiplication and the potential can be straightforward reconstructed by multiplying the density field with the Greens-function and summing over the single components. While this is exceedingly ($\mathcal{O}(N)$) fast, as one has only to compute the density field and carry out a one FT to obtain the Greens-function, it has the disadvantage that it becomes dominated by mesh noise on the grid scale. However, this is where the Tree can be used to further refine the structure enforced by gravity and one can solve the small scale force interactions on the Tree. Thus the force calculation is operator split in this framework and the long range force is computed by the PM-method while the short range force is computed on the Tree:

$$\Phi_{\mathrm{k}} = \Phi_{\mathrm{k}}^{\mathrm{long}} + \Phi_{\mathrm{k}}^{\mathrm{short}}. \tag{5.5}$$

The long range force contribution is then given as

$$\Phi_{\mathrm{k}}^{\mathrm{long}} = \Phi_{\mathrm{k}} \exp(-\mathbf{k}^2 r_{\mathrm{s}}^2), \tag{5.6}$$

which can be accurately computed in Fourier space. The factor r_{s} gives hereby the length scale on which the long range force computation is truncated and the short range forces are computed on the Tree via:

$$\Phi_{\mathrm{k}}^{\mathrm{short}}(\mathbf{r}) = -G \sum_i \frac{m_i}{r_i} \mathrm{erfc}\left(\frac{\mathbf{r}_i}{2r_{\mathrm{s}}}\right), \tag{5.7}$$

where r_i denotes the distance to the point $\mathbf{r}$. The parameter r_{s} is typically given by the mesh size plus a 20 per cent margin to ensure the highest accuracy in the force calculations.
Moreover, the Tree-PM method is extremely useful in cosmological zoom-in simulations as the low resolution large scale structure can be computed very fast on the PM-grid while the zoom-region is handled by the Tree. However, the memory imprint the of the Tree is much higher than the memory imprint of the PM-method. Thus for high-resolution zoom-simulations one can introduce a second PM-grid with higher resolution placed in the range of the zoom-region. This further speeds up the force calculation and ensures that the workload on the tree is minimised only to the particles below the nested grid scale. In today zoom-in simulation r_{s} is typically below the 100 pc scale, where it becomes really important to capture the orbits of the particles properly, which can be achieved well with the Tree, which will not capture the angular shape of the orbit but its eccentricity down to machine precision, while using a symplectic integrator.

5.2 Smoothed Particle Hydrodynamics

In this chapter we will introduce the state-of-the-art numerical methods that are used to model hydrodynmamical flows. Specifically, we will discuss Smoothed Particle Hydrodynamics (SPH) in its density-entropy, pressure-entropy and pressure-energy formulation as well as the highly related meshless finite mass (MFM) and Meshless Finite Volume (MFV) methods. Hereby, we will focus on the mathematical details of these methods. The MFM-method in our code Gadget will be tested in detail in chapter 6 to gauge that this method is a significant improvement over the state-of-the-art SPH-method. However, before we can implement and test it we have to understand how it works in detail.

5.2.1 Historical Overview

SPH was simultaneously introduced by Gingold and Monaghan (1977) and Lucy (1977) and has been successfully applied to various different physical problems over the last five decades. SPH is a numerical method for describing the physics of hydrodynamical flows, in the Lagrangian picture. In general SPH has been used on a wide variety of problems not only in astrophysics, but also in geophysics and engineering and in the movie and gaming industry. Typical problems that are still modelled with SPH to this day are the air stream around wings of an airplane and the airflow around skyscrapers. In the case of the airplane it is often cheaper to test a new wing design in the computer before it is actually produced and put in a windtunnel. In the case of the skyscraper it is an important safety measure with increasing building height that one can derive the effects of the wind that can be very different at bottom and the top of the building. This helps to understand how strong the building tends to swing in the wind and if the construction is safe in the first place. Further, SPH is often used to model viscous fluids in the movie industry. The most prominent example for this is the lava that streams down mount doom in the movie *Lord of the Rings: The return of the King* (NextLimitTechnologies, 1998). Another example is the movie *Poseidon* in which a cruise ship gets hit and is turned over by a water wave modelled with SPH. The method is also widely used in the gaming industry. For example SPH is an important part in fluid modelling in the *Nvidia* PhysiX engine which is for example used in the popular video game *CellFactor* (NvidiaCorporation, 2015).

5.2.2 The key to understand Hydrodynamical methods: Getting the density

Numerical methods to solve hydrodynamical flows are complicated. It is not at all straightforward to find a good point for entering this topic and explaining the fundamentals in a concise and understandable way. However, for most people (or at least for me) SPH is a method that can be understood relatively straightforward if the correct starting point is provided. Undoubtedly, this starting point has to be the density interpolation in the density-entropy formulation. Only by understanding how the fundamental density interpolation works one can ascend and understand not only SPH itself but also the need for pressure-entropy and pressure-energy SPH as well as the MFM and MFV methods. Thus we break the problem down and start with the task that is the least challenging in terms of numerical methods:

- Computing a density field for an arbitrary particle distribution

We already know several methods that can realise this if we implemented a gravity solver in our code that solves the Poisson-equation. One could go simply ahead and use the NGP, CSC or TSC method (e.g. Harlow and Welch, 1965) to obtain the density field and subdivide the computational domain into cubic grid cells. The hydrodynamic flux vectors would then be computed over the one-dimensional Riemann-problem on the edges of the grid cells. This would result in one of the popular Eulerian grid codes that are typically of second order in space and time (higher order extensions are possible but expensive). While this has the advantage that one has only to bin the particles on the grid, it can happen that dense regions get smoothed out if the grid is to coarse. This can be fixed by a higher resolution

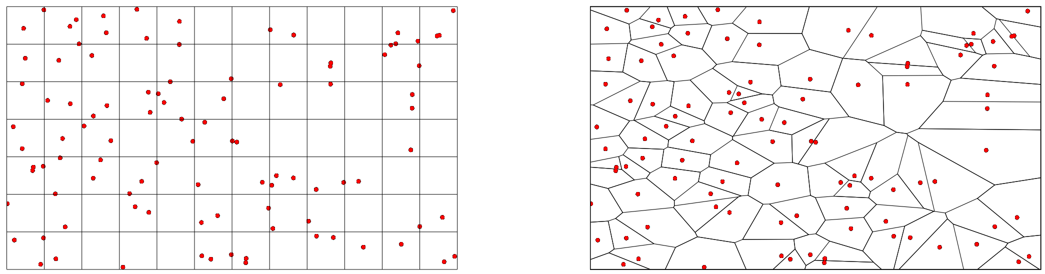

Figure 5.4: *Left:* This panel shows how density interpolation works with a particle mesh scheme. In this method the density is derived by interpolation of particles to a regular grid. For a fine grid this method is very accurate, but in can lead to spurious effects when the grid is to coarse. *Right:* This panel shows an alternative approach for getting the density on an irregular adaptive grid via the a Voronoi tessellation. For this methodology one constructs a grid based on the perpendicular bisector point of neighbouring cells.

mesh, which will become computational expensive very quickly. Moreover, the low dense regions are better resolved as well on the finer mesh which is obviously not necessary and a waste of computational time. Thus one can introduce the a technique that is called adaptive mesh refinement (AMR) which introduces a finer grid in the region of interest, while keeping the low resolution mesh in the low dense regions where we do not need higher resolution[1]. Another natural choice for the volume partition would be to construct a Voronoi mesh and calculate the density on this irregular mesh. This would be the strategy if one was to write a moving mesh code. In this scenario one would construct a Voronoi mesh by constructing the Wiegner-Seitz cells[2] of an arbitrary particle distribution. In this picture one would than calculate the fluxes over the edges of the neighbouring Wiegner-Seitz cells, again with a one-dimensional Riemann-solver with second order convergence. This method has the advantage that it is adaptive by construction and provides high resolution where the density increases. The above two methods are visualised in Figure 5.4. However, we want to construct a Lagrangian method based on particles. Thus the first option to realise this would be to calculate the density by summing the masses in a sphere around the particle of interest of which we want to have the density at the point $\mathbf{r} - \mathbf{r}'$ and dividing out the volume of the sphere. This approach would results in something that could be called Unsmoothed Particle Hydrodynamics (or USPH). Thus, one could go ahead and define the density in the following manner:

$$\rho(\mathbf{r}) = \frac{3}{4\pi R^3} \sum_{i}^{N.N.} m_i. \tag{5.8}$$

This is an interesting approach for a density interpolation as it intrinsically increases the resolution in high density regions. We can see this easily by assuming a constant neighbour number. In a high

[1]We note that there are cases where one would need higher resolution also in low density regions. A popular example these days is numerical simulations of galaxy and galaxy-cluster simulations with an emphasis of the properties in the circum galactic medium (CGM) and the Intra Cluster medium (ICM).

[2]This term comes from solid state physics and is usually not used in this context, but to this day I personally find no shorter explanation for constructing the perpendicular bisectors of an arbitrary particles distribution and determining the closest crossing point with one of the neighbouring perpendicular bisectors. Thus just labelling it by constructing the Wiegner-Seitz cells deems a good shortcut for me.

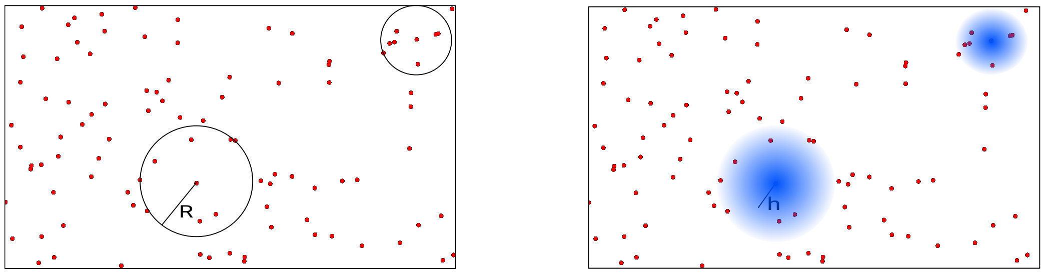

Figure 5.5: *Left:* This panel shows an alternative approach on how to construct the local volume of an arbitrary particle distribution, which represent an alternative approach compared to the methods that are shown in 5.4. This method is adaptive if it is based on the local particle distribution and resolve high density region by construction. *Right:* This can be further improved by weighting the particles with distance, thus smoothing out the density field, which is exactly the SPH approach.

density region this means that the same amount of particles occupies a smaller volume. Thus the resolution increases and the method is perfectly adaptive. This approach would keep the Lagrangian nature as it assigns one density value to a particle at the position $\mathbf{r} - \mathbf{r}'$ that might travel with the velocity $\mathbf{v}$. However, this approach would neglect that particles further away from the point $\mathbf{r}'$ contribute less to the density at the point $\mathbf{r}'$. Thus it would be useful to introduce some kind of distance weight to ensure that the density distribution at $\mathbf{r}'$ is not dominated by particles that are very far away. This is exactly the idea behind the SPH-density interpolation, where the density is calculated as a kernel weighted average over the neighbouring particles. In practice the approach of USPH is never used as it is too straightforward to directly ascend towards a proper SPH-density evaluation. In SPH the hydrodynamical fluxes are typically calculated as the so called SPH fluxes which will be discussed in section 5.2.6. However, one could also go ahead and construct the one-dimensional Riemann problem between two tracer particles and apply a proper second order gradient reconstruction for the fluid fluxes. In this case one would recover the new MFM and MFV methods. Which we will discuss in section 5.5.

5.2.3 SPH-density interpolation

As we discussed the fundamentals of density interpolation and briefly discussed the advantages and disadvantages of each method we can write down our the SPH-density interpolation which will be of paramount importance throughout this work. In the SPH formalism one assumes to calculate the density as a kernel weighted average over some specific nearest neighbour number. Following (e.g. Price, 2012) this is given as:

$$\rho(\mathbf{r}) = \sum_{i}^{N.N.} m_i W(\mathbf{r} - \mathbf{r}_i, h), \tag{5.9}$$

where W is a not yet specified weighting function which we will call 'kernel' and h is a scaling factor that we will call smoothing length which denotes the decrease of W with increasing distance from $\mathbf{r}_i$. We show the approach of USPH and SPH for obtaining densities from particle distributions in Figure 5.5. As we want to construct a mass conserving scheme (we forget about USPH), W has to fulfil the following norm:

$$\int_{V} W(\mathbf{r'} - \mathbf{r}_i, h) dV' = 1. \tag{5.10}$$

We directly see that the density interpolation is mainly given by the choice of the kernel function that has to fulfil the norm from equation 5.10. Thus the trick is to use a 'good' kernel function. However, this can be a tricky task as there are many different 'good' choices for the kernel-function that show specific advantages and disadvantages and ideally one has to find a kernel function that is best applicable to the problem at hand.

5.2.4 Kernel Functions

Apart from equation 5.10 a good kernel should obey:

1. Equation 5.9 with the kernel W has to be exact.
2. W is monotonically decreasing and is twice continuously differentiable.
3. Stable against the pairing-instability[3].
4. Flat central region, so that the density estimate is not dominated by minimal movements of close neighbours
5. Symmetric, which yields: $W(\mathbf{r'} - \mathbf{r}, h) \equiv W(|\mathbf{r'} - \mathbf{r}|, h)$

Given the criteria above a natural choice for the kernel function would be a Gaussian:

$$W(\mathbf{r'} - \mathbf{r}, h) = \frac{\sigma}{h^d} \exp\left[-\frac{(\mathbf{r'} - \mathbf{r})^2}{h^2}\right]. \tag{5.11}$$

The factor σ is a normalisation given by $\sigma = [1/\sqrt{\pi}, 1/\pi, 1/\pi\sqrt{\pi}]$ for dimension $d = [1,2,3]$. In principle the Gaussian is the ideal choice for the kernel if one is interested in the most accurate presentation of the density. However, the Gaussian converges at infinity, which implies that mass conservation is only given if we take all particles in the computational domain into account, resulting in a method with convergence order $O(N^2)$. Thus in theory the Gaussian is ideal, in practice it is not. Therefore, one has to take a class of functions that resembles the Gaussian in the central regions but drops faster in the outer regions to achieve a computational cost that scales with $O(N_{\text{neighbours}}N)$. While this leads to a fast density interpolation in practice, it has the disadvantage of distribution noise for low neighbour numbers. Thus one has to find a middle ground between computational cost and accuracy of the density interpolation.

B-Spline-Kernel

Historically, the first class of functions that has been used in the SPH-method are the so called B-spline functions. One can display them as the following Fourier transformation:

$$M_n(x, h) = \frac{1}{2\pi} \int_{-\infty}^{\infty} \operatorname{sinc}^n(kh/2) \cos(kx) dk \tag{5.12}$$

[3]The pairing instability is a phenomenon that occurs for large smoothing lengths h and a specific class of kernel functions that leads to artificial clumping of the particle distribution.

For a long time the most popular choice was the cubic spline ($n = 4$), which has been used successfully for many years in a lot of different simulations as it as the advantage of operating at a relatively low neighbour number (32 – 64). This is a trade-off between saving computational time and accurately capturing the fluid flow. In practice, the cubic spline is truncated at $2h$ and is piece wise defined as (see e.g. Price, 2012, for details).

$$W(q) = \frac{\sigma}{h^d} \begin{cases} \frac{1}{4}(2-q)^3 - (1-q)^3 & \text{für } 0 \leq q < 1; \\ \frac{1}{4}(2-q)^3 & \text{für } 1 \leq q < 2; \\ 0 & \text{für } q \geq 2, \end{cases} \tag{5.13}$$

where $\sigma = [2/3, 10/7\pi, 1/\pi]$ is the normalisation for the dimensions $d = [1, 2, 3]$ and q is given via $q = |\mathbf{r} - \mathbf{r}'|/h$. However, the small amount of neighbours can in practice lead to extensive distribution noise and one would like to use more neighbours to reduce this distribution noise. Thus one often uses higher order spline kernel to allow for larger neighbour numbers and popular choices other than the cubic spline are the M_5 (quartic) and the M_6 (quintic) that are truncated at larger radii of $2.5h$ and $3h$, which increases the average number of neighbours. A more detailed discussion of the B-spline kernel functions is given in Price (2012). Nowadays, the cubic and quartic splines are only very rarely used ins state-of-the-art SPH simulations, while the quintic spline is still used as the default kernel in some SPH codes (Price et al., 2018). This is due to the fact that these class of kernel functions falls victim to the pairing-instability for larger neighbour numbers. With increasing computational power this fact ruled out the cubic and the quartic spline as one wanted to increase the neighbour number to reduce distribution noise. The quintic spline however, allows a larger number of neighbours without being endangered by the paring-instability and is still used in todays practice. While the cubic and quartic spline have lost their field of use in classic SPH simulations they are lately rejuvenated in the newer MFM and MFV methods that reduce distribution noise by applying numerical diffusion over a Riemann-solver, so that these methods can be used with lower order kernels and only a few neighbours by still improving the accuracy of capturing the fluid quantities.
One class of kernel-function that can resolve the paring instability issue of B-spline kernel functions are the class of triangular shaped kernel functions. This class of functions has been used in some work (e.g. Read et al., 2010) and does not suffer from the paring instability as it has a proper infliction point leading to a smoother second order gradient and thus to a smoother force field. The triangular kernel functions have the disadvantage that their first derivative is not continuously differentiable which is not a good quality for a kernel as we discussed above. Nevertheless, some groups have explored the usage of this function as a smoothing kernel for SPH.

Wendland-Kernel

State-of-the-art SPH simulations use the class of Wendland functions as smoothing kernel. Specifically, the $C2$, $C4$ and $C6$. While all of these kernel functions are ideal choices, most commonly the $C4$ and $C6$ kernel are used in numerical SPH simulations of galaxy formation and evolution. This is again a trade-off between accuracy and speed. While the $C6$ kernel allows for neighbour numbers up to 800 and thus almost no distribution noise it is computationally very expensive to adapt so many neighbours. The $C2$ kernel on the other hand ideally operates with around 30 neighbours. While this makes the SPH-loop fast it again inflicts a lot of distribution noise. Thus the $C4$ kernel provides a good middle ground as it is ideally operated with 100 to 200 neighbours providing a good balance between accuracy and speed. The Wendland function are given as (e.g. Dehnen and Aly, 2012):

$$w(r) = C\psi_{lk}, \tag{5.14}$$

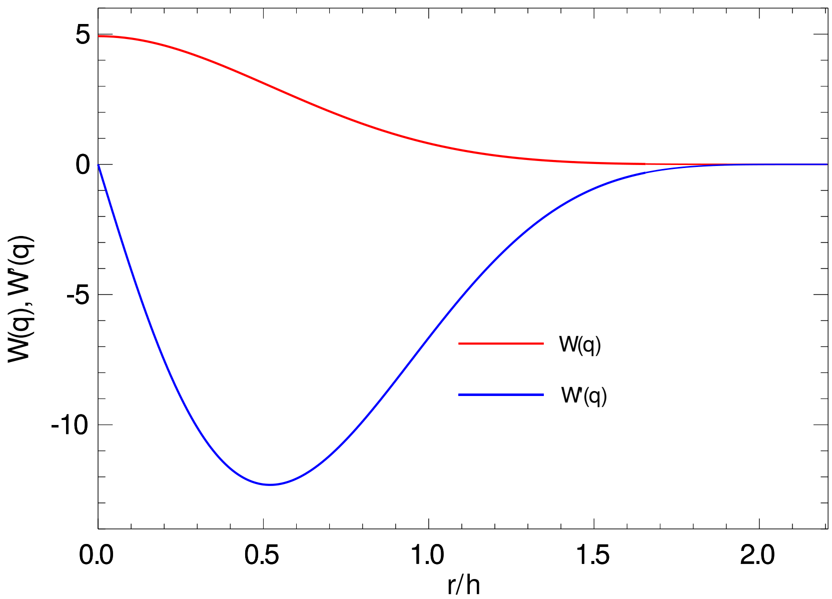

Figure 5.6: Wendland $C4$-kernel (red) and its derivation (blue).

with the following notation for ψ:

$$\psi(q) = \begin{cases} \mathcal{I}^k (1-q)^l & \text{for } 0 \le q < 1; \\ 0 & \text{everywhere else,} \end{cases} \tag{5.15}$$

where q is given as $q = |\mathbf{r} - \mathbf{r}'|/h$ and $\mathcal{I}$ is the linear operator:

$$\mathcal{I}[f(q)] \equiv \int_q^\infty s f(s) ds. \tag{5.16}$$

These functions are k-times continuously differentiable and approach the Gaussian for k towards infinity. Furthermore the Gaussian is also the only non-trivial Eigenvalue of the operator $\mathcal{I}$. The kernel that will be used in all SPH-simulations throughout this work is the $C4$ kernel:

$$W(q) = \begin{cases} \frac{495}{32\pi}(1-q)^6 \left(1 + 6q + \frac{35}{3}q^2\right) & \text{for } 0 \le q < 1; \\ 0 & \text{everywhere else,} \end{cases} \tag{5.17}$$

As this kernel is of importance in this work we display it in Figure 5.6 alongside with its first and second derivative. Finally, this leaves the question of how does one find such an exotic class of functions for the usage of a SPH-kernel. Basically, on searches for a class of functions that cannot fall victim under any circumstances to the pairing-instability. From the triangular kernel-functions we know that the existence of an infliction point is necessary to fulfil this criterion. Mathematically speaking, one could also formulate this statement by a class of functions with non negative Fourier transformation (e.g. Dehnen and Aly, 2012, for details) in the respective spatial dimension. Obviously, the Gaussian comes to mind again but for the reasons we discussed above this is not a good choice. So the question is, is there an iterative class of functions with non-negative Fourier transformation which higher order realisations approaches a Gaussian and the answer to that question is the Wendland-functions.

5.2.5 Setting the smoothing length

Before we can start to write down the basics of hydrodynamics in the SPH-formulation, we have to specify how one determines the smoothing length. First, we note that the easiest approach is obviously to assume a constant smoothing length however, this is not always the best choice for the problem at hand. Moreover, a constant smoothing length that we set in the beginning of a simulation could over smooth dense regions of interest that build-up during the simulation. Thus it is useful to introduce a scaling of the smoothing length with the number of particles n in the respective dimension d.

$$h(\mathbf{r}) \propto n(\mathbf{r})^{-d}, \tag{5.18}$$

with the number density n given via:

$$n(\mathbf{r}) = \sum_i^{N.N.} W[\mathbf{r} - \mathbf{r}_i, h_i(\mathbf{r})]. \tag{5.19}$$

For equal masses one can directly see that this means nothing else than connecting the smoothing length h with the SPH density estimate. This requires that we solve for the following system of equations for h:

$$\rho(\mathbf{r}_j) = \sum_i^{N.N.} m_i W(\mathbf{r}_j - \mathbf{r}_i, h_j); \quad h(\mathbf{r}_j) = \eta \left(\frac{m_j}{\rho_j}\right)^{-d} \tag{5.20}$$

This can straightforward be achieved by introducing the function ζ defined as:

$$\zeta(h_j) = m_j \left(\frac{\eta}{h_j}\right)^d - \sum_i^{N.N.} m_i W(\mathbf{r}_j - \mathbf{r}_i, h_j), \tag{5.21}$$

and solving for the zero points for example with the Newton-Raphson method or the bisection method. For the Newton-Rapshon method one iterates for $h_{j,\mathrm{new}}$ in the following manner until one reaches a specified tolerance value ε close to zero.

$$h_{j,\mathrm{new}} = h_j - \frac{\zeta(h_j)}{\zeta'(h_j)}. \tag{5.22}$$

The prime denotes the derivative with respect to h_j. By introducing the variable Ω

$$\Omega_j = 1 - \frac{\partial h_j}{\partial \rho_j} \sum_i^{N.N.} m_i \frac{\partial W(\mathbf{r}_j - \mathbf{r}_i, h_j)}{\partial h_j} = 1 + \frac{h_j}{\rho d} \sum_i^{N.N.} m_i \frac{\partial W(\mathbf{r}_j - \mathbf{r}_i, h_j)}{\partial h_j}, \tag{5.23}$$

it becomes possible to further simplify equation 5.22 and one obtains:

$$h_{j,\mathrm{new}} = h_j \left(1 + \frac{\zeta(h_j)}{\mathrm{d}\rho_j \Omega_j}\right). \tag{5.24}$$

The iteration continues until $(h_{j,\text{new}} - h_j)/h_j$ is smaller than ε which is often chosen to be around 10^{-3}. In practice, it can happen in rare cases that the Newton-Raphson method diverges, in these cases one could apply the bisection method that guarantees convergence by construction but is somehow slower than the Newton-Raphson method. The approach that we took here is to first order equivalent with the formulation of the smoothing length over mass conservation:

$$mN_{\text{neighbour}} \approx \frac{4}{3}\pi R^3_{\text{Kernel}}\rho_j, \tag{5.25}$$

but has the advantage that the neighbour number is not a free parameter of the modelling.

5.2.6 SPH equations of ideal Hydrodynamics

Choosing the SPH volume element

The last point that needs discussion before we can derive the SPH equations of ideal hydrodynamics is the definition of the SPH volume element.The classic choice for the SPH-volume is to define this via the density following:

$$V_j = \frac{m_j}{\rho_j}. \tag{5.26}$$

While this choice for the SPH volume seems to be the most straightforward given all the details of SPH that we discussed so far, it can introduce some problems. Saitoh and Makino (2013) and Hopkins (2013) discuss that this definition of the SPH-volume acts as a surface tension term at contact discontinuities with continuous pressure but with a jump in the internal energy and density. In those cases classic density SPH smooths the density distribution which can introduce an error in the pressure and the internal energy as they are derived from the smoothed density distribution. To solve this problem one can introduce artificial diffusion terms (or physical diffusion) or change the definition of the SPH-volume element (i.e. switching to pressure-based SPH, which will be discussed in section 5.3). A more general definition of the SPH-volume element can be achieved via Hopkins (2013):

$$V_j = \frac{X_j}{\sum_i^{N.N.} X_i W(\mathbf{r}_j - \mathbf{r}_i, h_j)}, \tag{5.27}$$

where X_j denotes an arbitrary scalar quantity. The density is then given as:

$$\rho_j^X = \frac{m_j}{V_j^X} = \frac{m_j}{X_j}\sum_i^{N.N.} X_i W(\mathbf{r}_j - \mathbf{r}_i, h_j). \tag{5.28}$$

For $X_j = m_j$ and $X_i = m_i$ equation 5.28 is reduced to equation (5.9) and we see that equation 5.28 is a generalisation of the usual SPH-density estimate for arbitrary scalar quantities as m_i and m_j. A popular example for when it is useful to not use m_i and m_j in the density estimate is given by the special and general relativity extensions of the SPH-method, as shown in Rosswog (2015) who use the baryon number density ν as the central scalar quantity.

Kernelinterpolation

The central point and the biggest advantage of the SPH-formalism is that any hydrodynamical variable can be expressed in terms of the SPH-volume element (often the density) and the kernel function. On the one hand this makes the scheme very easy understandable, on the other hand one could argue that the results depend to some degree on the quality of the kernel function, which is true and as we discussed above different problems might require different kernel function for optimal results. Thus the idea is that any variable A (vector or scalar) of fluid dynamics can be expressed in terms of the Dirac-delta function $\delta(\mathbf{r}-\mathbf{r}')$:

$$A(\mathbf{r}) = A(\mathbf{r})\delta(\mathbf{r}-\mathbf{r}')\mathrm{d}\mathbf{r}'. \tag{5.29}$$

To first order, we can approximate the delta function with the kernel function we use in our SPH simulation. Intuitively, we know that this is a good approximation as we know that all kernel function we discussed so far are closely related to a Gaussian and the Dirac-delta function is defined as the limit of the Gaussian as its width approaches zero. Following that one can approximate the variable A via:

$$A(\mathbf{r}) = \int A(\mathbf{r}')W(\mathbf{r}-\mathbf{r}',h)\mathrm{d}\mathbf{r}' + O(h^2). \tag{5.30}$$

The kernel has to take the shape of the delta function as h approaches zero and fulfil the norm $\int_V W\mathrm{d}V' = 1$. The next step is to expand equation 5.30 with $\rho(\mathbf{r}')/\rho(\mathbf{r}')$ and replace the integral with the sum[4]. This yields:

$$\langle A(\mathbf{r})\rangle = \int \frac{A(\mathbf{r}')}{\rho(\mathbf{r}')}W(\mathbf{r}-\mathbf{r}',h)\rho(\mathbf{r}')\mathrm{d}\mathbf{r}', \tag{5.31}$$

$$\approx \sum_{j=1}^{N.N.} m_j \frac{A_j}{\rho_\mathrm{j}} W(\mathbf{r}-\mathbf{r}_j,h). \tag{5.32}$$

$\rho(\mathbf{r}')\mathrm{d}\mathbf{r}'$ is the mass of each respective SPH-particle. For $A = \rho$ we find the standard SPH-density estimate. Based on this we can now straightforward formulate the gradient for our arbitrary SPH quantity A and we find:

$$\nabla A(\mathbf{r}) = \frac{\partial A(\mathbf{r})}{\partial \mathbf{r}} = \int \frac{A(\mathbf{r}')}{\rho(\mathbf{r}')}W(\mathbf{r}-\mathbf{r}',h)\rho(\mathbf{r}')\mathrm{d}\mathbf{r}', \tag{5.33}$$

$$\approx \sum_{j=1}^{N.N.} m_j \frac{A_j}{\rho_\mathrm{j}} \nabla W(\mathbf{r}-\mathbf{r}_j,h). \tag{5.34}$$

The advantage of equation 5.34 is obvious. To display the gradient of an arbitrary hydrodynamical variable A we only need the derivative of the kernel, which can be obtained analytical. This makes the method exceedingly fast and one can just generalise the formalism to vector quantities $\mathbf{A}$ and one

[4] We are allowed to do that as long as the integral converges, but we know that this is the case as the kernel fulfils the norm $\int_V W\mathrm{d}V' = 1$ as this is one of the central quantities that we select a 'good' kernel function by.

obtains.

$$\mathbf{A}(\mathbf{r}) \approx \sum_{j=1}^{N.N.} m_j \frac{\mathbf{A}_j}{\rho_j} W(\mathbf{r}-\mathbf{r}_j, h), \tag{5.35}$$

$$\nabla\cdot\mathbf{A}(\mathbf{r}) \approx \sum_{j=1}^{N.N.} m_j \frac{\mathbf{A}_j}{\rho_j} \cdot \nabla W(\mathbf{r}-\mathbf{r}_j, h), \tag{5.36}$$

$$\nabla\cdot\mathbf{A}(\mathbf{r}) \approx -\sum_{j=1}^{N.N.} m_j \frac{\mathbf{A}_j}{\rho_j} \times \nabla W(\mathbf{r}-\mathbf{r}_j, h), \tag{5.37}$$

$$\nabla^k A^l(\mathbf{r}) \approx \sum_{j=1}^{N.N.} m_j \frac{A_j^l}{\rho_j} \nabla^k W(\mathbf{r}-\mathbf{r}_j, h). \tag{5.38}$$

SPH equations of motion

Finally, we can derive the equations of hydrodynamics. We will derive the equations of motion from the principle of least action by using the Lagrangian $\mathcal{L}$ of hydrodynamics to which we will apply all the necessary approximations in the SPH limit. As the Lagrangian $\mathcal{L}$ of hydrodynamics describes a conservative, holomorphic system this directly implies that the resulting equation conserves energy, momentum and angular momentum down to machine precision. The Lagrangian of hydrodynamics is given as the difference of kinetic T and potential energy V of the system:

$$\mathcal{L} = T - V. \tag{5.39}$$

In a next step we discretise the Lagrangian as a system of point masses (particles) with velocities $\mathbf{v} = \mathrm{d}\mathbf{r}/\mathrm{d}t$ and internal energy per u_i per unit mass m_i. We start with the hydrodynamic continuum:

$$\mathcal{L} = \int [\frac{1}{2}\rho v^2 - \rho u(\rho, s)]\mathrm{d}^3\mathbf{r}. \tag{5.40}$$

We discretise equation 5.40 and obtain:

$$\mathcal{L} = \sum_i m_i \left[\frac{1}{2} v_i^2 - u_i(\rho_i, s_i)\right]. \tag{5.41}$$

Internal energy u can then be expressed as a general function of density ρ and entropy per unit mass s. From the discrete Lagrangian we can construct the Euler-Lagrange equations of motion via the principle of least action, where the action S is given via:

$$S = \int \mathcal{L}\mathrm{d}t. \tag{5.42}$$

The principle of least action requires that the variation of the action vanishes:

$$\delta S = \int \left(\frac{\partial\mathcal{L}}{\partial\mathbf{v}} \cdot \delta\mathbf{v} + \frac{\partial\mathcal{L}}{\partial\mathbf{r}} \cdot \delta\mathbf{r}\right)\mathrm{d}t = 0. \tag{5.43}$$

Through partially integrating this one finds:

$$\frac{\mathrm{d}}{\mathrm{d}t}\left(\frac{\partial\mathcal{L}}{\partial\mathbf{v}_j}\right) - \frac{\partial\mathcal{L}}{\partial\mathbf{r}_j} = 0. \tag{5.44}$$

Now we insert equation 5.41 in 5.44 and we obtain:

$$\frac{\partial \mathcal{L}}{\partial \mathbf{v}_j} = m_j \mathbf{v}_j, \frac{\partial \mathcal{L}}{\partial \mathbf{r}_j} = -\sum_{j=1} m_j \left(\frac{\partial u_j}{\partial \rho_j}\right)_s \frac{\partial \rho_j}{\partial \mathbf{r}_j}. \tag{5.45}$$

Moreover, we need the equation of state $U = T\mathrm{d}S - P\mathrm{d}V$ and as we insert $\mathrm{d}V = -m/\rho^2 \mathrm{d}\rho$ we can obtain an expression for $\partial u_j / \partial \rho_j$.

$$\left(\frac{\partial u_j}{\partial \rho_j}\right)_s = \frac{P}{\rho^2}. \tag{5.46}$$

Furthermore, we need the density gradient which is given by:

$$\frac{\partial \rho_j}{\partial \mathbf{r}_i} = \frac{1}{\Omega_j} \sum_k m_k \frac{\partial W_{jk}(h_j)}{\partial \mathbf{r}_i} (\delta_{ji} - \delta_{ki}), \tag{5.47}$$

with the correction factor Ω:

$$\Omega_i = \left[1 - \frac{\partial h_i}{\partial \rho_i} \sum_j m_j \frac{\partial W_{ij}(h_i)}{\partial h_i}\right], \tag{5.48}$$

where $\partial h / \partial \rho$ can be displayed via:

$$\frac{\partial h}{\partial \rho} = -\frac{h}{3\rho}, \tag{5.49}$$

This yields:

$$\frac{\partial \mathcal{L}}{\partial \mathbf{r}_i} = -\sum_j m_j \frac{P_j}{\Omega_j \rho_j^2} \sum_k m_k \frac{\partial W_{ij}(h_j)}{\partial \mathbf{r}_i}, \tag{5.50}$$

and one obtains the equation of motion for ideal hydrodynamics in the SPH-formalism:

$$\frac{\mathrm{d}\mathbf{v}_i}{\mathrm{d}t} = -\sum_j m_j \left[\frac{P_j}{\Omega_j \rho_j^2} \frac{\partial W_{ij}(h_i)}{\partial \mathbf{r}_j} + \frac{P_i}{\Omega_i \rho_i^2} \frac{\partial W_{ij}(h_i)}{\partial \mathbf{r}_i}\right]. \tag{5.51}$$

Linear and angular momentum conservation in SPH

That these equations conserve momentum and angular momentum can straightforward be seen for linear momentum via:

$$\frac{\mathrm{d}}{\mathrm{d}t} \sum_i m_i \mathbf{v}_i = \sum_i m_i \frac{\mathrm{d}\mathbf{v}_i}{\mathrm{d}t} = -\sum_i \sum_j m_i m_j \left(\frac{P_i}{\rho_i^2} + \frac{P_j}{\rho_j^2}\right) \nabla_i W_{ij} = 0. \tag{5.52}$$

This hold due to the double summation over the anti-symmetric gradient of the kernel function. For angular momentum one can make similar argument and one can see:

$$\frac{\mathrm{d}}{\mathrm{d}t} \sum_i \mathbf{r}_i \times m_i \mathbf{v}_i = \sum_i m_i \mathbf{r}_i \times \frac{\mathrm{d}\mathbf{v}_i}{\mathrm{d}t} = -\sum_i \sum_j m_i m_j \left(\frac{P_i}{\rho_i^2} + \frac{P_j}{\rho_j^2}\right) \mathbf{r}_i \times (\mathbf{r}_i - \mathbf{r}_j) F_{ij} = 0. \tag{5.53}$$

Energy conservation in SPH

We can write down the energy of the system in the SPH-formalism. Without dissipation, internal energy is given via:

$$\frac{\mathrm{d}u_i}{\mathrm{d}t} = \frac{P_i}{\rho_i^2}\frac{\mathrm{d}\rho_i}{\mathrm{d}t}. \tag{5.54}$$

If we insert the time derivative of the SPH-density we get:

$$\frac{\mathrm{d}u_i}{\mathrm{d}t} = \frac{P_i}{\Omega_i\rho_i^2}\sum_j m_j(\mathbf{v}_i - \mathbf{v}_j)\cdot\nabla_i W_{ij}(h_i). \tag{5.55}$$

The total energy in SPH is then given as the Legendre-transformation with respect to the velocity $\mathbf{v}_i$ of the Lagrangian. By doing this one obtains the Hamiltonian that represents the total energy in a conservative system:

$$\mathcal{H} = \sum_i \mathbf{v}_i\cdot\frac{\partial\mathcal{L}}{\partial\mathbf{v}_i} - \mathcal{L} = \sum_i m_i\left(\frac{1}{2}v_i^2 + u_i\right). \tag{5.56}$$

The rate of change of the total energy is then given as:

$$\frac{\mathrm{d}E}{\mathrm{d}t} = \sum_i m_i\left(\mathbf{v}_i\cdot\frac{\mathrm{d}\mathbf{v}_i}{\mathrm{d}t} + \frac{\mathrm{d}u_i}{\mathrm{d}t}\right) \tag{5.57}$$

$$= \sum_i m_i\frac{\mathrm{d}e_i}{\mathrm{d}t}. \tag{5.58}$$

If we insert the SPH-equation of motion we get:

$$\frac{\mathrm{d}E}{\mathrm{d}t} = -\sum_i\sum_j m_i m_j\left[\frac{P_i}{\Omega_i\rho_i^2}\mathbf{v}_j\cdot\nabla_i W_{ij}(h_i) + \frac{P_j}{\Omega_j\rho_j^2}\mathbf{v}_i\cdot\nabla_i W_{ij}(h_j)\right] = 0. \tag{5.59}$$

Because of the double summation we directly see that total energy is conserved. The specific energy e is then given by:

$$\frac{\mathrm{d}e_i}{\mathrm{d}t} = -\sum_j m_j\left[\frac{P_i}{\Omega_i\rho_i^2}\mathbf{v}_j\cdot\nabla_i W_{ij}(h_i) + \frac{P_j}{\Omega_j\rho_j^2}\mathbf{v}_i\cdot\nabla_i W_{ij}(h_j)\right]. \tag{5.60}$$

Finally, we need to discuss the entropy. In an ideal gas we find:

$$P = K(s)\rho^\gamma, \tag{5.61}$$

with the entropy function $K(s)$, which is given by (Springel and Hernquist, 2002):

$$\frac{\mathrm{d}K}{\mathrm{d}t} = \frac{\gamma-1}{\rho^{\gamma-1}}\left(\frac{\mathrm{d}u}{\mathrm{d}t} - \frac{P}{\rho^2}\frac{\mathrm{d}\rho}{\mathrm{d}t}\right) = \frac{\gamma-1}{\rho^{\gamma-1}}\left(\frac{\mathrm{d}u}{\mathrm{d}t}\right)_{diss}. \tag{5.62}$$

However, this term remains always zero without dissipation. In practice this is a problem and a weakness of the method as there can be no mixing without entropy. Thus to accurately capture shocks and fluid mixing instabilities one needs a prescription for artificial viscosity and artificial conduction.

5.2.7 Dissipative Terms in SPH

It has been pointed out by Agertz et al. (2007) that classic SPH-struggles with capturing fluid-mixing problems, because it intrinsically solved for $ds/dt = 0$. This can be resolved by introducing some numerical diffusion in the form of time dependant artificial viscosity and time dependant artifical conduction. The basic form of artificial viscosity is given via (Monaghan, 1997; Springel, 2005) and introduces as viscous term in the SPH-equations of motion of the form:

$$\left(\frac{d\mathbf{v}_i}{dt}\right)_{\text{visc}} = -\sum_i m_i \Pi_{ij} \nabla_j \overline{W}_{ij}, \tag{5.63}$$

which introduces a change in the entropy following:

$$\frac{dA_j}{dt} = \frac{\gamma - 1}{2\rho_j^{\gamma-1}} \sum_i m_i \Pi_{ij} \mathbf{v}_{ij} \cdot \nabla_j \overline{W}_{ij}. \tag{5.64}$$

The function Pi is given via:

$$\Pi_{ij} = \begin{cases} -\frac{1}{2}\overline{\alpha}_{ij}\frac{v_{\text{sig}}}{\overline{\rho}_{ij}}\omega_{ij} & \text{if } \omega_{ij} < 0; \\ 0 & \text{everywhere else,} \end{cases} \tag{5.65}$$

with $\omega = \mathbf{v}_{ij} \cdot \mathbf{x}_{ij}$ and the signal velocity $v_{\text{sig}} = c_i + c_j - 3\omega_{ij}$. $\overline{\rho}_{ij}$ is the arithmetic average of the density of particle i and j and $\overline{\alpha}_{ij}$ is the arithmetic average of the artificial conduction coefficients. This coefficient can either be a constant in time, or it can made time dependent, following a modified Balsara-switch as it is shown in Cullen and Dehnen (2010) which is implemented in out code version as well. The details of this switch can be found in Hu et al. (2014) ins section 2.3.

As every mixing process introduces entropy we further need artificial conductivity to provide the mixing entropy via the exchange of thermal energy between SPH-particle of the form:

$$\frac{du_j}{dt} = \sum_i \overline{\alpha}_{ij}^d v_{\text{sig}} L_{ij}^p m_i \frac{u_j - u_i}{\overline{\rho}_{ij}} \mathbf{x}_{ij} \cdot \nabla_j \overline{W}_{ij}. \tag{5.66}$$

$L_{ij}^p = |P_j - P_i|/(P_j + P_i)$ gives a limit for the pressure. In this form artificial conduction accounts fro the mixing entropy needed in fluid-mixing problems like the Rayleigh-Taylor or Kelvin-Helmholtz-Instability. However, a problem with this terms still remains and this is that they act highly non-linear. In practice the best values for these terms are obtained by bench marking against analytically known fluid problems. If those values are still good fits for more extreme environments like a galaxy merger remains unclear to this day.

5.3 Pressure based formulation of SPH

Although, this method has been very successful in solving hydrodynamic test cases (e.g. Beck et al., 2016a; Dolag and Stasyszyn, 2009; Springel et al., 2005b) and to tackle astrophysical problems in different systems (e.g. Johansson et al., 2009; Moster et al., 2010a) it has a weakness when it comes to fluid mixing quantities at contact discontinues (e.g. Agertz et al., 2007). The behaviour of SPH at contact discontinuities can be improved by reformulating SPH using the pressure as the smoothed quantity. This is leading to the 'pressure-entropy' (PE) formulation of SPH. In this formulation the pressure is smoothed which removes pressure gradients at contact discontinuities and leads to a better behaviour for fluid mixing problems (Hopkins, 2013; Hu et al., 2014). The system of equations changes and is given by (Hopkins, 2013; Hu et al., 2014)

$$P_i = \left[\sum_j m_j A_j W_{ij}(h_j)\right]^\gamma, \tag{5.67}$$

where A is the entropic function given by $P = A \cdot \rho^\gamma$. The EOM follows

$$\frac{\mathrm{d}\mathbf{v}_i}{\mathrm{d}t} = -\sum_j m_j (A_i A_j)^{1/\gamma} \times \tag{5.68}$$

$$\left[f_i^{\mathrm{co}} \frac{P_i}{P_i^{2/\gamma}} \nabla_i W_{ij}(h_i) + f_j^{\mathrm{co}} \frac{P_j}{P_j^{2/\gamma}} \nabla_i W_{ij}(h_j)\right] \tag{5.69}$$

The correction factor f_j^{co} is in this formulation given by

$$f_j^{\mathrm{co}} = 1 - \left(\frac{h_i}{3A_j^{1/\gamma} m_j \hat{n}_i} \frac{\partial P_i^{1/\gamma}}{\partial h_i}\right)\left[1 + \frac{h_i}{3\hat{n}_i} \frac{\partial \hat{n}_i}{\partial h_i}\right]^{-1} \tag{5.70}$$

5.4 Smoothed Particle Magnetohydrodynamics

5.4.1 The Lagrangian of ideal magneto hydrodynamics

One can take the same approach for the equations of ideal magnetohydrodynamics as for ideal hydrodynamics to derive the SPMHD equations of motion. The starting point for this is:

$$\mathcal{L}_{\mathrm{MHD}} = \int \left[\frac{1}{2}\rho v^2 - \rho u(\rho, s) - \frac{1}{2\mu_0 B^2}\right] \mathrm{d}^3\mathbf{r}. \tag{5.71}$$

From this one can make the transition towards the discrete Lagrangian:

$$\mathcal{L}_{\mathrm{MHD}} = \sum_i m_i \left[\frac{1}{2} v_i^2 - u_i(\rho_i, s_i) - \frac{1}{2\mu_0} \frac{B_j^2}{\rho_j}\right]. \tag{5.72}$$

Analogous to what we already did for the equations of motion of hydrodynamics, we can derive the equations of motion of magnetohydrodynamics in the SPH-form. However, as the Lagrangian is slightly more complex the derivation is somewhat more tedious and we will skip parts of the details of the derivation and only discuss the central equations of the SPMHD formalism. A slightly more comprehensive overview of the details of the calculation can be found in Price (2012).

5.4.2 SPMHD form of the induction equation

The largest difference between hydrodynamics and magnetohydrodynamics is the presence of a magnetic field. While this statement is trivial it is essential to understand where exactly this magnetic field comes into play and how it alters the system of equations one has to solve. Thus the starting point is that we acknowledge the fact that there is a magnetic field, which is already a large step to a more fundamental understanding of physical processes in numerical simulations.

$$\frac{\mathrm{d}}{\mathrm{d}t}\frac{\mathbf{B}}{\rho} = \left(\frac{\mathbf{B}}{\rho}\cdot\nabla\right)\mathbf{v}. \tag{5.73}$$

From this, one can obtain:

$$\frac{\mathrm{d}}{\mathrm{d}t}\frac{\mathbf{B}_i}{\rho_i} = -\sum_j m_j(\mathbf{v}_i - \mathbf{v}_j)\frac{\mathbf{B}_i}{\Omega_i\rho_i^2}\cdot\nabla W_{ij}(h_i). \tag{5.74}$$

This is the induction equation in its SPMHD discretised form.

5.4.3 SPMHD equation of motion

The equations of motion can again be derived form the discrete Lagrangian by determining the variation δ of the action of the Lagrangian of magnetohydrodynamics. Following the work of Dolag and Stasyszyn (2009) and Price (2012) one can find the equations of motion of magnetohydrodynamics:

$$\frac{\mathrm{d}\mathbf{v}_i}{\mathrm{d}t} = -\sum_j\left[\frac{P_i + \frac{1}{2\mu_0}B_i^2}{\Omega_i\rho_i^2}\nabla_i W_{ij}(h_i) + \frac{P_j + \frac{1}{2\mu_0}B_j^2}{\Omega_j\rho_j^2}\nabla_i W_{ij}(h_j)\right] \tag{5.75}$$

$$+\frac{1}{\mu_0}\sum_j m_j\left[\frac{\mathbf{B}_i(\mathbf{B}_i\cdot\nabla_i W_{ij}(h_i))}{\Omega_i\rho_i^2} + \frac{\mathbf{B}_j(\mathbf{B}_j\cdot\nabla_i W_{ij}(h_j))}{\Omega_j\rho_j^2}\right]. \tag{5.76}$$

To write equation 5.76 in a compact form on can introduce the formulation over the magnetic stress tensor:

$$\frac{\mathrm{d}v_i^k}{\mathrm{d}t} = \sum_j m_j\left[\frac{S_i^{kl}}{\Omega_i\rho_i^2}\nabla_i^l W_{ij}(h_i) + \frac{S_j^{kl}}{\Omega_j\rho_j^2}W_{ij}(h_j)\right]. \tag{5.77}$$

With the magnetic stress tensor S^{kl} given as:

$$S^{kl} = -\left(P + \frac{1}{2\mu_0}B^2\right)\delta^{kl} + \frac{1}{\mu_0}B^k B^l. \tag{5.78}$$

The conservation laws for linear momentum follow directly from the symmetry of the Lagrangian. However, it is worth noting that angular momentum is not strictly conserved in the SPMHD formulation, due to the second term on the right hand side of equation 5.76 which acts like an an-isotropic force term. Moreover, we note that this an-isotropic force term is entirely derived from the numerical representation of the induction equation in equation 5.74 while the isotropic part (the first term on the left hand side of equation 5.76) is a direct consequence of the symmetry of the magnetic energy in the Lagrangian of ideal magnetohydrodynamics. Thus, we introduce a breaking of the symmetry while dicscretising the induction equation.

5.4.4 Energy equation in SPMHD

Finally, we briefly note that there are only minor changes in the energy budget in SPMHD compared to SPH. Internal energy and entropy can be treated in the same fashion as in SPH. The total energy however, has to be corrected with the energy that is provided by the magnetic field, which leads to and additional term that scales with $\mathbf{B^2}$, which can directly be seen by deriving the Legendre transformation with respect to $\mathbf{v}$ of the Lagrangian in equation 5.71. This yields the Hamiltonian:

$$\frac{\mathrm{d}E}{\mathrm{d}t} = \sum_i m_i \left[\mathbf{v}_i \cdot \frac{\mathrm{d}v_i}{\mathrm{d}t} + \frac{\mathrm{d}u_i}{\mathrm{d}t} + \frac{1}{2}\frac{B_i^2}{\rho_i^2}\frac{\mathrm{d}\rho_i}{\mathrm{d}t} + \mathbf{B}_i \cdot \frac{\mathrm{d}}{\mathrm{d}t}\left(\frac{\mathbf{B}_i}{\rho_i}\right)\right]. \tag{5.79}$$

This can be presented in a compact form with the magnetic stress tensor S^{kl}:

$$\frac{\mathrm{d}E}{\mathrm{d}t} = \sum_i m_i \sum_j m_j \left[\left(\frac{S^{kl}}{\Omega\rho^2}\right)_i v_j^k \nabla_i^l W_{ij}(h_i) + \left(\frac{S^{kl}}{\Omega\rho^2}\right)_j v_j^k \nabla_i^l W_{ij}(h_j) \right] = 0, \tag{5.80}$$

which finally yields the rate of change of the specific energy:

$$\frac{\mathrm{d}e_i}{\mathrm{d}t} = \sum_j m_j \left[\left(\frac{S^{kl}}{\Omega\rho^2}\right)_i v_j^k \nabla_i^l W_{ij}(h_i) + \left(\frac{S^{kl}}{\Omega\rho^2}\right)_j v_j^k \nabla_i^l W_{ij}(h_j) \right]. \tag{5.81}$$

5.5 Meshless Methods for Hydrodynamics

To further improve the convergence quantities one can combine the fast volume partition of SPH with the higher order accuracy of a Riemann-solver. This results in the so called meshless finite mass (MFM) and meshless finite volume (MFV) methods first presented in Gaburov and Nitadori (2011). However, the first implementation in a state of the art galaxy formation code is carried out in Hopkins (2015) for the code GIZMO where similar performance of MFM and MFV is shown compared to the state of the art moving mesh code AREPO. While MFM and MFV share the kernel weighted density calculation with SPH, the hydrodynamical flux vectors are integrated over the one-dimensional Riemann-problem defined over the surface between two fluid particles. In combination with a second order reconstruction of the flux gradients it is possible to invent a proper second order hydrodynamical scheme with an appropriate mathematical consistency and convergence proof as shown in Lanson and Vila (2008). We follow the implementation of Gaburov and Nitadori (2011) and Hopkins (2015) by deriving the meshless equations from the general conversation law for hydrodynamics with velocity $\mathbf{a}$.

$$\frac{\partial \mathcal{U}}{\partial t} + \nabla \cdot (\mathcal{F} - \mathbf{a} \otimes \mathcal{U}) = 0, \tag{5.82}$$

with

$$\mathcal{U} = \begin{pmatrix} \rho \\ \rho\mathbf{v} \\ \rho e_{\mathrm{tot}} \end{pmatrix} = \begin{pmatrix} \rho \\ \rho\mathbf{v} \\ \rho u + \frac{1}{2}\rho|\mathbf{v}^2| \end{pmatrix}, \quad \mathcal{F} = \begin{pmatrix} \rho\mathbf{v} \\ \rho\mathbf{v}\otimes\mathbf{v} + P\mathcal{I} \\ \rho(e_{\mathrm{tot}} + P)\mathbf{v} \end{pmatrix} \tag{5.83}$$

where ρ is the density $\mathbf{v}$ the fluids velocity, e_{tot} the total energy, u the internal energy and P the pressure. $\mathcal{I}$ is the identity.
It is possible to derive a weak solution for equation 5.82 by multiplying it with a test function φ and integrating the resulting equation by parts over the whole spatial domain Ω.

$$\int_\Omega \left(\frac{d\mathcal{U}}{dt}\varphi - \mathcal{F}\nabla\varphi\right) d\Omega + \int_{\partial\Omega} (\mathcal{F}\varphi) \cdot \mathbf{n}_{\partial\Omega} d\partial\Omega = 0, \tag{5.84}$$

where we used the general definition of the Lagrangian co-moving derivative for an arbitrary function f with $df/dt = \partial f/\partial t + \mathbf{a}(\mathbf{x},t)\cdot\nabla f$. The vector $\mathbf{n}_{\partial\Omega}$ is the normal vector on the surface dΩ of the integration volume Ω. The test function $\varphi = \varphi(\mathbf{x},t)$ is continuous and differentiable with $d\varphi/dt = 0$. We assume that the surface term of equation 5.84 vanishes if we integrate over the whole domain Ω because the test function vanishes at infinity. Therefore, we find

$$\frac{d}{dt}\int_\Omega \mathcal{U}(\mathbf{x},t)\varphi d^\nu\mathbf{x} - \int_\Omega \mathcal{F}(\mathbf{x},t)d^\nu\mathbf{x} = 0. \tag{5.85}$$

The final goal of this calculation is to find a suitable volume discretization of equation 5.85 and different attempts have been made to do so. If we choose to partition the volume on by performing a Voronoi or Delauny triangulation between the reconstruction points $\mathbf{x}_i$ of the particle distribution that samples the Volume Ω we would resemble the structure of a moving mesh code. Although this approach has some advantages it is still computational expensive and relies on complicated re-meshing strategies to repair the mesh rather than build a new mesh after each time step to make the scheme efficient. However, we choose a different strategy of partitioning the volume between the fluid tracers $\mathbf{x}_i$. We therefore consider an 'SPH-like' approach for partitioning the volume amongst the particles by calculating the fractional volume ψ as a kernel weighted quantity via:

$$\psi_i(\mathbf{x}) = \frac{1}{\omega(\mathbf{x}_i)}W(\mathbf{x}-\mathbf{x}_i, h(\mathbf{x})), \tag{5.86}$$

$$\omega(\mathbf{x}) = \sum_j W(\mathbf{x}-\mathbf{x}_j, h(\mathbf{x})) \tag{5.87}$$

where h is some characteristic kernel size (i.e. the smoothing length from SPH). If we insert the volume partition from equation 5.86 and 5.87 to 5.85 and perform a Taylor-expansion up to second order we obtain

$$\sum_i \left[\varphi_i \frac{d}{dt}(V_i\mathcal{U}_i) - V_i\mathcal{F}_i\cdot(\nabla\varphi)_{\mathbf{x}_i}\right] = 0, \tag{5.88}$$

where $(\nabla\varphi)_{\mathbf{x}_i}$ is the product of the tensor $\mathcal{F}$ with the derivative of φ evaluated at the position x_i. So far this represents a second order reconstruction of the scheme. Again, there are different approaches to continue from here. The Ansatz which is the fastest but also the least accurate is to define 'SPH-gradients' and reduce the method again to order zero. We follow a different approach and keep the scheme second order by following Mocz et al. (2014) and Hopkins (2015) and introduce locally centred least-squares matrix gradient operators. We can write the second order gradient for an arbitrary function f via

$$(\nabla f)_i^\alpha = \sum_j\sum_{\beta=1}^{\nu}(f_j - f_i)\mathbf{B}_i^{\alpha\beta}(\mathbf{x}_j-\mathbf{x}_i)^\beta\psi_j(\mathbf{x}_i) + O(h_i^2) \tag{5.89}$$

$$= \sum_j (f_j - f_i)\tilde{\psi}_j^\alpha(\mathbf{x}_i). \tag{5.90}$$

with $\tilde{\psi}_j^\alpha(\mathbf{x}_i)$ given as

$$\tilde{\psi}_j^\alpha(\mathbf{x}_i) = \sum_{\beta=1}^{\nu}(f_j - f_i)\mathbf{B}_i^{\alpha\beta}(\mathbf{x}_j-\mathbf{x}_i)^\beta\psi_j(\mathbf{x}_i). \tag{5.91}$$

The matrix **B** can be determined by computing it as the inverse of the matrix **E** which is given by:

$$\mathbf{E}_i^{\alpha\beta} = \sum_j (\mathbf{x}_j - \mathbf{x}_i)^\alpha (\mathbf{x}_j - \mathbf{x}_i)^\beta \psi_j(\mathbf{x}_i). \tag{5.92}$$

Although this approach is in practice relatively stable it can happen that the matrix **E** can not be inverted. If we encounter such a rare case we approximate the gradient by building the gradient for the quantity using the derivative of the kernel. Finally, we can insert the second order gradients we constructed in equation 5.90 and insert it in equation 5.88.

$$\sum_i \varphi_i \left(\frac{d}{dt}(V_i \mathcal{U}_i) + \sum_j [V_i \mathcal{F}_i \tilde{\psi}_j^\alpha(\mathbf{x}_i) - V_i \mathcal{F}_i \tilde{\psi}_i^\alpha(\mathbf{x}_j)] \right) = 0. \tag{5.93}$$

However, φ is an arbitrary function therefore the term in the brackets of equation 5.93 has to vanish and we find:

$$\frac{d}{dt}(V_i \mathcal{U}_i) + \sum_j [V_i \mathcal{F}_i \tilde{\psi}_j^\alpha(\mathbf{x}_i) - V_j \mathcal{F}_j \tilde{\psi}_i^\alpha(\mathbf{x}_j)] = 0. \tag{5.94}$$

We do not evaluate the flux function at the particle positions i and j directly because there would be again the need to introduce some dissipation terms like in our default SPH-solvers to obtain a well behaving numerical scheme. Therefore we calculate the fluxes as the time-centred one dimensional Riemann-problem at the surface between the particles i and j. This procedure allows for the 'correct' value for the dissipation between any two given particles i and j. We therefore replace the fluxes at the particle positions i and j with the combined Riemann-Flux $\widetilde{\mathcal{F}}_{ij}$ and obtain:

$$\frac{d}{dt}(V_i \mathcal{U}_i) + \sum_j \widetilde{\mathcal{F}}_{ij} [V_i \tilde{\psi}_j^\alpha(\mathbf{x}_i) - V_j \tilde{\psi}_i^\alpha(\mathbf{x}_j)] = 0. \tag{5.95}$$

Finally, we define the effective face area $\mathcal{A}_{ij}$ as $\mathcal{A} = |A|_{ij} \hat{A}_{ij}$ with $\mathcal{A}_{ij}^\alpha = V_i \tilde{\psi}_j^\alpha(\mathbf{x}_i) - V_j \tilde{\psi}_i^\alpha(\mathbf{x}_j)$ and find the Godunov-type finite volume equation

$$\sum_i \frac{d}{dt}(V_i \mathcal{U}_i) + \sum_j \mathcal{F}_{ij} \cdot \mathcal{A}_{ij} \tag{5.96}$$

Further, we follow the slope limiting procedure of Springel (2010) and Hopkins (2015). The reconstruction procedure on the effective faces is following Hopkins (2015), although we calculate the quadrature point in first order via $\mathbf{x}_{ij} = (\mathbf{x}_i + \mathbf{x}_j)/2$. To solve the actual one dimensional Riemann-problem we adopted two different Riemann-solvers. Our default solver is a Harten-Lax-van-Leer (HLL) Riemann-solver with an approximate reconstruction of the contact wave (HLLC) following Toro et al. (1994). Finally, we point out that it makes a difference in which reference frame we solve the Riemann-problem. If we solve the Riemann problem in co-moving coordinates for the quadrature point, we obtain the MFM-method and conserve the mass-flux, if we solve it in a fixed zero reference frame for the quadrature-point we obtain the MFV-scheme, conserving the volume flux.

5.6 Time integration and adaptive time stepping

Now that we know how the equation of motion can be represented for gravity and hydrodynamics in either the classic SPH/SPMHD fashion or the more advanced Riemann-presentation of the MFM/MFV flux vectors, we need to integrate those equations. Thus we will discuss common numerical integration schemes and show their advantages/disadvantages before we choose our favoured integration scheme. Specifically, we note that we extended the gradient reconstruction for MFM and MFV to second order. Thus choosing an integrator for time integration of lower order would be unacceptable. This out qualifies the following methods that are still commonly used in a lot of physical applications:

- Explicit Euler method,
- Implicit Euler method.

The former is not energy conserving, while the later is energy conserving down to machine precision. However, both of these introduce a global error that is proportional to the step size, which makes the orbit integration in a collisionless N-body system highly inaccurate. Nevertheless, it is worth mentioning both methods as they are typically used as a starting point to construct a higher order scheme, like:

- Heun method,
- Runge-Kutta-method (up to order N),
- Leap-Frog method,

The first two are higher order realisations of the implicit Euler method, whereby the Heun-method is a special case of the Runge-Kutta method of convergence order two. The Runge-Kutta methods can in principal be expanded up to order N. However, this requires a massive overhead in computational time, due to multiple copies of a single physical state for the correction term in the higher order realisations of the scheme. Thus a preferred scheme would be one where you have to copy the physical state only once. This can be realised with the leap-frog integrator, which has the big advantage that it is phase-space conserving due to its symplectic nature. Generally, Hamiltonian systems are not stable against non Hamiltonian motions. Thus, one needs to reduce the non Hamiltonian perturbations to a minimum. But this is exactly the symplectic nature of the leap-frog method. While non-symplectic integrators (every integrator we discussed apart from the leap-frog) introduce a non-Hamiltonian perturbation to the system, the leap-frog conserves the phase space and thus the Hamiltonian nature of the integrated nature. The leap-frog method is thus Poincare-invariant and preserves the integral:

$$\frac{dI}{\mathrm{d}t} = \frac{\mathrm{d}}{\mathrm{d}t}\oint_{C(t)} \mathbf{p}\cdot d\mathbf{q}. \tag{5.97}$$

Springel et al. (2005b) point out that this has several advantages for orbit integration with high eccentricity. Thus Springel et al. (2005b) carried out simulations of a two body orbit with eccentricity of $\epsilon = 0.9$ with the Runge-Kutta method in second and fourth order and the leap frog in its Kick-Drift-Kick (KDK) and Drift-Kick-Drift (DKD) versions. While the Runge-Kutta methods preserve the orientation of the orbit, they are not capable of preserving the eccentricity of the system. Vice versa the Leap-frog method preserves the eccentricity while not being exact in preserving the orientation of the orbit. This means that the leap-frog-integrator is energy conserving in the sense that the energy can oscillate around the real value of the energy of the physical system that is modelled. However, this oscillatory motion can be described with Hamiltonian perturbation theory. The consequence of this is that all the orbits are stable but the Hamiltonian perturbation introduces a shift in orbit orientation as demonstrated in Springel et al. (2005b). The leap-frog method can be expressed as in its KDK-version via:

$$\mathbf{v}\left(t+\frac{\Delta t}{2}\right) = \mathbf{v}(t) + \frac{1}{2}\mathbf{a}(t)\Delta t, \tag{5.98}$$

$$\mathbf{r}(t+\Delta t) = \mathbf{r}(t) + \mathbf{v}\left(t+\frac{\Delta t}{2}\right)\Delta t, \tag{5.99}$$

$$\mathbf{v}(t+\Delta t) = \mathbf{v}\left(t+\frac{\Delta t}{2}\right) + \frac{1}{2}\mathbf{a}(t+\Delta t)\Delta t. \tag{5.100}$$

With the particle position $\mathbf{r}$, the particle velocity $\mathbf{v}$ and the particle acceleration $\mathbf{a}$. Δt is a constant time step in this context. We note that this system of equations could also be called symplectic Euler-method as one computes an explicit Euler-method on the half steps. This shows the beauty of this method, it is easy to code, conserves energy and is computationally fast.

Finally, we have to determine the time step that we use for the time integration. Hereby we distinguish between the gravity time step and the hydrodynamic time step. The time step for the gravitational interactions is given as:

$$\Delta t_i^{\mathrm{grav}} = \min\left[\Delta t_{\mathrm{max}}, \left(\frac{2\eta\varepsilon}{|\mathbf{a}_i|}\right)^{1/2}\right], \tag{5.101}$$

where η is a quality parameter, ε denotes the gravitational softening length and $\mathbf{a}_i$ is the acceleration on particle i. Δt_{max} is the initial guess for the time step that is chosen before or at the start of the simulation. For SPH-particles we further use a common CFL (Courant-Friedrichs-Levy) criterion following:

$$\Delta t_i^{\mathrm{hyd}} = \min\left[\Delta t_i^{\mathrm{grav}}, \frac{C_{\mathrm{Courant}} h_i}{\max_j(v_{ij}^{sig})}\right], \tag{5.102}$$

where v_{ij} is the signal velocity, which is basically given as the sum of the sound speed and the velocity of the fluid flow. We note that this time step is different in SPH and SPMHD as the signal velocity in MHD is the Alfvén velocity and not the sound speed. The maximum $\max_j(v_{ij}^{sig})$ is computed over the nearest neighbours and C_{Courant} is a numerical constant which we set to 0.15 in all our simulations. The factor h_i is the smoothing length. However, in a cosmological simulation one undoubtedly runs in limitations with time integration due to the dynamic range problem[5]. Thus these time steps are in practice not defined globally but follow a time step hierarchy where the time step is increased or decreased by a factor of two based on the time step calculations in 5.101 and equation 5.102. This has the advantage that the time resolution is high in high density region while we do not waste computational time in the low density regions as the time step is kept long there, which can be justified by the long cooling and long dynamical times in those regions. We show a schematic sketch of how the adaptive time stepping works in in Figure 5.7 .

[5]The dynamic range problem simply refers to the fact that in a cosmological simulation of galaxy formation one has to resolve several scales that differ over various orders of magnitude, from Mpc scales in galaxy clusters, over kpc scales in galaxy to pc scales in the ISM. These length scales correspond to different density regimes that have to be resolved

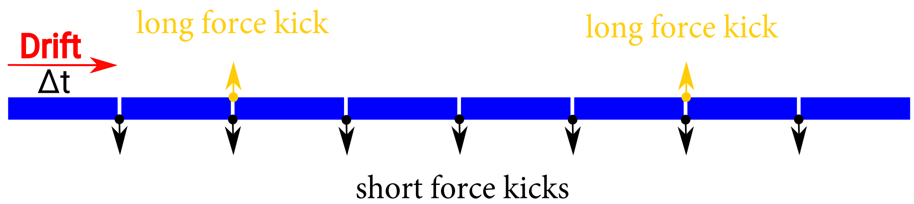

Figure 5.7: We show a schematic sketch of how the adaptive time stepping method can be realised and visualises the synchronisation between the long kicks and the short kicks. A similar view of this scheme is given in Springel (2005).

5.7 Subgrid modells for simulations of galaxy formation and evolution

In this section we discuss the numerical implementation of the hybrid multiphase model following Springel and Hernquist (2003), its consequences and limitations on galaxy formation and evolution. In large scale cosmological simulations one usually faces the issue that it is impossible to resolve physical processes that play a significant role on ISM scales. Today cosmological simulations achieve a particle mass resolution of a few times 10^3 $M_\odot$ per particle/cell. However, the latter resolution can only be achieved in cosmological zoom-in simulations of single galactic haloes of Milky Way-like galaxies. While single groups have made enormous progress over the past decade to run even higher resolution simulations of dwarf galaxies or high redshift galaxies at solar mass and sub-parsec resolution (Emerick et al., 2018; Forbes et al., 2016; Hopkins et al., 2018; Hu et al., 2017, 2016, 2019; Steinwandel et al., 2020b; Wheeler et al., 2019), large scale cosmological simulations will be unable to properly resolve the ISM in the near future. Thus some kind of subgrid modell for these unresolved processes (cooling, star formation, stellar winds, supernova-feedback, only to name a few) in the ISM has to be provided.

5.7.1 Radiative-Cooling

The stellar component of galaxies is forming from the cold fraction of the gas in the ISM. Thus heat has to be removed from the hot ambient medium via radiative cooling to obtain the cold phase from which we can form stars. While gas cooling involves very complicated physical processes, for cosmological simulations one can assume an optical thin approximation in collisional-ionisation equilibrium, which implies that there is an equilibrium between free electrons and ions in the plasma, where atoms are ionised by inter atom collisions. To first degree one can assume that primordial matter consists to 76 per cent ($X = 0.76$) of hydrogen and 24 per cent (Y=0.24) of helium. Under this assumption the major cooling processes would be:

- Collisional Excitation of H^0 and He^+,
- Collissional Ionisation of H^0, He^0 and He^+,
- One-electron-recombination of H^+, He^+ and He^{++},
- two-electron-recombination of He^{++},
- Thermal Bremsstrahlung,
- Inverse Compton-scattering at the cosmic microwave background,

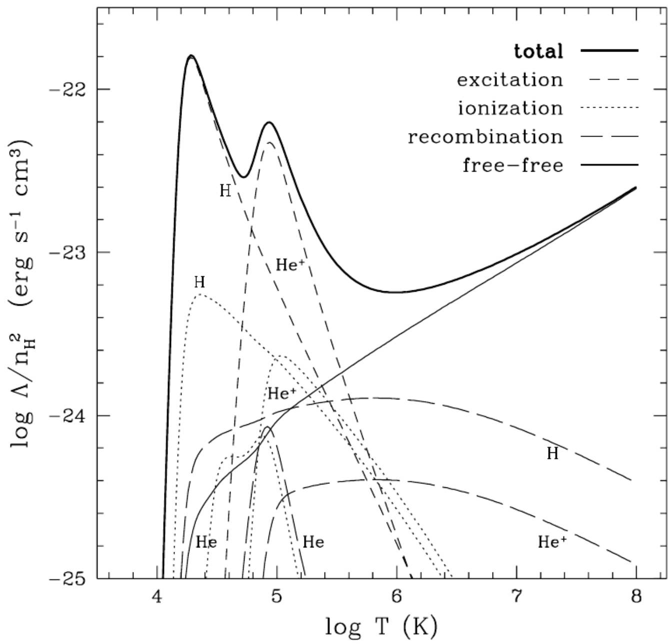

Figure 5.8: We show the cooling rate that one can calculate for an primordial gas composition in optically thin approximation with X = 76 and Y=0.24 in collision-ionisation equilibrium. The thick solid line shows the total cooling rate of the gas composition, the short-dashed line the shock absorption and the thin solid line the Bremsstrahlung continuum. The long-dashed lines show the recombination spectrum for different species in the primordial gas composition. The dotted lines show the spectrum of collisional ionisation processes. For small temperatures cooling is dominated by ionisation due to collisions and for larger temperatures Bremstrahlung radiates most of the energy away. We took this Figure from Katz et al. (1996).

which leads to the cooling rates in Figure 5.8 taken from Katz et al. (1996). However, one has to distinguish between actual physics and the numerical implementation, as it is obvious that this cooling function is basically not capturing any cooling contribution below 10^4 K. This none ability of self consistently capturing any of the cold phase of the gas within galaxies is a huge limitation of this cooling function and a more complicated cooling function has to be considered in order to self consistently capture the cold phase of the ISM. However, it is still possible to model the mass flux into the cold phase given this cooling rate and use it to build an effective model for star formation and feedback based on the theoretical understanding of the ISM of McKee and Ostriker (1977).

5.7.2 Hybrid-Multiphasen-Modell

The most popular and the most successful approach for a sub grid model for star formation and feedback is presented in Springel and Hernquist (2003), who account for the fact that there are unresolved scales in large scale simulations of galaxy formation and acknowledge the fact that the ISM is not resolved in those simulations. However, it can be treated in a sub grid fashion by assuming that stars form in old clouds, cold clouds are evaporated by supernova explosion which produces hot gas the subsequently cools down again into a cold, star forming phase. In this approach one assumes that every multiphase particle consists out of cold clouds and hot gas, where the cold fraction is the gas that can contribute to

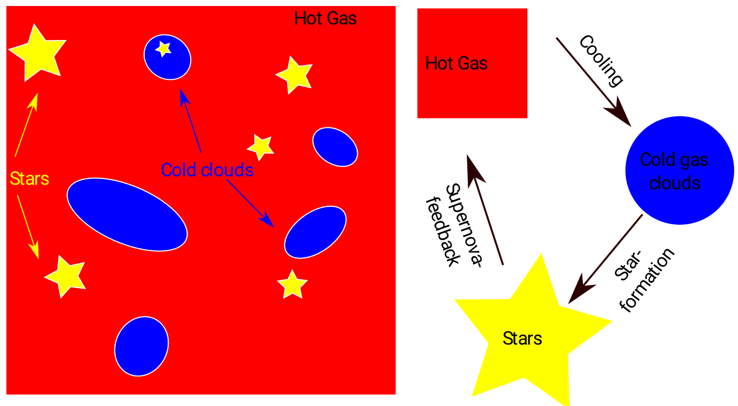

Figure 5.9: This Figure shows a schematic sketch of the multiphase model that is often used in galaxy formation simulations to this day. It demonstrates how the various components of the ISM interact with each other.

star formation. Thus one can assume that the density of multiphase particles is given via:

$$\rho = \rho_c + \rho_h, \tag{5.103}$$

where ρ_c is the cold gas and ρ_h is the hot gas. The thermal energy per unit volume is then given via (Springel and Hernquist, 2003):

$$\varepsilon = \rho_c u_c + \rho_h u_h, \tag{5.104}$$

with u_c and u_h as the energy per unit volume in the respective phase. The multiphase model captures the three main mechanisms for mass exchange between stellar component, and gas component. Those are star formation, cloud evaporation due to supernovae and cloud growth due to radiative cooling. In Figure 5.9 we show a schematic sketch of the processes that are modelled. The multiphase model is based on the assumption that star formation takes place in the cold clouds on a characteristic timescale $t_\star$. Further, one assumes that a fraction β of these stars is short lived and contributes to the energy release as supernova Type II where one assumes the canonical supernovae energy of 10^{51} erg, which results in an energy release of $4 \cdot 10^{48}$ erg per solar mass formed by assuming a Salpeter IMF Salpeter (1955). Other popular choices for the IMF are the Kroupa (Kroupa, 2001) and the Chabrier (Chabrier, 2003) IMF. Regardless of the IMF the fraction of massive stars β is usually around 0.1 and one obtains a rate equation for the rate of change of stellar mass:

$$\frac{\mathrm{d}\rho_\star}{\mathrm{d}t} = \frac{\rho_c}{t_\star} - \beta\frac{\rho_c}{t_\star} = (1-\beta)\frac{\rho_c}{t_\star} \tag{5.105}$$

The modelling ignores the time delay of the Type II supernova explosions of around 10 Myr. However, we note that recent studies show (Keller and Kruijssen, 2020) that this delay has an impact in further advanced sub grid models for feedback and thus we point to those studies for a deeper insight on this choice. Given the no delay constrain the heating rate by the supernovae can be calculated via:

$$\frac{\mathrm{d}}{\mathrm{d}t}(\rho_h u_h) = \varepsilon_{SN}\frac{\mathrm{d}\rho_\star}{\mathrm{d}t} = \beta u_{SN}\frac{\rho_c}{t_\star}, \tag{5.106}$$

with the specific supernova energy $u_{SN} = (1-\beta)\beta^{-1}$. From that on can calculate a specific temperature to which the ambient medium is heated by the supernovae given via $T_{\rm SN} = 2\mu u_{\rm SN}/(3k_{\rm B})$, which we tabulate in Table 7.1 in chapter 7. The cold clouds evaporate due to thermal conduction at the rate:

$$\frac{\mathrm{d}\rho_c}{\mathrm{d}t} = A\beta\frac{\rho_c}{t_\star} \tag{5.107}$$

where A describes how efficient this process is and follows the density (McKee and Ostriker, 1977):

$$A \propto \rho^{-\frac{4}{5}}, \tag{5.108}$$

In summary we see that this model has its short comings, if one wants to consider detailed physical processes of the ISM and this sub grid model approach has been heavily criticised in the past years. However, this model allowed for the first time to model galaxies in large scale simulations of the universe and is simply justified by its great success in explaining properties for galaxies, galaxy clusters and the large scale structure of the Universe. It is needless to say that the model can be improved. However, every improvement of a sub grid model with increasing resolution requires to remove old constraints of the modelling that can be resolved in the new iteration of the model. Obviously this introduces sub gird modelling on even smaller scales with the new iteration. It is inevitable that there will always be an unresolved scale in every numerical simulation.

5.7.3 Supernova-Seeding

It is straightforward to couple this multiphase model for star formation and feedback to a model that introduces a magnetic dipol field with every supernova that explodes in the galaxy. This is different from the usual treatment of magnetic fields as it is presented in similar research works (Pakmor et al., 2017; Pakmor and Springel, 2013; Rieder and Teyssier, 2016; Vazza et al., 2018) who assume that there is a magnetic seed field that has been generated either during inflation or via the Biermann-battery process where micro currents are quickly amplified due to a miss alignment of density and pressure gradient, resulting to a non-linear contribution in the generalised law of Ohm. In the this so called Supernova-seeding approach we assume that magnetic energy is generated on the sub grid. This assumption is more physical as other groups have to introduce magnetic seed fields above the limit of the Biermann-battery field strength of roughly 10^{-18} G to achieve saturated dynamo action. In the model we assume that stars generate a magnetic field quickly via their internal α-Ω dynamo. However, when the star dies it is also reasonable to assume that some of the magnetic field is ejected with the supernova explosion and magnetises the ambient ISM. Therefore we inject a magnetic dipol with every exploding supernova and let it expand to certain size (Beck et al., 2013). We implement the model by coupling it directly to the induction equation to which we add a seed term on the right hand side:

$$\frac{\partial \mathbf{B}}{\partial t} = \nabla\times(\mathbf{v}\times\mathbf{B}) + \eta\Delta\mathbf{B} + \left.\frac{\partial \mathbf{B}}{\partial t}\right|_{\rm seed}. \tag{5.109}$$

The first and second term denote the convection term and the resistivity term. The amplitude of the seed field is given per time step Δt:

$$\left.\frac{\partial \mathbf{B}}{\partial t}\right|_{seed} = \sqrt{N_{\rm SN}^{\rm eff}}\frac{B_{\rm Inj}}{\Delta t}\mathbf{e}_{\rm B}, \tag{5.110}$$

$\mathbf{e}_{\rm B}$ is the unity vector, $B_{\rm Inj}$ defines the amplitude of the seed field at the time Δt and $N_{\rm SN}^{\rm eff}$ is a normalisation that is directly linked to the supernova rate that we obtain out of the star formation model.

Table 5.1: Parameter for the Supernova-Seeding, motivated by Reynolds et al. (2012).

Multiphase model parameters		
SnSeedRadius in [kpc]	r_{SN}	0.005
SnSeedBubble in [kpc]	r_{SB}	0.025
SnSeedField in [G]	B_{SN}	$1 \cdot 10^{-5}$
SnSeedSoftening in [kpc]	r_{SNsoft}	0.25

We note that one can straightforward modify the already present star formation approach to directly account for magnetic fields[6]. We thus use the stellar mass that is obtained from the cold gas in the time frame Δt:

$$m_\star = \frac{\Delta t}{t_\star} m_{\mathrm{C}} \tag{5.111}$$

here m_{C} is the mass of the cold gas, $t_\star$ is the characteristic star formation time scale and $m_\star$ is the mass of newly formed stars. The time scale for this is:

$$t_\star = t_{\mathrm{SF}} \left(\frac{\rho_{\mathrm{th}}}{\rho} \right)^{\frac{1}{2}} \tag{5.112}$$

An one obtains the number of supernovae:

$$N_{\mathrm{SN}}^{\mathrm{eff}} = \alpha m_\star \tag{5.113}$$

α is the number of supernovae per solar mass and depends on the underlying IMF. The numerical value of α is given in Table 7.1. The total magnetic field amplitude is then given by:

$$B_{\mathrm{inj}}^{\mathrm{all}} = \sqrt{N_{\mathrm{SN}}^{\mathrm{eff}}} B_{\mathrm{SN}} \left(\frac{r_{SN}}{r_{\mathrm{SB}}} \right)^2 \left(\frac{r_{\mathrm{SB}}}{r_{\mathrm{Inj}}} \right)^3 . \tag{5.114}$$

In this case B_{SN} is the mean magnetic field strength in a spherical supernova remnant with radius r_{SN}. The magnetic field is than adiabatic and isotropic expanded from a radius r_{SN} to a radius r_{SB}. By doing so we obtain spherical gas bubbles which inject the magnetic field at r_{Inj} (e.g. Hogan, 1983a). The value for r_{Inj} is directly dependent on the achievable numerical resolution, in this case the smoothing length h of the underlying SPMHD equations. Finally, we obtain the seeding rate:

$$\dot{B} \approx B_{SN} \left(\frac{r_{\mathrm{SN}}}{r_{\mathrm{SB}}} \right)^2 \left(\frac{r_{\mathrm{SB}}}{r_{\mathrm{Inj}}} \right)^3 \frac{\sqrt{\dot{N}_{\mathrm{SN}}^{\mathrm{eff}} \Delta t}}{\Delta t}, \tag{5.115}$$

with supernova rate $\dot{N}$. The numerical values for r_{SN}, r_{SB} and B_{SN} are given in Table 5.1. The injected magnetic field has to obey the solonoidal constraint and thus we seed a dipol with dipol moment $\mathbf{m}$:

$$\left. \frac{\partial \mathbf{B}}{\partial t} \right|_{\mathrm{seed}} = \frac{1}{|\mathbf{r}|^3} \left[3 \left(\frac{\partial \mathbf{m}}{\partial t} \cdot \mathbf{e}_{\mathrm{r}} \right) \mathbf{e}_{\mathrm{r}} - \frac{\partial \mathbf{m}}{\partial t} \right], \tag{5.116}$$

[6] We have carried out this study with Master student Eirini Batziou at the USM. In her Master thesis we modified the star formation approach and removed the present density threshold and replaced it with a pressure threshold. In this way we can directly account the magnetic pressure $B^2/8\pi$ and account for the pressure contribution of the magnetic field in the star formation rate.

with the radial unity vector $\mathbf{e}_\mathrm{r}$ and the rate of change of the magnetic dipol field:

$$\frac{\partial \mathbf{m}}{\partial t} = \sigma \frac{B_\mathrm{Inj}^\mathrm{all}}{\Delta t} \mathbf{e}_\mathrm{B} \tag{5.117}$$

The parameter σ is simply a numerical constant. The unity vector $\mathbf{e}_\mathrm{B}$ constrains the direction of the dipol field and is calculated in weak field approximation (WFA) as the direction of the acceleration field $\mathbf{a}$:

$$\mathbf{e}_\mathrm{B} = \frac{\mathbf{a}}{|\mathbf{a}|}. \tag{5.118}$$

Moreover, we cut the field at r_Inj and smooth the field for $\mathbf{r} \rightarrow 0$. The smoothing is necessary to avoid a discontinuity at $\mathbf{r} = 0$. Finally, we define the numerical value of sigma:

$$\sigma = r_\mathrm{Inj}^3 \sqrt{\frac{1}{2} f^3 (1 + f^3)}, \tag{5.119}$$

with $f = r_\mathrm{soft}/r_\mathrm{Inj}$ and we are done writing our short supernova seeding model.

5.8 Resolved models for simulations of galaxy formation and evolution

Now that we have taken a look in the world of sub grid modelling, we want to improve this picture. However, this is a tedious step as there is a good motivation for sub grid models in simulations of galaxy formation and evolution. In principle the argumentation goes as follows. We know that there are a lot of process that play a crucial role in the ISM. The major processes are (magneto-) hydrodynamics, cooling, turbulence, star formation, stellar winds, photo-ionisation, photoelectric heating and supernovae. Usually, one argues that these processes cannot be resolved in a galaxy scale simulation and one needs sub grid models to mimic the processes in the ISM and tune them to CGM and ICM properties as these components can be very well observed from radio to X-rays and we basically now what expect here. This approach is valid and will be useful on large scales over the next decade. However, it raises the inevitable question if this is the only way to progress the field of galaxy formation and evolution? The answer to this question brings us on tricky terrain as the galaxy community is aware of the answer and it is no. There is another way to approach this problem of obtaining the CGM and ICM properties in numerical simulations. Namely, one could resolve all the process at the ISM scale where the energy is injected from stellar winds, supernovae and other relevant processes. This is tricky and in hind sight it is a lot of work and requires a detailed understanding of ISM physics and one needs a lot of resolution in a galaxy wide simulation (sub-parsec and at least solar mass in particle resolution)[7]. We already discussed the hydrodynamics issue in numerical simulations in depth and will present a full test suite for our new hydro-solver in section 6. Thus, we start by acknowledging that the cold phase of the ISM exists and it can actually be resolved in a galaxy scale simulation.

[7]Moreover, on a personal note it has a lot of potential to raise questions in the ISM community and the galaxy community. While the ISM community is convinced that the simulations are still not high enough resolution for detailed ISM studies, the galaxy formation community thinks that is an unnecessary effort. In reality the truth is somewhere in between. On the one hand I would like to have factor of 10 more in resolution to show convergence on our result, on the other hand this approach of resoling physical processes at the injection scale is the only one which will be able to explain which physical processes drive outflows in galaxies in a resolved fashion.

5.8.1 Chemistry Network

We couple the hydrodynamics and gravity routines to a non-equilibrium chemical model that is based on Glover and Mac Low (2007a) and Glover and Clark (2012) with an extension towards the inclusion of the carbon chemistry following Nelson and Langer (1997). The chemical network follows in total seven species: H, H_2, H^+, C^+, CO, O^+ and free electrons. While H_2, H^+ and CO are directly calculated from the non-equilibrium rate equations the others are obtained through the conservation laws for element and electrical charge. H_2 and H^+ follow several reaction which can are summarised in Table 1 of Micic et al. (2012). Carbon is always present as C^+ when not in CO missing an accurate treatment for the transition towards C as presented in Nelson and Langer (1999). O is always present as O^+ when not bound in CO. The formation of CO is driven by the reaction $C^+ + H_2 \rightarrow CH_2^+$. The CH_2^+ can experience two different reactions. Either it is destroyed due to photo ionising radiation or reacts with O to CO in a reaction that is catalysed by H_2. In reality there are two different formation channels for molecular hydrogen. The first is the more prominent 'dust-channel' in which H_2 is formed on the surface of dust grains where the dust acts as a catalyst for the formation process of molecular hydrogen. The second formation channel is the primordial channel that is driven by the process of a neutral hydrogen atom capturing a free electron that can attract ionised hydrogen. This channel requires free electrons and is quickly suppressed on strongly cooling fluids. In the simulations we only include the dust channel as this is a very good approximation even for lower metallicities following Glover (2003). On the other hand H_2 can be destroyed by photo-dissociation. H^+ is formed by collisional excitation of H due to free electrons or cosmic rays. H^+ can be destroyed by the recombination process with free electrons.

We include several non-equilibrium cooling and heating processes. There are 6 major cooling processes: fine structure line cooling of atom and ion species (mainly C+, Si+, O), cooling due to vibration and rotation lines of molecules (H_2, CO), Lyman-alpha cooling of hydrogen, collision that dissociate H_2 or ionise hydrogen and the recombination of H^+ (in gas phase and on the surface of dust grains). While not directly included in the chemistry network we assume that Silicon is present in the simulations as Si^+ and thus it is explicitly included in the non-equilibrium cooling channel. We track various heating processes. The major ones are given as photoelectric heating from dust grains and polycyclic aromatic hydrocarbonates (PAHs), cosmic ray ionisation, photodissociation of H_2, UV-pumping of H_2 and formation of H_2. Further, we include the heating of a temporarily and spatially evolved interstellar radiation field (ISRF) following Hu et al. (2017).

5.8.2 Star Formation

Star formation is modelled used the methods presented in Hu et al. (2016) and Hu et al. (2017) via an IMF-sampling approach. This is a middle ground between the sink particle method for star formation that is incorporated by smaller scale ISM simulations of disc patches and single molecular clouds and the Schmidt-type star formation relation often used in larger scale cosmological simulations. While the IMF-sampling approach keeps the basics of the Schmidt-type star formation relation it represents a star by star method that works very well at around solar mass resolution when stochastic star formation models that work on larger scales can not be representative anymore for a stellar population but sink particle methods cannot be applied yet as the resolution is not yet high enough to justify this choice. Star formation in the simulations thus has the following form

$$\dot{\rho}_\star = \epsilon_{\rm eff} \cdot \frac{\rho_{\rm gas}}{t_{\rm ff}} \propto \rho_{\rm gas}^{1.5}. \tag{5.120}$$

At sufficient low resolution (above scales of 0.1 kpc) one can build an nice subgrid-model for star formation and feedback by adopting this star formation recipe with $\dot{\rho}_\star$ as the local star formation rate density, $\epsilon_{\rm eff}$ the star formation rate efficiency parameter, $\rho_{\rm gas}$ the local gas density and $\mathrm{t_{ff}}$ the local free fall time of the gas. A star forming gas particle is not instantly converted to a star particle, but rather converted in a stochastic process over the timescale given by $\mathrm{t_{ff}}/\epsilon_{\rm eff}$. The advantage compared to the sink particle method is that there is a delay time for star formation included that prevents runway star formation just due to the low resolution of the simulation. This is directly controlled by the gas densities that can be achieved in a certain simulation and allows for a delay time to transfer the particle back into a diffuse non-star forming state taking care of the unresolved nature of the star forming gas. As the particle resolution of these types of simulations is low (10^3 - 10^6 $\mathrm{M_\odot}$) one can assume that the underlying IMF is always fully represented. If this is the case one can derive a a simple feedback scheme by applying calculations of stellar populations and determine the amount of massive stars (> 8 $\mathrm{M_\odot}$) in the star particle. This directly inherits the energy budget of each star particle. Assuming a Kroupa-IMF (Kroupa, 2001) one can determine that one core collapse supernova (CCSN) would take place per 100 $\mathrm{M_\odot}$ of stellar material formed. Thus a star particle of mass $\mathrm{m_\star}$ deposits ($\mathrm{m_\star}/100$ $\mathrm{M_\odot}$ $\mathrm{E_{51}}$), where $\mathrm{E_{51}}$ is the canonical supernova energy of 10^{51} erg (e.g. Janka et al., 2012, for a detailed review on CCSN). The exact injection mechanism for the energy in this scheme is still under debate which has been discussed in detail in Keller and Kruijssen (2020). However, this modelling breaks down when the stellar particle mass comes arbitrarily close to 100 $\mathrm{M_\odot}$, where mass resolution is still too low to capture the Sedov-Taylor phase of the SN-remnants properly by pure thermal injection given the motivation for stochastic feedback schemes as used in Dalla Vecchia and Schaye (2012) and Hu et al. (2016). However, at mass resolutions higher than 10 $\mathrm{M_\odot}$ the Sedov-Taylor phase is resolved over a dynamic range of at least seven orders of magnitude as a function of the environmental density of the supernova in a galaxy scale simulation (Steinwandel et al., 2020b). In these regimes a star by star approach seems to be the best approach to accurately treating the stellar feedback. As discussed above the sink-particles cannot be used yet as the mass resolution between 0.1 $\mathrm{M_\odot}$ and 10 $\mathrm{M_\odot}$ is still somewhat to poor to actually resolve the star forming gas properly. Thus to model star formation star by star we adopt the IMF-sampling approach from Hu et al. (2017) while applying a Schmidt-type star formation relation as given in equation 5.120. We sample the IMF in the following manner. First, we convert a gas particle with a specific mass to a star particle with the same specific mass. In the next step for each star particle of mass $\mathrm{m_\star}$ we randomly draw an array of assumed stellar masses from a Kroupa-IMF with a mass threshold that ranges from 0.08 $\mathrm{M_\odot}$ to 50 $\mathrm{M_\odot}$. The numbers that are chosen from the IMF are then assigned to the star particle until the mass is equal to $\mathrm{m_\star}$ or exceeds $\mathrm{m_\star}$. Hence we sum up the mass of in the array $\mathrm{m_{IMF}}$ by calculating $M_{\rm IMF} = \sum m_{\rm IMF}$ until we reach $\mathrm{m_\star}$. As we draw random numbers from the IMF in practice it is unlikely to exactly sum towards $\mathrm{m_\star}$. In almost every case there will be a rest mass given by $\mathrm{M_{IMF}}$ - $\mathrm{m_\star}$. This mass is transferred to the next star particle which is assigned masses from the IMF. If mass resolution is low, this rest mass will be only a tiny fraction of the mass of the star particle $\mathrm{m_\star}$. However, if mass resolution is in the regime of a few $\mathrm{M_\odot}$ one massive star drawn from the IMF easily exceeds the mass $\mathrm{m_\star}$. At our mass resolution that is used in our set of simulations this happens quite regularly. In these cases the subsequent events are assigned the mass zero until the rest mass has vanished. The star particles with zero mass are then removed from the simulation. As this method is providing a source for none physical mass transfer between star particles this should be limited by a distance criterion to ensure that the stars generated at a certain point $\mathbf{r}$ in the simulation do not get there mass from a gas particles across the galaxy. In practice this only happens sparsely, but non the less we employ a distance criterion of 50 pc to ensure that all the mass comes roughly from the same converging flow of gas. The sampling process itself is carried out with the acceptance rejection method, while applying a powerlaw envelope function with

an acceptance rate of 65 per cent. We note that we do not store particles below two solar masses to optimise the memory imprint of the code. Still, we add them to M_{IMF}.
We adopt a Jeans star formation threshold to separate the star forming from the none star forming population of gas particles. This model only involves one free parameter. The Jeans mass is evaluated by:

$$M_{J,i} = \frac{\pi^{5/2} \cdot c_{s,i}^3}{6 \cdot G^{3/2} \rho_i^{1/2}}, \tag{5.121}$$

where $c_{s,i}$ is the sound speed and ρ_i is the density of the gas particle. The star formation rate is instantaneous in this context and a star particle i becomes star forming when the following two conditions are met. The first is that $M_{J,i}$ is smaller than the mass inherited within a constant factor multiplied by the mass that is inside the kernel. In other words $M_{J,i} < N_{\mathrm{thresh}} \cdot M_{\mathrm{kernel}}$. With the kernel mass given as the number of neighbours times particle mass in the simulation $N_{\mathrm{ngb}} \cdot m_{\mathrm{gas}}$. We choose N_{thresh} to be 8 through all of our simulations. The second is that the gas has to have local negative velocity divergence (it has to be in a converging flow). Finally, we note an important difference to the work of Hu et al. (2017). Although Hu et al. (2017) used the same value for N_{thresh} as we do in this work, the method for solving the equations of hydrodynamics is a different one, as we use the MFM-method with a lower neighbour number. Effectively this would be the same as reducing N_{thresh} to 2.6 in the SPH simulations of Hu et al. (2017). However, they tested in their Appendix B (Figure B2) that there is only a weak influence of N_{thresh} on the star formation rate and the outflow rate with the values N_{thresh} set to two and 32.

5.8.3 Interstellar radiation field for UV

We use a UV radiation field following the implementation of Hu et al. (2017), who implemented a method for variable interstellar radiation fields that is valid as long as we consider the system to be gas poor, like it is in the here presented application of SN-feedback in small an intermediate sized dwarf galaxies. In larger galaxies like the Milky Way the dust-to-gas ratio is larger and dust extinction is a significant process that would not be captured by the current approach. In this case one has to apply a proper methodology for radiative transfer. In dwarf galaxies with low dust-to-gas ratio we can assume that dust extinction is not present (to first order). If this is the case then we can assume that we only have to sum over the single contributions to the UV field given by each individual star following an inverse squared law. In our implementation we use the results by Georgy et al. (2013) to obtain stellar lifetimes and effective temperature of the individual stars in the simulation, who carried out a detailed study of rotating and non-rotating stellar evolution calculations for stars from 0.08 $M_\odot$ to 120 $M_\odot$ for metal poor POP-II stars as they are present in dwarf galaxies or at very high redshift. The single stars are then cross correlated with the stellar library BASEL (Lejeune et al., 1997, 1998; Westera et al., 2002) to obtain their UV-luminosity within the energy band of $6 - 13.6$ eV, which is dominating the photoelectric heating rate in the ISM. We can then construct the energy density for each gas particle by summing over (time dependent) UV-luminosity's of the single stellar particles via:

$$u_{6-13.6\mathrm{eV}} = \sum_i \frac{L_{i,6-13.6\mathrm{eV}}}{4\pi c r_i^2}, \tag{5.122}$$

with the speed of light c, the luminosity $L_{i,6-13.6\mathrm{eV}}$ of star particle i in the respective UV energy range and the distance r_i at which the gas particle is located relative to the star. We note that one star particle can contain more than one star in this respect as we trace the UV-radiation form all stars with masses larger than 2 $M_\odot$. However, for star particles more massive than 4 solar masses the stars represent single stars. The computation of the energy density due to the UV-radiation of the stars (see 5.122) can be evaluated cheaply if we incorporate the computation while we walk GADGETS tree.

5.8.4 Stellar Feedback

Photoelectric heating

We incorporate the effect of photoelectric heating following Bakes and Tielens (1994); Wolfire et al. (2003) and Bergin et al. (2004) in the implementation that is presented in Hu et al. (2016) who adopt the photoelectric heating rate:

$$\Gamma_{\mathrm{pe}} = 1.3 \cdot 10^{-24} \epsilon D G_{\mathrm{eff}} n \ \ \mathrm{erg\ s^{-1} cm^{-3}}, \tag{5.123}$$

with the hydrogen number density n, the effective attenuation radiation field $G_{\mathrm{eff}} = G_0 \exp{-1.33 \cdot 10^{-21} D N_{\mathrm{H,tot}}}$, the dust-to-gas ratio D, the total hydrogen column density $N_{\mathrm{H,tot}}$ and the photoelectric heating rate ϵ that can be determined via

$$\epsilon = \frac{0.049}{1 + 0.004\psi^{0.73}} + \frac{0.037(T/10000)^{0.7}}{1 + 2 \cdot 10^{-4}\psi} \tag{5.124}$$

where ψ is denoted as $\psi = G_{\mathrm{eff}}\sqrt{T}/n^-$, with the electron number density n^- and the gas temperature T. Similar to Hu et al. (2017) we adopt a variable G_0 that is obtained locally by taking the UV-radiation of the individual stars into account. However, to account for the extragalactic UV-radiation we take a floor for $G_{0,\mathrm{min}}$ into account that is given via $G_0 = 0.00324$ and is obtained by integrating the UV-background from Haardt and Madau (2012) over the energy range of $6 - 13.6$ eV. Furthermore, we account for self-shielding against radiation in the dense regions of the ISM utilising the TREECOL algorithm (see Clark et al., 2012, for the details of the algorithm), where we calculate the column densities for H_2 and CO alongside with a 12 ray healpix scheme that can be efficiently carried out while evaluating GADGETS force tree algorithm. However, some simulations that are shown in this thesis will use the PM-algorithm. If the PM-part is active one has to make sure that TREECOL is calculating the self shielding only on the short range forces that are handled by the tree code. This has a potential complication as we have to make sure that the PM-part of the code is coarse enough to ensure that particles below a distance of 50 pc, which we adopt for our self shielding distance, are all handled by the tree and not the PM part of the code which would ultimately lead to a crash of the code. In practice, however, every physically motivated PM-mesh is coarse enough to ensure this, even at the high resolution at which we carry out some of our simulations.

Photo Ionising Radiation

Massive stars can distribute a massive amount of up to 10^{53} erg of energy in the form of ionising radiation over their total lifetime to the ambient ISM. This radiation output of the stars can blow massive HII-regions and can lead to a decrease in the ambient density in the close vicinity of the star, decreasing the ambient densities before a CCSN event takes place. The lower ambient density affects the cooling properties and thus the momentum and the hot phase generation by SN-events, enhancing the capability to drive winds (e.g. Hu et al., 2017, 2019).

Ideally, this task would require a proper radiative transfer scheme to accurately model the photo ionising feedback. However, this is computationally expensive. Thus we model the photo ionising feedback in a Stroemgren-approximation locally around each photo ionising source in the simulation (e.g. Hopkins

et al., 2012).
Every star particle that fulfils the criterion of having one ore more constituent with $m_{IMF} > 8\ M_\odot$, is treated as a photo ionising source in our simulations. Thus all of the neighbouring gas particles are labelled as photo ionised within the radius R_S around the star and the all of the inherent molecular and neutral hydrogen is destroyed and transferred to H^+ (we set the ionising fraction to 1 in our chemical model). Alongside this procedure we heat the surrounding gas within R_S to 10^4 K, which is the temperature in HII-regions, by providing the necessary energy input from the ionising source. This procedure is straightforward if R_S is known. However, while determining R_S is easy in a uniform medium as one can assume that R_S is just the classical Stroemgren-radius given by

$$R_{\mathrm{S}} = \left(\frac{3S_\star}{4\pi n^2\beta)}\right)^{\frac{1}{3}}, \tag{5.125}$$

with the photo ionising flux rate $S_\star$, the hydrogen nuclear number density $n = \rho_{\mathrm{gas}} X_{\mathrm{H}}/m_{\mathrm{proton}}$ and the recombination coefficient of hydrogen $\beta = 2.56 \cdot 10^{-13}$ cm^3 s^{-1}. In this case we use the case B hydrogen recombination rate that takes into account that the electrons might cascade over several energy levels to the hydrogen ground state, releasing a cascade of lower energy photons in the ambient medium. In a uniform medium this approximation for the Stroemgren-radius is valid. However, the ISM of galaxies has a complicated mulit phase structure in temperature and density that spans several orders of magnitude. Moreover, this definition of R_S would lead to an underestimation of R_S in the case of two radiation sources in close proximity to one another due to accounting twice for the photo ionising flux for each neighbouring gas particle that is accounted as a neighbour for both sources, thus we find R_S via iteration to obtain a more accurate result.
In equilibrium, the recombination rate of hydrogen in the neighbouring gas should be balanced by the ionising flux rate of the photo ionising source. The recombination rate per gas particle can be evaluated by

$$R_{i,\mathrm{rec}} = \beta n_{i,\mathrm{H}} N_{i,\mathrm{H}}. \tag{5.126}$$

with $N_{i,\mathrm{H}} = m_{i,\mathrm{gas}} X_{i,\mathrm{H}}/m_{\mathrm{proton}}$. The total recombination rate can then be obtained by summing over all the individual $R_{\mathrm{rec}} = \sum_i R_{i,\mathrm{gas}}$ in the respective region. This initial region is usually defined as a few 10 gas particles around the star. If there are two stars in close proximity, it could potentially happen that two gas particles are ionised twice by different stars. Thus we mark the ionised gas particles and exclude them from the summation of the total recombination rate if they are already ionised by a different star. Then we calculate $S_\star - R_{\mathrm{rec}}$ and check for its sign. If $S_\star - R_{\mathrm{rec}} > 0$ this means that we have to expand R_S if. We do this in 10 per cent margins. If $S_\star - R_{\mathrm{rec}} < 0$, R_S is too large and we decrease the estimate for R_S by a 10 per cent margin and mark the particles outside this new estimate for R_S to be not photo ionised any longer. This is controlled by a quality parameter which exits the iterative search for R_S. This is given as $|S_\star - R_{\mathrm{rec}}| < 10\beta m_{\mathrm{gas,in}} X_{\mathrm{H}}/m_{\mathrm{proton}}$. Hu et al. (2017) showed that this approach captures the ionisation front well in a uniform medium compared to more accurate radiative transfer calculations. However, Hu et al. (2017) also notes that this approach is strongly mass biased in a non-uniform medium as it discards all angular information which is partially due to the Lagrangian nature of SPH in their case. However, this restriction stays in MFM which is used in our implementation as well. This could be potentially improved by introducing a healpix scheme that subdivides the space around the star in pixels. If we would then ensure that we met the above criterion for each pixel separately (devided by the solid angle that is captured by each pixel) we would include the angular information and account for an asymmetric estimate for R_S capturing the irregular shape of the HII-region along different lines of sight. Thus how well we capture the structure of the

HII-region would then depend on the resolution of the Healpix sphere. In this methodology we would then increase the size of the Healpix sphere until every channel fulfils the exit criterion. However, the channels that already fulfil the criterion will not mark anymore particles as photoionised, removing the mass bias of the method. This implementation will be subject of future work to further improve the scheme. However, currently we have implemented a scheme with an angular resolution of 4π and thus we set a maximum Stroemgren radius $R_{S,max} = 50$ pc to overcome the mass bias and preserve dense molecular region from being artificially ionised.

Supernovae

We include the feedback of Type Ia and Type II (CCSN) supernovae in our simulations. The supernova feedback routines presented in this section are the core feedback mechanism in our current galaxy formation and evolution framework. While present, the Type Ia population is subdominant in our simulations due to the long delay time distribution of these type of supernovae, given our maximum simulation time of 1 Gyr, that we will apply to almost all our simulations which we show in this thesis. For the Type-II population we follow the metal enrichment given by the yields of Chieffi and Limongi (2004) who present stellar yields for stars from zero metallicity to solar metallicity for progenitors ranging from 13 $M_{\odot}$ to 35 $M_{\odot}$ from which we interpolate via metal enrichment routines. When a star explodes in a CCSN the mass is added to the surrounding 32 (one kernel) gas particles with the respective metal mixture that is expected from the above yields. To include the metal yields is of importance to obtain the correct cooling properties of the ambient medium and thus in the end the correct density structure of the ISM. However, as the amount of metal mass that is distributed into the neighbours of the star particle can be much larger than the mass of one gas particle we split the gas particles after the enrichment has taken place if they exceed the initial particle mass resolution of the simulation by a factor of two to avoid numerical artefacts. The split particles inherit all the physical properties that where present in the parent particle alongside specific internal energy, kinetic energy, metallicity and chemical abundances. The particle mass is split by a factor of two and the position is offset by one fifth of the parent particle smoothing length in a random direction to avoid the overlap of the two newly spawned particles. The spawning process requires a new domain decomposition and a re-build of the gravity tree which makes the code somewhat slower.
We close with the following statement. We do not say that this approach is superior compared to the sub grid model approach but we are convinced that it is a significant improvement to some constraints of the sub grid modelling approach as we can resolve the feedback in the ISM over at least seven orders of magnitude which we will show in great detail chapter 9 before we show our latest results in galaxy scale simulations with this model in section 10.

Chapter 6

Implementation and testing of the Meshless Finite Mass solver

In this chapter we will test the new MFM method and test it against the present pressure SPH implementation that is already present in GADGET. For the most tests we will present the MFM run and pressure SPH runs and directly compare the results. However, we want to note one thing in the beginning. Some of the SPH tests will look very bad compared to the MFM results and I cannot stress enough that the presented performance of SPH is by no means the best achievable performance for SPH. It is also unique and usually not done in comparisons of hydro solvers that we run identical setups. We run neither of the tests with optimised setups but rather choose a setup which I would apply in a production run in two or three dimensions. In this scenario we will see that MFM performs 'better' in almost all scenarios. However, the parameter choices we took are intrinsically a better fit for MFM than for SPH. Thus we advice caution, if one was to drive a conclusion from the presented simulations on the real performance of SPH.

6.1 Hydrodynamical test cases

6.1.1 Square test

In recent years the square or box test has become popular to benchmark hydrodynamical codes against advection and surface tension errors. While the former can be problematic in grid based codes, the later ones are known to appear in SPH codes as a manifestation of the SPH 'E0' errors. The test is initialised as a box of side length $L = 1/2$, with pressure $P = 2.5$ and density $\rho = 4$. This box is surrounded by a medium of pressure $P = 2.5$, density $\rho = 1$, thus the square is in pressure equilibrium with the surrounding medium. We use an adiabatic index of 5/3. We note that this is slightly different from other work where this test is carried out with an adiabatic index of 1.4. We choose 5/3 only to demonstrate that the test is generally not effected by the choice of the adiabatic index. However, we have to modify the internal energies in the initial conditions to ensure equilibrium conditions. Last but not least we follow Hopkins (2015) and give the fluid a very large velocity $\mathrm{v_x} = 142.3$ and $\mathrm{v_y} = -31.4$. We note that we set this velocity to test advection errors in Riemann based methods. The test is trivial for Riemann based methods if the fluid is initially at rest. The test is carried out with a corresponding resolution of 64^2 particles in two dimensions with pressure SPH and the MFM method. We show the results for the SPH version of the test in Figure 6.1 and for the MFM version in Figure 6.2, for $t = 0$ (plot on the top in the respective Figure) and $t = 10$ (plot on the bottom in the respective Figure).

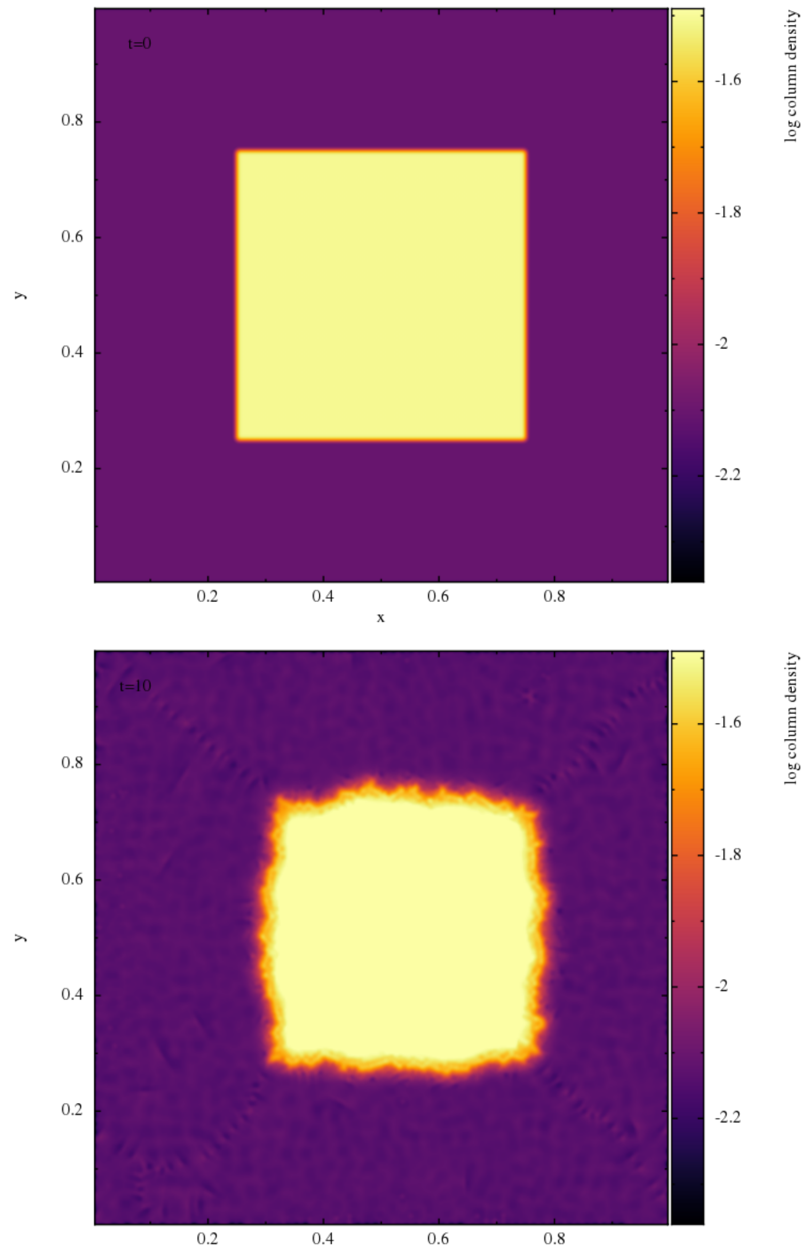

Figure 6.1: Pressure SPH version of the square test for a resolution of 64^2. While the box is initially in pressure equilibrium the artificial conduction prescription present in our implementation and the 'E0'-error of SPH leads to a rounding of the edges at later times.

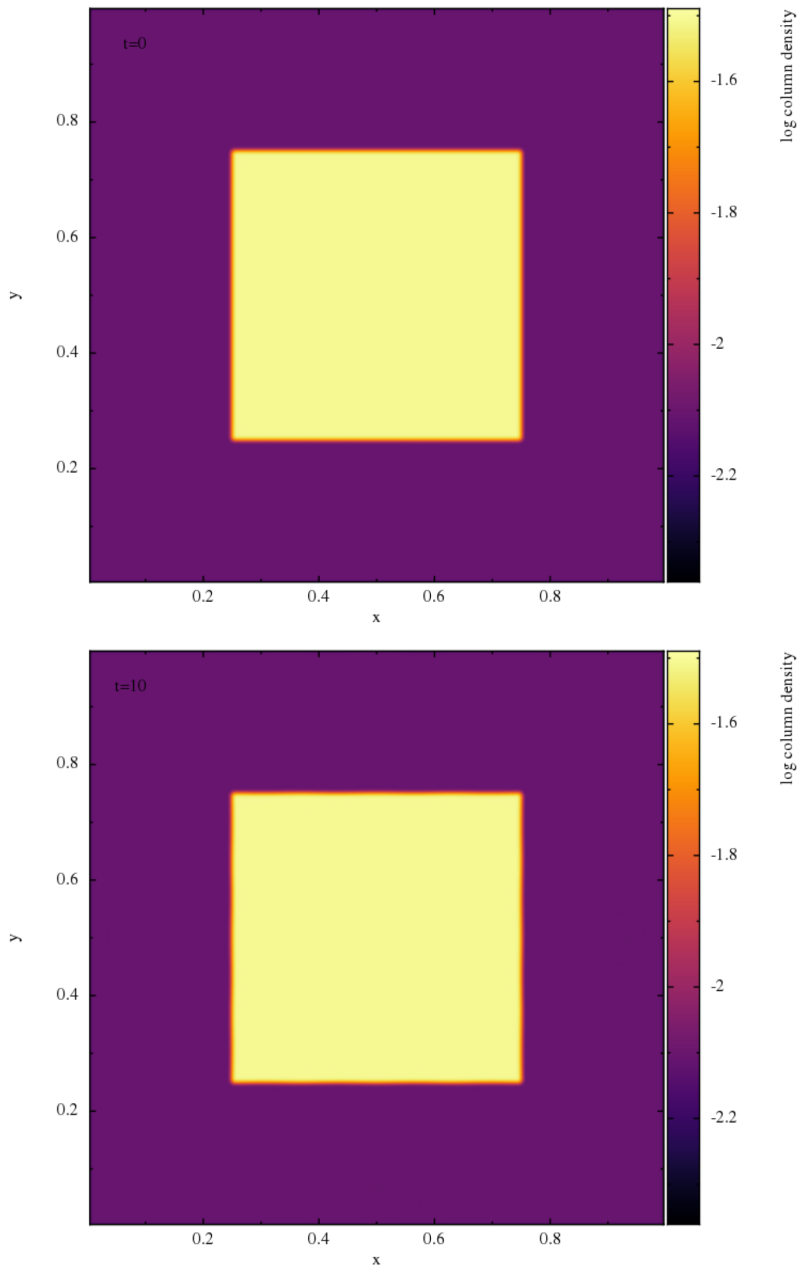

Figure 6.2: MFM version of the square test. This test is perfectly captured by the MFM method, down to machine precision. This demonstrates that the MFM method is minimising advection errors compared to grid codes and is not suffering from the common 'E0'-error in SPH.

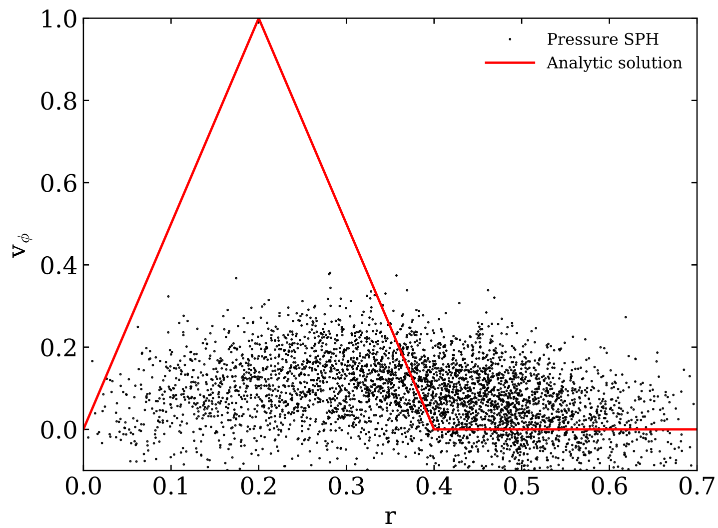

Figure 6.3: Pressure SPH version of the Gresho-vortex test at $t = 3.0$. We see a lot of noise in the particle distribution and the density peak is significantly reduced.

Pressure SPH struggles to keep the equilibrium condition in which the test is initialised. This has two major reasons. The first reason is connected to the well known and well studied 'E0'-error of SPH that leads to a net force even if the initial conditions are in perfect pressure equilibrium. This behaviour is especially strong if the initial particle distribution shows large anti-symmetries at the contact discontinuity. However, this is not the case here. The second reason is connected to the artificial conductivity that is implemented to resolve the issues that SPH shows in fluid mixing. What is crucial for fluid mixing (i.e. allowing for exchange of internal energy and thus generating mixing entropy, see 6.1.6) leads to a destabilisation of the pressure equilibrium in this test. The consequences for for numerical simulations are crucial as artificial conduction in SPH allows for mixing entropy that is needed to capture fluid mixing instabilities at the cost of capturing the pressure equilibrium correctly in numerical simulations.
The MFM method on the other hand captures this test perfectly and is capable of preserving the equilibrium condition down to machine precision. MFM captures this test so well because it advects the fluid tracers (particles) with the bulk velocity of the fluid, while it applies a linear reconstruction of the gradients. This is a significant improvement compared to SPH and the performance is at least as good as in state of the art moving mesh codes like Arepo Springel (2010). For classical grid codes this test is trivial as long as the fluid is at rest. However, for a moving fluid a grid code needs to be second order in space and time to properly advect the fluid motion. Further, a static grid code will always advect stronger along the grid axis. This behaviour can be reduced by adaptive mesh refinement (AMR) techniques, but this introduces other problems (i.e. a reduction of the convergence order at the borders from refined to de-refined areas of the simulation domain.)

6.1.2 Gresho vortex

The Gresho-vortex test is carried out to test the ability of a code to capture sub-sonic turbulence and angular momentum. The test is initialised in a two dimensional box with a constant background density of $\rho = 1$ with periodic boundary conditions on the domain $0 < L < 1$. The pressure profile of the system

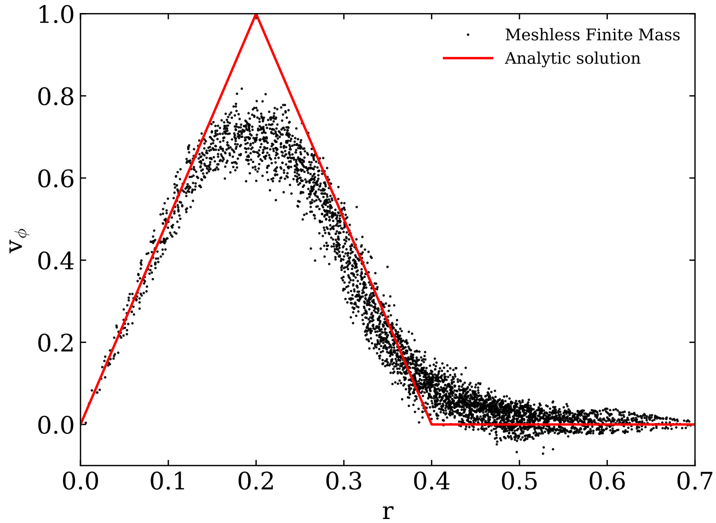

Figure 6.4: MFM version of the Gresho-Vortex test. Overall the structure of the vortex is preserved. The test shows the ability of the MFM-solver to capture sub-sonic turbulent flows and is a benchmark for angular momentum conservation. The noise can be further reduced with higher order kernel-functions but is a clear improvement over the results obtained with SPH.

is given as:

$$P(r) = \begin{cases} 5 + 12.5r^2 & 0 \le r < 0.2, \\ 9 + 12.5r^2 - 20r + 4\ln(5r) & 0.2 \le r < 0.4 \\ 3 + 4\ln 2 & r \ge 0.4. \end{cases} \tag{6.1}$$

The azimutally velocity is given by:

$$v_\varphi = \begin{cases} 5r & 0 \le r < 0.2, \\ 2 - 5r & 0.2 \le r < 0.4 \\ 0.0 & r \ge 0.4, \end{cases} \tag{6.2}$$

where r is given as $r = \sqrt{x^2 + y^2}$. we carry out th test with 64^2 particles and evolve the vortex until $t = 3$. We show the results for this test for pressure SPH and the MFM methods in the Figures 6.3 and 6.4 respectively, where we plot the radial velocity structure as a function of the radius and compare to the analytic result (red solid line). With the new MFM-solver we can preserve the vortex easily until $t = 3$, while SPH diffuses the vortex away rather quickly. This test is extremely difficult for SPH to capture. The shear motion leads to constant deformation of the fluid tracers (i.e. the kernel volume is distorted). Thus the particle volume of the SPH-particles is constantly re-calculated. This leads to a large error in the SPH-volume estimation and the SPH-volume is not conserved in SPH. However, other local quantities like energies and particle masses are obliged to conservation laws. This leads to a lot of partition noise when calculating the central fluid variable in pressure SPH (the pressure). On the other hand artificial viscosity leads to a quick damping of the velocity field. Both effects together lead to q quick diffusion of the vortex and it becomes almost impossible to preserve the vortex over more

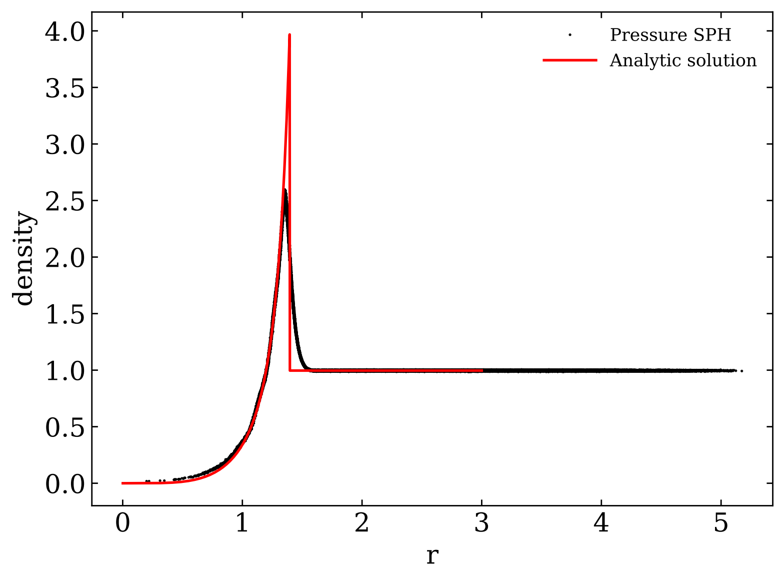

Figure 6.5: Pressure SPH version of a Sedov-Taylor blastwave at time $t = 0.03$. The shock is captured very well compared to the analytic solution.

then one dynamical time. However, we note that the SPH result can be very much improved by using higher order kernels like the Wendland-C6 kernel with 600 neighbours in three dimensions. However, this comes with a huge increase of computational cost as the SPH-loop becomes significantly slower by increasing the neighbour number.
The MFM-method significantly increases the ability of Gadget to capture sub-sonic turbulence in shear flows as we can preserve the vortex until $t = 3$, even at the very low resolution we used in this test. Despite the improvement we can still see a lot of partition noise. This is dependent on the slope-limiter choice and the fact that MFM is still using a particle weighted density interpolation. Generally, this problem can be captured in a more accurate fashion by static grid or moving mesh codes due to their more accurate volume partition, that reduces the partition noise.

6.1.3 Sedov-Taylor-Blastwave

The Sedov-Taylor solution is widely study in the literature (e.g. Kim and Ostriker, 2015; Steinwandel et al., 2020b) and provides a standard test for the ability to capture strong (high-machnumber) shocks and preserve the spherical structure of a point explosion. The test is initialised in a large box with density $\rho = 1$ the pressure $P = 10^{-6}$ and the energy $E = 1$, which is distributed kernel-weighted over the central 32 particles and is deposited entirely in thermal energy. We choose an adiabatic index of $\gamma = 5/3$. Given the Rankine-Hugenoit conditions this directly defines the density contrast of the blastwave which is then given as $(\gamma + 1)/(\gamma - 1) = 4$. Thus this means the closer we get to capture the maximum density of 4 in the shock the better. The test is initialised with 64^3 particles. However, this test has been carried out at higher resolutions in $3d$, with 128^3 and 256^3 particles. We note that we find less distribution noise and better convergence of the density peak at higher resolution. However, we show the results for 64^3 particles as it is sufficient to capture the shock properly (we reach roughly $\rho = 3.2$ in the MFM case). We show the results for pressure SPH and the MFM-method in the Figure 6.5 and Figure 6.6 for the density as a function of the radius at time $t = 0.03$ and compare to the analytic

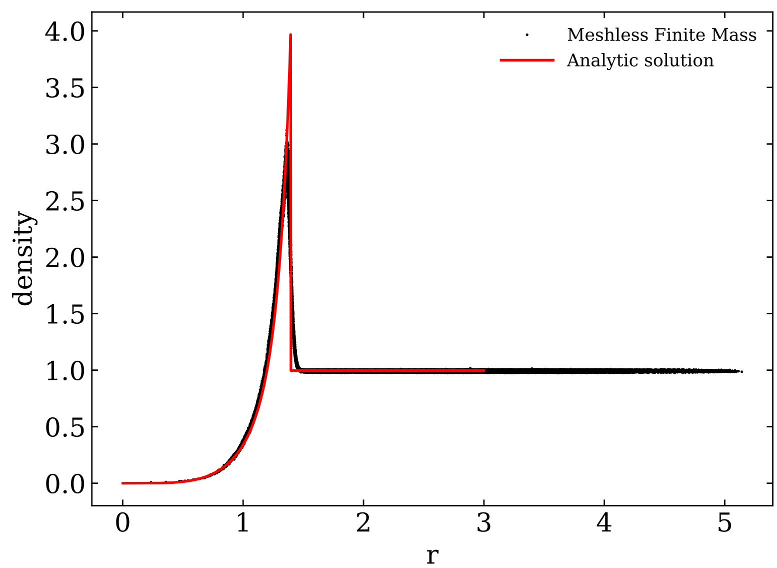

Figure 6.6: MFM version of a Sedov-Taylor blastwave at time $t = 0.03$. The shock is captured properly compared to the analytic solutions.

solution (red solid lines).
Both pressure SPH and the MFM-method are very well capable of capturing this high Machnumber point explosion and preserve the spherical structure of the blast wave. However, pressure SPH tends to underestimate the maximum density of the shock compared to the MFM result. It is very hard to improve this for SPH, even by changing the artificial conduction. Despite this too low peak density, SPH is perfectly capable to capture the position of the shock accurately, which directly shows that SPH has no-problem in terms of shock capturing. The MFM solver captures the location of the blastwave with very high accuracy. We note that the height of the density peak depends on the details of the slope-limiting procedure and of course the resolution. If we increase the resolution from 64^3 to 128^3 it is possible to get a peak density of roughly 3.8 compared to the peak density of 3.2 that we currently achieve. Another way to come closer to the predicted density peak from the Rankine-Hugeniot jump conditions is do decrease the dimensionality. However, we have to test the code also in three dimensions as the final goal is to use the MFM-solver in galaxy scale simulations. In this context the Sedov-Taylor solution is of importance in three dimensions as it is a direct test how well the method is capturing high Machnumber shocks introduced for example by the feedback of supernovae. This demonstrates that the MFM-method is capable of resolving the adiabatic phase supernova-blastwaves in the ISM, even if the resolution is relatively low (as it is typically the case in galaxy simulations in comparisons to smaller scale ISM simulations). However, one of the main goals of this thesis is to exceed the current subgrid limitations for stellar feedback, rendering this test of paramount importance when it comes to feedback modelling in the next generation of galaxy scale simulations that resolve the feedback from individual stars.

6.1.4 Noh implosion test

The Noh implosion test is a very tricky test for many hydrodynamical solvers. According to Liska and Wendroff (2003) this test could only be carried out by four of eight solvers they tested. Thus this

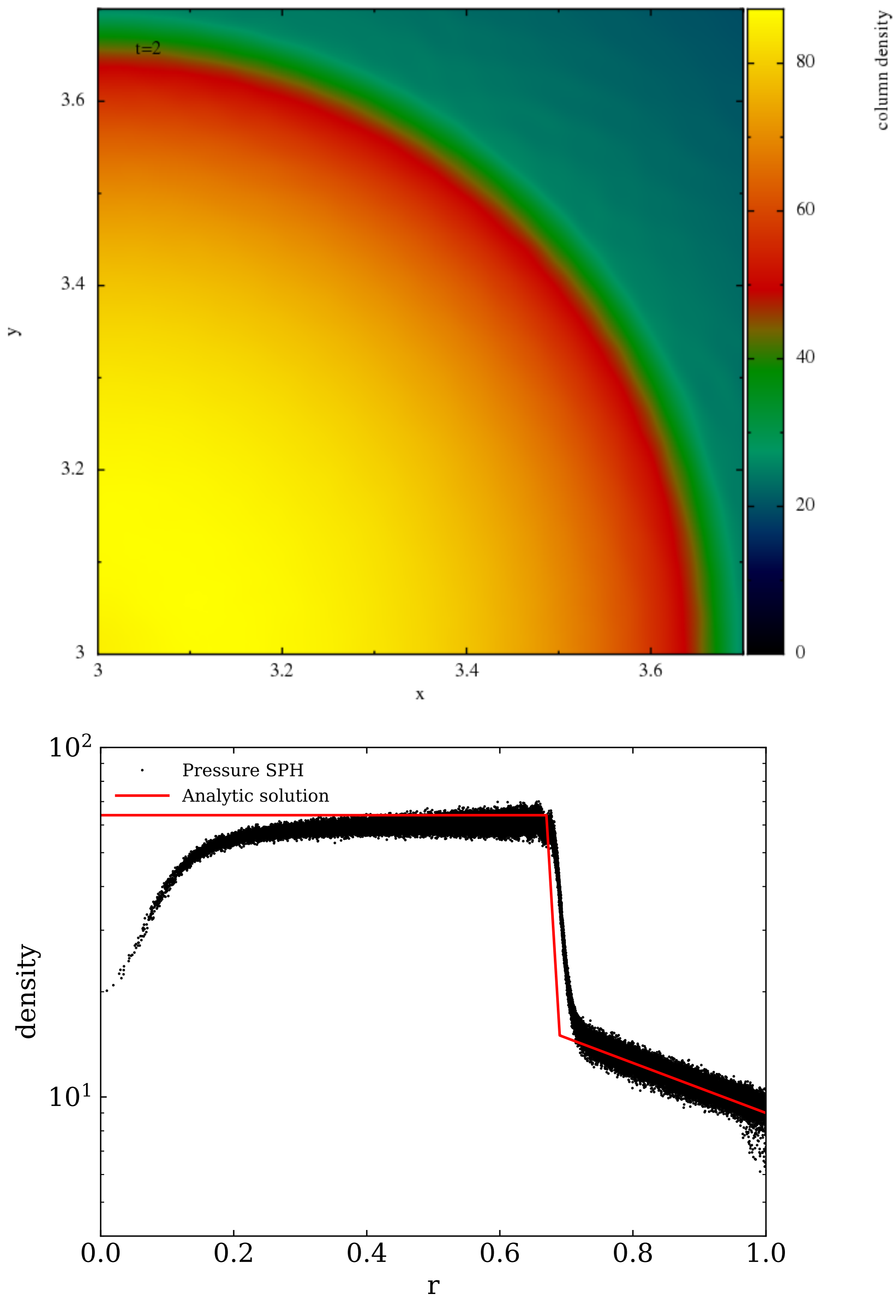

Figure 6.7: Pressure SPH version of the Noh implosion test. The inner region is not captured properly in SPH.

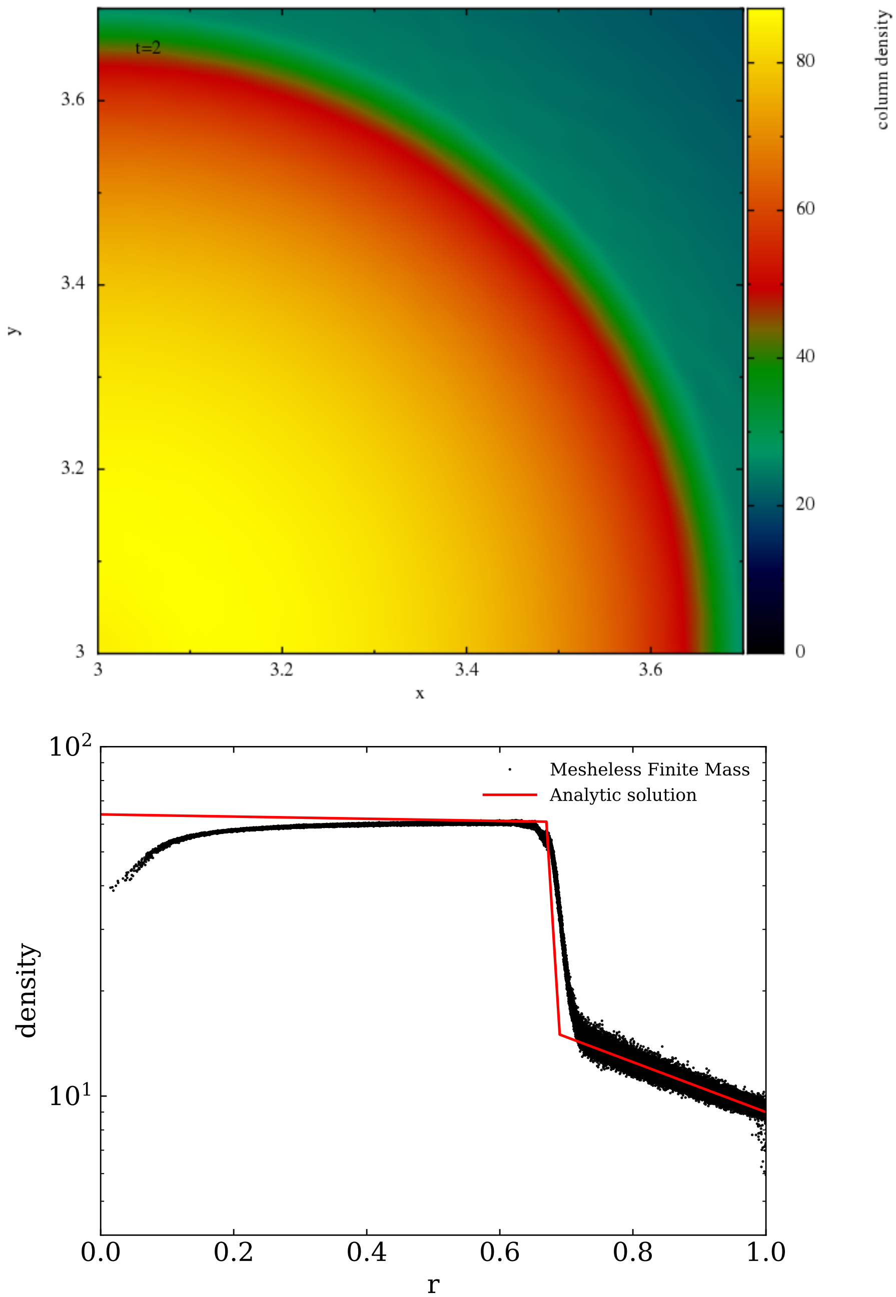

Figure 6.8: MFM version of the Noh-implosion test. The inner region can be captured more appropriately in MFM.

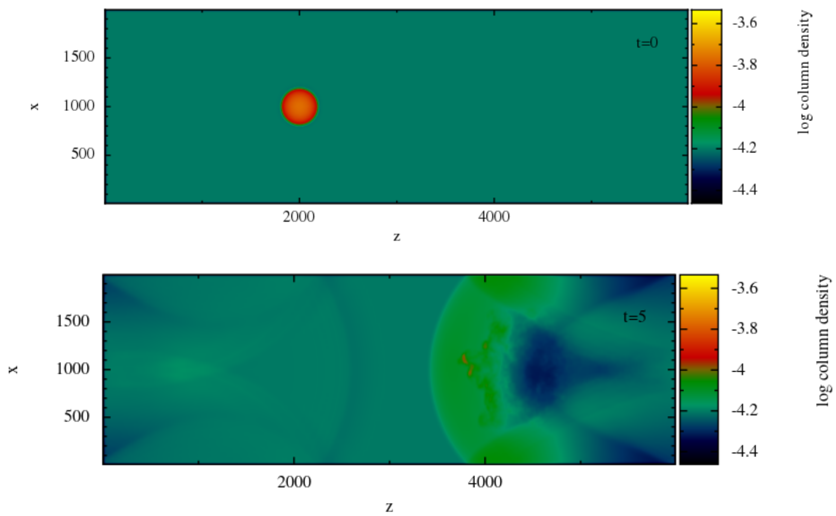

Figure 6.9: Pressure SPH version of the blob test. This test caused a lot of trouble for the SPH community around the year 2007, but can be handled very well with nowadays applicable artificial diffusion terms.

test is a make or break test for our hydrodynamical method. The test is initialised in an arbitrarily large domain with a background density $\rho = 1$. We set the radial velocity v_r to $v_r = -1$ and adapt the adiabatic index $\gamma = 5/3$. The analytic solution leads to an infinitely strong shock with a density contrast of 64. We note that for this test is makes a difference if we setup the initial particle distribution as a glass or a regular lattice. We carry the test out in three dimensions. There are two things that are important in this test. The first is to capture the density profile of the implosion correctly. The second is to preserve the spherical structure of the implosion. These two facts combined make this test extremely difficult for grid codes as grid codes struggle with preserving the spherical structure.
We carry out the test with pressure SPH and the MFM-method. We show our results in the Figures 6.7 and 6.8. In the top panel we show a density rendering of the test to demonstrate that the solvers keep the spherical shape of the implosion as the system is evolved in time. In the bottom panels of these two figures we show the density structure of the implosion and compare to the analytic solution (red solid line). As we can see from Figure 6.7 SPH struggles to capture the implosion properly. The density field in the centre is underestimated. However, the spherical structure is more less kept while the implosion evolves in time. Even the MFM-solver underestimates the central density field and seems to converge against 63 instead of 64. The outward shock structure is very well captured by MFM and the spherical shape of the implosion is preserved until the end of the simulation. In this test MFM shows a significant improvement over SPH and regular static grid codes and performs on the same level as state of the art moving mesh methods.

6.1.5 Cloud-Dissruption

This test caused some controversy due to the study of Agertz et al. (2007) who compared different particle based codes with different grid codes. The outcome of the study was that classic (vanilla) SPH is very bad in capturing fluid mixing. However, the community draw the conclusion that SPH is sub optimum for fluid-mixing and shock capturing. While the first statement is true, the second is simply wrong. SPH is excellent at shock capturing as we already demonstrated in the tests we carried out so

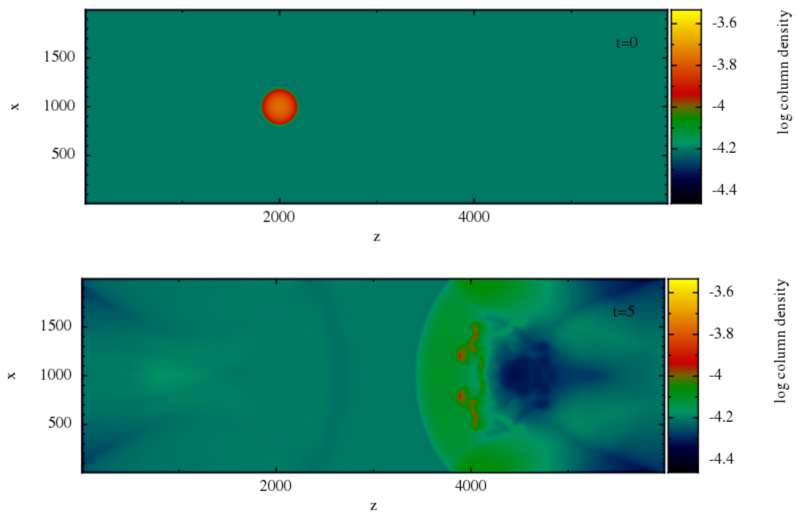

Figure 6.10: MFM version of the blob test. The numerical diffusion that is applied by the Riemann-solver intrinsically provides the mixing entropy that is needed to disperse the cold cloud by the hot wind.

far. The correct statement should be that vanilla SPH under performs when it comes to fluid mixing as it intrinsically solves for $dS/dt = 0$ and thus not allowing for mixing entropy. This can be solved by introducing artificial conduction routines. However, it remains tricky and the artificial conduction has to be tuned at the right amount to get the correct growth rate of the instabilities. Riemann methods have a clear advantage when it comes to this test because they apply some numerical diffusivity while solving for the hydrodynamical flux vectors. Thus the 'correct' amount of mixing entropy is intrinsically provided by the solver. This makes the blob test a very interesting benchmark test for the MFM-method as it should resolve the issues other particle based methods have with this test by construction. In practice, this problem is not a real issue anymore, as long as the environment is predictable, because artificial diffusion term in SPH can be tuned very effectively and we find only little difference for this test case as we demonstrate for this test case in the bottom panel of Figure 6.9 and Figure 6.10. The test is initialised as a cold dense blob with a four times higher density than the ambient medium that streams around the blob with a high velocity of 1000 km s^{-1}. We show the initial configuration in the upper panels of the respective figures.

6.1.6 Kelvin-Helmholtz-Instability

Another important test for fluid mixing instabilities is the Kelvin-Helmholtz-Instability (KH) test. To safe some space we skip the two dimensional version of the test and directly run th test in three dimensions. We construct the ICs of the test following McNally et al. (2012) with a fluid with density ρ_1 on top of fluid layer with density ρ_2, that again is placed on a flui layer with density ρ_1. To trigger the instability we disturb the fluids velocity and density at the edges of the fluid layers alongside the y-direction in a small interval Δy. The detailed structure of the velocity perturbations can be found in McNally et al. (2012). We further use the $\rho_1 = 2$ and $\rho_2 = 1$. We then obtain the results, we show in Figure 6.11 if we run the ICs with PSPH and the results we show in Figure 6.12 if we run the test with the MFM-solver. For this test we do not have a lot to say, as our main goal is to make the fluid mix.

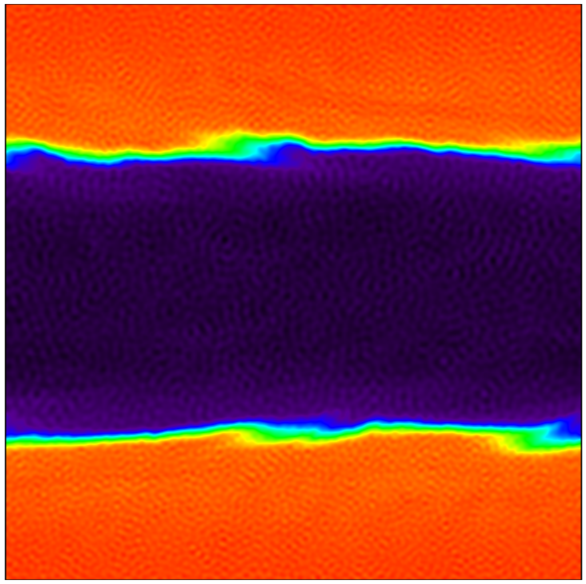

Figure 6.11: Pressure SPH version of the KH-instability in three dimensions.

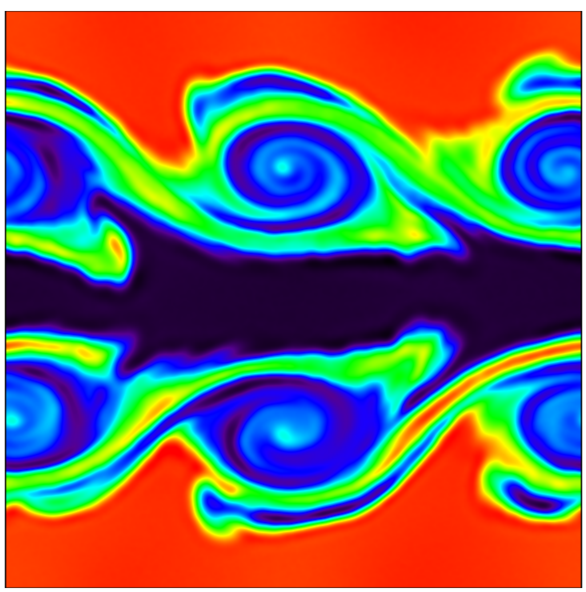

Figure 6.12: MFM version of the KH-instability in three dimensions.

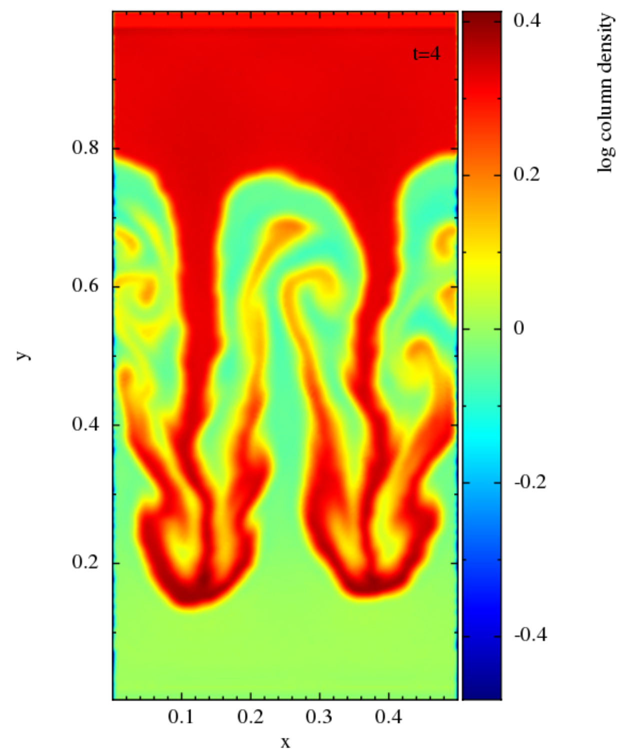

Figure 6.13: MFM version of the Rayleigh-Taylor Instability. The test show that we can mix a fluid under the influence of gravity.

From this point of view, we achieved this goal. However, the story of the KH-test is more complicated since the paper of Lecoanet et al. (2016) who provide converged results for the two dimensional version of the test with the grid-code ATHENA++ (Stone et al., 2020) and the spectral code DEADALUS. For us this basically means that there must be a more detailed study for SPH, MFM, MFV and the moving mesh codes like AREPO to investigate weather the other solvers can find converged solutions for this test as well. Essentially, this is an important study to begin with, as it allows us to predict at which Reynolds-number the different methods operate. If you want to see a simulator cry ask him at which Reynolds number his/her favoured code operates. I am quite certain that 99 per cent will not know the exact answer as I do not know it for my code at this time. However, since the study of Lecoanet et al. (2016) I suspect that the Reynolds number of GADGET must be around 10^5 if we compare mixing properties. Despite this, a more detailed study is needed here and will be carried out at a later point. We note that this is one of the test-cases where the current parameter-option of SPH is not optimal. Different choices for the normalisation of thermal conduction will greatly improve the result. However, we want to show that even at low resolution MFM can achieve a good results, while SPH tends to struggle here. I cannot stress enough that this is not the true performance of SPH, but a results of one-to-one comparison between MFM and SPH.

6.1.7 Rayleigh-Taylor-Instability

We can add more complexity to fluid mixing tests by considering the fluid under gravity. This is known as the Rayleigh-Taylor-Instability (RT). The test is similar to the KH-test but we add an analytic potential alongside the z axis to model a two phase fluid with density $\rho_1 = 2$ on top an density $\rho_2 = 1$ below. To trigger the instability we add a sinus-perturbation on the fluids contact discontinuity in the density. The fluids are in pressure equilibrium The heavy fluid will then start to fall down under gravity and penetrate the low density fluid, forming tow cones the fragment o the edges due to the KH-Instability. Again, there is not much to report for this test either, as the fluid is supposed to mix which is given in Figure 6.13. We do not show this test for SPH, because we find with the current parameter choices a similar results that we obtained for the SPH-version of the KH-instability. There is an interesting complication to this test, which can give some information on how well the code at hand handles advection errors. To investigate this one could shift the simulation domain with constant velocity through the box. Grid codes typically struggle with this, apart from when they use extensive AMR-refinement. However, we already know from section 6.1.1 that there are basically no advection errors in MFM and we skip the advection version of the RT-test at this point.

6.1.8 Evrard Collpase test

The Evrard-collapse test is a test that is often carried out for SPH-codes to demonstrate the proper coupling between gravity and hydrodynamic routines on the one hand side and the energy conservation on the other hand side. The test is initialised in an arbitrarily large box (we adopt a box size of 10). In this box we setup a sphere with a total mass $M = 1$ and a radius with $R = 1$, The initial density profile is given by $\rho(r) = M/(2\pi R^2 \cdot r) = 1/(2\pi r)$ if $r < R$. Otherwise the density is set to $\rho = 0$. Thus the test not only shows the proper coupling of the MFM to the gravity routines of GADGET, it also demonstrates that the MFM can handle vacuum boundary conditions perfectly in situations where the fluid is behaving relatively smooth. However, we note that the MFM-method can struggle with Vacuum boundary conditions if single particles are ejected to far from their neighbours (this can be triggered by feedback in galaxy scale simulations). The gas is initially at rest and we set the internal energy per unit mass to $u = 0.05$. We sample the sphere with 30^3 particles like in Hopkins (2015) and Springel (2010). Initially, the sphere starts to collapse and begins to convert gravitational energy into kinetic energy. Kinetic energy is then thermalised and converted into internal energy in the centre. This drives a strong (accretion) shock in the centre. The inner regions bounce back and the shock evolves outwards, moving through the outer regions and the in-falling gas until the the shock has propagated through the whole sphere and an hydrostatic virial equilibrium is reached at $t = 0.8$. We show the radial profile of the density at $t = 0.8$ as a function of the radius and compare to the solution of a high resolution one dimensional PPM run (red line) for pressure SPH and the MFM-method in the bottom panels of the Figures 6.14 and 6.15 respectively. In the top panels we show a projected density rendering to quantify how the Evrard-collapse test looks like. Overall, both methods capture the shock very well. Surprisingly, this is the only test where SPH seems to perform better than MFM and MFM slightly under predicts the central density. This could be related to the somewhat more tedious coupling of MFM to GADGETS gravity routines that can introduce some noise on the grid scale. We note that there is a similar trend found in the code AREPO, even in its moving mesh-configuration (see Springel, 2010, in his Figure 40). This can potentially be resolved by increasing the resolution.

6.1.9 Isolated Galaxy

Finally, we apply the MFM-solver to a galaxy scale simulation. We simulate the high resolution MW-model that is presented in Steinwandel et al. (2019). The model consists out of an isolated disc galaxy with a dark matter halo, a stellar disc, a gas disc and a bulge. Moreover, we model the circum galactic medium with a hot atmosphere that is following a β-profile. The particle mass is 4000 $M_\odot$

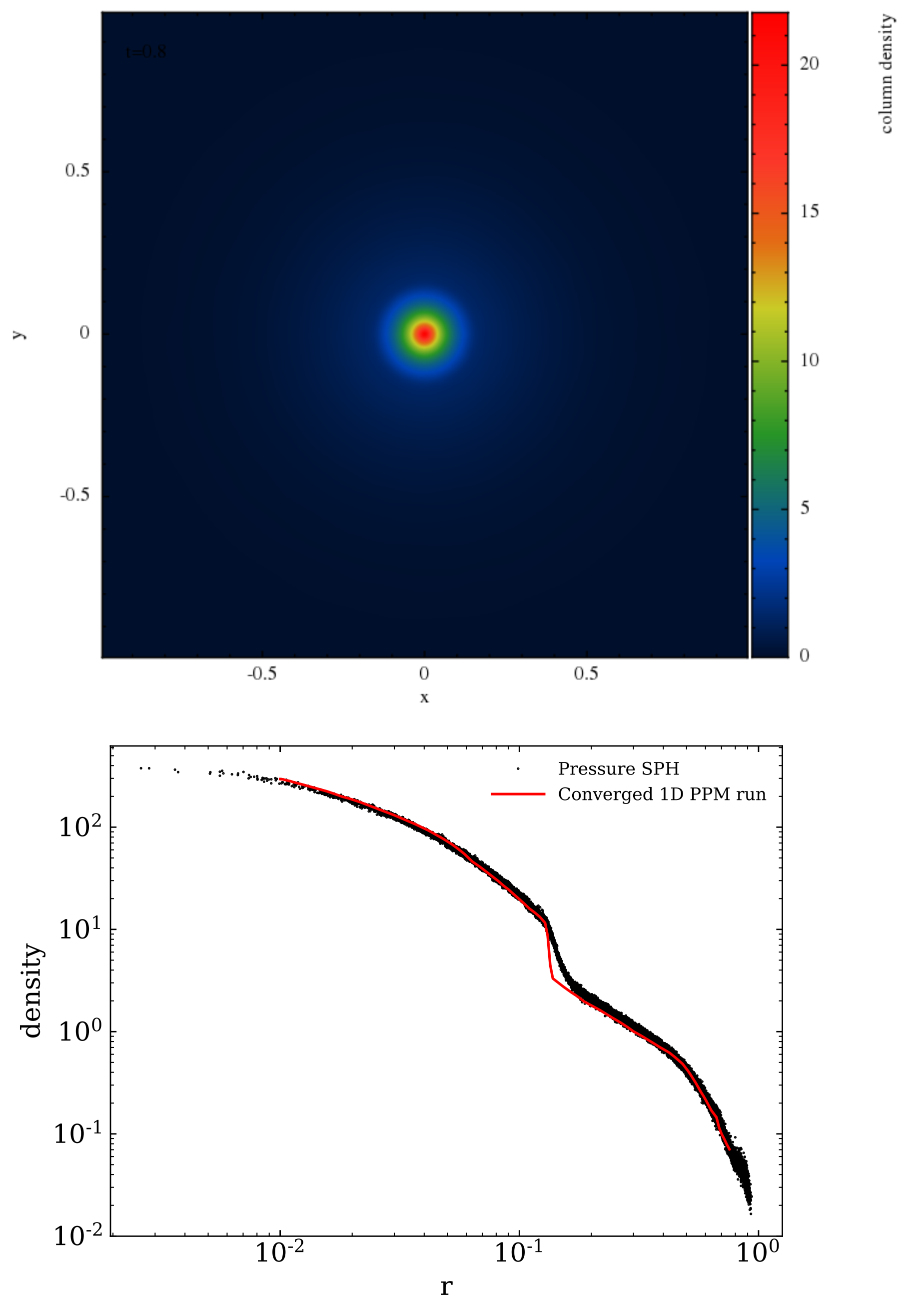

Figure 6.14: Pressure SPH version of the Evrard-collapse test at $t = 0.8$

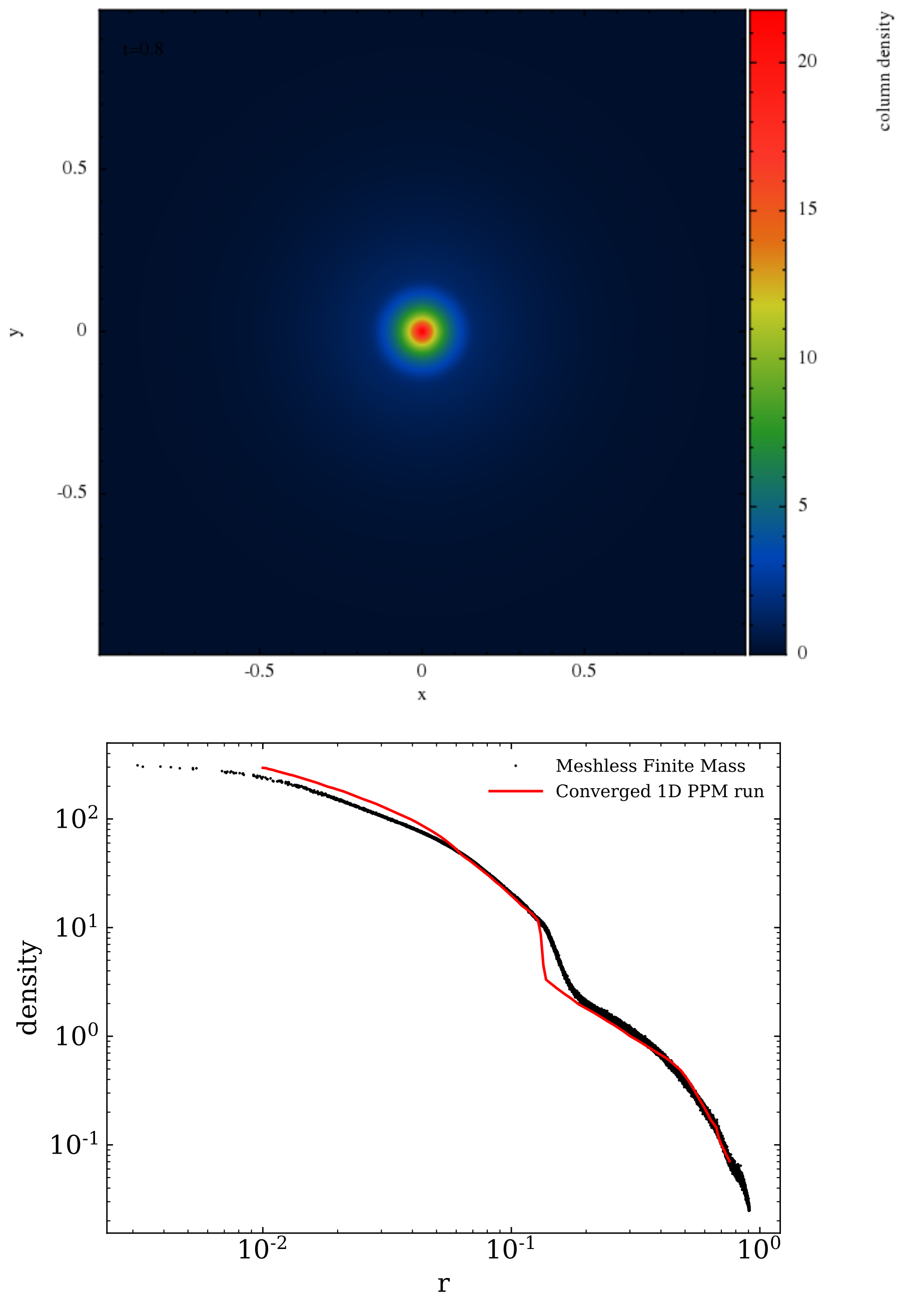

Figure 6.15: MFM version of the Evrard-collapse test at $t = 0.8$. This demonstrates that the MFM method is properly coupled to Gadgets gravity routines and the conversion between gravitational, kinetic and internal energy is captured.

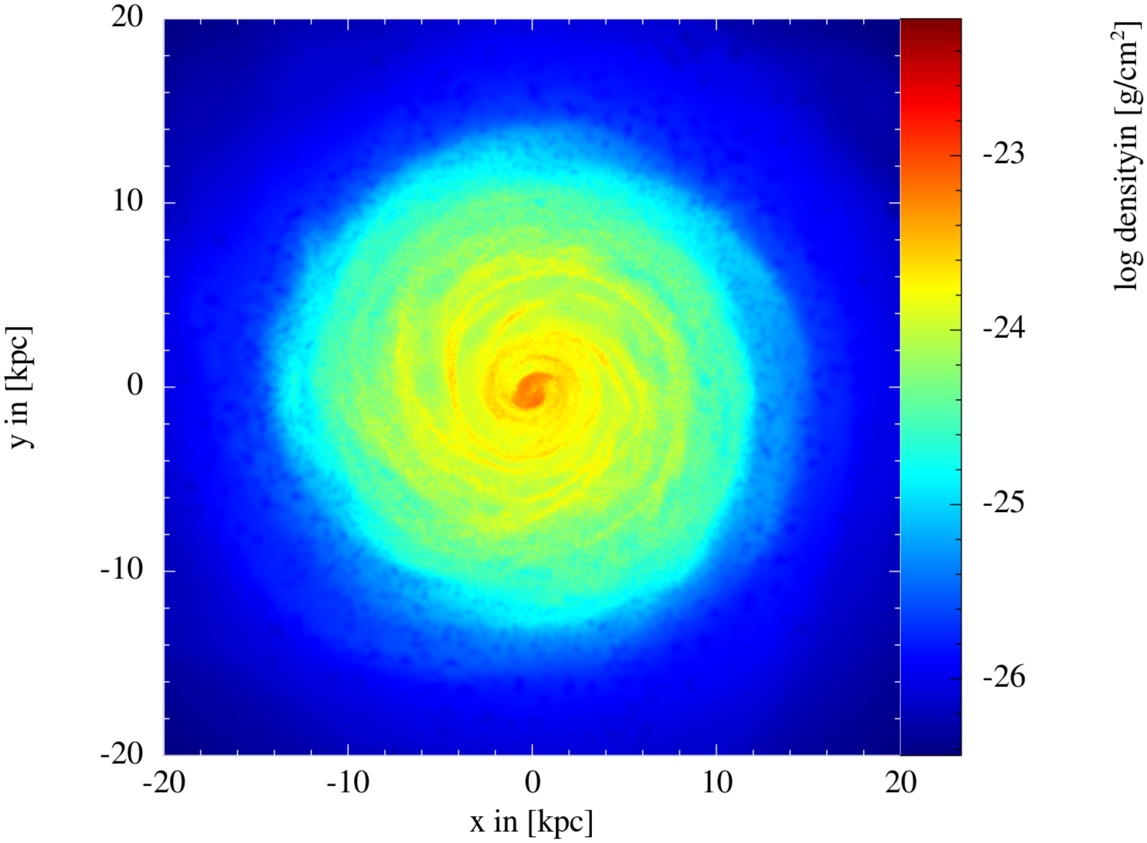

Figure 6.16: MFM-version of the hydrodynamics version of the the Milky Way-like galaxy model presented in Steinwandel et al. (2019). The simulation was a factor of six faster with improved accuracy in capturing hydrodynamical flows and sub sonic turbulence. The galaxy has been evolved for 1 Gyr.

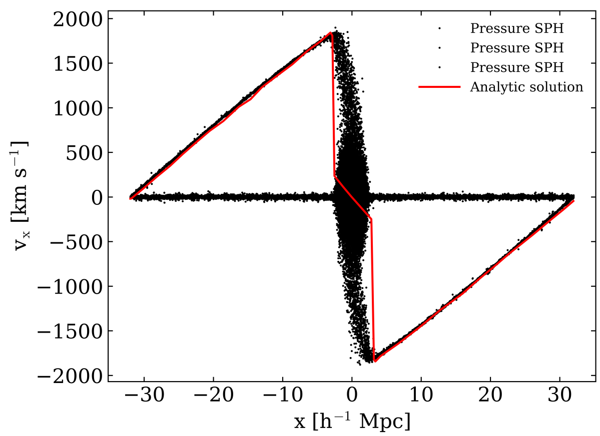

Figure 6.17: Pressure SPH version of the Zeldovich Pancake test. While the shape of the velocity structure is captured very well, it show a lot of distribution noise.

and we model star formation and feedback following Springel and Hernquist (2003). The details and the initial condition generating strategy are explained in detail in chapter 7. We evolve the disc for 1 Gyr. We show the density evolution at the final time of the simulation for the MFM-version in the face-on view in Figure 6.16. We note that the simulation was faster by a factor of six compared to the runs that we carried out with SPH due to the fact that the MFM allows us to decrease the neighbour number by a factor of six while capturing the fluid flow with the same accuracy. This demonstrates the advantage of the MFM-solver in terms of speedup and the importance of further developing the hydrodynamics routines is astrophysical simulation codes like Gadget as they can lead to a significant speedup of current galaxy formation models and open the door to higher resolution galaxy simulations with resolved feedback from individual stars.

6.1.10 Zeldovich Pancake

A good test case for cosmological integration is the Zeldovich-pancake. The test is initialised as a perturbation of the form:

$$x(q,z) = q - \frac{1+z_c}{1+z}\frac{\sin(kq)}{k}, \tag{6.3}$$

$$\rho(q,z) = \frac{\rho_0}{1-\frac{1+z_c}{1+z}\cos(kq)}, \tag{6.4}$$

$$v_{\mathrm{pec}} = -H_0\frac{1+z_c}{\sqrt{1+z}}\frac{\sin(kq)}{k}, \tag{6.5}$$

$$T(x,z) = T_i\left[\left(\frac{1+z}{1+z_i}\frac{\rho(x,z)}{\rho_0}\right)\right]^{2/3}. \tag{6.6}$$

with the wavenumber $k = 2\pi/\lambda$, the background density $\rho_0 = 1$, temperature $T_i = 100$ K, initial redshift $z_i = 100$ and the redshift of caustic formation z_c. We set the test up in a periodic co-moving box with a

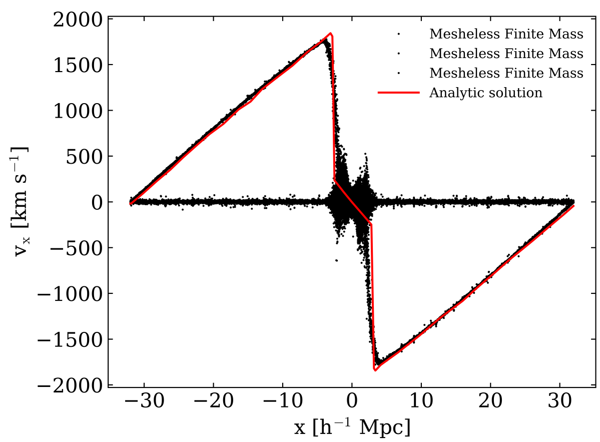

Figure 6.18: MFM version of the Zeldovich Pancake test. We find less distribution noise if we apply a Riemann-solver compared to the SPH case and we find more clearly defined edges as the velocity profile deceases towards the box centre.

side-length of 64 Mpc. We show the results for the velocity-structure at redshift zero for pressure SPH in Figure 6.17 and for the new MFM-solver in Figure 6.18. Generally, we find that the results that are obtained with SPH show more noise than the results obtained with the MFM method. Both solvers capture the linear increase and the linear decrease in the the velocity similarly well. However, the steep decline of the velocity profile by approaching the centre of the box is captured more accurately by the MFM-solver. Further, we note that different from how the test is often displayed in various code papers, we plot every-single data point we have in the simulation domain. This reveals that the SPH-solver is not able of capturing the tilt in the velocity profile, while the MFM-method can capture it, but it shows a lot of distribution noise, which is a sign of inadequate resolution in the box centre, combined with a too aggressive slope limit setting of the Riemann-solver. The constant background line comes from gas that is moving at zero velocity.

Chapter 7

Magnetic buoyancy in simulated galactic discs with a realistic circum galactic medium

This work has been published in the Monthly Notices of the Royal astronomical Society, Volume 483, Pages 1008-1028.

We present simulations of isolated disc galaxies in a realistic environment performed with the Tree-SPMHD-Code GADGET-3. Our simulations include a spherical circum-galactic medium (CGM) surrounding the galactic disc, motivated by observations and the results of cosmological simulations. We present three galactic models with different halo masses between $10^{10} M_{\odot}$ and $10^{12} M_{\odot}$, and for each we use two different approaches to seed the magnetic field, as well as a control simulation without a magnetic field. We find that the amplification of the magnetic field in the centre of the disc leads to a biconical magnetic outflow of gas that magnetises the CGM. This biconical magnetic outflow reduces the star formation rate (SFR) of the galaxy by roughly 40% compared to the simulations without magnetic fields. As the key aspect of our simulations, we find that small-scale turbulent motion of the gas in the disc leads to the amplification of the magnetic field up to tens of μG, as long as the magnetic field strength is low. For stronger magnetic fields turbulent motion does not lead to significant amplification but is replaced by an α - ω dynamo. The occurrence of a small-scale turbulent dynamo becomes apparent through the magnetic power spectrum and analysis of the field lines' curvature. In accordance with recent observations we find an anti-correlation between the spiral structure in the gas density and in the magnetic field due to a diffusion term added to the induction equation.

7.1 Introduction

Magnetic fields are a fundamental aspect in astrophysics and cosmology. They are essential for describing many processes in theoretical astrophysics properly. The relevance of magnetic fields ranges from the small scales in star formation and in the ISM over galactic scales up to galaxy-clusters and the large scale structure of the Universe. While there is a large amount of observational data on magnetic fields, especially in the area of galaxy formation and evolution (i.e. Beck, 2007; Chyży et al., 2007, 2003; Hummel, 1986) the situation is different for numerical studies that investigate the behaviour of magnetic fields in detail (Beck et al., 2016b; Kotarba et al., 2011; Pakmor et al., 2017; Pakmor and Springel, 2013; Rieder and Teyssier, 2016). In the case of galaxies the magnetic field becomes important for several reasons. It acts as an additional pressure component, and thus it is needed as a correction of the equations of hydrodynamics, resulting in the well known equations of magnetohydrodynamics. Moreover, the magnetic pressure in galaxies can reach the same order of magnitude as the turbulent pressure in the ISM, and thus it can completely dominate over the thermal pressure in the disc. Hence, it should be taken into account in simulations of galaxy formation and evolution. However, this is often not the case and pure hydrodynamical simulations are used to study the formation and evolution of galactic discs. On the other hand magnetic fields can be very important for star formation and the regularization of cosmic rays and should not be excluded when these processes are taken into account.

Still, the origin of magnetic fields in the Universe is unclear. It is possible to generate magnetic seed fields below 10^{-20} G by either battery processes in the early Universe (e.g. Biermann, 1950; Mishustin and Ruzmaĭkin, 1972; Zeldovich et al., 1983) or the phase transitions that appear in the standard model, shortly after the Big Bang (e.g. Hogan, 1983b; Ruzmaikin et al., 1988a,b; Widrow, 2002). Those initial magnetic fields can then be amplified by various dynamo processes, namely the α-ω-dynamo (Ruzmaikin et al., 1979), the cosmic ray driven dynamo (Hanasz et al., 2009; Lesch and Hanasz, 2003) or the small-scale turbulent dynamo (Kazantsev, 1968; Kraichnan, 1968). While, the first and the second dynamo process operate on 10^8 yr-scales, the third process has typical timescales in the Myr-regime (Kulsrud, 2005). The magnetic energy is exponentially amplified on the small scales and random motion regulates it on the largest turbulent scales (Kulsrud and Anderson, 1992; Kulsrud et al., 1997; Malyshkin and Kulsrud, 2002; Schekochihin et al., 2002, 2004; Schleicher et al., 2010; Zeldovich et al., 1983).

Observationally, there are several methods to measure the magnetic field strength in galaxies. Brown et al. (2007) investigated the magnetic field of the inner Milky Way by using rotation measurements of 148 objects behind the galactic disc. More recent observations from Han et al. (2018) present rotation measurements of 477 pulsars and compared their distribution with extra galactic radio sources (EGRS) showing that the magnetic field of the Milky Way has a bisymmetric structure. Further, magnetic fields of nearby galaxies can be determined using their radio synchrotron emission. In this case the unpolarised component of the synchrotron emission is important because it is needed to explain galactic dynamics and outflows (e.g. Beck, 2007). Radio synchrotron emission is also used to calculate the magnetic field strengths in nearby galaxies which leads to values between 20 and 30 μG in the spiral arms and up to 50 to 100 μG in the galactic centre, as described in Beck (2007) or Beck (2009). Robishaw et al. (2008) presented measurements of magnetic fields due to Zeeman-splitting emission in OH megamasers of five ultra luminous infrared galaxies leading to magnetic field strengths along the line of sight between 0.5 and 18 mG.

Beyond the observations of the magnetic fields in galactic discs there are also those of their CGM. Carretti et al. (2013) present measurements of magnetised outflows towards the CGM of the Milky Way in two giant lobes located in the north and south of the galactic centre with a magnetic field strength of

around 15 μG, known as the 'Fermi-bubbles'.
Simulations of galactic magnetic fields are often carried out with hydrodynamical grid codes. Wang and Abel (2009) investigated the magnetic field in isolated disc galaxies without star formation using the grid code ENZO (Bryan and Norman, 1997; Bryan et al., 2014; O'Shea et al., 2004). Dubois and Teyssier (2010) studied the magnetic field of dwarf galaxies with a closer look on winds driven by the feedback of stars using the grid code RAMSES (Teyssier, 2002). Pakmor and Springel (2013) and Rieder and Teyssier (2016) present studies of magnetic fields for isolated galaxy formation by collapsing a giant gaseous halo in a dark matter potential using the moving mesh code AREPO (Springel, 2010) and the grid code RAMSES, respectively. While Pakmor and Springel (2013) investigate general properties of the magnetic field, Rieder and Teyssier (2016) point out the importance of supernova feedback on the structure of the ISM and its magnetic field.
Another detailed study of magnetic fields in isolated discs is presented in Butsky et al. (2017) where they find a small-scale turbulent dynamo of the magnetic field. The same behaviour can be found in Rieder and Teyssier (2017a) for an isolated disc galaxy as well as in Pakmor et al. (2017) and Rieder and Teyssier (2017b) for cosmological zoom-in simulations. The evolution of magnetic fields has been extensively studied with particle-based methods for magnetohydrodynamics as well. Kotarba et al. (2009) investigate the magnetic field in an isolated disc galaxy using the SPH-code VINE (Wetzstein et al., 2009). In Kotarba et al. (2010) VINE is used for studies of the magnetic field in the Antennae-galaxies. In Kotarba et al. (2011), Geng et al. (2012b), and in Geng et al. (2012a), GADGET-3 is used to study the magnetic field in other galaxy mergers. Beck et al. (2016b) is investigating the magnetic field structure of the Milky Way in more detail, by calculating its synchrotron-emission. Many of these simulations study the evolution of galaxies in isolation by sampling a dark matter halo, a stellar bulge, and a stellar and gaseous disc as the initial condition. The hot CGM is typically neglected to save computational effort and as it is mainly irrelevant for galactic dynamics. However, cosmological simulations show that galaxies are constantly accreting gas from their hot haloes, such that this component is essential to model realistic galactic systems. Moreover, a hot gaseous halo around the Milky Way can now be detected observationally (Miller and Bregman, 2013). These observations indicate that the density profile of the CGM can be described with a β-power law (Cavaliere and Fusco-Femiano, 1978), which is common in studies of globular clusters (Plummer, 1911) and cosmological simulations of galaxy-clusters (e.g. Donnert, 2014). Consequently, it may be critical to include the hot gaseous component in simulations of isolated galaxies. In SPMHD simulations the presence of the CGM has a further advantage. In the SPMHD formalism the magnetic field is a property of the gas particles. Therefore, a carrier for the magnetic field is needed which gives further justification for the presence of the CGM in magnetohydrodynamic simulations.
In this work we present a set of nine high-resolution simulations that include a spherical hot CGM for each galaxy. The paper is structured as follows. We give a short summary of our simulation method in section 7.2, where we point out recent improvements of our numerical methods and the physical models that are considered. In section 7.3 we present the methods that we use to build our numerical model for an isolated disc galaxy that includes an observationally constrained CGM. We then examine the general properties of each galactic system and investigate the interaction between the galactic disc and the CGM in section 7.4. Our conclusions are presented in section 7.5.

7.2 Simulation Method

The simulations we present in this paper are performed using the Tree-SPMHD-Code GADGET-3, the developers version of the public available GADGET-2 code (Springel, 2005). We use a modern implementation of SPH, as presented in Beck et al. (2016a). This SPH formulation includes various improvements like a higher order SPH-kernel described by Dehnen and Aly (2012), a timestep limiter (Dalla Vecchia and Schaye, 2012), time-dependent artificial viscosity and a new model for time-dependent artificial conduction. Our version of GADGET-3 further includes magnetic fields and magnetic dissipation as presented in Dolag and Stasyszyn (2009). We also include star formation, cooling, supernova-feedback and metals following Springel and Hernquist (2003). Further, one of our models for the magnetic field couples the seed rate of the magnetic field directly to the supernova rate within the ISM, as presented in Beck et al. (2013). In this section we summarise the adopted SPH formalism and the physical models in a very compact way.

7.2.1 Kernel function and density estimate

We use the density-entropy formulation of SPH, i.e. we smooth the density distribution such that

$$\rho_i = \sum_j m_j W_{ij}(x_{ij}, h_i), \tag{7.1}$$

where h_i is the smoothing-length. The sum in equation 7.1 is calculated over the neighbouring particles. $W_{ij}(x_{ij}, h_i)$ is the smoothing kernel with the property

$$W_{ij}(x_{ij}, h_i) = \frac{1}{h_i^3} w(q). \tag{7.2}$$

In our simulations we use the Wendland C4 function for $w(q)$, with 200 neighbouring particles. The function $w(q)$ is given by

$$w(q) = \frac{495}{32\pi}(1-q)^6\left(1 + 6q + \frac{35}{3}q^2\right), \tag{7.3}$$

for $q < 1$. For $q > 1$ we set $w(q)$ to zero.

7.2.2 SPH and SPMHD formulation

It is possible to derive the equations of motion (EOM) in both the hydrodynamical and the magnetohydrodynamical case from a discrete Lagrangian, via the principle of least action, as been presented in Price (2012).
This leads to the SPH-formulation of the EOM:

$$\frac{\mathrm{d}\mathbf{v}_i}{\mathrm{d}t} = -\sum_j m_j \left[f_i^{\mathrm{co}} \frac{P_j}{\rho_j^2} \frac{\partial W_{ij}(h_i)}{\partial \mathbf{r}_i} + f_j^{\mathrm{co}} \frac{P_j}{\rho_j^2} \frac{\partial W_{ij}(h_j)}{\partial \mathbf{r}_i} \right]. \tag{7.4}$$

with f_j^{co} given by

$$f_j^{\mathrm{co}} = \left[1 + \frac{h_j}{3\rho_j} \frac{\partial \rho_j}{\partial h_j} \right]^{-1}. \tag{7.5}$$

The formulation given by equation 7.4 conserves energy, momentum and angular momentum per construction. For the case of SPMHD, the EOM takes the form:

$$\begin{aligned}\frac{\mathrm{d}\mathbf{v}_i}{\mathrm{d}t} = -\sum_j m_j \Bigg[& f_i^{\mathrm{co}} \frac{P_i + \frac{1}{2\mu_0} B_i^2}{\rho_i^2} \nabla_i W_{ij}(h_i) \\ & + f_j^{\mathrm{co}} \frac{P_j + \frac{1}{2\mu_0} B_j^2}{\rho_j^2} \nabla_i W_{ij}(h_j) \Bigg] \\ + \frac{1}{\mu_0} \sum_j m_j \Bigg[& f_i^{\mathrm{co}} \frac{\mathbf{B}_i [\mathbf{B}_i \cdot \nabla_i W_{ij}(h_i)]}{\rho_i^2} \\ & + f_j^{\mathrm{co}} \frac{\mathbf{B}_j [\mathbf{B}_j \cdot \nabla_i W_{ij}(h_j)]}{\rho_j^2} \Bigg]. \end{aligned} \tag{7.6}$$

We note, that the magnetic field influences the EOM in two ways. At first the presence of the magnetic field generates a pressure alongside the thermal pressure of the fluid, which scales as $\mathbf{B}^2$. The second term is needed to fulfil the $\nabla \cdot \mathbf{B} = 0$ constraint. Further, we note that for the SPMHD formulation, energy and linear momentum are conserved down to machine precision, while angular momentum is violated due to the fact that the second term in equation 7.6 is anisotropic and therefore not invariant under rotation of the system.

7.2.3 Cooling, star formation and supernova-seeding

We briefly describe the cooling, star formation and the supernova-seeding approach that is used in a subset of our simulations. We include cooling as described by Katz et al. (1996). In this framework, cooling is mainly driven due to collisional excitation of H^0 and He^+, and free-free emission (thermal Bremsstrahlung). The cooling rates are then calculated via the assumption of collisionless ionisation equilibrium and an optically thin gas. We use the stochastic star formation approach, presented in Springel and Hernquist (2003), where stars are formed according to the Kennicutt-Schmidt relation (Kennicutt, 1989; Schmidt, 1959). The adopted values for the star formation model are given in Table 7.1. Simulations without magnetic fields are referred to as *noB*. Additionally, we perform runs with two different magnetic field models. The first one is set up with a primordial magnetic field of 10^{-9} G in x-direction in the disc and 10^{-12} G in the CGM, and is referred to as *primB*. The second model does not employ a primordial magnetic field, but follows the magnetic supernova-seeding presented in Beck et al. (2013), and is referred to as *snB*. Here, a dipole field is seeded in the ISM when a supernova explodes, such that it directly couples to the stellar feedback routines. The induction equation is modified with an additional seeding term on the right hand side:

$$\frac{\partial \mathbf{B}}{\partial t} = \nabla \times (\mathbf{v} \times \mathbf{B}) + \eta \Delta \mathbf{B} + \left(\frac{\partial \mathbf{B}}{\partial t} \right)_{\mathrm{seed}}, \tag{7.7}$$

with the magnetic resistivity η and the magnetic seeding amplitude per timestep, calculated via:

$$\left(\frac{\partial \mathbf{B}}{\partial t} \right)_{\mathrm{seed}} = \sqrt{N_{\mathrm{SN}}^{\mathrm{eff}}} \frac{B_{\mathrm{Inj}}}{\Delta t} \mathbf{e}_{\mathrm{B}}, \tag{7.8}$$

where $N_{\mathrm{SN}}^{\mathrm{eff}}$ is the effective number of supernovae directly given by the Springel and Hernquist (2003) star formation model. The parameter $\mathbf{e}_{\mathrm{B}}$ is a normalization vector and B_{Inj} is the injected magnetic field

Table 7.1: Parameters for the multiphase model.

Multiphase model parameters		
Gas consumption time-scale in [Gyr]	t_{MP}	2.1
Mass fraction of massive stars	β_{MP}	0.1
Evaporation parameter	A_0	1000
Effective supernova temperature in [K]	T_{SN}	$1 \cdot 10^8$
Temperature of cold clouds in [K]	T_{CC}	1000

amplitude given by

$$B_{\mathrm{Inj}} = \sqrt{N_{\mathrm{SN}}^{\mathrm{eff}}}\, B_{\mathrm{SN}} \left(\frac{r_{\mathrm{SN}}}{r_{\mathrm{SB}}}\right)^2 \left(\frac{r_{\mathrm{SB}}}{r_{\mathrm{r_{Inj}}}}\right)^3, \tag{7.9}$$

with $B_{\mathrm{SN}} = 10^{-5}$ G as the magnetic seed field strength within the supernova-radius $r_{\mathrm{SN}} = 5$ pc. The bubble radius $r_{\mathrm{SB}} = 25$ pc is the radius where the isotropic expansion of the magnetic field within the shell ends. The bubbles are randomly placed within the injection radius r_{Inj} and mix with the surrounding medium.

7.3 Initial conditions

Our setup consists of an isolated disc galaxy, surrounded by a spherical CGM. To set the system up, we use the method described in Hernquist (1993). A more detailed documentation can be found in Springel and White (1999) and Springel et al. (2005a). The model for a spiral disc galaxy consists of a dark matter halo, a bulge, a stellar disc and a gaseous disc. We prepare initial conditions for three systems with virial masses of 10^{10}, 10^{11}, and $10^{12}\mathrm{M}_\odot$, representing a dwarf galaxy (DW), a medium-mass galaxy (MM), and a Milky Way-like galaxy (MW), respectively. In Table 7.2 we present the particle numbers used in our models and list the mass resolution as well as the gravitational softening lengths.

7.3.1 Galactic system

The dark matter halo is modelled using the spherical Hernquist (1993) density profile:

$$\rho_{\mathrm{dm}}(r) = \frac{M_{\mathrm{dm}}}{2\pi} \frac{a}{r(r+a)^3}, \tag{7.10}$$

where M_{dm} is the total mass of the dark matter halo, and a is a scale parameter. For the corresponding Navarro et al. (1997) profile with an equal inner density profile and a scale length of r_{s}, the parameter a can be related to the halo concentration c by

$$a = r_{\mathrm{s}} \sqrt{2\left[\ln(1+c) - c/(1+c)\right]}. \tag{7.11}$$

The density profile of the stellar bulge follows the Hernquist-profile:

$$\rho_{\mathrm{b}}(r) = \frac{M_{\mathrm{b}}}{2\pi} \frac{l_{\mathrm{b}}}{r(r+l_{\mathrm{b}})^3}, \tag{7.12}$$

where l_{b} is the scale length of the bulge. Its mass is given by $M_{\mathrm{b}} = m_{\mathrm{b}} M_{200}$, where m_{b} is the dimensionless bulge mass fraction.

Table 7.2: Number of particles, mass resolution, and gravitational softening lengths for our three galactic systems.

Particle Numbers [10^6]				
		DW	MM	MW
Gas disc	N_{gd}	0.8	1.0	1.2
Gas halo	N_{gh}	5.0	6.0	7.0
Stellar disc	N_{sd}	3.2	4.0	4.8
Stellar bulge	N_{b}	1.3	1.6	2.0
Dark matter	N_{dm}	4.6	5.7	6.9
Mass resolution [$M_\odot$]				
		DW	MM	MW
Gas particles	m_{gas}	72	510	4800
Star particles	m_{star}	72	510	4800
Dark matter	m_{dm}	1440	10200	96000
Gravitational softening [pc]				
		DW	MM	MW
Gas particles	ϵ_{gas}	5	10	20
Star particles	ϵ_{star}	5	10	20
Dark matter	ϵ_{dm}	40	20	10

The surface densities of the stellar and gaseous discs $\Sigma_\star$ and Σ_{gas} follow an exponential profile:

$$\Sigma_\star = \frac{M_\star}{2\pi l_{\mathrm{d}}^2} \cdot \exp\left(-\frac{r}{l_{\mathrm{d}}}\right), \tag{7.13}$$

$$\Sigma_{\mathrm{gas}} = \frac{M_{\mathrm{gas}}}{2\pi l_{\mathrm{d}}^2} \cdot \exp\left(-\frac{r}{l_{\mathrm{d}}}\right), \tag{7.14}$$

where l_{d} is the scale length of the disc. The mass of the disc is given by $M_{\mathrm{d}} = (M_\star + M_{\mathrm{gas}}) = m_{\mathrm{d}} M_{200}$, with the dimensionless disc mass fraction m_{d}. We take a fraction f of the disc mass to compose the gaseous disc. The total mass of the dark matter halo is then given by $M_{\mathrm{dm}} = M_{200} - (m_{\mathrm{b}} + m_{\mathrm{d}}) \cdot M_{200}$. Finally, the angular momentum of the system is determined by the spin parameter λ, as described by Mo et al. (1998). The parameters we used for each model are listed in Table 7.3.

7.3.2 Circum galactic medium

Our implementation of the CGM follows that of Moster et al. (2010a) and Donnert (2014), but samples the particles from a glass distribution rather than from a random distribution. We assume a radial symmetric density distribution for the gas medium surrounding the galaxy. For this we use the radial density profile of the beta-model (Cavaliere and Fusco-Femiano, 1978), that has also been found by observations (i.e. Croston et al., 2008; Miller and Bregman, 2013). The density distribution in the beta-model takes the form

$$\rho_{\mathrm{gh}} = \rho_0 \left(1 + \frac{r^2}{r_c^2}\right)^{-\frac{3}{2}\beta} . \tag{7.15}$$

We follow Mastropietro and Burkert (2008) and set $\beta = 2/3$, which is underpinned by recent observations by Miller and Bregman (2013), who find a value for β close to this value. We choose the central gas

Table 7.3: Adopted parameters for our three galactic systems.

Disc parameters				
		DW	MM	MW
Total mass [$10^{10} M_\odot$]	M_{200}	1	10	100
Virial radius [kpc]	r_{200}	31	67	145
Halo concentration	c	8	10	12
Spin parameter	λ	0.033	0.033	0.033
Disc mass fraction	m_d	0.041	0.041	0.041
Bulge mass fraction	m_b	0.013	0.013	0.013
Disc spin fraction	j_d	0.041	0.041	0.041
Gas fraction	f	0.2	0.2	0.2
Disc scale length [kpc]	l_d	0.8	1.5	2.1
Disc height	z_0	$0.2\ l_\mathrm{d}$	$0.2\ l_\mathrm{d}$	$0.2\ l_\mathrm{d}$
Bulge size	l_b	$0.2\ l_\mathrm{d}$	$0.2\ l_\mathrm{d}$	$0.2\ l_\mathrm{d}$

Table 7.4: Parameters for the gaseous halo

General parameters				
		DW	MM	MW
Total Mass [$10^{10} M_\odot$]	M_gh	0.05	0.5	5.0
Virial temperature [K]	T_vir	10^4	10^5	10^6
Settings for the β-model				
Exponent	β		2/3	
Density in [g/cm^3]	ρ_0		$5 \cdot 10^{-26}$	
Core radius	r_c	$0.22 \cdot r_\mathrm{s}$	$0.25 \cdot r_\mathrm{s}$	$0.33 \cdot r_\mathrm{s}$

density ρ_0 to be between 10^{-27} and $5 \cdot 10^{-26}$g/cm^3 , motivated by the electron density found through cosmological simulations (Dolag et al., 2015), as well as the observations of Milky Way's hot gaseous halo (Miller and Bregman, 2013). The core radius r_c has been chosen between 0.22 and 0.33kpc, which is again motivated by observations (Miller and Bregman, 2013). The value of r_c conforms well with $r_\mathrm{s}/40$ where r_s is the scale length of the corresponding NFW-halo. The value of $\beta = 2/3$ allows us to calculate the mass distribution of the gaseous halo analytically. By integrating the density profile set by equation 7.15, the hot gas mass within a radius r is given by

$$M_\mathrm{gh}(< r) = 4\pi r_c^3 \rho_0 \left[\frac{r}{r_\mathrm{c}} - \arctan\left(\frac{r}{r_\mathrm{c}}\right)\right]. \tag{7.16}$$

As we require the density distribution to be as close as possible to equilibrium, we sample the particle positions of the CGM with a normalized glass distribution. The glass is constructed with the Wendland C4 kernel to be consistent with the disc galaxy simulations. We introduce the variable q as

$$q = \frac{M_\mathrm{gh}(< r_\mathrm{new})}{M_\mathrm{gh}}, \tag{7.17}$$

which corresponds to the hot gas mass within a radius r_new, normalized by the total gas mass of the CGM. To sample the particle distribution, we thus need to solve the equation

$$\frac{4\pi r_c^3 \rho_0}{M_\mathrm{gh}} \left[\frac{r}{r_\mathrm{c}} - \arctan\left(\frac{r}{r_\mathrm{c}}\right)\right] - q = 0. \tag{7.18}$$

We take a normalized, equally distributed glass distribution and transform its components to spherical coordinates r', θ and ϕ. As we can see from equation 7.16, the mass distribution of the β-profile is only a perturbation in the radial coordinate. We determine the value of q that corresponds to r' by solving equation 7.18 with the Newton-Raphson-Method.

This leads to a new radial component with a smaller value than r', in agreement with the density distribution given by equation 7.15. As this procedure distorts the initial glass sampling, the advantages of using a glass are somewhat weakened. However, the particle noise is kept low enough to justify the procedure (a more rigorous approach will be presented in Arth et al. in prep.) Further, we observe better results compared to other initial configurations (random distribution, cubic or hcp lattice). The angular coordinates stay unchanged and we can perform the transformation from spherical coordinates back to Cartesian coordinates with the new radial coordinate. As a result, we get a particle distribution for the CGM which is as close as possible to its dynamical equilibrium. In the last step the gaseous halo is balanced in the dark matter profile of the galactic disc. The condition for hydrostatic equilibrium between the dark matter halo of the galaxy and the CGM are

$$\frac{1}{\rho_{\mathrm{gh}}}\frac{\mathrm{d}P_{\mathrm{gh}}}{\mathrm{d}r} = -\frac{G\,M_{\mathrm{total}}(<r)}{r^2} \tag{7.19}$$

This allows us to calculate the temperature profile of the CGM by integrating the equilibrium condition using the ideal equation of state for an atomic gas:

$$T(r) = \frac{\mu m_{\mathrm{p}}}{k_{\mathrm{B}}}\frac{G}{\rho_{\mathrm{gh}}}\int_r^{R_{\max}} \frac{\rho_{\mathrm{gh}}(t)}{t^2} M_{200}(<t)\,\mathrm{d}t\,, \tag{7.20}$$

which leads to

$$T(r) = G\frac{\mu m_{\mathrm{p}}}{k_{\mathrm{B}}}\left(1+\frac{r^2}{r_{\mathrm{c}}^2}\right)[M_{\mathrm{dm}}F_0(r) + 4\pi r_{\mathrm{c}}^3\rho_0 F_1(r)]. \tag{7.21}$$

The temperature profile consists out of two parts. The first part comes from the dark matter halo and the second part is the influence of the CGM itself. The functions $F_0(r)$ and $F_1(r)$ are given via

$$\begin{aligned} F_0(r) = &\frac{r_{\mathrm{c}}}{a^2+r_{\mathrm{c}}^2}\left[\frac{\pi}{2}(a^2-r_{\mathrm{c}}^2) + r_{\mathrm{c}}\frac{a^2+r_{\mathrm{c}}^2}{a+r}\right. \\ &\left. -(a^2-r_{\mathrm{c}}^2)\arctan\left(\frac{r}{r_{\mathrm{c}}}\right) - r_{\mathrm{c}}a\ln\left(\frac{(a+r)^2}{r^2+r_{\mathrm{c}}}\right)\right], \end{aligned} \tag{7.22}$$

and

$$F_1(r) = \frac{\pi^2}{8r_{\mathrm{c}}} - \frac{\arctan^2(r/r_{\mathrm{c}})}{2r_{\mathrm{c}}} - \frac{\arctan(r/r_{\mathrm{c}})}{r}. \tag{7.23}$$

From an observational point of view it is useful to calculate a virial temperature for the gaseous halo $T_{\mathrm{c}} = T(r_{\mathrm{c}})$. It can be calculated as

$$\begin{aligned} T_{\mathrm{c}} = &\frac{2G\mu m_{\mathrm{p}}}{k_{\mathrm{B}}}\left\{M_{\mathrm{dm}}\frac{r_{\mathrm{c}}^2}{(a^2+r_{\mathrm{c}}^2)}\cdot\left[\frac{\pi}{4r_{\mathrm{c}}^2}(a^2-r_{\mathrm{c}}^2) + \frac{a^2+r_{\mathrm{c}}^2}{a+r_{\mathrm{c}}}\right.\right. \\ &\left.\left. -a\ln\left(\frac{(a+r_{\mathrm{c}})^2}{2r_{\mathrm{c}}^2}\right)\right] + \pi^2 r_{\mathrm{c}}^2\rho_0\left(\frac{3\pi}{8}-1\right)\right\}. \end{aligned} \tag{7.24}$$

In table 7.4 we summarize the values used to construct realistic gaseous haloes for the three galactic system in this study. Finally we note that the CGM is truncated at $R200$.

7.3.3 Combination of the galactic disc with the CGM

Finally, we need to combine the galactic disc with the CGM in a way that keeps the initial conditions as close as possible to equilibrium. Further, we want to avoid an overlap between the particles of the galactic disc and the CGM. Therefore, we implement a procedure to cut out the central part of the CGM and place the disc in the resulting gap. An obvious choice would be to cut out a cylinder, with the radius of the disc and the height of the disc height. This procedure has the advantage, that it is very simple. However, this method results in a relatively large gap between the disc and the CGM. Luckily, the density profile of the galactic disc and the CGM are slightly different and we can use this for selecting the part of the CGM we want to cut out, by introducing a quality condition for the density in the overlap region of galactic disc and CGM. To do so, we bring the SPH data of the galactic disc on a grid by using the triangular shaped cloud method. Then we compare the density of each grid cell to the density of the CGM. To minimize the gap between disc and gaseous halo we remove the particles of the CGM, if their density is ten percent different to that of the grid cell they are related to. The grid we use for this purpose has a spatial resolution of $20^3 = 8000$ cells.

7.4 Results

We perform three types of simulations with the same initial conditions but with different approaches for the magnetic field, a primordial field, a field seeded by supernovae, and, for reference, without a magnetic field. In this section we present our results for the morphology of the disc, the SFR, the growth rate of the magnetic field, the magnetic field structure and the interaction between the galactic disc and the CGM. We mainly focus on the Milky Way-like galaxies MW, MW-primB and MW-snB.

7.4.1 Morphology of the galactic disc and the magnetic field

We first focus on the most important morphological structures in the simulations, i.e. face-on and edge-on slices of the density and the magnetic field strength for the Milky Way-like models MW-snB and MW-primB. The slices of the face-on view are centred in the mid-plane, the ones for the edge-on view are perpendicular to it. Figure 7.1 shows our results for the model MW-snB after $t = 2$ Gyr (first and second columns) and $t = 3$ Gyr (third and fourth columns). The upper left panel shows that the gas in the disc builds up a well defined spiral structure. The lower left panel indicates that the system evolved to a thin disc that is surrounded by the lower density gas of the CGM. However, because of the density gradient of the underlying β-profile one can see a brighter blue halo closer to the disc. This density gradient is a quantity which has been introduced by our galactic model itself and is only weakly influenced by the boundary layer between the gas disc and the CGM. In the second panel on the top, we show the face-on view of the absolute magnetic field strength. While the gas density on average decreases monotonically towards the outer parts of the disc, the situation is different for the galactic magnetic field which is of the order of a few μG in two different regions. This is in good agreement with observations of several spiral galaxies (Beck, 2015; Beck and Wielebinski, 2013; Han, 2017). The first region with strong magnetic fields is the very centre of the galactic disc (i.e. the innermost kpc). The second region is a ring-shaped structure further outside in the galactic disc and approximately located at 10 kpc distance from the galactic centre. The former originates from the large SFR in the very centre of the galaxy. A consequence of strong star formation is a large rate of supernovae in the same region. In the model MW-snB this is directly correlated with the amount of magnetic dipoles that are seeded into the surrounding ISM, leading to a strong magnetic field. Furthermore, in this regime the magnetic field is exponentially amplified by the small-scale turbulent motion of the ISM.

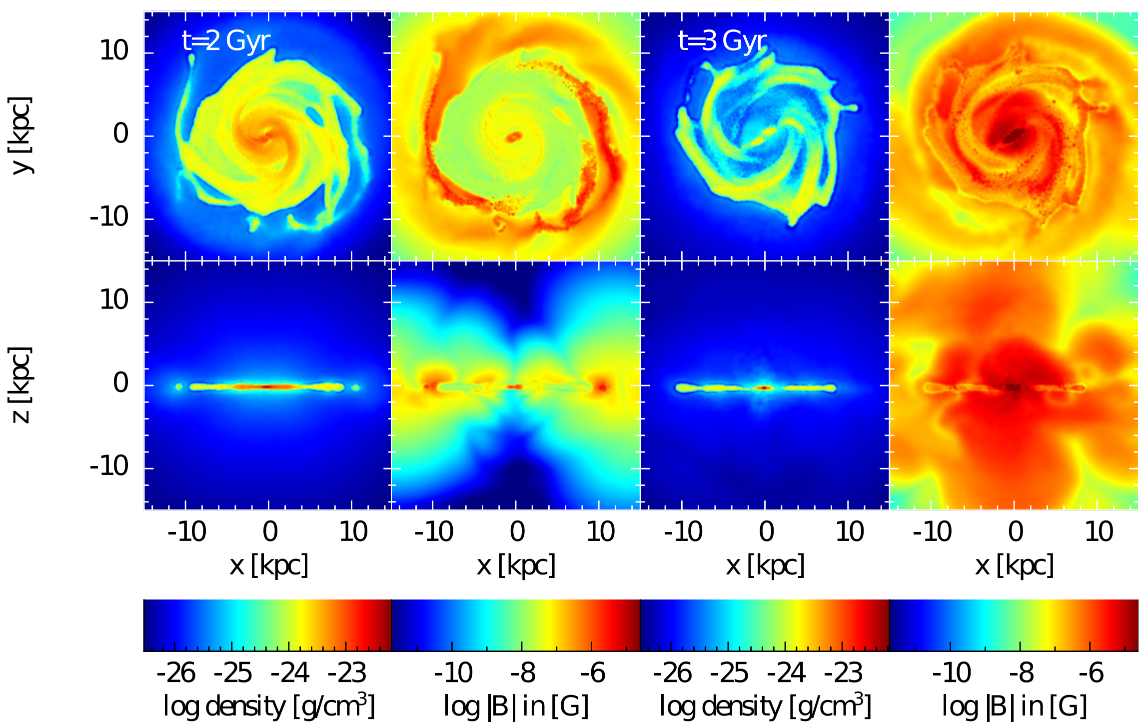

Figure 7.1: Slice through the gas density and the magnetic field strength for the simulation *MW-snB* for the face-on and edge-on view. The four panels on the left-hand-side are at $t = 2$ Gyr, while the four panels on the right-hand-side are at $t = 3$ Gyr.

This small-scale turbulence is mainly driven by the higher supernova rate in the centre of the galaxy. We will discuss this in more detail in section 7.4.3. In contrast, the amplification process in the outer parts of the disc is most likely not driven by small-scale turbulence. There, we observe very high rotation velocities of the gas due to the differential rotation of the disc. This leads to an exponential amplification of the magnetic field through the kinematic motion known as the $\alpha-\omega$-dynamo. This explains the strong magnetic field at the edge of the disc, although the amount of supernovae in the ambient medium in the outer parts of the disc is significantly lower compared to the galactic centre. Nevertheless, turbulent motion could also play a crucial role in this regime.

We note that the large magnetic field strengths are correlated with the location of the spiral arms in the gas density, but they do not explicitly follow each other. It seems that the magnetic field strength between or at the edges of the spiral arms in the gas density is higher than in the gaseous spiral arms itself. This behaviour is indicated by observations (see Beck (2015) for a review) and can be explained in galaxies with high density. Strong density waves lead to a compression of the magnetic field at the inner edges of the spiral arms. This can lead to turbulent motion and further amplification of the magnetic field. However, on e can hardly see whether the magnetic field follows the spiral structure of the gas density by only comparing the two top left panels of figure 7.1 at this point in time. The anti-corellation becomes clearer later at $t = 3$. We will evaluate this behaviour in closer detail in section 7.4.5. In the bottom row of figure 7.1 we plot the edge-on view of the gas density (first panel) and the magnetic field strength (second panel). Perpendicular to the galactic disc, the magnetic field strength declines much more weakly than the gas density. This is especially true at the edge and is a result of the interaction between the outer parts of the disc with the surrounding CGM. The large magnetic field at the edge leads to a weak magnetization of the nearby CGM. Due to the magnetic pressure the gas particles near the edge of the disc gain momentum in z-direction, move into the CGM, slow down, magnetize the nearby particles in the CGM, stop and fall back towards the disc. After $t = 3$ Gyr (third and fourth columns), the face-on view of the gas density shows that the spiral structure is more depleted than at $t = 2$ Gyr. We note that this effect is the strongest in the galactic centre. This can be explained by the higher SFR in the centre of the galaxy. A large fraction of the original gas mass in the centre has been converted into stars which leads to a significant drop in the gas density. In the third panel on the top, we present the face-on view of the magnetic field for $t = 3$ Gyr. To this point in time the magnetic field strength in the galactic disc has significantly increased and evolved towards a prominent spiral structure. It reaches values of a few 10μG in the magnetic spiral arms to a few 100μG in the galactic centre. The magnetic field in the spiral arms is still in agreement with the observations of magnetic fields in spiral galaxies (e.g. Beck and Wielebinski, 2013). The magnetic field in the central region has a maximum value that is around 350μG. Although, this is a high magnetic field strength there is observational evidence that the magnetic field in the centre reaches values between 50μG (Crocker et al., 2010) and 4 mG (Yusef-Zadeh et al., 1996).

We further note that at $t = 3$ Gyr, we can clearly observe the magnetic field in the inter-arm regions to be stronger than in the gaseous spiral arms. We are also able to reproduce the correct field strengths in the inter arm regions of a few 10μG that are known from observations (Beck, 2007, 2009). Our simulations reach larger field strengths in the inter-arm regions than in the gaseous spiral arms with the correct field strengths compared to observations. However, the physical reason for this behaviour cannot be clearly determined. There are several possibilities that can lead to stronger magnetic fields in the inter-arm regions, like the buoyancy, Parker, or magneto-rotational instability (MRI)[1] (Beck,

[1] At early times we do not resolve the fastest growing mode of the MRI. For later times when the magnetic field is saturated the resolution scale of the fastest growing mode is ~ 20 pc depending on the exact location across the disc. This length scale is of the same order of magnitude as our force softening and therefore the simulations weakly resolve the MRI at later times.

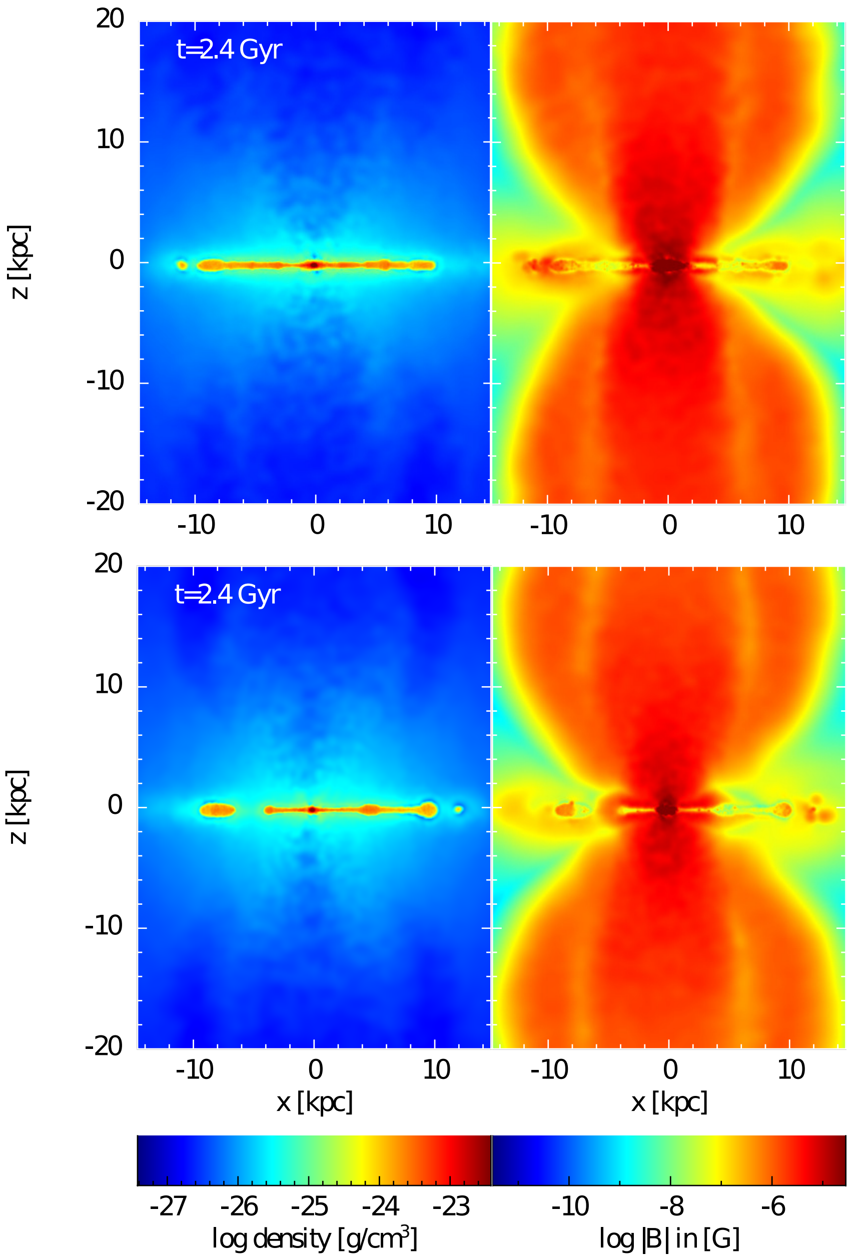

Figure 7.2: Cross section slices for the *MW-snB* run (top panels) and the *MW-primB* run (bottom panels) at $t = 2.4$ Gyr. On the left we show the edge-on view of the gas density and on the right we show the edge-on view of the magnetic field strength. For both models we observe a strong biconical outflow in the magnetic field strength with an x-shaped structure.

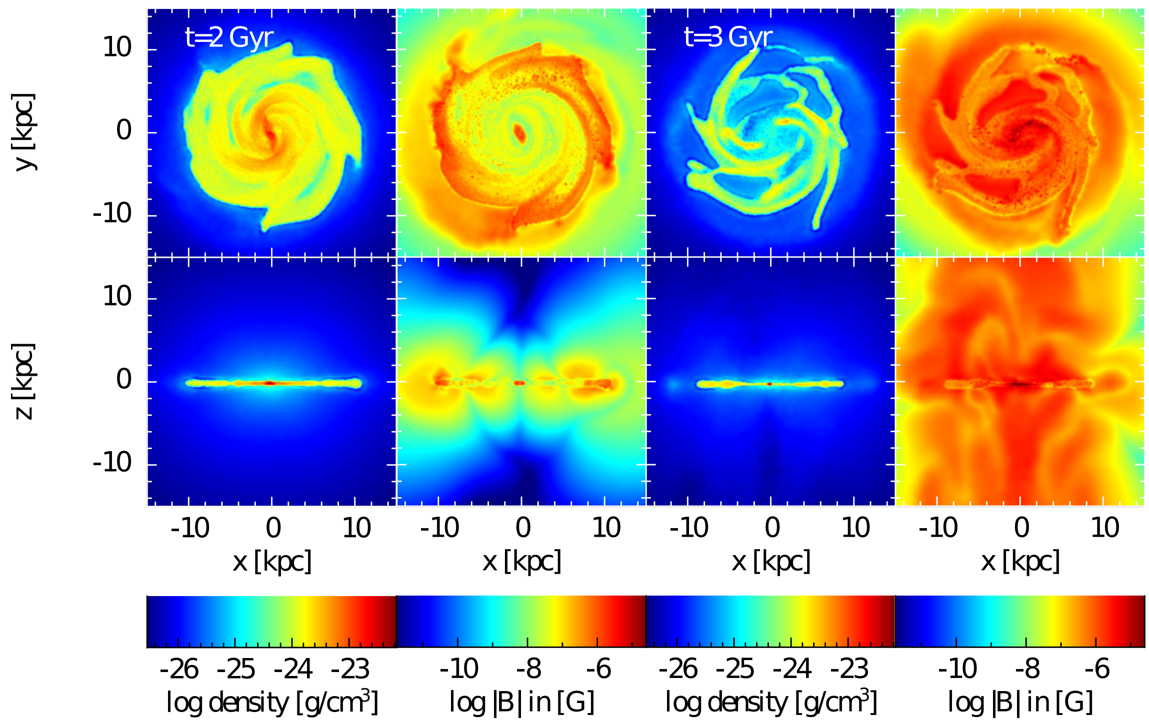

Figure 7.3: Same as figure 7.1 but for the *MW-primB* simulations. A similar behaviour as in figure 7.1 is observed.

2015). In the centre of the galactic disc the magnetic field is further amplified by the small-scale turbulent motion of the ISM. This leads to a very huge magnetic pressure in the very innermost kpc of the galactic disc. When the magnetic pressure becomes large enough it can accelerate particles alongside the z-direction. The strong magnetic field drives the system out of equilibrium, leading to a sharp pressure gradient between the magnetic dominated disc and the thermal dominated, hot gaseous halo. As a result the magnetic field lines break up in z-direction to reduce the sharp pressure gradient at the edge of the disc and we can observe a biconical outflow of magnetic energy perpendicular to the disc. We note that it has its origin in the very centre of the disc.

Because this biconical magnetic tube is one of the central morphological features we show it for both magnetic field models (*MW-snB* and *MW-primB*) in figure 7.2 shortly after it sets in at $t = 2.3$ Gyr. The top row of figure 7.2 shows the edge-on gas density (left) and magnetic field (right) for the *MW-snB* run. The bottom row shows the same quantities for the *MW-primB* run. Although magnetic fields are seeded differently in both models, we observe this biconical magnetic tube in both simulations at the exact same time. In the beginning the magnetic tube rises symmetrically above the disc. It moves forward into the outer parts of the CGM, with a mean velocity of around $400 - 500$ km/s. The biconical tube transports a significant amount of magnetic energy into the CGM, leading to its magnetization.

Moreover, this effect leads to morphological features in the gas density of the CGM close to the disc at the onset of the biconical magnetic tube at around $t = 2.3$ Gyr. The nearby CGM shows a X-shaped or H-shaped structure. These structures of the CGM around galaxies are a well known morphological feature in observations of galaxies with an active galactic nucleus (AGN) in the centre (i.e. Veilleux et al., 2005). In these observations it is known as an indicator for a biconical galactic outflow. We note that we do not include such an AGN, but we observe the CGM structures that indicate such an

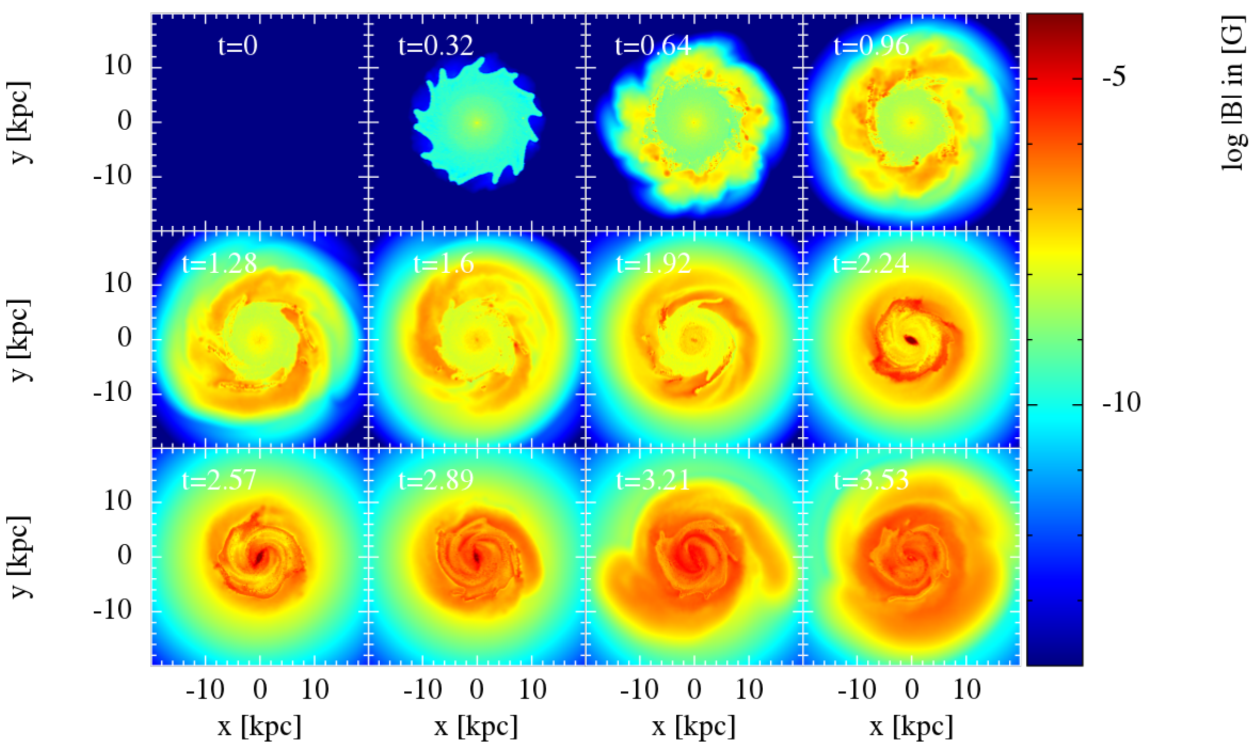

Figure 7.4: Face-on time sequences for the simulation *MW-snB*. The sequence shows the amplification of the magnetic field strength in the galactic disc, as well as the development of the outflow of highly magnetized material perpendicular to the disc.

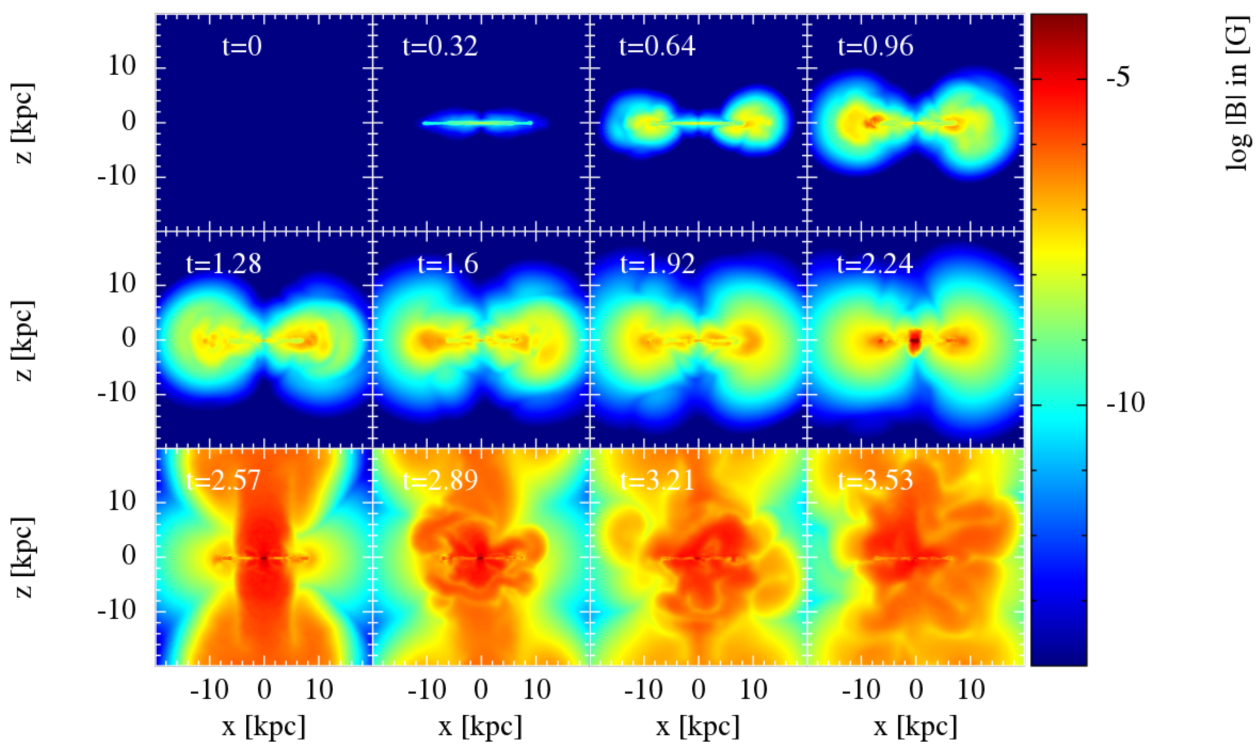

Figure 7.5: Edge-on time sequences for the simulation *MW-snB*. The sequence shows the amplification of the magnetic field strength in the galactic disc, as well as the development of the outflow of highly magnetized material perpendicular to the disc.

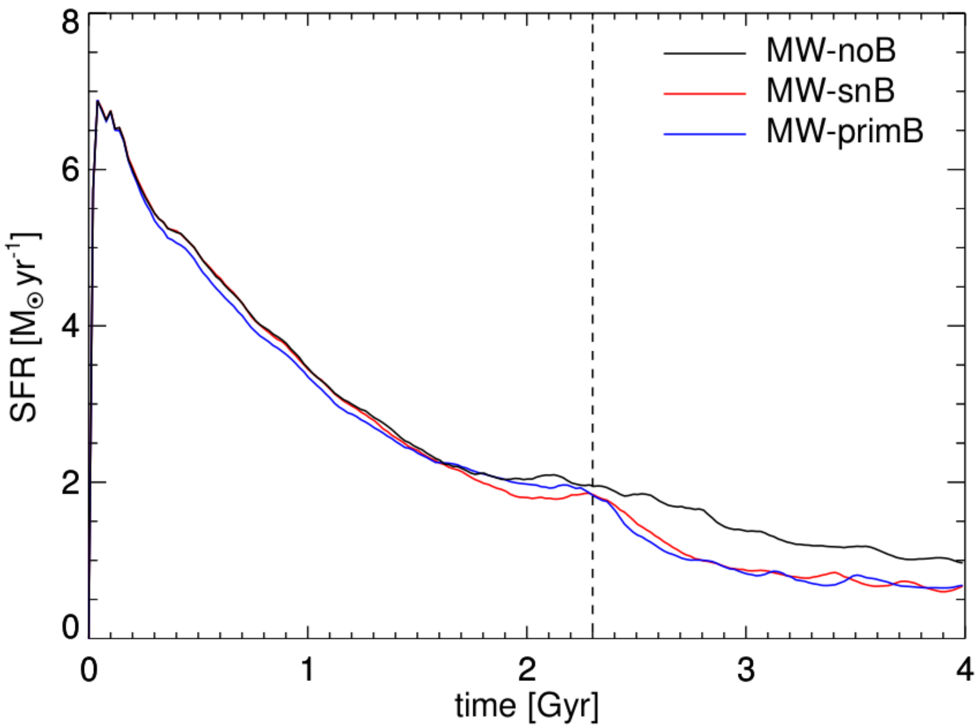

Figure 7.6: SFRs for the simulations *MW-noB* (black line), *MW-primB* (red line), and *MW-primB* (blue line). For all three runs the SFR peaks shortly after the simulation starts due to the non-equilibrium initial condition. At t = 2.3 Gyr the SFR drops for both models that include magnetic fields.

outflow. In our simulations this outflow would be driven by the magnetic field. Therefore, we discuss the possibility of magnetic driven biconical outflows in more detail in section 7.4.4. We note that we observe these X-shaped structures of the CGM around the galaxy only in the first few 100 Myr after the onset of the biconical magnetic tube and thus we conclude that the magnetic wind should be the strongest shortly after it sets in. We do not find a huge difference in the X-shaped structures around the galaxy between the models *MW-snB* and *MW-primB*. Nevertheless, we observe slightly higher magnetic field strengths in the biconical tube for the model *MW-snB*. In figure 7.3 we present the exact same properties as in the figure 7.1 for the model *MW-primB*. The overall morphological structure is comparable to the model *MW-snB*. We observe a prominent gas disc in the face-on view for $t = 2$ Gyrs as well as a thin gas disc in the edge-on view. Further, we see that the magnetic field is mainly amplified in the galactic centre and in a ring around the centre with a radius of around 10 kpc. As we do not seed magnetic field with supernovae, we emphasize that the amplification of the magnetic field in the model *MW-snB* is not caused by a higher magnetic field seeding in the central region due to the higher amount of supernovae. In both cases the supernovae are a crucial component for the amplification of the magnetic field in the galactic centre. But the cause for the amplification is the turbulent motion that is driven by supernova-feedback in the galactic centre leading to an exponential amplification of the magnetic field in the centre. By comparing models *MW-snB* and *MW-primB* it becomes clear that turbulence induced by supernova-feedback is the crucial component for the amplification of the magnetic field in the centre. We present more evidence of the small-scale turbulent dynamo in section 7.4.3. Further, our results justify the common choice of a primordial seed field which has often been used by other groups (e.g. Butsky et al., 2017; Pakmor and Springel, 2013).

The edge-on view (bottom panels of figure 7.3) shows the same biconical magnetic outflow. Its appearance in the model *MW-primB* leads to the conclusion that this structure in the magnetic field is not driven by the supernova-seeding. Furthermore, we observe a similar behaviour of the magnetic field in the inter-arm regions which becomes even clearer for the model *MW-primB* at $t = 3$ Gyr. The model *MW-primB* is also capable of reproducing the observed field strengths in spiral galaxies. To give a more detailed overview of the evolution of the magnetic field, we show a time sequence of the evolution of the magnetic field strength for the model MW-snB in the figures 7.4 and 7.5. The top panels show the face-on view, and the bottom panels show the edge-on view. The evolution of the magnetic field in the *MW-primB* model is very similar, with only minor differences.

7.4.2 Star formation rate within the different models

In figure 7.6 we show the SFR for the simulations *MW-snB*, *MW-primB* and *MW-noB* as a function of time. All simulations were evolved for $t = 4$ Gyr. The SFR at the beginning of the simulation is very similar in all three runs, and peaks shortly after the start of the simulation to a value of around $7 M_{\odot}/yr$. The initial peak can be explained by the non-equilibrium configuration and the large amount of cold gas at the start of the simulation. It is entirely set by the initial conditions, and does not depend on the magnetic field model. After the initial peak, the SFR declines rapidly. In the first 1.5 Gyr, there is no significant difference between the three models, except for a slightly lower SFR for the *MW-primB* run. This small deviation can simply be explained by the difference in the initial magnetic field strength. While the simulations *MW-snB* and *MW-noB* start without any magnetic field the simulation *MW-primB* starts with a field strength of 10^{-9} G in the disc. This is demonstrated in figure 7.7, which shows the magnetic field strength for the simulations *MW-snB* (red solid line) and *MW-primB* (blue solid line). The mean magnetic field strength of the *MW-primB* run is three orders of magnitude higher in the beginning than in the *MW-snB* run, leading to a higher magnetic pressure, which can results in a lower SFR if gas is pushed out of the star-forming regions of the disc. The SFRs in the simulations *MW-snB*

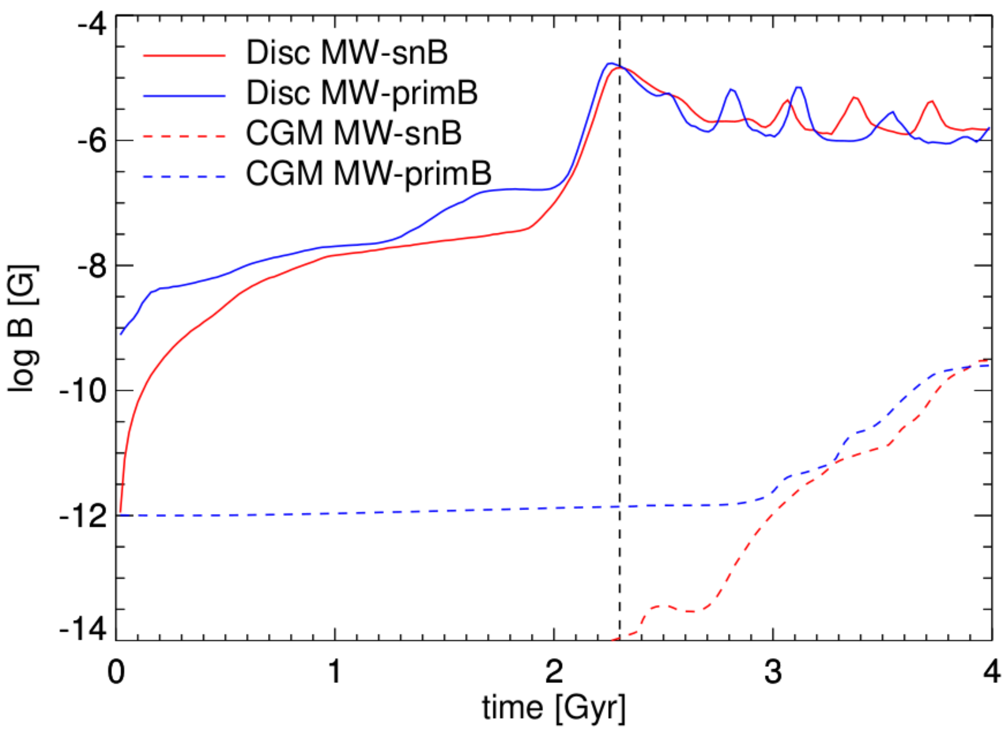

Figure 7.7: Magnetic field strength for the simulations *MW-snB* (red line) and *MW-primB* (blue line). In the disc, it first growth exponentially and then saturates at $\sim 10^{-6}$ G with oscillations that reach up to a few 10^{-5} G. The dashed lines show the evolution of magnetic field strength in the CGM. The mean magnetic field strength in the CGM is around 10^{-10} G and is still rising when the simulation stops.

and *MW-noB* are identical in the beginning, since the small initial magnetic field corresponds to the run without a magnetic field and therefore does not change the SFR. After the SFR drops, it remains nearly constant between 1.7 Gyr and 2.3 Gyr for all three simulations. Then the SFR in the simulations with magnetic fields drops by about 50 per cent for the rest of the simulation compared to the simulation without magnetic fields. This indicates that in the *MW-snB* and *MW-primB* runs, a significant amount of the star-forming gas is removed from the disc. This can be explained by the results of section 7.4.1, which showed strong magnetized biconical outflows that set in at around $t = 2.3$ Gyr in both runs. This indicates that the SFR is reduced due to a magnetized outflow of gas from the disc to the CGM. This outflow is driven by the magnetic pressure, i.e. the magnetic field strength within the disc, that rises mainly in the centre due to amplification via small-scale turbulence. This results in a smaller gas reservoir in the disc leading to a lowered SFR. In the star-formation model used in our simulations, all gas above the threshold density forms stars, independent of its temperature and magnetic field strength. Thus, we cannot follow the impact of the magnetic field on the SFR directly, but only its indirect influence, such as outflows that are driven by the contribution of the magnetic pressure in the ISM. For a more detailed analysis on how the magnetic field influences the galactic SFR, the density threshold in the star formation recipe would have to be changed to a pressure threshold, such that the magnetic pressure $\mathbf{B}^2/8\pi$ can be taken into account directly.

7.4.3 Amplification of the magnetic field

A very important aspect of disc galaxy simulations with SPMHD is to reproduce the observed magnetic field strengths in the disc. There are many observations of magnetic fields in galactic discs (e.g. Beck, 2007; Chyży et al., 2007, 2003; Hummel, 1986), which show that the field strength in discs ranges from $10\mu G$ between the spiral arms up to $50\mu G$ within the spiral arms. We present the growth rate of the magnetic field in our three models in figure 7.7. The solid lines represent the magnetic field strength in the galactic disc, for the models with supernova-seeding (red) and a constant magnetic seed-field (blue). The dashed lines represent the magnetic field strength in the CGM. The vertical dashed line marks the point in time when the magnetic pressure becomes dynamically important at around $t = 2.3$ Gyr. At the beginning of the simulation the magnetic field in the disc roughly grows exponentially in both models, in good agreement with the findings of dynamo theory. In galaxies there are in general two amplification processes for the magnetic field. The first is the small-scale turbulent dynamo and the second is the mean-field α-ω-dynamo. Both dynamos can lead to either exponential or linear growth of the magnetic field. In the case of the small-scale turbulent dynamo, the amplification of the magnetic field happens due to the turbulent motion in the ISM as long as we can neglect the pressure caused by the magnetic field itself, so that the dynamo operates in the kinetic regime (Pakmor et al., 2017). The magnetic energy rises exponentially until an equilibrium with the kinetic energy is reached. At this point the magnetic energy can be transported to large scales due to an inverse energy cascade. In this regime the small-scale dynamo is only able to follow linear amplification (Federrath, 2016). In the case of the α-ω-dynamo, the differential rotation and the α-effect (small-scale vertical motion of the gas particles) in the galactic disc itself can lead to both, exponential or linear growth of the magnetic field. Initially it is not clear which of those two amplification processes is favoured in our simulations. However, we can deduce the dominant amplification process from the power spectrum of the magnetic field, which is shown for both models in figure 7.8. These power spectra have been obtained with the tool SPHMAPPER (Röttgers and Arth, 2018), which carries out an appropriate binning for SPH data on a regular grid using the same kernel that is used in the simulations (Wendland C4). The left panel of figure 7.8 shows the power spectra at five different points in time for the model *MW-snB*. The right panel of figure 7.8 shows the power spectra at the same points in time for the models *MW-primB*

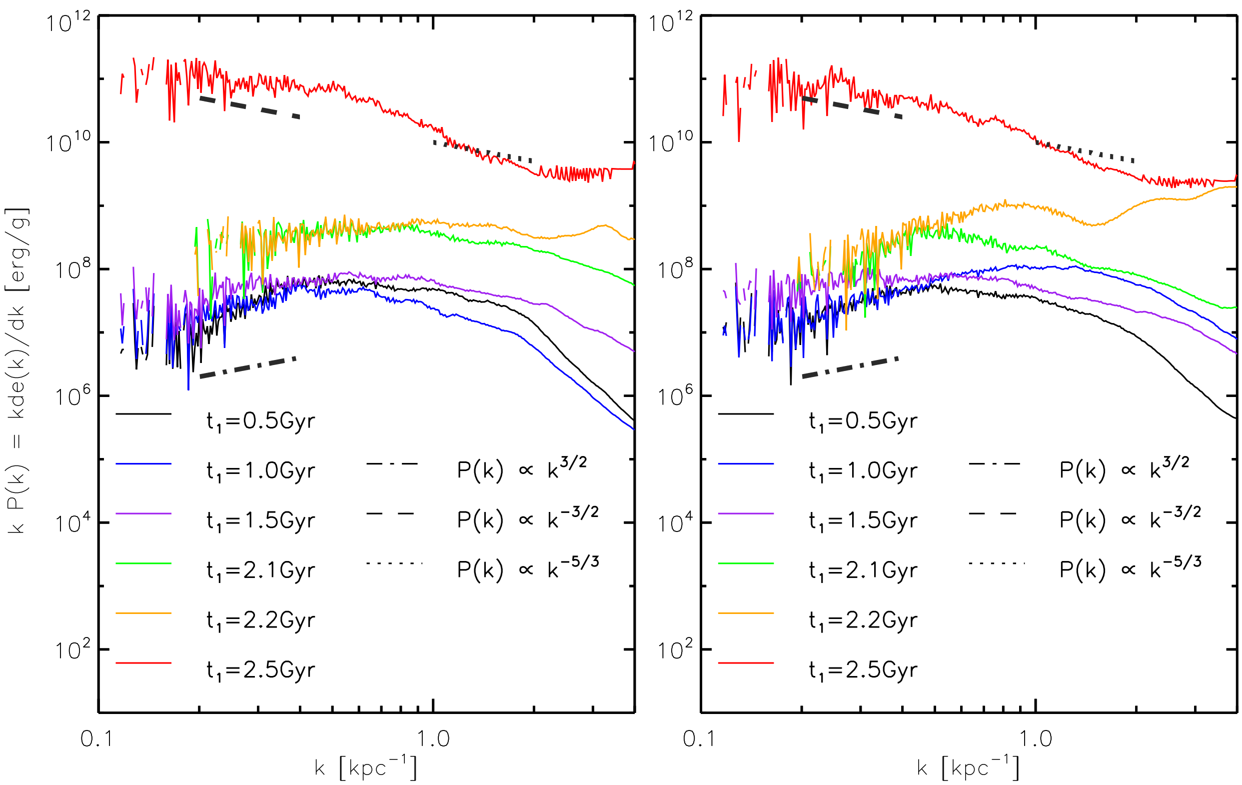

Figure 7.8: Magnetic power spectra for the simulations *MW-snB* (left panel) and MW-primB (right panel). Both models result in very similar power spectra, independent of the seeding model. The magnetic field is amplified by turbulent motion on small scales, which is transported to large scales through an inverse energy cascade. This Kazantsev (1968) spectrum is an indicator for a small-scale turbulent dynamo, resulting in an increase of the power $P(k) \propto k^{3/2}$ on large scales. The small-scale dynamo stops at later times due to the large magnetic field resulting in an Iroshnikov (1963) spectrum with $P(k) \propto k^{-3/2}$.

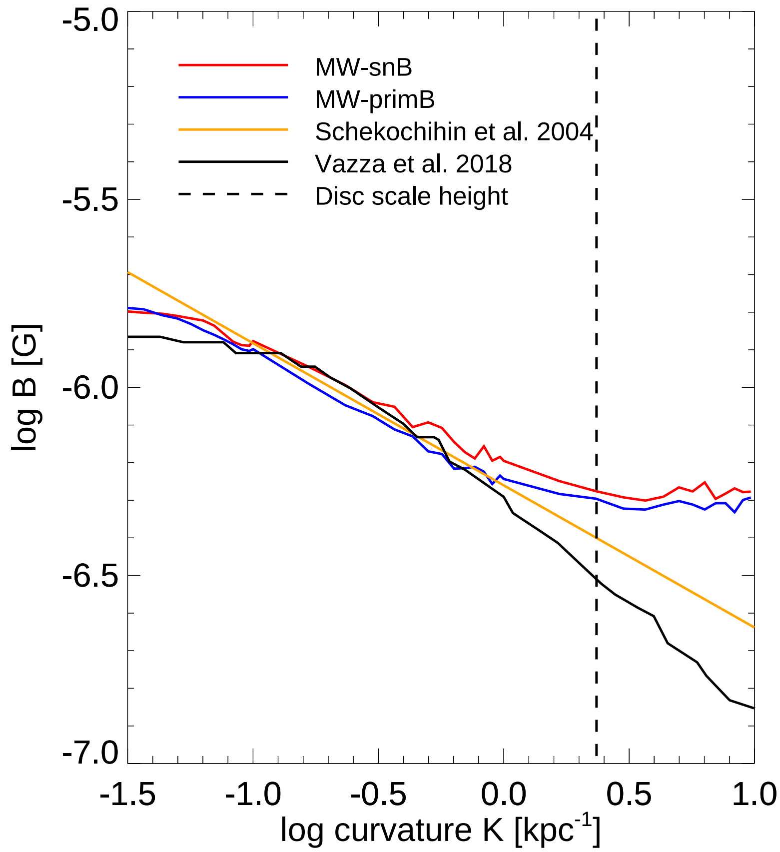

Figure 7.9: Median of the magnetic field strength as a function of the curvature of the magnetic field lines for $t = 2$ Gyr. The red line represents the *MW-snB* run and the blue line the *MW-primB* run. The field strength and curvature are anti-correlated with a power law slope of 0.5, as the field lines are harder to bend in the presence of stronger magnetic fields. The slope indicates that the amplification is driven by small-scale turbulence in agreement with the results by Schekochihin et al. (2004) (orange line). The black line shows the recent result of MHD-simulations of galaxy-clusters by Vazza et al. (2018).

field. Both magnetic field models reproduce a relatively smooth distribution of the magnetic power from small scales to large scales. We find strong evidence for a small-scale turbulent dynamo for both magnetic field models. From dynamo theory we expect a power spectrum $P(k) \propto k^{3/2}$ in the case of a small-scale turbulent dynamo. We can see this behaviour in both power spectra very clearly, especially at the beginning of the simulation, when the equilibrium state between the magnetic and the kinetic energy has not been reached yet. The magnetic field is amplified by turbulent motion on small scales and transported to large scales by an inverse energy cascade, as predicted by dynamo theory. We note, that the power spectrum on the large scales is fully consistent with a Kazantsev-spectrum (Kazantsev, 1968; Kraichnan, 1968), known from a small-scale turbulent dynamo (Brandenburg and Subramanian, 2005; Tobias et al., 2011). This is also consistent with the findings of other simulations of isolated disc galaxies (Butsky et al., 2017; Rieder and Teyssier, 2016, 2017a), as well as those of cosmological zoom-in simulations (Pakmor et al., 2017; Rieder and Teyssier, 2017b). As this small-scale dynamo is one of the central findings of our study, we provide more evidence based on the Kazantsev (1968) theory. For this, we calculate the magnetic curvature $\mathbf{K}$ given by Schekochihin et al. (2004)

$$\mathbf{K} = \frac{(\mathbf{B}\cdot\nabla)\,\mathbf{B}}{|\mathbf{B}^2|}. \tag{7.25}$$

By using vector identities we can reformulate equation 7.25. Thus we obtain

$$\mathbf{K} = \frac{1}{|\mathbf{B}^2|}\left[\frac{1}{2}\nabla(\mathbf{B}\cdot\mathbf{B}) - \mathbf{B}\times(\nabla\times\mathbf{B})\right]. \tag{7.26}$$

The magnetic curvature can be used to distinguish the regime where the magnetic field is amplified by adiabatic compression (i.e. the magnetic field strength stays constant with increasing curvature) and the regime where a dynamo is acting (Schekochihin et al., 2004; Schober et al., 2015). In this case, an anti-correlation can be found between the magnetic field strength and the curvature with the relation $KB^{0.5} = const$. We show the median magnetic field strength as a function of curvature in figure 7.9. The red and blue lines corresponds to the *MW-snB* and *MW-primB* runs, respectively. The orange line represents the power law slope indicated by Schekochihin et al. (2004). Further, the black line shows the recent results by Vazza et al. (2018), where the same power law behaviour is found for a galaxy cluster simulated with the grid code ENZO. We note that the curvature is a very noisy quantity. This has two different origins. The first one is the rapidly changing distributions of both the magnetic field strength, and the curvature in agreement with Schekochihin et al. (2004). The second one is the low order gradient estimates that we used for calculating the curvature as a real SPH-quantity (e.g. Price, 2012). In our simulations, we find the same power law behaviour as Schekochihin et al. (2004) for the intermediate curvatures between 0.1 and 1, which provides further evidence for a small-scale dynamo in both our magnetic field models. Moreover, in figure 7.9 we indicate the curvature corresponding to the disc scale height with a vertical dashed line. While in a cluster environment the power law slope of Schekochihin et al. (2004) can be recovered also in the high curvature regime, this is not the case for our isolated galactic systems. The reason for this may be that the interface between the rotating disc and the halo gives a natural scale on which the field has to be bend. At low curvatures and very strong magnetic fields we see that the trend of the curvature deviates from the Schekochihin et al. (2004)-power law. In this regime the magnetic field is weakly increasing while the curvature is staying nearly constant. This can be identified as a regime where the amplification is driven by adiabatic compression. We find further evidence for this statement by taking figure 7.10 into account where we present the median magnetic field strength as a function of the gas density for the simulation *MW-snB*. The largest magnetic field strengths coincide with the densest gas in the very centre of the

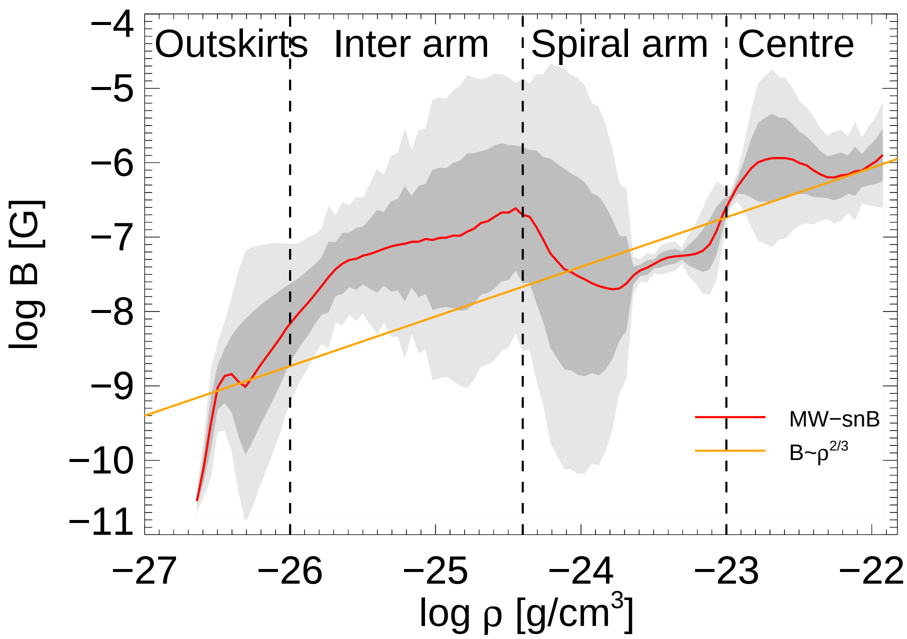

Figure 7.10: Median magnetic field strength for the model *MW-snB* (red) alongside with its 1σ (dark gray shaded region) and 2σ (light gray shaded region) errors. The orange line shows the relation that is known from the flux freezing argument of MHD, indicating amplification by adiabatic compression which can be found in several recent simulations (Marinacci et al., 2015, 2018; Pakmor et al., 2017). The highest magnetic field strengths correlate with the highest gas densities. In the centre the gas density is driven by both, adiabatic compression and small scale turbulence. In the spiral arms the magentic field is lower compared to the inter arm region and is amplified by adiabtic compression. The magnetic field strength in the inter arm regions is amplified by small scale trubulence and not adiabatic compression. In the outskirts of the galaxy the amplification is not driven by adiabatic compression.

galaxy (in a radius less than 1 kpc). Here we find that the magnetic field is amplified by adiabatic compression, where we expect a scaling following $B \propto \rho^{2/3}$. This relation can be derived from the flux freezing argument of ideal MHD where we assume that the flux of the magnetic field is conserved. This behaviour is comparable to findings of other simulations like Marinacci et al. (2015, 2018) and Pakmor et al. (2017). However, the central region is complex due to the fact the all gas particles above $2.5 \cdot 10^{-25}$ g/cm^3 are star forming.

Although we can present strong evidence for a small-scale turbulent dynamo in the power spectra (figure 7.8) and the magnetic curvature (figure 7.9), at later times, the slope of the power spectrum is no longer in agreement with the Kazantsev (1968) power spectrum. This indicates that the amplification process is not dominated by the small-scale dynamo at later times. In this case we find that our power spectra are similar to an Iroshnikov (1963, 1964) spectrum that is acting in the regime of strong magnetic fields. Examining this behaviour we believe that the small-scale dynamo is turned off at later times due to the strong dominating magnetic field in the galaxy. This is in agreement with the behaviour we observed in figure 7.7, where we see an exponential growth in the beginning, which becomes linear at later times. The interplay between the Iroshnikov-spectrum and the linear growth of the magnetic field at later times leads to the conclusion that the amplification process of the magnetic field in this regime is either driven by the α-ω-dynamo instead of the small-scale turbulent dynamo, or switched off completely. The more likely option of those two is the former one which is indicated by the abrupt increase (about 2 orders of magnitude) of the magnetic field strength at around 2.1 Gyr (see figure 7.7). We can identify this region as a transition region from the small-scale turbulent dynamo to the α-ω-dynamo where both processes are acting but the α-ω-dynamo finally takes over once the magnetic fields in the disc are strong enough to effectively suppress turbulence. This point is strengthened by the fact that in figure 7.8 the slope of the power spectra for $t = 2.1$ and $t = 2.2$ starts to deviate from the proposed Kazantsev (1968) spectrum showing first evidence that the small-scale turbulent dynamo is about to shut down. Finally, we note that in the CGM there is nearly no growth of the magnetic field visible. In the *MW-primB* run, there is a small amplification of the magnetic field in the beginning, because of the none-zero magnetic field in the CGM in this model and the slight rotation of the CGM. However, the amplification in this case is minimal, and, as expected from dynamo theory, we can see a small exponential growth due to an α-ω-dynamo. Because the CGM is in hydrostatic equilibrium due to our initial conditions there is no amplification of the magnetic field strength over small-scale turbulence.

Although there is no relevant magnetic field in the CGM in the first 2.3 Gyr of the simulation, after around 2.3 Gyr we see a jump in the magnetic field strength in the CGM of several orders of magnitude in both models. There is no observable difference in the behaviour of the magnetic field strength in the CGM between both our models. This underpins the fact that the observed magnetic field in our simulations depends mainly on the dynamical structure of the galaxy and is not dominated by the seeding of the magnetic field.

7.4.4 Halo accretion and magnetic driven ouflows

A new and very important aspect of our simulations is the inclusion of the CGM, unlike in previous simulations of isolated disc galaxies (e.g. Butsky et al., 2017; Kotarba et al., 2011). This allows us to observe the interaction of an isolated disc galaxy with its CGM in an idealised environment without any perturbations. In section 7.4.3, we have shown that the CGM gets strongly magnetized because of outflows that transport a lot of the magnetic power, which is amplified in the galactic disc via the small-scale turbulent dynamo and the mean field α-ω dynamo, to the outer parts of the CGM. We observe a prominent tube with a radius of approximately 2 kpc near the disc, which opens up to 5 kpc in its outer parts with a magnetic field strength between 10^{-7}-10^{-6} G. It reaches the outer parts of the CGM with a total length of around 40 kpc. This magnetic tube transports gas out of the disc in positive and negative z-direction at nearly the same rate, with a speed of a few 100 km/s. Some of the gas particles are close to reaching the galactic escape velocity. The gas is moving outwards along the magnetized tube and falls back to the disc from outside of the tube, such that there is an active exchange of the disc's gas with the hot gas of the CGM. Further, we note that after the onset of the magnetic tube we see heavily magnetized, low density bubbles rising from the galactic disc to the CGM reaching a hight of a few kpc above the disc, which is in agreement with the findings of Pakmor and Springel (2013). In addition to the gas which is initially located in the disc, moves to the CGM, and falls back, there is also a cooling flow of hot gas from the CGM onto the disc. To demonstrate this, we show the evolution of the total mass of the baryonic disc for our three models in figure 7.11. While cold gas is turned into stars, the total disc mass increases with time, as the disc is fuelled by cooling gas from the hot halo. Interestingly, the cooling rate ($1\ M_\odot\ yr^{-1}$) is roughly of the same order as the SFR ($\sim 3\ M_\odot\ yr^{-1}$), indicating, that the disc can compensate the loss of gas mass due to star

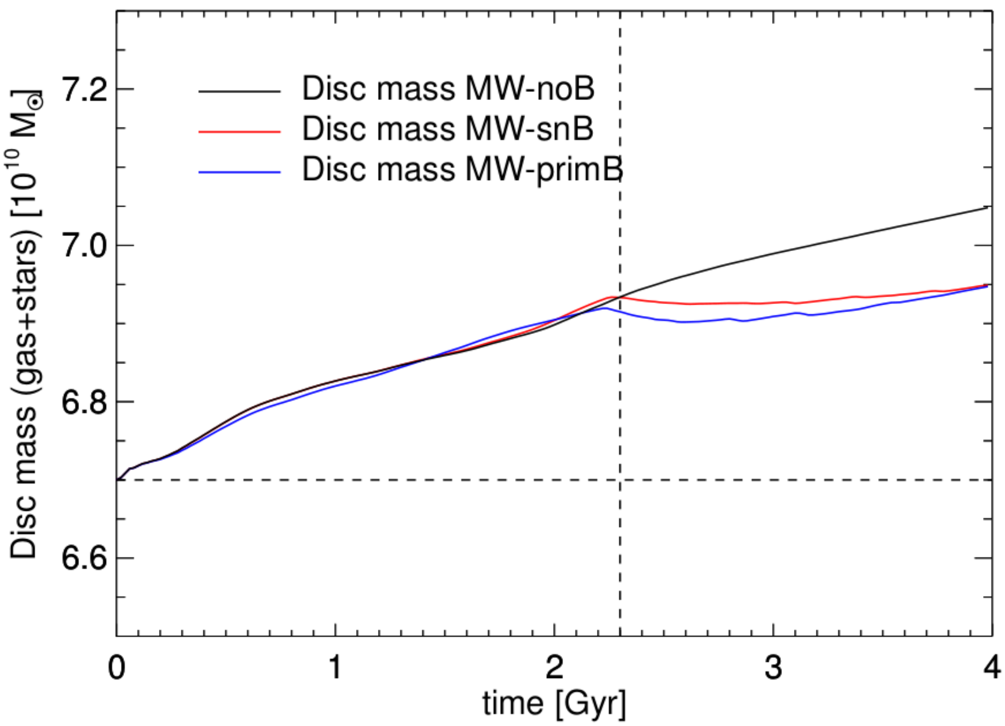

Figure 7.11: Total mass of the disc for the simulations *MW-noB* (black), *MW-snB* (red), and *MW-primB* (blue). While the disc is accreting a large amount of gas in *MW-noB*, the net growth of the disc is suppressed in *MW-snB* and *MW-primB*, after the magnetic outflow sets in at 2.3 Gyr.

formation by accreting hot gas from the CGM. Because of the immense gas reservoir, the SFR in the disc is thus stabilized, and eventually reaches an equilibrium. After the magnetic outflow sets in, the total disc mass stays roughly constant, while in the simulation without magnetic fields the disc still grows by accreting gas from the CGM at a constant rate. Thus, for both magnetic field models the strong magnetic driven wind with about one solar mass per year, compensates the incoming cooling flow. This equilibrium between inflow and outflow results in a constant disc mass, although within the disc, cold gas is still converted into stars. We note that the outflow velocties and mean magnetic field strengths in the biconal outflow we observe are failry similar to the properties observed in the 'Fermi-bubbles'. In Carretti et al. (2013) a magnetic field strength between 6 and 12μG is observed for the two lobes which is comparable to the field strenghts between 1 and 30μG we find in the biconal outflow in our simulations. Furhter, in our simulations we find that these biconal structures propagate with a velocity of between 400 and 500 km/s into the CGM, while kinematic modelling of the Fermi bubbles leads to outflow velocities between 1000 and 1300 km/s as presented by Bordoloi et al. (2017).

Along with the outflowing gas, the metals which are returned to the disc by supernova feedback are transported to the CGM. We show this behavior for the models *MW-snB* (red), and *MW-primB* (blue) in figure 7.12. The solid lines represent the metals in the disc and the dashed lines the metals in the CGM. We observe metal enrichment in the CGM due to the magnetic outflow which is normally believed to be caused only by supernova driven winds from either late supernova driven winds in massive galaxies (e.g. Adelberger et al., 2003; Aguirre et al., 2001; Shen et al., 2012) or outflows from dwarf galaxies at higher redshift (e.g. Dekel and Silk, 1986; Furlanetto and Loeb, 2003; Mac Low and Ferrara, 1999).

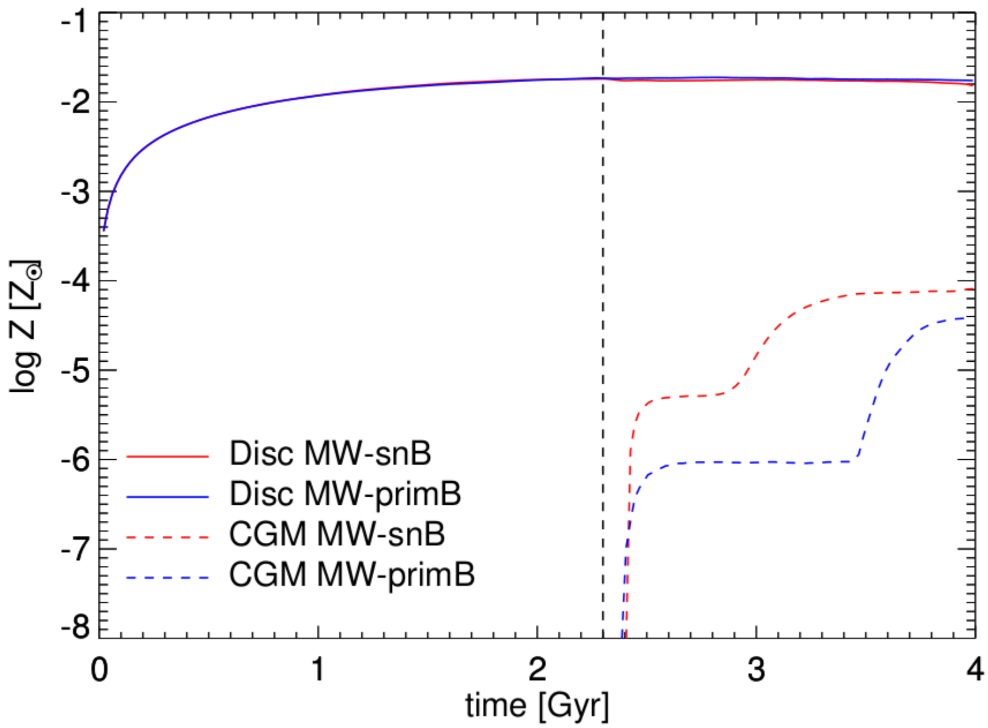

Figure 7.12: Time evolution of metals in the disc (solid lines) and the CGM (dashed lines) for *MW-snB* (red), and *MW-primB* (blue). The black vertical dashed line indicates the onset of the outflow driven by magnetic fields, leading to a net magnetization of the CGM in both models that is normally believed to be obtained by the wind feedback induced by supernovae.

Another mechansim for the metal enrichment of the CGM is proposed by Scannapieco and Oh (2004) due to quasar driven winds. Gnedin (1998) point out the importance of proto galaxy mergers at high redshift to enrich the surrounding medium with metals. Finally, we note that we could not observe any metal enrichment towards the CGM in the simulation *MW-noB*.

7.4.5 Magnetic field structure

The general morphological properties of the magnetic field have been discussed in section 7.4.1. Here, we present a more detailed study on the galactic magnetic field in our simulations. For this we show a more detailed comparison between the structure of the gas density and the magnetic field strength in polar coordinates for the *MW-snB* and *MW-primB* runs in figures 7.13 and 7.14, respectively. The left-hand side panels show the gas density and the right-hand side panels show the magnetic field strength, while the panels on the top give the results after $t = 2$ Gyr and the panels on the bottom give the results after $t = 3$ Gyr. Plotting these quantities in polar coordinates allows us to directly compare our results to observations of spiral galaxies, e.g. by Bittner et al. (2017). These plots have been obtained by using a two dimensional grid of the size 100×66, with a pixel corresponding to a specific r and φ. For each pixel we calculate the gas density and the magnetic field using the triangular shaped cloud (TSC) method for calculating densities on a regular grid. The plots then show a slice for a fixed r for one circulation over the whole galaxy. This allows us to determine the positions of the more

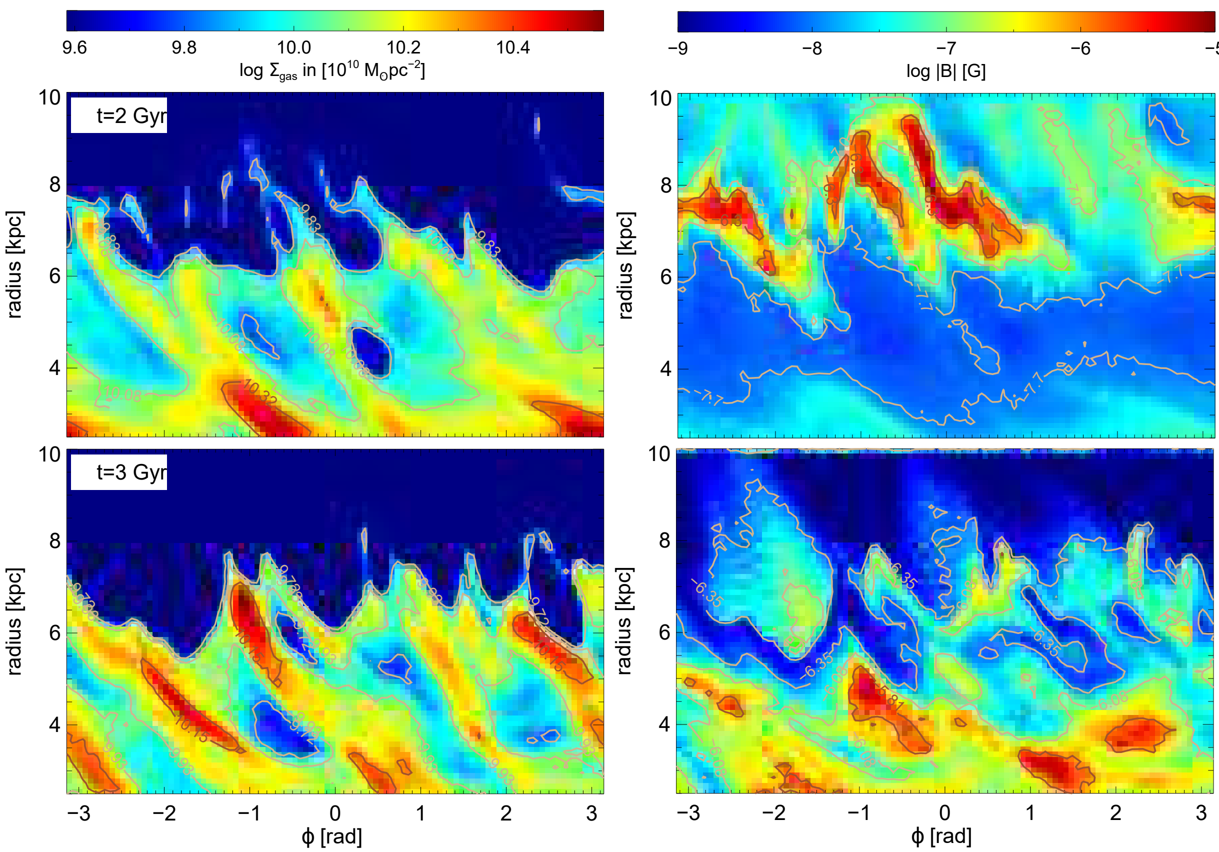

Figure 7.13: Surface density of the gas (left-hand-side panels) and magnetic field strength (right-hand-side panels) in cylindrical coordinates for the *MW-snB* run at 2Gyr (top panels) and 3 Gyr (bottom panels). The spiral structures in the magnetic field and the gas surface density are correlated in the centre at $t = 3$ Gyr, while they are not at $t = 2$ Gyr. In the outer regions of the disc the magnetic field and the gas density are anti-correlated at $t = 3$ Gyr.

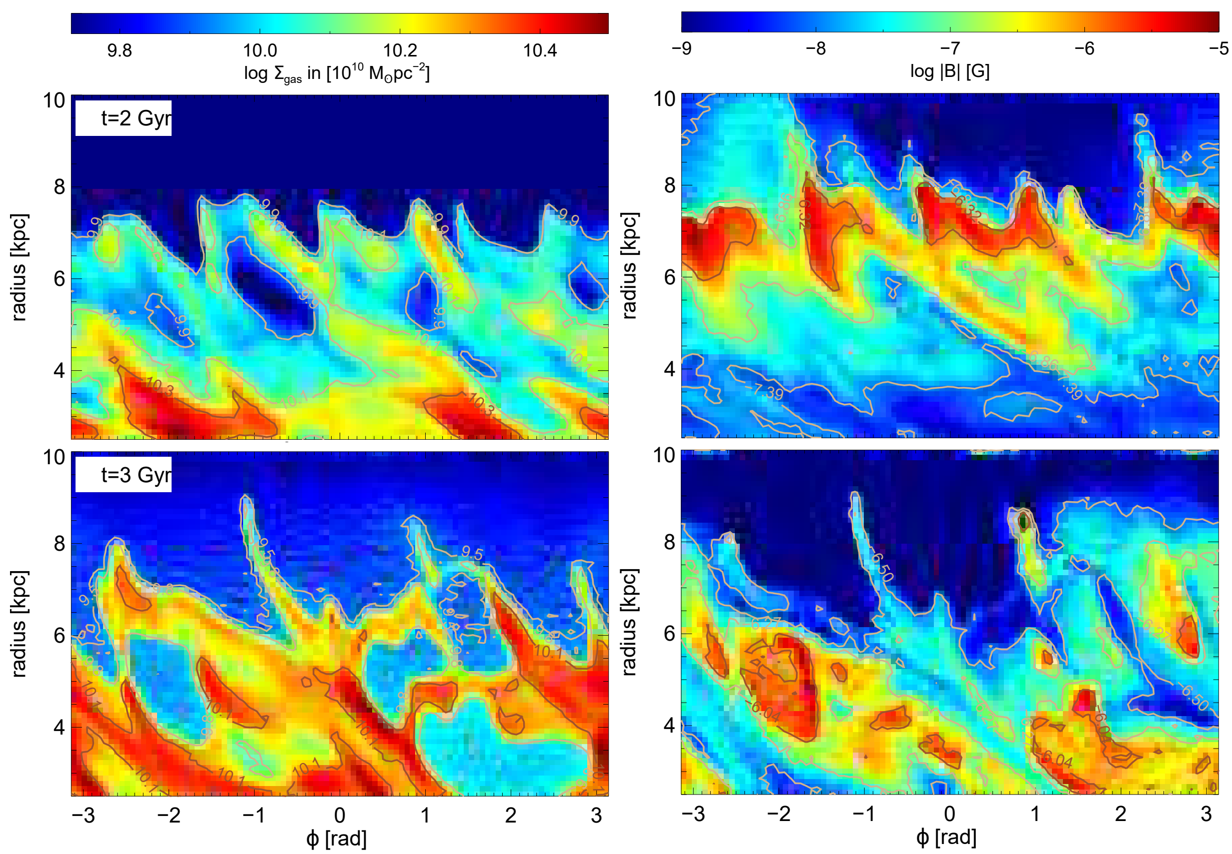

Figure 7.14: Same as figure 7.13, but for the simulation *MW-primB*.

prominent areas in the structure of a spiral galaxy. The panel on the top left of figure 7.13 nicely shows four density peaks, corresponding to at least four spiral arms in the *MW-snB* simulation, as expected for a Milky Way analogue. Comparing our results for the gas density to the magnetic field strength, we find that they are not strongly correlated. Moreover, early in the simulation, we observe that the magnetic field is stronger in the outer parts of the galactic disc, compared to the centre. This behaviour changes at later times (bottom panels), when the magnetic field is stronger in the centre and shows a spiral structure. The magnetic field strength is highest between the spiral arms of the gas disc, which is most obvious at late times, when the gas of the disc is already depleted due to star formation and outflows. While Beck and Wielebinski (2013) have noted this effect before, they have not found this behaviour in gas rich galaxies. Although, we can give an explanation for the connection between the gas density and the magnetic field strength we note that our implementation of MHD follows mainly ideal MHD with a small magnetic diffusion term. In the limit of small magnetic fields this leads to a direct correlation between high densities and high magnetic fields. Thus, at early times the strongest magnetic fields are located in the high density areas due to adiabatic collapse and increased turbulent amplification due to the higher supernova rate in this regime. At later times the non-linear term we include in the induction equation makes it possible to trigger diffusive processes that can transport the magnetic field energy from high density regions to low density regions. The inter arm regions have lower densities and higher temperatures compared to the spiral arms. This leads to a stronger turbulence in this regions than in the spiral arms itself. Once the magnetic field energy is transported via diffusive processes from the spiral arms to the inter arm regions, it can be amplified easily via small-scale turbulence on Myr timescales. This can lead to a dominating magnetic field in the inter arm regions. Moreover, we quantify that in figure 7.10 where we can see an overall decrease of the magentic field strength in the spiral arms compared to the inter arm regions of the galaxy.

We now focus on the detailed structure of the magnetic field and the comparison of the differences in the structure for both presented magnetic field models. We present two ways to evaluate this. The first one is based on the evaluation of the quantity ζ_1 given by

$$\zeta_1 = \frac{|\mathbf{B} - \mathbf{B}_{\mathrm{sm}}|}{|\mathbf{B}_{\mathrm{sm}}|}, \tag{7.27}$$

where $\mathbf{B}$ is the magnetic field and $\mathbf{B}_{\mathrm{sm}}$ is the magnetic field smoothed by a Gaussian-kernel. As our simulations were performed with an SPH code, ζ_1 cannot be directly computed, but the particle properties first need to be transformed to a regular grid. To achieve this, an obvious choice would be the TSC method that was used to obtain figures 7.13 and 7.14. However, the TSC method is based on a triangular kernel and thus not accurate enough to resolve the detailed structure of the magnetic field in an SPMHD simulation. Therefore, we work out an proper SPH-binning for which we use a two dimensional grid with a very high resolution of 1024×1024 grid points. For each element, we then calculate the magnetic field with the Wendland C4 Kernel using 200 neighbouring particles. In this way, we use exactly the same configuration to bin the data as for our underlying SPH-formalism. The data binning has been performed using the code SPHMAPPER presented by Röttgers and Arth (2018). The property ζ_1 describes the deviation of the magnetic field in our simulations from the smoothed magnetic field. This method called unsharp masking, is very common in image editing, and allows us to achieve a stronger contrast in the magnetic field, making it is easier to find detailed structure lines. A high value of ζ_1 indicates a large difference between the smoothed magnetic field and the original magnetic field, indicating a highly turbulent magnetic field. A small value of ζ_1 shows little deviation between the smoothed magnetic field and the original one, indicating a region of highly correlated magnetic field lines.

The upper left panel of figure 7.15 shows ζ_1 for the *MW-snB* simulation at $t = 2.0$ Gyr, shortly

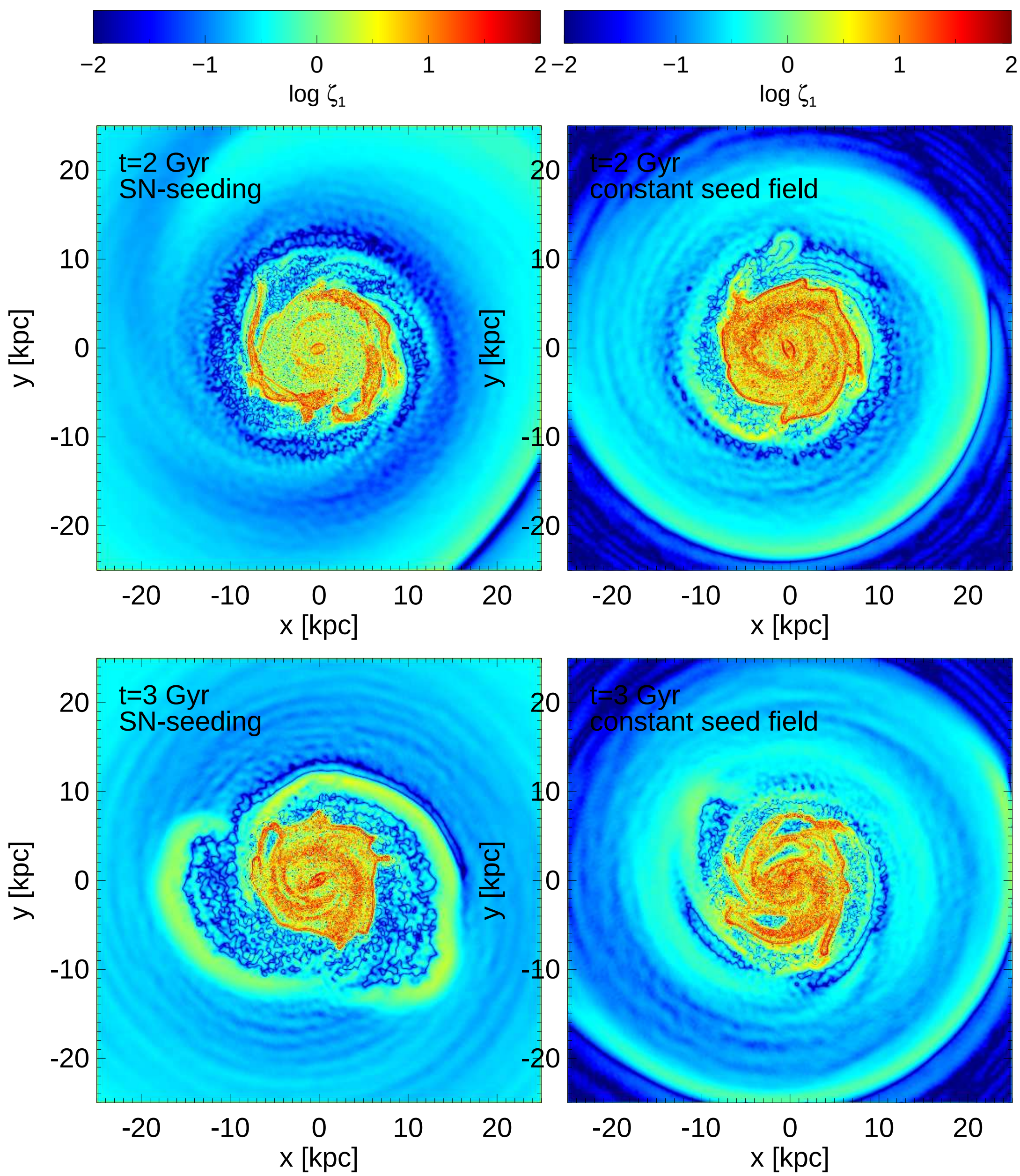

Figure 7.15: Structure of the magnetic field for the *MW-snB* run (left-hand-side panels) and the *MW-primB* run (right-hand-side panels) at $t = 2$ Gyr (upper panels) and $t = 3$ Gyr (bottom panels). The colour bar indicates the normalized relative deviation of the magnetic field from a smoothed magnetic field (unsharp masking, see eqn. 7.27). Red indicates that turbulence is dominating while blue indicates high order in the magnetic field.

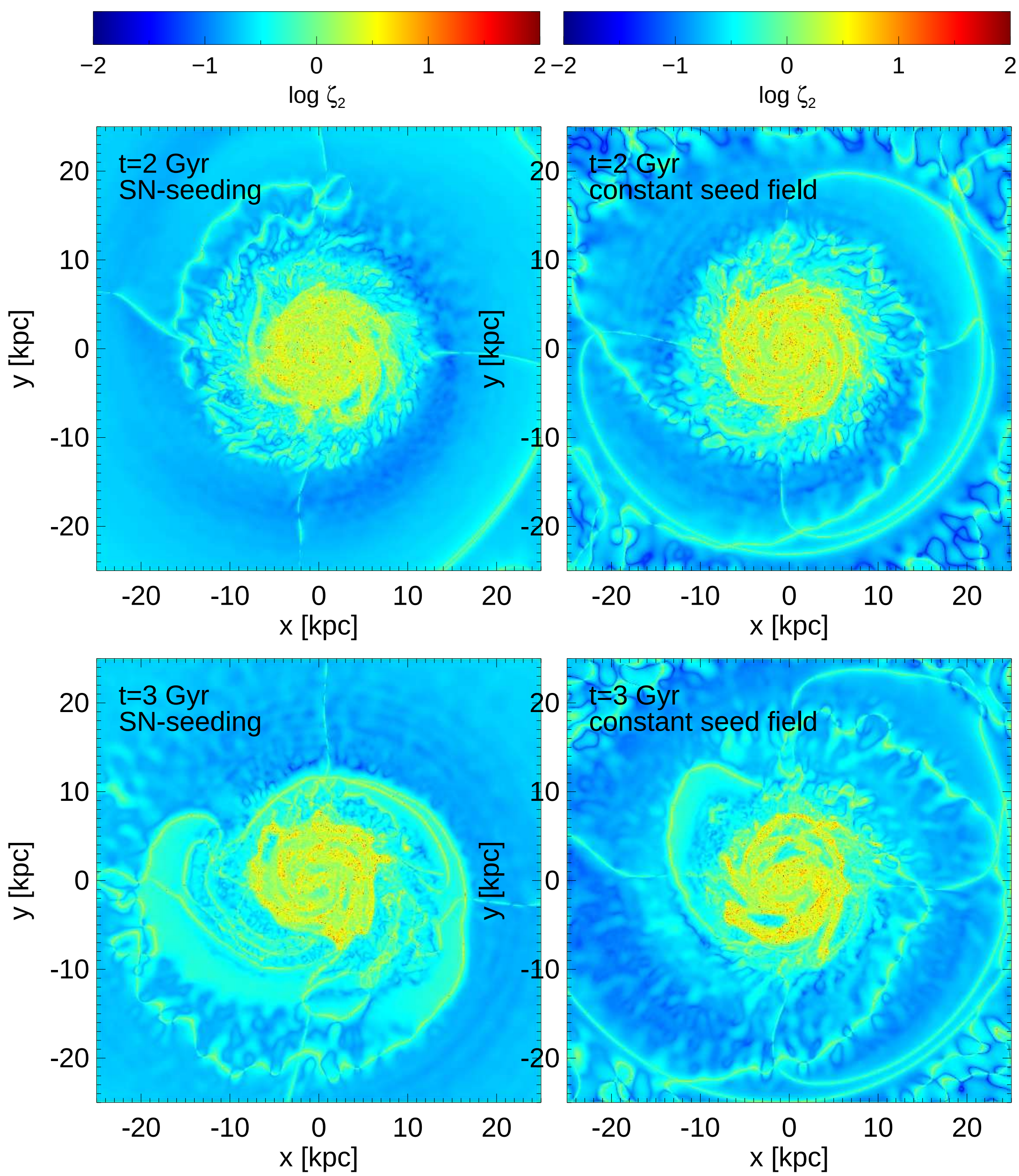

Figure 7.16: Same as figure 7.15, but each spatial magnetic field direction is normalized to the smoothed magnetic field in that certain direction (see eqn. 7.28).

before the outflow sets in. It demonstrates that there are detailed structures in the magnetic field beyond the spiral arms. Furthermore, the turbulent structures are mostly located in the centre of the galactic plane. This nicely illustrates that the magnetic field is amplified via a small-scale dynamo, as we argued in section 7.4.3. On the small scales, i.e. in the galactic centre, the turbulent character of the magnetic field dominates. The upper right panel of figure 7.15 shows ζ_1 for the *MW-primB* simulation. Also here, we observe the spiral structure of the magnetic field, but the disc is more dominated by turbulence than in the *MW-snB* run. The bottom panels of figure 7.15 show ζ_1 at $t = 3$ Gyr, demonstrating that the structure of the magnetic field is not diminished by the magnetic outflow which sets in around $t = 2.3$ Gyr. The quantity ζ_1 evaluates the total magnetic field, ignoring the spatial behaviour of each magnetic field component. We therefore present a second method to evaluate the structure of the magnetic field, and introduce the variable ζ_2:

$$\zeta_2 = \sqrt{\left(\frac{B_x - B_{\mathrm{x/sm}}}{B_{\mathrm{x/sm}}}\right)^2 + \left(\frac{B_y - B_{\mathrm{y/sm}}}{B_{\mathrm{y/sm}}}\right)^2 + \left(\frac{B_z - B_{\mathrm{z/sm}}}{B_{\mathrm{z/sm}}}\right)^2}. \tag{7.28}$$

Compared to ζ_1, it takes into account the structure of the magnetic field in each spatial direction, and prevents an overestimation due to the strong magnetized outflows in z-direction. The resulting maps are presented in figure 7.16. While the ζ_1 maps clearly show the underlying magnetic structure of the disc in the x-y-plane, the ζ_2 maps are far smoother, though we can see the structures we already saw in figure 7.15. Finally, we note that the magnetic field becomes much more turbulent when the magnetic outflow sets in.

7.4.6 Different halo masses

So far, we focused on the simulations *MW-noB*, *MW-snB* and *MW-primB*, as these systems were constrained by X-ray observations. Here, we investigate the effects in haloes of lower mass, i.e. $M_{\mathrm{h}} = 10^{11} M_\odot$ (*MM-noB*, *MM-snB*, *MM-primB*) and $M_{\mathrm{h}} = 10^{10} M_\odot$ (*DW-noB*, *DW-snB*, *DW-primB*). While the intermediate mass systems (MM) show a similar behaviour as the Milky Way-like systems (MW) for the amplification of the magnetic field and the observed morphological features, the point in time where the biconical magnetic tube sets in is is delayed to $t = 3.0$ Gyr. This is a consequence of the magnetic field amplification being driven by small-scale turbulence induced by feedback, mainly in the galactic centre. In the lower mass galaxies the efficiency of the feedback is lower, resulting in a slower amplification of the magnetic field. Moreover, the lower rotational velocity in a halo with $M_{\mathrm{h}} = 10^{11} M_\odot$ delays the amplification process further. As a consequence, the magnetic pressure rises at a lower rate compared to the Milky Way-like systems, such that the magnetic pressure needed to expell gas from the centre towards the CGM is reached at a later point in time. The total magnetic field strength rises to similar values as for the Milky Way-like models, but the peak values of the magnetic field is slightly lower, reaching values between 10^{-7} to 10^{-5} G. While the magnetic field properties of the MM simulations are similar to the MW simulations, i.e. a small-scale turbulent dynamo drives the amplification of the magnetic field resulting in an outflow of gas, we notice a considerable difference in the evolution of the SFR. Moreover, we can observe the same transition from the small-scale turbulent dynamo to the α-ω-dynamo as in the MW models including a transition regime where both dynamos seem to act before the small-scale turbulent dynamo is ultimately switched off and the α-ω-dynamo takes over. For the system with the lowest mass of $M_{\mathrm{h}} = 10^{10} M_\odot$ (DW), we only find minor changes for the simulations with magnetic fields compared to the reference simulation without magnetic fields. For this halo mass scale the magnetic field is dynamically unimportant, as the amplification of the magnetic field is very slow. Since the SFR in these systems is very low, the effects of the SN feedback are minor, resulting in no significant small-scale turbulence that could amplify the magnetic field in the centre. Moreover, the amplification of the magnetic field can not be supported via the α-ω-dynamo either, because the gas orbits with a peak velocity of 50 km/s. Lastly, the magnetic field can also not be amplified by adiabatic compression of the gas because the potential wells are too shallow to trigger the formation of high density regions which would result in an amplification of the magnetic field. Consequently, there are no outflows for the DW simulations. We conclude that outflows are only present when the magnetic field becomes dynamically important. This is the case for the MW and MM haloes, because the amplification of the magnetic field is strong enough to reach a magnetic pressure that is higher than the thermal pressure. Therefore, we also do not find transition regions from one dynamo process to the other. Overall, these lower mass systems seem to be mostly inactive regarding dynamo amplification.

7.4.7 Divergence Cleaning

Every numerical simulation that includes magnetic fields has to deal with the $\nabla \cdot \mathbf{B} = 0$ constraint, we need to prove that our simulations are not contaminated by magnetic monopoles. For this, we present the relative magnetic divergence $h \cdot \nabla\mathbf{B}/|\mathbf{B}|$, where h is the smoothing length, for the *MW-snB* run in figure 7.17, and for *MW-primB* in figure 7.18. The panels on the left-hand-side and right-hand-side show the result before (t = 2.0 Gyr), and after (t = 3.0 Gyr)the magnetic outflow sets in. The more turbulent structure after the outflow sets in leads to an increase of the divergence of the magnetic field due to the sharper gradients. The maximum value of the relative divergence error of ~ 1 is reached where turbulence is dominating, such as in the galactic centre, and at the edges of the spiral arms. This is comparable to the error in other simulations (e.g. Pakmor and Springel, 2013).[2] However, the typical value of $h \cdot \nabla\mathbf{B}/|\mathbf{B}|$ is below 0.1, which is very good for a SPMHD-Code. We note that there are methods in grid codes such as RAMSES, which can reduce the relative divergence error to machine precision. Although, these cleaning methods perform very well in test studies they have the disadvantage of being computationally very expensive. However, Pakmor and Springel (2013) used a cleaning scheme (Powell et al., 1999) similar to ours and find that it is sufficient on a moving mesh. Compared to a regular grid, it is significantly more complicated to control the divergence error on a moving mesh because of the irregularity of the Voronoi-grid, which is similar for a SPH particle distribution. Although our SPMHD formulation includes higher order hyperbolic cleaning schemes (Dedner et al., 2002; Dolag and Stasyszyn, 2009), the findings of Pakmor and Springel (2013) show that it is sufficient to use a lower order cleaning scheme for the type of systems we are simulating. To save computational power we follow this approach and use a lower order cleaning scheme. We can further observe that the higher values of the relative divergence error appear around the spiral arms, as this is where the magnetic field has strong gradients. This behaviour improves with higher resolution, because the gradients become better resolved. Lastly, we note that the divergence is smaller in the case of the supernova-seeding, since magnetic dipoles are inserted into the ISM. By construction, this leads to a lower divergence, as the dipole structure is forced to appear with the supernova explosions, resulting in a smoother distribution of the magnetic field.

[2] We note that the magnetic energy density is about a factor of 100 below the kinetic energy density within one resolution element of the simulation in its very centre.

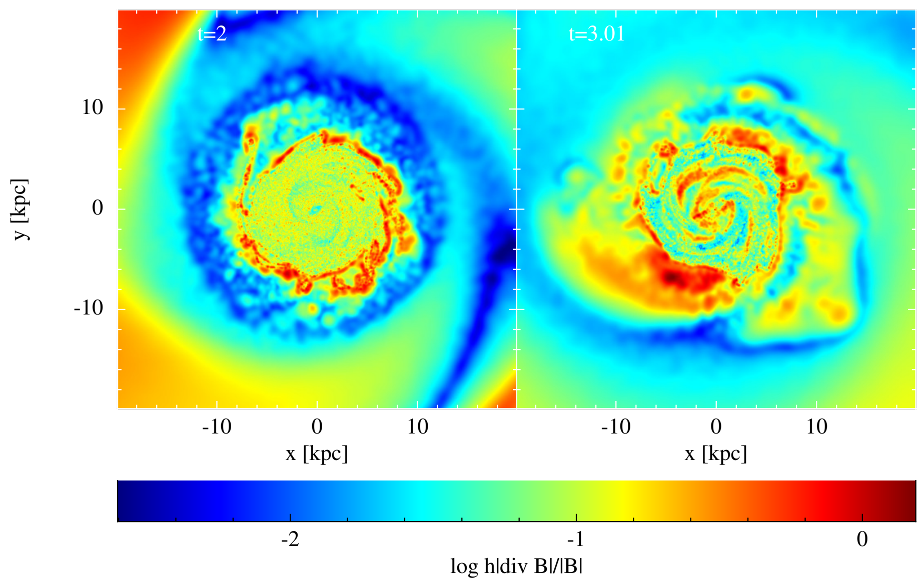

Figure 7.17: Relative divergence errors for the simulation *MW-snB* at $t = 2$ Gyr (left-hand-side panel) and $t = 3$ Gyr (right-hand-side panel). Typical values are between 1 and 10 per cent.

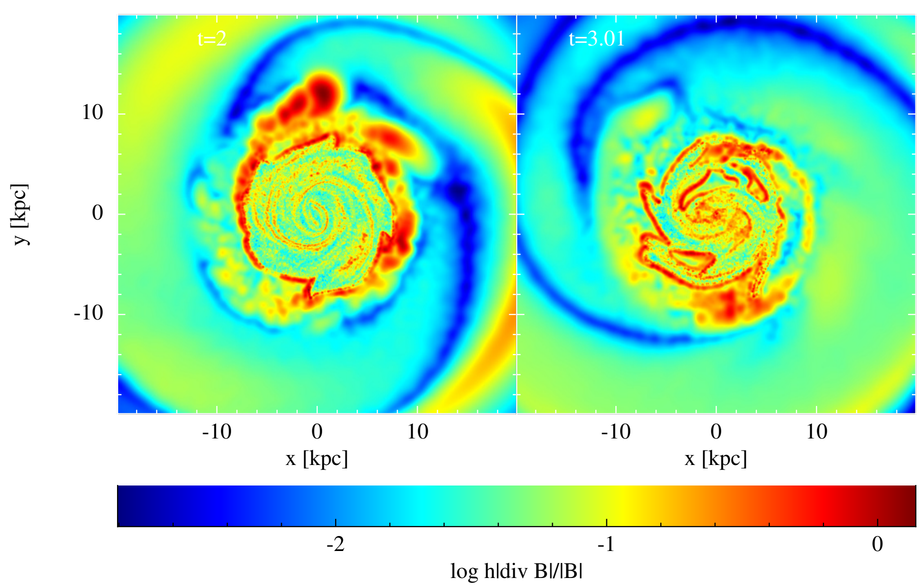

Figure 7.18: Same as figure 7.17 but for the simulation *MW-primB*.

7.5 Conclusions

We present a modified model for isolated disc galaxies including a realistic CGM. Using this model we simulate a set of galaxies with different halo masses ranging from $10^{10} M_\odot$ over $10^{11} M_\odot$ to $10^{12} M_\odot$ and study the general properties (like the morphological structure and the SFR) of these systems. We focus on the Milky Way-like system, and present a detailed study of the morphological structure of the gas density, as well as the magnetic field. We observe a mean magnetic field strength of a few μG in the galactic disc, which is in good agreement with observations. In the galactic centre we find higher field strengths up to a few 100μG. In the spiral arms the magnetic field strength is about an order of magnitude lower compared to the galactic centre. We find that the structure of the magnetic field strength does not follow exactly the spiral arms in the gas density, but is strongest between two neighbouring spiral arms. This result differs from those reported by other groups (Butsky et al., 2017; Pakmor and Springel, 2013). The reason for that is that we include a magnetic diffusion term in our simulations, which makes it possible to follow the magnetic field evolution in the non-linear regime. Furthermore, this effect is in agreement with many observations (see Beck (2015) for and references therein). The amplification of the magnetic field in our simulations is mainly driven by small-scale turbulence. We show clear evidence for this in the magnetic power spectra (figure 7.8), in agreement with simulations by other groups (Butsky et al., 2017; Pakmor and Springel, 2013; Rieder and Teyssier, 2016).

Moreover, we find further evidence for a small-scale dynamo by examining the curvature of the magnetic field lines, which can be used to distinguish between amplification by adiabatic compression and by a small-scale dynamo (figure 7.9). Our simulations indicate that at later times the slope of the magnetic power spectra turns around. This shows that the galaxies are entering a new regime that is dominated by strong magnetic fields instead of small-scale turbulence. Thus, the dominating amplification process in this regime is either driven by the $\alpha-\omega$-dynamo or completely saturated and thus switched off. In the simulations with $M_\mathrm{h} = 10^{12} M_\odot$ and $M_\mathrm{h} = 10^{11} M_\odot$, we find galactic outflows that are driven by the magnetic field. In this regime the magnetic pressure is several orders of magnitude higher than the thermal pressure. In our simulations with $M_\mathrm{h} = 10^{10} M_\odot$ this is not the case, so that we do not observe a dominating magnetic outflow in haloes below $M_\mathrm{h} = 10^{11} M_\odot$. A more detailed study of the interaction between galactic disc and CGM shows that a certain amount of magnetic energy is released in the outer regions of the CGM having its origin in the centre of the galactic disc. Studying the turbulence in the magnetic field, we find that the highly magnetized outflows are mainly driven by the turbulent magnetic field in the centre of the galactic disc. The structural analysis of the magnetic field indicates that it follows a complex structure besides the obvious spiral patterns and does not necessarily follow the spiral structure of the gas density because of magnetic diffusion. Finally, we summarize the three most important findings of this study.

1. The amplification of the magnetic field strength can be devided in different regimes. In the very centre we find that the magnetic field is amplified by adiabatic compression. However, the main amplification process is driven by small-scale turbulence until the magnetic field in the disc is strong enough so that the dynamo saturates. We provide evidence for this Kazantsev (1968) dynamo in the magnetic power spectra as well as the anti-correlation of the magnetic field strength and the curvature of the magnetic field lines for a small-scale dynamo (e.g. Schekochihin et al., 2004; Vazza et al., 2018). Finally, at later times when strong magnetic fields are present the small-scale turbulent dynamo is switched off and the system is dominated by the α-ω-dynamo.

2. Galaxies in which the magnetic pressure dominates the thermal pressure show magnetic-driven

outflows that can lead to a significant mass loss of the baryonic disc. The outflows appear as low density bubbles reaching a several 100 km/s before they mix with the CGM and fall back to the disc.

3. Diffusive terms in the induction equation can transport the magnetic field energy from the spiral arms to the inter arm regions. In the inter arm regions the density is lower but the temperature is higher which leads to more turbulence and therefore stronger amplification due to the small-scale turbulent dynamo. Thus we can see an anti-correlation between the spiral structure of the gas disc and the spiral structure within the magnetic field strength that can be seen in observations (Beck, 2015).

Future work will need to focus on detailed resolution studies to determine the spatial and the mass resolution that is needed to actually resolve the small-scale turbulent dynamo, which may be crucial in the framework of cosmological zoom-in simulations of Milky Way-like galaxies. Furthermore, none of the current models for star formation in hydrodynamical simulations includes the pressure given by the magnetic field directly. Only indirect effects on the SFR can be captured by the current simulations. In future studies the magnetic pressure may be directly included by using pressure-based star formation models.

Acknowledgments

We thank the anonymous referee for his/her comments that helped to improve this work. We thank Eirini Batziou, Andreas Burkert, Julien Devriendt, Timo Halbesma, Stefan Heigl, Thorsten Naab, Rüdiger Pakmor, Rhea Silvia Remus, Felix Schulze, Romain Teyssier and Simon White for useful discussions and their insights on magnetic fields and galaxies. We thank Franco Vazza for his insights on the magnetic curvature. The authors gratefully acknowledge the computing time granted by the John von Neumann Institute for Computing (NIC) provided on the supercomputer JURECA at Jülich Supercomputing Centre (JSC) under the project number hmz07 and the computing time provided by the Leibniz Rechenzentrum (LRZ) of the Bayrische Akademie der Wissenschaften on SuperMuc in Garching with the porject number pe86re. UPS and BPM are funded by the Deutsche Forschungsgemeinschaft (DFG, German Research Foundation) with the project number MO 2979/1-1. KD acknowledges support by the DFG Cluster of Excellence 'Origin and Structure of the Universe'

Chapter 8

On the origin of magnetic driven winds and the structure of the galactic dynamo in isolated galaxies

This work has been published in the Monthly Notices of the Royal astronomical Society, Volume 494, Pages 4393–4412.

We investigate the build-up of the galactic dynamo and subsequently the origin of a magnetic driven outflow. We use a setup of an isolated disc galaxy with a realistic circum-galactic medium (CGM). We find good agreement of the galactic dynamo with theoretical and observational predictions from the radial and toroidal components of the magnetic field as function of radius and disc scale height. We find several field reversals indicating dipole structure at early times and quadrupole structure at late times. Together with the magnetic pitch angle and the dynamo control parameters R_α, R_ω and D we present strong evidence for an α^2-Ω dynamo. The formation of a bar in the centre leads to further amplification of the magnetic field via adiabatic compression which subsequently drives an outflow. Due to the Parker-Instability the magnetic field lines rise to the edge of the disc, break out and expand freely in the CGM driven by the magnetic pressure. Finally, we investigate the correlation between magnetic field and star formation rate. Globally, we find that the magnetic field is increasing as function of the star formation rate surface density with a slope between 0.3 and 0.45 in good agreement with predictions from theory and observations. Locally, we find that the magnetic field can decrease while star formation increases. We find that this effect is correlated with the diffusion of magnetic field from the spiral arms to the inter-arm regions which we explicitly include by solving the induction equation and accounting for non-linear terms.

8.1 Introduction

Magnetic fields are a quantity of paramount importance in the Universe. Their influence ranges from the interior of the earth and the sun over interactions with dust in proto planetary and proto stellar discs to molecular clouds and finally galaxies, galaxy clusters and the large scale structure of the Universe.

Observationally, there are a few common tracers to quantify the presence of magnetic fields in the nearby Universe, like the radio synchrotron emission and its polarization along the line of sight, the Faraday rotation measure or the Zeeman-splitting of star light within galaxies. Using these methods the magnetic field strengths of nearby galaxies are very well constrained. By assuming that the magnetic field is in equipartition with the other energetic components of a galaxy the magnetic field strength can be determined to a few μG (e.g. Fletcher, 2010; Niklas et al., 1995). Higher magnetic field strengths up to 50 μG are observed in the spiral arms of galaxies (e.g. Beck, 2015; Han, 2017). The highest magnetic fields can be found in starburst galaxies (Beck, 2005; Chyży et al., 2003; Heesen et al., 2011) or in the galactic centre (e.g. Robishaw et al., 2008) and can reach values up to 1 mG. There is observational evidence that the energy density generated by the magnetic field can be dynamically important. Beck (2007), Basu and Roy (2013), Tabatabaei et al. (2008) find in different galaxies that the magnetic energy density can be in the same order of magnitude as the energy density induced by the turbulent motions within the ISM, indicating that the ISM is a low β-plasma where β is the ratio between thermal and magnetic pressure. The morphology of magnetic fields can be investigated by the emission of synchrotron radiation in spiral galaxies. The results indicate that the magnetic fields of spiral galaxies can show a spiral structure itself which is especially prominent in so called grand design spiral galaxies like M51 and M83 (Beck et al., 2013; Houde et al., 2013; Patrikeev et al., 2006). In spiral galaxies with strong density wave structure the magnetic fields morphology is often tightly bound to the spiral structure of the density waves. However, if the density waves are sub-dominant the large scale ordered magnetic fields do not necessarily align with the spiral structure of the gaseous arms (Beck, 2015; Han, 2017). Faraday rotation measurements of polarized sources in the radio continuum can be utilized to determine the morphology and the strength of magnetic fields in nearby spiral galaxies and the Milky Way(e.g. Han et al., 2018). However, the Faraday rotation measure is a not single valued estimate of the magnetic field structure if there are various sources with different rotations and a variety of internal structure. In this cases the physical meaning of the RM measurements remains unclear. In those cases the RM-measurements can be replaced by the Faraday depth (Rotation measure synthesis) method to obtain information about the magnetic field strength and structure (e.g. Brentjens and de Bruyn, 2005; Burn, 1966; Heald et al., 2015; Kim et al., 2016; Sun et al., 2015). To interpret and understand the data obtained from these methods it is important to build detailed theoretical models that lead to a more detailed picture of the physical interpretation. Further, the magnetic field can play an important role in regulating the star formation process on galactic scales. In observations it has been observed that the total magnetic field strength is directly correlated with the star formation rate density with a power law scaling exponent that is measured between 0.18 (Chyży et al., 2007) and 0.3 (Heesen et al., 2014). However, recent observations of molecular clouds in NGC 1097 indicate that locally the star formation surface density might also show an anti correlation with increasing magnetic field (Tabatabaei et al., 2018). Although the field strengths of magnetic fields in nearby galaxies are very well known, the origin of those magnetic fields is still under debate. It is possible to generate tiny seed fields with 10^{-20} G via the Biermann-battery process (e.g. Biermann, 1950; Mishustin and Ruzmaĭkin, 1972; Zeldovich et al., 1983) or by phase transitions in the early universe. (e.g. Hogan, 1983b; Ruzmaikin et al., 1988a,b; Widrow, 2002). Once these seed fields are present they can be amplified via different dynamo processes. The three major ones are given by the cosmic ray driven dynamo (Hanasz et al., 2009; Lesch and Hanasz, 2003), the $\alpha-\Omega$-dynamo (Ruzmaikin et al., 1979) and the small scale turbulent dynamo (Kazantsev, 1968; Kazantsev et al., 1985; Kraichnan, 1968). While the cosmic ray driven dynamo and the α-Ω dynamo operate close to Gyr timescales the small scale turbulent dynamo operates on Myr timescales and can therefore lead to a rapid growth of the magnetic field on short galactic timescales. In the small scale turbulent dynamo the magnetic field lines are stretched, twisted and folded due to turbulence on the smallest scales in the ISM which leads to an amplification of the magnetic field. The field is then regulated by random motion on the larger scales (Kulsrud and Anderson, 1992; Kulsrud et al., 1997; Malyshkin and Kulsrud, 2002; Schekochihin et al., 2002, 2004; Schleicher et al., 2010; Zeldovich et al., 1983). The turbulence on the smallest scales can be driven by various physical processes with SN-feedback being the most prominent one (e.g. Elmegreen and Scalo, 2004). Further, theoretical calculations can predict the structure of the magnetic field which turns out to be either dipolar or quadrupolar (Shukurov et al., 2019), whereby the quadrupolar structures decay faster if the dynamo action is switched off. The field structure can then be determined by the symmetry of the magnetic field around the mid plane, where uneven symmetry determines a dipolar field while even symmetry indicates a quadrupolar field. Recently, there have been various simulations of isolated galaxies, cosmological zoom-in simulations and larger cosmological volumes that include a prescription for solving the equations of magneto hydrodynamics. These simulations provide strong evidence for a small scale turbulent dynamo on scales of galaxies (Beck et al., 2012; Butsky et al., 2017; Pakmor et al., 2017; Pakmor and Springel, 2013; Rieder and Teyssier, 2016, 2017a; Steinwandel et al., 2019) and galaxy clusters (Dolag et al., 1999, 2001; Roh et al., 2019; Vazza et al., 2018; Xu et al., 2009). All of these simulations find indications in the magnetic power spectra for small scale turbulence driven amplification of the magnetic field. The origin of the turbulence on the small scales is in all cases mostly dominated by the feedback of supernovae (e.g. Naab and Ostriker, 2017; Somerville and Davé, 2015). Pakmor and Springel (2013) and Steinwandel et al. (2019) discuss the possibility of outflows that are driven by the magnetic pressure only, finding a slight decrease in the star formation rates in systems that are more massive than 10^{10} $M_{\odot}$. Both studies note that the condition for magnetic outflows are given if the magnetic pressure is dominating over the thermal pressure of the galaxy. Low mass systems are only weakly influenced by magnetic outflows because the amplification process of the magnetic field is merely inactive due to shallow potential wells and the low star formation rate that leads to a small amount of supernovae and therefore no source for small scale turbulence (apart from accretion shocks). Moreover, the α-Ω dynamo is not contributing much to the amplification of the magnetic field, but can order the field on larger scales. In the higher mass systems there is a magnetic driven wind which has the potential to contribute as an additional feedback process to the matter cycle within galaxies. Usually, there are two main sources that can drive galactic outflows that are well studied in both, observations an simulations and regulate the baryon-cycle in galaxies, namely supernova-feedback and the feedback of active galactic nuclei (AGN). This paper is structured as follows. In chapter 8.2 we present some of the fundamental findings of galactic dynamo theory. In chapter 8.3 we present the simulation suite that we use for our analysis alongside with the galactic model and the applied physics modules. In chapter 8.4 we investigate the origins and the properties of magnetic driven winds. In chapter 8.5 we discuss the results, presenting different properties from the dynamo theory. In chapter 8.6 we discuss the correlation between the magnetic field and the star formation rate. Finally, we present a summary of our work alongside with the conclusions and limits of the model in section 8.7.

8.2 Fundamentals of Dynamo-Theory

As the magnetic field is enhanced by the acting galactic dynamo we can follow the build-up of its structure. The fundamentals of dynamo theory can be derived from the induction equation of magneto hydrodynamics (MHD).

$$\frac{\partial \mathbf{B}}{\partial \mathbf{t}} = \nabla \times (\mathbf{v} \times \mathbf{B}) - \nabla \times \eta(\nabla \times \mathbf{B}). \tag{8.1}$$

where η is the magnetic resistivity, $\mathbf{B}$ the magnetic field and $\mathbf{v}$ the gas velocity. Regarding this equation, magnetic fields can be amplified when small magnetic seed fields are twisted by fluid flows. In classical MHD the magnetic field is tightly coupled to the movement of the gas. In this picture the galaxy provides the large scale velocity structure due to differential rotation of the disc. Therefore, the understanding of the velocity structure of a galaxy can lead to the understanding of the build-up of the magnetic field within the galaxy. In spiral galaxies the gas is rotating differentially within the potential that is provided by the dark matter halo of the galaxy and its stellar disc and bulge. Various processes like bar-instabilities or tidal forces due to gravitational interaction, in spiral galaxies transport angular momentum outwards and mass inwards. Therefore, the centre of the galaxy is constantly provided with gas that moves towards the centre. This gas cools, forms stars and eventually generates feedback by star-burst driven winds or winds driven by the feedback of Supernovae (SNe) which can lead to enrichment of the galactic halo. In disc galaxies the dominant component of the velocity is given as the axis symmetric rotation with usually only very small velocity components perpendicular to the galactic disc (which can be interpret as the turbulent motion of the fluid). This rotational velocity structure of the galactic disc is therefore highly complicated but its evolution is tightly coupled to the large scale components of the galaxy, like its dark matter halo, the stellar disc and the bulge.

Apart from the large scale velocity structure of the galaxy, small scale perturbations in the velocity can be generated by various feedback processes within the ISM (e.g. stellar wind feedback, supernova-feedback, collisions of molecular clouds, feedback of active galactic nuclei) which stir the gas and introduce small scale vertical motions that lead finally to the build-up of ISM-MHD turbulence. This introduces two effects that have to be considered to understand the build-up of magnetic fields in spiral galaxies. The first one is the so called helicity (convective turbulent motion of the gas, perpendicular to the disc) which enhances the magnetic field strength and supports the galactic dynamo. The second one is the turbulent diffusion which leads to a loss of magnetic energy due to (partially) reconnecting magnetic field lines. In this process magnetic energy that is carried by the magnetic field lines is converted into thermal energy. Therefore, this process works against the galactic dynamo. By including the small scale perturbations that are introduced over various feedback processes in the ISM one can derive the mean field dynamo equation following for example Wielebinski and Krause (1993), Sur et al. (2007) and Brandenburg (2009). Within the scope of the mean field dynamo the velocity field and the magnetic field can be written as follows

$$\mathbf{v} = \langle \mathbf{v} \rangle + \mathbf{v}^{(1)}, \tag{8.2}$$

$$\mathbf{B} = \langle \mathbf{B} \rangle + \mathbf{B}^{(1)}, \tag{8.3}$$

where $\mathbf{v}^{(1)}$ and $\mathbf{B}^{(1)}$ denote the small scale fluctuations of the velocity field and the magnetic field, respectively. The small scale fluctuations in the velocity field are locked to the small scale fluctuations in the magnetic field and coupled via $\nabla \times \alpha \langle \mathbf{B} \rangle$ with α given by Zeldovich et al. (1983) via $\frac{1}{3}\tau\langle \mathbf{v}^{(1)} \cdot$

$(\nabla \times \mathbf{v}^{(1)})\rangle$ and $\eta_T \Delta\langle \mathbf{B}\rangle$ where η_T is the turbulent diffusion coefficient. It is directly proportional to the turbulent length scale l_{turb} and the turbulent velocity v_{turb}. This leads to the dynamo equation given by

$$\frac{\partial \mathbf{B}}{\partial t} = \nabla \times (\mathbf{v} \times \mathbf{B}) + \nabla \times \alpha \mathbf{B}. \tag{8.4}$$

We assume that the magnetic diffusivity is small and not strongly dependent on the environment. However, this is a rough approximation that breaks down in strong shocks that give an upper limit on the magnetic field amplification. In this picture the magnetic field is amplified in a two stage process. First the radial component B_r is amplified via small scale radial motion (convective turbulence and/or buoyancy). In the second step B_φ is generated via the Ω-effect (large scale rotation of the axis-symmetric component) from B_r. This behaviour can be directly seen from writing down the rate of change of the single magnetic field components in cylindrical coordinates given as:

$$\begin{aligned}\frac{\partial B_r}{\partial t} &= -B_r\frac{v_r}{r} - \frac{1}{r}B_r\frac{\partial v_\varphi}{\partial \varphi} - B_r\frac{\partial v_z}{\partial z} + \frac{1}{r}B_\varphi\frac{\partial v_r}{\partial \varphi}\\ &\quad + B_z\frac{\partial v_r}{\partial z} - v_r\frac{\partial B_r}{\partial r} - \frac{v_\varphi}{r}\frac{B_r}{\partial \varphi} - v_z\frac{\partial B_r}{\partial z},\end{aligned} \tag{8.5}$$

$$\begin{aligned}\frac{\partial B_\varphi}{\partial t} &= -B_\varphi\frac{\partial v_r}{\partial r} - B_\varphi\frac{\partial v_z}{\partial z} + B_r\frac{\partial v_\varphi}{\partial r} + B_z\frac{\partial v_\varphi}{\partial z}\\ &\quad - v_r\frac{\partial B_\varphi}{\partial r} - \frac{v_\varphi}{r}\frac{\partial B_\varphi}{\partial \varphi} - v_z\frac{B_\varphi}{\partial z} - v_\varphi\frac{\partial B_r}{\partial r},\end{aligned} \tag{8.6}$$

$$\begin{aligned}\frac{\partial B_z}{\partial t} &= -B_z\frac{v_r}{r} - B_z\frac{\partial v_r}{\partial r} - \frac{1}{r}B_z\frac{\partial v_\varphi}{\partial \varphi} + B_r\frac{\partial v_z}{\partial r}\\ &\quad + \frac{1}{r}B_\varphi\frac{\partial v_z}{\partial \varphi} - v_r\frac{\partial B_z}{\partial r} - \frac{v_\varphi}{r}\frac{B_z}{\partial \varphi} - v_z\frac{\partial B_z}{\partial z}.\end{aligned} \tag{8.7}$$

If we assume the system of interest to be a razor thin, differentially rotating galactic disc then we can cross out some terms from the above equations. Because differentially rotating systems have a flat rotation curve all terms with $\partial v_\varphi/\partial r$ cancel out. Further, we can assume axis symmetry for the velocity. This means that the velocity is independent of the angle φ and a vanishing magnetic field in z-direction. The magnetic field within the disc can then be written as follows

$$\frac{\partial B_r}{\partial t} = -B_r\frac{v_r}{r}, \tag{8.8}$$

$$\frac{\partial B_\varphi}{\partial t} = -B_\varphi\frac{\partial v_r}{\partial r} - v_\varphi\frac{B_r}{r} = B_\varphi\frac{\partial v_r}{\partial r} + rB_r\frac{\partial \Omega}{\partial r}, \tag{8.9}$$

with the angular velocity Ω. From the last term of equation 8.9 we directly see that a toroidal field is generated from an already existing radial field by the large scale rotation of the galactic disc. This effect is limited when all of the radial field is wound up and therefore has been converted into a toroidal field. However, due to radial inflow the radial field can be compressed and subsequently amplified. Due to the Ω-effect this radially amplified magnetic field can again be converted into a toroidal field and the process continues until the equipartition field strength is reached and the dynamo saturates.

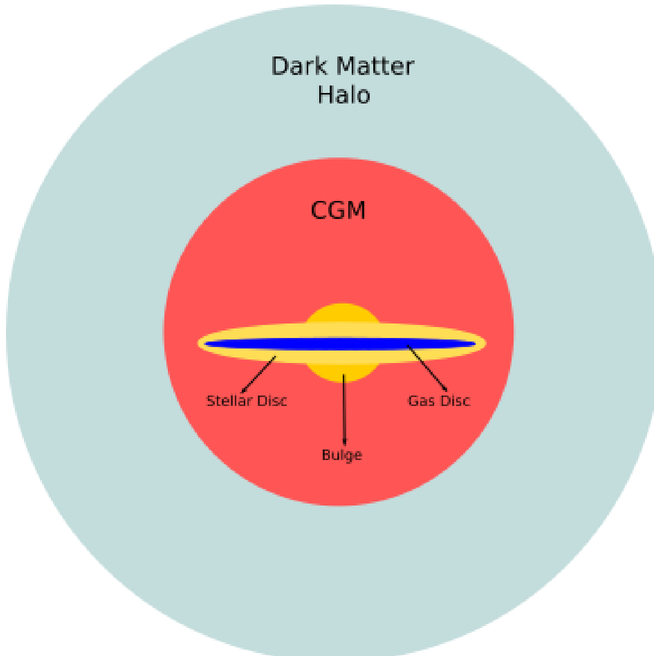

Figure 8.1: Schematic sketch of the galactic model we employ. The system is consisting out of a stellar disk (light yellow), a stellar bulge (dark yellow), a cold gas disc (blue) and a hot CGM (red). The whole system is embedded in a large dark matter halo (light blue).

8.3 Simulations

8.3.1 Simulation-code

All presented simulations are carried out with the Tree-SPMHD code *Gadget-3* (Springel et al., 2005b). *Gadget-3* solves the equations of Newtonian gravity via a Tree-code (Barnes and Hut, 1986). The fluid equations are solved with a particle ansatz utilising the Smoothed Particle Hydrodynamics (SPH)-method. We use a modern version of SPH that is presented in Beck et al. (2016a) with artificial viscosity and conduction terms to overcome known problems of the method in terms of shock-capturing and fluid mixing instabilities (Agertz et al., 2007; Junk et al., 2010). The details of the implementation of the magnetohydrodynamics version is presented in (Dolag and Stasyszyn, 2009) and has been used successfully in different studies (e.g. Beck et al., 2013, 2012; Geng et al., 2012a,c; Kotarba et al., 2011; Steinwandel et al., 2019). We are aware of the divergence cleaning constraints that can be problematic in particle methods. Therefore, we use a divergence cleaning method following Powell et al. (1999). For the presented set of simulations we showed in Steinwandel et al. (2019) that the magnetic energy density stays below the kinetic energy density for all times within the simulation by at least a factor of 100, proofing the Powell et al. (1999) cleaning scheme to be sufficient for the purpose at hand. We note that we tested the Dedner et al. (2002) cleaning scheme on the Milky Way-like models showing little differences. This is expected as the simulations have quite high resolution and large differences in the cleaning scheme are only expected at low resolution with the Dedner et al. (2002) cleaning scheme being more diffusive than the Powell et al. (1999) cleaning scheme.

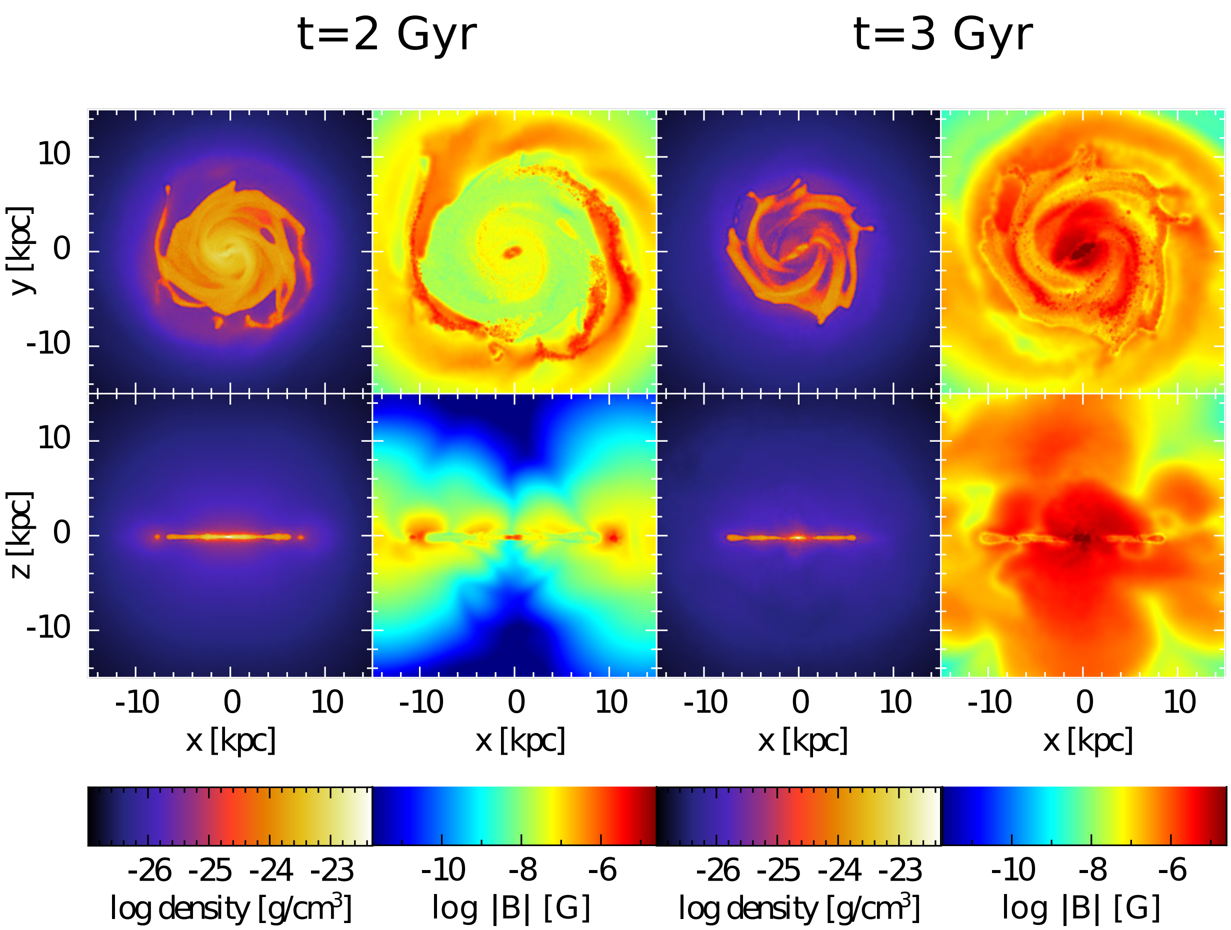

Figure 8.2: Projected gas densities (first and third row) and projected magnetic field strengths (second and fourth row) for the model *MW-SnB* for two different points in time. The four panels on the left show the galaxy at t= 2 Gyr and the four panels on the right show th galaxy at t=4 Gyr. For t= 2 Gyr, the thermal pressure is the dominating component in the ISM. The gas is captured in the potential minimum and forms a razor thin disc. For t= 3 Gyr the situation has changed and the magnetic pressure is dominating the system driving winds with mass loss rates of the order of a few $M_\odot$ yr^{-1}. We find three amplification processes at work in this kind of simulation. In the beginning the magnetic field is amplified in the centre via adiabatic compression and a small scale turbulent dynamo in the centre, while in the outer parts the magnetic field is amplified by the α-Ω dynamo. At later times the small scale turbulent dynamo is ultimately switched off by the strong magnetic fields and only the α-Ω dynamo remains.

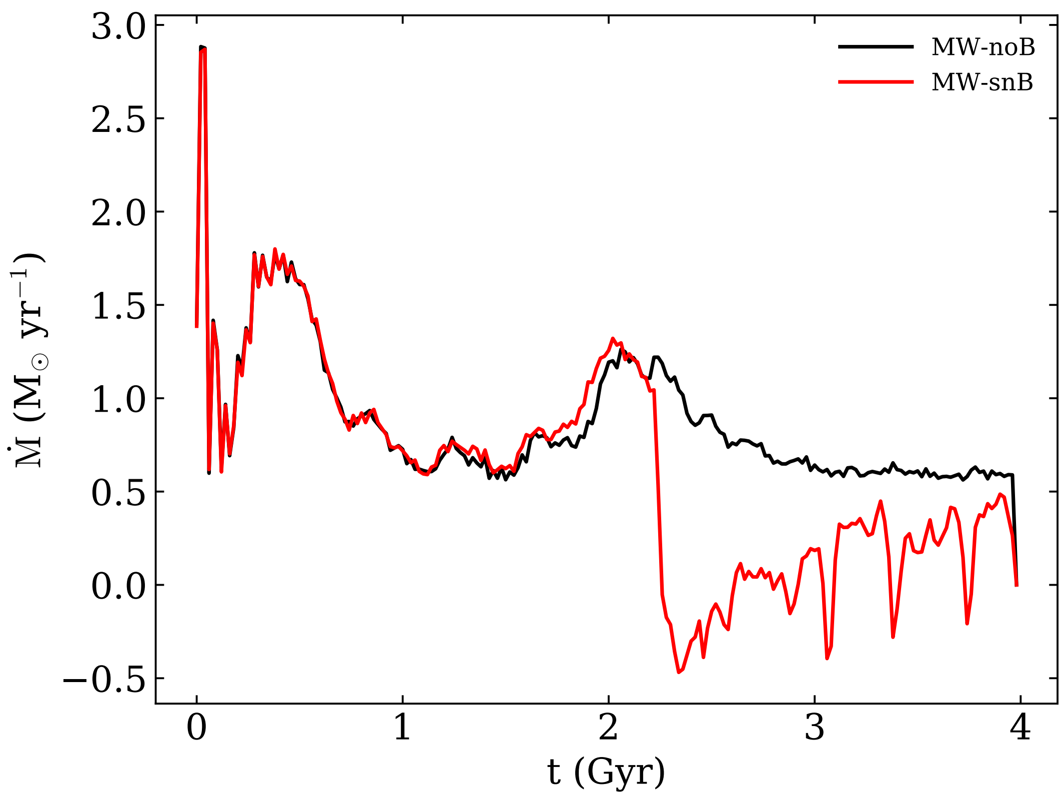

Figure 8.3: We show the mass budget of the models MW-snB that utilizes magnetic seed fields via the seeding of supernovae compared to the model MW-noB that represents an fluid with infinite plasma β (hydro-dynamic limit). We clearly see that the mass budget of the simulation without magnetic field stays positive all the time due to smooth accretion from the hot CGM (black line). The simulation with magnetic field is also smoothly accreting material. However at roughly 2.3 Gyr we see a drop with a peak outflow rate of 0.5 solar masses per year. While this outflow is small compared to mass loadings of supernova-feedback or even AGN-feedback it is not only capable to prevent the smooth accretion from the CGM,but also the remove star forming gas from the galactic disc.

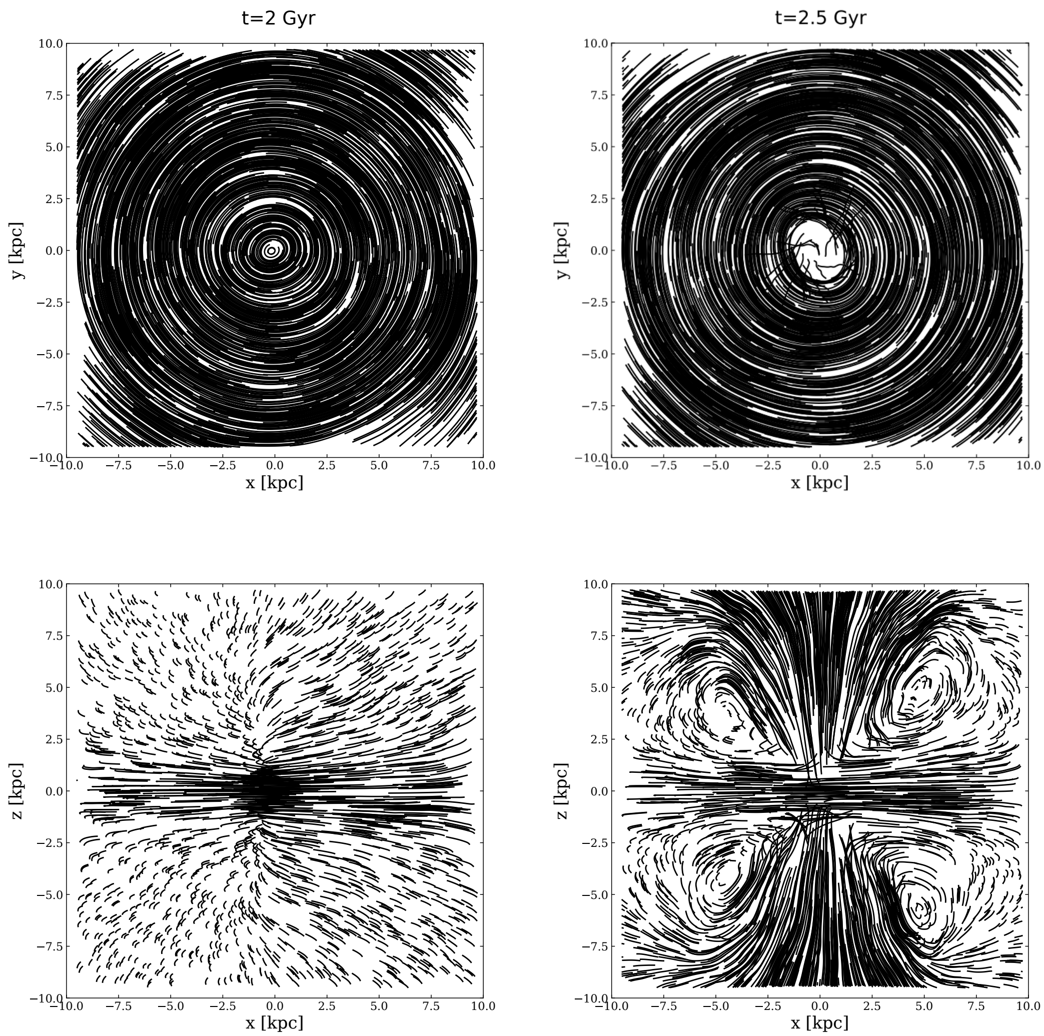

Figure 8.4: Structure of the velocity field for t=2 Gyr on the left face-on (top) and edge-on (bottom) and for t=2.5 Gyr on the right. The gas within the disc rotates differentially until the outflow sets in. Shortly, before the outflow sets in we find that there is an in fall from the CGM to the very centre of the galaxy which subsequently increases the density in the centre and adiabatic compression leads to an increase of the magnetic pressure that subsequently drives the outflows. When the outflow is present we see that the gas is moving in z-direction and falls back at later times.

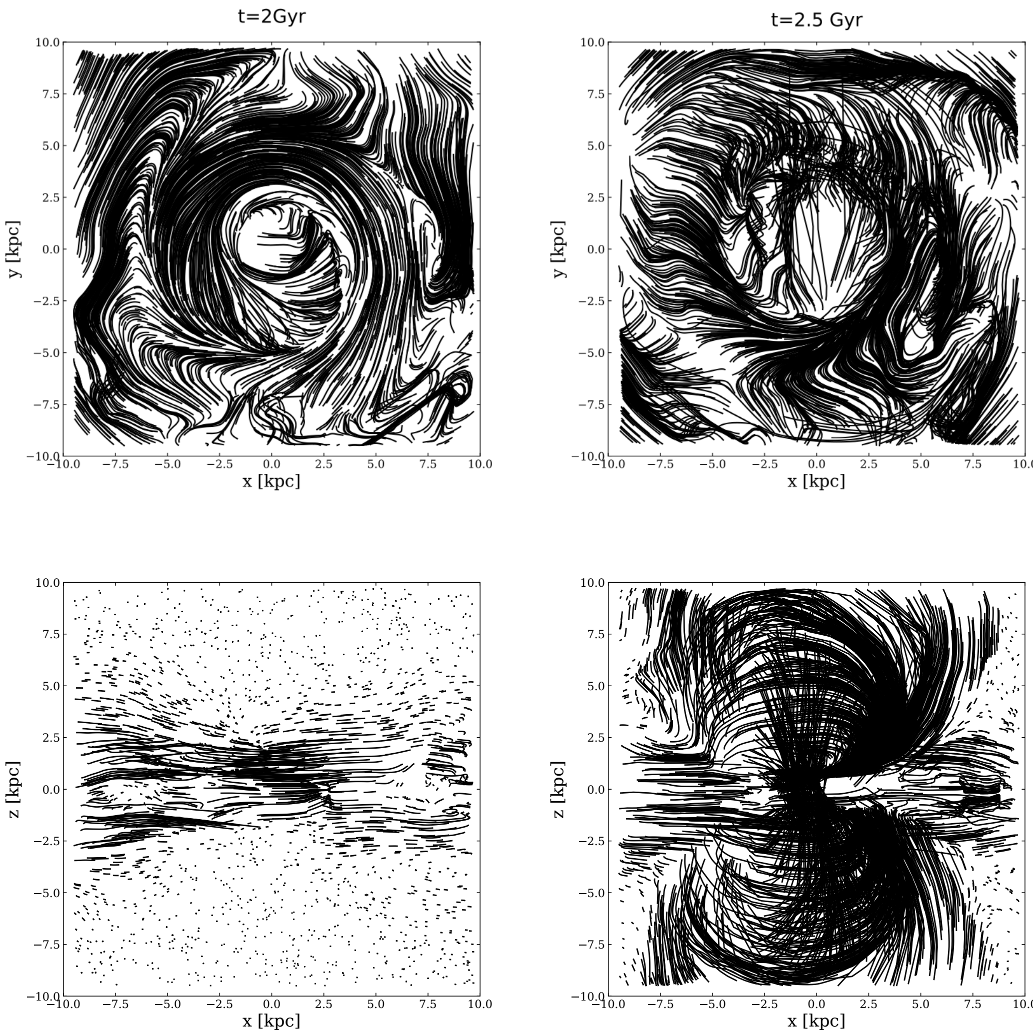

Figure 8.5: Structure of the magnetic field for t=2 Gyr on the left face-on (top) and edge-on (bottom) and for t=2.5 Gyr on the right. Already in the beginning of the simulation we find a highly complicated structure in the magnetic field that is kept once the outflow is present at later times. In the z-direction we find at later times that the field lines rise and their structure is in good agreement with what is expected from the Parker-Instability.

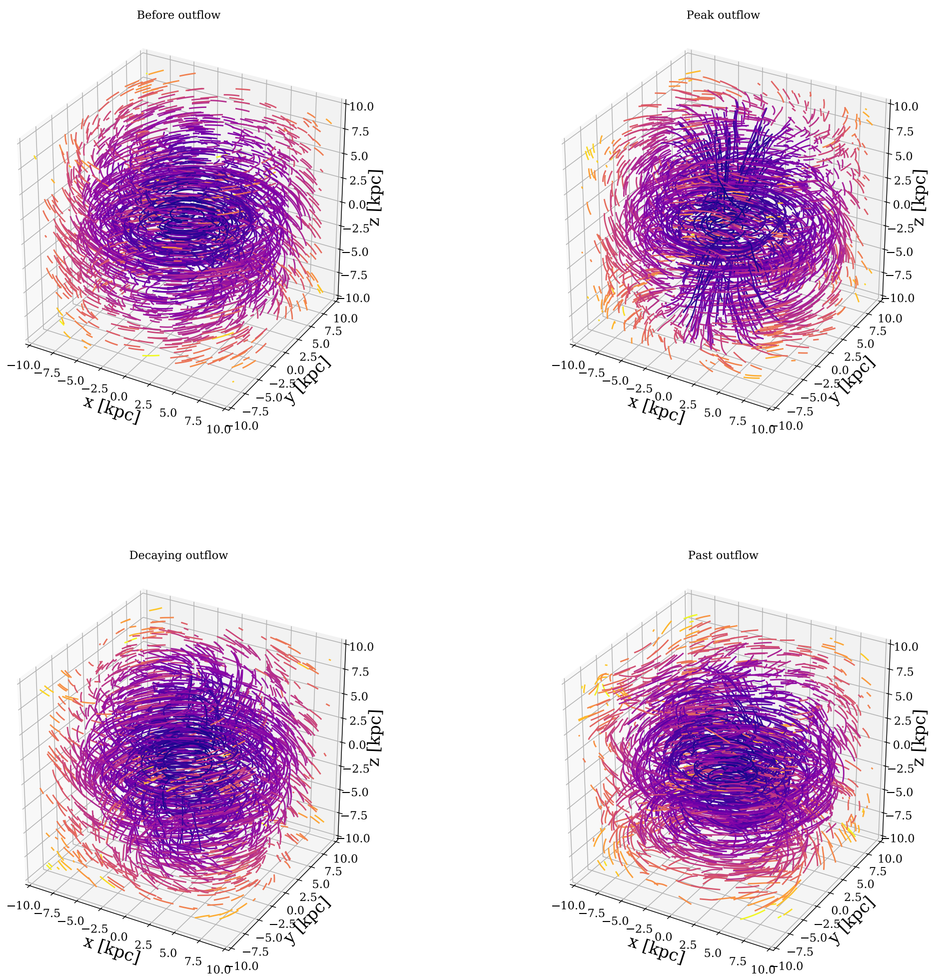

Figure 8.6: Three-dimensional structure of the velocity field at four different points in time, before the outflow (top left), at peak outflow rate (top right), as the outflow decays and the material is falling back to the disc (bottom left) and after the outflow has vanished (bottom right). The colour is indicating the speed of the particles alongside the streamlines, with darker colour showing higher velocities. We can see that once the outflow is emerging the regular velocity structure of the disc that originates from differential rotation is disturbed as the outflow rises with very high velocities from the centre of the disc towards both sides of the CGM. Once the outflow starts to decay the out flowing material falls back to the disc. After the outflow is over the disc relaxes to a more regular rotating state.

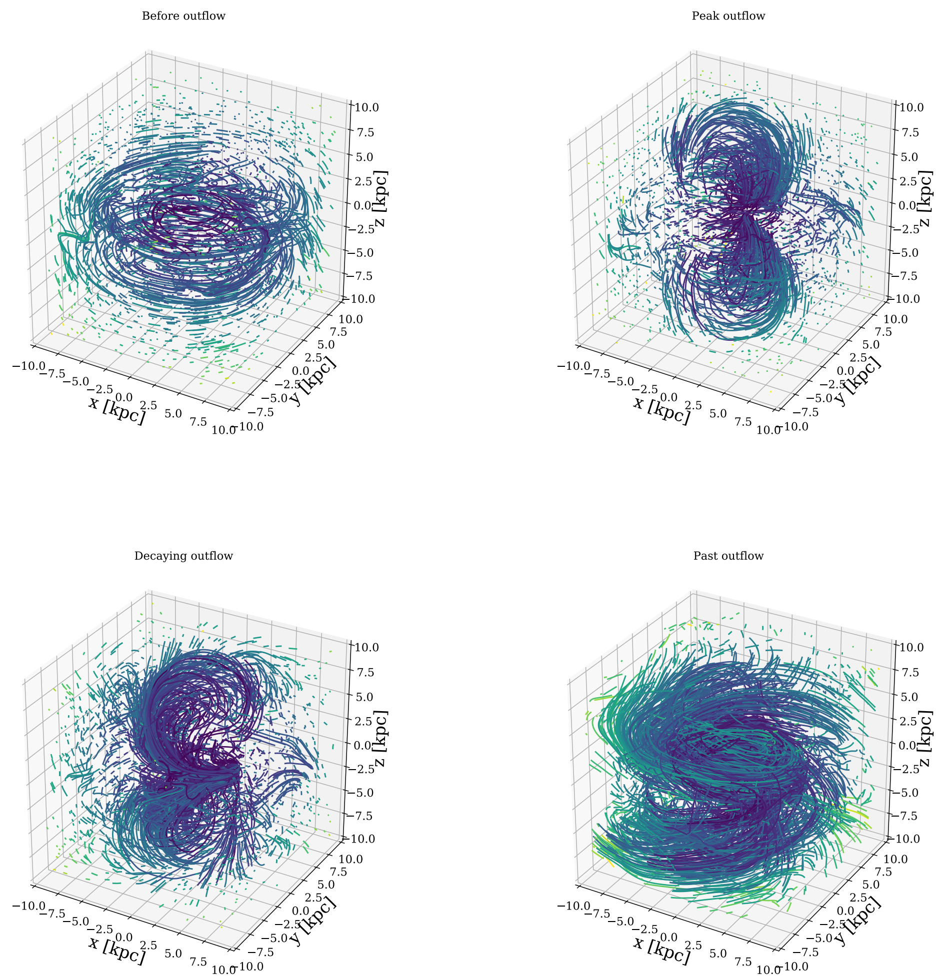

Figure 8.7: Three-dimensional structure of the magnetic field at four different points in time, before the outflow (top left), at peak outflow rate (top right), as the outflow decays and the material is falling back to the disc (bottom left) and after the outflow has vanished (bottom right). The colour is indicating the strength of the magnetic field with darker colour showing higher magnetic field values. we can see that once the outflow is present we can observe two Parker-like lobes rising above and below the disc. This clearly shows the bending of the magnetic field lines by the Parker-instability which is the initial process for the outflow to form. At later times when the material starts to fall back towards the disc we can see that the structured of these lobes is altered which finally results in a highly complicated magnetic field structure once the outflow has vanished.

Table 8.1: Number of particles, mass resolution, and gravitational softening lengths for our three galactic systems.

Particle Numbers [10^6]				
		DW	MM	MW
Gas disc	N_{gd}	0.8	1.0	1.2
Gas halo	N_{gh}	5.0	6.0	7.0
Stellar disc	N_{sd}	3.2	4.0	4.8
Stellar bulge	N_{b}	1.3	1.6	2.0
Dark matter	N_{dm}	4.6	5.7	6.9
Mass resolution [$M_\odot$]				
		DW	MM	MW
Gas particles	m_{gas}	72	510	4800
Star particles	m_{star}	72	510	4800
Dark matter	m_{dm}	1440	10200	96000
Gravitational softening [pc]				
		DW	MM	MW
Gas particles	ϵ_{gas}	5	10	20
Star particles	ϵ_{star}	5	10	20
Dark matter	ϵ_{dm}	40	20	10

Table 8.2: Adopted parameters for our three galactic systems.

Disc parameters				
		DW	MM	MW
Total mass [$10^{10} M_\odot$]	M_{200}	1	10	100
Virial radius [kpc]	r_{200}	31	67	145
Halo concentration	c	8	10	12
Spin parameter	λ	0.033	0.033	0.033
Disc mass fraction	m_{d}	0.041	0.041	0.041
Bulge mass fraction	m_{b}	0.013	0.013	0.013
Disc spin fraction	j_{d}	0.041	0.041	0.041
Gas fraction	f	0.2	0.2	0.2
Disc scale length [kpc]	l_{d}	0.8	1.5	2.1
Disc height	z_0	0.2 l_{d}	0.2 l_{d}	0.2 l_{d}
Bulge size	l_{b}	0.2 l_{d}	0.2 l_{d}	0.2 l_{d}

Table 8.3: Parameters for the gaseous halo

General parameters				
		DW	MM	MW
Total Mass [$10^{10} M_\odot$]	M_{gh}	0.05	0.5	5.0
Virial temperature [K]	T_{vir}	10^4	10^5	10^6
Settings for the β-model				
Exponent	β		2/3	
Density in [g/cm^3]	ρ_0		$5 \cdot 10^{-26}$	
Core radius	r_{c}	$0.22 \cdot r_{\mathrm{s}}$	$0.25 \cdot r_{\mathrm{s}}$	$0.33 \cdot r_{\mathrm{s}}$

8.3.2 Galactic model

We use the Milky Way-like model of the set of simulations that are presented in Steinwandel et al. (2019). This set consists out of three galaxies with halo masses 10^{10} (*DW*), 10^{11} (*MM*) and 10^{12} $M_\odot$ (*MW*) with an explicit modeled circum-galactic medium (CGM) that is motivated by observations of the CGM of the Milky Way (Miller and Bregman, 2013) for the 10^{12} $M_\odot$ galaxy. We show the specifics of all models in Table 8.1, 8.2 and 8.3 in terms of particle numbers, disc parameters and CGM properties. The CGMs for the lower mass galaxies are scaled down versions of the high mass model for the sake of simplicity. This model gives us the advantage to provide accretion from the CGM to the disc and allows detailed studies of the interaction between the disc and the CGM in a controlled environment. We utilize two different implementations of the magnetic field. In the first one a primordial magnetic field of 10^{-9} G is applied in x-direction (denoted with the identifier *primB* if used). We note that the equatorial plane is in the x-y plane. In the second one the magnetic field is coupled to the supernova-explosions and seeds a magnetic dipole in a certain region around an exploding star. For the model details we refer to Beck et al. (2013). This model is indicated with the identifier *snB*. As we find almost no difference in the structure of the magnetic field and the dynamical behaviour of the galaxy between the models *primB* and *snB* we only perform the analysis of the more realistic model *snB* and comment on the (slight) differences within the model *primB* if necessary. For completeness we show all the necessary parameters for all disc and CGM properties in the whole simulation set in Table 8.1 to Table 8.3.

All galaxies consist out of a dark matter halo that is modeled via a Hernquist-profile (Hernquist, 1993) a bulge, a stellar disc and a gas disc that is consisting out of SPH-particles. While the bulge is following a Hernquist-profile, the stellar and the gas disc follow exponential surface density profiles which are motivated by observations. These components are modeled with the method that is presented in Springel et al. (2005b) with explicitly modelled particle profiles for all components of the galaxy. The CGM is modeled separately as a β-profile (Cavaliere and Fusco-Femiano, 1978) as SPH-particles from a glass-distribution with the given radial density in spherical coordinates:

$$\rho(r) = \left(1 + \frac{r^2}{r_c^2}\right)^{\frac{3}{2}\beta} \tag{8.10}$$

The method that is used to build the galactic model is presented in detail in Steinwandel et al. (2019) and follows similar implementations on galactic scales (e.g. Moster et al., 2010a) and cluster scales (e.g. Donnert, 2014). However, we note that we introduced some small modifications to these models to fit the environment of isolated galaxies without perturbing the original system. We illustrate the model in Figure 8.1. With this model it is possible to simulate a Milky Way-like galaxy with the focus on resolving the galactic dynamo. We show an example of the resulting galactic system in Figure 8.2.

8.3.3 Previous Work

In Steinwandel et al. (2019) we already discussed the amplification processes for the magnetic field that we can resolve in our simulations and find strong evidence for three processes, adiabatic compression, the α-Ω dynamo and the small scale turbulent dynamo and showed agreement with other work (e.g. Pakmor et al., 2017; Rieder and Teyssier, 2016; Vazza et al., 2018). We identified the regimes of adiabatic compression via the scaling law $B \propto \rho^{2/3}$ which can be obtained from the flux freezing argument of ideal MHD that states that the magnetic flux through the surface of a collapsing gas cloud is constant. The magnetic field can then only be amplified due to collapse perpendicular to the magnetic field lines. We identified the α-Ω over the large scale rotation of the galactic disc. The small scale turbulent dynamo could be identified by the power-law slope that is predicted via Kazantsev (1968) in the low magnetic power regime. Turbulence is driven on the scales of a few 100 pc due to SN-feedback and leads to small scale turbulent motion (similar to the α-effect). We further found this process in the behaviour of the curvature of the magnetic field lines in good agreement with the results of Schekochihin et al. (2004). While these quantities are a good observable for comparison with dynamo-theory they cannot straight forward be obtained from observations. However, there are a few observables that can quantify the dynamo process and the higher order structure of the magnetic field that can be observed, which we will discuss in section 8.5. Further, we probed the effect of the magnetic driven outflow as a function of time on the star formation rate and found that the star formation rate is reduced by 40 per cent in the presence of magnetic field compared to a reference simulation that does not incorporate magnetic fields (Steinwandel et al., 2019). Further we find a mass outflow rate of a 0.5 solar masses (peak outflow rate) with a saturation value of roughly around zero solar masses per year, once an equilibrium between outflow-rate and accretion rate is established. We show this behaviour in Figure 8.3 where we show the mass budget of the galactic disc as a function of time. We compare our fiducial supernova-seeding model (red line) with a model that does not include the effects of MHD (black line). While we find that the peak outflow rate is too low compared to the outflow rate of the Milky Way or even compared to galaxies at high redshift, the effect could still be of importance. At very high redshift, when galaxies mainly grow due to smooth accretion and supernova-feedback is not yet dominating, magnetic driven outflows could delay star formation and thus contribute to the quenching of the first galaxies by internally regulating their star formation efficiencies. Moreover, it is expected that the outflow properties are set by all thermal and non-thermal components of the ISM and not by the magnetic field alone (e.g. cosmic rays). The interplay of all these components has to be studied in future simulations.

8.4 Bar formation and magnetic driven outflows

8.4.1 Formation of the magnetic driven outflow

In Steinwandel et al. (2019) we discussed the possibility of outflows that are driven by the magnetic field alone. Due to the amplification of the weak magnetic field in the beginning of the simulation the system is in a high plasma β regime. In this regime the system is completely supported by the thermal pressure in the disc and the magnetic field has no dynamic impact on the structure of the ISM. At later times when the plasma β is of order 1 and the magnetic pressure is of the same order of magnitude as the thermal pressure (or even higher) the magnetic field becomes dynamically important and can launch a highly magnetised, weak wind into the outer regions of the surrounding CGM. The gas is accelerated to a few 100 km s^{-1} during this process. In the following we want to describe the launch process of the wind in more detail. It is a combination of the acting small scale turbulent dynamo in the innermost kpc of the disc, adiabatic compression of the field lines, the acting Parker-Instability[1] that lifts the magnetic field lines above the disc within a few 100 Myrs and the formation process of a bar which is destabilising the central region of the galaxy. The launching process can be subdivided in four stages.

1. Small scale turbulent dynamo: The magnetic field in the centre of the galaxy is amplified

[1] The fastest growing mode of the Parker-Instability is proportional to the disc scale height. Therefore, to resolve the Parker Instability one has to resolve the disc scale height in the simulation. As our resolution is 10 pc (limited by the gravitational-softening) we resolve the disc scale height of roughly 200 pc well enough to capture the buoyancy driven Parker-lobes.

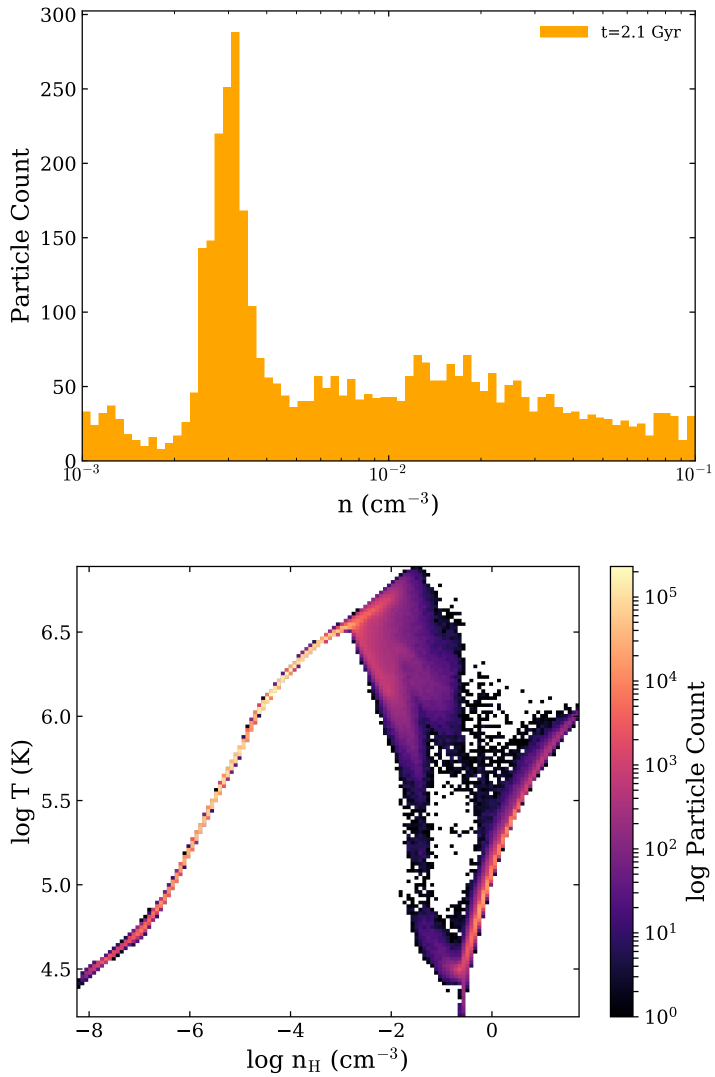

Figure 8.8: *Top:* Density structure of the out-flowing gas that is pushed out by the magnetic pressure. The peak number density is around 0.003 cm^{-3} which is in good agreement with results from Girichidis et al. (2016) who find a similar peak number density of the out-flowing gas. In the case of Girichidis et al. (2016) the outflow is driven by the feedback of supernovae. Surprisingly, we find that our outflow which is driven by the magnetic pressure can generate a similarly structured outflow. *Bottom:* Temperature-Density phase space diagram. We can easily distinguish between the galactic disc (low temperature and high densities) and the CGM (high temperature and low densities). These two phases interact via cooling from the CGM to the disc and the out-flowing gas from the disc to the CGM. Hereby the out-flowing gas can be seen as the branch that is walking up from low densities in the disc towards higher temperatures and lower densities to the CGM between 0.001 and 0.01 cm^{-3}. Thus the gas first cools due to adiabatic expansion (switching off star formation in the process) before it is lifted above the disc and heated by the surrounding medium of the CGM.

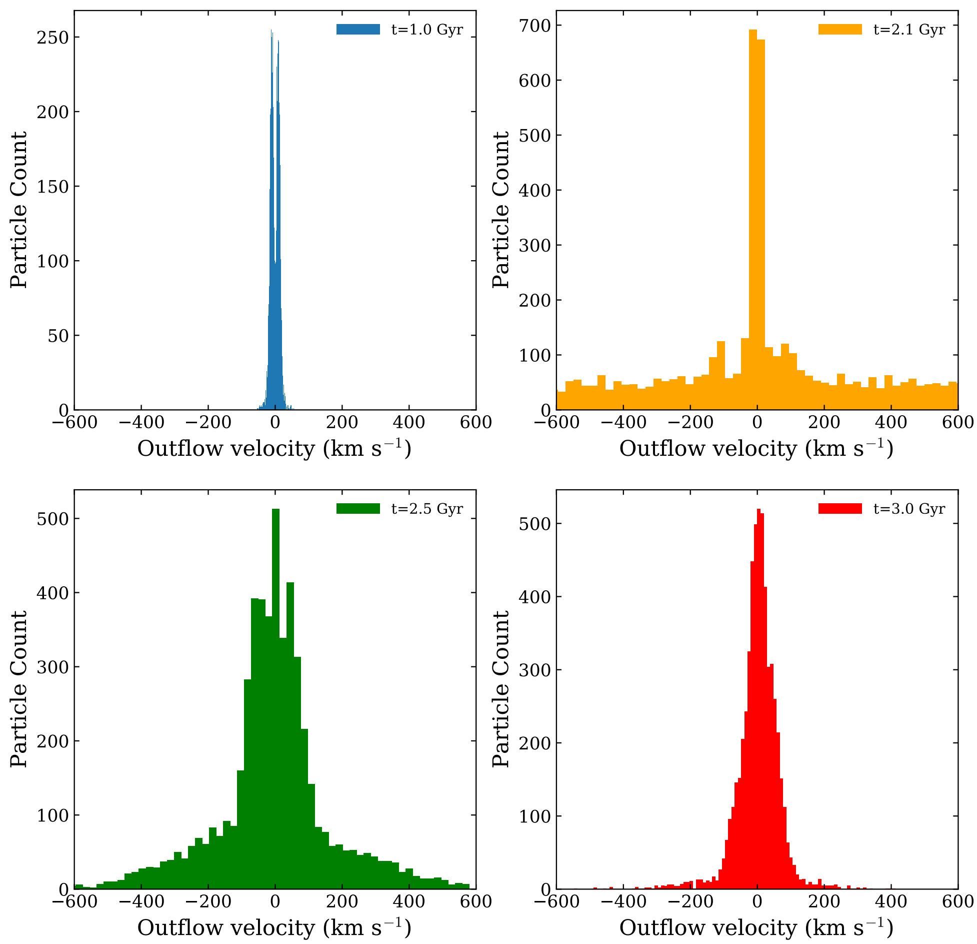

Figure 8.9: Histograms of the out-flowing gas for four different points in time at t= 1 Gyr before the magnetic driven outflow sets in (top left), at t= 2.1 Gyr shortly after the onset of the outflow (top right), at t=2.5 Gyr during the outflow (bottom left) and at t=3 Gyr (bottom right) when the outflow becomes weaker again. We only investigate the star forming gas that is evacuated from the disc. This process reduces star formation rate and magnetizes the CGM. The high outflow velocities are in good agreement with he upper limit for a pressure driven wind, set by the sound speed within the CGM. Further, we note that the magnetic outflow produces a variety of outflow velocities that are in good agreement with what is expected from supernova-driven outflows. However, here the magnetic pressure of the galactic magnetic field drives the outflow. The field lines rise due to the Parker-Instability until they break out of the galactic mid plane. Then they are pushed forward by the magnetic pressure from the galactic centre.

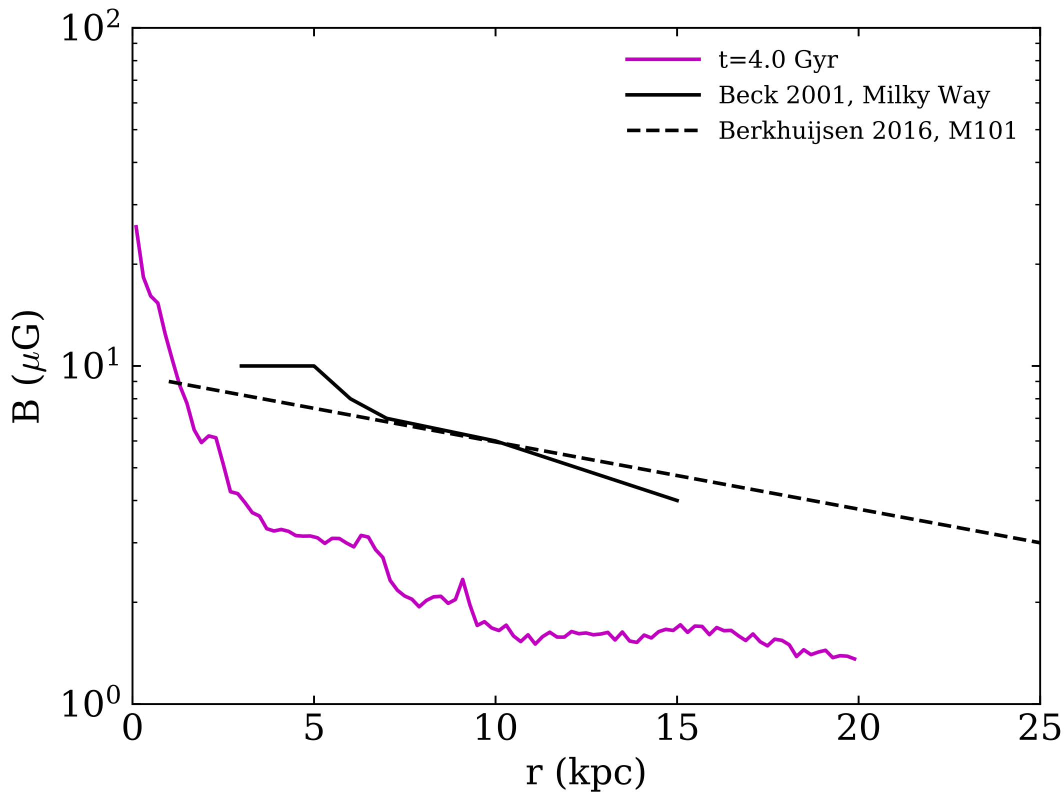

Figure 8.10: Radial profile of the total magnetic field for our final simulation time (magenta). The black solid and the black dashed lines show observations from Beck (2001) and Berkhuijsen et al. (2016) for the Milky way and M101. We calculated the square root of the mean magnetic field components and excluded the star forming gas to have a consistent comparison with observations. We note that for a better comparison we should construct the RM-signal and calculate the total magnetic field from this RM-signal. Generally we find that our simulation predicts a total radial magnetic field that is too low by a factor of 2.5. However, the scatter in both our simulations and the observations is within this range and we capture the declining radial trend.

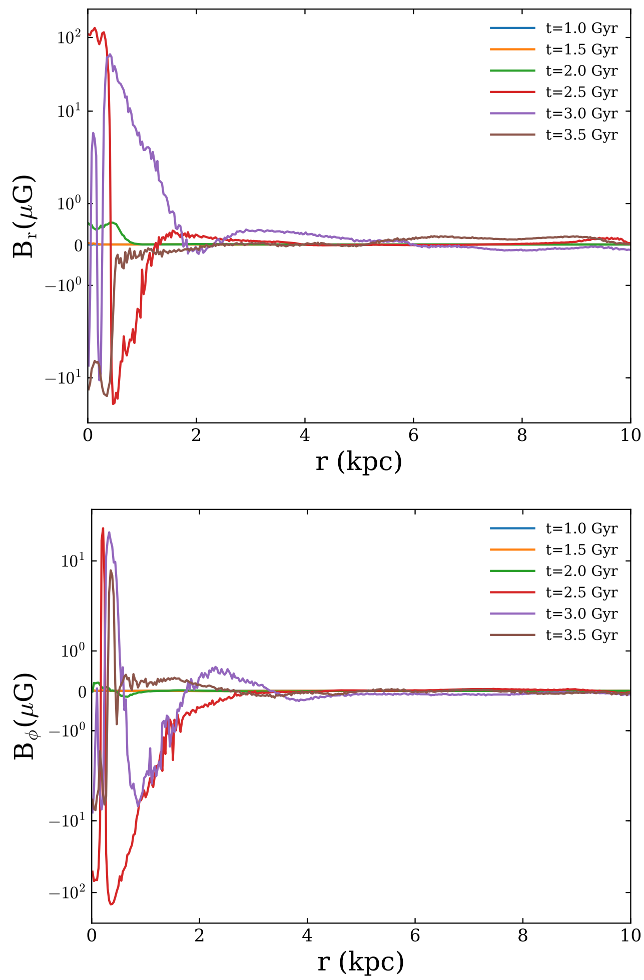

Figure 8.11: Radial profiles in the disc of the radial (top) and toroidal components (bottom) of the magnetic field for the simulation *MW-SnB*, for six different points in time, t=1 Gyr (blue), t=1.5 Gyr (orange), t=2 Gyr (green), t=2.5 Gyr (red), t=3 Gyr (purple) and t=3.5 Gyr (brown). The highest magnetic field strengths can be observed in the centre. Both radial profiles indicate ongoing dynamo action at later stages. In the beginning there is only a weak background field present which is only weakly amplified within the first Gyr. The field is seeded by SNe in the ambient ISM where it is amplified due to small scale turbulence and large scale rotation. At later stages the radial magnetic field components change the sign several times as function of the radius. From observations this is known as a first indicator for ongoing dynamo action (Stein et al., 2019).

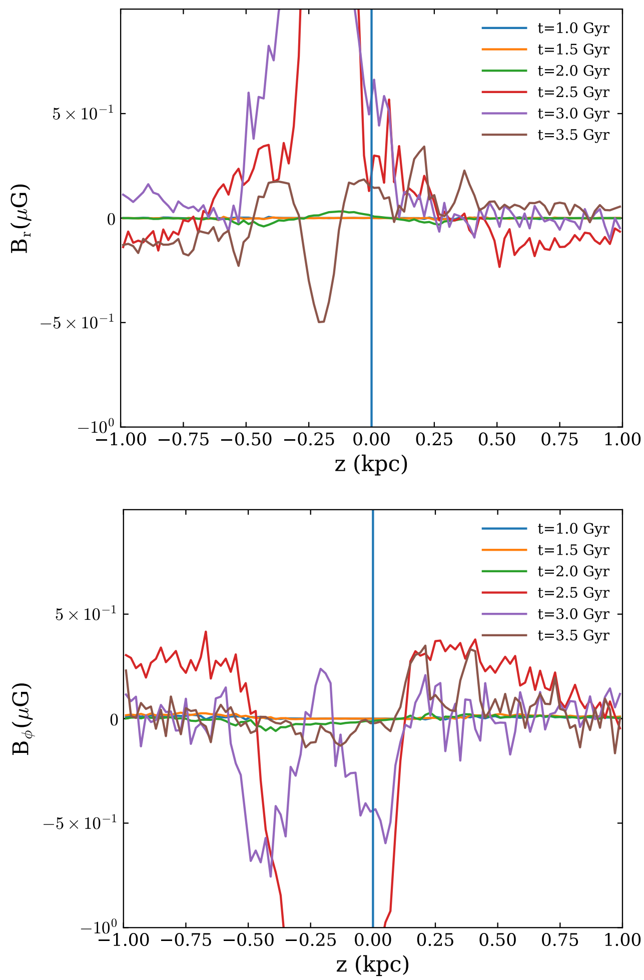

Figure 8.12: We show the dependence of the radial and the toroidal magnetic field component as a function of the disc scale height for six different points in time, t=1 Gyr (blue), t=1.5 Gyr (orange), t=2 Gyr (green), t=2.5 Gyr (red), t=3 Gyr (purple) and t=3.5 Gyr (brown). At early times we find that the magnetic field distribution is anti-symmetric around the mid plane. This indicates a dipole structure of the magnetic field at early stages of the dynamo. At later stages we find an even symmetry in the outer part of the galaxy which is indicating a quadrupole field structure. However, we note that at this point the galaxy has build-up a wind which is disturbing the magnetic field structure. We find indicators for dipole and quadrupole structure as well in the distribution of the toroidal field. The vertical blue line indicates the position of the mid plane.

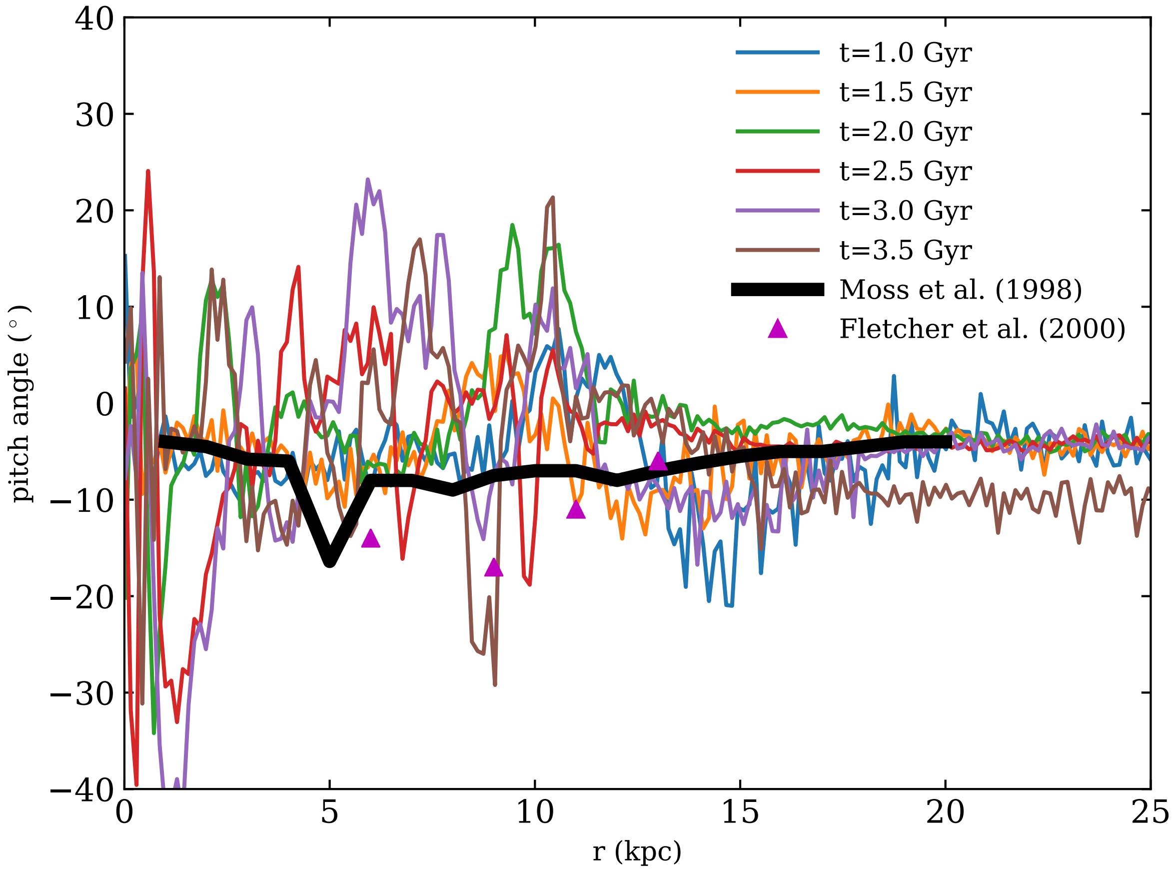

Figure 8.13: Pitch angle as the function of the radius for different points in time, t=1 Gyr (blue), t=1.5 Gyr (orange), t=2 Gyr (green), t=2.5 Gyr (red), t=3 Gyr (purple) and t=3.5 Gyr (brown). At early times before the system is dominated by the outflow in the very centre we can see negative values for the pitch angle ranging from −30 degree to roughly −5 degree. At alter times we find positive pitch angles because the systems is heavily perturbed by the magnetic pressure driven wind. However, on average we can still reproduce the correct radial trend. This agrees very well with the observations of M31 presented in Fletcher et al. (2000). Moreover, we find a saturation value of roughly −5 degree in the outer parts of the disc which is in good agreement with dynamo models Haud (1981). We find very good agreement with the dynamo model from Moss (1998) who predict an α^2-Ω dynamo. Further, we find good agreement with the Milky Way value which is around -15 degree at the solar orbit of roughly 8 kpc.

via the small scale turbulent dynamo. The small scale turbulence is induced by SN-feedback and accretion shocks generated by the in falling gas from the CGM. The central regions of the galaxy have the highest star formation rates (SFR) and subsequently the highest SN-rates. The turbulence in the central region leads to more effective star formation and amplifies the magnetic field further. However, the amplification process of the magnetic field over the dynamo saturates at a few 10 μG in the centre.

2. Bar-formation: At around 1.8 Gyr the galaxy starts to form a bar in the innermost kpc. Due to the high SFR in this region the gas is quickly depleted, leading to the radial gas in-fall due to the steep potential wells of the dark matter potential in Milky Way-like galaxies. Subsequently this leads to the formation of a bar, which gravitationally destabilises the central region of the galaxy.

3. Mass accretion through the bar: Once the bar has formed the central region of the galaxy can quickly accrete mass by transporting mass along the bar towards the centre while angular momentum is deposited in the outer region of the bar. The magnetic field can then be amplified by adiabatic compression if there is a mass flux perpendicular to the magnetic field lines and reach values of a few 100 μG in the very centre of the galaxy.

4. Buoyancy Instability: Finally, magnetic field lines are moving upwards (or downwards) driven by the Parker or buoyancy instability. Due to the density gradient in z-direction of the disc the magnetic field lines start to bend and form a sinusoidal shape around the mid plane. The mass on top of the field lines starts to flow down as mass can move freely alongside the field lines in direction of the strongest gravitational potential in the centre. This is significantly reducing the mass that confined the magnetic field line against the uprising pressure and the field lines rise. This process continues until the field line reaches the edge of the disc. The density in the ambient CGM is orders of magnitude lower than in the disc. The magnetic pressure drives a wind into the CGM. The outflow velocity is hereby limited by the speed of sound within the CGM which is a few 100 km s^{-1}.

In Figure 8.4 we show the streamlines of the velocity within 10 kpc for two different points in time, t=2 Gyr (left) and t=2.5 Gyr (right) in the face-on view (top) and the edge on view (bottom). The face-on velocity structure is very regular. The gas is orbiting the centre of the galaxies in circular orbits before the outflow sets in. In vertical direction the centre of the galaxy is accumulating mass from the CGM, which gravitationally destabilizes the central region and leads to the formation of a bar in the innermost kpc of the disc. To obtain a more detailed insight in the velocity structure, we show the three-dimensional velocity structure for four different points in time before (top left) during peak outflow (top right), in transition to a decaying outflow (bottom left) and past the outflow (bottom right) in Figure 8.6. The darker color shows higher velocities. We can see that the regular rotating velocity structure is disturbed by the out-flowing material that eventually falls back to the disc. After this material settles again and the outflow stops, the disc circular motion is dominating the system again. In Figure 8.5 we show the same streamline maps as in Figure 8.4 but for the magnetic field lines. Adiabatic compression amplifies the magnetic field, the magnetic pressure rises and magnetic field lines are pushed towards the CGM on the time scales of roughly 500 Myr in good agreement with the timescale of the Parker-Instability. We find that the magnetic field structure is highly complicated due to the ongoing dynamo action in the disc. This is present before and after the outflow sets in. Once the field lines reach the edge of the disc they expand freely into the CGM until they reach the speed of sound where the pressure support becomes weak and the outflow velocity saturates. The wind itself is then driven by uprising magnetic field lines due to the Parker-Instability and can be imagined as a magnetic supper bubble of Parker-lobes forming in the centre and rising to the edge of the disc where they finally break up and expand towards the CGM (bottom right of Figure 8.5). This can be seen even more clear in the corresponding three-dimensional streamline maps of the magnetic field that we show in Figure 8.7 for the same points in time at which we determined the three dimensional velocity maps from Figure 8.6. While the magnetic field structure only builds-up in the disc in the beginning due to the fact that the dynamo action is restricted to the disc (top left of Figure 8.7) at later times we can observe Parker-like bending of the magnetic field lines which supports our proposed outflow mechanism (top right panel of Figure 8.7). Once the outflow starts to decay these Parker like lobes start to get twisted while they are falling back (see bottom left of Figure 8.7) to the disc generating the highly complicated magnetic field structure after the outflow settles (bottom right of Figure 8.7). Moreover we note, that the direction of the outflow by this mechanism can be determined a priori. The field lines within the disc basically see the same density contrast in the xy-plane. However, in the xz-plane the see the highest density contrast which leads to the highest pressure gradient which makes the Parker-Instability very effective in the z-direction in our simulations while it is suppressed in the disc by the relatively constant pressure background.

8.4.2 Structure of the outflow

We briefly discuss the structure of the magnetic driven outflow. In Figure 8.8 we show the distribution of the densities within the outflow. The distribution peaks at a number density of around 0.003 cm^{-3} leading to the conclusion that most of the gas in the outflow is very low density gas which is not star forming. This is in agreement with the picture of the Parker-Instability as the driver for the outflow. The mass on top of the field lines that bend due to the Parker-Instability is falling down along the field lines reducing the mass that supports the line against the uprising magnetic pressure. The top of the field line consists therefore of lower density gas that is pushed out by the pressure. This becomes even more clear by considering the bottom panel of Figure 8.8 in which we show a temperature-density phase space diagram. We can clearly identify the galactic disc as the branch that is at high densities and low temperatures . Vice versa we can see the CGM clearly at low densities and high temperatures. The structure between those two components can be explained by considering cooling from the CGM to the disc and out-flowing gas from the disc to the CGM. The out-flowing gas is hereby the low density gas branch of the connection between CGM and disc, while the cooling gas is feeding the centre of the galaxy toward higher densities. This finally leads to a bar-instability that initiates the outflow process. The gas is then first adiabatically expanded and cools before it is lifted above the disc where it is heated by the hot halo gas, stabilizing the complicated baryon cyclce between the disc and the CGM.

Further, we investigate the outflow velocities. In Figure 8.9 we show the structure of the out-flowing velocities for four different points in time, before the outflow (upper left), at the beginning of the outflow (upper right), during the outflow (lower left) and at a later stage where the outflow gets weaker again. Before the outflow sets in we find a very narrow distribution of the velocities perpendicular to the disc with velocities of a few km s^{-1}. When the outflow starts we find a very wide distribution of velocities that reaches out to roughly 600 km s^{-1}. The peak in the centre are the particles that belong to the disc. At a later stag of the outflow most of the particles are flowing out with velocities between 50 km s^{-1} and 250 km s^{-1} with an extended tail of particles that can reach still velocities up to 600 km s^{-1}. We note that these particles are located in the outer regions of the CGM. At late stages the outflow gets weaker due to the declining gas mass fractions as a result of star formation and the outflow itself. As the outflow-velocities are smaller than the escape velocity, the majority of the particles falls back to the disc on the time scales of a few 100 Myrs. This recycling flow can be seen in the bottom right panel of Figure 8.4.

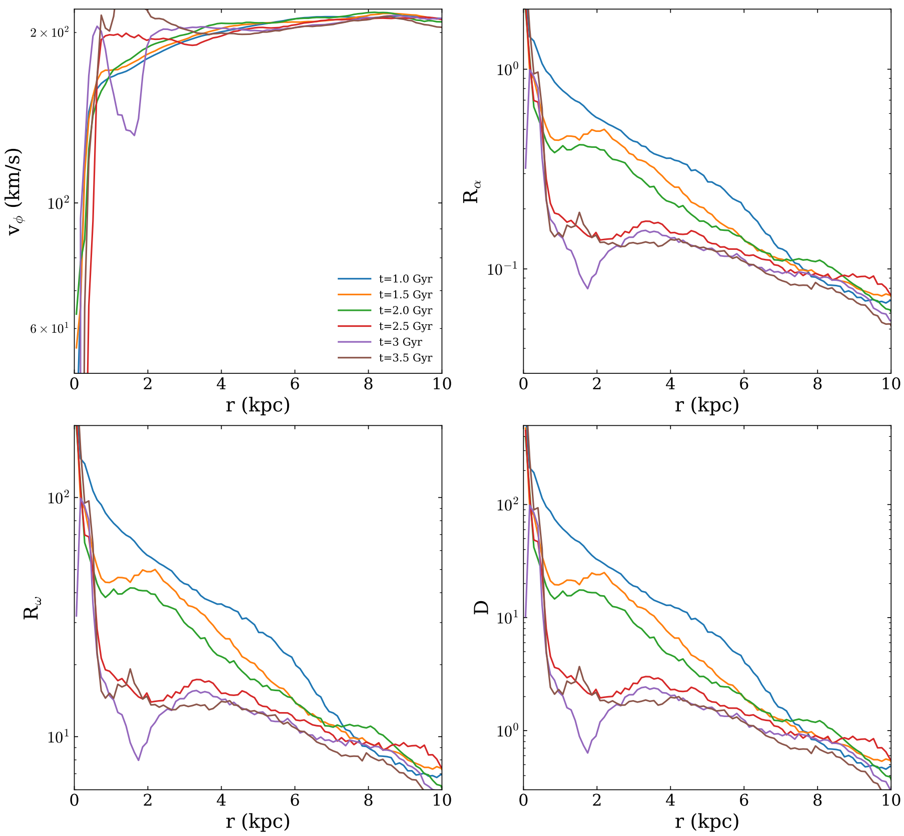

Figure 8.14: Physical properties that are important to classify the galactic dynamo of the galaxy MW-snB for six different points in time,t=1 Gyr (blue), t=1.5 Gyr (orange), t=2 Gyr (green), t=2.5 Gyr (red), t=3 Gyr (purple) and t=3.5 Gyr (brown). The first two points in time are before the outflow sets in, the third point in time is after the outflow is present. *Top Left:* Rotation curve of the galaxy as a function of the radius. The rotation curve shows the typical behaviour of a Milky Way-like disc galaxy with a steep increase in the innermost three kpc and a saturation at around 200 km s^{-1} in its outer parts. The oscillation at small radii at later times is a result of the formation process of the bar in the very centre. *Top Right:* R_α as a function of the radius. This parameter quantifies the contribution of the small scale vertical motion (α-effect) that is either introduced by small scale turbulence or rising buoyant bubbles in the inner parts of the galaxy. It decreases with radius as there is only weak feedback present and the gas is mostly in pressure equilibrium. *Bottom Left:* R_ω as a function of the radius. This parameter quantifies the contribution of the large scale rotation of the galactic disc (Ω-effect) to the dynamo process. *Bottom Right:* dynamo number D as a function of the radius. If the dynamo number is larger than 10 a large scale galactic dynamo is acting. In the beginning of the simulation we see a strong dynamo acting up to 6 kpc. At later times when the bar starts to form the dynamo is suppressed and magnetic fields in the centre are amplified via adiabatic compression until the mass inflow to the centre becomes only possible alongside the magnetic field lines due to the rising magnetic pressure.

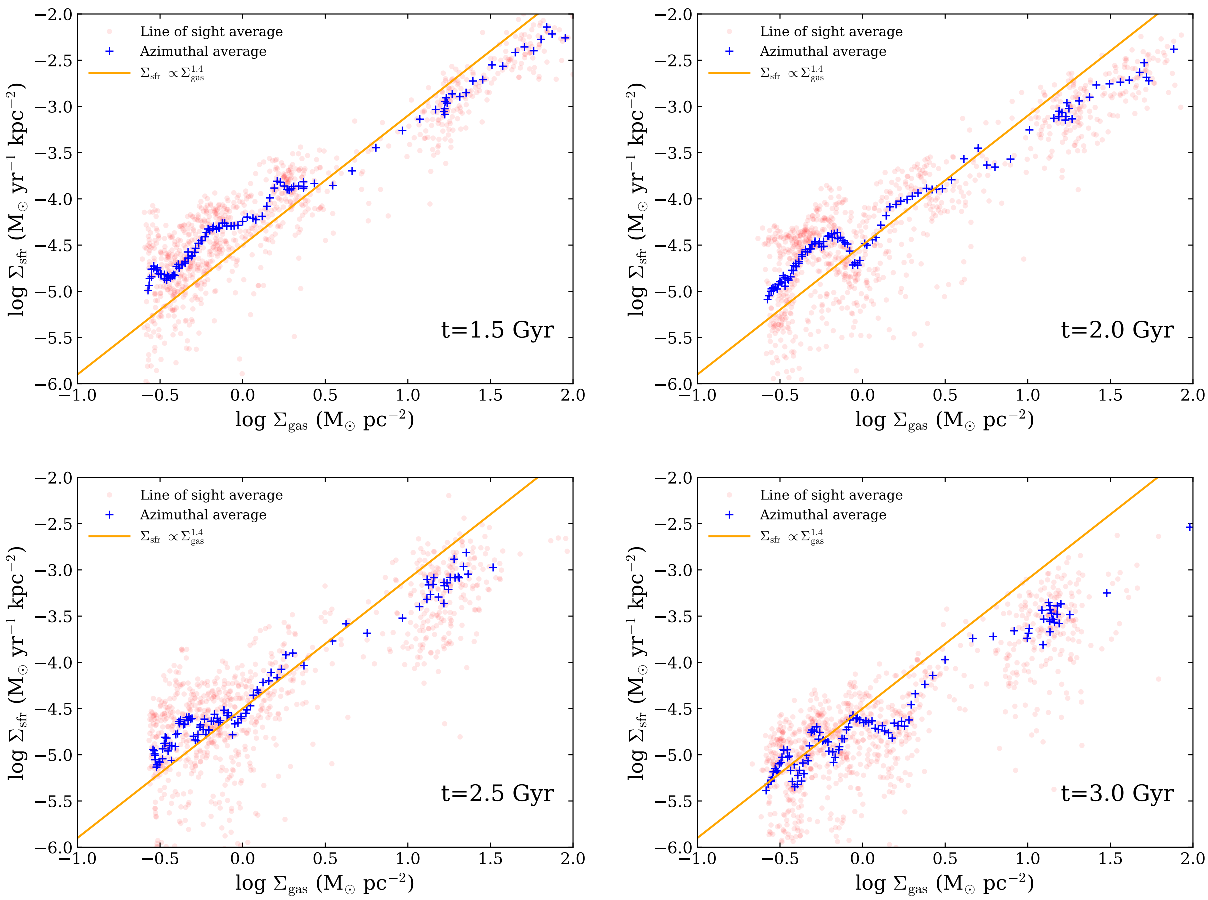

Figure 8.15: Star formation rate surface density as function of the gas surface density for four different points in time, t=1.5 Gyr (top left), t=2.0 Gyr (top right), t=2.5 Gyr (bottom left) and t=3.0 Gyr (bottom right). The data was obtained by binning the data on a grid with 256x256 bins. For every bin we calculated gas surface density and the star formation rate density per pixel (red dots). The blue stars indicate the azimuthally averaged values of the red data cloud. In our simulations star formation follows the Kennicutt-relation which we reproduce very good, also at later times within the galaxy.

8.5 Galactic Dynamo in MW-like galaxies

8.5.1 Structure of the magnetic field

First, we discuss the general magnetic field structure. In Figure 8.2 we show the projected gas densities and projected magnetic field strengths for two different points in time. We are able to follow three different amplification processes of the magnetic field in this simulation, adiabatic compression of the field lines, the small scale turbulent dynamo (on timescales of a few tens of Myrs) and the α-Ω-Dynamo (on Gyr timescales). In the beginning of the simulation the magnetic field is amplified in the outer parts due to large scale rotation and in the centre through amplification via turbulence induced by the feedback of SNe. Later, the formation of the bar in the centre leads to an increase of the magnetic field strength due to adiabatic compression. Material can effectively be transported to the centre due to the bar following the radial field lines within the bar. The Parker Instability determines the threshold for increase of the magnetic field within the disc until the field lines break out of the disc and form two giant magnetised lobes that lead to the magnetic outflow. In Figure 8.10 we show the total magnetic field as a function of the radius and compare to the observations of Beck (2001) and Berkhuijsen et al. (2016). We show the total magnetic field at the end of the simulation and excluded the star forming gas from the calculation to have the closest comparison possible to the observations at hand. We note that we find values that are a factor of 2.5 too low compared to these observations. However, we do not follow the discs cosmological evolution and thus we do not expect the disc to have a fully developed field in the outer parts of the galaxy. Moreover, the disc is accreting gas from the halo which is not enriched with magnetic field yet. This can substantially reduce the discs magnetic field in the outer parts compared to galactic models that do not exclude a hot CGM and can easily lead to a factor of a few lower values of the magnetic field in the radial trend. Furthermore, to self-consistently derive the magnetic field strength we would need to generate RM-mock observations to have a closer comparison with observations, which we will focus on in future work. In Figure 8.11 we show the radial profiles in the galactic disc for the radial and toroidal components of the magnetic field. In the beginning of the simulation both components appear to be flat as a function of the radius. This is due to the fact that at this point in time only a weak background field is present in the simulation, that is only seeded by the SNe in the ambient ISM due to our SN-seeding mechanism. This small seed fields have to be amplified first. This indicates that there is only weak dynamo action in the first Gyr of the simulation. However, after that point in time we can see that both the radial and the toroidal magnetic field component change its sign as a function of radius. Observationally, this behaviour is correlated with ongoing dynamo action within the galactic disc (Beck, 2015; Stein et al., 2019). In a dynamo the toroidal magnetic field component is generated via differential rotation from the radial field. This effect is captured in the appearing asymmetry of the radial and the toroidal magnetic field components.

Moreover, we can investigate the structure of the magnetic field as a function of the height above the mid plane. We show the results for the radial and toroidal magnetic field component in Figure 8.12. We show the radial field as a function of the scale height on the left for six different points in time and the toroidal field as a function of the disc height on the right. We can use both of these quantities to work out the magnetic field structure that is present around the mid plane. Dynamo theory predicts a dipole structure or a qudrupolar field structure which results in a certain behaviour of the radial and the toroidal component around the mid plane. If the radial and toroidal components are anti symmetric around the mid plane this is an indicator for a dipolar structure of the magnetic field. This picture is consistent with the early stages of the dynamo within our simulations. We find relatively weak magnetic fields in radial and toroidal direction indicating a dipole structure of the magnetic field. However, at later stages the symmetry becomes even which indicates quadrupolar field structure. However, we note that we find an increase of the magnetic field in the mid plane for both components once the system becomes outflow dominated. Further, we note that we find several field reversals at later stages with an even symmetry which not only predicts a quadrupolar field structure but also predicts a dynamo with several higher modes.

8.5.2 Pitch angle

From observations there are two strong indicators for ongoing dynamo action within a galaxy. The first one is the behaviour of the radial and toroidal components of the magnetic field, the second one is the pitch angle p which provides straightforward evidence for dynamo action. This is the shape of the projected magnetic field lines onto the plane of the galactic disc and is given by

$$\tan p = \frac{B_{\mathrm{r}}}{B_{\varphi}}, \tag{8.11}$$

where B_{r} and B_{φ} are the radial and toroidal component of the magnetic field given in cylindrical coordinates given by

$$B_{\mathrm{r}} = B_{\mathrm{x}} \sin(\varphi) + B_{y} \cos(\varphi), \tag{8.12}$$

$$B_{\varphi} = -B_{\mathrm{x}} \cos(\varphi) + B_{y} \sin(\varphi). \tag{8.13}$$

From observations the pitch angle can be constrained between -30 and -10 degree (e.g. Fletcher et al., 2000) which is in good agreement with our results. We derived the pitch angle from our simulation via equation 8.11 and show the result for six different points in time in Figure 8.13. At early times the pitch angle is negative at a value of around -5 degree and stays roughly constant as a function of the radius. At later times we find pitch angles between -30 (in the centre) and -5 degrees (in the outer parts). We note that we find also positive pitch angles due to the structure in the distribution of the magnetic field. At early stages this fluctuations of the magnetic field are mostly due to the noise of our underlying numerical scheme. At later stages the structure of the magnetic field is mostly introduced by the outflow in the centre which leads to a perturbation of the system. The bump at roughly 12 kpc can be explained by hot gas that is cooling down to the disc and a resulting accretion shock. Once our system becomes dominated by the outflow in the very centre the spiral structure becomes disrupted in the innermost area of the galactic disk. Therefore, we can see a positive pitch angle in this regime where our trailing spiral arms lifted and twisted by uprising material from the disc that is accelerated by the magnetic pressure. The pitch angle can be estimated directly from dynamo theory in different limits. We find good agreement with the results of Shukurov (2000) who computed the pitch angle via

$$\tan p = -\frac{l}{h} \sqrt{\frac{\Omega/r}{\partial\Omega/\partial r}}, \tag{8.14}$$

with l as the disc scale length and h as the disc scale height. For a flat rotation curve the term in the square-root of equation 8.14 is one and the pitch angle is only dependent on the ratio l/h. For a Milky Way-like galaxy this gives a pitch angle of roughly -15 degree. However, we note that this limit is only valid if the parameter $\mathrm{D}_{\mathrm{crit}}$ is close to one. A more detailed calculation with a better treatment for $\mathrm{D}_{\mathrm{crit}}$ is presented by Ruzmaikin et al. (1988b). Further, we find agreement of the pitch angle with the results from Moss (1998) and Haud (1981) and note that our structure for the pitch angle is close to the α^2-Ω dynamo shown in Moss (1998). This is especially true in the outer parts of the disc which we show as the thick black solid line in Figure 8.13. Moreover, we over plotted the observational results of Fletcher et al. (2000) for the Andromeda galaxy as the magenta triangles.

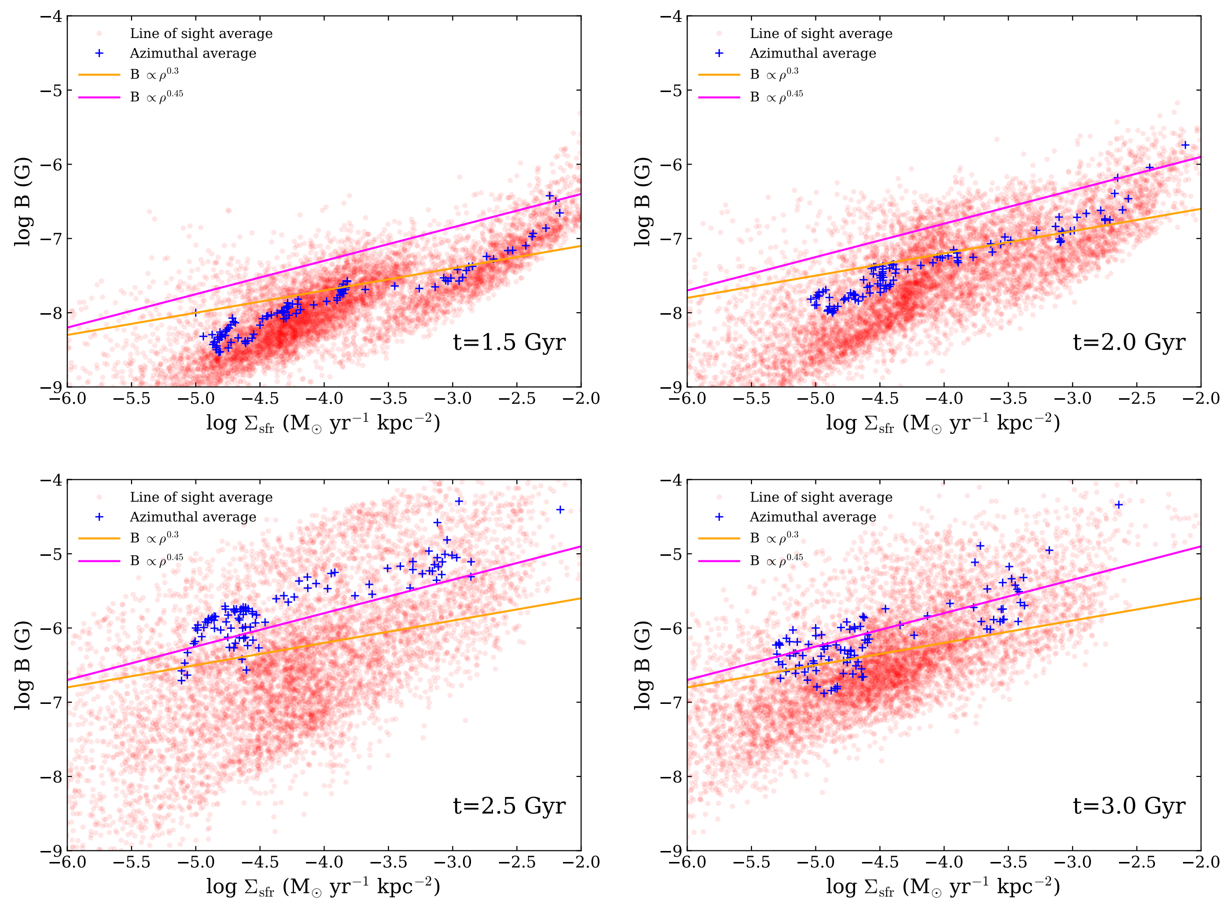

Figure 8.16: Magnetic field as function of the star formation rate density for four different point in time, t=1.5 Gyr (top left), t=2.0 Gyr (top right), t=2.5 Gyr (bottom left) and t=3.0 Gyr (bottom right). The data was obtained by binning the data on a grid with 256x256 bins. For every bin we calculated the integrated magnetic field and the star formation rate density per pixel (red dots). The blue stars indicate the azimuthally averaged values of the red data cloud. Further, the data we obtain is in good agreement with observations (e.g. Beck, 2015). The slope of the underlying Kennicutt-relation lies between 1 and 1.4 which leads to a variation in the relation between B and $\Sigma_{\rm sfr}$ between 0.3 (for molecular gas, orange line) and 0.45 (atomic gas, magenta line). However, we note that the scatter in the distribution is relatively large which is a consequence of our stochastic star formation procedure which aims to reproduce the azimuthally averaged Schmidt-Kennicutt relation. Therefore, the agreement with the theoretical prediction between of Schleicher and Beck (2013) that yield $B \propto \Sigma_{\rm sfr}^{1/3}$ is a consequence of our star formation law in combination with ideal MHD in the flux freezing regime.

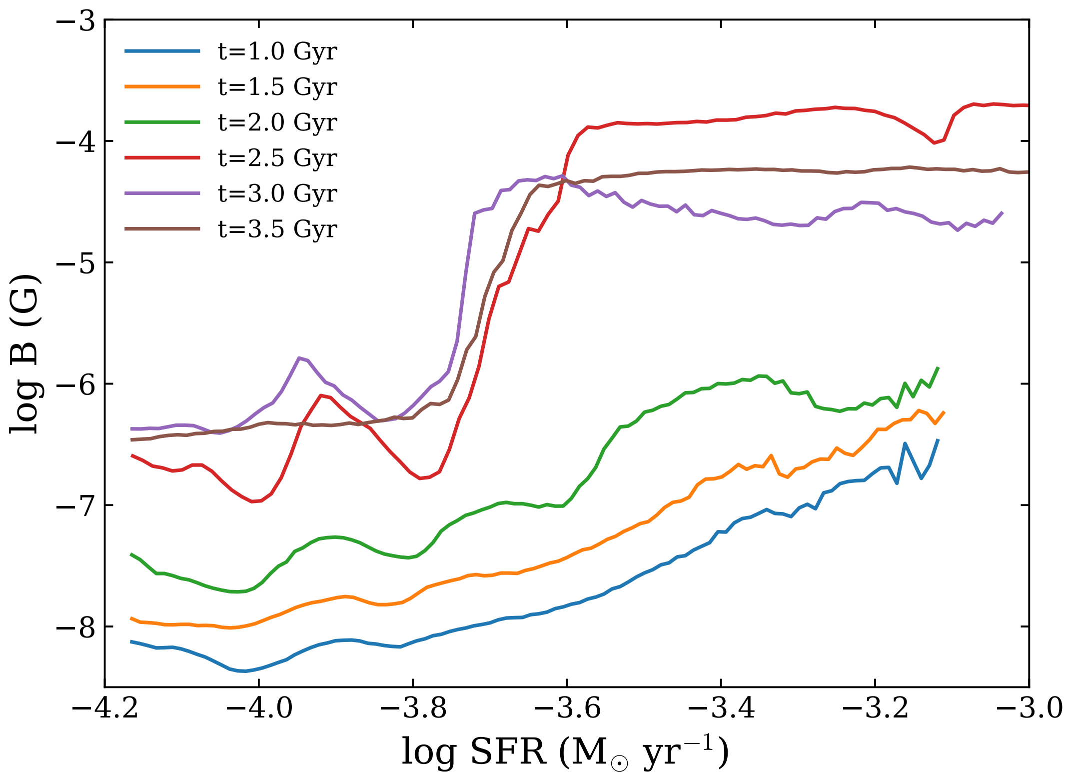

Figure 8.17: Magnetic field as a function of the local star formation rate for six different points in time, t=1 Gyr (blue), t=1.5 Gyr (orange), t=2 Gyr (green), t=2.5 Gyr (red), t=3 Gyr (purple) and t=3.5 Gyr (brown). At early times we find that the magnetic field is increasing with star formation rate. However, at later points magnetic field tends to be constant as a function of the local star formation rate or is even decreasing. At intermediate time we find that the magnetic field is oscillating with increasing star formation rate which indicates that there are regions in the galaxy where the local star formation rate is increasing but the magnetic field is decreasing.

8.5.3 Dynamo control parameters

We determine the so called dynamo control parameters. In the literature there are two Dynamo parameters of interest that measure the contribution of the α-effect (R_α) and the contribution of the Ω-effect (R_ω). They are given by

$$R_\alpha = \frac{\alpha h}{\beta}, \tag{8.15}$$

$$R_\omega = \frac{G h^2}{\beta}, \tag{8.16}$$

where α is the strength of small scale vertical flows given by $\alpha = l^2\Omega/h$ with the turbulent length scale l, the angular velocity Ω and h the scale height of the disc. $G = r\partial\Omega/\partial r$ is the shear rate that we can directly obtain from the shape of the rotation curve of our Milky Way-like galaxy. The factor $\beta = 1/3 l v_{\mathrm{turb}}$ with the turbulent length scale l and the turbulent velocity v_{turb}. R_α and R_ω define the dynamo number $D = R_\alpha \cdot R_\omega$ which indicates Dynamo action for $|D| > |D_{\mathrm{crit}}|$, with $|D_{crit}| \approx 10$. Before we start the determination of the dynamo control parameters we justify the assumptions under which we choose some of the parameters from above to actually determine the dynamo control parameters. Especially, we want to justify our choices regarding the turbulent length scale l and the turbulent velocity v_{turb} that we assume for our simulated galaxy. First, we note that within our galactic model it is hard to track turbulence in the first place which is due to our pressure floor sub grid model. However, keeping this issue in mind, determining the turbulent length scale can be self-consistently done by computing the velocity power spectra and measuring the injection scale for our induced turbulence before the start of the turbulent cascade. We obtain the power spectra with the code SPHMapper (Röttgers and Arth, 2018) by properly binning the data to a mesh with the same kernel that we used for our SPMHD-simulation. By doing this we obtain an injection scale of roughly 100 pc. This value is in very good agreement with the radius of SN-remnants at the time of pressure equilibrium (e.g. Kim and Ostriker, 2015). For the turbulent velocity we assume the mean rms of the velocities in each bin. For most bins this value is roughly around 10 km s^{-1}. We show radial profiles of the our rotation curve (top left), and the dynamo control parameters R_α (top right) and R_ω (bottom left) and D (bottom right) for six different points in time in Figure 8.14. We note that the shape of the dynamo control parameters is very similar between R_α, R_ω and D but the normalisation is different. This is mainly driven by the similar shape of the rotation curves and the fact that radial change of the shear goes as $-\Omega$ (in the leading term). We find radially declining dynamo parameters for all times that we display. Moreover, we note that we plot the absolute value of the dynamo numbers. At early times we find that D is greater than 10 in the very centre, indicating ongoing dynamo action (e.g. Shukurov et al., 2019). At later times the dynamo parameters decrease faster and go below 10 in the centre. Although that would indicate that dynamo action is suppressed we note that the launching outflow introduces a lot of noise within our bins for the turbulent velocity as we measure it as the velocities z-component. Therefore, we over-estimate the turbulent velocity in the central bins by at least a factor of two which would then lead to dynamo control parameters larger than 10 showing still ongoing dynamo action in the presence of the outflow.

8.6 Correlation between star formation rate and magnetic field

We investigate the dependence of the magnetic field on the star formation rate. Schleicher and Beck (2013) find that the magnetic field scales with the star formation rate in the following manner

$$B \propto \Sigma_{\mathrm{SFR}}^{1/3}. \tag{8.17}$$

In Figure 8.15 we show that the star formation is following the Kennicutt-relation for four different points in time. This fact has an direct impact on the correlation of the star formation rate with the magnetic field. This is shown in Figure 8.16 where we show the dependence of the magnetic field and the star formation rate surface density Σ_{SFR} for four different points in time, t= 1.5 Gyr (top left), t= 2.0 Gyr (top right), t= 2.5 Gyr (bottom left) and t= 3.0 Gyr (bottom right). The orange and the magenta solid lines show the power law dependencies that can be obtained from observations in the neutral and the molecular regime. The red dots are obtained by binning the whole galaxy on a grid with 256 x 256 cells. The magnetic field is then obtained by integrating the LOS magnetic field. The star formation surface density is obtained by integrating the LOS star formation rate and normalizing it by the unit area. Therefore, we can follow the global dependence of the SFR-surface density and the LOS magnetic field. Globally, we find very good agreement with the results of Schleicher and Beck (2013) and observations from Tabatabaei et al. (2013) and Niklas and Beck (1997). However, we note that in a global picture of our Milky Way-like galaxy we are constrained to this behaviour because our star formation is constrained by the Kennicutt-relation with a slope of 1.4 for neutral gas and a slope of 1 for molecular gas. For a saturated dynamo where amplification of the magnetic flux can only be obtained by adiabatic compression of the field lines this leads directly to a relation with a similar slope than obtained by Schleicher and Beck (2013). In dwarf irregulars smaller values are obtained (Chyży et al., 2011), but we find good agreement with observations of Milky-Way like spirals (e.g. Niklas and Beck, 1997). Further, we note the results of Tabatabaei et al. (2018) who observed the centre of NGC 1097 and found a antic correlation between the magnetic field strength and the star formation rate surface density. We find the same if we look on more local regions of the galaxy. While globally we are constrained by the Schmidt-Kennicutt relation, locally we can find that the magnetic field can behave differently. We show evidence for this behaviour in Figure 8.17. Here we plot the magnetic field as a function of the star formation rate. This gives us the local dependence of the magnetic field and the star formation rate. We find regions within the galaxy that do not follow the global power law scaling and the magnetic field is decreasing as a function of the star formation rate. This is consistent with the findings of Tabatabaei et al. (2018) who observed several molecular clouds in the nearby galaxy NGC 1097 and find a power law scaling with a negative exponent. In our simulations this effect is due to the effect that we include a diffusion term within our induction equation. Magnetic field lines can be transported from the spiral arms to the inter arm regions where they can be twisted and folded by small scale turbulent motion and due to the slightly lower densities but higher temperatures in the spiral arms and subsequently be amplified. Although our resolution is not high enough to properly follow the formation of molecular clouds within the Milky Way ISM, we propose that a similar effect could be responsible for the observed anti correlation between magnetic field and the star formation rate in molecular clouds where the magnetic field can be transported and dissipated away from star forming regions due to non-linear MHD effects and a smaller magnetic field remains in regions with high star formation activity.

8.7 Conclusions

8.7.1 Summary

We investigated the build-up of the galactic dynamo in a high resolution simulation of a Milky Way-like disc galaxy. We find that the galactic dynamo is supported by the small scale buoyant bubbles that rise and are twisted by the large scale rotation of the disc. Further, the dynamo is supported by supernova induced turbulence. Due to the amplification of the magnetic field in the dynamo the magnetic pressure in the disc quickly amplifies. In combination with the formation of a bar at 1.8 Myr this generates a large scale galactic outflow that is driven by the magnetic pressure. Further, we investigated the magnetic fields morphology in more detail and computed the pitch angle and the dynamo numbers. In the following we summarize our most important results.

1. *Magnetic driven outflows:* We find a magnetic driven outflow driven by the magnetic pressure. Due to the formation of a bar in the galactic centre the mass can be efficiently accreted onto the very centre of the galaxy. The magnetic field is amplified due to adiabatic compression of the field lines which increases the magnetic pressure. On timescales of a few 100 Myr the field lines in the centre begin to rise due to the buoyancy instability. Once the field lines reach the edge of the disc, the bubble that is supported by the magnetic pressure can further push out the material at the edge of the disc. The outflow velocity is limited to the speed of sound within the galactic CGM and can reach a few 100 km s^{-1}. Although the peak outflow rate is at around 200 km s^{-1} the outflow shows an extended tail towards higher velocities. Therefore, the pressure provided by the magnetic field could indeed play a role for the interpretation of results from Genzel et al. (2014) who observe a similar outflow structure. While they can identify very high outflow velocities with the activity of an AGN the exact origin of the lower velocities remains unclear, but is believed to have supernova-feedback as an origin.

2. *Structure of the magnetic field:* We investigated the detail morphological structure of the magnetic field as function of the radius and disc scale height. In agreement with predictions from dynamo theory we find that field reversals in the radial and toroidal field components. The reversals in the radial component are in agreement with recent observations from Stein et al. (2019) who showed for the first time radial field reversals in observations of the nearby galaxy NGC 4666. Moreover, we find toroidal field reversals which can be observed as well (Beck, 2015). Further, we find an indication for an uneven symmetry of the radial magnetic field and the toroidal magnetic field as a function of the disc scale height in the beginning of the simulation. At later times we find an even symmetry which is especially prominent in the outer parts of the disc. From dynamo theory it is known that the former is related to a dipole structure of the magnetic field while the latter is indicating a quadrupolar field structure.

3. *Pitch-angle:* We investigate the magnetic pitch angle as a function of the radius. Overall, we find good agreement with our estimated magnetic pitch-angles from our simulations and observations given by Fletcher et al. (2000). Further, we note that our radial trend and the values for the pitch angle are in good agreement with the results of Moss (1998) who find evidence for an α^2-Ω-dynamo which settles in the outer part of the galaxy at roughly -5 degree. We note that we also find positive magnetic pitch angles which do not fit into the picture of the dynamo-theory. However, we mostly find them at late times and in the centre of the galactic disc, where the system becomes outflow dominated and the magnetic field structure becomes much more complicated.

4. *Dynamo control parameters:* Finally, we compute the dynamo control parameters from our simulation. We measured the turbulent length scale as the injection scale of a velocity power spectrum and calculated the turbulent velocity as the (random) movement of the particles within the disc in z-direction, by assuming that the motion within the galactic plane is ordered by the large scale rotation of the disc. From that we obtained dynamo numbers that suggest ongoing dynamo action until the outflow sets in. At later stages the system is outflow dominated and the calculation of the dynamo number becomes more complicated and becomes polluted by particles that belong to the outflow that should not be included in the calculation of the dynamo parameters.

5. *Relation between SFR and magnetic field:* Globally we find that the SFR scales with the star formation rate surface density with a power law slope between 0.3 and 0.45 in good agreement with the results from Schleicher and Beck (2013), Niklas and Beck (1997) and Tabatabaei et al. (2013). However, locally in the spiral arms we find that the star formation rate can increase while the magnetic field is decreasing due to magnetic dissipation and diffusion which is included in our MHD equations (Tabatabaei et al., 2018).

8.7.2 Model limitations

Although our galactic model works well in reproducing some features known from a galactic dynamo its predictive power is still limited. First of all, the galactic system is isolated. While this setup is ideal to gain a deeper understanding of how the galactic dynamo operates it still misses the cosmological background that would be provided by the large scale structure of the Universe in close proximity of the galaxy. Therefore, we cannot follow the cosmological build-up of the galactic dynamo in a Milky Way-like disc galaxy and the model can by no means be interpreted as a simulation that represents the ab-initio generation of a galactic dynamo. As we miss the cosmological framework of the assembly of the Halo via mergers (smooth accretion from the CGM is modelled with the hot Halo) we cannot investigate the influence of major (mass ratio 1:4), minor (up to mass ratio 1:10) and mini mergers (below mass ratio 1:10) on the build-up of the dynamo and the magnetic field evolution of the galaxy. Depending on the type of merger, different scenarios are possible. In the case of minor and mini mergers e.g. Karademir et al. (2019) have shown that the mass of these kind of mergers is mostly deposited in the outer parts of Milky Way like galaxies. Therefore, for these kind of mergers the dynamo properties and the magnetic field evolution is supposedly only weakly influenced. However, major mergers could trigger an overlay star-burst of the merging systems (Karademir et al., 2019; Lahén et al., 2019) leading to a significant increase in star formation and turbulence and a more effective amplification of the magnetic field due to the small scale turbulent dynamo and compression of the gas (Steinwandel et al., 2019). This should be investigated in more detail in future studies cosmological zoom-in simulations on galaxy and galaxy cluster scales. However, the consequences for the large-scale α-ω dynamo that we mainly focused on in this study which orders the field on larger scales are potentially more severe. We note that the small scale dynamo can amplify the magnetic field on 100 Myr time-scales to the equipartition value (with the turbulent component of the galactic ISM), while the large scale dynamo operates on Gyr time-scales and is more important for re-ordering the magnetic field on larger scales and supporting the field growth once the small scale dynamo saturates. Thus, major mergers can disturb the gas dynamics to a degree that the large-scale dynamo is never fully operating as it is supported by the large-scale disc rotation. This is especially an issue when the merging system consists out of a pro- and counter rotator (miss aligned angular momentum vectors). Another important physics part that is missing within the simulation is the impact of cosmic rays. While the magnetic field alone already has an impact on the evolution of the galaxy the interaction of cosmic rays with magnetic fields is potentially important and has shown to have the capability to drive large scale galactic winds (e.g. Jacob and Pfrommer, 2017). Further, we note that we rely on the cooling, star formation and feedback prescription which is presented in Springel and Hernquist (2003). While this allows us to follow the build-up of interstellar turbulence it mostly remains sub-sonic. Other studies like Hu (2019) and Su et al. (2018) use a more detailed prescription for cooling and feedback that accounts for a proper treatment of momentum generation during the Sedov-Taylor-phase of a SN-remnant. While this is unlikely to have an effect on the behaviour of the large-scale dynamo, the rapid build-up of supersonic turbulence within the galactic ISM can effect can potentially change the growth rate of the small-scale-turbulent dynamo. Thus, future studies should investigate the build-up of the galactic dynamo with a sub-grid model for cooling, star formation and feedback that accounts for a proper treatment of the small scale physics of the ISM. Resolving the small scale structure of the ISM within galaxy formation simulations can therefore help to better understanding the detailed build-up of the dynamo in Milky Way-like galaxies.

Acknowledgements

We thank the anonymous referee for his/her comments on the paper draft, which helped to improve the quality of the paper. We thank, Joseph O'Leary, Marcel Lotz, Rhea-Silvia Remus and Felix Schulze for helpful discussions. UPS thanks Anvar Shukurov and Rashid Sunyaev for useful discussion and insights on dynamo theory and their connection to galaxy dynamics and high energy astrophysics. UPS acknowledges the discussion with Eugene Churazov, Marat Gilfanov and Ildar Khabibullin on the details of outflow mechanisms. The authors gratefully acknowledge the computing time granted by the Leibniz Rechenzentrum (LRZ) on SuperMUC under the project number pr86re and the on the c2pap-cluster under the project number pr27mi in Garching where most of this work has been carried out. UPS and BPM are funded by the Deutsche Forschungsgemeinschaft (DFG, German Research Foundation) with the project number MO 2979/1-1. UPS, KD and AB are supported by the Deutsche Forschungsgemeinschaft (DFG, German Research Foundation) under Germanys Excellence Strategy-EXC-2094 - 390783311. KD and AB acknowledge support by the DFG Cluster of Excellence 'Origin and Structure of the Universe' and its successor 'ORIGINS'.

Chapter 9

Hot phase generation by supernovae in ISM simulations: resolution, chemistry and thermal conduction

This work has been published in the Monthly Notices of the Royal astronomical Society, Volume 495, Pages 1035–1060.

Supernovae (SN) generate hot gas in the interstellar medium (ISM), help setting the ISM structure and support the driving of outflows. It is important to resolve the hot gas generation for galaxy formation simulations at solar mass and sub-parsec resolution which realise individual supernova (SN) explosions with ambient densities varying by several orders of magnitude in a realistic multi-phase ISM. We test resolution requirements by simulating SN blast waves at three metallicities ($Z = 0.01, 0.1$ and $1Z_{\odot}$), six densities and their respective equilibrium chemical compositions ($n = 0.001$ cm^{-3} - 100 cm^{-3}), and four mass resolutions (0.1 - 100 M$_{\odot}$), in three dimensions. We include non-equilibrium cooling and chemistry, a homogeneous interstellar radiation field, and shielding with a modern pressure-energy smoothed particle hydrodynamics (SPH) method including isotropic thermal conduction and a meshless-finite-mass (MFM) solver. We find stronger resolution requirements for chemistry and hot phase generation than for momentum generation. While at 10 M$_{\odot}$ the radial momenta at the end of the Sedov phase start converging, the hot phase generation and chemistry require higher resolutions to represent the neutral to ionised hydrogen fraction at the end of the Sedov phase correctly. Thermal conduction typically reduces the hot phase by 0.2 dex and has little impact on the chemical composition. In general, our 1, and 0.1 M$_{\odot}$ results agree well with previous numerical and analytic estimates. We conclude that for the thermal energy injection SN model presented here resolutions higher than 10 M$_{\odot}$ are required to model the chemistry, momentum and hot phase generation in the multi-phase ISM.

9.1 Introduction

The galactic interstellar medium is shaped by the feedback of massive stars. A physical process which is of paramount importance in this picture are SN-explosions. Core-collapse-supernovae (SNe) eject gas at supersonic velocities of several thousand kilometres per second (e.g. Blondin et al., 1998; Janka et al., 2012) and drive blast waves into the ISM. The evolution of SN-remnants has been extensively investigated analytically, and can be divided in four phases (e.g. Woltjer, 1972): the phase of 'free-expansion' which is terminated when the swept up mass equals the ejecta mass (roughly a few 100 years), the energy conserving Sedov-Taylor (ST) phase (e.g. Sedov, 1946, 1959; Taylor, 1950), the pressure driven snow plough (PDS) phase and the momentum conserving snow plough phase (MCS; Falle 1975). In the PDS-phase the pressure of the bubble interior further generates momentum until pressure equilibrium with the shell is reached and the bubble evolves the remnant in the low pressure regime (Cioffi et al., 1988; Cohen et al., 1998; Cox, 1972; Gaffet, 1983; Haid et al., 2016). In the MCS-phase the momentum of the shell is conserved and the further evolution of the shell is driven by the generated inertia of the swept up mass (Cioffi et al., 1988; Haid et al., 2016). The energy conserving ST-phase is of particular importance as it is the main momentum generating phase with an expanding hot bubble. This momentum build up due the ST-phase drives turbulence within the ISM and regulates star formation within galaxies. It can last from a few 1000 years in dense environments to several million years in low density environments. The duration of the ST-phase and the momentum and hot phase generation during this phase is highly dependent on the cooling properties of the ambient ISM. In this phase the SN-remnant behaves adiabatically because there are (nearly) no cooling losses that can remove energy from the system.

Blast waves replenish the hot phase of the ISM (Cox and Smith, 1974; McKee and Ostriker, 1977) through shocks (e.g. Gotthelf et al., 2001), generate momentum and build up turbulence (Elmegreen and Scalo, 2004; Scalo and Elmegreen, 2004) in the warm neutral medium (WNM) of the ISM (Mac Low and Klessen, 2004). The hot phase generated by SNe fills a large fraction of the turbulent ISM volume (e.g. Ferrière, 1998; Könyves et al., 2007; McKee and Ostriker, 1977) in which smaller and cooler clouds are embedded, as observed in the local ISM (e.g. Frisch et al., 2011). SNe also enrich the ISM with metals and dust (e.g. Dwek, 1998; Indebetouw et al., 2014; Kobayashi et al., 2011; Matsuura et al., 2011), different atomic species, and form molecules in their remnants (Fransson et al., 2016; Grefenstette et al., 2014; Kamenetzky et al., 2013; Spyromilio et al., 1988). When multiple SNe occur in a low density environment, subsequent explosion add mass to the shell and heat the interior of the bubble which can lead to the formation of 'super-bubbles' (Castor et al., 1975; Koo and McKee, 1992; Mac Low and McCray, 1988; McCray and Kafatos, 1987; Tomisaka and Ikeuchi, 1986; Weaver et al., 1977). Theses can drive strong galactic outflows which redistribute the gas on galactic scales and moves a fraction of it towards the circum galactic medium (CGM) of the galaxy. In more general terms, the feedback from SNe can regulate the cosmic baryon cycle and the star formation rate (SFR) of galaxies across cosmic time (c.f. Naab and Ostriker, 2017; Somerville and Davé, 2015).

In cosmological simulations of galaxy formation, stellar feedback leads to a better agreement with the properties of the observed stellar and gaseous components, such as the low conversion efficiency of gas into stars which are determined empirically (e.g. Behroozi et al., 2010; Moster et al., 2010a, 2013) and disk-like galaxy morphologies (Naab and Ostriker, 2017; Somerville and Davé, 2015). However, most simulations cannot resolve the momentum and hot medium generating phases of blast waves and rely on "sub-resolution" implementations to mimic the SN impact. Simulations adopting these methods have been able to produce galaxy morphology and population properties in agreement with observations (e.g. Agertz et al., 2013; Aumer and White, 2013; Guedes et al., 2011; Hopkins et al., 2018; Marinacci et al., 2014; Wang et al., 2015), and empirical predictions (e.g. Behroozi et al., 2019;

Moster et al., 2018). However, it remains unclear how well the underlying physical processes are really captured, and to what degree these results are achieved by fine-tuning model parameters.

Recently, it has become possible to simulate low mass galactic systems like dwarf galaxies at such high resolution that the impact of supernovae from individual massive stars can be captured in the relevant temperature and density regimes of the multi-phase ISM (Emerick et al., 2019; Forbes et al., 2016; Hu et al., 2017, 2016). In particular studies by (Lahén et al., 2019) have extended previous galactic ISM studies to environments with much more extreme densities and star formation rates. This approach, however, requires a detailed understanding of the resolution requirements for accurately tracking the impact of individual blast waves in the turbulent cold, warm and hot ISM. Many high-resolution simulations of SN blast waves in ambient homogeneous media or turbulent ISM patches have been carried out to understand their evolution in detail (e.g. Badjin et al., 2016; Blondin et al., 1998; Draine, 2011; Gatto et al., 2015; Haid et al., 2016; Kim and Ostriker, 2015; Martizzi et al., 2015; Ohlin et al., 2019; Ostriker and McKee, 1988; Thornton et al., 1998; Walch et al., 2015). While some of these studies aim for detailed blast-wave evolution (e.g. Badjin et al., 2016; Thornton et al., 1998) in one or two dimensional simulations, others aim for the effects of supernova feedback in a three-dimensional approach for investigating the effects on the three-dimensional galactic ISM (e.g. Kim and Ostriker, 2015; Ohlin et al., 2019) or investigate the effect of multiple feedback events on the galactic ISM (e.g. Gatto et al., 2015).

Apart from emerging resolution requirements, it has become clear that the distribution of ambient densities of SN blast waves play an important role for how efficiently they can drive turbulence and outflows (Gatto et al., 2017; Girichidis et al., 2016; Hu et al., 2017, 2016; Lahén et al., 2020; Naab and Ostriker, 2017; Seifried et al., 2018). While the turbulent component of the ISM can be generated by adopting some feedback prescription that injects the momentum of SNe, the galactic winds are driven by the pressure that is generated by the SNe within the turbulent ISM. In simulations, many factors like spatial resolution, stellar winds, radiation, SN clustering and binary or runaway stars can affect the ambient SN density distributions (Fielding et al., 2018; Gentry et al., 2017; Kim et al., 2017; Naab and Ostriker, 2017; Peters et al., 2017). However, not only numerical implementation, resolution constraints and ambient density distribution of blast waves determine their impact but also the complexity of the physical modelling. For example magnetic fields, cosmic rays (e.g. Diesing and Caprioli, 2018; Gupta et al., 2018) and thermal conduction (e.g. El-Badry et al., 2019; Keller et al., 2014) change their evolution.

In this paper we use two particle based hydrodynamical methods: modern smoothed particle hydrodynamics (SPH) and the meshless finite mass (MFM) method (Gaburov and Nitadori, 2011; Hopkins, 2015). We couple both solvers to a non-equilibrium chemical network to estimate their ability to converge on blast wave evolution in cold, warm and hot ambient media at different numerical resolutions. Furthermore we use the SPH implementation to probe the impact of thermal conduction on individual blast waves. While these studies have been carried out extensively using different grid codes in one or two dimensions, results in three dimensions are rare and detailed studies for particle codes are missing. However, as the ISM is a highly structured, turbulent and multi phase fluid it is of importance to investigate the effects of supernovae on the galactic ISM at the highest resolutions we can achieve today in galaxy formation and evolution simulations in three dimensions to work out the limitations on the physics of the ISM in galactic scale simulations. We test our results against detailed blast wave studies carried out in one or two dimensions Badjin et al. (e.g. 2016); Blondin et al. (e.g. 1998); Thornton et al. (e.g. 1998) and check how well we can resolve the global evolution of the Sedov-Taylor phase with momentum injection and hot phase generation under controlled boundary conditions. We also address resolutions requirement for current and next generation galaxy formation simulations without sub-grid modelling of individual supernovae.

The paper is structured as follows. In section 9.2 we briefly present the numerical and physical methods that are important for this study and discuss the simulation setup and the initial parameters that are important for our cooling and chemistry network. In section 9.3 we discuss our results for isolated SNe blast waves in a homogeneous medium (e.g. structure of the blast wave its environmental dependence). In section 9.4 we use the physical properties from our simulations to constrain the expectation value for a hot phase to form as a function of their environmental densities. In section 9.5 we discuss the effect of isotropic heat conduction on the SN-remnant evolution in our highest resolution runs. In section 9.6 we derive the consequences of the presented supernova-feedback scheme on the ISM in galaxy scale simulations and show results for supernova-driven ISM-patches, remnants in structured media and finally full galactic disc simulations at solar mass and sub-parsec resolution. Finally, we summarise our results in section 9.7.

9.2 Simulation method

9.2.1 Hydrodynamics

We run our set of simulations with our version of Gadget-3 (Springel et al., 2005b), which includes implementations for several hydrodynamics solvers, such as pressure-energy SPH (Hu et al., 2014) and the meshless finite mass (MFM) (e.g. Gaburov and Nitadori, 2011; Hopkins, 2015). In Hu et al. (2014) it is shown that the improved pressure-energy SPH accurately captures shocks and instabilities in several idealised test problems. While MFM shares the kernel weighted density computation with SPH, the hydrodynamical flux vectors are integrated over the one-dimensional Riemann-problem defined on the surface between two reconstruction points of the fluid equations (particles). In combination with a second order reconstruction of the flux gradients (Gaburov and Nitadori, 2011; Mocz et al., 2014) it is possible to obtain a second order hydrodynamical scheme with an appropriate mathematical consistency and convergence proof as shown in Lanson and Vila (2008). We follow the slope limiting and reconstruction procedures by Hopkins (2015). We calculate the quadrature point in first order via $\mathbf{x}_{ij} = (\mathbf{x}_i + \mathbf{x}_j)/2$ and solve the one dimensional Riemann-problem with a Harten-Lax-van-Leer (HLL) Riemann-solver with an approximate reconstruction of the contact wave (HLLC) following Toro et al. (1994). The time integration scheme that we adopt follows the description of Springel (2010) with a common CFL-criterion for the timestep. In strong shocks driven by supernova blast waves particles can move very fast and interact with other particles, which might be on much longer time steps and cannot react accurately. To avoid this we activate all nearby particles (within a kernel radius) and put them on the same short time step. The procedure is similar to the methods described in Saitoh and Makino (2009) and Durier and Dalla Vecchia (2012).

9.2.2 Thermal conduction

Some of our simulations employ a prescription for thermal conduction. We follow the implementation of Jubelgas et al. (2004) with updates for this scheme presented by Petkova and Springel (2009). We implement isotropic conduction given as a local transport process for the internal energy of a fluid tracer with the heat flux $\mathbf{j}$.

$$\mathbf{j} = -\kappa \nabla T, \tag{9.1}$$

where κ is the conduction coefficient and T is the temperature. The total change of energy is

$$\rho \frac{du}{dt} = -\nabla \mathbf{j}, \tag{9.2}$$

with the thermal energy u and the density of the fluid ρ. The conduction equation can be obtained by inserting equation 9.1 into 9.2:

$$\frac{du}{dt} = \frac{1}{\rho}\nabla \cdot (\kappa \nabla T). \tag{9.3}$$

However, we note that in astrophysical plasmas the conductivity is not constant but shows a dependence on the temperature. In the Spitzer limit this is given by

$$\kappa_{\mathrm{sp}} = 1.31 n_e \lambda_e k_B \left(\frac{k_B T_e}{m_e}\right)^{1/2}, \tag{9.4}$$

with the electron density n_e, its temperature T_e and its mass m_e. However, $n_e\lambda_e$ is only a function of the temperature T_e and the Coulomb-logarithm following

$$n_e \lambda_e = \frac{3^{3/2}(k_B T_e)^2}{4\pi^{1/2} e^4 \ln \Lambda}. \tag{9.5}$$

In the case of a constant value for the Coulomb-logarithm the Spitzer conductivity remains strongly temperature dependent

$$\kappa_{\mathrm{sp}} = 8.2 \cdot 10^{20} \left(\frac{k_{\mathrm{B}} T}{10\mathrm{keV}}\right)^{5/2} \frac{\mathrm{erg}}{\mathrm{cm\ s\ keV}}. \tag{9.6}$$

However, the behaviour changes for very low plasma densities where the scale length of the temperature gradient is of order the electron mean free path or even smaller. In this regime the heat flux saturates and no longer increases even if the temperature gradient rises. The saturation flux is given by

$$j_{\mathrm{sat}} \approx 0.4 n_e k_B T \left(\frac{2 k_B T}{\pi m_e}\right)^{1/2}. \tag{9.7}$$

In this case κ is modified to an effective κ_{eff} to smoothly change between the Spitzer and the saturated regime in the following manner

$$\kappa_{\mathrm{eff}} = \frac{\kappa_{\mathrm{sp}}}{1 + 4.2\lambda_e / l_T}, \tag{9.8}$$

where l_T is the length scale of the temperature gradient given as $T/|\nabla T|$. While the saturation limit is mostly relevant on galaxy-cluster scales and not in the ISM, we carried out some test simulations without the heat flux limit and even without a temperature dependence of κ itself. For isolated events we do not find large differences and it seems to be more important to have a heat diffusion term in the first place. The reason for that is, that we cannot resolve the process of thermal conduction within the bubble or the shell respectively. However, what we can resolve is the interface between bubble and shell. Therefore, even a constant value for κ leads to similar results (as long as it is physically motivated), as κ at the interface of bubble and shell stays (roughly) constant.

9.2.3 Chemistry model

We adopt a non-equilibrium chemical model following the implementation of the 'SILCC' project (Gatto et al., 2017; Girichidis et al., 2016; Peters et al., 2017; Walch et al., 2015). This chemical model is based on Nelson and Langer (1997), Glover and Mac Low (2007a), Glover and Mac Low (2007b) and Glover and Clark (2012). We track six individual species, H_2, H^+, CO, H, C^+ and O as well as free electrons and assume that silicon is present in the simulation as Si^+. Carbon is present either in single ionised from as C^+ or CO. Oxygen is present as O. H_2 and H^+ undergo several reactions, which are summarised in table 1 of Micic et al. (2012). The formation of H_2 is a dust catalysed reaction in which a dust grain captures two hydrogen atoms and the reaction becomes possible on dust surfaces. Most important for the destruction of H_2 is photo-dissociation due to the inter-stellar radiation field (ISRF), ionisation due to cosmic rays and via collisional dissociation (collisions with other species). The main channels for the formation of H^+ are collisional excitation with cosmic rays and free electrons. The destruction of H^+ is driven by recombination processes with free electrons. In the case of thermal conduction we directly assume the amount of free electrons that is predicted from solving the non-equilibrium rate equations to perform our computation of heat transfer.

9.2.4 Cooling and heating processes

The non-equilibrium cooling rates take into account the local density, temperature and the local chemical abundances. There are six major non-equilibrium cooling processes that are relevant for our studies, fine structure line cooling of atoms and ions (C^+, Si^+, O), vibration and rotation line cooling of molecules (H_2, CO), Lyman-alpha cooling of hydrogen, collisional dissociation of H_2, collisional ionisation of hydrogen and recombination of H^+ (both in gas phase and condensed on dust grains). The main sources for heating are given by photo-electric heating from dust grains and polycyclic aromatic hydrocarbonates (PAHs), cosmic ray ionisation, photo-dissociation of H_2, UV-pumping of H_2 and formation of H_2. For high temperatures ($T > 3 \cdot 10^4$ K) we adopt the cooling function by Wiersma et al. (2009). It assumes that the ISM is in equilibrium where the cooling due to collisional ionisation is balanced by the heating of the cosmic UV-radiation (Haardt and Madau, 2001). Further, the absolute cooling rate is determined by following the model of Aumer and White (2013) and depends on the local gas density, gas temperature and includes metal line cooling from 11 species (H, He, C, N, O, Ne, Mg, Si, S, Ca and Fe).

9.2.5 Shielding mechanisms from the interstellar radiation field

For the hydrogen chemistry the ISRF photo dissociation rate R_{pd,H_2} acting on H_2 is affected by the shielding of dust and the self shielding of H_2. Dust has the ability to absorb photons of the ISRF field and re-emit in the infrared while absorbing the energy difference. Self-shielding by molecular hydrogen is more complicated. The process normally refers to a mechanism where the photo excitation transitions become optically thick and shield each other if UV radiation is coming from a single direction. However, in the optical thick limit (high column densities) this process is prevented by the line broadening of the Lyman and Werner bands (e.g. Gnedin and Draine, 2014). In this regime the self shielding by dust becomes the more important process. We include both processes, the self-shielding by dust and molecular hydrogen. This is implemented with the TreeCol-algorithm (Clark et al., 2012; Hu et al., 2016).

9.2.6 Numerical resolution and performance

Although the single particles have very small masses ranging from 0.1 $M_\odot$ to 100 $M_\odot$ this is not the effective resolution of the simulations. For methods that follow an SPH-like volume distribution the relevant spatial resolution is the size of the kernel or to be more specific the radius of compact support. For the SPH runs we use a Wendland C4 kernel with 100 neighbours while we use a cubic spline

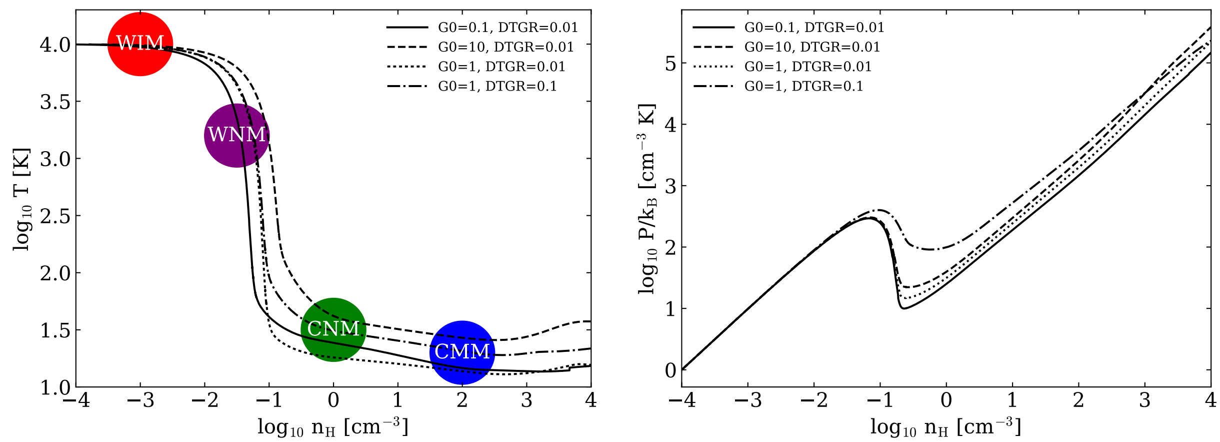

Figure 9.1: Equilibrium phase diagrams for temperature (top) and pressure (bottom) for a metallicity of 0.1 $Z_\odot$. We show the curves for different values of G_0 and dust-to-gas ratios (DTGR). These variations only affect the high density and low temperature regimes. The four different ISM regimes, warm ionised medium (WIM), warm neutral medium (WNM), cold neutral medium (CNM) and cold molecular medium (CMM) for the SN blast wave simulations are indicated by the coloured circles. The thermally unstable regime at densities 10^{-2} to 10^{-1} cm^{-3} can be identified in the bottom panel.

with 32 neighbours for the MFM runs to capture the fluid properties. The effective spatial and mass resolution is higher for the runs with MFM as the radius of compact support is smaller for the cubic spline and it can operate with a smaller number of neighbours. The resulting mass resolution can be calculated via

$$m_{\rm resolved} = N_{\rm ngb} m_{\rm gas} \left(\frac{h}{H}\right)^3, \tag{9.9}$$

where h is the smoothing length and H is the radius of compact support of the respective kernel. For the cubic spline we find the relation $h = 0.55H$ and for the Wendland C4 kernel $h = 0.45H$. Therefore, the resolution for MFM is better by about a factor of 2. While the MFM method requires more memory than SPH methods (a factor of 1.5) it is overall faster in solving the equations of hydrodynamics compared to our state-of-the-art SPH solver (for the same number of neighbours).

9.2.7 Initialisation and naming convention

In our default runs we adopt a metallicity of $Z = 0.1$ Z$_\odot$ with a constant the dust to gas ratio mass ratio of 0.01. The constant UV-background (Haardt and Madau, 2012) has a normalisation factor of $G_0 = 1.7$ for the interstellar radiation field, which corresponds to the value of the solar neighbourhood. For resolution we refer to the gas particle mass. The four resolution levels are 100 M$_\odot$ (L1), 10 M$_\odot$ (L2), 1 M$_\odot$ (L3) and 0.1 M$_\odot$ (L4). The SN blast waves are simulated in the cold molecular medium (CMM) with $n = 100$ cm^{-3}, the cold neutral medium (CNM) with $n = 1$ cm^{-3}, the warm neutral medium (WMN) with $n = 0.1$ cm^{-3} and the warm ionised medium. Some runs have lower $Z = 0.01$ $Z_\odot$ (Z-001) and and higher $Z = 1 Z_\odot$ (Z-1) metallicities. A different number density compared to our defaults is indicated with n and the number density in units of cm^{-3}. Runs with isotropic thermal conduction are indicated by *cond*.

Table 9.1: Simulation parameters for supernovae in homogeneous ambient media

Simulation Name	ambient n [cm^{-3}]	ambient T [K]	metallicity [$Z_\odot$]	chemistry	m_{gas} [$M_\odot$]	solver	SN-feedback resolved
Cold Molecular Medium							
CMM-L1	100	10	0.1	100% H_2	100	MFMH	✗
CMM-L2	100	10	0.1	100% H_2	10	MFM	•
CMM-L3	100	10	0.1	100% H_2	1	MFM	✓
CMM-L4	100	10	0.1	100% H_2	0.1	MFM, SPH	✓
CMM-cond-L4	100	10	0.1	100% H_2	0.1	SPH	✓
CMM-Z1-L1	100	10	1	100% H_2	100	MFM	✗
CMM-Z1-L2	100	10	1	100% H_2	10	MFM	•
CMM-Z1-L3	100	10	1	100% H_2	1	MFM	✓
CMM-Z1-L4	100	10	1	100% H_2	0.1	MFM	✓
CMM-Z001-L1	100	10	0.01	100% H_2	100	MFM	✗
CMM-Z001-L2	100	10	0.01	100% H_2	10	MFM	•
CMM-Z001-L3	100	10	0.01	100% H_2	1	MFM	✓
CMM-Z001-L4	100	10	0.01	100% H_2	0.1	MFM	✓
Cold Neutral Medium							
CNM-n10-L1	10	100	0.1	100% H	100	MFM	✗
CNM-n10-L2	10	100	0.1	100% H	10	MFM	•
CNM-n10-L3	10	100	0.1	100% H	1.0	MFM	✓
CNM-n10-L4	10	100	0.1	100% H	0.1	MFM, SPH	✓
CNM-n10-cond-L4	10	100	0.1	100% H	0.1	SPH	✓
CNM-L1	1	100	0.1	100% H	100	MFM, SPH	✗
CNM-L2	1	100	0.1	100% H	10	MFM, SPH	•
CNM-L3	1	100	0.1	100% H	1.0	MFM, SPH	✓
CNM-L4	1	100	0.1	100% H	0.1	MFM, SPH	✓
CNM-cond-L4	1	100	0.1	100% H	0.1	SPH	✓
CNM-Z1-L1	1	100	1	100% H	100	MFM, SPH	✗
CNM-Z1-L2	1	100	1	100% H	10	MFM, SPH	•
CNM-Z1-L3	1	100	1	100% H	1.0	MFM, SPH	✓
CNM-Z1-L4	1	100	1	100% H	0.1	MFM, SPH	✓
CNM-Z001-L1	1	100	0.01	100% H	100	MFM, SPH	✗
CNM-Z001-L2	1	100	0.01	100% H	10	MFM, SPH	•
CNM-Z001-L3	1	100	0.01	100% H	1.0	MFM, SPH	✓
CNM-Z001-L4	1	100	0.01	100% H	0.1	MFM, SPH	✓
Warm Neutral Medium							
WNM-L1	0.1	4000	0.1	100% H	100	MFM	✗
WNM-L2	0.1	4000	0.1	100% H	10	MFM	✓
WNM-L3	0.1	4000	0.1	100% H	1.0	MFM	✓
WNM-L4	0.1	4000	0.1	100% H	0.1	MFM, SPH	✓
WNM-cond-L4	0.1	4000	0.1	100% H	0.1	SPH	✓
WNM-Z1-L1	0.1	4000	1	100% H	100	MFM, SPH	✗
WNM-Z1-L2	0.1	4000	1	100% H	10	MFM	✓
WNM-Z1-L3	0.1	4000	1	100% H	1.0	MFM	✓
WNM-Z1-L4	0.1	4000	1	100% H	0.1	MFM	✓
WNM-Z001-L1	0.1	4000	0.01	100% H	100	MFM	✗
WNM-Z001-L2	0.1	4000	0.01	100% H	10	MFM	✓
WNM-Z001-L3	0.1	4000	0.01	100% H	1.0	MFM	✓
WNM-Z001-L4	0.1	4000	0.01	100% H	0.1	MFM, SPH	✓
Warm Ionised Medium							
WIM-L1	0.01	8000	0.1	100% H^+	100	MFM	✗
WIM-L2	0.01	8000	0.1	100% H^+	10	MFM	✓
WIM-L3	0.01	8000	0.1	100% H^+	1.0	MFM	✓
WIM-L4	0.01	8000	0.1	100% H^+	0.1	MFM, SPH	✓
WIM-cond-L4	0.01	8000	0.1	100% H^+	0.1	SPH	✓
WIM-Z1-L1	0.01	8000	1	100% H^+	100	MFM	✗
WIM-Z1-L2	0.01	8000	1	100% H^+	10	MFM	✓
WIM-Z1-L3	0.01	8000	1	100% H^+	1.0	MFM	✓
WIM-Z1-L4	0.01	8000	1	100% H^+	0.1	MFM	✓
WIM-Z001-L1	0.01	8000	0.01	100% H^+	100	MFM	✗
WIM-Z001-L2	0.01	8000	0.01	100% H^+	10	MFM	✓
WIM-Z001-L3	0.01	8000	0.01	100% H^+	1.0	MFM	✓
WIM-Z001-L4	0.01	8000	0.01	100% H^+	0.1	MFM	✓
WIM-n0001-L1	0.001	10000	0.1	100% H^+	100	MFM, SPH	✗
WIM-n0001-L2	0.001	10000	0.1	100% H^+	10	MFM	✓
WIM-n0001-L3	0.001	10000	0.1	100% H^+	1.0	MFM	✓
WIM-n0001-L4	0.001	10000	0.1	100% H^+	0.1	MFM	✓
WIM-n0001-cond-L4	0.001	10000	0.1	100% H^+	0.1	SPH	✓
WIM-Z1-L4	0.001	10000	1	100% H^+	0.1	MFM, SPH	✓
WIM-Z001-L4	0.001	10000	0.01	100% H^+	0.1	MFM, SPH	✓

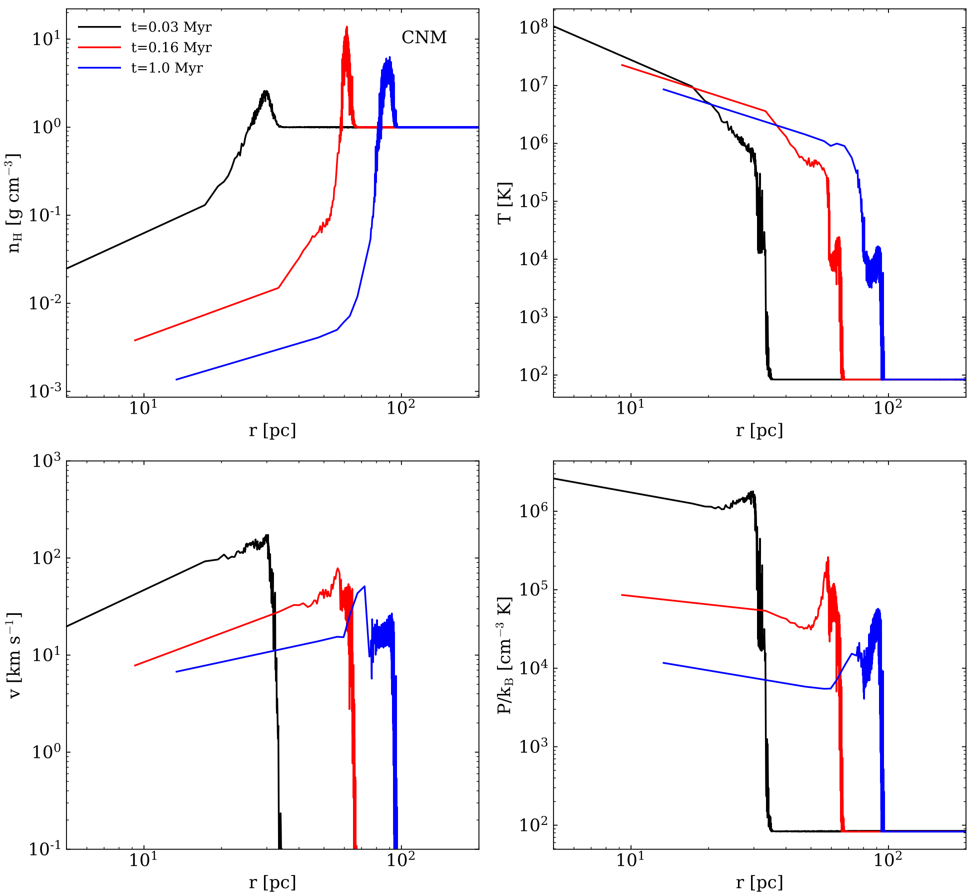

Figure 9.2: Hydrogen number density (top left), temperature (top right), velocity (bottom left) and pressure (bottom right) for the simulation CNM-L4 as a function of the radius. We display the results at three different points in time that represent different phases of the blast wave. The black lines indicate $t = 0.04$ Myr where the shock is at the end of the energy conserving ST-phase. The red lines show $t = 0.14$ Myr. In this regime the cooling time is shorter than the total time of the simulation (roughly 0.08 Myr) and the system is dominated by cooling. The blue lines show the properties of the shock at the end of the simulation when the shock merges with the ambient medium. All properties of the shock are resolved in each investigated regime of the shock. *Top Left:* In the ST-phase (black line) the shock is resolved in the adiabatic regime. In the cooling dominated regime (red line) the maximum density exceeds the expected adiabatic solution by a factor 3.5. At the end of the simulation (blue line) the density decreases again and the shock starts to merge with the ambient medium. *Top Right:* The temperatures in the post-shock region are very high (above 10^8 K). When cooling dominates energy is radiated away and the temperature starts to decrease by an order of magnitude. *Bottom Left:* In the beginning the shock moves very fast outwards (a few 100 km s^{-1}) but gets slower at later times. *Bottom Left:* The pressure is roughly constant during the ST-phase of the shock but starts to decrease very fast after shell formation.

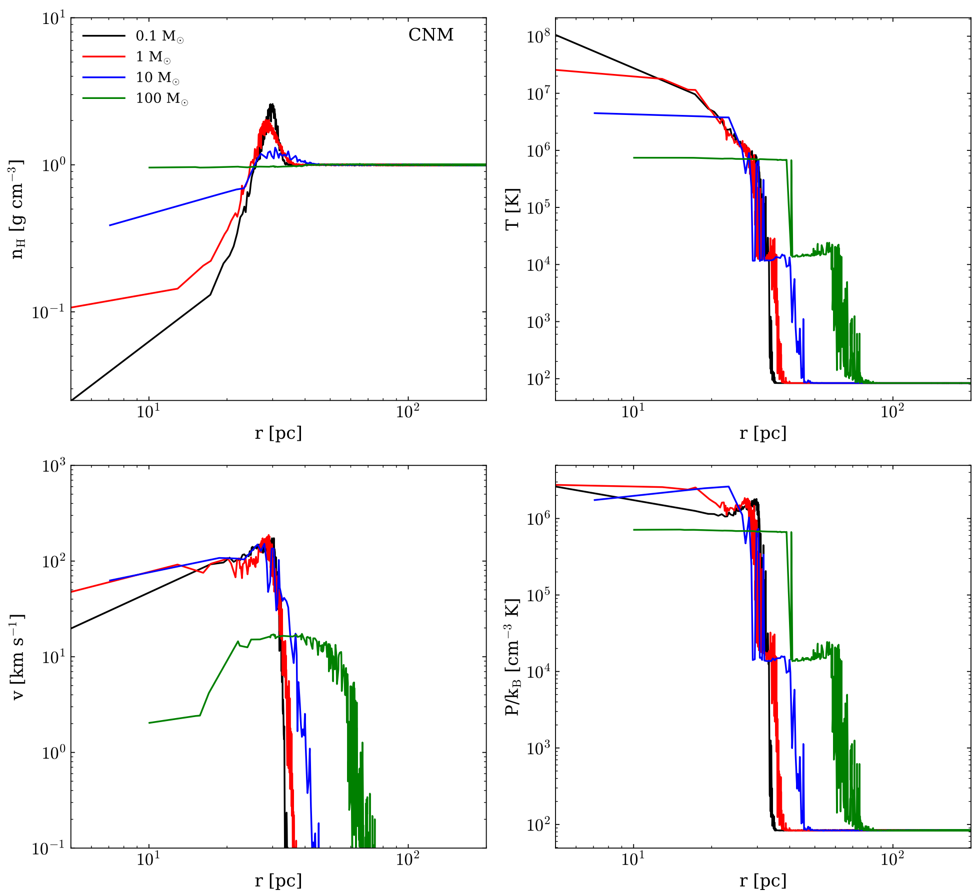

Figure 9.3: Different properties of the SN-remnant as a function of the radius in the ST-phase (t= 0.04 Myr) for all mass resolutions in the CNM. The black lines show the 0.1 $M_\odot$, the red lines the 1 $M_\odot$ resolution, the blue lines the 10 $M_\odot$ and the green lines the 100 $M_\odot$ resolution. *Top Left:* Density of the shock as a function of radius. With decreasing resolution the shock becomes less and less resolved. At the two highest mass resolutions we can detect the shock very well in the ST-phase. A the highest mass resolution we find the maximum density increased by a factor 3.5 compared to the ambient density. While we can still detect the shock in the ST-phase for the 10 $M_\odot$ resolution the shock in the density completely vanishes at the lowest resolution. *Top Right:* Temperature structure of the shock. The three highest mass resolutions agree well apart from the maximum temperature within the bubble. At the lowest mass resolution, we find that the shock is at a different radial position which corresponds to the larger injection region in this regime. *Bottom Left:* Velocity structure of the shock in the ST-phase. The three highest mass resolutions agree very well, while at the lowest resolution the velocity structure remains unresolved. *Bottom Right:* Pressure in the remnant. For the three highest resolutions we find that the pressure is well resolved. For the lowest resolution the pressure in the bubble is already significantly lower, compared to the higher resolution runs.

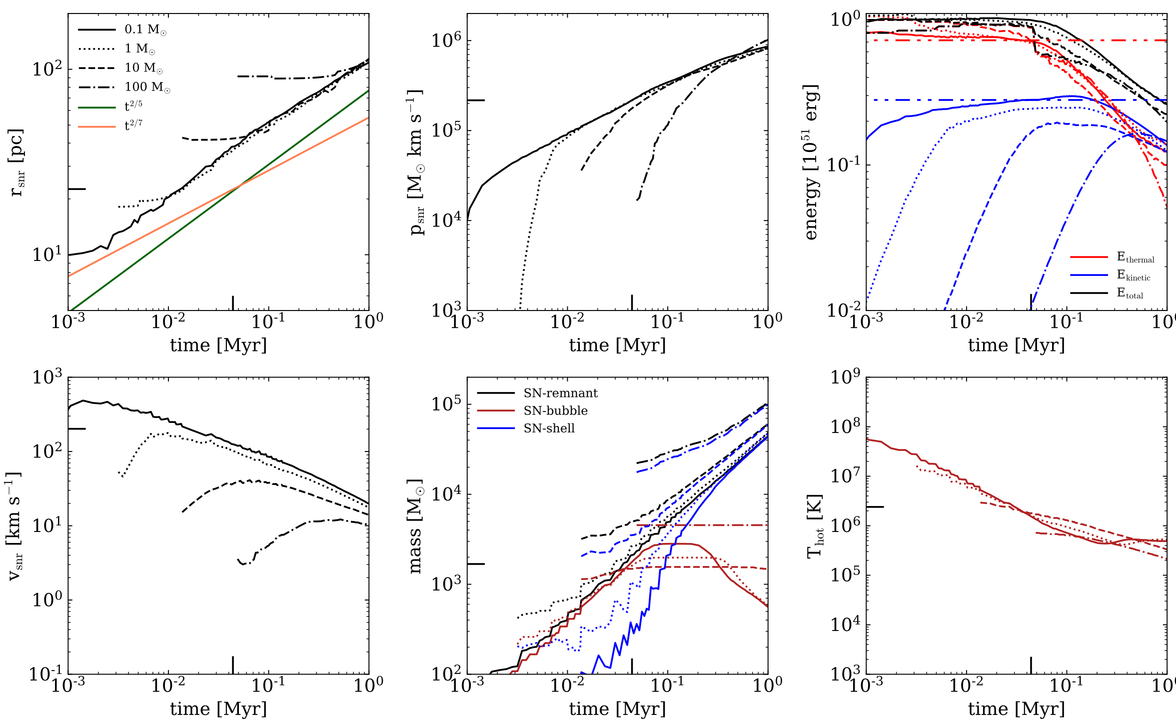

Figure 9.4: Evolution of supernova remnants in the CNM at four different resolution levels of 0.1 $M_\odot$ (solid), 1 $M_\odot$ (dotted), 10 $M_\odot$ (dashed) and 100 $M_\odot$ (dashed-dotted). The black markers on the axis represent the physical values at the end of the ST-phase. *Top Left:* Time evolution of the shell radius with the analytical values of $r \propto t^{2/5}$ (green) and $r \propto t^{2/7}$ (red) for Sedov phase and the momentum conserving phase, respectively. Our results converge for mass resolution higher than 10 $M_\odot$. *Top Middle:* The shell momentum as a function of time is relatively insensitive to resolution. *Top right:* Total energy (black), kinetic energy (blue) and thermal energy (red) as a function of time. The total energy is conserved in the ST-phase with 28 per cent kinetic and 72 per cent thermal energy (dot-dot-dashed lines). The kinetic energy builds up during shell formation (we inject only thermal energy) and reaches the ST-solution only for the highest mass resolution. The 10 $M_\odot$ run only creates $\sim$ 20 per cent kinetic energy. *Bottom Left:* The shell velocity as a function of time strongly depends on resolution. At the end of the Sedov phase it ranges from 30 km s^{-1} to $200 kms-1$ for low and high resolution, respectively. *Bottom Middle:* The shell mass a function of time is smaller at higher resolution. *Bottom right:* Bubble temperature (red) as a function of time. At low mass resolution the bubble temperature and therefore its pressure remain unresolved. At mass resolution higher than 10 $M_\odot$ the bubble temperature at the Sedov time is captured. At 100 $M_\odot$ the temperature evolution is unresolved.

9.3 Individual supernova blast waves

We present a set of simulations of individual SN blast waves in six different environments at equilibrium conditions of the ISM for our cooling model. In the upper panel of Figure 9.1 we show the temperature as a function of hydrogen number density for different values for a (constant) interstellar radiation field and the dust to gas ratio (DTGR). The coloured circles indicate the ISM conditions for WIM, WNM, CNM and CMM. The CMM represents regimes in dense molecular clouds (n_H = 100cm^{-3}, T = 10 K, fully molecular). The CNM has higher temperatures and densities such that hydrogen is present in neutral atomic form (n_H = 1cm^{-3}, T = 100 K, fully neutral). The WNM is warmer but still neutral (n_H = 0.1cm^{-3}, T = 8000 K, fully neutral) and the WIM is fully ionised with long cooling times (n$_H$ = 0.001cm^{-3}, T= 10000 K, fully ionised). The pressure vs. density plot in the bottom panel highlights the pressure-unstable regime between 10^{-2} and 10^{-1} cm^{-3}. We initialise each supernova event by a kernel-weighted injection of 10^{51} erg of thermal energy into all kernel particles. For the MFM-solver we hereby use 32 particles and cubic-spline (M4) kernel. For the respective SPH runs we use a Wendland C4 kernel with 100 neighbours. Experience has shown that MFM with a cubic spline and 32 neighbours shows the same quality of capturing fluid flows as the SPH reference runs with 100 neighbours and a Wendland C4 kernel. In the case of SPH the higher neighbour number is needed to suppress the intrinsic noise of particles methods by smoothing over the fluid field. However, the well known and investigated pairing-instability makes it than necessary to use a higher order kernel with positive Fourier transformation. The initial phase of free expansion is very short (only a few 100 yr) and is not modelled here. The initial conditions are summarised in Table 9.1.

9.3.1 Blast wave evolution

In Figure 9.2 we show the radial profiles of the hydrogen number density (top left), the temperature (top right), the relative velocity of the shock (bottom left) and the thermal pressure (bottom right) for a blast wave in the CNM at the highest resolution of 0.1 M$_\odot$, which implies a spatial resolution of around 1 pc. The different colours show the system at time t = 0.04 Myr (black) during the ST-phase, at t = 0.16 Myr (red) after the formation of a dense cooling shell, and at t = 1.0 Myr (blue) when the remnant starts to merge with the ISM. In the ST-phase the maximum value of the density is around 3.53 cm^{-3}. In the case of the pure adiabatic solution we would expect a maximum density of 4 cm^{-3} under constraint of the Rankine-Hugoniot jump-conditions with an adiabatic index of $5/3$ which is adopted in all our simulations. After the end of the ST-phase shell remnant has formed a thin, cooling dominated shell with a maximum density of roughly 20 times the initial ambient density. At the end of the simulation the amplitude of the density decreases again and the remnant starts to merge with the ambient ISM. In all three stages the temperature declines as a function of the radius. After shell we can observe a bump in the temperature distribution at around 10^4 K which can be identified as the dense cooling shell of the remnant. This shell grows over time as more and more gas from the initially hot bubble starts to cool. The velocities within the ST-phase are high which can lead to a velocity dispersion of roughly 10 km s^{-1} that is observed within the ISM. At later stages the remnant slows down until it finally reaches the point where it merges with the ISM. Initially, the pressure is large (especially in the bubble) but decreases about an order of magnitude within the later evolutionary stages. While the results do not compare well with studies that are carried out in fewer dimensions (Badjin et al., 2016; Blondin et al., 1998; Thornton et al., 1998) in terms of peak density in the Sedov-Taylor phase and in terms of resolving fluid instabilities that are certainly important in supernova-remnant modelling, we note that we compare well to other grid code results in three dimensions (e.g. Kim and Ostriker, 2015) who find a maximum value between 3.3 and 3.5 in their respective Sedov-Taylor phase.

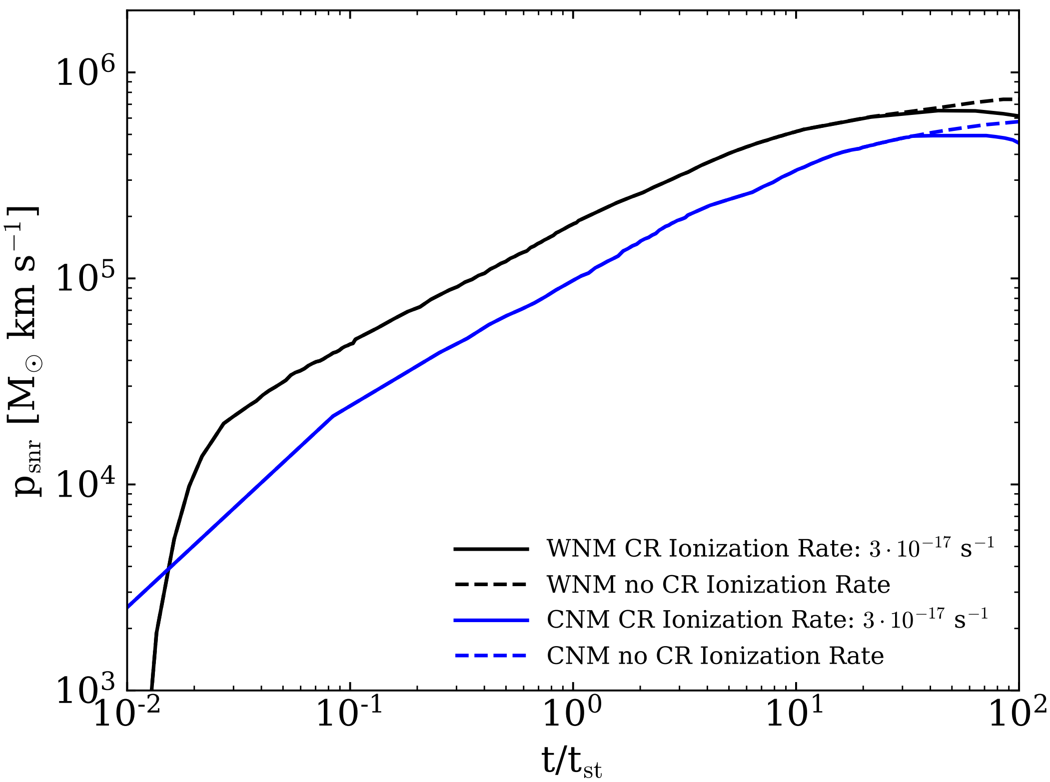

Figure 9.5: Momentum evolution normalised to the end of the ST-phase as defined in section 9.3 for two remnants with and without cosmic-ray ionisation heating included in the cooling function in the WNM and the CMM. The momentum conserving snow-plough phase is reached later and at higher shell momentum if cosmic-ray ionisation heating is not included. This is due to a lower ambient equilibrium temperature and a longer PDS phase. The pressurised shell is evolving into the lower pressure ambient medium, by 20 per cent, and delays saturation of momentum. This happens slightly earlier at lower ambient densities as the ambient temperature is higher than in the higher density regime.

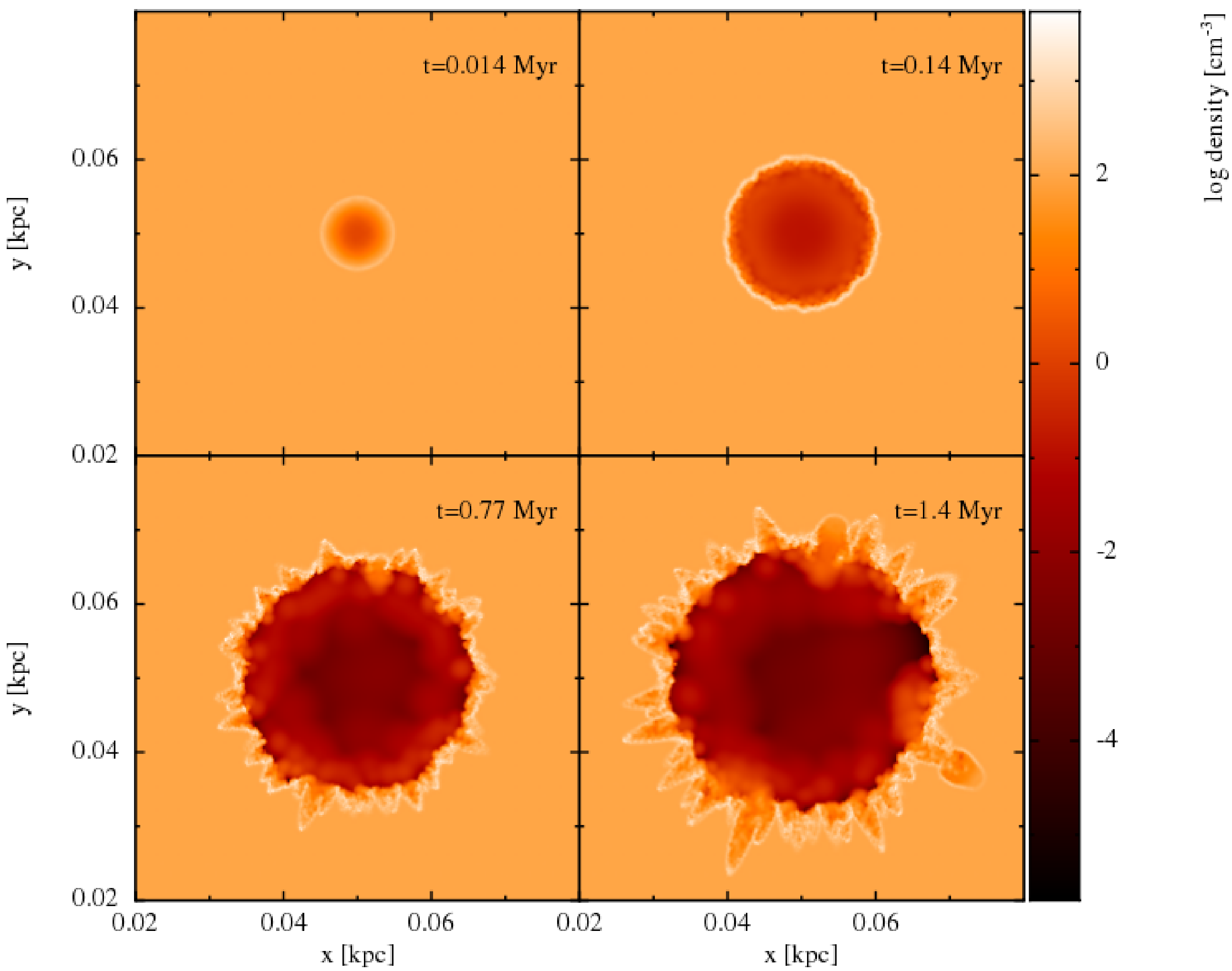

Figure 9.6: Time evolution for four different point in time of a supernova-feedback event in the cold molecular medium. Initially, in the ST-phase we can observe a spherical remnant (top left). Once the thin shell has formed (top right), the bubble supports the evolution of the shell until it they reach pressure equilibrium and the remnant moves outwards with constant velocity. At later times, the shell starts to become unstable due to Ryu-Vishniac-instabilities, that start to grow after roughly 100 ST-times (bottom left), until they dominate the structure in the outer parts of the remnant (bottom right).

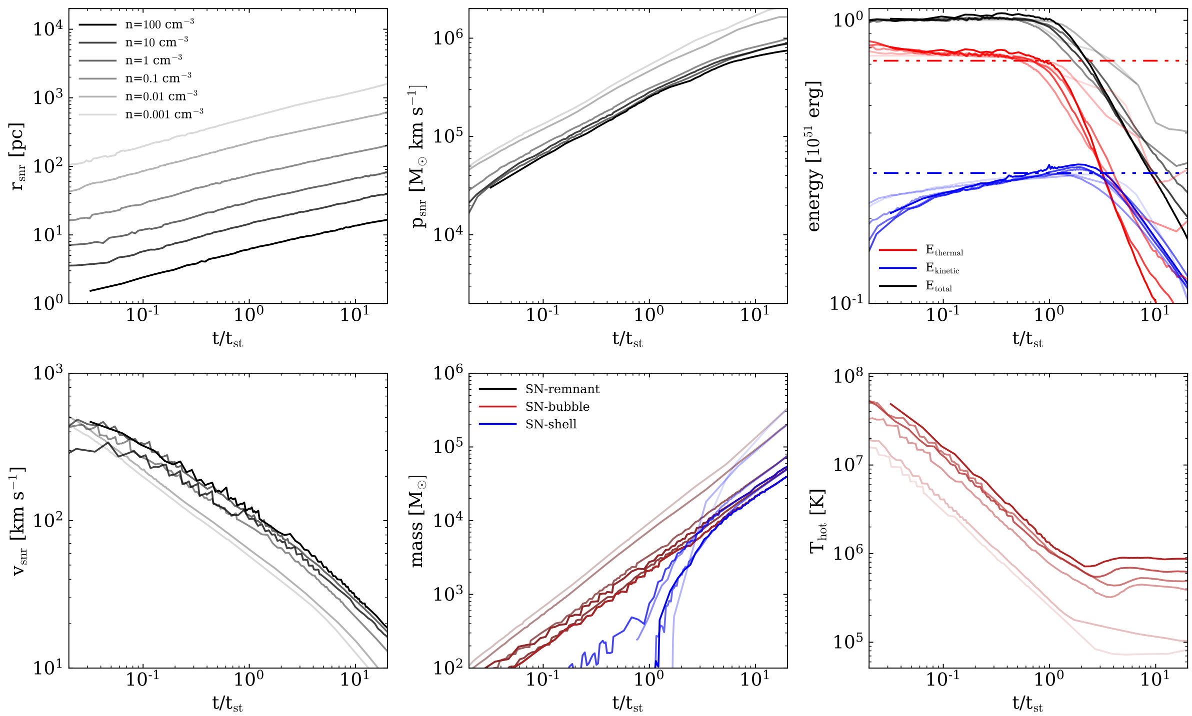

Figure 9.7: Comparison of physical properties of SN-blastwaves for different ambient densities for our highest all our highest resolution runs. For all runs the ST-phase is well resolved at our highest mass resolution. For better comparison we normalised the time axis to the respective ST-time that we derive in Figure 9.8. *Top Right:* In the high ambient media the radii become significantly smaller. While at the highest ambient medium the remnant has a size of a few parsec at the end of the ST-phase, we find that in the lowest ambient medium the remnant has a size of roughly 700 parsec at the end of the ST-phase. *Top Middle:* The remnants in ambient media with the highest density generate most momentum within the ISM. These remnants have the longest cooling times but fill the highest volume and therefore generate most momentum at the end of the ST-phase *Top Right:* Energy in the shocked region split up in kinetic energy (blue), thermal energy (red) and total energy (black). In all environments the evolution towards the ST-phase is given and we find that 28 per cent of the energy is deposited in kinetic energy while 72 per cent is in thermal energy before cooling takes over and thermal energy is radiated away after the end of the ST-phase. *Bottom Left:* In the beginning the remnants in the lowest density environments are the fastest, while at the end of the ST-phase they are the slowest. *Bottom Middle:* The remnants with the highest mass at the end of ST-phase are those in the low density environments. Therefore, they have the highest momenta at the end of the ST-phase but also the lowest velocity. *Bottom Right:* The temperature in the bubble decreases with decreasing ambient density. This phase is important because it generates the pressure in the bubble which makes it possible to drive outflows.

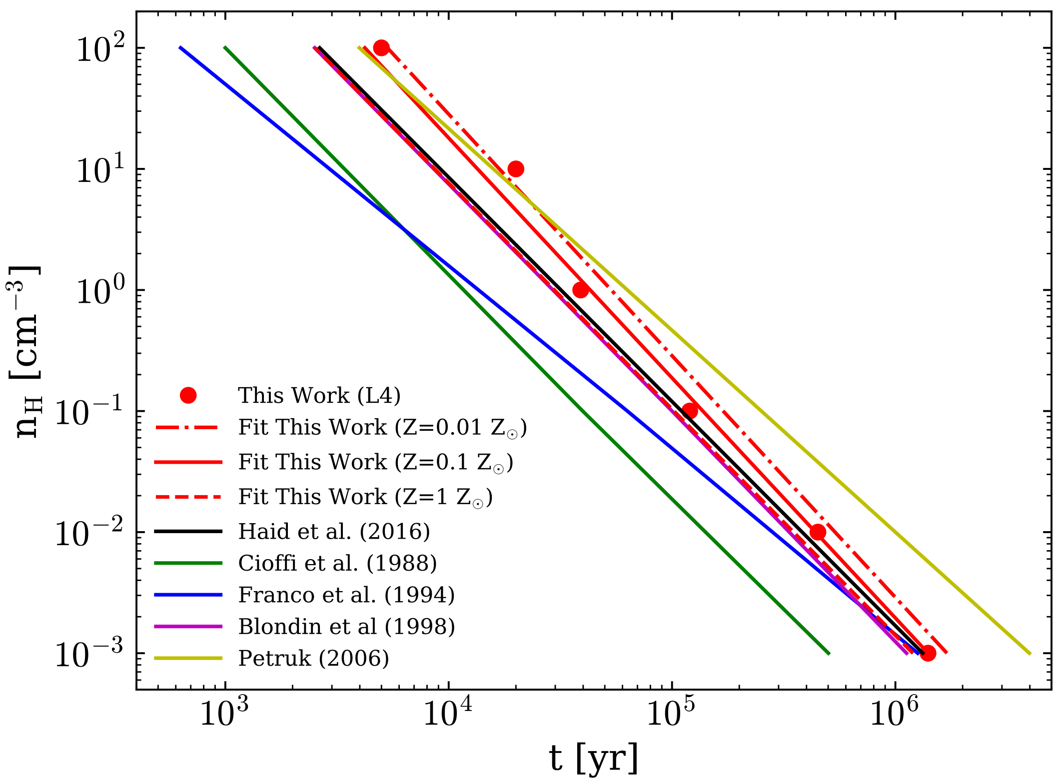

Figure 9.8: Shell formation times for different ambient densities at our highest resolution level. We show the data for our highest resolution run (red dots) for a metallicity of $Z = 0.1\ Z_\odot$ (red solid line). For the two other metallicities we tested we only show the fitting function that we obtain in the $Z = 1\ Z_\odot$ regime (red dashed line) and in the $Z = 0.01\ Z_\odot$ regime (red dashed-dotted line). We find reasonable agreements with the fits provided by Blondin et al. (1998), Haid et al. (2016), Cioffi et al. (1988), Franco et al. (1994) and Petruk (2006). Note that all authors use slightly different cooling functions and some results are from (semi-)analytical computations.

However, we note that we focus on low metalicity environments while (Kim and Ostriker, 2015) is focusing on solar metallicity environments. This leads to differences in blast wave evolution which we discuss in section 9.3.3. Moreover, we note that we observe a clear drop in the pressure between bubble and shell which indicates some contribution of the thermal instability in our highest resolution runs, although we see only a drop of 0.5 dex while higher resolution state-of-the-art simulations of detailed blast wave evolution report 1 dex (e.g. Badjin et al., 2016) and we do not properly resolve it at the presented resolutions throughout the paper. However, as we carry out these simulations to test which supernova-remnant properties can be modelled in current high resolution galaxy formation simulations, resolving the thermal instability in the remnant is not the main goal of the paper. Nevertheless, it would be very interesting to study the detailed effect of the thermal instability on momentum and hot phase generation in higher resolution simulations with our code in future studies. In this context, we have to consider the inability of capturing the analytic predicted value of the density and the inability of fully capturing the thermal instability as a limitation that has to be noted. However, despite this limitations which can be resolved at higher resolution or in lower dimensionality, the ability to model radial momentum input and hot phase at our target resolutions is worth noting as it enables the galaxy scale studies of outflows that are self-consistently driven by the the supernova-feedback without the limitations that common subgrid-models are tied to.

To understand the details of the blast waves evolution we investigate the remnant at different mass resolutions. In Figure 9.3 we show the remnant in the CNM during the ST-phase for all four mass resolutions that we investigated. We note that the shock is well resolved at the highest mass resolutions for the simulations CNM-L4 and CNM-L3. While the shock is still sufficiently resolved in the adiabatic regime in CNM-L2 it is completely unresolved for CNM-L1. This is mainly due to the fact that we have a lower amount of resolution elements in the same spatial region to actually resolve the shock properly in the adiabatic regime. Therefore, to capture the shock within the ST-phase a mass resolution of smaller than 10 solar masses is needed for the MFM-solver. We mark runs that are resolved (green check), weakly resolved (black dot) and unresolved (red crosses) in Table 9.1. Further, we note differences in the cooling dominated regime. At the highest mass resolutions a thin, cooling dominated shell is forming following the end of the ST-phase. The density within this supernova shell is up to 10 times higher than what we would expect to see in a pure adiabatic simulation of the shock front. However, with lower resolution this dense cooling shell becomes less and less resolved and remains unresolved at a mass resolution of 100 $M_\odot$. We note that this becomes even worse for a different ambient configuration. If we consider the runs in the CMM the shock is less well resolved even at higher mass resolution. In the last evolution stage of the remnant the density decreases again and starts to merge with the ambient medium for all mass resolutions. We note that in these simulations we cannot capture the phase in which the SN-remnant merges with the ambient medium as the configuration of our ambient medium is chosen to be of uniform density and zero velocity. Consequently, our ambient medium is not turbulent which would be necessary to properly capture the merging phase of the shock with the ambient medium.

9.3.2 Resolution effects

For an accurate simulation of a supernova blast wave for applications in galaxy scale simulations it is important to capture the formation of the swept-up shell, which also determines the cooling properties of a supernova remnant (e.g. Kim and Ostriker, 2015). For example Hu et al. (2016) have shown for SPH that the shell momentum is relatively insensitive to numerical resolution. However, the shell mass and velocity are strongly affected by higher velocities and lower shell masses at high resolution. At insufficient resolution the shell becomes too massive, slower and cools too early, resulting in a too

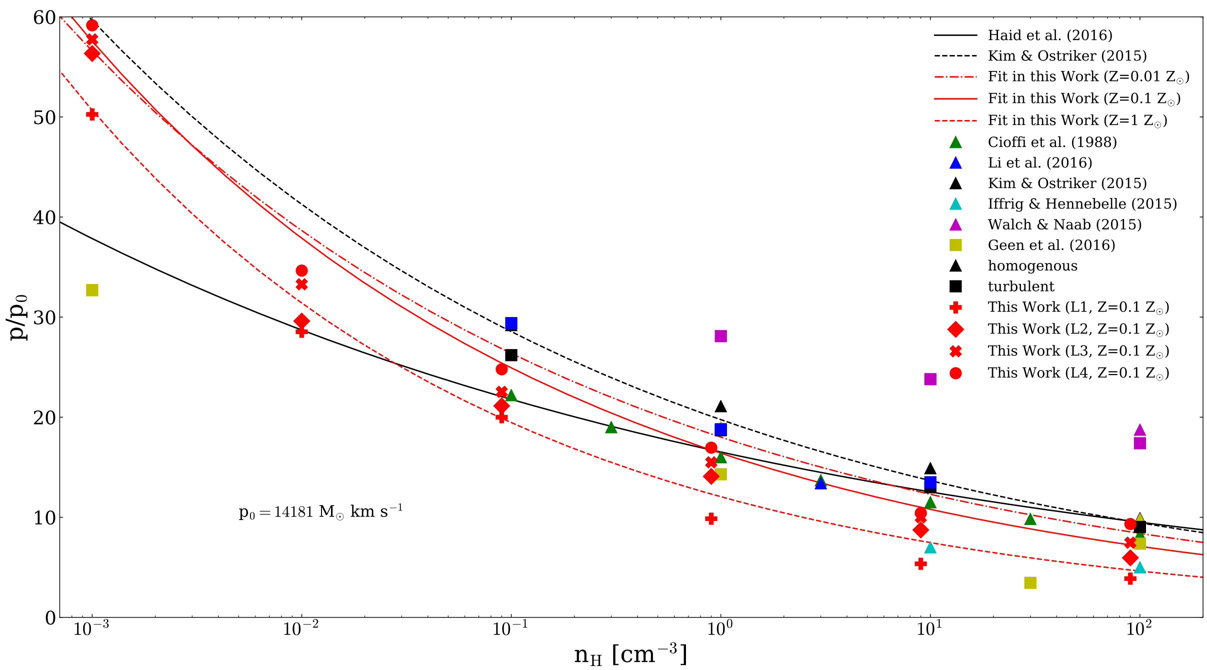

Figure 9.9: Momentum boost at the time of shell formation for blast waves at various environmental densities normalised to a fiducial initial momentum of p_0 = 14181 $M_{\odot}$km s^{-1}. The coloured symbols show results from three dimensional numerical simulations (apart from Cioffi et al. (1988) and Haid et al. (2016)) with homogeneous (triangles), structured or turbulent (cubes) ambient media carried out with three different grid codes and a particle based SPH code. The red symbols show the supernova momenta obtained in this work at the end of the energy conserving ST-phase for our four different resolution levels in a homogeneous medium. At the lowest resolution the momenta can be underestimated by up to a factor 2. The lines show the fits from Haid et al. (2016), Kim and Ostriker (2015), and the highest resolution of this work for all three adopted metallicities. We show the results obtained for a metallicity of 0.1 $Z_{\odot}$ as red symbols for all environmental densities and mass resolutions. We note that we shifted the red symbols slightly to the left to show the results of other work below.

rapid termination of the ST-phase. Similar results have been found by Kim and Ostriker (2015) for Eulerian grid simulations. However, they focused on solar metallicity environments while we focus our study on sub-solar metallicities. The material in the shell has a temperature below $2 \cdot 10^4$ K. All material above this temperature cut belongs to the hot phase of the remnant. Additionally, we set a velocity cut of 0.1 km s^{-1} to select the ambient medium which is at rest form the bubble and the shell. The shell radius is defined by the position of the 10 particles with the highest densities. The radial shell momentum is computed by summing up the individual particle momenta, and the shell velocity is the shell momentum divided by the shell mass.

In Figure 9.4 we show shell radius (top left), shell momentum (top middle), shell energy (top right), split in kinetic (blue) and thermal energy (red), shell velocity (bottom left), shell mass and bubble mass (bottom middle), as well as the bubble temperature (bottom right). We present the four resolution levels with 0.1 $M_\odot$ (solid line), 1.0 $M_\odot$ (dashed-line), 10 $M_\odot$ (dash-dot-line), 100 $M_\odot$ (dash-dot-dot-line) for a medium with $n = 1$ cm^{-3} consisting of neutral hydrogen (CNM-L4 to CNM-L1). The small black dashes on the axis indicate the end of the ST-phase and the numerical values of the respective quantity for this point in time. We note that instead of showing the pressure in shell and bubble, we show the temperature structure within the hot bubble. The pressure within the bubble can be computed at any time by multiplying the densities within shell and bubble with the related temperatures. Moreover, we note that the lines for different resolutions start at different points in time because in the lower resolution runs the shock can not be separated from the ambient density field by the time at which the respective lines start. This is due to the fact that the shock remains unresolved until the respective points in time. In the top left panel of Figure 9.4 before shell formation $t < t_{sf}$ at the end of the Sedov phase, the radius is increasing as $r \propto t^{2/5}$ (Sedov, 1946; Taylor, 1950) (green line). At shell formation ($t_{sf} = 45000$ yr) the slope changes $r \propto t^{2/7}$ for the momentum conserving phase. We define our Sedov-Taylor time t_{st} as the (final) time when the thermal energy drops below the analytical value of 72 per cent. The three highest resolution levels capture the shell radius at formation and its evolution within 10 per cent. The shell momentum (top middle panel of Figure 9.4) is relatively insensitive to resolution and well captured at the three highest resolution levels. Further, our results are in good agreement with results from Kim and Ostriker (2015) and Hu et al. (2016). The shell velocity and mass, however, depend strongly on resolution (bottom left and middle panel of Figure 9.4). With higher resolution the remnant velocity increases and the remnant mass decreases as the shock is better resolved. However, we note that a part of this trend is related to our feedback scheme. We further distinguish between the total mass of the remnant (black), the mass in the cold shell (blue) and the mass in the hot bubble (red). With decreasing resolution the mass within the bubble is lower apart from the lowest resolution run where the initially heated particles generate a too high hot mass. However, as the structure of the shell is so poorly resolved in these runs those particles cool very inefficiently and the hot mass is over predicted. For lower mass resolution we inject initially in more mass, leading to more initial swept-up material. This has consequences for the shell momentum at lower resolution. In the 10 $M_\odot$ run the shell momentum is too high because of this reason, which renders the shell momentum a bad tracer to determine whether the ST-phase is resolved. The evolution of shell and bubble temperature is shown in the lower right panel. At the two highest resolution levels the bubble temperatures are resolved to within 10 per cent. At the lowest mass resolution the temperature structure of the hot bubble is unresolved.

9.3.3 Blastwave evolution past the ST-phase

While we focus on the evolution of the blastwaves within the ST-phase to investigate how momentum and hot mass are generated in this evolutionary state we briefly want to discuss the transition from the

ST-phase to the PDS and finally the MCS phase. However, we note two major differences to other studies (e.g. Kim and Ostriker, 2015). Our main focus is on sub-solar metallicity environments, as they can be found in present day dwarf-galaxies or at higher redshifts. Moreover, our cooling-function is non static and we excluded the effect of cosmic-ray ionisation to study SN-feedback in high density and very low temperature environments. Thus, we find three times higher terminal momenta compared to solar metallicity studies with higher equilibrium temperatures in the ambient ISM. First, metal-line cooling is less efficient in lower metallicity environments. This leads to an increased momentum boost past the ST-phase as the bubble cools less efficiently. Second, as we exclude cosmic ray ionisation th equilibrium temperature is lower and we can gain a little momentum boost after the PDS-phase as the shell is pushing into the ISM until the ambient ISM reaches pressure-equilibrium with the shell. Thus our momentum input gives an upper limit for the momentum boost which will generally be lower in practice as we will discuss in 9.6. In Figure 9.5 we show two examples for the CMM (blue) and the WNM (black) without (dashed) and with (solid) cosmic ray ionisation heating of the ISM at a rate of $3 \cdot 10^{-17}$ s^{-1}. We see a decrease of the final momentum by roughly 20 per cent if we switch on cosmic ray ionisation heating as the ambient pressure is higher and the shell cannot generate momentum anymore while pushing into the ambient ISM. Further, the exclusion of the cosmic-ray ionisation rate has an effect on the chemistry. While the molecular hydrogen is not effected (less than the per cent level), the cosmic-ray ionisation leads to higher fractions of ionised hydrogen by a roughly 10 per cent and subsequently reduces the fraction neutral hydrogen. There is no effect on the formation of CO. Finally, we note that at the two highest mass resolutions we start to observe the fragmentation of the shell by Ryu-Vishniac type of instabilities. While we do not claim that these instabilities are fully resolved at the presented resolution, we note that they can further affect the cooling-rates that we calculate on the fly in our simulations. A detailed modelling of the cooling rate in shell and bubble plays a crucial role in modelling a supernova-event in a galactic context. The Ryu-Vishniac instabilities (even though our results are not fully converged yet) only appear in more than one dimensional simulations and thus it is important to model the SN-feedback event in three spatial dimensions as they can influence the detailed cooling rates in our chemical model. We show this for our highest resolution simulation in a time evolution of four different snapshots, in the CMM-medium in density of 100 cm^3 in Figure 9.6. We can see clear fragmentation of the remnant at very late times which is potentially caused by the Ryu-Vishniac instabilities. However, at this resolution the results could be also influenced by amplification of initial numerical noise of our particle distribution. We carefully checked the results by applying higher time resolution (i.e. decreasing the Courant number by a factor of 4) and find similar results. Moreover, we carried out a higher resolution simulation with a particle mass resolution of 10^{-4} M$_\odot$ and find similar structures.

9.3.4 Environmental dependence

The evolution of SN remnants is strongly dependent on the environment. The cooling-time scales as n^2 which has consequences for remnants in a high density environment as well as remnants in a low density environment and leads to various different shell formation times. In Figure 9.8 we show the ambient densities for all our SN-remnants at the highest resolution (L4) as a function of the shell formation time t$_{\rm sf}$. With increasing ambient densities the shell formation times become shorter and can last from a few 1000 years at 100 cm^{-3} to roughly 1.5 Myr at 0.001 cm^{-3}. As we simulate in three different metallicity regimes we show our best fits for the shell formation time individually for each metallicity as the dashed red line ($Z = 1Z_\odot$), the solid red line ($Z = 0.1Z_\odot$) and the dashed-dotted red line ($Z = 0.01Z_\odot$). For $Z = 0.1Z_\odot$ we additionally show the data from our six highest resolution runs to visualise the data with which we obtained the red solid line. The best fit relations as functions of the metallicity are given by:

$$t_{\rm st}(Z = 0.01Z_\odot) = 5.3 \cdot 10^4 {\rm yr} \cdot n^{-0.50}, \tag{9.10}$$

$$t_{\rm st}(Z = 0.1Z_\odot) = 4.2 \cdot 10^4 {\rm yr} \cdot n^{-0.50}, \tag{9.11}$$

$$t_{\rm st}(Z = 1Z_\odot) = 2.9 \cdot 10^4 {\rm yr} \cdot n^{-0.53}. \tag{9.12}$$

We compare these shell formation times to previous numerical and analytical results by Blondin et al. (1998), Cioffi et al. (1988), Franco et al. (1994), Petruk (2006) and Haid et al. (2016) and find good agreement with the recent results of Haid et al. (2016) and Petruk (2006).

In Figure 9.7 we show the blast wave evolution for all environmental densities at the highest resolution level (L4) corresponding to 0.1 $M_\odot$ for different properties of the individual SN-remnants for an ambient metallicity of $Z = 0.1Z_\odot$. With increasing ambient number density the size of the remnants at the end of the ST-phase becomes shorter and can vary over more than an order of magnitude. The momentum at the end of the ST-phase is the largest for remnants in low density environments. For all environments apart from the highest ambient density we find a trend of an increasing kinetic energy in the PDS-phase of the remnant while the thermal energy is radiated away quickly after the end of the ST-phase. The shell velocities are the highest in the low density media where the shell and bubble masses are the highest. Further, we find that the bubble temperature is higher for higher mass densities after 10 shell formation times, while the shell temperature significantly drops due to the shorter cooling times. Finally, we note that we can resolve the ST-phase for all ambient densities at our highest mass resolution. At lower mass resolution convergence can still be obtained for the three highest mass resolutions up to an ambient density of 10 cm^{-3}. For higher ambient media a mass resolution of 1 $M_\odot$ is required to resolve the ST-phase.

The shell formation time terminates the radial momentum generation phase (see Haid et al. 2016 for a detailed discussion of the momentum generating phases) and the remnant transits to the momentum conserving snow plough phase. However, we note that given our cooling function and initial conditions our simulations indicate that the momentum is further increasing past pressure balance of bubble an shell is reached. However, as we have relatively low ambient temperatures due to our cooling function that does not contain the contribution of cosmic ray heating. While this provides relative extreme conditions with high cooling rates to determine how well the code can handle blast waves in rapidly cooling environments we lack comparability towards other studies like Kim and Ostriker (2015) who employ a static cooling function with a higher equilibrium value for the temperature. For the high density environments we thus observe that the dense shell pushes further into the ISM and thus increases the momentum further until it reaches pressure equilibrium with the ambient ISM. In reality, this would be prevented by the much more complex structure of the ISM (e.g. overlapping remnants or interactions with stellar wind or magnetic fields), which we will discuss in more detail in section 9.6. For the remnants in the lower density media the situation is different as they have an equilibrium temperature of around 10^4 K in the surrounding ISM, resulting in quickly after the ST-phase established equilibrium state between shell and ambient medium, where we then fully capture the momentum conserving snow-plough phase.

In Figure 9.9 we show an updated version of Figure 4 of Naab and Ostriker (2017) with a comparison of the momentum gain for different ambient densities to previous estimates by Cioffi et al. (1988); Geen et al. (2016); Iffrig and Hennebelle (2015); Kim and Ostriker (2015); Li et al. (2017); Martizzi et al. (2015); Walch et al. (2015). Our results agree well in particular with Kim and Ostriker (2015) (despite a different cooling function) and show a momentum boost compared to the assumed initial SN momentum of $p_0 = 14181$ $M_\odot$ km s^{-1} from a factor ~ 10 at $n = 100$ cm^{-3} to a factor ~ 50 at $n = 0.001$ cm^{-3}. At low resolution this boost can be lower up to a factor of two at the highest densities. As we carried out all simulations at three different ambient metallicities, we can obtain best fit relations for all three metallicities that are given by:

$$p_{\rm st}(Z = 0.01) = 18.0 \cdot p_0 \cdot n^{-0.16}, \tag{9.13}$$

$$p_{\rm st}(Z = 0.1) = 16.4 \cdot p_0 \cdot n^{-0.18}, \tag{9.14}$$

$$p_{\rm st}(Z = 1) = 12.0 \cdot p_0 \cdot n^{-0.17}. \tag{9.15}$$

These fitting relations are shown as the red dashed-dotted ($Z = 0.01Z_\odot$), the red solid ($Z = 0.1Z_\odot$) and the red dashed line ($Z = 1Z_\odot$) in Figure 9.9. The momentum is always measured at the end of the ST-phase. We note that a remnant can still generate momentum in the pressure driven snow-plough phase until pressure equilibrium between the bubble and the shell is reached, which can lead to higher momenta by a factor of two (Haid et al., 2016; Kim and Ostriker, 2015). Compared to other studies (e.g. Haid et al., 2016; Kim and Ostriker, 2015) we follow the momentum gain for $Z = 0.1Z_\odot$ and $Z = 0.01Z_\odot$. We find a weak dependence of the final terminal momenta generated by each remnant in different metallicity environments which mostly affects the terminal momenta in the high ambient density regimes (roughly a factor of 2) while the momenta in the lowest ambient environments remain unchanged.

Finally, we show the results for the runs CMM (Figure 9.11) and WNM (Figure 9.12) with the MFM-solver to investigate the solvers behaviour in capturing the ST-phase as a function of environment fro different resolutions. For the higher density environment it is much more difficult to resolve the ST-phase at low mass resolution. While most properties are still within 50 per cent in comparison to Kim and Ostriker (2015) the hot phase remains less and less resolved at low mass resolution. The terminal momentum is still well resolved even at lower resolution. However, as we pointed out in section 9.3.2 this is a result of the feedback scheme where the thermal energy is injected into the 32 nearest neighbours which leads to an overestimate of the shell momentum that scales with the particle mass. Therefore, the terminal momentum remains a weak measure to determine whether the ST-phase is resolved or not. Even, if 'correct' terminal momentum is injected and particles move through the volume the feedback remains ineffective as long as the temperatures in shell and bubble are unresolved which then generate the pressure in the ISM. For the low density environments all important physical quantities can be properly captured with a mass resolution of 10 $M_\odot$. The crucial point in this regime is the long cooling times which are longer than 0.1 Myr. Because of this long cooling time and the negligible cooling losses it the hot phase in the bubble has time to build up and can be resolved even at lower mass resolutions. As already pointed out above the momentum seems to be converged between all mass resolutions in this environment which is again due to the fact that we sweep up too much mass with our feedback scheme within the ST-phase which counterbalances the poorly resolved velocity structure of the shell which leads to the correct momentum even at lowest mass resolution. However, because in this regime we also revolve the temperature structure of the shell and the bubble the feedback remains resolved because it generates enough pressure within the ISM.

9.3.5 Chemical composition

We show the chemical evolution of SN-remnants for H_2, H, and H^+ in the WNM, the CNM, the CNM-n10, and the CMM in Figure 9.10. In the WIM (top left) the initial material is fully ionised and

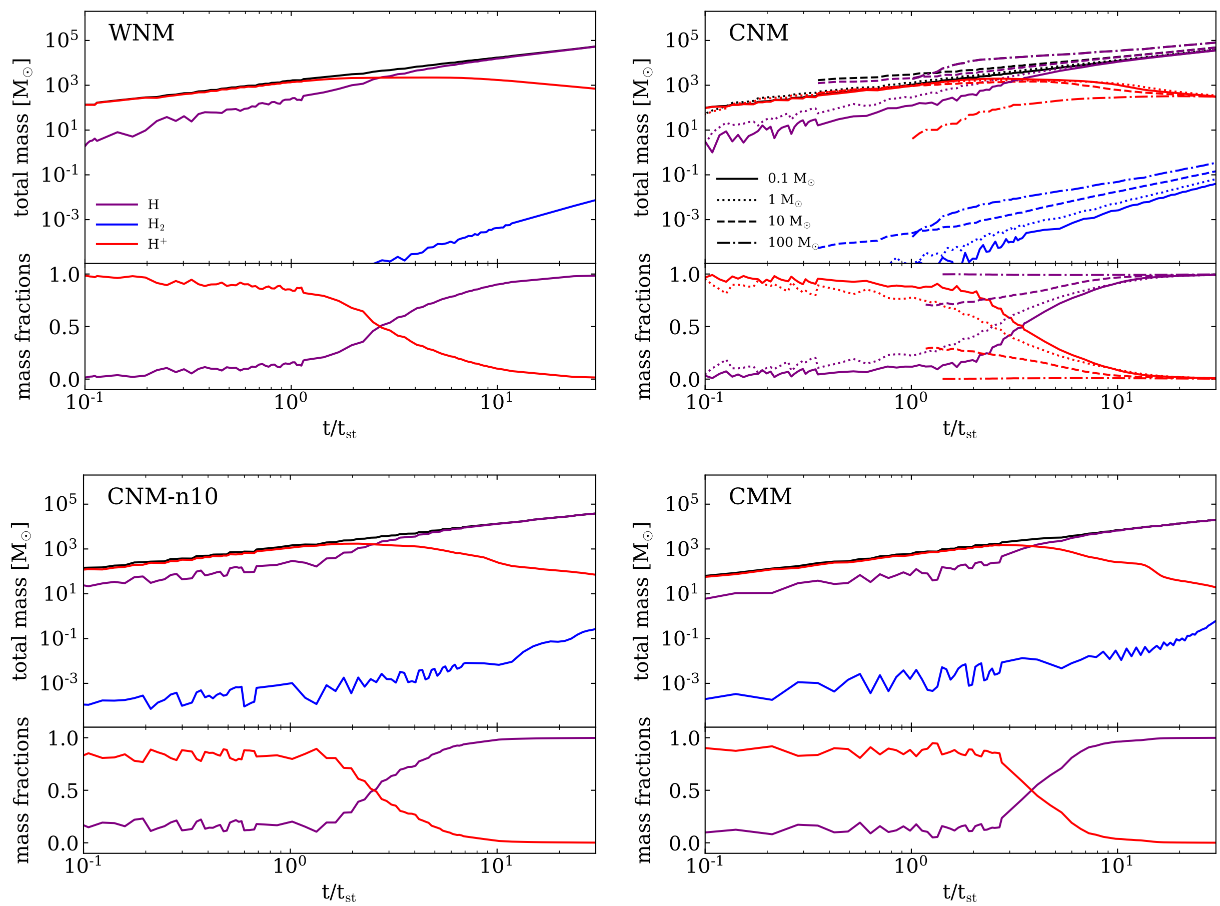

Figure 9.10: Chemical composition of the masses of SN-remnants in different environments of the non-equilibrium species H_2 (blue), H^+ (red) and H (purple) for the runs WNM-L4 (top right), CNM-L4 (top right), CNM-n10-L4 (bottom left) and CMM-L4 (bottom right) as a function of time. The top panels show the total mass in each species while the bottom panels show the mass fraction of each species. We observe that initially most of the molecular and neutral hydrogen is destroyed due to the heating of the injection energy. The remnants in the high density environments can preserve a small fraction of their mass in neutral hydrogen. At later times the shell becomes fully neutral again in all remnants. In all cases we can see that a little mass in molecular hydrogen builds up. However, it is below the per cent level within 10 Sedov-times. The black lines indicate the total mass in the remnant.

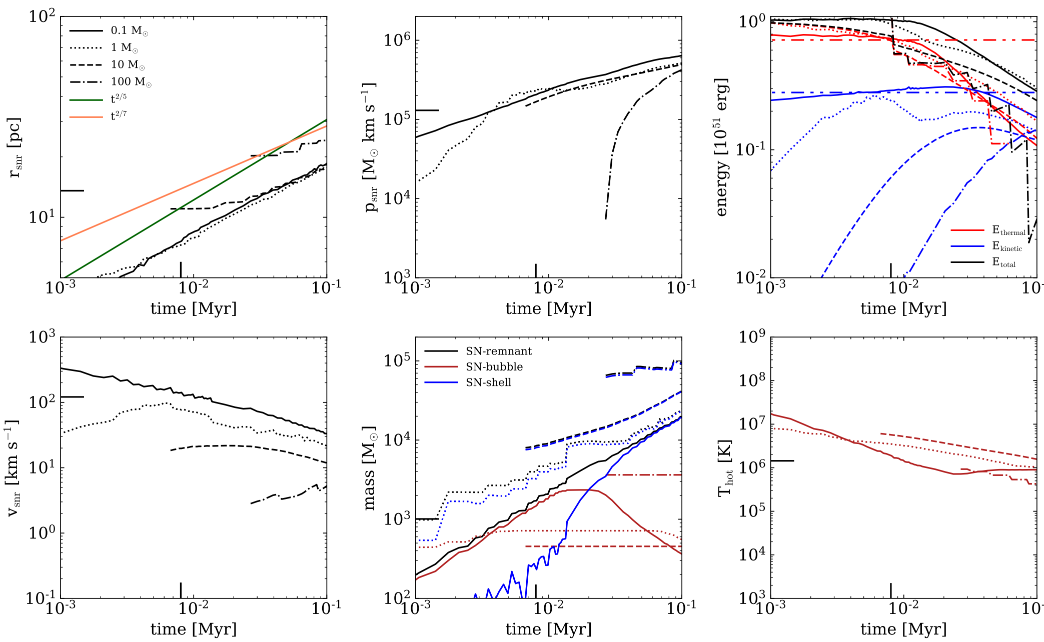

Figure 9.11: Same as Figure 9.4 for an ambient density of 100 cm^{-3}

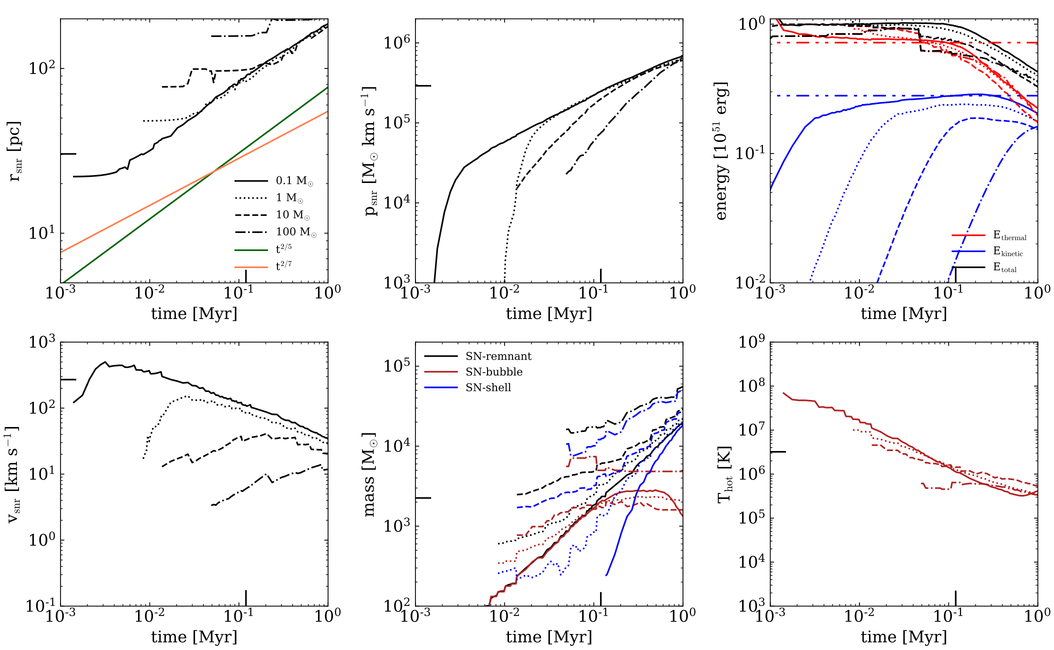

Figure 9.12: Same as Figure 9.4 for an ambient density of 0.1 cm^{-3}

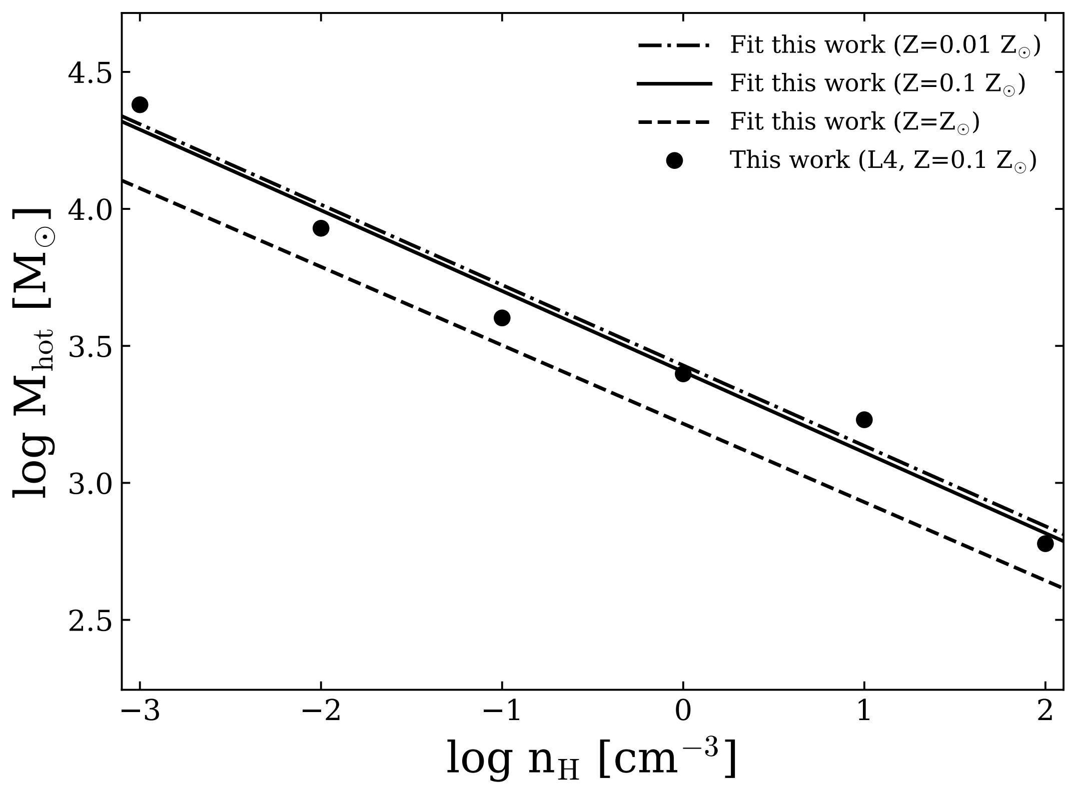

Figure 9.13: Peak hot mass as a function of the environmental density in which the SNe occur. We show the peak hot mass for a metallicity of Z=0.1 $Z_\odot$ as red dots. The red dashed, the red solid and the red dash-dotted line are the best fit relations that are obtained for the metallicities Z=$Z_\odot$, Z=0.1 $Z_\odot$ and Z=0.01 $Z_\odot$. We find that remnants in low density generate one order of magnitude more hot gas mass as remnants in high density environments.

H^+ stays the dominating chemical component of the shell even after 2 shell formation times where roughly 60 per cent of the remnant are in full ionisation. However, at ten shell formation times the remnant becomes fully neutral and also forms a tiny fraction of molecular hydrogen (below a solar mass). The CNM (top right panel) initially consists of neutral hydrogen but the whole remnant is ionised by the blast wave. Only after shell formation the remnant cools and the shell is becoming 100 per cent neutral again after 10 shell formation times. In these remnants molecular species can be ignored. For the CNM, we show a resolution study for the chemical fractions within the remnant. At the lowest mass resolutions the chemical composition of the single remnant is not captured accurately. At this resolution the remnant is not fully ionised in the beginning and initially more mass is kept in the neutral state rather than fully ionised by the blast wave as expected. The remnant is fully neutral before shell formation. The same is true for the 10 $M_\odot$ runs, although we note that here we already find a slightly dominating ionisation fraction of the remnant compared to the neutral component. For the two highest resolution runs we find that the blast wave is fully ionising the ambient medium, keeping 70 to 80 per cent of the gas ionised until shell formation. After that, cooling is dominating and the remnant starts to form neutral hydrogen and reaches the fully neutral state roughly 10 shell formation times after the appearance of the blast wave. Despite the fact that the molecular fractions are low, they also vary within at least an order of magnitude at the end of the simulation, where the low resolution remnants produce more molecular hydrogen than the high resolution ones, which leads to a more dominant cooling process through molecules at low resolution. This indicates that the non-equilibrium chemical model overestimates the cooling rate at low resolution increasing the issues with the well known cooling problem.

In higher density media (CNM-n10) we find the same behaviour (bottom left panel of Figure 9.10). However, we note that initially a small fraction of hydrogen of around 20 per cent is kept in the neutral phase and the formation rate of molecular hydrogen is slightly enhanced (half an order of magnitude) towards the end of the simulation. In the CMM medium (bottom left of Figure 9.10) we find that the some of the initially swept up mass is kept in the neutral state (again roughly 20 per cent) while the rest if fully ionised. The formation rate of molecular hydrogen increases again and at the end of the simulation we find about half an order of magnitude lower molecular fractions than ionised rest mass of the remnant. If we continued the simulation longer the built-up of molecular hydrogen would be significant. However, we assume that remnants overlap before they reach more than 30 Sedov-times. Finally, we briefly discuss the dynamical impact of the chemical model. We carry out one reference run where we override the evolution of the chemical abundances and only enable our non-equilibrium cooling routines. Not evolving the chemical abundances has mainly an impact on the cooling behaviour of the gas. We only find a marginal impact of the chemical model on the overall evolution of the supernova remnant on the percent level. However, the chemistry effects the initial momentum build-up and the peak hot mass in the beginning. The initial momentum is slightly increased in the run without the active chemical evolution, but converges quickly to the momentum evolution that is observed with the active chemistry. The peak hot mass is slightly increased without the chemical evolution, which can be explained by the missing cooling channel over the molecules. Furthermore, we want to point out that the radiation which is emitted by the remnant would certainly impact its chemical evolution which is a potential caveat of the model. However, the simulations are also too low in resolution to make valuable prediction for X-ray properties of supernova-remnants. To accurately investigate this, one would have to carry out higher resolution simulations with lower dimensionality like Thornton et al. (1998), Blondin et al. (1998), or more recent Badjin et al. (2016). However, We investigate a possible feedback scheme that aims for the input of the terminal momentum and the generation of the hot phase in galaxy scale simulations in a resolved fashion. Although the chemistry might be insignificant in isolated events that picture can be quickly altered if we consider multiple events that

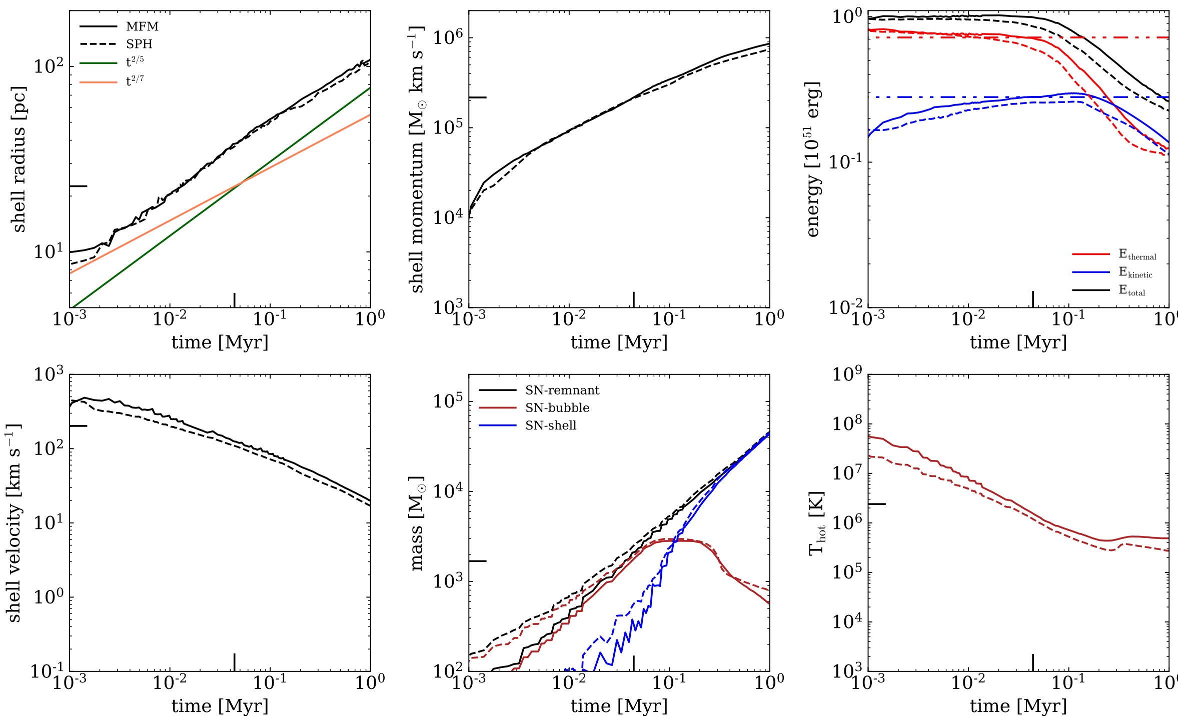

Figure 9.14: Comparison of the shock capturing behaviour for two different solvers, MFM (solid) and SPH (dashed). Most physical properties agree within a few percent.

lead to overlapping higher density remnants with shorter cooling times and higher formation rates for molecular hydrogen, which will certainly influence the distribution of internal energy and therefore its dynamics within the ISM.

9.3.6 Comparison of different Hydro-solvers

We carried out some of our simulations employing different solvers for hydrodynamics. All simulations at our highest mass resolution are carried out with our pressure-energy SPH solver. In Figure 9.14 we show the comparison between the MFM-solver (solid) and the SPH-solver (dashed) for all physical quantities that we investigate. Overall, we find good agreement of the two solvers at the highest mass resolution. Most of the physical properties of the shock are captured within a few per cent. The major differences between the solvers are given in the behaviour of the thermal and kinetic energy (upper left panel of Figure 9.14). For the SPH-solver we find that the thermal energy is radiated away at a slightly earlier time compared to the MFM solver leading to shorter shell formation times (c.f. equation 9.16). Further, the SPH-solver under predicts the kinetic energy within the ST-phase. The other difference that we point out is that the SPH-solver predicts a lower temperature in the hot bubble by half an order of magnitude. Therefore, the pressure within the bubble is slightly lower, which can potentially lead to less momentum generation within the PDS phase for this method. For the SPH-solvers we evaluate the results in section 9.5 in more detail.

9.4 Build up of the hot phase

Following Naab and Ostriker (2017) we can derive the expectation value for a hot phase to be established by SN-feedback. To derive the expectation value we follow a semi-analytic approach. From our simulations we can derive the radii of the remnant as a function of the environmental density. As we do not have data for different explosion energies we lack the dependence on the explosion energy compared to similar studies (e.g. Kim and Ostriker, 2015). However, we tested different metallicities and can therefore carry out the semi-analytic calculations for different metallicity regimes. First, we need to derive the dependence of the radius on the ambient density. We can fit our results for all three different regimes. Therefore, we obtain the radius of the shell at the end of the ST-phase. We find the following relations.

$$r_{\mathrm{st}}(Z = 0.01 Z_{\odot}) = 18.0 \text{ pc } n^{-0.53} \tag{9.16}$$

$$r_{\mathrm{st}}(Z = 0.1 Z_{\odot}) = 16.4 \text{ pc } n^{-0.52} \tag{9.17}$$

$$r_{\mathrm{st}}(Z = 1 Z_{\odot}) = 13.15 \text{ pc } n^{-0.52} \tag{9.18}$$

The expectation value for the hot phase of a SN-explosion that goes off within the hot phase of a previously occurred SNe can be written as follows

$$\epsilon_{\mathrm{hot}} = S \frac{4\pi}{3} r_{st}^3 t_{st}, \tag{9.19}$$

where S is the SN-rate and r_{st} is the remnants radius at the end of the ST-phase. By substituting r_{st} with the equations 9.16 to 9.18 and t_{st} with equations 9.10 to 9.12 we find a strong power law dependence for the expectation value of the hot phase for all three different metallicity regimes. The expectation value for the hot phase can then be determined via:

$$\epsilon_{\mathrm{hot}}(Z = 0.01 Z_{\odot}) = S \cdot 1.310^{-6} \mathrm{kpc}^3 \mathrm{Myr}^{-1} n^{-2.1}, \tag{9.20}$$

$$\epsilon_{\mathrm{hot}}(Z = 0.1 Z_{\odot}) = S \cdot 9.7410^{-7} \mathrm{kpc}^3 \mathrm{Myr}^{-1} n^{-2.1}, \tag{9.21}$$

$$\epsilon_{\mathrm{hot}}(Z = 1 Z_{\odot}) = S \cdot 6.6210^{-7} \mathrm{kpc}^3 \mathrm{Myr}^{-1} n^{-2.1}. \tag{9.22}$$

Thus, we see that the expectation value for the hot phase varies only very weakly with the metallicity and we can determine it for typical values within the ISM. We assume a typical surface density of the Milky Way within the solar neighbourhood around 10 $M_{\odot}$ kpc^{-2}. We follow Naab and Ostriker (2017) and assume a Salpeter mass function and a disc height of 250 pc. From that we can determine the SN-rate S for solar neighbourhood conditions and obtain 280 kpc^{-3} Myr^{-1}. By assuming the typical medium density within the Milky Way of $n = 1\mathrm{cm}^{-3}$ this gives a very low number for the expectation value for the hot phase in order of 10^{-5} to 10^{-4}. However, for SNe in lower density environments the expectation value for the hot phase becomes quickly larger and for environmental densities below 0.01 we find an expectation value greater than one due to the strong power law dependence of the expectation value with the density of the ambient medium. We note that this has consequences for the hot phase in the ISM. Once a configuration of the ISM is reached where SNe go off in low density environments our model predicts higher and higher expectation values with decreasing densities. SNe tend to go off in lower and lower density media. Cooling times for the gas increase alongside with the sizes of the remnants. Finally, this becomes a runaway process with dominating volume filling hot phase. This picture is in very good agreement with the findings from our simulations. Further, the model is in good agreement with the simulations carried out by Girichidis et al. (2016) who investigated the gas densities in galactic outflows and find a peak of the number density of roughly 0.01 cm^{-3}. While the remnants in the CMM have a size of a few pc, the size of remnants in the warm and hot ionised phase of the ISM can reach values up to 800 pc. Moreover, in Figure 9.13 we show that the hot mass of the remnant significantly increases as a function of the environment. We measured the peak hot mass (maximum mass of the bubble) that is generated by SN-blastwaves in different environments and find strongly increasing masses in the hot phase in remnants below 0.1 cm^{-3}. We find the following best fit relations.

$$M_{\mathrm{hot}}(Z = 0.01Z_{\odot}) = 2570 \cdot M_{\odot} \cdot n^{-0.29}, \tag{9.23}$$

$$M_{\mathrm{hot}}(Z = 0.1Z_{\odot}) = 2398 \cdot M_{\odot} \cdot n^{-0.29}, \tag{9.24}$$

$$M_{\mathrm{hot}}(Z = 1Z_{\odot}) = 1584 \cdot M_{\odot} \cdot n^{-0.28}, \tag{9.25}$$

Therefore, remnants in low density environments contribute much more to the build up of the hot phase by generating high expectation values for the hot phase alongside with high mass fractions of the hot gas. Remnants in high density media on the other hand have very low expectation values for a hot phase to form and generate only around 600 $\mathrm{M}_{\odot}$ of hot gas in the bubble which quickly cools away once the shell forms.

This has consequences for the formation of a wind driven by SNe. In this picture a wind is driven by the hot phase via the formation of a superbubble which interior is heated by SNe expanding into the bubbles of preceding SNe. Once the bubble breaks out of the disc the pressure within the bubble interior can push the shell outwards into the CGM. Hereby the outflow velocity would be limited by the sound speed within the CGM. Given a virial temperature of 10^6 K for the CGM of the Milky Way this can drive outflows with a few 100 km s^{-1} as they are observed (e.g. Genzel et al., 2011).

9.5 Effects of thermal conduction

Using our fiducial SPH-solver we investigate the behaviour of SN-remnants under the effect of thermal conduction. In supernova remnants, thermal conduction can influence the interface between the hot bubble and the shell by redistributing thermal energy from the bubble into the shell and mass from the shell into the bubble (El-Badry et al., 2019; Keller et al., 2014). With a temperature dependent thermal conduction coefficient in the Spitzer-limit (see Sec. 9.2.2) we investigate differences in remnant morphology and chemistry. All our highest resolution runs have been carried out including the effect of thermal conduction. In Figure 9.15 we show the radial profiles of the density (top left), the temperature (top left), the velocity (bottom right) and the pressure (bottom right) for the simulation CNM-Lv4. Comparing to Figure 9.2, we find that the temperature in the run with thermal conduction is about an order of magnitude lower than in the case without thermal conduction, while the pressure remains roughly constant. The lower bubble temperatures result form heat flux from the hot bubble to the colder shell. The pressure is similar due to mass flux from the shell to the bubble. This effect has a general impact on the evolution of the remnants when thermal conduction is included.

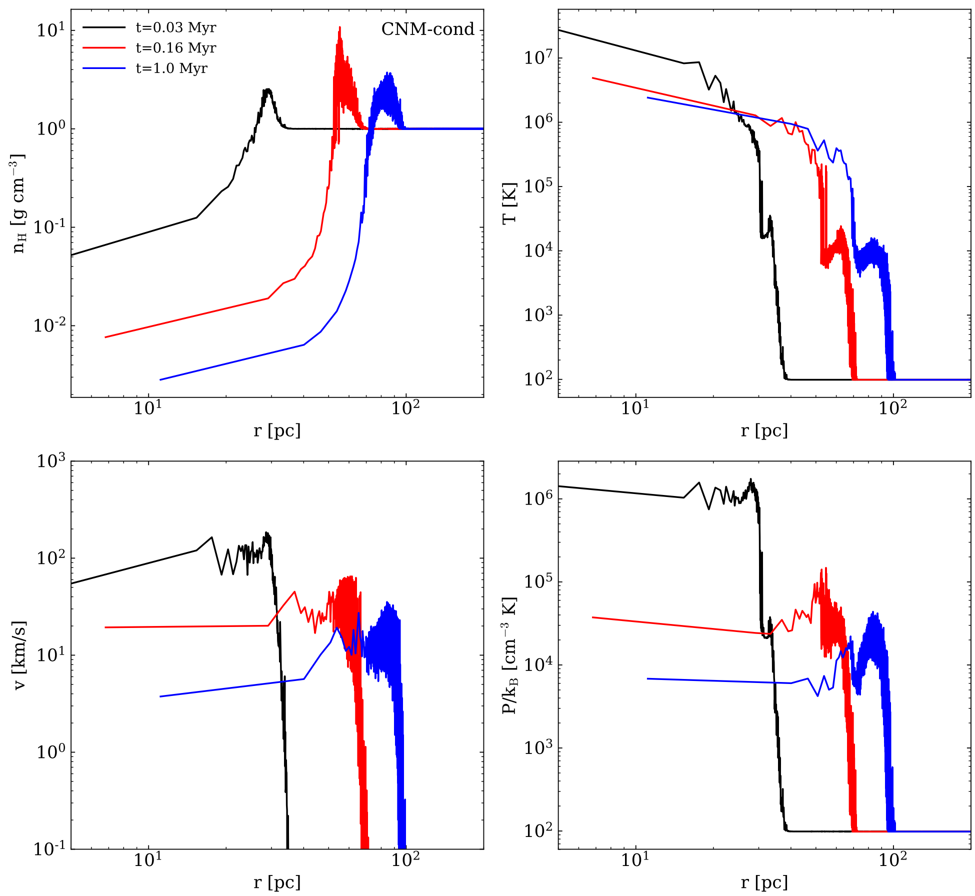

Figure 9.15: Same as Figure 9.4 but with the effect of isotropic thermal conduction. We find slightly lower temperatures in the bubble and higher densities in the shell.

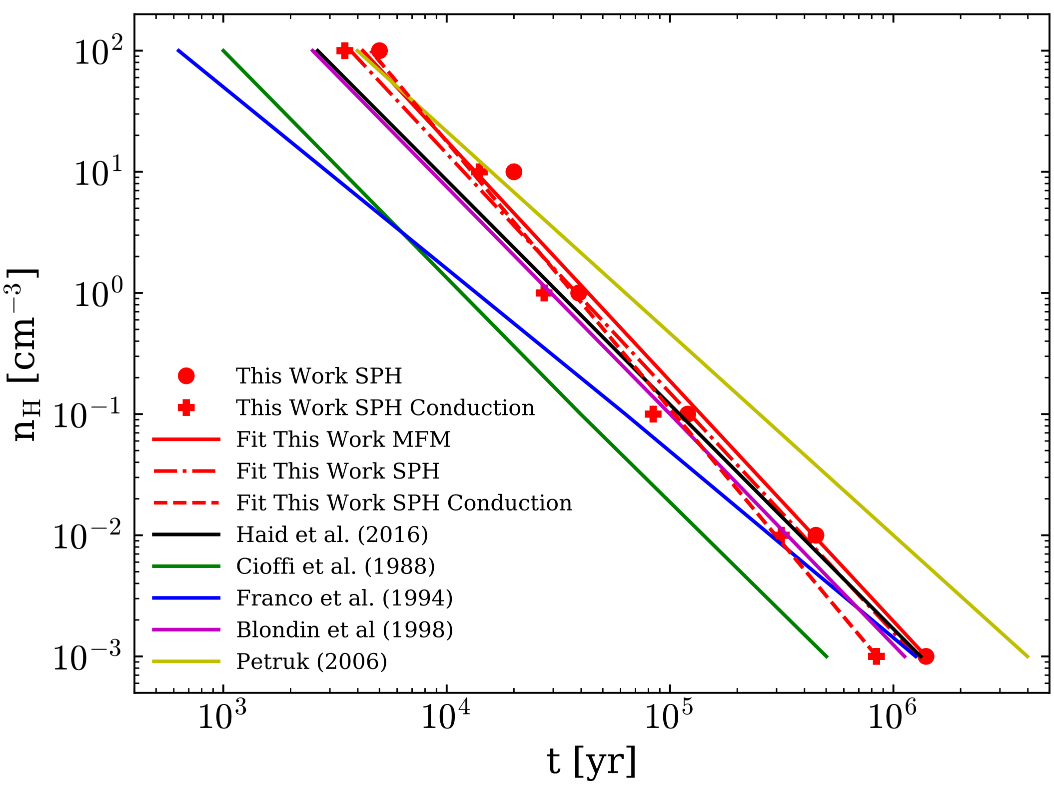

Figure 9.16: Same as Figure 9.8 for the results that we obtain with SPH (red dashed) and SPH with heat conduction (red dashed dotted). For reference we overplot the results we obtained with MFM. We find slightly shorter shell formation times for the SPH-solver than we find for the MFM solver. Moreover, thermal conduction further shortens the shell formation time.

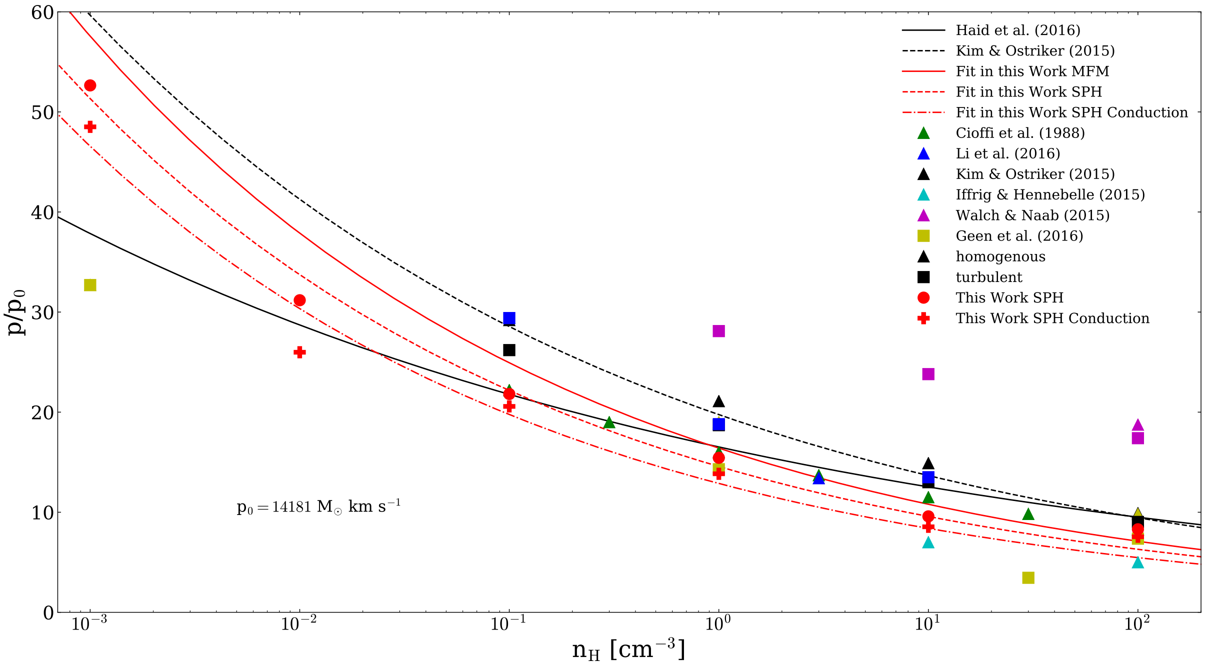

Figure 9.17: Same as Figure 9.9 for the runs with SPH (red dashed) and thermal conduction (red dashed dotted). We directly overplot the data points we obtained for SPH (red dots) and for the runs including heat conduction (red crosses). In comparison with MFM we generally find that the momentum is reduced by roughly 10 per cent for SPH and 20 per cent with SPH and heat conduction.

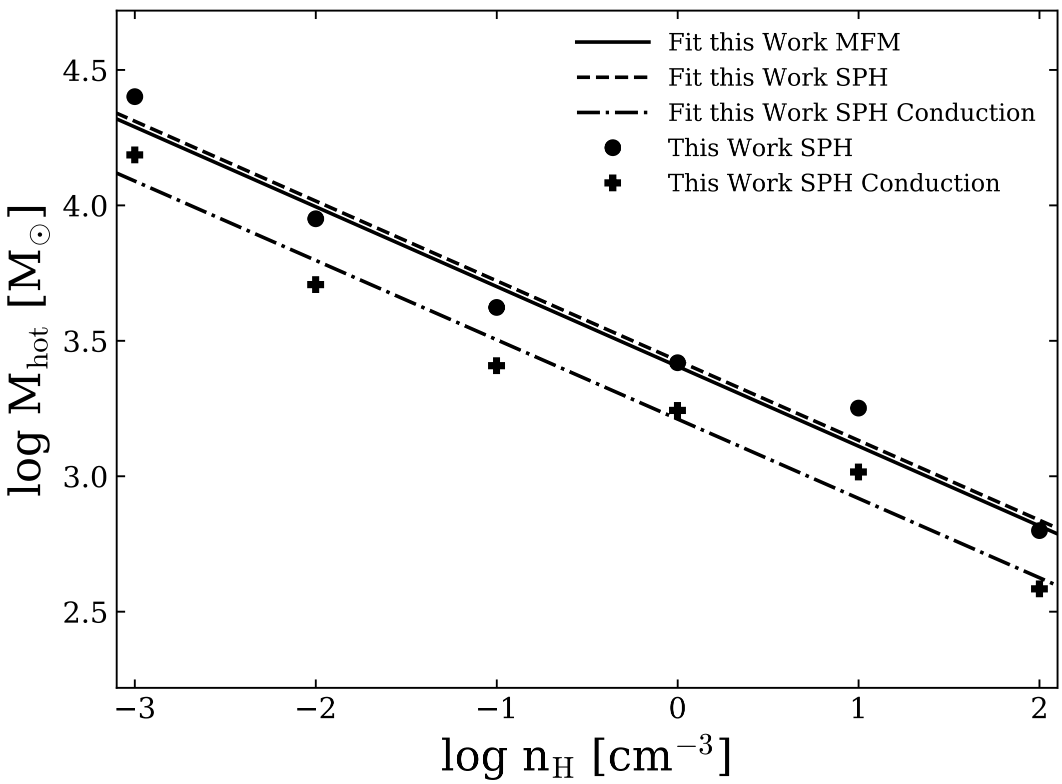

Figure 9.18: Same as Figure 9.13 for the runs that are carried out with SPH (dashed) and with SPH and conduction (dashed-dotted). While we only find weak differences between MFM and SPH in the peak hot mass we find that thermal conduction can reduce the peak hot mass by roughly 40 per cent.

Conduction describes a heat flux from the hot gas to the cold gas, which is counterbalanced by a mass flux from the cold gas to the hot gas constrained by energy conservation. This is valid before shell formation and leads to slightly higher mass fractions of the hot gas. However, in SN-remnants cooling is active after shell formation and energy conservation is violated. Therefore, the mass flux from cold to warm gas is prohibited and the energy from the bubble that enters the shell is radiated away immediately. This can impact the general physical properties of SN-remnants. Temperature is reduced and density slightly increases. While there are quantities that are only weakly affected by thermal conduction (e.g. remnants size, velocity structure), there are others which are affected significantly. First, we note that the ST-times (times of shell formation) are shorter in the presence of thermal conduction by roughly 20 per cent. We show this in Figure 9.16 where we plot a comparison of the shell formation times that we find in our fiducial runs with MFM (red solid line), the SPH (red dashed line) and with SPH plus thermal heat conduction (red dahsed dotted line). Conduction leads to a redistribution of internal energy from the hot gas to the cold. This reduces temperatures and leads to a slightly enhanced cooling. Therefore, cooling times shorten and the energy conserving ST-phase terminates earlier. We find modified fitting formulas with conduction. For completeness we give the fit we obtained with SPH.

$$t_{\rm st,sph} = 3.8 \cdot 10^4 {\rm yr} \cdot n^{-0.50}, \tag{9.26}$$

$$t_{\rm st,cond} = 3.6 \cdot 10^4 {\rm yr} \cdot n^{-0.46}. \tag{9.27}$$

Because of the earlier termination of the ST-phase, the momentum input with thermal conduction is lowered compared to the runs without thermal conduction. In Figure 9.17 we show the momentum input as a function of the environmental density and find that the SPH solver gives lower momenta by roughly 10 per cent while thermal conduction again reduces the terminal momentum by 20 per cent compared to the results that we obtain with our fiducial MFM solver. We overplot the data points from the simulation as red dots (SPH) and red crosses (SPH plus thermal conduction). The modified fitting formulas for the results with SPH and conduction yield:

$$p_{\rm st,sph} = 14.6 \cdot p_0 \cdot n^{-0.18}, \tag{9.28}$$

$$p_{\rm st,cond} = 12.9 \cdot p_0 \cdot n^{-0.18}. \tag{9.29}$$

However, the largest impact can be seen in the build up of the hot mass which is reduced by 40 per cent. We show the results in 9.18 for MFM (solid line), SPH (dashed line) and conduction (dashed-dotted line). While the results for MFM and SPH only differ in the per cent regime, the hot mass is reduced 40 per cent in the runs with thermal conduction. We note that before cooling takes over the hot mass slightly increased due to the mass flux from warm to hot gas. For thermal conduction we find the dependence of the hot mass as function of the environmental density as follows:

$$M_{\rm hot,cond} = 1580 \cdot M_\odot \cdot n^{-0.29}. \tag{9.30}$$

Further, we find an impact of thermal conduction on the chemical composition of the SN-remnant. Overall, the effect is minor. Therefore, we show the results for the run CNM-cond in Figure 9.19. Initially, the majority of the gas is ionised in the case with and without conduction but with conduction the ionising fraction is lightly reduced (by roughly 5 per cent). Because cooling is slightly more efficient in the presence of conduction, the build-up of neutral hydrogen in the shell is slightly enhanced. This then leads to higher formation rates of molecular hydrogen which is increased by a factor of two.

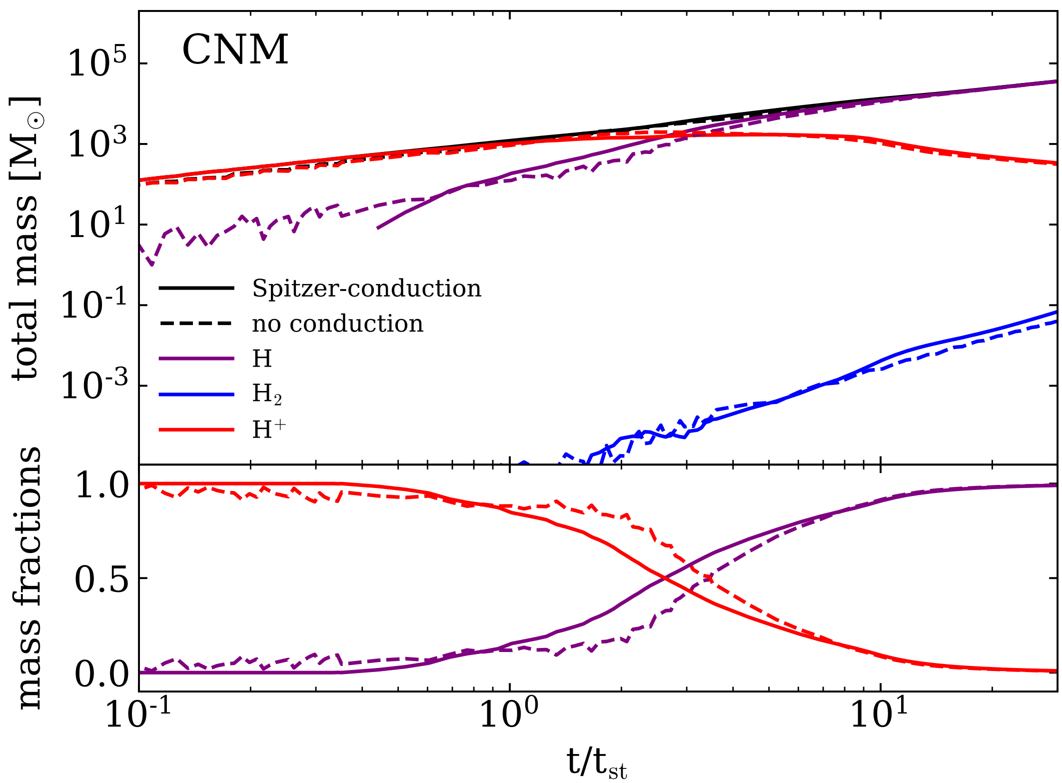

Figure 9.19: Comparison between the chemical evolution of the shell without the effect of thermal conduction (solid) and with thermal conduction (dashed) for the different species that the non-equilibrium model follows. We find slightly increased fractions for the H^+ in the runs that include thermal conduction in the beginning of the simulation. At later times the ionising fraction of hydrogen decreases faster than in the run without thermal heat conduction.

9.6 Applications to astrophysical systems

In this section we briefly discuss applications to larger scale ISM and galactic scale systems to show that it is possible to use the presented feedback scheme at the target resolution of solar mass and sub-parsec resolution and achieve convergence on the momentum and hot phase generation in a global large scale simulations just by resolving the momentum and hot phase of isolated remnants. Moreover, we provide an insight into SN-remnants in structured media which can not be handled in higher resolution one dimensional SN-blast waves studies as these systems miss the radial symmetry needed for justifying a lower dimensional approach.

9.6.1 The supernova driven ISM

The first example we want to study is the SN-driven ISM. In Figure 9.20 we show the density distribution of the SN-driven ISM in a periodic box with a side length of 256 pc with solar neighbourhood conditions for the background UV-field but 0.1 $Z_{\odot}$ which represents an ISM environment as present at high redshift. However, we adopt a lower SN-rate of 1.5 supernova per Myr and follow the evolution of the SN-driven ISM for 100 Myr. The four different panels in Figure 9.20 represent the four different mass resolutions after 100 Myr of evolution. Visually, we note some differences in density structure. In the lowest resolution run we observe that the resulting ISM-structure is only very badly resolved and the hot phase is mostly missing in this simulation as the canonical SN-energy falls to over cooling and is radiated away shortly after deposition without depositing momentum or generating the hot phase ans subsequently it does not provide the ISM-pressure to subsequently generate a SN-driven outflow. Finally, we investigate the SN-remnant properties that we obtain from a feedback event in a structured (SN-driven) medium. In Figure 9.22 we show the blast wave evolution for 4 different point of a blast wave that evolves into the SN-driven ISM for our highest resolution runs. In this scenario we generate the initial conditions by using the SN-driven ISM simulations that we show in Figure 9.20 and select a snapshot with a nicely build-up turbulent structure that provides an realistic environment for the explosion of massive star as we would obtain it in galactic scale simulation. The canonical SN-energy of 10^{51} is hereby distributed over the 32 particles closest to the centre of the box. Thus the SN-even occurs in the centre of the box at $x = 180$ pc and $y = 180$ pc. The supernova goes of in the dense filamentary structure that can be observed in the upper left panel of Figure 9.22. With this event we represent a supernova-explosion in the CMM. As the blast wave occurs in the centre of a filament the feedback is most effective into the direction of the steepest pressure gradient. In this scenario this coincides with the steepest density-gradient. Therefore, we obtain a highly asymmetric blast wave structure with a faster expansion of the blast wave in negative and positive z-direction. While the blastwave can expand freely in negative y-direction it expands into an already bubble-like in positive y-direction and heats the material in this already present bubble even more (upper right panel of Figure 9.22). Despite the fact that the feedback is ineffective parallel to the filament we can still observe in the upper right panel of Figure 9.22 that it get disrupted, by the momentum that is deposited during the ST-phase which remains resolved in this simulation. After the end of the ST-phase (bottom panels of Figure 9.22) the material in the irregular formed shell is further pushed out via the pressure-support by the hot material inside the newly formed bubble, generated in the resolved ST-phase.Finally, we show the detailed blast wave properties in Figure 9.23 and point out the differences to the results of the runs that we obtained with a non-structured, constant density ambient medium at rest. The main difference is that in the context of an already structured ambient medium the heating by the supernova-explosion is most effective in the direction of the steepest pressure gradient. Thus the remnant becomes highly non-isotropic. While it is relatively easy to follow the momentum, the energy distribution and the

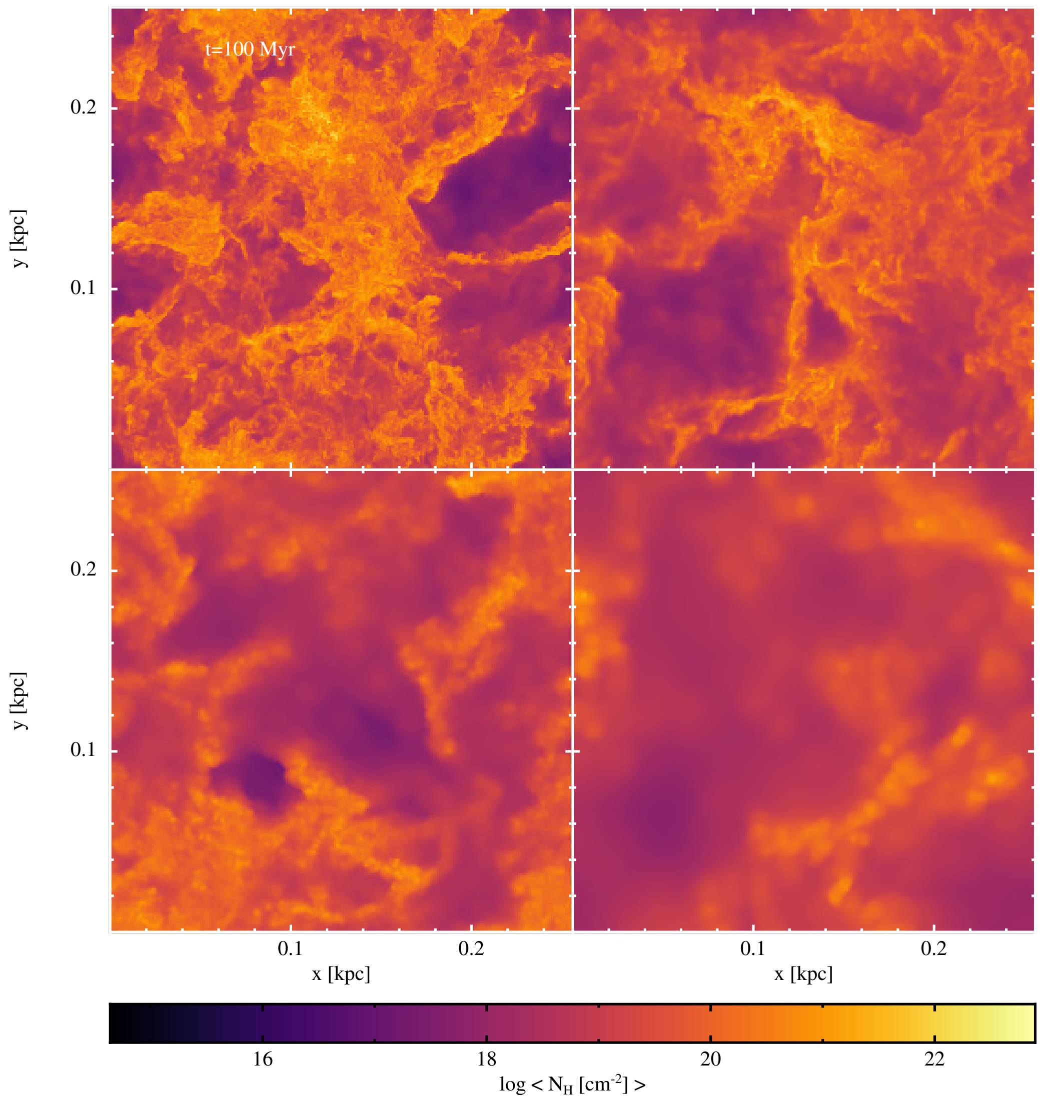

Figure 9.20: We show the effect of multiple supernova events on the resulting ISM-structure as a function of particle mass. The upper left panel shows our highest mass resolution of 0.1 $M_\odot$, the upper right the 1 $M_\odot$, the bottom left the 10 $M_\odot$ and the bottom right the 100 $M_\odot$ resolution. While the two highest resolution runs show significant substructure from filaments and cloud like structures, the lower resolution runs with 10 solar masses but specifically the 100 solar mass run, show a far less structured and much more blurred out medium.

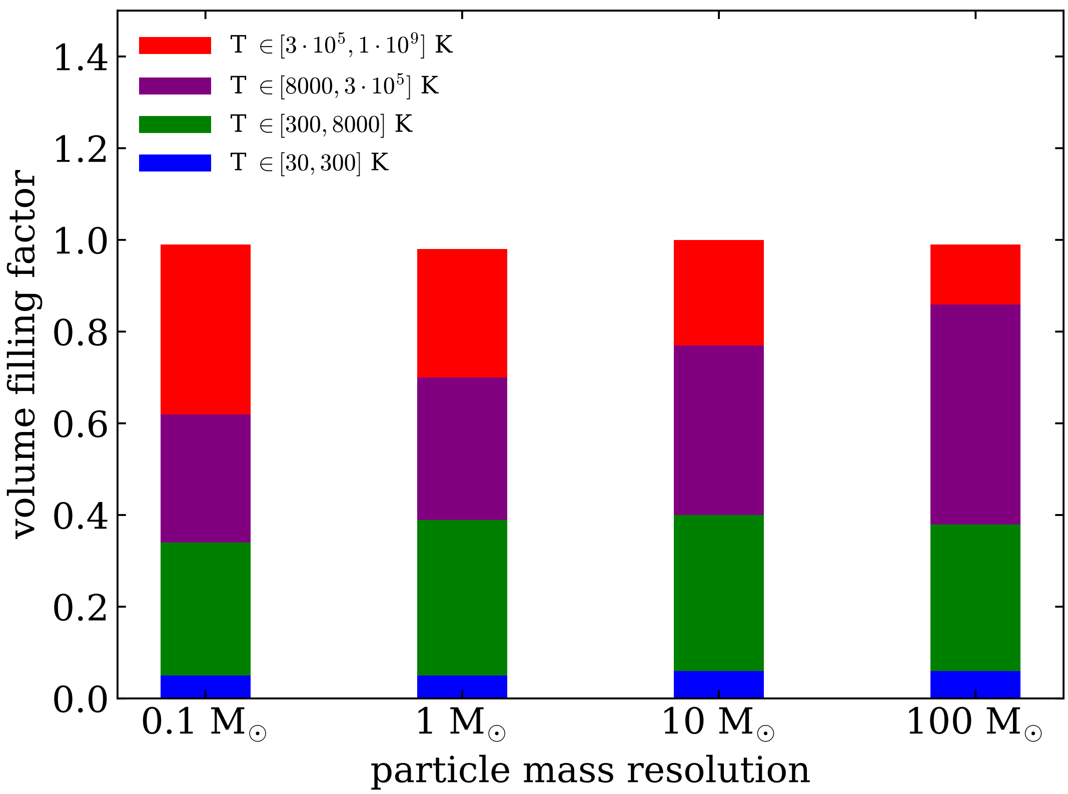

Figure 9.21: We show the mass weighted Volume filling fractions for the simulations that are shown in 9.20 for all different mass resolutions. For the highest mass resolutions it is possible to generate a Volume filling hot and warm phase as it is observed within the local ISM.

hot mass fraction, of this non-isotropic remnant it is not straight forward to determine the cold mass as most of the other parts of the ISM are still cooling while they are not yet effected by the heating from the supernova. The velocity can only be determined as averaged value out of shell mass and shell momentum. We show the central quantities of the remnant in a structured medium in Figure 9.23 with the momentum (top left), the energy (top right), the velocity (bottom left) and the remnant mass (bottom right). We can see that the remnant, despite its irregular shaped form still undergoes the ST-phase, the PDS-phase and the MCS-phase, which can be identified in the momentum and energy distribution. Velocity and cold mass are harder to track in this context while the hot mass can be determined more easily. we note that we find a factor of 2.5 more hot mass in the structured medium compared to the remnants in homogeneous media. This can again be explained by the more efficient heating alongside the steepest density gradient.

9.6.2 Galaxy scale simulations

One major achievement that can be realised at the target resolution is a full galactic disc simulation that resolves the feedback of massive stars, with the focus on SN-feedback of Type II core collapse supernovae. In Figure 9.24 we show a simulation of an isolated dwarf galaxy that has been simulated with our code and the feedback scheme that we have tested into depth in the scope of this work to investigate the momentum and hot-phase generating properties that can be obtained with a very simple SN-feedback scheme at target resolutions where the the single feedback events' ST-phase is resolved. This kind of simulation shows that SN-feedback can be effective once the ST-phase can be resolved in the majority of the ambient media in which the supernova occurs. With this simple, but resolved feedback scheme it becomes possible to self-consistently study ISM-turbulence and galactic scale outflows in a galaxy scale simulation, without the need for more complicated and less accurate treatments of sub-grid feedback physics, like direct momentum input or a mixed injection scheme that assumes the ST-solution by construction. For our scheme we are able to show that the vast majority of SN-events occurs in environmental densities for which our isolated blast wave studies clearly indicate convergence on momentum and hot phase generation at a mass resolution of 1 $M_\odot$. Together, with the results of our presented SN-driven ISM-environments it becomes possible to also achieve hot phase-dominating Volume filling fractions in a galactic scale simulation. Thus far, this has only been achieved in small galactic patches. Finally, we note that with this kind of galaxy-scale simulation we are able to achieve one major step forward in the modelling of ISM-physics in a galactic context. Although, we treat the stars that we form as single stars by randomly drawing them from the IMF, this still represents a sub-grid model for star formation. We then follow the massive stellar population in terms of photo-ionising radiation and photo-electric heating in a Stroemgren-approximation (e.g. Hopkins et al., 2011) by mapping the density distribution with a healpix-algorithm and calculating the local column densities with TREECOL (Clark et al., 2012). Although, we neglect re-emission in this context, we still include an approximation for radiation of the massive stars. Once these massive stars reach the end of their life times they explode as core collapse SNe and every single remnant is able to provide its momentum and hot-phase in the ST-phase removing the sub-grid constraint for supernova-feedback from our galaxy simulations.

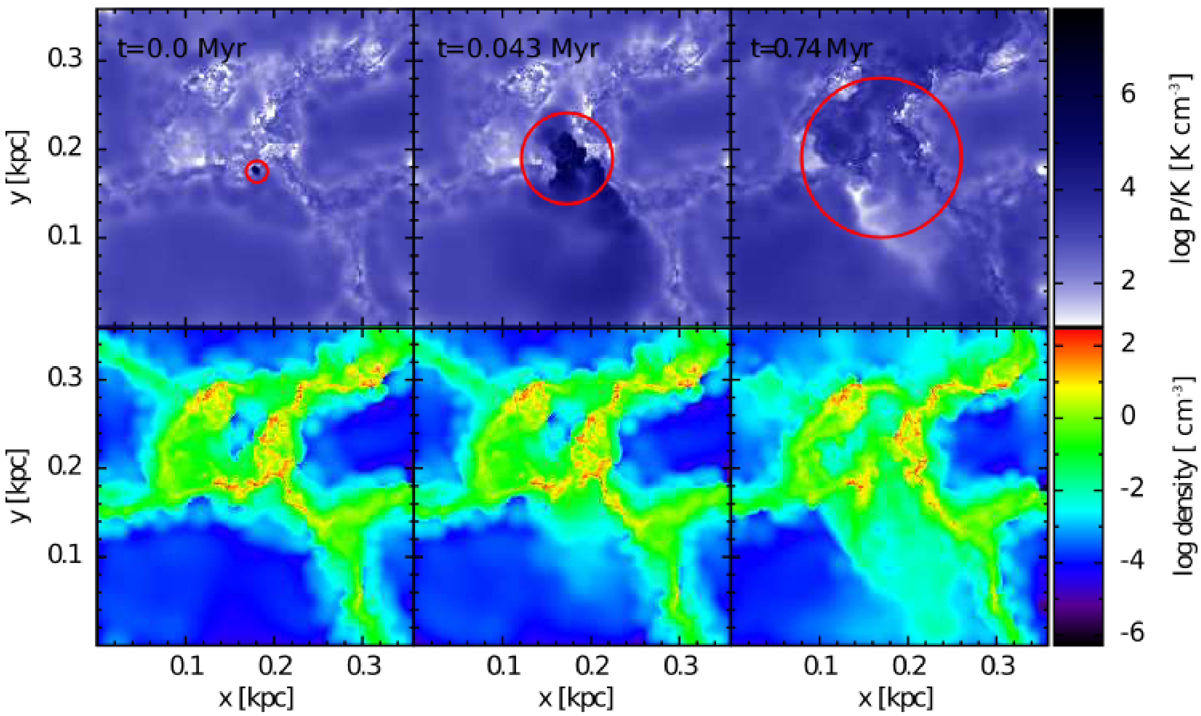

Figure 9.22: We show the evolution of a supernova-blast wave that evolves into a supernova-driven ISM as pressure slices (top row) and density slices (bottom row) at the height at which the blast wave event occurs (box center, $z = 0.168$ pc). We show the irregular evolution of this blast wave for three different points in time. In the upper left panel we show the initial density configuration. The supernova-event is placed in the very centre of the box in the densest filament we could identify. The blast wave is then evolving into the direction of the steepest pressure gradient (in positive and negative y-direction). Alongside the filament the action of the feedback-event is suppressed due to the higher environmental densities in this direction. The middle panel shows the end of the ST-phase. We immediately see that the remnant looks much more irregular and shows much more detailed structure compared to the isolated events, capturing the full three dimensional nature of this problem. Past the ST-phase we observe the evolution of an irregular blast wave structure that is supported by the internal pressure provided by the hot material in the bubble (right panels), until the bubble is in pressure equilibrium with the shell at which point the remnant starts to merge with the ambient medium.

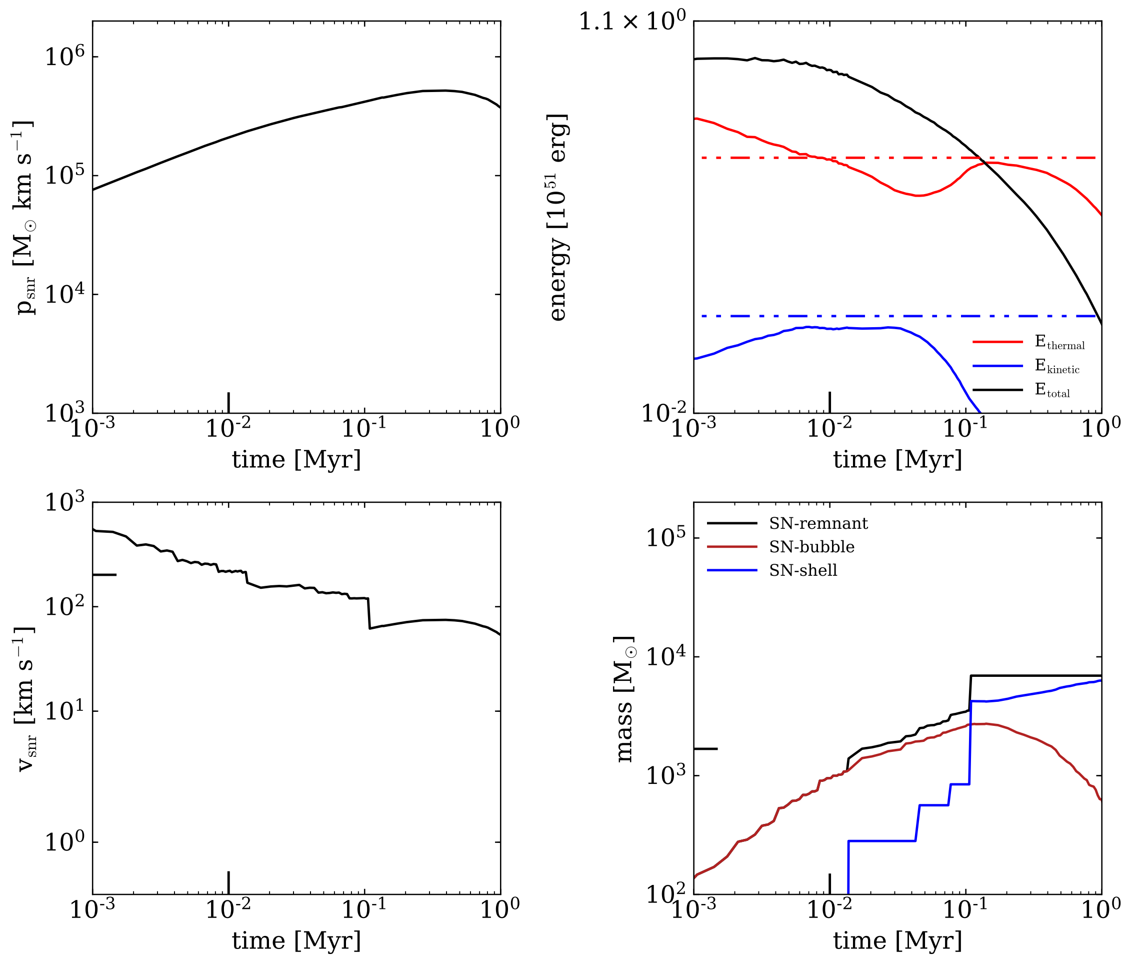

Figure 9.23: We show the most important SN-remnant properties (momentum, energy, velocity and mass) that can be modelled with a simple SN-feedback scheme at our highest resolution level. Generally we find that the remnant undergoes a proper ST-phase with a split of 72 % in thermal and 28 % in kinetic energy, before the cooling losses start to dominate and the remnant goes onto the pressure driven snow-plough phase before entering the momentum conserving phase which is indicated by a flattening of the momentum curve (bottom left). After this the momentum drops and starts to merge with the ambient (turbulent) ISM. Compared to the isolated events we observe roughly the same terminal momentum build-up towards the end of the ST-phase. The momentum is increased by a factor of two in the pressure-driven snow plough phase. The hot mass seems to be increased by a factor of three compared to the isolated events. This is related to the asymmetry of the remnant. In the structure medium feedback is most effective alongside the direction of the highest pressure gradient. Thus energy is deposited into lower density gas which can be heated very effectively, resulting in a more effective heating mechanism.

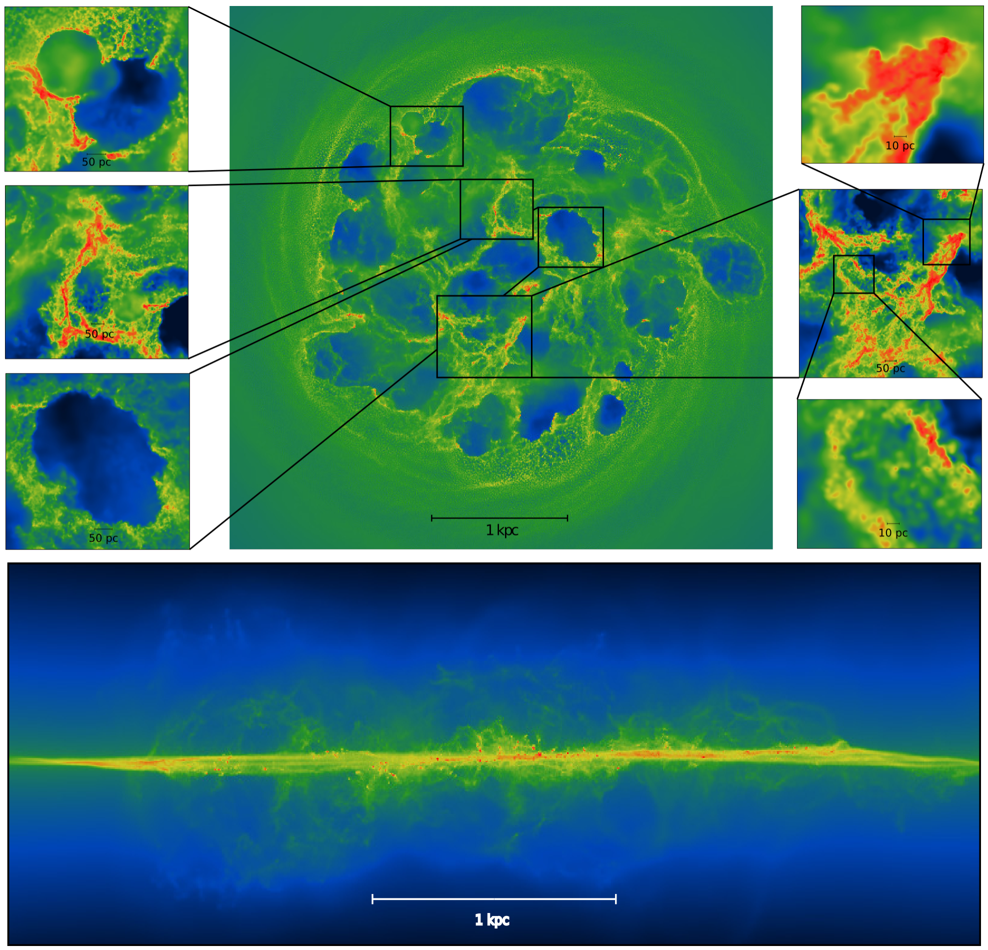

Figure 9.24: Simulation of an isolated dwarf galaxy with the MFM-solver at a mass resolution of 1 $M_{\odot}$ and a spatial resolution of 0.1 parsec. The color-coding indicates total gas surface density (covering 10^{16} (blue) to 10^{22} (red) cm-2). We show various zoom-ins on overlapping SN-remnants (top left), filaments (middle panels), an isolated SN-remnant (bottom left), dense cores (top right) and fragmented clouds (bottom right). In the bottom panel we show the edge-on view of the galaxy with filamentary outflows driven by SNe. In simulation the main driver for the resulting complex ISM-structure is the combined effect of the turbulence driving and heating by the feedback of supernovae and the cooling due to the employed non-equilibrium cooling and chemistry routines. The stars in this simulations represent single stars and are sampled with the IMF-sampling approach from Hu et al. (2016). At the end of their lifetimes the massive stars explode in a core collapse SN-event and distribute 10^{51} erg into the ambient ISM. Every single remnant can be tracked and undergoes a resolved ST-phase in which it generates momentum to drive turbulence and hot mass that is needed to self-consistently provide the pressure support for driving galactic outflows.

9.7 Conclusions

9.7.1 Summary

We carried out three dimensional simulations of isolated SNe that include a non-equilibrium cooling and a chemical model that tracks the formation (and destruction) of H_2. The canonical SN-energy of 10^{51} erg is coupled by pure thermal injection to one kernel size the centre of a box with uniform density and tested four different mass resolutions of 0.1 $M_\odot$, 1 $M_\odot$, 10 $M_\odot$ and 100 $M_\odot$. The energy is distributed weighted by the kernel. We focus on the convergence of physical properties at the end of the ST-phase to constrain the resolution requirements for a SN-feedback scheme that can be applied in high resolution simulations of galaxy formation and evolution. Specifically, we tested the behaviour of two different, widely used numerical methods for solving Euler's equations. We tested the implications of this feedback scheme with a modified 'pressure-energy' SPH solver and the higher order meshless finite mass (MFM) solver which utilises a second order reconstruction of Euler's equations by solving the Riemann problem on the one dimensional surface between two fluid tracers to obtain the fluid fluxes. The usage of the chemical model allows us to follow the formation and destruction processes of molecular, neutral and ionised gas within isolated SN-remnants as they currently can be modelled in simulations of galaxy formation and evolution. We carried out reference runs with thermal conduction to investigate the effects of the heat flux between SN-bubble and the cold material in the remnant.

1. *Morphology of the shock:* We can capture three stages in the evolution of a SN-remnant. In the ST-phase we resolve the adiabatic regime defined by the Rankine-Hugoniot jump conditions with an accuracy of up to 10 per cent that is limited by the behaviour of our underlying numerical scheme. After the ST-phase the remnants enters the PDS-phase in which they can further increase momentum due to the high pressure in the bubble behind the shell. This pushes the shell further outwards until pressure equilibrium with the shell is reached and the shell moves forward with roughly constant momentum and reaches the MCS-phase. Finally, the remnant starts to merge with the ambient ISM. We can capture the shocks morphology reasonably well at our three highest resolution levels. However, at the lowest resolution level the shock remains unresolved.

2. *Dependence on the environment:* We carried out explosions for six different environmental densities of SN-remnants alongside the equilibrium cooling curve. For all these remnants we computed the end of the ST-phase and find a power law scaling of the termination time of the ST-phase which is within a 30 per cent agreement compared to the work of Blondin et al. (1998), Petruk (2006) and Haid et al. (2016). We investigate eight physical quantities as a function of time including radius, momentum, energy distribution, velocity structure, remnant mass, bubble-mass, shell-mass as well as the bubble temperature. At the end of the ST-phase our resolved runs agree very well with the results of studies of the same kind (e.g. Haid et al., 2016; Kim and Ostriker, 2015), although we note that our default metallicity is 0.1 $Z_\odot$ because we aim for understanding SN-feedback in low metallicity environments. Most quantities can be resolved at a resolution of 10 $M_\odot$ in all relevant density regimes of the ISM. We specifically highlight this in the context of the momentum that has been generated during the ST-phase and the generation of the hot phase (the hot mass and the temperature evolution in the bubble). The feedback can then be resolved as a combination of those two quantities. Momentum is needed to move particles through the ISM and generate turbulence. The hot phase is needed to generate pressure in the ISM which is necessary to launch galactic winds that can impact the CGM of a galaxy. Further, we determine a fit to the SN-momenta that are injected in different regions of

the ISM based on our highest resolution remnants which can be adopted for feedback schemes in simulations of galaxy formation and evolution that do not resolve the ST-phase explicitly.

3. *Chemistry of single SN-remnants:* We investigate the chemical composition in the simulated SN-remnants. We note that the remnants in the low density environments contribute to the build up of the hot phase but the remnants become fully neutral after a few cooling times. They do not contribute to the formation of molecular hydrogen because the densities in the swept up mass remain low. In the CNM the mass in the swept up region is fully ionised. After cooling sets in the remnant becomes neutral after a few cooling times again. However at the end of the simulation (t=1 Myr) we find around one per cent of the remnant mass in neutral hydrogen. In the CMM the SN destroys most of the molecular hydrogen and leads to an ionisation of the swept up mass. We find that a small fraction (around 10 per cent) of the remnants mass remain in the neutral hydrogen phase. After cooling set in most of the material cools quickly and recombination with the free electrons leads to the formation of neutral hydrogen.

4. *Role of thermal conduction:* Thermal conduction leads to a decrease in temperature and to an increase in density in the shell. Thermal energy can be transported from the hot phase to the cold phase while mass from the cold phase is transported to the hot phase. Once cooling becomes relevant the mass flux towards the hot bubble is suppressed because the thermal energy that is transported from the bubble to the shell is instantly radiated away. Thermal conduction makes cooling slightly more efficient and leads to slightly less momentum generation (by 10 per cent). The quantity that is most affected by thermal conduction is the peak hot mass within the hot bubble which decreases by roughly 40 per cent compared to the runs without conduction. Due to an increase of the densities within the shell the formation rate of molecular hydrogen increases roughly by a factor of two. Moreover, we find good agreement of our results with the recent work of El-Badry et al. (2019) who investigated the effects of cooling and thermal conduction in simulations of one-dimensional super-bubbles.

5. *Applications of the presented feedback scheme:* The presented feedback scheme is perfectly suited to be used in future simulations of galaxy formation and evolution that focus on sufficient modelling of the momentum build-up and hot phase generation that can be obtained at a target resolution of a few solar masses to obtain convergence on these quantities over a dynamic range of at least six orders of magnitude. While we extensively tested the properties that can be obtained in isolated unstructured ambient media, we also investigate the case of a feedback event in a highly supersonic, turbulent medium to investigate the momentum and hot-phase build-up in a more realistic environment. Moreover, we investigate the effect of multiple SNe in a closed box model to accurately derive the Volume filling factors for the hot-phase that can be obtained with the feedback scheme. The volume filling hot phase is of importance for the explanation of large scale galactic outflows as we already discussed in section 9.4. We find a dominating hot and warm volume filling fraction for our highest mass resolutions while we generally find that at lower mass resolution the hot volume filling fraction remains low. Thus to self-consistently drive galactic outflows with the feedback that we present it is necessary to have a mass resolution higher than 10 solar masses.

9.7.2 Model limitations

Although we find good agreement of our results with other theoretical studies we are still limited by some assumptions we already made in section 9.2. For the isolated remnants we assumed that they occur in an environment with a constant ambient density. Given the highly turbulent structure of the ISM (e.g. Elmegreen and Scalo, 2004) this is a rather simplified assumption. Further, we excluded the fact that massive stars normally shape their environment and ionise the surrounding ambient medium due to stellar winds prior to the core collapse event, which renders our assumption of a core collapse event in a fully molecular medium untrue. However, because in this regime we initially destroy all of the molecular hydrogen it does not influence the formation rate after shell formation. Further we neglected that each remnant ejects mass in the explosion, which initially alters the chemical composition of the remnant prior to shell formation. The injection of metals and dust in the explosion would significantly shorten the cooling time and increase the formation rate of the molecules. In a galactic context we can resolve the momentum and the hot phase in the Sedov-Taylor phase, while other properties of the a SN-remnant cannot be captured accurately. For example at the presented mass resolutions it is not possible to reach the predicted analytic value of the density in the adiabatic phase (before cooling dominates) of the remnant which can certainly change the on the fly updated cooling and molecular formation rates. Further, we do not consider magnetic fields in the shock. This could change the picture again because of the additional pressure component (the same is valid or cosmic rays). Moreover, in the case of the runs including thermal conduction it remains unclear to which degree the behaviour is driven by the numerics of the underlying scheme. Here, the crucial point is to resolve the structure of the hot and the cold phase which we do in our two highest resolution runs. If this can be done the effect is physical, if not it remains unclear whether the results have any physical impact. Further, we note that our resolution is far too low to resolve the internal heat fluxes within the bubble or the shell (once it has formed).

Acknowledgements

We thank the referee of this paper S.A.E.G. Falle for careful comments on the draft which significantly improved the quality of the paper. UPS thanks Eirini Batziou, Andreas Burkert, Chris Byrohl, Klaus Dolag, Joseph O'Leary, Rhea Silvia Remus, Felix Schulze and Simon White for helpful discussions and insights on the physics of the interstellar medium. UPS thanks Volker Springel and Prateek Sharma for useful discussion on thermal heat conduction. UPS thanks Jeong-Gyu Kim for his comments on the ISM in equilibrium. The authors gratefully acknowledge the computing time granted by the c2pap-cluster in Garching under the project number pr27mi where most of this work has been carried out. UPS and BPM are funded by the Deutsche Forschungsgemeinschaft (DFG, German Research Foundation) with the project number MO 2979/1-1. UPS and TN acknowledge support from the Deutsche Forschungsgemeinschaft (DFG, German Research Foundation) under Germanys Excellence Strategy - EXC-2094 - 390783311 from the DFG Cluster of Excellence 'ORIGINS'. The Flatiron Institute is supported by the Simons Foundation. SWG acknowledges support by the European Research Council via ERC Starting Grant RADFEEDBACK (no. 679852) and by the German Science Foundation via CRC956, Project C5.

Chapter 10

Outlook: Prospects in galaxy formation and evolution

Finally, we briefly want to discuss future prospects in the field of galaxy formation and evolution. Therefore, this is a more personal view on the field which will highlight the prospects that I think are important to focus on if one wants to progress the field of galaxy formation and evolution. As we already mentioned in chapter 1 there are basically two different approaches to galaxy formation nowadays. The first approach is Semi-analytic-modelling (SAMs) and the second is the one by means of direct numerical simulation. While I asses that the first approach is very useful for example for galaxy counts (e.g. Kauffmann et al., 1994), galaxy clustering (e.g. Wechsler et al., 2001), galaxy colours and metallicities (e.g Springel et al., 2001a), chemical enrichment histories (De Lucia et al., 2004) and galaxy abundances in the local group (e.g. Somerville, 2002), its results are clearly limited by the validity of the underlying physical models. However, the same statement can be made for large scale cosmological simulations like Magneticum (Hirschmann et al., 2014), Illustris (Vogelsberger et al., 2014), Eagle (Schaye et al., 2015) or Illustris-TNG (Pillepich et al., 2018) with the difference that those simulations are an 'one-shot' experiment and parameter studies are simply impossible due to limited computational power. Thus, if one is interested in exploring parameter space, this can be done much more efficiently by applying SAMs.

Despite the disadvantage in terms of computational run time, the approach of direct numerical simulation has the advantage that it directly includes a treatment of HD or MHD. Therefore, theses simulations resolve the baryon structure by construction much better than a SAM. However, how meaningful the results are, depends heavily on the tuning of the underlying physical models and progress can only be made by constantly checking the validity of the sub-grid models against results from smaller scale, higher resolution simulations on the sub-grid scale. While this works for some processes, the problem is typically that the coupling of most physical processes to the hydrodynamical flow is resolution dependent in a non-linear fashion. Moreover, the testing against resolved simulations is typically ignored as well, as there is not conclusive study to this day which shows that the subgrid model can successfully be tuned against resolved small-scale simulations.

Despite the fact that large scale simulations are limited there is at least one extremely important take away from the last decade, which is usually referred to as the importance of feedback. Feedback processes in galaxies and clusters prevent gas from cooling and control the baryon cycle. This actually has a more crucial implication which is the importance of the hot-phase of the gas in the ISM, CGM and ICM. I personally think that this is one of the most important results of the last 10 years is that one can make realistic galaxies in numerical simulations, if the hot phase of the gas is modelled appropriately.

This is a bit counter intuitive, because star formation occurs in cold dense regions, and therefore the trick is to establish a reservoir of hot gas by some process to prevent gas from undergoing the transition to the cold star forming phase. There are two obvious physical processes that can in principle keep gas in the hot phase in galaxies and clusters of galaxies, the feedback of (massive) stars and the feedback of AGN.

For stellar feedback one could argue that supernova-feedback of the massive star population with over 8 $M_{\odot}$ is the most important stellar feedback process as the canonical SN-energy is around 10^{51} erg and thus quite large[1]. Further, the process is instantaneous and has therefore and immediate effect on the surrounding structure on 100 pc spatial and 1 Myr time-scale. We showed in chapter 9 that it is now possible to model SN-feedback by pure thermal injection over a wide variety of densities and resolve the ST-phase and therefore the hot and diffuse ISM by construction. Furthermore, at least at solar metallicity, one also has to consider stellar wind mass loss, while ionising radiation and photo-electric heating play a crucial role also in low-metallicity stars. However, the effect of those is mainly that they reduce the environmental density for the subsequent supernova, which makes it very easy to establish the hot phase of the ISM by supernova-feedback. However, the modelling of photo-ionisation and photo-electric heating has to be improved in future simulations to make a conclusive statement, ideally by means of direct radiative transfer.

For stellar feedback processes one question remains. What about low mass stars. Low mass stars come in the picture as Type Ia supernova following some delay time distribution for the process, allowing them to travel large-distances before they explode, potentially in lower density environments. A feedback channel that is typically ignored but could be of importance for low mass stars are proto-stellar outflows and one goal for future galaxy simulations could be to include feedback by proto-stellar outflows (jets), not only for low mass but also for high mass stars. There are other feedback channels that could be of importance for stellar feedback. For example there is a large fraction of observed O/B runaway stars that seem to travel with significant velocities (above 30 km s^{-1}) across the Galaxy. Similar to the Type Ia channel those stars can travel very far from their birth place and can potentially contribute to galaxy outflows, CGM heating and metal enrichment. I have implemented two such models and we will discuss one of them briefly in section 10.1 to see the effect.

Another factor that could play a role is the variabiltiy of the canonical supernova-energy as a function of stellar main sequence mass. We know from one dimensional modelling of Type II SNe (Ertl et al., 2016) that there is a variation in the energy output of these type of SNe[2]. In the resolved galaxy feedback models we discussed in chapter 9 this could be directly tested by implementing the obtained explosion energies from Ertl et al. (2016) as a function of zero-age-main-sequence (ZAMS) mass, which is already implemnted and will be subject of future work.

For AGN feedback the situation is more complicated and while stellar feedback can now be resolved in galaxy-scale simulations this is not possible for AGN-feedback and subgrid-modelling will be of importance over the next decade. In depth discussion of AGN-feedback is out of the scope of this thesis, but I would rather want to point out some issues with it. First, while stellar feedback couples very efficiently to the ISM, this is not true for AGN feedback and it is not clear if the impact of AGN-feedback is overestimated in numerical simulations just simply because it can easily heat the hot gas in the current numerical implementations. Future galaxy simulations in a cosmological context,

[1] Still after working with this number for a couple of years now, its hard for me to imagine how significant the explosion is that is set free by that amount of energy. For comparison the largest explosion that was generated by humans is the Zar-hydrogen-bomb, with an energy release of around 10^{25} erg and therefore a supernova explosion is supposedly 26 orders of magnitude above that scale and I think its fair to say that this is a pretty significant explosion.

[2] Not relevant for the Type Ia, as they all explode at the Chandrasekhar-limit of around 1.5 $M_{\odot}$ for a rotating White Dwarf (WD) progenitor, making them standard candles.

with resolved stellar feedback have to be used to study this in more detail and we currently prepare a cosmological zoom-in suite of 5 galaxies to clarify the situation at the highest redshifts (see 10.3). Another interesting opportunity is to investigate the formation of star clusters in simulations with single stars and we have done that in Lahén et al. (2020). However, as this simulation was still carried out with SPH, the direct comparison with the newer MFM method is of interest, which will also be subject of future work and is briefly discussed in section 10.2. Furthermore, at some point during the next decade all these simulations have to ascend towards a two-fluid approach in terms of dust modelling, which will enable to possibility to investigate the wind launching process of cool stars in galaxy-simulations that drive their winds via radiation pressure on dust. We have carried pathfinder simulations for this task and present them in section 10.5.

10.1 Accounting for more processes in isolated galaxy simulations

As discussed above, efficient driving of outflows with supernova feedback is strongly dependent on the supernova environmental density. If the bulk of the SNe explodes in the high density regime the generation of the hot-phase is suppressed and outflows will remain inefficient. However, if the SNe explode in the low density environment this changes and one can generate the dominating hot phase naturally. Recently, Andersson et al. (2020) suggested that outflow rates and mass loading factors can be enhanced by a factor of 10 if the so called O/B runaway stars are included. These stars are massive stars that travel through the galaxy in a random fashion, seemingly decoupled from the ordered motion of the bulk of the stars in the Milky Way. There are two scenarios for the generation of runaway stars. The first is that a fraction of the massive star population obtains a velocity kick due to dynamical three body scattering. This is called dynamical ejection scenario (DES). While this process it not resolved within the scope of current galaxy simulations due to the current treatment of the N-body force integration, it can effectively be modelled in a sub-grid fashion, by assuming a certain velocity distribution, which is either a power-law or a Maxwell-Boltzmann-distribution for a given velocity dispersion (width of the distribution function). The second scenario is given via the binary ejection scenario (BES). Hereby, a star is ejected out of a massive binary system when the first star explodes in a core collapse supernova due to the combination of the kick during the supernova and the change of the gravitational potential due to ejecta and the subsequent the mass loss of the neutron star or black hole progenitor star. Of these two scenarios only the first one can be effectively modelled in the current scope of our code. The idea is that this fast travelling stars can explode in much lower density environments, as they can explode in inter arm region or further out in the CGM.
However, the study of Andersson et al. (2020) has raised some controversial discussion about the effect of runaway stars. On the one hand they only find a strong effect in MW-like galaxies in isolated galaxy evolution simulations that are evolved for roughly 300 Myrs. This generates two problems. The first is, that these isolated simulations undergo a starburst phase after start up because because there is no feedback to prevent initial star formation if not turbulent driving is present (which they did not use). The second problem is their base resolution of 9 pc in combination with their claim that they resolve the ST-phase by pure thermal injection, which is in tension with the results of Kim and Ostriker (2015) and Steinwandel et al. (2020b), who suggest that a five times higher spatial resolution is needed to resolve the ST-phase, even in isolated SN-remnant studies. However, Andersson et al. (2020) conclude that runaway stars burst the mass loading significantly in MW-like galaxies. On the other hand they report a weak effect in dwarf galaxies and argue this would be due to the porous structure of the ISM in dwarf galaxies. The problem is that while their 9 pc resolution might not be suitable to resolve the ST-phase in MW-like galaxies, it is enough for the low column density dwarf-galaxy regime. Thus the

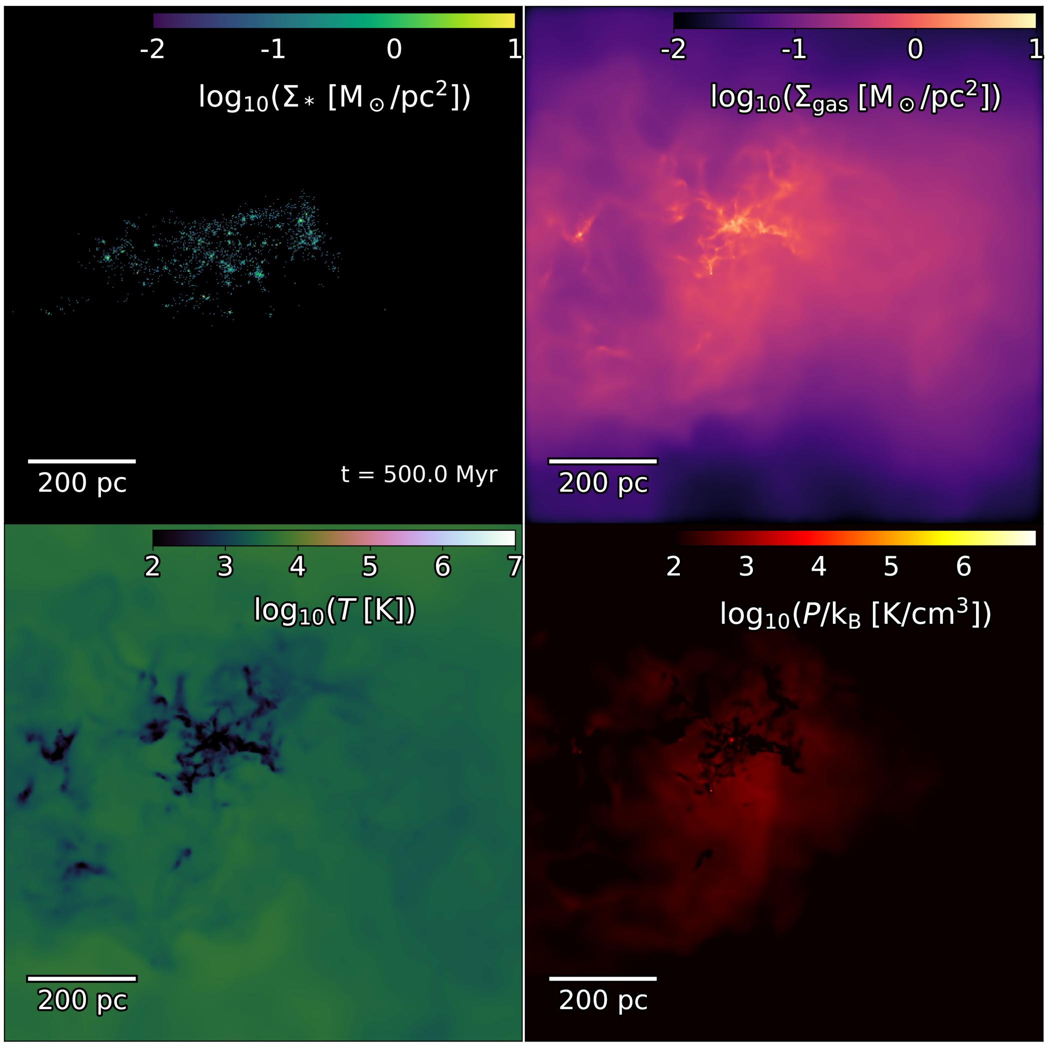

Figure 10.1: Stellar surface density (top left), gas surface density (top right), temperature (bottom left) and thermal pressure (bottom right) in the edge-on view of the galaxy at t= 500 Myr for the reference simulation without the runway stars.

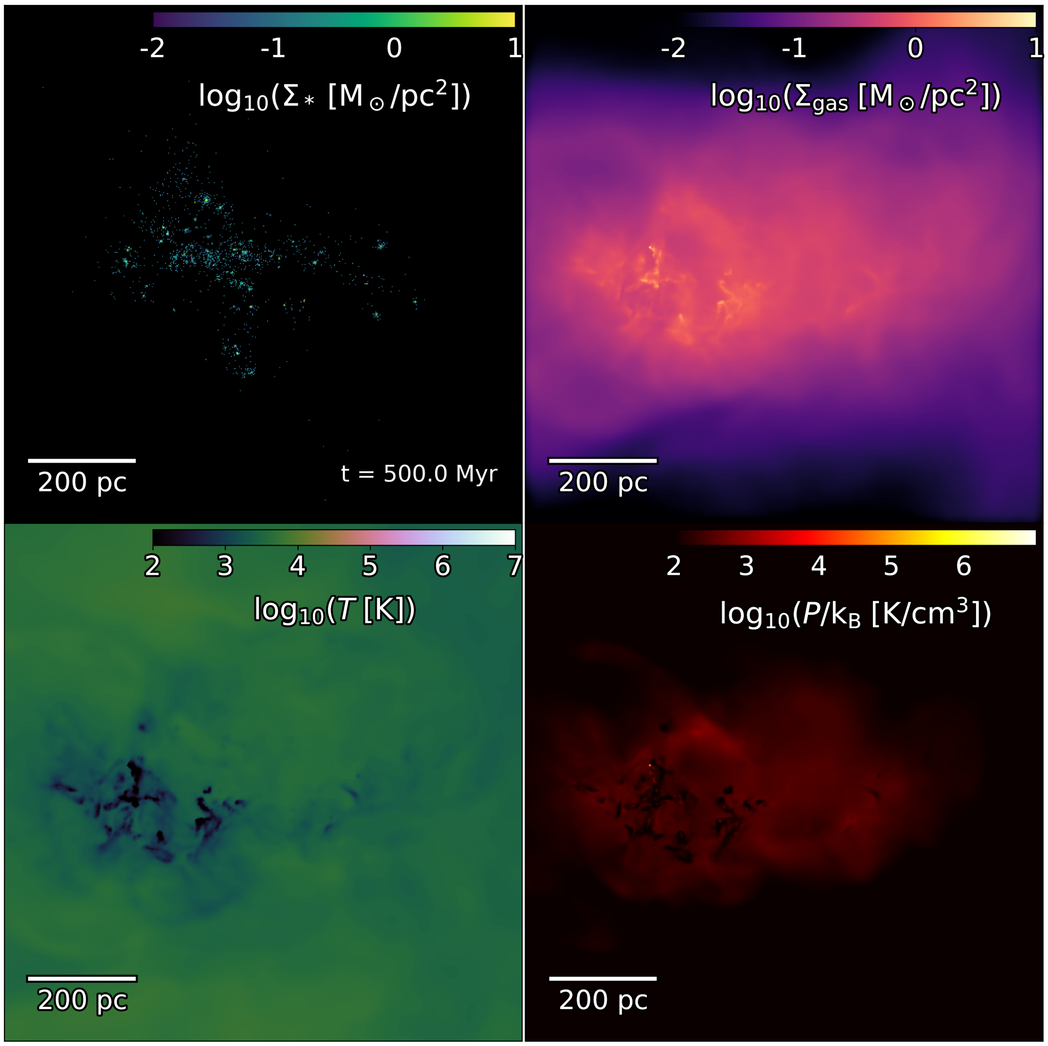

Figure 10.2: Stellar surface density (top left), gas surface density (top right), temperature (bottom left) and thermal pressure (bottom right) in the edge-on view of the galaxy at t= 500 Myr for the simulation with runaway stars in the power-law implementation.

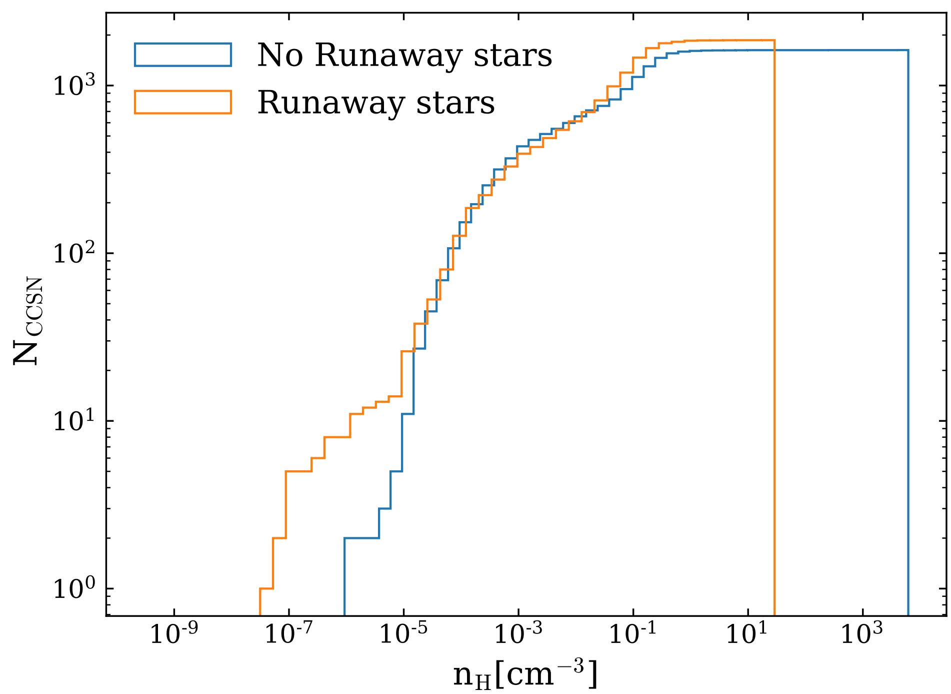

Figure 10.3: We show the cumulative distribution of the SN-environmental densities for the reference simulation without runaway stars (blue) and with runaways stars (orange). While the extreme environments differ and runaway stars suppress the explosions in the very high densities regimes, the overall structure remains unaltered.

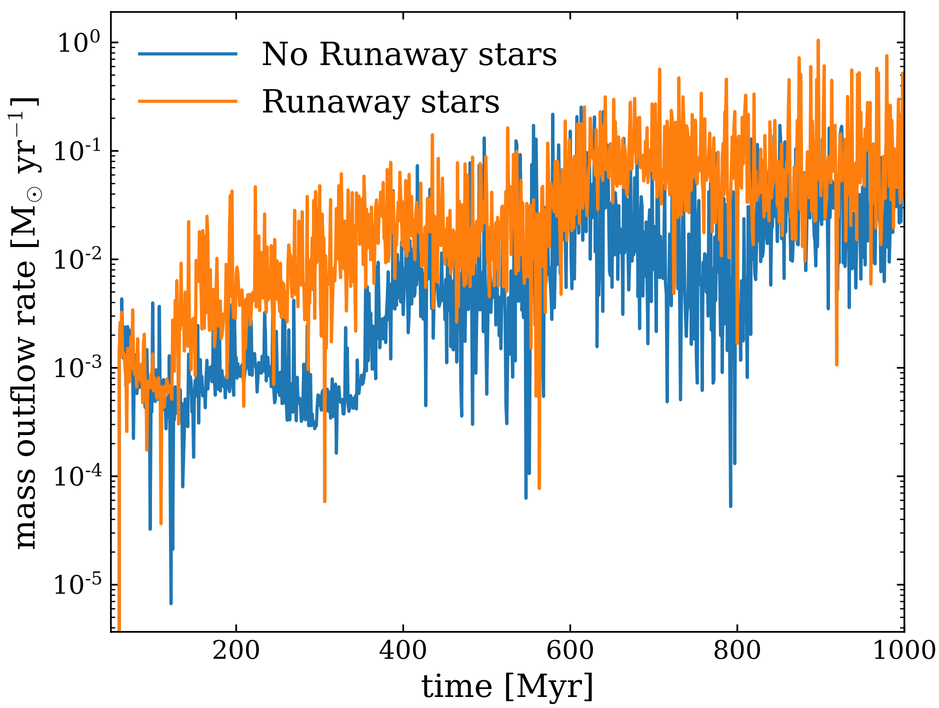

Figure 10.4: Mass outflow rate for our dwarf galaxy simulations. The blue line shows the outflow rate without runaway stars. The orange line shows the outflow rate with the effect of runaway stars.

conclusion should have been that there is a weak effect in dwarf galaxies and a non-conclusive result in MW-like galaxies due to unresolved SNe. The enigma is in the MW-model they present. In the run without runaway stars they have too few SNe in the resolved regime to launch an outflow. With runaway stars they suddenly push enough SNe in the low density media to launch the outflow, because the ST-phase is resolved with the applied 9 pc resolution in the diffuse ISM.

Further, there is some tension with their assumed velocity distribution as most studies assume a Maxwellian distribution instead of a power-law. In summary, the paper raised enough questions for a detailed study with our own ISM model, that has still some significant advancements, especially in the dwarf galaxy regime. First, we will carry out a one-to-one comparison to Andersson et al. (2020) before we extend the modelling to the more realistic Maxwellian distribution. In Figure 10.1 we show a reference simulation without runaway stars in the edge in view of the galaxy for stellar surface density (upper left), gas surface density (upper right), gas temperature (bottom left) and gas pressure (bottom right) at t=500 Gyr. In Figure 10.2 we show the same system with the effect of runaway stars, following a power-law velocity distribution. The overall morphology is only weakly influenced by the effect of runaway stars. However, we can also investigate and compare the outflow rate and the metal outflow rate (Figure 10.4 and Figure 10.5) to see if there is a strong effect caused by runaway stars in dwarf galaxies where we know that all the supernovae are resolved. We show this in Figure 10.3 where we show that most of the SNe explode in the regime of which we showed in Steinwandel et al. (2020b) that the applied mass resolution of 1 M$_\odot$ that we have in this dwarf galaxy with a stellar mass of $4 \cdot 10^6$ M$_\odot$, is enough to resolve most SNe. In the simulation with runaway stars it seems that the extreme regimes are mostly impacted, i.e. the distribution shifts order of 20 SNe in the very low density regime, compared to the simulation with runaway stars and reduces the maximum SN-environmental density.

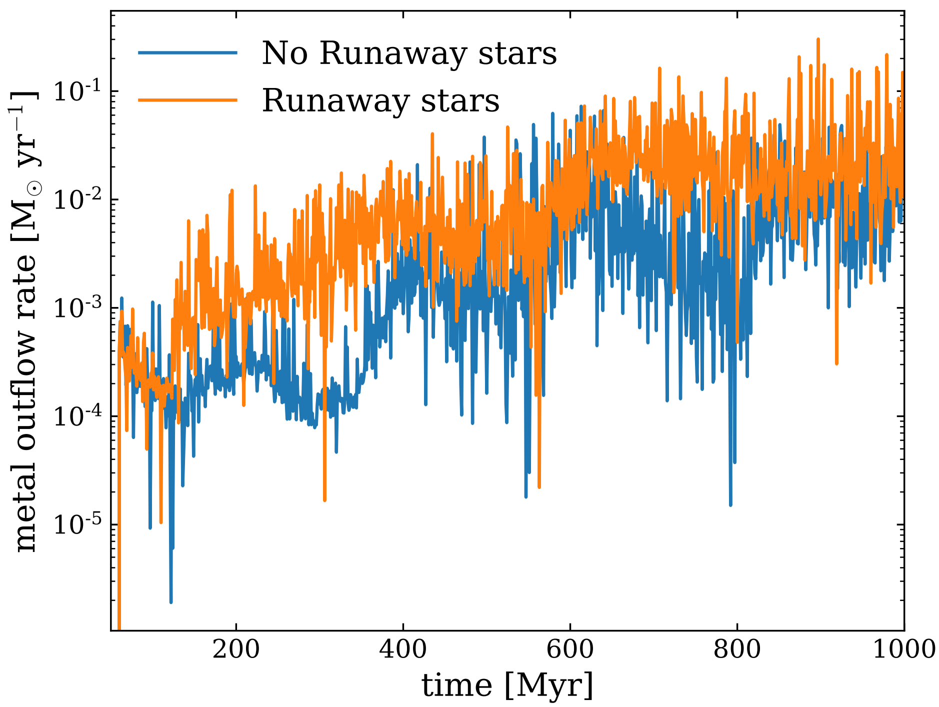

Figure 10.5: Metal mass outflow rate for our dwarf galaxy simulations. The blue line shows the metal outflow rate without runaway stars. The orange line shows the metal outflow rate with the effect of runaway stars.

However, this would indicate a small effect in our test simulation, which we expect. We find similar results in terms of the outflow rate and the metal loss rate which we show in Figure 10.4 and Figure 10.5, respectively as a function of time in direct comparison to the reference simulation that does not account for runaway stars. Overall, we find a weak effect of runaway stars, which is in line with the results of Andersson et al. (2020), but we would conclude that this changes with decreasing resolution and there will mostly be no outflow present as the feedback remains unresolved, which remains to be seen in our future studies. The more interesting question would then, if one can increase the outflow rate by including runway stars and push more and more SNe back into a resolved regime. From this one could even determine which fraction of the massive stars needs to get a velocity kick to obtain at which resolution a similar effect can be achieved as in the resolved case. This could be an interesting approach to improve stellar feedback models in large scale galaxy simulations. However, the last part of the study which is not carried out yet is to explicitly show that there is no outflow in an inverse resolution study. Furthermore, we implemented a different method from Andersson et al. (2020) for the kick velocity of the runaway star. Observationally, there is little evidence for the power-law implementation for the velocity kicks, as the typical distribution seems to be rather Maxwellian (e.g. Renzo et al., 2019, for a more detailed discussion). The other difference of the implementation of Andersson et al. (2020) is that they kick every massive star particle, while in practice a maximum of 50 per cent is estimated for kicks by three-body scattering. Therefore, in a second approach we implemented a Maxwellian distribution with a variable width as it is not finally decided what is the best value here. Observations indicate values from $\sigma = 5$ km s^{-1} to $\sigma = 256$ km s^{-1}. We further implemented a variable fraction for the massive stars that receive a velocity kick between zero and 100 per cent.

10.2 Galaxy merger simulations

Other aspects of galaxy formation and evolution can be investigated in major merger simulations. Lahén et al. (2020) were able to carry out a simulation of a major merger with our model for resolved stellar feedback in galaxy simulations. However, this simulation was still carried out with SPH at the time and we re-simulated the system with the new MFM technique to investigate the differences and in the long run report them in a comparison paper where we investigate the impact of the hydrodynamical method on the results of resolved numerical simulations. In Figure 10.6 we show the SPH version of the simulation and in Figure 10.7 the MFM-version. While the overall structure seems to agree very well, there are some differences in the details of the simulations, in the stellar structure and the structure of the gaseous component. The gas structure in the SPH run appears to be more smooth compared to the MFM run, which seems to further fragment to smaller scale clouds and filaments further out in the CGM. Further, the star cluster structure seems to be visually different. This kind of simulation is the perfect test bed for studies of star cluster formation. This has been shown in Lahén et al. (2020) who derived the star cluster mass function and showed that it has a slope of −1.7, which is actually quite close to the observed value of −2. In principle, it is not surprising that this is the outcome of the simulation. As we discussed in 4 there seems to be a tight correlation between the clump mass function and the IMF. However, star formation is still modelled stochastic and in fact we draw masses from the IMF that has a power-law mass function, which will give us hierarchical clustering in star forming regions by construction. That being said, it still implies that the model in its current scope was able to reproduce the clump mass function and the star forming regions to some degree. This could be tested in future studies with the new run. Further, we point out that the star clusters that have been found in the simulation so far are relatively close to the resolution limit of the simulation, up to a factor of two. This fact makes it necessary to investigate the star cluster formation in more detail in future studies,

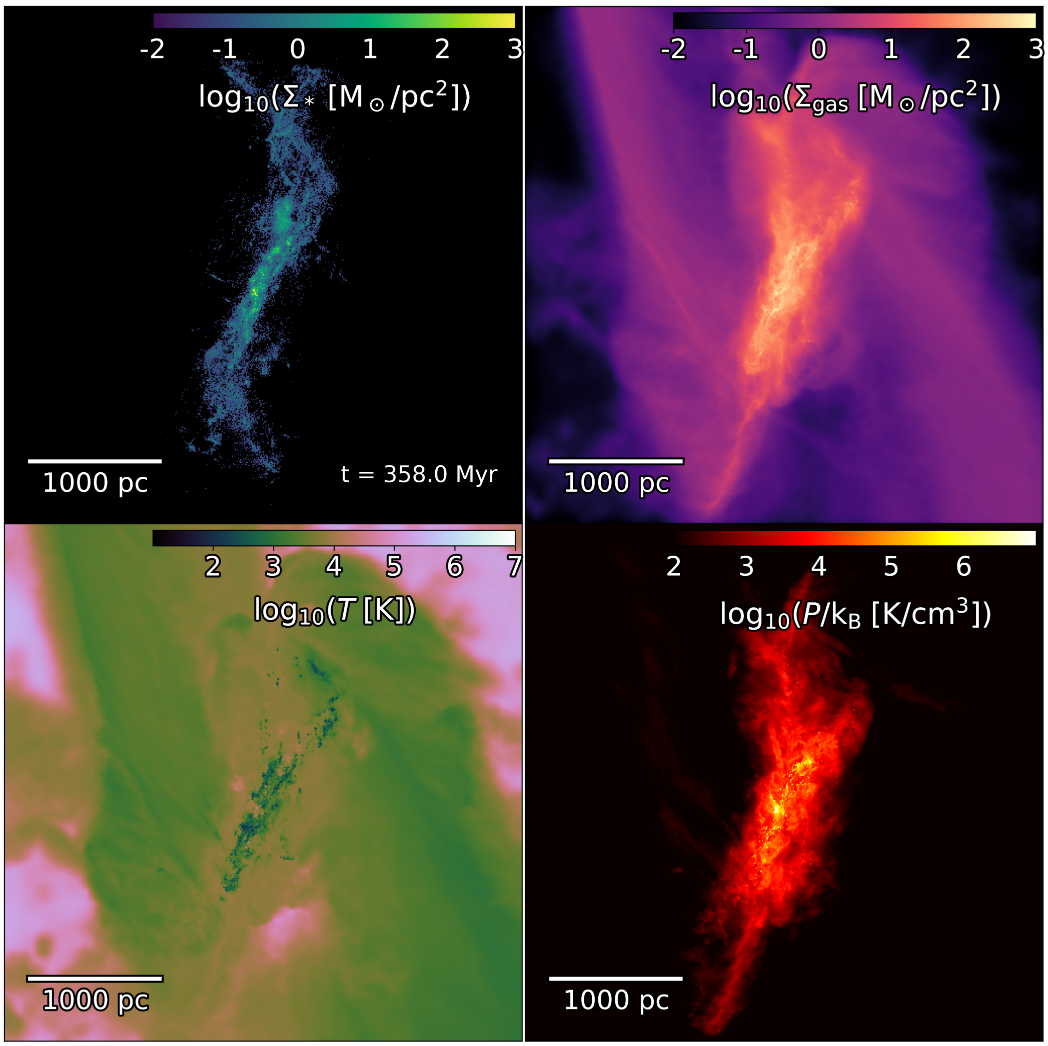

Figure 10.6: SPH dwarf merger simulation after 157 Myr, after the first encounter. We show the stellar surface density (top left), the gas surface density (top right), the gas temperature (bottom left) and the gas pressure (bottom right), shortly before the system enters a star burst event.

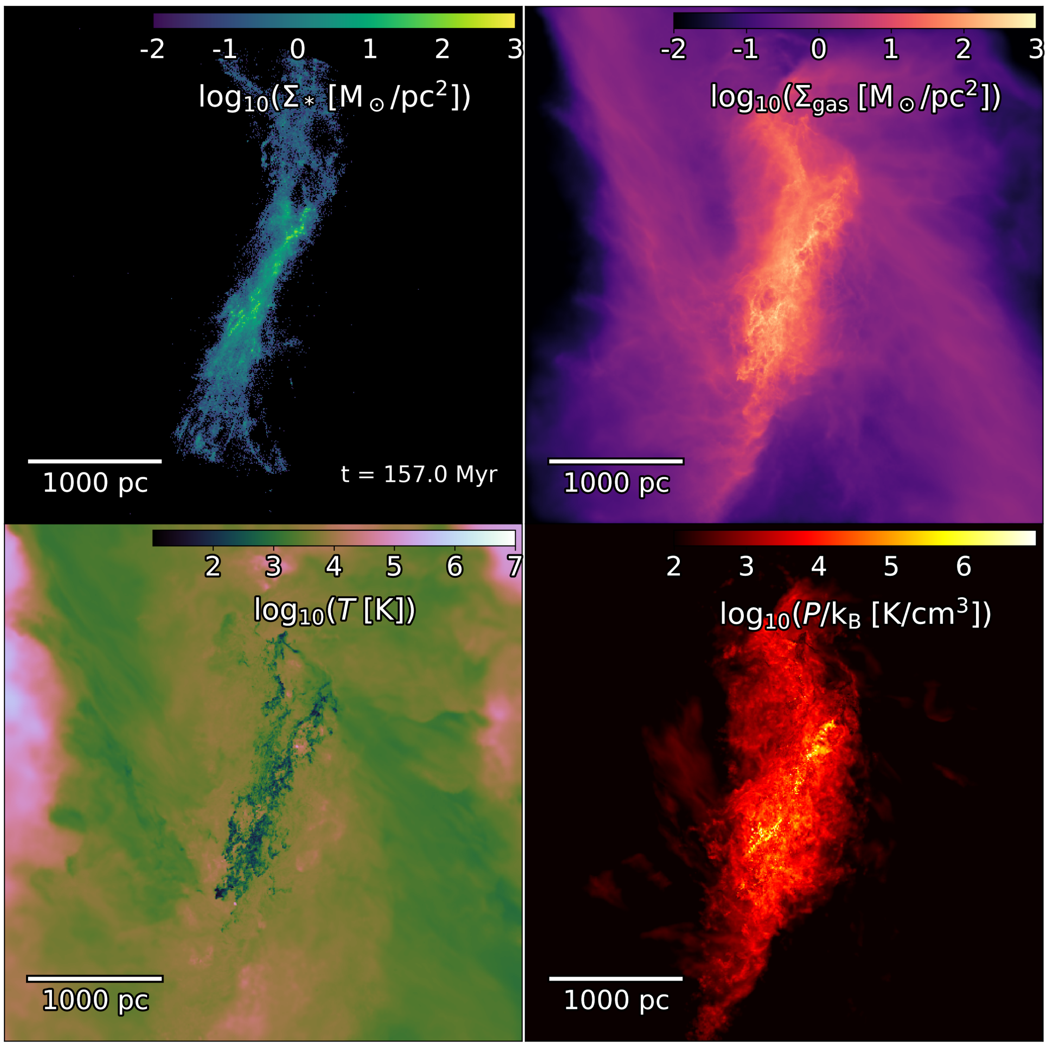

Figure 10.7: MFM dwarf merger simulation after 157 Myr, after the first encounter. We show the stellar surface density (top left), the gas surface density (top right), the gas temperature (bottom left) and the gas pressure (bottom right), shortly before the system enters a star burst event.

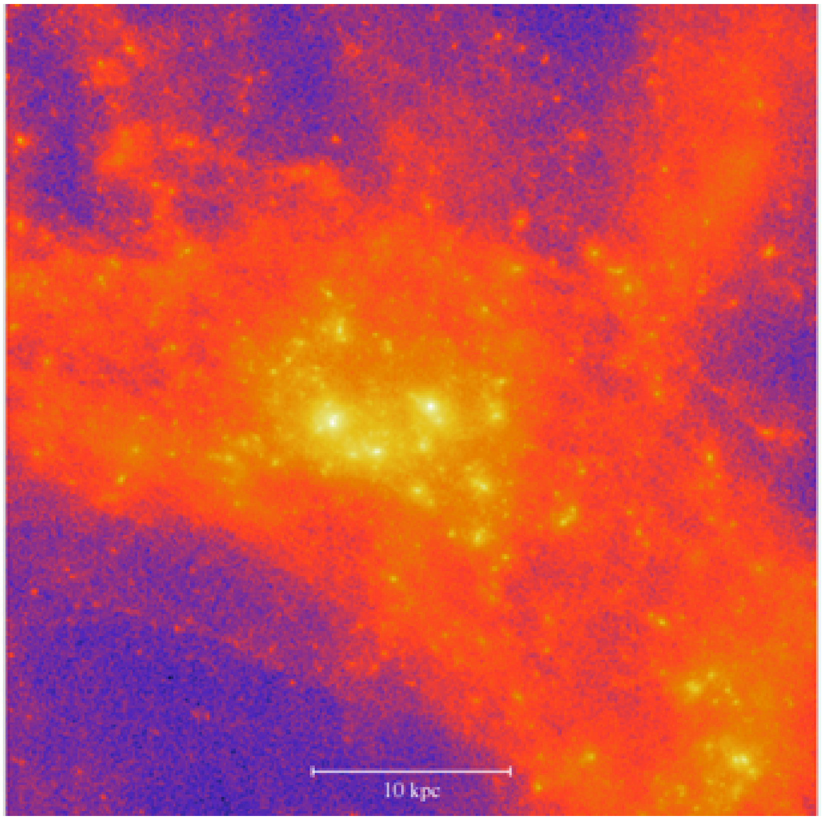

Figure 10.8: We show a pathfinder dark matter simulation selected for re-simulation with the full physics model at down to redshift 8.

especially in the scope of the new MFM-method as issues with the star cluster formation rate could be issues with the hydro-solver as well and the MFM provides us with a converged fluid flow.

10.3 Cosmological zoom simulations

The next step in the modelling of realistic galaxies is to investigate the effect of a resolved model for stellar feedback, like that one we presented in a huge part of this thesis, in cosmological-zoom simulations. However, this has proven to be a relatively complicated task, that has some major complications. The first and most crucial one is that the cooling and chemistry model that we have applied so far is not one-to-one applicable in a cosmological context. The first reason for this is that the primordial cooling channels have been excluded from the scope so far. For this reason Simon Glover and I developed an extension to the current scope of the chemical model that is now coupled to our code version of Gadget. This model combines the primordial cooling and chemistry channels at high redhsift with the dust dominated regime at low redshift and allows a smooth transition between those two regimes. This is of great importance as we want to carry out cosmological zoom-simulations, first at high redshift and later in the dwarf galaxy regime at redshift zero. This model allows us to do both without changing the cooling function too much. These simulations are currently under development and subject of research in the immediate future. We have selected the halos for re-simulation under high redshift conditions and have carried out some dark matter only runs at 20 $M_{\odot}$ resolution in the dark matter particles. This allows us to have a 3 $M_\odot$ resolution in the baryons in our production runs. We show an example halo for one of our dark matter only simulations in Figure 10.8 at $z = 8$ with a total mass of 10^{10} $M_\odot$.

10.4 Non thermal outflow mechanisms in galaxies

After we briefly discussed the road that lays ahead in the modelling of resolved stellar feedback, we want to follow up in the outflow driving process by magnetic fields, that was a huge part of this thesis, of which we were not only able to show that the effect is not driven by numerics, but we were also able to derive key features of the process in a more in depth analysis from the simulation and were finally able to derive an analytic approach to explain the magnetic field growth (see section 3.3.4) and accurately predict the outflow rate we see in the simulation. Why is this so important? For two reasons. The first is simple and everyone working on numerical simulations should do that anyway, namely obtaining a detailed understanding of how our simulated systems operate and corner out the physics from the numerical artefacts. The second one comes down to this. If we look at state-of-the-art numerical simulations of galaxy formation (Eagle, Illustris, Illustris-TNG, Magneticum) we have to understand the following. While they all incorporate models for AGN-outflows and stellar-feedback outflows, none of these simulations are suited to understand how outflows are driven in detail. The modelling simply does not account for it. What it does account for is pushing enough gas in the hot phase to obtain galaxy populations at redshift zero. It does not tell us that this is done by stellar feedback or AGN-feedback in reality, it tells us that it is driven by the modelling in the simulation. When we look at the results from outflow studies for example from the TNG-collaboration (Nelson et al., 2019) and look at predicted mass loading factors, specifically at the peak of star formation for massive halos, around $z \sim 2$, we see that the mass loading factors (even the ones at injection) are intrinsically too high when compared to observations of these systems (Förster Schreiber et al., 2019). This means that either the simulation or the observation show strange behaviour or the mass-loading in the simulation (the one which is tuned to at injection) is not the same as in the observations. We think that the latter is the case and the mass-loading is just a free parameter of the underlying galaxy formation model. Therefore, we will investigate now if our magnetic-driven outflow process might play a role at the peak of star formation by deriving the mass loading that can be obtained by our proposed outflow mechanism via the radial inflow dynamo from section 3.3.4.

Major observational results from high redshift observations show that the high redshift galaxy population is very compact and turbulent with thick discs, strong galactic outflows and declining ration curves (e.g. Genzel et al., 2014, 2017). This is in also in line with theoretical predictions for the high redshift galaxy population from numerical simulations (Teklu et al., 2018). There are good indicators that these outflows are driven by the feedback of AGN or star-burst events. However, we can use our derived outflow process and generalise it for the high redshift population to predict the impact of magnetic outflows in this environment.

First, we can rule out the α-Ω dynamo as the source of the magnetic field amplification in galaxies at $z \sim 2$ as its timescale goes as the disc scale height squared (h^2) and these galaxies show thicker discs with declining gas rotation. This increases the turbulent resistivity and decreases the rotational support, suppressing any α-Ω dynamo action. However, these systems are highly turbulent. The high amount of turbulence in discs at $z \sim 2$ can start magnetic field growth via the small-scale turbulent dynamo (kinematic regime) on Myr time scales and the magnetic energy density would quickly establish equipartition with the turbulent energy density, yielding $B \propto \sigma_{\rm turb}$ and increasing the magnetic field strength in high redshift systems easily by a factor of 5.

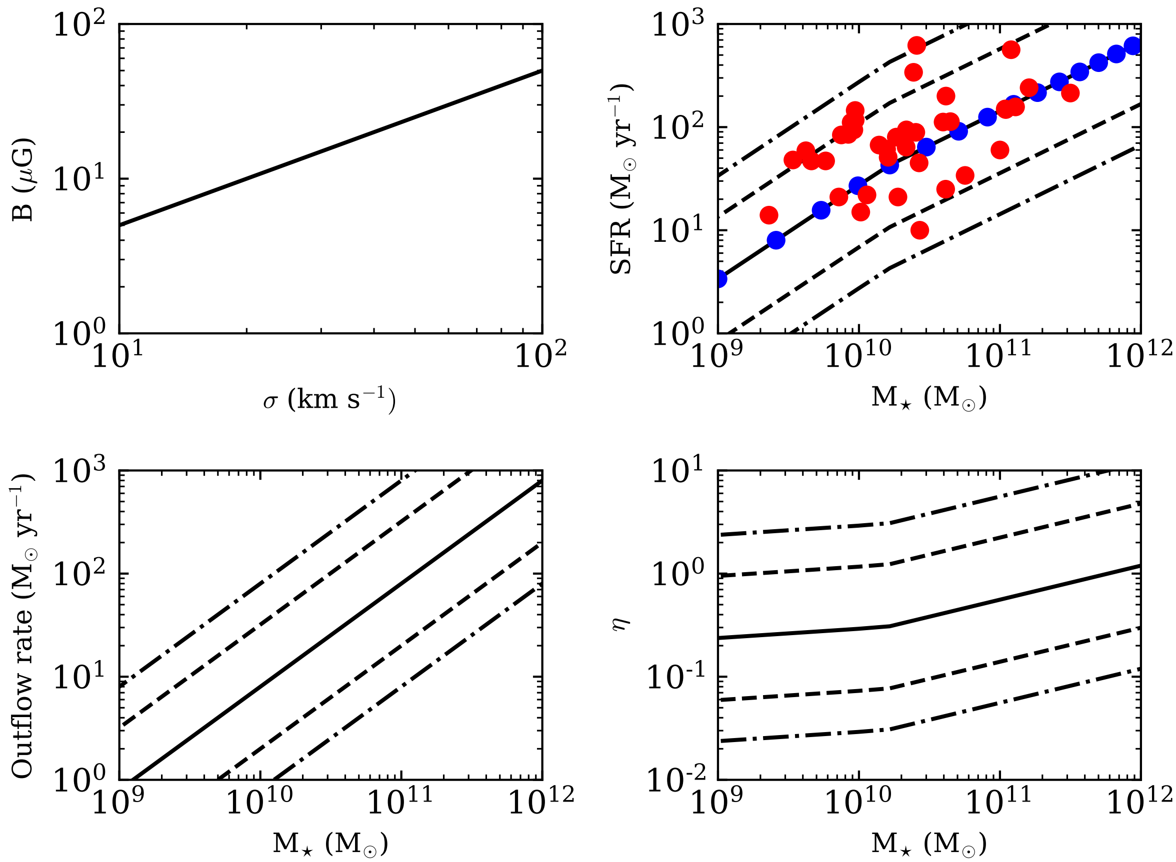

Figure 10.9: This figure shows the main results of our simple analytic prescription for predicting star formation rates, outflow rates and mass loading factors at high redshift. We assume that the magnetic field strength in equipartition scales with the turbulent velocity dispersion of the galaxy at hand, which would imply magnetic field that are of order 30 to 50 μG in high redshift galaxies that typically have velocity dispersion of order 40 to 120 km s^{-1} (top left). Via the magnetic field-star formation correlation of Schleicher and Beck (2013) we obtain the star formation rate that corresponds to the higher magnetic field strength and cross-match this against the star formation main sequence at $z = 2$ (Whitaker et al., 2014). Finally, we can derive the outflow rate in thin disc approximation by calculating the increase in the magnetic field via the radial inflow dynamo, yielding a power law increase of the outflow rate with stellar mass (bottom left). Finally, we can obtain the mass loading factor η by dividing the outflow rate by the star formation rate (bottom right).

From this we can directly estimate the star formation rate of these systems by applying the theoretical scaling of $B \propto \Sigma_{\rm sfr}$ that can be obtained analytically following Schleicher and Beck (2013). A non-axis symmetric instability like a bar, but also disc fragmentation (e.g. Behrendt et al., 2015) or cold filament accretion (e.g. Dekel et al., 2009, usually referred to as Dekel-Birnboim accretion of cold filaments) can now trigger the radial inflow dynamo and we can calculate the resulting outflow rate over the boundary condition of $B_r = B_\varphi = 0$ on the edges of the disc as we derived our results in thin disc approximation. Finally, we can cross match the obtained star formation rates of our model with the star formation main sequence at redshift $z = 2$ and obtain the mass loading factor as a function of the stellar mass, typically yielding values below 1. We show our results for this simple model in Figure 10.9.
However, we note that this intrinsically depends on the shape of the star forming main sequence, which is a clear limitation of the model which we plan to incorporate in future work. Nevertheless, the resulting outflow rates and mass loading factors are consistent with the theoretical expectations for an energy/entropy driven outflow. Our predictions could be tested by evaluating the magnetic field strengths in redshift 2 galaxies in an angular resolved fashion. If observations would indicate a linear scaling of magnetic field strength and velocity dispersion, our proposed wind driving process could play a crucial role in explaining outflow rates in high mass redshift galaxies.

10.5 Optical properties of dust driven winds

Future simulations of galaxy formation have to go even beyond hydrodynamics, magnetohydrodynamics, radiation and resolved feedback. A next natural step would be to include dust, first in a one-fluid approach by treating the dust as a fraction of the gas particles and physically evolve the dust-to-gas ratio by including ablation or sputtering processes as destruction processes and SNe as formation processes. The other way to include dust is to model it directly in a two fluid approach, where the dust is modelled as a separate species, like it is done with the dark matter and the gas in galaxy scale simulations. However, this is computationally expensive as all the interactions of the gas with the dust have to be modelled physically, and there has to be some momentum exchange between the dust and the gas species, plus a back reaction of the dust on the gas due to the drag-force. This has for example be done in Squire and Hopkins (2018) and Hopkins et al. (2018) who first derived an analytic prescription of the interaction of dust streaming through gas. Their very interesting result is that they find that the system of dust streaming at constant velocity through a gas generally renders to be unstable and tends to form instabilities in the dust. The basic idea is that the dust is capable to deposit momentum in the background drift of the gas and become unstable. Moreover, they were able to show that the streaming instability is a special case of this super class of dust-gas instabilities. They called this super class of instabilities Resonant Drag Instabilities (RDIs). In a second step they were able to find several of those instabilities in numerical magnetohydrodynamical simulations by solving:

$$\frac{d\mathbf{v}_{\rm d}}{dt} = -\frac{\mathbf{w}_{\rm s}}{t_{\rm s}} + \frac{\mathbf{w}_{\rm s} \times \mathbf{B}}{t_{\rm L}} + \mathbf{a}, \tag{10.1}$$

where $\mathrm{t_L}$ is the Lamor-time given as

$$t_{\rm L} = \frac{m_{\rm d} c}{|q_{\rm d}\mathbf{B}|} = \frac{4\pi\rho_{\rm d}\epsilon_d^3 c}{3e|Z_{\rm d}\mathbf{B}|}, \tag{10.2}$$

with m_d as the grain mass and Z_d as the grain charge. This Larmor time corresponds to a Larmor frequency $\omega_{\rm L}$ at which charged particles gyrate under the influence of the magnetic field. This yields the equation of motion:

$$\rho_{\mathrm{g}}\left(\frac{\partial}{\partial t}+\mathbf{u}_{\mathrm{g}}\cdot\nabla\right)\mathbf{u}_{\mathrm{g}}=-\nabla P_{\mathrm{g}}+\frac{\mathbf{B}\times(\nabla\times\mathbf{B})}{4\pi}+\int d^3v_{\mathrm{d}}f_{\mathrm{d}}(\mathbf{v}_{\mathrm{d}},\mathbf{x}_d)\frac{\mathbf{w}_{\mathrm{s}}}{t_{\mathrm{s}}}. \tag{10.3}$$

In practice this is solved with the MFV method. However, the integral on the right hand side of equation 10.3 is non-trivial with the default integration scheme of the code Gizmo which uses a Leap-Frog integrator. The problem is the following. The distribution function f is a phase-space integral and thus dependent on the position vector $\mathbf{x}_{\mathrm{d}}$ and the velocity vector $\mathbf{v}_{\mathrm{d}}$. We immediately see why this is a problem for the Leap-Frog integrator because it integrates on the halfsteps. Thus $\mathbf{x}_{\mathrm{d}}$ and $\mathbf{v}_{\mathrm{d}}$ are never known at the same time, only shifted by a halfstep. Therefore, there is some intrinsic numerical error that is integrated by including the momentum exchange in equation 10.3 using the Leap-Frog method. In practice the error can be controlled by a small Courant-number, which has the drawback of increasing the run time of the simulations. Hopkins et al. (2020) also tested a higher order Boris-integrator which is based on a velocity-Verlet method, but they find little difference on the impact of the results.
In collaboration with Philip. F. Hopkins and Sasha Kaurov we investigated the optical properties of these RDIs, by reconstructing their optical depth signal in an AGB-star atmosphere. We chose the AGB-atmosphere because AGB-wind are dust-driven and thus a perfect test-bed for testing the observational significance of the RDIs. Thus we carried out simulations of the RDIs by constantly accelerating dust particles in a small patch over the AGB-atmosphere. The acceleration is constrained to the acceleration that can be obtain by the radiation pressure that is acting on the dust in the upper atmosphere of the AGB star.

10.5.1 Initial Conditions and units

Hopkins and Squire (2018) showed the existence of an equilibrium solution with a constant dust- to-gas ratio $\mu=\langle\rho_{\mathrm{d}}\rangle/\langle\rho_{\mathrm{g}}\rangle$, the gas velocity $\langle\mathbf{u}_{\mathbf{g}}\rangle=\langle\mathbf{u}_0\rangle+\mathbf{a}t\mu/(1+\mu)$ and the dust drift $\langle\mathbf{w}_{\mathrm{s}}\rangle=\mathbf{a}\langle t_{\mathrm{s}}\rangle/(1+\mu)$. The parameter $\mathbf{u}_0$ determines the velocity of the fluid for $t=0$ and $\mathbf{a}$ specifies the acceleration (e.g. acceleration due to radiation pressure). Further, the system is specified by the stopping time given by $\langle t_{\mathrm{s}}\rangle=t_{\mathrm{s}}(\langle\rho_g\rangle\mathbf{w}_{\mathrm{s}})$. The simulations are initialised by assuming this equilibrium solutions at $t=0$ in a fully periodic 3D Box with the box length $L0$ with $\langle\mathbf{u}_0\rangle=0$ and $\langle\mathbf{w}_{\mathrm{s}}\rangle=\mathbf{a}\langle t_{\mathrm{s}}\rangle/(1+\mu)$. While Moseley et al. (2019) focus on resolution studies of these systems to study the non linear growth regime of the RDIs using constant grain sizes we want to investigate a more specific case. We investigate the system in a regime when the grains have variable sizes following the grain size distribution given by equation 10.4, following Mathis et al. (1977):

$$\frac{dN}{da}\propto a_{\mathrm{d}}^{-3.5}, \tag{10.4}$$

The simulations are carried out with 256^3 gas particles and $4\cdot256^3$ dust particles for the two different cases. For the HD-simulations we carry out two different runs. In the first one we assume that the dust particles feel the same acceleration regardless of their size. In the second configuration we assume the more realistic/physical case of dust particles which feel an acceleration depending on their grain size. In the MHD-simulations we only utilise the latter. The particles are initialised on a uniform grid. This leads to very good results and seems to perform very well compared to other methods for initialising the particle positions (e.g. using a glass-distribution) as shown in Moseley et al. (2019). In the MHD-case we make some slight modifications to the setup. The drift velocity is given by

$$w_s^0=\frac{at_s^0}{1+\mu}\left[\frac{\hat{\mathbf{a}}-t_s^0/t_L^0(\hat{\mathbf{a}}\times\hat{\mathbf{B}}_0)+(t_s^0/t_L^0)^2(\hat{\mathbf{a}}\cdot\hat{\mathbf{B}}_0)}{1+(t_s^0/t_L^0)^2}\right]. \tag{10.5}$$

Further, we have to initialise the grain charge and the angle between the magnetic field vector and the drift velocity. The charge of the grain is given by the grain charge parameter $\tilde{\phi} = 3Z_\mathrm{d}e/4\pi c\epsilon_\mathrm{d}^2\rho_\mathrm{g}^{1/2}$ and the angle between the magnetic field vector and the drift velocity defined by $\cos\theta_\mathbf{Ba} = |\hat{\mathbf{B}}_0 \cdot \hat{\mathbf{a}}|$. However, we restrict the results that we show in this thesis to the hydrodynamics case only, we generally find very little difference in the optical properties of the instabilities between the HD and MHD case.

The setup is initialised in the most general way that is possible. We work in dimensionless units in terms of the equilibrium sound speed $\langle c_\mathrm{s}\rangle$ and gas density $\langle\rho_\mathrm{g}\rangle$ and the box size L_0. In this context, the system has only three free parameters, the dust-to-gas ratio μ, the acceleration of the dust particles $\mathbf{a}L_0/\langle c_\mathrm{s}^2\rangle$ and the grain size parameter α given by $\rho_\mathrm{d}a_\mathrm{d}/\langle\rho_\mathrm{g}L_0\rangle$. The choice of dimensionless units is motivated by two aspects. The first one is to focus on the detailed structure of the RDI. The second one is to keep the system as general as possible. Potentially there are a lot of regions within the universe where this instabilities can have a huge impact on the dynamics, like in giant molecular clouds (GMCs), winds of the AGB stars or the surrounding medium of the AGN. The systems for which we can work out a more detailed framework in physical coordinates will be presented in chapter 10.6.

10.6 Constraints given by an AGB-star atmosphere

We assume that the RDIs appear in the atmosphere of AGB stars which winds are mainly driven by dust (Höfner and Olofsson, 2018). In this section we discuss how we can constrain the physical system of an AGB-star. The whole simulation is characterised by three physical parameters, the dust-to-gas-ratio μ, the drift velocity of the dust (i.e. the external acceleration on the dust particles) and the grain-size-parameter. However, the grain size-parameter is not a full physical parameter and is numerically given through:

$$\frac{a_\mathrm{d}\rho_\mathrm{d}}{L_\mathrm{Box}\rho_\mathrm{g}} = \text{const.}, \tag{10.6}$$

To constrain the system of an AGB-star properly we therefore need the dust-to-gas-ratio around this objects, an estimate for the acceleration parameter that is given by a typical AGB-star and a value for the minimum and maximum size for the grain size parameter. Typically, the wind of an AGB-star is defined by its luminosity L_AGB, its mass loss rate $\dot{M}_\mathrm{AGB}$ and the velocity v_AGB. Moreover, the size of the AGB-star R_AGB is an important quantity to define the system. Further, we need to assume a typical value for the optical depth τ_AGB in the close neighbourhood of the system. We show typical values for this parameters in table 10.1 and discuss them briefly in the following section. Stars on the AGB-branch are in the stage of burning helium to carbon in the so called triple-α process. In this process, three helium-cores fuse to one single carbon core and put out an energy of around 25 MeV. While the stars are on the AGB-branch they are in hydro static equilibrium. Although, the stars are stable once they reach the AGB-branch there are requirements on the initial mass for the stars to populate the AGB-branch. The lower limit is roughly $0.6M_\odot$ dominated by the fact that the star must be heavy enough to survive the Helium-flash, when the core abruptly expands due to the transition from a degenerate equation of state to a adiabatic equation of state. The upper limit is set to around $10M_\odot$ by the fact that stars with a higher mass never reach hydro static equilibrium via the triple-α-process. While moving towards the AGB-branch the stars increase in size due to the fact that the core is contracting and heating the caveat from below leading to enhanced hydrogen burning in the envelope at a larger radius. The objects can reach radii up to 1 Au($\propto 250R_\odot$). The increase of the radius leads to a drop of the effective temperature to a value of between 2000 and 3000 K. However the effective temperature and the radius of the star determine its luminosity, given by $L/L_\odot = (R/R_\odot)^2(T/T_\odot)^4$. While the effective temperature drops but

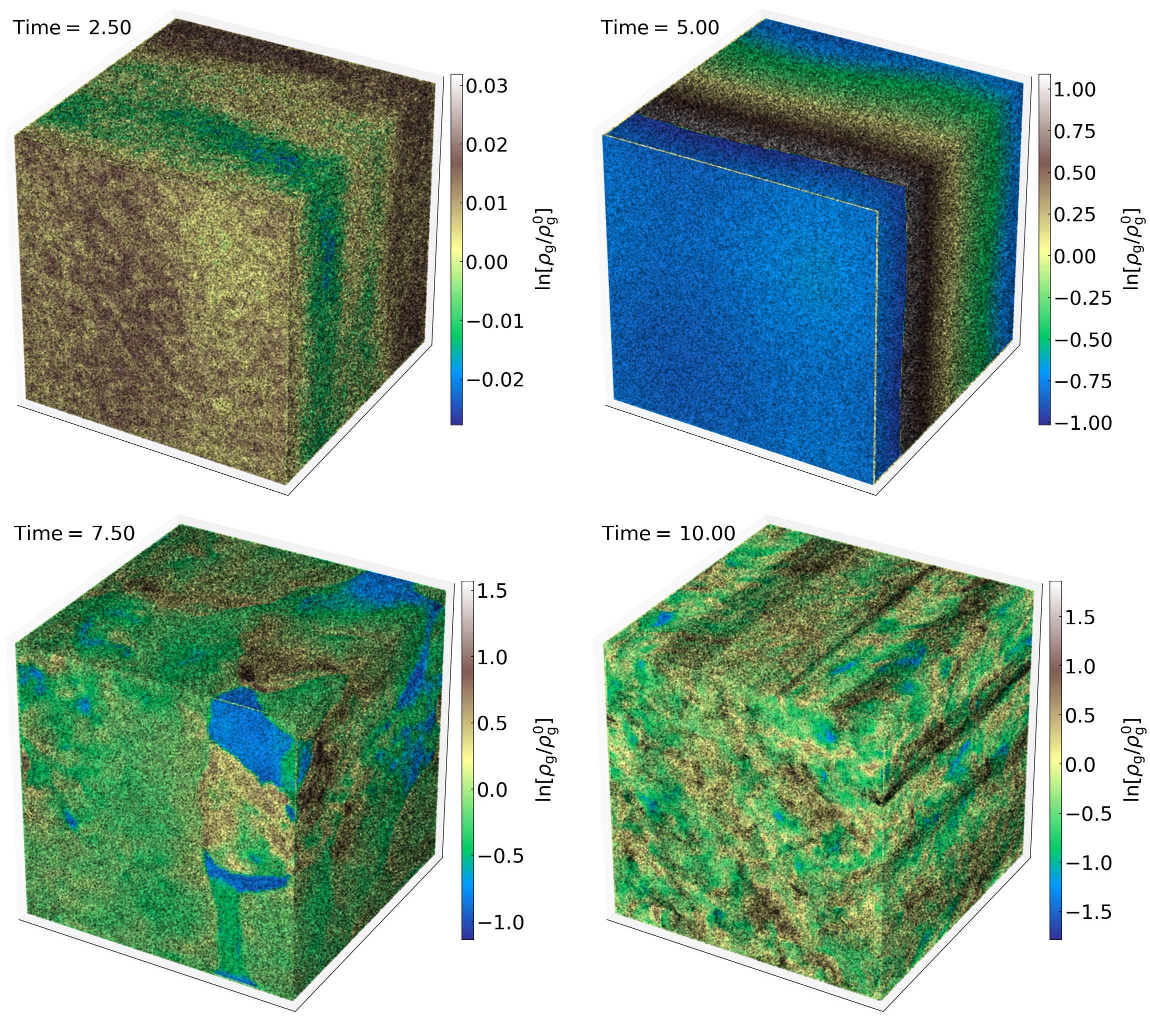

Figure 10.10: Time evolution of the RDIs for the simulation HD-c in which we apply a constant acceleration independent of the size of the grains. We show the structure of the RDIs for four different points in time. For a constant acceleration all grains move initially with the same velocity and the dust particles start to form a sheet. This sheet stars to to collapse to more complex structures due the rapid non-linear growth phase of the RDIs. Finally, the structure of the RDIs saturates in elongated cylinders within the box.

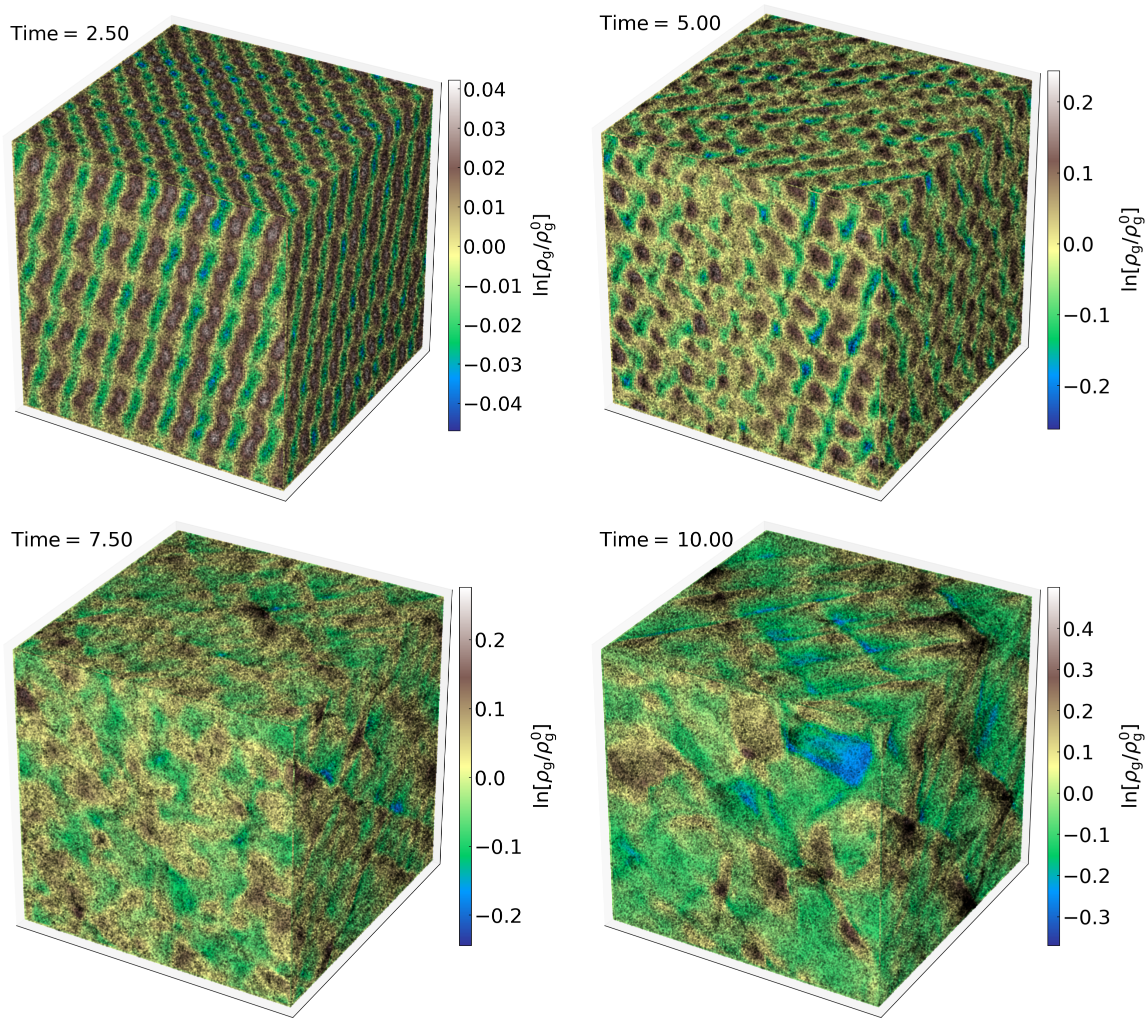

Figure 10.11: Time evolution of the RDIs for the simulation HD-no-c in which we apply a grain size dependent acceleration. We show the structure of the RDIs for four different points in time. For a non constant acceleration all grains move initially already with a velocity offset leading to a more violent build-up of the RDIs that shows a less regular structure compared to the simulations that use a constant acceleration on the grains. Here, the RDIs form isolated regions with large dust over-densities.

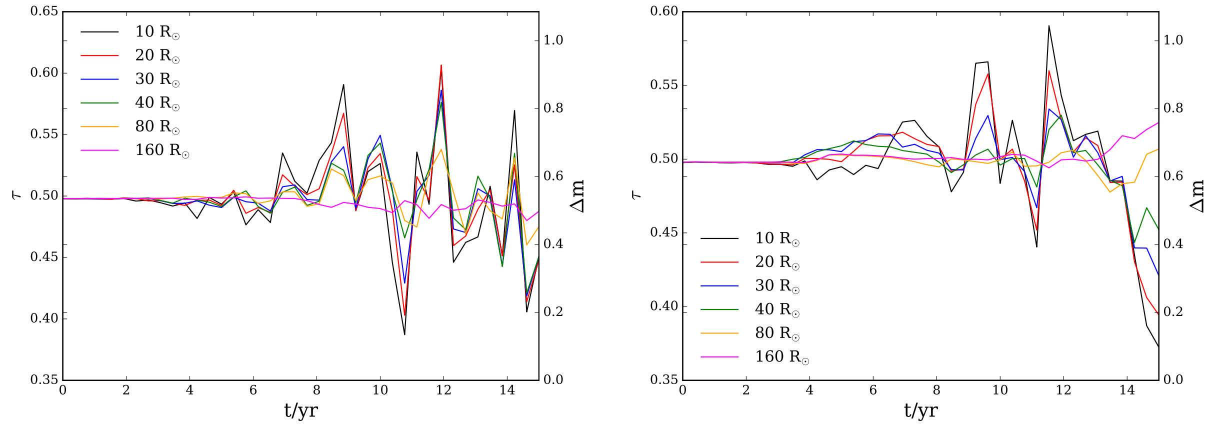

Figure 10.12: Fluctuations of the optical depth as a function of time for different sizes of the observed star constrained to the unit system for the AGB-star that we obtained in section 10.6. For small AGB-stars we find that the fluctuations of the optical depth can be relatively large due to the fact that the RDIs generate either over or under densities of the dust which can block the escaping radiation from the star. For larger stars we find that the optical depth remains more less flat. This can be explained by the fact that the large stars reach the box size of the simulation domain. Therefore they converge to the fixed optical depth within the box. We show the results for two different sight lines through the box. The top panel shows the line of sight that is perpendicular to the xy-plane of the system. The bottom panel shows the line of sight that is perpendicular to the xz-plane. The last line of sight is statistically insignificant.

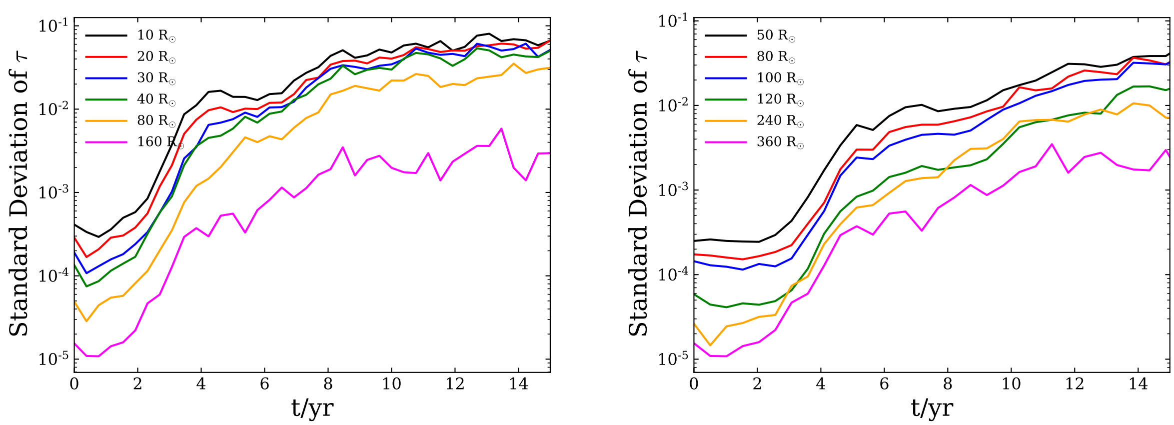

Figure 10.13: Standard deviation of the optical depth for stars of different sizes and along different line of sights through the boxes. In the top panel we show the line of sight perpendicular to the xy-plane and on the bottom perpendicular to the xz-plane. In all cases the standard deviation of the optical depth increases due to the built-up of the RDIs.

Table 10.1: Typical physical AGB-star parameter

Typical values for AGB stars from Observations	
Stellar mass [$M_\odot$]	$0.6 - 10$
Stellar radius [$R_\odot$]	$10 - 250$
Effective temperature [K]	$2000 - 3000$
Envelope density [g cm^{-3}]	$10^{-12} - 10^{-10}$
Luminosity [$L_\odot$]	10^3 - 10^4
Wind velocity [km s^{-1}]	$5 - 30$
Mass loss rate [$M_\odot$ yr^{-1}]	$10^{-8} - 10^{-4}$
Dust-to-gas ratio μ	$10^{-4} - 6 \cdot 10^{-3}$
Optical depth τ	$0.5 - 1.2$

stays inside the same order off magnitude but the radius can easily increase by a factor of 100 the typical luminosity's can reach values up to $10^4 L_\odot$. While most values of AGB-stars are quite extreme compared to low mass stars on the main sequence, the wind velocities of these objects are quite low compared to solar-like main-sequence stars and reach maximum values between 5 and 30 km s^{-1}. These winds are driven by the radiation pressure acting on dust grains in the lower atmosphere of the star, triggered by high mass loss rates of AGB-stars between 10^{-8} and $10^{-4} M_\odot$ /yr^{-1}, leading to values of μ in the neighbourhood of the star between 10^{-4} and $6 \cdot 10^{-3}$. The optical depths are between 0.5 and 1.2. This parameter space can be used to constrain the ICs for a box that represents a patch of an AGB-star wind in the close neighbourhood (a few $R_\star$) of the star. In three steps we constrain a unit system for an AGB-star environment.

1. Choose a set of parameters by selecting a certain optical depth for the box.
2. Calculate the grain-size-parameter in code units for a given optical depth of the box.
3. Use the grain-size-distribution to calculate the acceleration parameter in code units for a given Luminosity of the star.

We note that we do not want the system to be to extreme in either direction and therefore we assume intermediate values for all parameters.

10.6.1 Constraints for the optical depth

We want to choose the optical depth to be 0.5 within the simulation. The optical depth of the Box depends on a few parameters, especially the dust-to-gas-ratio μ, the distance from the stars surface and the mass loss rate of the star. We can approximate the optical depth by calculating

$$\tau = \frac{\mu}{0.01} \frac{R}{1000 R_\odot} \frac{\dot{M}}{10^{-6}} \tag{10.7}$$

If we choose not to extreme values for the dust-to-gas we can obtain a reasonable value for the optical depth. We choose the dust-to-gas ratio to be $\mu = 0.01$ (as an upper limit), the distance from the star to $1000 R_\odot$ and an intermediate to high outflow rate of $M_\odot$ of $5 \cdot 10^{-5} M_\odot$ yr^{-1}. This gives an optical depth of 0.05. While this value seems to be to low if we apply single grain sizes it fits very well if we apply the more physical case of a grain size distribution, as the optical depth is dominated by the grains with smaller size. This is pointed out in section 10.8. In the case of this grain size distribution we get a value of the optical depth which is exactly a factor of 10 larger. Therefore, this set of parameters is appropriate for a box with an optical depth of 0.5.

10.6.2 Calculating the grain size parameter α

Under the assumption of the optical depth that we calculated in section 10.6.1 we can derive the value for the grain-size-parameter α. If we set the minimum of the grain size parameter to 1 per cent of the maximum grain size we will automatically obtain an optical depth of 0.5. We can therefore calculate the maximum grain size parameter with the relation

$$\alpha_{\mathrm{max}} = \frac{3}{4}\frac{\mu}{\tau} \tag{10.8}$$

This sets the numerical value for α_{max} to 0.015. The minimum for the grain size parameter is therefore set to 0.00015. This parameters are chosen to obey the physical system of an AGB-star system in the unit-system we use for running the simulations.

10.6.3 Calculating the acceleration parameter

Finally, we can calculate the acceleration parameter by taking the grain size parameter into account. A lengthy calculation leads to the relation between the acceleration parameter a_{cc} in code units and the grain size parameter α given by

$$a_{\mathrm{cc}} = \frac{3}{4}\alpha\frac{10^3 L_{\odot}\dot{M}}{4\pi r^2}, \tag{10.9}$$

This constraints our physical unit system to the internal reduced unit system with which we ran the boxes.

10.6.4 The physical unit system

So far we set the parameters for the boxes in reduced units in a way that it is connected to the framework of an AGB star. However, the final step that is missing is to convert the unit less system into physical units. We adopt the units for the dust grains as follows. The maximum grain size a_{max} is set to $1\mu m$ which is in agreement with observations Draine and Salpeter (1979); Weingartner and Draine (2001). Using this definition we directly find the minimum grain size which is given by $a_{\mathrm{max}}/100$ given via the initial grain size distributions that has been used in the original setup. To calculate the particle masses of the dust grains we assume the mean density for the dust grains given by $\langle\rho_{\mathrm{d}}\rangle = 2$ g/cm^{-3} which is also in good agreement with the observations of dust particles in the ISM and protoplanetary discs. Further, we assume the dust particles to be spherical. Therefore, the mass m_{d} of the dust particles is given by

$$m_{\mathrm{d}} = \langle\rho_{\mathrm{d}}\rangle \cdot \frac{4}{3}\pi a_{\mathrm{d}}^3. \tag{10.10}$$

Using this definitions it becomes possible to define our system of units for the surroundings of an AGB-star. We can calculate a physical box size by using equation 10.6 and specify the grain size density $\langle\rho_{\mathrm{g}}\rangle = 2g/cm^3$, the grain size $a_{\mathrm{g}} = 0.0001cm$, and the gas density $\langle\rho_{\mathrm{gas}}\rangle = \dot{M}/4\pi r^2 v_{\mathrm{w}}$. This leads to a box size of the physical system of $330R_{\odot}$. Using that we can derive the time unit over the wind speed of roughly 10 km s^{-1} to 0.75 years. Therefore, we see that the box simulation can represent a patch of an AGB-star atmosphere with 330 $\mathrm{R}_{\odot}$ that is 1000 $\mathrm{R}_{\odot}$ away from the AGB-stars surface.

10.7 Obscuration effects due to the RDIs in AGB-star atmospheres

10.7.1 Morphology of the instabilities

We start our discussion of the results by visualising the results we obtain from the two simulations on which we base our studies on the general optical properties that arise in the presence of the RDIs. We introduce the shortcuts HD-c and HD-no-c for the two simulations based on the fact that in the model HD-c the acceleration that the particles feel is independent of the grain size, while in the model HD-no-c we present the more realistic case of a grain size dependent acceleration, as we pointed out in section 10.5.1. In figure 10.10 we show a time sequence of the model HD-c for four different points in time. In figure 10.11 we show the time evolution of the model HD-no-c for the same points in time. Although, both simulations start from the exact same initial conditions the build up of the RDIs is completely different between both simulations. In the case of the model HD-c we can observe that the RDIs build up in sheets which are moving through the box, before they build up elongated cylinders through the whole box. The initial behaviour of the movement of the dust in the model 10.10 can be explained by the fact that all dust particles are initialised with the same acceleration within the simulation domain. Therefore, the dust particles move initially with the exact same velocity and their movement is strongly coupled. Once the RDIs build up and begin to dominate the system we see different structures like isolated islands of dust or elongated cylinders. As one can see from the comparison with the model HD-no-c which we present in 10.11 the morphology of the RDIs is heavily influenced by a grain sized dependent acceleration. In this case the instabilities show initially up as sheets and form elongated cylinders in which the dust is captured to finally form more complex structures in which the dust is concentrated. This is different in the model HD-c in which the build up of the instabilities is also slower compared to the model HD-no-c.

10.7.2 Optical depth

In this section we want to evaluate the influence of the RDIs on the geometrical optical depth. Despite the fact that the optical depth is a constant averaged over the whole simulation domain, given by the fact the the amount of dust particles is fixed, it is still intuitively clear that the build up of the RDIs in the system can have a huge impact on the local properties of the geometrical optical depth. This is due to the simple fact that the geometrical optical depth is mainly dependent on the total number of dust particles along a certain line of sight. Because the RDIs lead to an overpopulation (or under population respectively) of dust particles in certain regions of the box the geometrical optical depth can increase (or decrease) significantly. This is even more crucial if the certain region contains a lot of dust particles that follow the lower end of the grain size distribution as we pointed out in section 10.8 as the lower end dominates the behaviour of the geometrical optical depth. In the following we investigate the obscuration effects that are caused by the RDIs in a physical unit system constraint by an AGB-star as a function of time for the pure acoustic case of the RDIs. Therefore, we take different radial-sizes for AGB-stars and evaluate the fluctuations of the optical depth as a function of time. We already constrained the size of the simulation domain to 330 $R_\odot$. As AGB-star sizes range from 10 $R_\odot$ to 250 $R_\odot$ we can constrain stars with sizes up to 160 $R_\odot$. We calculate the optical depth in the cylinders above the cross section of stars of different sizes in the following way. We sum up particles in a specific cylinder with the radius of the cross section of the star through the box. This large cylinder can be subdivided in smaller cylinders. For each cylinder we calculate the the geometrical optical depth by summing up over the grain sizes within this cylinder. Now, we have two options to calculate the geometrical optical depth within the cylinders. The most simple one is by calculating the geometrical optical depth of the large cylinder by building the mean value of the geometrical optical depths of the smaller cylinders which leads to

$$\tau_{\mathrm{large}} = \frac{1}{N}\sum_{i}^{N}\tau^{i}_{\mathrm{small}}, \tag{10.11}$$

with τ_{large} as the geometrical depth of the large cylinder, N as the number of small cylinders and $\tau^{i}_{\mathrm{small}}$ as the individual geometrical optical depth of the cylinder with the index i. However, this is only a first order approximation of the optical depth in the large cylinder. The better approach is to calculate the covering fraction and then calculating the optical depth from the mean of the covering fraction. This method is more robust towards out layers in the distribution and therefore more accurate. We calculate the covering fraction of the small cylinders via

$$f_{\mathrm{c}} = \frac{1}{N}\sum_{i}\exp -\tau_{\mathrm{c}}{}^{i}. \tag{10.12}$$

We can then calculate the geometrical optical depth of the large cylinder by evaluating the expression

$$\tilde{\tau} = -\ln f_{\mathrm{c}}. \tag{10.13}$$

As it is quite expensive to subdivide the large cylinders in a number of smaller ones that is statistically significant for each time step we tabulate the optical depth on a grid to speed up the procedure. This means that the small cylinders actually become small rectangular cuboids. We note that this does not change the methodology described above but reduces the computational effort by a significant amount. For the size of the grid we choose 256x256 pixels. This is given by the resolution of our simulations. Given our resolution of $4 \cdot 256^3$ dust particles, we have (on average) 1000 dust particles in one bin which we assume a reasonable number. It is small enough to not get the box average of the optical depth but large enough to not be dominated by shot noise. We then draw a cylinder of a certain size around the grid points and make sure that we capture enough grid points to have enough values of τ_{small} in each cylinder to calculate the geometrical optical depth in each large cylinder by an appropriate set of data points. We show our results in Figure 10.12 in the case that the line of sight is alongside the xy-direction in the left panel for the simulation *HD-no-c*. In the right panel of Figure 10.12 we show the results from the optical depth calculations if the line of sight is alongside the xz-direction. The fluctuations of the optical depths directly translate in fluctuations in the magnitude of the object, which we derived as the V-band delta magnitudes in the second y-axis in Figure 10.12. We note that we do not have to consider the third line of sight along the yz-direction because it is statistically identical to the xz-direction. Along both line of sights there is initially no change in the optical depth. We can understand this by keeping in mind that the RDIs need a certain formation time before they build up. This is in order of the stopping time of the system. Further, we can see that the smaller the cylinder is, the larger are the jumps in the geometrical optical depths once the RDIs dominate the system. This can be understood by the fact that the RDIs can keep a large amount of dust particles in a relatively small spatial region. However, for larger radii it is straight forward to see that the optical depth is not fluctuating very strong as function around the initial value of the optical depth of the box. We further notice that the fluctuations in the optical depth are stronger along the xy-direction due to the fact that this is the line of sight in which the instabilities build up. In Figure 10.13 we show the standard deviations for the optical depths of the instabilities in the xy-direction on the left and for the xz-direction on the right. We find that the instabilities quickly go through a phase of non-linear growth, before the saturate.

10.8 Calculating the optical depth

In this section we discuss the calculation of the optical depths for constant grain size and varying grain size given by the Mathis et al. (1977) grain size distribution.

10.8.1 Constant grain sizes

For constant grain sizes we can calculate the optical depth for the box analytically from the initial setup that has been used in the simulations. In the case of constant grain sizes our system is characterised by the grain size parameter which takes the form

$$\frac{a_\mathrm{d}\rho_\mathrm{d}}{L_\mathrm{Box}\rho_\mathrm{g}} = \mathrm{const.} = 0.15, \tag{10.14}$$

with a_d as the grain size, ρ_d as the mean grain density, L_Box as the box size and ρ_g as the mean gas density in the box. For this system we can calculate the optical depth τ_opt of the box by:

$$\tau_\mathrm{opt} = \sigma_\mathrm{d} N_\mathrm{d}, \tag{10.15}$$

with the cross-section of the dust particles σ_d and the column density of the dust N_d within the box. Further, we make the assumption of perfectly spherical grains (which is a very simplified assumption). Therefore, the cross section of the dust particles σ_d is given by the projected surface area of one dust particle.

$$\sigma_\mathrm{d} = \pi a_\mathrm{d}^2. \tag{10.16}$$

The column density of the dust grains in the box can be calculated via

$$N_\mathrm{d} = \frac{\Sigma_\mathrm{d}}{m_\mathrm{d}}, \tag{10.17}$$

where Σ_d is the surface density of the dust particles in the Box and m_d is the mass of one dust particle. Σ_d can be calculated straightforward with the dust-to-gas ratio $\mu = 0.01$ and, the box size L_Box and the gas density ρ_gas in the box. Thus, the $\Sigma_\mathrm{d} = \mu L_\mathrm{Box}\rho_\mathrm{gas}$. For spherical dust particles the mass of one dust particle is $m_\mathrm{d} = \frac{4}{3}\pi a_\mathrm{d}^3 \rho_\mathrm{d}$. Thus the column density N_d is given by

$$N_\mathrm{d} = \frac{\mu L_\mathrm{Box}\rho_\mathrm{g}}{\frac{4}{3}\pi a_\mathrm{d}^3 \rho_\mathrm{d}}. \tag{10.18}$$

We obtain the optical depth of the system if we use 10.16 and equation 10.18 and plug them into equation 10.15. This leads to the following result.

$$\tau_\mathrm{opt} = \frac{3}{4}\mu \frac{L_\mathrm{Box}\rho_\mathrm{g}}{\rho_\mathrm{d} a_\mathrm{d}} = \frac{3}{4}\frac{\mu}{\alpha}. \tag{10.19}$$

By using equation 10.14 in equation 10.19 we obtain the optical depth $\tau_{\text{opt}} = 0.05$. From equation 10.19 one can immediately see that the optical depth of the box is only dependent on the initial configuration of the grain size parameter alpha and the dust to gas ratio μ.

Moreover, one can calculate τ_{opt} numerically by summing over all dust particles in the box and taking into account that we use the super particle approach for the dust particles where each dust particle in the simulation represents a statistical ensemble of dust particles. Thus, we have to renormalise with the particle mass. We obtain τ_{opt} by

$$\tau_{\text{opt}} = \frac{3}{4}\mu \frac{\sum_i a_{\text{i,d}}^2}{\sum_i m_i} \frac{m_{\text{d}}}{\frac{4}{3}a_d^3} = 0.05. \tag{10.20}$$

This is just a simple sanity check to make sure that we obtain the same values for τ_{opt} analytically and numerically. Moreover, we note that the optical depth for constant grain sizes is given by the initial value we choose in equation 10.14. If we keep this value fixed while transforming the unit less system into a physical system we keep the optical depth of the system fixed.

10.8.2 Variable grain sizes

Obtaining the optical depth in the case of variable grain sizes is more complicated but we will show that the result is a renormalised version of equation 10.19 . In this case the optical depth can be calculated from the dust opacity κ_{d}.

$$\tau_{\text{opt}} = \int \kappa_{\text{d}}\rho_{\text{g}} dl. \tag{10.21}$$

This means we can calculate τ_{opt} by averaging κ_{d} and ρ_{g} over the total box size L_{Box}. This implies for τ_{opt}

$$\tau_{\text{opt}} = \overline{\kappa}_{\text{d}}\overline{\rho}_{\text{g}} L_{\text{Box}} \tag{10.22}$$

To evaluate $\overline{\kappa}$ we need to take the distribution of the grains into account. The grains are distributed following the power law given by equation 10.4 We can use equation 10.4 to get $\overline{\kappa}_{\text{dust}}$ introduced in equation 10.22.

$$\overline{\kappa}_{\text{d}} = \frac{\int \pi a_{\text{d}}^2 \frac{dN_{\text{d}}}{da} da}{\frac{1}{\mu}\int \frac{4}{3}\pi a_{\text{d}}^3 \overline{\rho}_{\text{d}} \frac{dN_{\text{d}}}{da} da}, \tag{10.23}$$

again we calculate the particle mass by assuming that the dust particles are perfect spheres. We can then obtain a similar form as in equation 10.19 re scaled by the factor $\widetilde{a}$ with

$$\widetilde{a}_{\text{d}} = \frac{\int a_{\text{d}}^3 \frac{dN_{\text{d}}}{da}}{\int a_{\text{d}}^2 \frac{dN_{\text{d}}}{da}} \tag{10.24}$$

By inserting $\widetilde{a}_{\text{grain}}$ of equation 10.24 into equation 10.23 we find for the optical depth τ_{opt}

$$\tau_{\rm opt} = \frac{3}{4}\mu\frac{L_{\rm Box}\overline{\rho}_{\rm gas}}{\overline{\rho}_{\rm d}\widetilde{a}_{\rm grain}}. \tag{10.25}$$

However, $\widetilde{a}_{\rm grain}$ can directly be calculated from the grain distribution by inserting equation 10.4 in equation 10.24 and integrating the expression between $a_{\rm min}$ and $a_{\rm max}$. Therefore, one obtains

$$\widetilde{a}_{\rm grain} = \frac{\int_{a_{\rm min}}^{a_{\rm max}} a^{-\frac{1}{2}}\,da}{\int_{a_{\rm min}}^{a_{\rm max}} a^{-\frac{-3}{2}}\,da} \approx \sqrt{a_{\rm min}a_{\rm max}}. \tag{10.26}$$

If we insert all the numbers we obtain an optical depth which is one order of magnitude larger than in the case of constant grain sizes. Thus $\tau_{\rm opt} = 0.5$.
Further, we can do the same calculation numerically by evaluating the expression

$$\tau_{\rm opt} = \mu\frac{\sum_i a^2_{\rm i,grain}\frac{m_i}{\frac{4}{3}a^3_{\rm i,grain}}}{\sum_i m_i}. \tag{10.27}$$

By evaluating this expression over the total box we obtain $\tau_{\rm opt} = 0.5$.
From this calculations we can see that the optical depth within the boxes is a fundamental constant when we switch to a physical reference frame, because it is just a physical re scaling of the reduced unit system that has been applied in the simulations to study various modes of the RDIs. For both cases we adopt some similar unit conversions regarding the grain sizes and the mean grain density.

Chapter 11

Summary and Conclusions

In this work we presented a detailed discussion on how galaxies over different mass ranges can drive outflows. In this chapter we briefly conclude with our main findings.

- For the first time we showed that magnetic fields are more likely to be amplified by the small-scale turbulent dynamo then by the well established α-Ω dynamo that simply has a growth-rate issue in combination with the findings of galaxy formation theory, that does not allow a thin undisturbed disc early on in the formation history of a galaxy.

- Galactic magnetic fields can play a major role in driving galactic outflows, by the magnetic pressure support in their centre that is supported by runaway magnetic field growth due to a process that we named radial inflow dynamo, that can occur in all galaxies that become Ostriker-Peebles unstable (i.e. that are prone for bar-like instabilities), where excess mass is transported to the centre resulting, that triggers the Parker-Instability in the fluid flow, which launches the outflow as soon as the Parker-lobes can freely expand into the CGM.

- SN-feedback remains one of the most effective mechanisms to drive outflows in low mass galaxies, were we showed that magnetic field growth in dynamo processes remains ineffective. However, this results could change with the next generation of resolved MHD-disc simulations. We find that SN-feedback can be resolved in the current scope of galaxy evolution simulations over Gyr timescales with a particle mass resolution of around 1 $M_{\odot}$. Furthermore, we find that SN-feedback is setting 90 per cent of the mass loading in dwarf galaxies and photo-electric heating remains subdominant. Photo ionising radiation might play an important role for the SN-environment. However, a full radiative transfer prescription has to be implemented to test this in more detail.

Bibliography

Adebahr, B., Krause, M., Klein, U., Weżgowiec, M., Bomans, D. J., and Dettmar, R. J. (2013). <ASTROBJ>M 82</ASTROBJ> - A radio continuum and polarisation study. I. Data reduction and cosmic ray propagation. A&A, 555:A23.

Adelberger, K. L., Steidel, C. C., Shapley, A. E., and Pettini, M. (2003). Galaxies and Intergalactic Matter at Redshift z˜3: Overview. ApJ, 584:45–75.

Agertz, O., Kravtsov, A. V., Leitner, S. N., and Gnedin, N. Y. (2013). Toward a Complete Accounting of Energy and Momentum from Stellar Feedback in Galaxy Formation Simulations. ApJ, 770:25.

Agertz, O., Moore, B., Stadel, J., Potter, D., Miniati, F., Read, J., Mayer, L., Gawryszczak, A., Kravtsov, A., Nordlund, Å., Pearce, F., Quilis, V., Rudd, D., Springel, V., Stone, J., Tasker, E., Teyssier, R., Wadsley, J., and Walder, R. (2007). Fundamental differences between SPH and grid methods. MNRAS, 380:963–978.

Aguirre, A., Hernquist, L., Schaye, J., Katz, N., Weinberg, D. H., and Gardner, J. (2001). Metal Enrichment of the Intergalactic Medium in Cosmological Simulations. ApJ, 561:521–549.

Alves, J., Lombardi, M., and Lada, C. J. (2006). The mass function of dense molecular cores and the origin of the imf. *Astronomy Astrophysics*, 462(1):L17–L21.

Andersson, E. P., Agertz, O., and Renaud, F. (2020). How runaway stars boost galactic outflows. MNRAS, 494(3):3328–3341.

Arbutina, B., Urošević, D., Andjelić, M. M., Pavlović, M. Z., and Vukotić, B. (2012). Modified Equipartition Calculation for Supernova Remnants. ApJ, 746(1):79.

Aumer, M. and White, S. D. M. (2013). Idealized models for galactic disc formation and evolution in 'realistic' ΛCDM haloes. MNRAS, 428:1055–1076.

Badjin, D. A., Glazyrin, S. I., Manukovskiy, K. V., and Blinnikov, S. I. (2016). On physical and numerical instabilities arising in simulations of non-stationary radiatively cooling shocks. MNRAS, 459(2):2188–2211.

Bakes, E. L. O. and Tielens, A. G. G. M. (1994). The Photoelectric Heating Mechanism for Very Small Graphitic Grains and Polycyclic Aromatic Hydrocarbons. ApJ, 427:822.

Bardeen, J. M., Steinhardt, P. J., and Turner, M. S. (1983). Spontaneous creation of almost scale-free density perturbations in an inflationary universe. Phys. Rev. D, 28(4):679–693.

Barnes, J. and Hut, P. (1986). A hierarchical O(N log N) force-calculation algorithm. Nature, 324:446–449.

Basu, A. and Roy, S. (2013). Magnetic fields in nearby normal galaxies: energy equipartition. MNRAS, 433:1675–1686.

Baumgardt, H. and Klessen, R. S. (2011). The role of stellar collisions for the formation of massive stars. MNRAS, 413(3):1810–1818.

Beck, A. M., Dolag, K., Lesch, H., and Kronberg, P. P. (2013). Strong magnetic fields and large rotation measures in protogalaxies from supernova seeding. MNRAS, 435:3575–3586.

Beck, A. M., Lesch, H., Dolag, K., Kotarba, H., Geng, A., and Stasyszyn, F. A. (2012). Origin of strong magnetic fields in Milky Way-like galactic haloes. MNRAS, 422:2152–2163.

Beck, A. M., Murante, G., Arth, A., Remus, R. S., Teklu, A. F., Donnert, J. M. F., Planelles, S., Beck, M. C., Förster, P., Imgrund, M., Dolag, K., and Borgani, S. (2016a). An improved SPH scheme for cosmological simulations. MNRAS, 455(2):2110–2130.

Beck, M. C., Beck, A. M., Beck, R., Dolag, K., Strong, A. W., and Nielaba, P. (2016b). New constraints on modelling the random magnetic field of the MW. J. Cosmology Astropart. Phys., 5:056.

Beck, R. (2001). Galactic and Extragalactic Magnetic Fields. Space Sci. Rev., 99:243–260.

Beck, R. (2005). Magnetic Fields in Galaxies. In Wielebinski, R. and Beck, R., editors, *Cosmic Magnetic Fields*, volume 664 of *Lecture Notes in Physics, Berlin Springer Verlag*, page 41.

Beck, R. (2007). Magnetism in the spiral galaxy NGC 6946: magnetic arms, depolarization rings, dynamo modes, and helical fields. A&A, 470:539–556.

Beck, R. (2009). Galactic and extragalactic magnetic fields - a concise review. *Astrophysics and Space Sciences Transactions*, 5:43–47.

Beck, R. (2011). Cosmic Magnetic Fields: Observations and Prospects. In Aharonian, F. A., Hofmann, W., and Rieger, F. M., editors, *American Institute of Physics Conference Series*, volume 1381 of *American Institute of Physics Conference Series*, pages 117–136.

Beck, R. (2015). Magnetic fields in spiral galaxies. A&A Rev., 24:4.

Beck, R. and Wielebinski, R. (2013). *Magnetic Fields in Galaxies*, page 641. Springer, Dordrecht.

Behrendt, M., Burkert, A., and Schartmann, M. (2015). Structure formation in gas-rich galactic discs with finite thickness: from discs to rings. MNRAS, 448(1):1007–1019.

Behroozi, P., Wechsler, R. H., Hearin, A. P., and Conroy, C. (2019). UNIVERSEMACHINE: The correlation between galaxy growth and dark matter halo assembly from z = 0-10. MNRAS, 488(3):3143–3194.

Behroozi, P. S., Conroy, C., and Wechsler, R. H. (2010). A Comprehensive Analysis of Uncertainties Affecting the Stellar Mass-Halo Mass Relation for 0 z 4. ApJ, 717:379–403.

Bell, A. R. (1978). The acceleration of cosmic rays in shock fronts - II. MNRAS, 182:443–455.

Bell, M. R., Junklewitz, H., and Enßlin, T. A. (2011). Faraday caustics. Singularities in the Faraday spectrum and their utility as probes of magnetic field properties. A&A, 535:A85.

Bergin, E. A., Hartmann, L. W., Raymond, J. C., and Ballesteros-Paredes, J. (2004). Molecular Cloud Formation behind Shock Waves. ApJ, 612(2):921–939.

Bergin, E. A. and Tafalla, M. (2007). Cold Dark Clouds: The Initial Conditions for Star Formation. ARA&A, 45(1):339–396.

Berkhuijsen, E. M., Urbanik, M., Beck, R., and Han, J. L. (2016). Radio polarization and magnetic field structure in M 101. A&A, 588:A114.

Biermann, L. (1950). Über den Ursprung der Magnetfelder auf Sternen und im interstellaren Raum (miteinem Anhang von A. Schlüter). *Zeitschrift Naturforschung Teil A*, 5:65.

Binney, J. (1977). The physics of dissipational galaxy formation. ApJ, 215:483–491.

Bittner, A., Gadotti, D. A., Elmegreen, B. G., Athanassoula, E., Elmegreen, D. M., Bosma, A., and Muñoz-Mateos, J.-C. (2017). How do spiral arm contrasts relate to bars, disc breaks and other fundamental galaxy properties? MNRAS, 471(1):1070–1087.

Black, J. H. (1981). The physical state of primordial intergalactic clouds. MNRAS, 197:553–563.

Blondin, J. M., Wright, E. B., Borkowski, K. J., and Reynolds, S. P. (1998). Transition to the Radiative Phase in Supernova Remnants. ApJ, 500:342–354.

Boldyrev, S. and Cattaneo, F. (2004). Magnetic-Field Generation in Kolmogorov Turbulence. Phys. Rev. Lett., 92(14):144501.

Bond, J. R., Efstathiou, G., and Silk, J. (1980). Massive Neutrinos and the Large-Scale Structure of the Universe. Phys. Rev. Lett., 45(24):1980–1984.

Bondi, H. (1952). On spherically symmetrical accretion. MNRAS, 112:195.

Bonnor, W. B. (1956). Boyle's Law and gravitational instability. MNRAS, 116:351.

Bordoloi, R., Fox, A. J., Lockman, F. J., Wakker, B. P., Jenkins, E. B., Savage, B. D., Hernandez, S., Tumlinson, J., Bland-Hawthorn, J., and Kim, T.-S. (2017). Mapping the Nuclear Outflow of the Milky Way: Studying the Kinematics and Spatial Extent of the Northern Fermi Bubble. ApJ, 834:191.

Boylan-Kolchin, M., Bullock, J. S., and Kaplinghat, M. (2011). Too big to fail? The puzzling darkness of massive Milky Way subhaloes. MNRAS, 415(1):L40–L44.

Boylan-Kolchin, M., Bullock, J. S., and Kaplinghat, M. (2012). The Milky Way's bright satellites as an apparent failure of ΛCDM. MNRAS, 422(2):1203–1218.

Brandenburg, A. (2009). The critical role of magnetic helicity in astrophysical large-scale dynamos. *Plasma Physics and Controlled Fusion*, 51(12):124043.

Brandenburg, A., Moss, D., and Shukurov, A. (1995). Galactic Fountains as Magnetic Pumps. MNRAS, 276:651.

Brandenburg, A. and Stepanov, R. (2014). Faraday Signature of Magnetic Helicity from Reduced Depolarization. ApJ, 786(2):91.

Brandenburg, A. and Subramanian, K. (2005). Astrophysical magnetic fields and nonlinear dynamo theory. Phys. Rep., 417:1–209.

Brentjens, M. A. and de Bruyn, A. G. (2005). Faraday rotation measure synthesis. A&A, 441:1217–1228.

Brown, J. C., Haverkorn, M., Gaensler, B. M., Taylor, A. R., Bizunok, N. S., McClure-Griffiths, N. M., Dickey, J. M., and Green, A. J. (2007). Rotation Measures of Extragalactic Sources behind the Southern Galactic Plane: New Insights into the Large-Scale Magnetic Field of the Inner Milky Way. ApJ, 663:258–266.

Bryan, G. L. and Norman, M. L. (1997). Simulating X-Ray Clusters with Adaptive Mesh Refinement. In Clarke, D. A. and West, M. J., editors, *Computational Astrophysics; 12th Kingston Meeting on Theoretical Astrophysics*, volume 123 of *Astronomical Society of the Pacific Conference Series*, page 363.

Bryan, G. L., Norman, M. L., O'Shea, B. W., Abel, T., Wise, J. H., Turk, M. J., Reynolds, D. R., Collins, D. C., Wang, P., Skillman, S. W., Smith, B., Harkness, R. P., Bordner, J., Kim, J.-h., Kuhlen, M., Xu, H., Goldbaum, N., Hummels, C., Kritsuk, A. G., Tasker, E., Skory, S., Simpson, C. M., Hahn, O., Oishi, J. S., So, G. C., Zhao, F., Cen, R., Li, Y., and Enzo Collaboration (2014). ENZO: An Adaptive Mesh Refinement Code for Astrophysics. ApJS, 211:19.

Burbidge, E. M., Burbidge, G. R., and Rubin, V. C. (1964). A Study of the Velocity Field in M82 and its Bearing on Explosive Phenomena in that Galaxy. ApJ, 140:942.

Burn, B. J. (1966). On the depolarization of discrete radio sources by Faraday dispersion. MNRAS, 133:67.

Butsky, I., Zrake, J., Kim, J.-h., Yang, H.-I., and Abel, T. (2017). Ab Initio Simulations of a Supernova-driven Galactic Dynamo in an Isolated Disk Galaxy. ApJ, 843:113.

Carr, B. J., Bond, J. R., and Arnett, W. D. (1984). Cosmological consequences of Population III stars. ApJ, 277:445–469.

Carretti, E., Crocker, R. M., Staveley-Smith, L., Haverkorn, M., Purcell, C., Gaensler, B. M., Bernardi, G., Kesteven, M. J., and Poppi, S. (2013). Giant magnetized outflows from the centre of the Milky Way. Nature, 493:66–69.

Castor, J., McCray, R., and Weaver, R. (1975). Interstellar bubbles. ApJ, 200:L107–L110.

Cavaliere, A. and Fusco-Femiano, R. (1978). The Distribution of Hot Gas in Clusters of Galaxies. A&A, 70:677.

Cen, R. (1992). A Hydrodynamic Approach to Cosmology: Methodology. ApJS, 78:341.

Chabrier, G. (2003). Galactic Stellar and Substellar Initial Mass Function. PASP, 115(809):763–795.

Chandrasekhar, S. and Fermi, E. (1953). Magnetic Fields in Spiral Arms. ApJ, 118:113.

Chieffi, A. and Limongi, M. (2004). Explosive Yields of Massive Stars from Z = 0 to Z = Z_{solar}. ApJ, 608(1):405–410.

Cho, J., Lazarian, A., and Vishniac, E. T. (2002). New Regime of Magnetohydrodynamic Turbulence: Cascade below the Viscous Cutoff. ApJ, 566(1):L49–L52.

Cho, J. and Vishniac, E. T. (2000). The Anisotropy of Magnetohydrodynamic Alfvénic Turbulence. ApJ, 539(1):273–282.

Chyży, K. T. and Beck, R. (2004). Magnetic fields in merging spirals - the Antennae. A&A, 417:541–555.

Chyży, K. T., Bomans, D. J., Krause, M., Beck, R., Soida, M., and Urbanik, M. (2007). Magnetic fields and ionized gas in nearby late type galaxies. A&A, 462:933–941.

Chyży, K. T., Knapik, J., Bomans, D. J., Klein, U., Beck, R., Soida, M., and Urbanik, M. (2003). Magnetic fields and ionized gas in the local group irregular galaxies IC 10 and NGC 6822. A&A, 405:513–524.

Chyży, K. T., Weżgowiec, M., Beck, R., and Bomans, D. J. (2011). Magnetic fields in Local Group dwarf irregulars. A&A, 529:A94.

Cioffi, D. F., McKee, C. F., and Bertschinger, E. (1988). Dynamics of radiative supernova remnants. ApJ, 334:252–265.

Clark, P. C., Glover, S. C. O., and Klessen, R. S. (2012). TreeCol: a novel approach to estimating column densities in astrophysical simulations. MNRAS, 420:745–756.

Clark, S. E., Peek, J. E. G., and Putman, M. E. (2014). Magnetically Aligned H I Fibers and the Rolling Hough Transform. ApJ, 789(1):82.

Clowe, D., Bradač, M., Gonzalez, A. H., Markevitch, M., Randall, S. W., Jones, C., and Zaritsky, D. (2006). A Direct Empirical Proof of the Existence of Dark Matter. ApJ, 648(2):L109–L113.

Cohen, E., Piran, T., and Sari, R. (1998). Fluid Dynamics of Semiradiative Blast Waves. ApJ, 509:717–727.

Cowling, T. G. (1934). The stability of gaseous stars. MNRAS, 94:768–782.

Cowsik, R. and McClelland, J. (1972). An Upper Limit on the Neutrino Rest Mass. Phys. Rev. Lett., 29(10):669–670.

Cox, D. P. (1972). Cooling and Evolution of a Supernova Remnant. ApJ, 178:159–168.

Cox, D. P. (2005). The Three-Phase Interstellar Medium Revisited. ARA&A, 43(1):337–385.

Cox, D. P. and Smith, B. W. (1974). Large-Scale Effects of Supernova Remnants on the Galaxy: Generation and Maintenance of a Hot Network of Tunnels. ApJ, 189:L105.

Crenshaw, D. M., Kraemer, S. B., and George, I. M. (2003). Mass Loss from the Nuclei of Active Galaxies. ARA&A, 41:117–167.

Crocker, R. M., Jones, D. I., Melia, F., Ott, J., and Protheroe, R. J. (2010). A lower limit of 50 microgauss for the magnetic field near the Galactic Centre. Nature, 463:65–67.

Croston, J. H., Pratt, G. W., Böhringer, H., Arnaud, M., Pointecouteau, E., Ponman, T. J., Sanderson, A. J. R., Temple, R. F., Bower, R. G., and Donahue, M. (2008). Galaxy-cluster gas-density distributions of the representative XMM-Newton cluster structure survey (REXCESS). A&A, 487:431–443.

Cullen, L. and Dehnen, W. (2010). Inviscid smoothed particle hydrodynamics. MNRAS, 408(2):669–683.

Dalla Vecchia, C. and Schaye, J. (2012). Simulating galactic outflows with thermal supernova feedback. MNRAS, 426:140–158.

Davis, Leverett, J. and Greenstein, J. L. (1951). The Polarization of Starlight by Aligned Dust Grains. ApJ, 114:206.

De Lucia, G., Kauffmann, G., and White, S. D. M. (2004). Chemical enrichment of the intracluster and intergalactic medium in a hierarchical galaxy formation model. MNRAS, 349(3):1101–1116.

Dedner, A., Kemm, F., Kröner, D., Munz, C.-D., Schnitzer, T., and Wesenberg, M. (2002). Hyperbolic Divergence Cleaning for the MHD Equations. *Journal of Computational Physics*, 175:645–673.

Dehnen, W. and Aly, H. (2012). Improving convergence in smoothed particle hydrodynamics simulations without pairing instability. MNRAS, 425:1068–1082.

Dekel, A., Birnboim, Y., Engel, G., Freundlich, J., Goerdt, T., Mumcuoglu, M., Neistein, E., Pichon, C., Teyssier, R., and Zinger, E. (2009). Cold streams in early massive hot haloes as the main mode of galaxy formation. Nature, 457(7228):451–454.

Dekel, A. and Silk, J. (1986). The origin of dwarf galaxies, cold dark matter, and biased galaxy formation. ApJ, 303:39–55.

Demozzi, V., Mukhanov, V., and Rubinstein, H. (2009). Magnetic fields from inflation? J. Cosmology Astropart. Phys., 2009(8):025.

Diesing, R. and Caprioli, D. (2018). Effect of Cosmic Rays on the Evolution and Momentum Deposition of Supernova Remnants. *Physical Review Letters*, 121(9):091101.

Dobbs, C. L. (2008). GMC formation by agglomeration and self gravity. MNRAS, 391(2):844–858.

Dolag, K., Bartelmann, M., and Lesch, H. (1999). SPH simulations of magnetic fields in galaxy clusters. A&A, 348:351–363.

Dolag, K., Borgani, S., Schindler, S., Diaferio, A., and Bykov, A. M. (2008). Simulation Techniques for Cosmological Simulations. Space Sci. Rev., 134(1-4):229–268.

Dolag, K., Gaensler, B. M., Beck, A. M., and Beck, M. C. (2015). Constraints on the distribution and energetics of fast radio bursts using cosmological hydrodynamic simulations. MNRAS, 451:4277–4289.

Dolag, K., Schindler, S., Govoni, F., and Feretti, L. (2001). Correlation of the magnetic field and the intra-cluster gas density in galaxy clusters. A&A, 378:777–786.

Dolag, K. and Stasyszyn, F. (2009). An MHD GADGET for cosmological simulations. MNRAS, 398:1678–1697.

Donnert, J. M. F. (2014). Initial conditions for idealized clusters mergers, simulating 'El Gordo'. MNRAS, 438:1971–1984.

Draine, B. T. (2011). *Physics of the Interstellar and Intergalactic Medium*. Princeton University Press.

Draine, B. T. and Salpeter, E. E. (1979). On the physics of dust grains in hot gas. ApJ, 231:77–94.

Dubois, Y. and Teyssier, R. (2010). Magnetised winds in dwarf galaxies. A&A, 523:A72.

Durier, F. and Dalla Vecchia, C. (2012). Implementation of feedback in smoothed particle hydrodynamics: towards concordance of methods. MNRAS, 419:465–478.

Dwek, E. (1998). The Evolution of the Elemental Abundances in the Gas and Dust Phases of the Galaxy. ApJ, 501:643.

Ebert, R. (1955). Über die Verdichtung von H I-Gebieten. Mit 5 Textabbildungen. ZAp, 37:217.

Efstathiou, G. and Jones, B. J. T. (1979). The rotation of galaxies: numerical investigations of the tidal torque theory. MNRAS, 186:133–144.

Eggen, O. J., Lynden-Bell, D., and Sandage, A. R. (1962). Evidence from the motions of old stars that the Galaxy collapsed. ApJ, 136:748.

Einasto, J., Saar, E., Kaasik, A., and Chernin, A. D. (1974). Missing mass around galaxies - Morphological evidence. Nature, 252:111–113.

El-Badry, K., Ostriker, E. C., Kim, C.-G., Quataert, E., and Weisz, D. R. (2019). Evolution of supernovae-driven superbubbles with conduction and cooling. MNRAS, 490(2):1961–1990.

Ellis, R. S. and Axon, D. J. (1978). Stellar Polarization and the Structure of the Magnetic Field of Our Galaxy. Ap&SS, 54(2):425–443.

Elmegreen, B. G. (1993). The H to H 2 Transition in Galaxies: Totally Molecular Galaxies. ApJ, 411:170.

Elmegreen, B. G. and Scalo, J. (2004). Interstellar Turbulence I: Observations and Processes. ARA&A, 42:211–273.

Emerick, A., Bryan, G. L., and Mac Low, M.-M. (2018). Stellar Radiation Is Critical for Regulating Star Formation and Driving Outflows in Low-mass Dwarf Galaxies. ApJ, 865(2):L22.

Emerick, A., Bryan, G. L., and Mac Low, M.-M. (2019). Simulating an isolated dwarf galaxy with multichannel feedback and chemical yields from individual stars. MNRAS, 482:1304–1329.

Ertl, T., Janka, H. T., Woosley, S. E., Sukhbold, T., and Ugliano, M. (2016). A Two-parameter Criterion for Classifying the Explodability of Massive Stars by the Neutrino-driven Mechanism. ApJ, 818(2):124.

Falle, S. A. E. G. (1975). Numerical calculation of thin shell formation in supernova remnants. MNRAS, 172:55–84.

Fatuzzo, M. and Adams, F. C. (2002). Enhancement of Ambipolar Diffusion Rates through Field Fluctuations. ApJ, 570(1):210–221.

Federrath, C. (2016). On the universality of interstellar filaments: theory meets simulations and observations. MNRAS, 457:375–388.

Fendt, C., Beck, R., and Neininger, N. (1998). Spiral pattern in the optical polarization of NGC 6946. A&A, 335:123–133.

Ferriere, K. (1992a). Effect of an Ensemble of Explosions on the Galactic Dynamo. I. General Formulation. ApJ, 389:286.

Ferriere, K. (1992b). Effect of the Explosion of Supernovae and Superbubbles on the Galactic Dynamo. ApJ, 391:188.

Ferriere, K. (1993a). Magnetic Diffusion Due to Supernova Explosions and Superbubbles in the Galactic Disk. ApJ, 409:248.

Ferriere, K. (1993b). The Full Alpha-Tensor Due to Supernova Explosions and Superbubbles in the Galactic Disk. ApJ, 404:162.

Ferriere, K. (1996). Alpha-tensor and diffusivity tensor due to supernovae and superbubbles in the Galactic disk near the Sun. A&A, 310:438–455.

Ferrière, K. (1998). Global Model of the Interstellar Medium in Our Galaxy with New Constraints on the Hot Gas Component. ApJ, 497:759–776.

Ferrière, K. and Schmitt, D. (2000). Numerical models of the galactic dynamo driven by supernovae and superbubbles. A&A, 358:125–143.

Field, G. B. (1965). Thermal Instability. ApJ, 142:531.

Field, G. B., Goldsmith, D. W., and Habing, H. J. (1969). Cosmic-Ray Heating of the Interstellar Gas. ApJ, 155:L149.

Fielding, D., Quataert, E., and Martizzi, D. (2018). Clustered supernovae drive powerful galactic winds after superbubble breakout. MNRAS, 481:3325–3347.

Fletcher, A. (2010). Magnetic Fields in Nearby Galaxies. In Kothes, R., Landecker, T. L., and Willis, A. G., editors, *The Dynamic Interstellar Medium: A Celebration of the Canadian Galactic Plane Survey*, volume 438 of *Astronomical Society of the Pacific Conference Series*, page 197.

Fletcher, A., Beck, R., Berkhuijsen, E. M., and Shukurov, A. (2000). The regular magnetic fields of M31 and M33, from radio polarization observations. In Berkhuijsen, E. M., Beck, R., and Walterbos, R. A. M., editors, *Proceedings 232. WE-Heraeus Seminar*, pages 201–204.

Forbes, J. C., Krumholz, M. R., Goldbaum, N. J., and Dekel, A. (2016). Suppression of star formation in dwarf galaxies by photoelectric grain heating feedback. Nature, 535:523–525.

Förster Schreiber, N. M., Übler, H., Davies, R. L., Genzel, R., Wisnioski, E., Belli, S., Shimizu, T., Lutz, D., Fossati, M., Herrera-Camus, R., Mendel, J. T., Tacconi, L. J., Wilman, D., Beifiori, A., Brammer, G. B., Burkert, A., Carollo, C. M., Davies, R. I., Eisenhauer, F., Fabricius, M., Lilly, S. J., Momcheva, I., Naab, T., Nelson, E. J., Price, S. H., Renzini, A., Saglia, R., Sternberg, A., van Dokkum, P., and Wuyts, S. (2019). The KMOS^{3D} Survey: Demographics and Properties of Galactic Outflows at z = 0.6-2.7. ApJ, 875(1):21.

Franco, J., Miller, III, W. W., Arthur, S. J., Tenorio-Tagle, G., and Terlevich, R. (1994). Thin shell formation in radiative shocks. 1: Supernova remnants in low-density media. ApJ, 435:805–814.

Fransson, C., Larsson, J., Spyromilio, J., Leibundgut, B., McCray, R., and Jerkstrand, A. (2016). Discovery of Molecular Hydrogen in SN 1987A. ApJ, 821:L5.

Frick, P., Sokoloff, D., Stepanov, R., and Beck, R. (2011). Faraday rotation measure synthesis for magnetic fields of galaxies. MNRAS, 414(3):2540–2549.

Frisch, P. C., Redfield, S., and Slavin, J. D. (2011). The Interstellar Medium Surrounding the Sun. ARA&A, 49:237–279.

Furlanetto, S. R. and Loeb, A. (2003). Metal Absorption Lines as Probes of the Intergalactic Medium Prior to the Reionization Epoch. ApJ, 588:18–34.

Gaburov, E. and Nitadori, K. (2011). Astrophysical weighted particle magnetohydrodynamics. MNRAS, 414:129–154.

Gaffet, B. (1983). Semianalytical treatment of the hydrodynamics of supernova remnants during the snowplow phase. ApJ, 273:267–279.

Gamow, G. and Teller, E. (1939). On the Origin of Great Nebulae. *Physical Review*, 55(7):654–657.

Garrison-Kimmel, S., Boylan-Kolchin, M., Bullock, J. S., and Kirby, E. N. (2014). Too big to fail in the Local Group. MNRAS, 444(1):222–236.

Gatto, A., Walch, S., Low, M.-M. M., Naab, T., Girichidis, P., Glover, S. C. O., Wünsch, R., Klessen, R. S., Clark, P. C., Baczynski, C., Peters, T., Ostriker, J. P., Ibáñez-Mejía, J. C., and Haid, S. (2015). Modelling the supernova-driven ISM in different environments. MNRAS, 449:1057–1075.

Gatto, A., Walch, S., Naab, T., Girichidis, P., Wünsch, R., Glover, S. C. O., Klessen, R. S., Clark, P. C., Peters, T., Derigs, D., Baczynski, C., and Puls, J. (2017). The SILCC project - III. Regulation of star formation and outflows by stellar winds and supernovae. MNRAS, 466:1903–1924.

Geen, S., Hennebelle, P., Tremblin, P., and Rosdahl, J. (2016). Feedback in Clouds II: UV photoionization and the first supernova in a massive cloud. MNRAS, 463:3129–3142.

Geller, M. J. and Huchra, J. P. (1989). Mapping the Universe. *Science*, 246(4932):897–903.

Geng, A., Beck, A. M., Dolag, K., Bürzle, F., Beck, M. C., Kotarba, H., and Nielaba, P. (2012a). Synthetic X-ray and radio maps for two different models of Stephan's Quintet. MNRAS, 426:3160–3177.

Geng, A., Kotarba, H., Bürzle, F., Dolag, K., Stasyszyn, F., Beck, A., and Nielaba, P. (2012b). Magnetic field amplification and X-ray emission in galaxy minor mergers. MNRAS, 419:3571–3589.

Geng, A., Kotarba, H., Bürzle, F., Dolag, K., Stasyszyn, F., Beck, A., and Nielaba, P. (2012c). Magnetic field amplification and X-ray emission in galaxy minor mergers. MNRAS, 419:3571–3589.

Gentry, E. S., Krumholz, M. R., Dekel, A., and Madau, P. (2017). Enhanced momentum feedback from clustered supernovae. MNRAS, 465:2471–2488.

Genzel, R., Förster Schreiber, N. M., Rosario, D., Lang, P., Lutz, D., Wisnioski, E., Wuyts, E., Wuyts, S., Bandara, K., Bender, R., Berta, S., Kurk, J., Mendel, J. T., Tacconi, L. J., Wilman, D., Beifiori, A., Brammer, G., Burkert, A., Buschkamp, P., Chan, J., Carollo, C. M., Davies, R., Eisenhauer, F., Fabricius, M., Fossati, M., Kriek, M., Kulkarni, S., Lilly, S. J., Mancini, C., Momcheva, I., Naab, T., Nelson, E. J., Renzini, A., Saglia, R., Sharples, R. M., Sternberg, A., Tacchella, S., and van Dokkum, P. (2014). Evidence for Wide-spread Active Galactic Nucleus-driven Outflows in the Most Massive z ˜ 1-2 Star-forming Galaxies. ApJ, 796:7.

Genzel, R., Newman, S., Jones, T., Förster Schreiber, N. M., Shapiro, K., Genel, S., Lilly, S. J., Renzini, A., Tacconi, L. J., Bouché, N., Burkert, A., Cresci, G., Buschkamp, P., Carollo, C. M., Ceverino, D., Davies, R., Dekel, A., Eisenhauer, F., Hicks, E., Kurk, J., Lutz, D., Mancini, C., Naab, T., Peng, Y., Sternberg, A., Vergani, D., and Zamorani, G. (2011). The Sins Survey of z ˜ 2 Galaxy Kinematics: Properties of the Giant Star-forming Clumps. ApJ, 733:101.

Genzel, R., Schreiber, N. M. F., Übler, H., Lang, P., Naab, T., Bender, R., Tacconi, L. J., Wisnioski, E., Wuyts, S., Alexander, T., Beifiori, A., Belli, S., Brammer, G., Burkert, A., Carollo, C. M., Chan, J., Davies, R., Fossati, M., Galametz, A., Genel, S., Gerhard, O., Lutz, D., Mendel, J. T., Momcheva, I., Nelson, E. J., Renzini, A., Saglia, R., Sternberg, A., Tacchella, S., Tadaki, K., and Wilman, D. (2017). Strongly baryon-dominated disk galaxies at the peak of galaxy formation ten billion years ago. Nature, 543(7645):397–401.

Georgy, C., Ekström, S., Eggenberger, P., Meynet, G., Haemmerlé, L., Maeder, A., Granada, A., Groh, J. H., Hirschi, R., Mowlavi, N., Yusof, N., Charbonnel, C., Decressin, T., and Barblan, F. (2013). Grids of stellar models with rotation. III. Models from 0.8 to 120 M at a metallicity Z = 0.002. A&A, 558:A103.

Gershtein, S. S. and Zel'dovich, Y. B. (1966). Rest Mass of Muonic Neutrino and Cosmology. *Soviet Journal of Experimental and Theoretical Physics Letters*, 4:120–122.

Gingold, R. A. and Monaghan, J. J. (1977). Smoothed particle hydrodynamics - Theory and application to non-spherical stars. MNRAS, 181:375–389.

Girichidis, P., Walch, S., Naab, T., Gatto, A., Wünsch, R., Glover, S. C. O., Klessen, R. S., Clark, P. C., Peters, T., Derigs, D., and Baczynski, C. (2016). The SILCC (SImulating the LifeCycle of molecular Clouds) project - II. Dynamical evolution of the supernova-driven ISM and the launching of outflows. MNRAS, 456:3432–3455.

Glover, S. C. O. (2003). Comparing Gas-Phase and Grain-catalyzed H_2 Formation. ApJ, 584(1):331–338.

Glover, S. C. O. and Clark, P. C. (2012). Is molecular gas necessary for star formation? MNRAS, 421:9–19.

Glover, S. C. O., Federrath, C., Mac Low, M. M., and Klessen, R. S. (2010). Modelling CO formation in the turbulent interstellar medium. MNRAS, 404(1):2–29.

Glover, S. C. O. and Mac Low, M.-M. (2007a). Simulating the Formation of Molecular Clouds. I. Slow Formation by Gravitational Collapse from Static Initial Conditions. ApJS, 169:239–268.

Glover, S. C. O. and Mac Low, M.-M. (2007b). Simulating the Formation of Molecular Clouds. II. Rapid Formation from Turbulent Initial Conditions. ApJ, 659:1317–1337.

Gnat, O. and Sternberg, A. (2007). Time-dependent Ionization in Radiatively Cooling Gas. ApJS, 168(2):213–230.

Gnedin, N. Y. (1998). Metal enrichment of the intergalactic medium. MNRAS, 294:407.

Gnedin, N. Y. and Draine, B. T. (2014). Line Overlap and Self-Shielding of Molecular Hydrogen in Galaxies. ApJ, 795:37.

Gnedin, N. Y., Ferrara, A., and Zweibel, E. G. (2000). Generation of the Primordial Magnetic Fields during Cosmological Reionization. ApJ, 539(2):505–516.

Gnedin, N. Y. and Hollon, N. (2012). Cooling and Heating Functions of Photoionized Gas. ApJS, 202(2):13.

Godard, B., Falgarone, E., and Pineau Des Forêts, G. (2009). Models of turbulent dissipation regions in the diffuse interstellar medium. A&A, 495(3):847–867.

Goldreich, P. and Kylafis, N. D. (1981). On mapping the magnetic field direction in molecular clouds by polarization measurements. ApJ, 243:L75–L78.

Goldreich, P. and Sridhar, S. (1995). Toward a Theory of Interstellar Turbulence. II. Strong Alfvenic Turbulence. ApJ, 438:763.

González-Casanova, D. F. and Lazarian, A. (2017). Velocity Gradients as a Tracer for Magnetic Fields. ApJ, 835(1):41.

Gott, J. R., I. and Thuan, T. X. (1976). On the formation of spiral and elliptical galaxies. ApJ, 204:649–667.

Gotthelf, E. V., Koralesky, B., Rudnick, L., Jones, T. W., Hwang, U., and Petre, R. (2001). Chandra Detection of the Forward and Reverse Shocks in Cassiopeia A. ApJ, 552:L39–L43.

Gould, R. J. and Salpeter, E. E. (1963). The Interstellar Abundance of the Hydrogen Molecule. I. Basic Processes. ApJ, 138:393.

Grefenstette, B. W., Harrison, F. A., Boggs, S. E., Reynolds, S. P., Fryer, C. L., Madsen, K. K., Wik, D. R., Zoglauer, A., Ellinger, C. I., Alexander, D. M., An, H., Barret, D., Christensen, F. E., Craig, W. W., Forster, K., Giommi, P., Hailey, C. J., Hornstrup, A., Kaspi, V. M., Kitaguchi, T., Koglin, J. E., Mao, P. H., Miyasaka, H., Mori, K., Perri, M., Pivovaroff, M. J., Puccetti, S., Rana, V., Stern, D., Westergaard, N. J., and Zhang, W. W. (2014). Asymmetries in core-collapse supernovae from maps of radioactive ^{44}Ti in CassiopeiaA. Nature, 506:339–342.

Guedes, J., Callegari, S., Madau, P., and Mayer, L. (2011). Forming Realistic Late-type Spirals in a ΛCDM Universe: The Eris Simulation. ApJ, 742:76.

Gunn, J. E. and Gott, J. Richard, I. (1972). On the Infall of Matter Into Clusters of Galaxies and Some Effects on Their Evolution. ApJ, 176:1.

Gupta, S., Nath, B. B., Sharma, P., and Eichler, D. (2018). Lack of thermal energy in superbubbles: hint of cosmic rays? MNRAS, 473:1537–1553.

Guth, A. H. and Pi, S. Y. (1982). Fluctuations in the New Inflationary Universe. Phys. Rev. Lett., 49(15):1110–1113.

Haardt, F. and Madau, P. (2001). Modelling the UV/X-ray cosmic background with CUBA. In Neumann, D. M. and Tran, J. T. V., editors, *Clusters of Galaxies and the High Redshift Universe Observed in X-rays*, page 64.

Haardt, F. and Madau, P. (2012). Radiative Transfer in a Clumpy Universe. IV. New Synthesis Models of the Cosmic UV/X-Ray Background. ApJ, 746:125.

Habing, H. J. (1968). The interstellar radiation density between 912 A and 2400 A. Bull. Astron. Inst. Netherlands, 19:421.

Haid, S., Walch, S., Naab, T., Seifried, D., Mackey, J., and Gatto, A. (2016). Supernova blast waves in wind-blown bubbles, turbulent, and power-law ambient media. MNRAS, 460:2962–2978.

Han, J. L. (2017). Observing Interstellar and Intergalactic Magnetic Fields. ARA&A, 55:111–157.

Han, J. L., Manchester, R. N., van Straten, W., and Demorest, P. (2018). Pulsar Rotation Measures and Large-scale Magnetic Field Reversals in the Galactic Disk. ApJS, 234:11.

Hanasz, M., Otmianowska-Mazur, K., Kowal, G., and Lesch, H. (2009). Cosmic-ray-driven dynamo in galactic disks. A parameter study. A&A, 498:335–346.

Harlow, F. H. and Welch, J. E. (1965). Numerical Calculation of Time-Dependent Viscous Incompressible Flow of Fluid with Free Surface. *Physics of Fluids*, 8:2182–2189.

Harrison, E. R. (1970a). Fluctuations at the Threshold of Classical Cosmology. Phys. Rev. D, 1(10):2726–2730.

Harrison, E. R. (1970b). Generation of magnetic fields in the radiation ERA. MNRAS, 147:279.

Haud, U. (1981). Gas kinematics in M31. Ap&SS, 76:477–490.

Hawking, S. W. (1982). The development of irregularities in a single bubble inflationary universe. *Physics Letters B*, 115(4):295–297.

Heald, G., Beck, R., de Blok, W. J. G., Dettmar, R. J., Fletcher, A., Gaensler, B., Haverkorn, M., Heesen, V., Horellou, C., Krause, M., Mao, S. A., Oppermann, N., Scaife, A., Sokoloff, D., Stil, J., Tabatabaei, F., Takahashi, K., Taylor, A. R., and Williams, A. (2015). Magnetic Field Tomography in Nearby Galaxies with the Square Kilometre Array. *Advancing Astrophysics with the Square Kilometre Array (AASKA14)*, page 106.

Heesen, V., Beck, R., Krause, M., and Dettmar, R.-J. (2011). Cosmic rays and the magnetic field in the nearby starburst galaxy NGC 253 III. Helical magnetic fields in the nuclear outflow. A&A, 535:A79.

Heesen, V., Brinks, E., Leroy, A. K., Heald, G., Braun, R., Bigiel, F., and Beck, R. (2014). The Radio Continuum-Star Formation Rate Relation in WSRT SINGS Galaxies. AJ, 147:103.

Heiles, C. and Crutcher, R. (2005). *Magnetic Fields in Diffuse HI and Molecular Clouds*, volume 664, page 137.

Heitsch, F. and Hartmann, L. (2008). Rapid Molecular Cloud and Star Formation: Mechanisms and Movies. ApJ, 689(1):290–301.

Heitsch, F., Zweibel, E. G., Slyz, A. D., and Devriendt, J. E. G. (2004). Turbulent Ambipolar Diffusion: Numerical Studies in Two Dimensions. ApJ, 603(1):165–179.

Hennebelle, P. and Chabrier, G. (2008). Analytical Theory for the Initial Mass Function: CO Clumps and Prestellar Cores. ApJ, 684(1):395–410.

Hennebelle, P. and Chabrier, G. (2013). Analytical Theory for the Initial Mass Function. III. Time Dependence and Star Formation Rate. ApJ, 770(2):150.

Hennebelle, P. and Ciardi, A. (2009). Disk formation during collapse of magnetized protostellar cores. A&A, 506(2):L29–L32.

Hennebelle, P. and Pérault, M. (1999). Dynamical condensation in a thermally bistable flow. Application to interstellar cirrus. A&A, 351:309–322.

Hennebelle, P. and Pérault, M. (2000). Dynamical condensation in a magnetized and thermally bistable flow. Application to interstellar cirrus. A&A, 359:1124–1138.

Hernquist, L. (1993). N-body realizations of compound galaxies. ApJS, 86:389–400.

Hirschmann, M., Dolag, K., Saro, A., Bachmann, L., Borgani, S., and Burkert, A. (2014). Cosmological simulations of black hole growth: AGN luminosities and downsizing. MNRAS, 442:2304–2324.

Hoang, T. and Lazarian, A. (2008). Radiative torque alignment: essential physical processes. MNRAS, 388(1):117–143.

Hoang, T. and Lazarian, A. (2014). Grain alignment by radiative torques in special conditions and implications. MNRAS, 438(1):680–703.

Höfner, S. and Olofsson, H. (2018). Mass loss of stars on the asymptotic giant branch. Mechanisms, models and measurements. A&A Rev., 26(1):1.

Hogan, C. J. (1983a). Magnetohydrodynamic effects of a first-order cosmological phase transition. *Physical Review Letters*, 51:1488–1491.

Hogan, C. J. (1983b). Magnetohydrodynamic effects of a first-order cosmological phase transition. *Physical Review Letters*, 51:1488–1491.

Hopkins, P. F. (2013). A general class of Lagrangian smoothed particle hydrodynamics methods and implications for fluid mixing problems. MNRAS, 428:2840–2856.

Hopkins, P. F. (2015). A new class of accurate, mesh-free hydrodynamic simulation methods. MNRAS, 450:53–110.

Hopkins, P. F., Quataert, E., and Murray, N. (2011). Self-regulated star formation in galaxies via momentum input from massive stars. MNRAS, 417:950–973.

Hopkins, P. F., Quataert, E., and Murray, N. (2012). Stellar feedback in galaxies and the origin of galaxy-scale winds. MNRAS, 421(4):3522–3537.

Hopkins, P. F. and Squire, J. (2018). The resonant drag instability (RDI): acoustic modes. MNRAS, 480(2):2813–2838.

Hopkins, P. F., Squire, J., and Seligman, D. (2020). Simulating diverse instabilities of dust in magnetized gas. MNRAS, 496(2):2123–2154.

Hopkins, P. F., Wetzel, A., Kereš, D., Faucher-Giguère, C.-A., Quataert, E., Boylan-Kolchin, M., Murray, N., Hayward, C. C., Garrison-Kimmel, S., Hummels, C., Feldmann, R., Torrey, P., Ma, X., Anglés-Alcázar, D., Su, K.-Y., Orr, M., Schmitz, D., Escala, I., Sanderson, R., Grudić, M. Y., Hafen, Z., Kim, J.-H., Fitts, A., Bullock, J. S., Wheeler, C., Chan, T. K., Elbert, O. D., and Narayanan, D. (2018). FIRE-2 simulations: physics versus numerics in galaxy formation. MNRAS, 480:800–863.

Horellou, C. and Fletcher, A. (2014). Magnetic field tomography, helical magnetic fields and Faraday depolarization. MNRAS, 441(3):2049–2057.

Houde, M., Fletcher, A., Beck, R., Hildebrand, R. H., Vaillancourt, J. E., and Stil, J. M. (2013). Characterizing Magnetized Turbulence in M51. ApJ, 766:49.

Hoyle, F. (1949). On the Cosmological Problem. MNRAS, 109:365.

Hoyle, F. and Ellis, G. R. A. (1963). On the Existence of an Ionized Layer about the Galactic Plane. *Australian Journal of Physics*, 16:1.

Hoyle, F. and Lyttleton, R. A. (1939). The Evolution of the Stars. Nature, 144(3659):1019–1020.

Hu, C.-Y. (2019). Supernova-driven winds in simulated dwarf galaxies. MNRAS, 483:3363–3381.

Hu, C.-Y., Naab, T., Glover, S. C. O., Walch, S., and Clark, P. C. (2017). Variable interstellar radiation fields in simulated dwarf galaxies: supernovae versus photoelectric heating. MNRAS, 471:2151–2173.

Hu, C.-Y., Naab, T., Walch, S., Glover, S. C. O., and Clark, P. C. (2016). Star formation and molecular hydrogen in dwarf galaxies: a non-equilibrium view. MNRAS, 458:3528–3553.

Hu, C.-Y., Naab, T., Walch, S., Moster, B. P., and Oser, L. (2014). SPHGal: smoothed particle hydrodynamics with improved accuracy for galaxy simulations. MNRAS, 443(2):1173–1191.

Hu, C.-Y., Zhukovska, S., Somerville, R. S., and Naab, T. (2019). Thermal and non-thermal dust sputtering in hydrodynamical simulations of the multiphase interstellar medium. MNRAS, 487(3):3252–3269.

Hu, Y., Lazarian, A., Li, Y., Zhuravleva, I., and Gendron-Marsolais, M.-L. (2020). Probing Magnetic Field Morphology in Galaxy Clusters with the Gradient Technique. *arXiv e-prints*, page arXiv:2007.06219.

Hummel, E. (1986). The radio continuum-far infrared correlation and magnetic fields in SBC galaxies. A&A, 160:L4–L6.

Icke, V. (2016). Which side are you on? *Nature Physics*, 12(4):374.

Iffrig, O. and Hennebelle, P. (2015). Mutual influence of supernovae and molecular clouds. A&A, 576:A95.

Imara, N. and Blitz, L. (2011). Angular Momentum in Giant Molecular Clouds. I. The Milky Way. ApJ, 732(2):78.

Indebetouw, R., Matsuura, M., Dwek, E., Zanardo, G., Barlow, M. J., Baes, M., Bouchet, P., Burrows, D. N., Chevalier, R., Clayton, G. C., Fransson, C., Gaensler, B., Kirshner, R., Lakićević, M., Long, K. S., Lundqvist, P., Martí-Vidal, I., Marcaide, J., McCray, R., Meixner, M., Ng, C.-Y., Park, S., Sonneborn, G., Staveley-Smith, L., Vlahakis, C., and van Loon, J. (2014). Dust Production and Particle Acceleration in Supernova 1987A Revealed with ALMA. ApJ, 782:L2.

Inutsuka, S.-i. (2001). The Mass Function of Molecular Cloud Cores. ApJ, 559(2):L149–L152.

Iroshnikov, P. S. (1963). Turbulence of a Conducting Fluid in a Strong Magnetic Field. AZh, 40:742.

Iroshnikov, P. S. (1964). Turbulence of a Conducting Fluid in a Strong Magnetic Field. Soviet Ast., 7:566.

Jacob, S. and Pfrommer, C. (2017). Cosmic ray heating in cool core clusters - II. Self-regulation cycle and non-thermal emission. MNRAS, 467(2):1478–1495.

Janka, H.-T., Hanke, F., Hüdepohl, L., Marek, A., Müller, B., and Obergaulinger, M. (2012). Core-collapse supernovae: Reflections and directions. *Progress of Theoretical and Experimental Physics*, 2012(1):01A309.

Jeans, J. H. (1902). The Stability of a Spherical Nebula. *Philosophical Transactions of the Royal Society of London Series A*, 199:1–53.

Jensen, M. J., Bilodeau, R. C., Safvan, C. P., Seiersen, K., Andersen, L. H., Pedersen, H. B., and Heber, O. (2000). Dissociative Recombination of H_3O^+, HD_2O^+, and D_3O^+. ApJ, 543(2):764–774.

Johansson, P. H., Naab, T., and Burkert, A. (2009). Equal- and Unequal-Mass Mergers of Disk and Elliptical Galaxies with Black Holes. ApJ, 690:802–821.

Johnstone, D., Fich, M., Mitchell, G. F., and Moriarty-Schieven, G. (2001). Large Area Mapping at 850 Microns. III. Analysis of the Clump Distribution in the Orion B Molecular Cloud. ApJ, 559(1):307–317.

Jubelgas, M., Springel, V., and Dolag, K. (2004). Thermal conduction in cosmological SPH simulations. MNRAS, 351:423–435.

Junk, V., Walch, S., Heitsch, F., Burkert, A., Wetzstein, M., Schartmann, M., and Price, D. (2010). Modelling shear flows with smoothed particle hydrodynamics and grid-based methods. MNRAS, 407:1933–1945.

Jura, M. (1975). Interstellar clouds containing optically thin H_2. ApJ, 197:575–580.

Kalberla, P. M. W. and Kerp, J. (2009). The Hi Distribution of the Milky Way. ARA&A, 47(1):27–61.

Kamenetzky, J., McCray, R., Indebetouw, R., Barlow, M. J., Matsuura, M., Baes, M., Blommaert, J. A. D. L., Bolatto, A., Decin, L., Dunne, L., Fransson, C., Glenn, J., Gomez, H. L., Groenewegen, M. A. T., Hopwood, R., Kirshner, R. P., Lakicevic, M., Marcaide, J., Marti-Vidal, I., Meixner, M., Royer, P., Soderberg, A., Sonneborn, G., Staveley-Smith, L., Swinyard, B. M., Van de Steene, G., van Hoof, P. A. M., van Loon, J. T., Yates, J., and Zanardo, G. (2013). Carbon Monoxide in the Cold Debris of Supernova 1987A. ApJ, 773:L34.

Karademir, G. S., Remus, R.-S., Burkert, A., Dolag, K., Hoffmann, T. L., Moster, B. P., Steinwandel, U. P., and Zhang, J. (2019). The outer stellar halos of galaxies: how radial merger mass deposition, shells, and streams depend on infall-orbit configurations. MNRAS, 487:318–332.

Katz, N., Weinberg, D. H., and Hernquist, L. (1996). Cosmological Simulations with TreeSPH. ApJS, 105:19.

Kauffmann, G., Guiderdoni, B., and White, S. D. M. (1994). Faint galaxy counts in a hierarchical universe. MNRAS, 267:981–999.

Kauffmann, G., White, S. D. M., and Guiderdoni, B. (1993). The formation and evolution of galaxies within merging dark matter haloes. MNRAS, 264:201–218.

Kazantsev, A. P. (1968). Enhancement of a Magnetic Field by a Conducting Fluid. *Soviet Journal of Experimental and Theoretical Physics*, 26:1031.

Kazantsev, A. P., Ruzmaikin, A. A., and Sokolov, D. D. (1985). Magnetic field transport by an acoustic turbulence-type flow. *Zhurnal Eksperimentalnoi i Teoreticheskoi Fiziki*, 88:487–494.

Keller, B. W. and Kruijssen, J. M. D. (2020). Below the subgrid: uncertainties in supernova input rates drive qualitative differences in simulations of galaxy evolution. *arXiv e-prints*, page arXiv:2004.03608.

Keller, B. W., Wadsley, J., Benincasa, S. M., and Couchman, H. M. P. (2014). A superbubble feedback model for galaxy simulations. MNRAS, 442:3013–3025.

Kennicutt, Jr., R. C. (1989). The star formation law in galactic disks. ApJ, 344:685–703.

Keto, E. (2002). On the Evolution of Ultracompact H II Regions. ApJ, 580(2):980–986.

Keto, E. (2003). The Formation of Massive Stars by Accretion through Trapped Hypercompact H II Regions. ApJ, 599(2):1196–1206.

Keto, E. (2007). The Formation of Massive Stars: Accretion, Disks, and the Development of Hypercompact H II Regions. ApJ, 666(2):976–981.

Kim, C.-G. and Ostriker, E. C. (2015). Momentum Injection by Supernovae in the Interstellar Medium. ApJ, 802:99.

Kim, C.-G., Ostriker, E. C., and Raileanu, R. (2017). Superbubbles in the Multiphase ISM and the Loading of Galactic Winds. ApJ, 834:25.

Kim, K. S., Lilly, S. J., Miniati, F., Bernet, M. L., Beck, R., O'Sullivan, S. P., and Gaensler, B. M. (2016). Faraday Rotation Measure Synthesis of Intermediate Redshift Quasars as a Probe of Intervening Matter. ApJ, 829:133.

Klessen, R. S. (2011). Star Formation in Molecular Clouds. In Charbonnel, C. and Montmerle, T., editors, *EAS Publications Series*, volume 51 of *EAS Publications Series*, pages 133–167.

Klessen, R. S. and Glover, S. C. O. (2016). Physical Processes in the Interstellar Medium. *Saas-Fee Advanced Course*, 43:85.

Klinkhamer, F. R. and Norman, C. A. (1981). Massive neutrinos and galaxy formation. ApJ, 243:L1–L4.

Klypin, A., Kravtsov, A. V., Valenzuela, O., and Prada, F. (1999). Where Are the Missing Galactic Satellites? ApJ, 522(1):82–92.

Kobayashi, C., Karakas, A. I., and Umeda, H. (2011). The evolution of isotope ratios in the Milky Way Galaxy. MNRAS, 414:3231–3250.

Kolmogorov, A. (1941). The Local Structure of Turbulence in Incompressible Viscous Fluid for Very Large Reynolds' Numbers. *Akademiia Nauk SSSR Doklady*, 30:301–305.

Komatsu, E., Smith, K. M., Dunkley, J., Bennett, C. L., Gold, B., Hinshaw, G., Jarosik, N., Larson, D., Nolta, M. R., Page, L., Spergel, D. N., Halpern, M., Hill, R. S., Kogut, A., Limon, M., Meyer, S. S., Odegard, N., Tucker, G. S., Weiland, J. L., Wollack, E., and Wright, E. L. (2011). Seven-year Wilkinson Microwave Anisotropy Probe (WMAP) Observations: Cosmological Interpretation. ApJS, 192(2):18.

Könyves, V., Kiss, C., Moór, A., Kiss, Z. T., and Tóth, L. V. (2007). Catalogue of far-infrared loops in the Galaxy. A&A, 463:1227–1234.

Koo, B.-C. and McKee, C. F. (1992). Dynamics of wind bubbles and superbubbles. I - Slow winds and fast winds. II - Analytic theory. ApJ, 388:93–126.

Kotarba, H., Karl, S. J., Naab, T., Johansson, P. H., Dolag, K., Lesch, H., and Stasyszyn, F. A. (2010). Simulating Magnetic Fields in the Antennae Galaxies. ApJ, 716:1438–1452.

Kotarba, H., Lesch, H., Dolag, K., Naab, T., Johansson, P. H., Donnert, J., and Stasyszyn, F. A. (2011). Galactic ménage à trois: simulating magnetic fields in colliding galaxies. MNRAS, 415:3189–3218.

Kotarba, H., Lesch, H., Dolag, K., Naab, T., Johansson, P. H., and Stasyszyn, F. A. (2009). Magnetic field structure due to the global velocity field in spiral galaxies. MNRAS, 397:733–747.

Koyama, H. and Inutsuka, S.-i. (2002). An Origin of Supersonic Motions in Interstellar Clouds. ApJ, 564(2):L97–L100.

Kraichnan, R. H. (1965). Inertial-Range Spectrum of Hydromagnetic Turbulence. *Physics of Fluids*, 8:1385–1387.

Kraichnan, R. H. (1968). Small-Scale Structure of a Scalar Field Convected by Turbulence. *Physics of Fluids*, 11:945–953.

Kraichnan, R. H. and Nagarajan, S. (1967). Growth of Turbulent Magnetic Fields. *Physics of Fluids*, 10:859–870.

Krolik, J. H. (1999). *Active galactic nuclei : from the central black hole to the galactic environment*.

Krolik, J. H., McKee, C. F., and Tarter, C. B. (1981). Two-phase models of quasar emission line regions. ApJ, 249:422–442.

Kroupa, P. (2001). On the variation of the initial mass function. MNRAS, 322(2):231–246.

Krumholz, M. R. (2012). Star Formation in Atomic Gas. ApJ, 759(1):9.

Krumholz, M. R. (2014). The big problems in star formation: The star formation rate, stellar clustering, and the initial mass function. Phys. Rep., 539:49–134.

Krumholz, M. R., Leroy, A. K., and McKee, C. F. (2011). Which Phase of the Interstellar Medium Correlates with the Star Formation Rate? ApJ, 731(1):25.

Krumholz, M. R., McKee, C. F., and Tumlinson, J. (2008). The Atomic-to-Molecular Transition in Galaxies. I. An Analytic Approximation for Photodissociation Fronts in Finite Clouds. ApJ, 689(2):865–882.

Kulsrud, R. M. (2005). *Plasma physics for astrophysics, N.J. : Princeton University Press*.

Kulsrud, R. M. and Anderson, S. W. (1992). The spectrum of random magnetic fields in the mean field dynamo theory of the Galactic magnetic field. ApJ, 396:606–630.

Kulsrud, R. M., Cen, R., Ostriker, J. P., and Ryu, D. (1997). The Protogalactic Origin for Cosmic Magnetic Fields. ApJ, 480:481–491.

Kulsrud, R. M. and Zweibel, E. G. (2008). On the origin of cosmic magnetic fields. *Reports on Progress in Physics*, 71(4):046901.

Kwan, J. (1979). The mass spectrum of interstellar clouds. ApJ, 229:567–577.

Lada, C. J. and Lada, E. A. (2003). Embedded Clusters in Molecular Clouds. ARA&A, 41:57–115.

Lada, C. J., Muench, A. A., Rathborne, J., Alves, J. F., and Lombardi, M. (2008). The Nature of the Dense Core Population in the Pipe Nebula: Thermal Cores Under Pressure. ApJ, 672(1):410–422.

Lahén, N., Naab, T., Johansson, P. H., Elmegreen, B., Hu, C.-Y., and Walch, S. (2019). The Formation of Low-metallicity Globular Clusters in Dwarf Galaxy Mergers. ApJ, 879:L18.

Lahén, N., Naab, T., Johansson, P. H., Elmegreen, B., Hu, C.-Y., Walch, S., Steinwand el, U. P., and Moster, B. P. (2020). The GRIFFIN Project—Formation of Star Clusters with Individual Massive Stars in a Simulated Dwarf Galaxy Starburst. ApJ, 891(1):2.

Landau, L. D. and Lifshitz, E. M. (1959). *Fluid mechanics, Oxford: Pergamon Press, 1959*.

Lanson, N. and Vila, J. (2008). . *SIAM J. Numer. Anal*, 46:1935.

Larmor, J. (1919). *How could a rotating body Such as the Sun become a Magnet?* Rep. 87th Meeting Brit. Assoc. Adv. Sci.

Larson, R. B. (1974). Effects of supernovae on the early evolution of galaxies. MNRAS, 169:229–246.

Larson, R. B. (1975). Models for the formation of elliptical galaxies. MNRAS, 173:671–699.

Larson, R. B. (1976). Models for the formation of disc galaxies. MNRAS, 176:31–52.

Lazarian, A. and Vishniac, E. T. (1999). Reconnection in a Weakly Stochastic Field. ApJ, 517(2):700–718.

Lecoanet, D., McCourt, M., Quataert, E., Burns, K. J., Vasil, G. M., Oishi, J. S., Brown, B. P., Stone, J. M., and O'Leary, R. M. (2016). A validated non-linear Kelvin-Helmholtz benchmark for numerical hydrodynamics. MNRAS, 455(4):4274–4288.

Leitherer, C., Schaerer, D., Goldader, J. D., Delgado, R. M. G., Robert, C., Kune, D. F., de Mello, D. F., Devost, D., and Heckman, T. M. (1999). Starburst99: Synthesis Models for Galaxies with Active Star Formation. ApJS, 123(1):3–40.

Lejeune, T., Cuisinier, F., and Buser, R. (1997). Standard stellar library for evolutionary synthesis. I. Calibration of theoretical spectra. A&AS, 125:229–246.

Lejeune, T., Cuisinier, F., and Buser, R. (1998). A standard stellar library for evolutionary synthesis. II. The M dwarf extension. A&AS, 130:65–75.

Leroy, A., Bolatto, A. D., Simon, J. D., and Blitz, L. (2005). The Molecular Interstellar Medium of Dwarf Galaxies on Kiloparsec Scales: A New Survey for CO in Northern, IRAS-detected Dwarf Galaxies. ApJ, 625(2):763–784.

Lesch, H. and Hanasz, M. (2003). Strong magnetic fields and cosmic rays in very young galaxies. A&A, 401:809–816.

Li, M., Bryan, G. L., and Ostriker, J. P. (2017). Quantifying Supernovae-driven Multiphase Galactic Outflows. ApJ, 841:101.

Li, Z.-Y. and Nakamura, F. (2004). Magnetically Regulated Star Formation in Turbulent Clouds. ApJ, 609(2):L83–L86.

Lifshitz, E. M. (1946). On the gravitational stability of the expanding universe. *Zhurnal Eksperimentalnoi i Teoreticheskoi Fiziki*, 16:587–602.

Liska, R. and Wendroff, B. (2003). Comparison of several difference schemes on 1d and 2d test problems for the euler equations. *SIAM Journal on Scientific Computing*, 25(3):995–1017.

Lucy, L. B. (1977). A numerical approach to the testing of the fission hypothesis. AJ, 82:1013–1024.

Lynden-Bell, D. (1969). Galactic Nuclei as Collapsed Old Quasars. Nature, 223(5207):690–694.

Lynds, C. R. and Sandage, A. R. (1963). Evidence for an Explosion in the Center of the Galaxy M82. ApJ, 137:1005.

Lyubimov, V., Novikov, E., Nozik, V., Tretyakov, E., and Kosik, V. (1980). An Estimate of the electron-Neutrino Mass from the beta Spectrum of Tritium in the Valine Molecule. *Phys. Lett. B*, 94:266–268.

Mac Low, M.-M. and Ferrara, A. (1999). Starburst-driven Mass Loss from Dwarf Galaxies: Efficiency and Metal Ejection. ApJ, 513:142–155.

Mac Low, M.-M. and Klessen, R. S. (2004). Control of star formation by supersonic turbulence. *Reviews of Modern Physics*, 76:125–194.

Mac Low, M.-M. and McCray, R. (1988). Superbubbles in disk galaxies. ApJ, 324:776–785.

Malyshkin, L. and Kulsrud, R. M. (2002). Magnetized Turbulent Dynamos in Protogalaxies. ApJ, 571:619–637.

Marinacci, F., Pakmor, R., and Springel, V. (2014). The formation of disc galaxies in high-resolution moving-mesh cosmological simulations. MNRAS, 437:1750–1775.

Marinacci, F., Vogelsberger, M., Mocz, P., and Pakmor, R. (2015). The large-scale properties of simulated cosmological magnetic fields. MNRAS, 453:3999–4019.

Marinacci, F., Vogelsberger, M., Pakmor, R., Torrey, P., Springel, V., Hernquist, L., Nelson, D., Weinberger, R., Pillepich, A., Naiman, J., and Genel, S. (2018). First results from the IllustrisTNG simulations: radio haloes and magnetic fields. MNRAS, 480:5113–5139.

Martizzi, D., Faucher-Giguère, C.-A., and Quataert, E. (2015). Supernova feedback in an inhomogeneous interstellar medium. MNRAS, 450:504–522.

Maschberger, T. (2013). On the function describing the stellar initial mass function. MNRAS, 429(2):1725–1733.

Mastropietro, C. and Burkert, A. (2008). Simulating the Bullet Cluster. MNRAS, 389:967–988.

Matarrese, S., Mollerach, S., Notari, A., and Riotto, A. (2005). Large-scale magnetic fields from density perturbations. Phys. Rev. D, 71(4):043502.

Mathis, J. S., Mezger, P. G., and Panagia, N. (1983). Interstellar radiation field and dust temperatures in the diffuse interstellar matter and in giant molecular clouds. A&A, 500:259–276.

Mathis, J. S., Rumpl, W., and Nordsieck, K. H. (1977). The size distribution of interstellar grains. ApJ, 217:425–433.

Matsuura, M., Dwek, E., Meixner, M., Otsuka, M., Babler, B., Barlow, M. J., Roman-Duval, J., Engelbracht, C., Sandstrom, K., Lakićević, M., van Loon, J. T., Sonneborn, G., Clayton, G. C., Long, K. S., Lundqvist, P., Nozawa, T., Gordon, K. D., Hony, S., Panuzzo, P., Okumura, K., Misselt, K. A., Montiel, E., and Sauvage, M. (2011). Herschel Detects a Massive Dust Reservoir in Supernova 1987A. *Science*, 333:1258.

Matzner, C. D. and McKee, C. F. (2000). Efficiencies of Low-Mass Star and Star Cluster Formation. ApJ, 545(1):364–378.

McCray, R. and Kafatos, M. (1987). Supershells and propagating star formation. ApJ, 317:190–196.

McElroy, D., Walsh, C., Markwick, A. J., Cordiner, M. A., Smith, K., and Millar, T. J. (2013). The UMIST database for astrochemistry 2012. A&A, 550:A36.

McKee, C. F. and Ostriker, E. C. (2007). Theory of Star Formation. ARA&A, 45(1):565–687.

McKee, C. F. and Ostriker, J. P. (1977). A theory of the interstellar medium - Three components regulated by supernova explosions in an inhomogeneous substrate. ApJ, 218:148–169.

McNally, C. P., Lyra, W., and Passy, J.-C. (2012). A Well-posed Kelvin-Helmholtz Instability Test and Comparison. ApJS, 201(2):18.

Menci, N., Grazian, A., Castellano, M., and Sanchez, N. G. (2016). A Stringent Limit on the Warm Dark Matter Particle Masses from the Abundance of z = 6 Galaxies in the Hubble Frontier Fields. ApJ, 825(1):L1.

Micic, M., Glover, S. C. O., Federrath, C., and Klessen, R. S. (2012). Modelling H_2 formation in the turbulent interstellar medium: solenoidal versus compressive turbulent forcing. MNRAS, 421:2531–2542.

Mierkiewicz, E. J., Reynolds, R. J., Roesler, F. L., Harlander, J. M., and Jaehnig, K. P. (2006). Detection of Diffuse Interstellar [O II] Emission from the Milky Way Using Spatial Heterodyne Spectroscopy. ApJ, 650(1):L63–L66.

Milgrom, M. (1983). A modification of the Newtonian dynamics as a possible alternative to the hidden mass hypothesis. ApJ, 270:365–370.

Miller, G. E. and Scalo, J. M. (1979). The Initial Mass Function and Stellar Birthrate in the Solar Neighborhood. ApJS, 41:513.

Miller, M. J. and Bregman, J. N. (2013). The Structure of the Milky Way's Hot Gas Halo. ApJ, 770:118.

Mishustin, I. N. and Ruzmaĭkin, A. A. (1972). Occurrence of "Priming" Magnetic Fields During the Formation of Protogalaxies. *Soviet Journal of Experimental and Theoretical Physics*, 34:233.

Mo, H. J., Mao, S., and White, S. D. M. (1998). The formation of galactic discs. MNRAS, 295:319–336.

Mocz, P., Vogelsberger, M., Sijacki, D., Pakmor, R., and Hernquist, L. (2014). A discontinuous Galerkin method for solving the fluid and magnetohydrodynamic equations in astrophysical simulations. MNRAS, 437:397–414.

Monaghan, J. J. (1997). SPH and Riemann Solvers. *Journal of Computational Physics*, 136(2):298–307.

Moore, B. (1994). Evidence against dissipation-less dark matter from observations of galaxy haloes. Nature, 370(6491):629–631.

Moore, B., Ghigna, S., Governato, F., Lake, G., Quinn, T., Stadel, J., and Tozzi, P. (1999). Dark Matter Substructure within Galactic Halos. ApJ, 524(1):L19–L22.

Moseley, E. R., Squire, J., and Hopkins, P. F. (2019). Non-linear evolution of instabilities between dust and sound waves. MNRAS, 489(1):325–338.

Moss, D. (1998). The relation between magnetic and gas arms in spiral galaxies. MNRAS, 297:860–866.

Moster, B. P., Macciò, A. V., Somerville, R. S., Johansson, P. H., and Naab, T. (2010a). Can gas prevent the destruction of thin stellar discs by minor mergers? MNRAS, 403:1009–1019.

Moster, B. P., Naab, T., and White, S. D. M. (2013). Galactic star formation and accretion histories from matching galaxies to dark matter haloes. MNRAS, 428:3121–3138.

Moster, B. P., Naab, T., and White, S. D. M. (2018). EMERGE - an empirical model for the formation of galaxies since z
10. MNRAS, 477:1822–1852.

Moster, B. P., Somerville, R. S., Maulbetsch, C., van den Bosch, F. C., Macciò, A. V., Naab, T., and Oser, L. (2010b). Constraints on the Relationship between Stellar Mass and Halo Mass at Low and High Redshift. ApJ, 710:903–923.

Motte, F., Andre, P., and Neri, R. (1998). The initial conditions of star formation in the rho Ophiuchi main cloud: wide-field millimeter continuum mapping. A&A, 336:150–172.

Motte, F., Nguyên Luong, Q., Schneider, N., Heitsch, F., Glover, S., Carlhoff, P., Hill, T., Bontemps, S., Schilke, P., Louvet, F., Hennemann, M., Didelon, P., and Beuther, H. (2014). The formation of the W43 complex: constraining its atomic-to-molecular transition and searching for colliding clouds. A&A, 571:A32.

Mouschovias, T. C. (1976). Nonhomologous contraction and equilibria of self-gravitating, magnetic interstellar clouds embedded in an intercloud medium: star formation. I. Formulation of the problem and method of solution. ApJ, 206:753–767.

Naab, T. and Ostriker, J. P. (2017). Theoretical Challenges in Galaxy Formation. ARA&A, 55:59–109.

Navarro, J. F., Eke, V. R., and Frenk, C. S. (1996). The cores of dwarf galaxy haloes. MNRAS, 283(3):L72–L78.

Navarro, J. F., Frenk, C. S., and White, S. D. M. (1997). A Universal Density Profile from Hierarchical Clustering. ApJ, 490:493–508.

Nelson, D., Pillepich, A., Springel, V., Pakmor, R., Weinberger, R., Genel, S., Torrey, P., Vogelsberger, M., Marinacci, F., and Hernquist, L. (2019). First results from the TNG50 simulation: galactic outflows driven by supernovae and black hole feedback. MNRAS, 490(3):3234–3261.

Nelson, R. P. and Langer, W. D. (1997). The Dynamics of Low-Mass Molecular Clouds in External Radiation Fields. ApJ, 482:796–826.

Nelson, R. P. and Langer, W. D. (1999). On the Stability and Evolution of Isolated BOK Globules. ApJ, 524(2):923–946.

NextLimitTechnologies (1998). RealFlow: A Fluid dynamics simulation tool for the 3D and visual effects industry, `http://www.realflow.com/?_ga=1.60118378.699335925.1484139950`.

Niklas, S. and Beck, R. (1997). A new approach to the radio-far infrared correlation for non-calorimeter galaxies. A&A, 320:54–64.

Niklas, S., Klein, U., Braine, J., and Wielebinski, R. (1995). A radio continuum survey of Shapley-Ames Galaxies at λ2.8 cm. I. Atlas of radio data. A&AS, 114:21.

Nisini, B., Benedettini, M., Codella, C., Giannini, T., Liseau, R., Neufeld, D., Tafalla, M., van Dishoeck, E. F., Bachiller, R., Baudry, A., Benz, A. O., Bergin, E., Bjerkeli, P., Blake, G., Bontemps, S., Braine, J., Bruderer, S., Caselli, P., Cernicharo, J., Daniel, F., Encrenaz, P., di Giorgio, A. M., Dominik, C., Doty, S., Fich, M., Fuente, A., Goicoechea, J. R., de Graauw, T., Helmich, F., Herczeg, G., Herpin, F., Hogerheijde, M., Jacq, T., Johnstone, D., Jørgensen, J., Kaufman, M., Kristensen, L., Larsson, B., Lis, D., Marseille, M., McCoey, C., Melnick, G., Olberg, M., Parise, B., Pearson, J., Plume, R., Risacher, C., Santiago, J., Saraceno, P., Shipman, R., van Kempen, T. A., Visser, R., Viti, S., Wampfler, S., Wyrowski, F., van der Tak, F., Yıldız, U. A., Delforge, B., Desbat, J., Hatch, W. A., Péron, I., Schieder, R., Stern, J. A., Teyssier, D., and Whyborn, N. (2010). Water cooling of shocks in protostellar outflows. Herschel-PACS map of L1157. A&A, 518:L120.

NvidiaCorporation (2015). Nvidia Physx System Software, `http://www.nvidia.de/object/physx-9.15.0428-driver-de.html`.

Offner, S. S. R., Clark, P. C., Hennebelle, P., Bastian, N., Bate, M. R., Hopkins, P. F., Moraux, E., and Whitworth, A. P. (2014). The Origin and Universality of the Stellar Initial Mass Function. In Beuther, H., Klessen, R. S., Dullemond, C. P., and Henning, T., editors, *Protostars and Planets VI*, page 53.

Ohlin, L., Renaud, F., and Agertz, O. (2019). Supernovae feedback propagation: the role of turbulence. MNRAS, 485(3):3887–3894.

Oort, J. H. (1932). The force exerted by the stellar system in the direction perpendicular to the galactic plane and some related problems. Bull. Astron. Inst. Netherlands, 6:249.

Oort, J. H. (1954). Outline of a theory on the origin and acceleration of interstellar clouds and O associations. Bull. Astron. Inst. Netherlands, 12:177.

O'Shea, B. W., Bryan, G., Bordner, J., Norman, M. L., Abel, T., Harkness, R., and Kritsuk, A. (2004). Introducing Enzo, an AMR Cosmology Application. *ArXiv Astrophysics e-prints*.

Ostriker, J. P. (1980). Elliptical Galaxies are not Made by Merging Spiral Galaxies. *Comments on Astrophysics*, 8:177.

Ostriker, J. P. and McKee, C. F. (1988). Astrophysical blastwaves. *Reviews of Modern Physics*, 60:1–68.

Ostriker, J. P., Peebles, P. J. E., and Yahil, A. (1974). The Size and Mass of Galaxies, and the Mass of the Universe. ApJ, 193:L1.

Padoan, P. and Nordlund, Å. (2002). The Stellar Initial Mass Function from Turbulent Fragmentation. ApJ, 576(2):870–879.

Padoan, P., Nordlund, A., and Jones, B. J. T. (1997). The universality of the stellar initial mass function. MNRAS, 288(1):145–152.

Pakmor, R., Gómez, F. A., Grand, R. J. J., Marinacci, F., Simpson, C. M., Springel, V., Campbell, D. J. R., Frenk, C. S., Guillet, T., Pfrommer, C., and White, S. D. M. (2017). Magnetic field formation in the Milky Way like disc galaxies of the Auriga project. MNRAS, 469:3185–3199.

Pakmor, R. and Springel, V. (2013). Simulations of magnetic fields in isolated disc galaxies. MNRAS, 432:176–193.

Pan, L. and Padoan, P. (2009). The Temperature of Interstellar Clouds from Turbulent Heating. ApJ, 692(1):594–607.

Parker, E. N. (1955). Hydromagnetic Dynamo Models. ApJ, 122:293.

Parker, E. N. (1966). The Dynamical State of the Interstellar Gas and Field. ApJ, 145:811.

Parker, E. N. (1979). *Cosmical magnetic fields. Their origin and their activity*.

Patrikeev, I., Fletcher, A., Stepanov, R., Beck, R., Berkhuijsen, E. M., Frick, P., and Horellou, C. (2006). Analysis of spiral arms using anisotropic wavelets: gas, dust and magnetic fields in M 51. A&A, 458:441–452.

Peebles, P. J. E. (1965). The Black-Body Radiation Content of the Universe and the Formation of Galaxies. ApJ, 142:1317.

Peebles, P. J. E. (1971). Rotation of Galaxies and the Gravitational Instability Picture. A&A, 11:377.

Peebles, P. J. E. and Yu, J. T. (1970). Primeval Adiabatic Perturbation in an Expanding Universe. ApJ, 162:815.

Penzias, A. A. and Wilson, R. W. (1965). A Measurement of Excess Antenna Temperature at 4080 Mc/s. ApJ, 142:419–421.

Peters, T., Banerjee, R., Klessen, R. S., Mac Low, M.-M., Galván-Madrid, R., and Keto, E. R. (2010a). H II Regions: Witnesses to Massive Star Formation. ApJ, 711(2):1017–1028.

Peters, T., Klessen, R. S., Mac Low, M.-M., and Banerjee, R. (2010b). Limiting Accretion onto Massive Stars by Fragmentation-induced Starvation. ApJ, 725(1):134–145.

Peters, T., Naab, T., Walch, S., Glover, S. C. O., Girichidis, P., Pellegrini, E., Klessen, R. S., Wünsch, R., Gatto, A., and Baczynski, C. (2017). The SILCC project - IV. Impact of dissociating and ionizing radiation on the interstellar medium and Hα emission as a tracer of the star formation rate. MNRAS, 466:3293–3308.

Petkova, M. and Springel, V. (2009). An implementation of radiative transfer in the cosmological simulation code GADGET. MNRAS, 396:1383–1403.

Petruk, O. (2006). On the transition of the adiabatic supernova remnant to the radiative stage in a nonuniform interstellar medium. *arXiv Astrophysics e-prints*.

Phillips, J. P. (1999). Rotation in molecular clouds. A&AS, 134:241–254.

Pillepich, A., Springel, V., Nelson, D., Genel, S., Naiman, J., Pakmor, R., Hernquist, L., Torrey, P., Vogelsberger, M., Weinberger, R., and Marinacci, F. (2018). Simulating galaxy formation with the IllustrisTNG model. MNRAS, 473(3):4077–4106.

Planck Collaboration, Adam, R., Ade, P. A. R., Aghanim, N., Akrami, Y., Alves, M. I. R., Argüeso, F., Arnaud, M., Arroja, F., Ashdown, M., Aumont, J., Baccigalupi, C., Ballardini, M., Band ay, A. J., Barreiro, R. B., Bartlett, J. G., Bartolo, N., Basak, S., Battaglia, P., Battaner, E., Battye, R., Benabed, K., Benoît, A., Benoit-Lévy, A., Bernard, J. P., Bersanelli, M., Bertincourt, B., Bielewicz, P., Bikmaev, I., Bock, J. J., Böhringer, H., Bonaldi, A., Bonavera, L., Bond, J. R., Borrill, J., Bouchet, F. R., Boulanger, F., Bucher, M., Burenin, R., Burigana, C., Butler, R. C., Calabrese, E., Cardoso, J. F., Carvalho, P., Casaponsa, B., Castex, G., Catalano, A., Challinor, A., Chamballu, A., Chary, R. R., Chiang, H. C., Chluba, J., Chon, G., Christensen, P. R., Church, S., Clemens, M., Clements, D. L., Colombi, S., Colombo, L. P. L., Combet, C., Comis, B., Contreras, D., Couchot, F., Coulais, A., Crill, B. P., Cruz, M., Curto, A., Cuttaia, F., Danese, L., Davies, R. D., Davis, R. J., de Bernardis, P., de Rosa, A., de Zotti, G., Delabrouille, J., Delouis, J. M., Désert, F. X., Di Valentino, E., Dickinson, C., Diego, J. M., Dolag, K., Dole, H., Donzelli, S., Doré, O., Douspis, M., Ducout, A., Dunkley, J., Dupac, X., Efstathiou, G., Eisenhardt, P. R. M., Elsner, F., Enßlin, T. A., Eriksen, H. K., Falgarone, E., Fantaye, Y., Farhang, M., Feeney, S., Fergusson, J., Fernandez-Cobos, R., Feroz, F., Finelli, F., Florido, E., Forni, O., Frailis, M., Fraisse, A. A., Franceschet, C., Franceschi, E., Frejsel, A., Frolov, A., Galeotta, S., Galli, S., Ganga, K., Gauthier, C., Génova-Santos, R. T., Gerbino, M., Ghosh, T., Giard, M., Giraud-Héraud, Y., Giusarma, E., Gjerløw, E., González-Nuevo, J., Górski, K. M., Grainge, K. J. B., Gratton, S., Gregorio, A., Gruppuso, A., Gudmundsson, J. E., Hamann, J., Handley, W., Hansen, F. K., Hanson, D., Harrison, D. L., Heavens, A., Helou, G., Henrot-Versillé, S., Hernández-Monteagudo, C., Herranz, D., Hildebrandt, S. R., Hivon, E., Hobson, M., Holmes, W. A., Hornstrup, A., Hovest, W., Huang, Z., Huffenberger, K. M., Hurier, G., Ilić, S., Jaffe, A. H., Jaffe, T. R., Jin, T., Jones, W. C., Juvela, M., Karakci, A., Keihänen, E., Keskitalo, R., Khamitov, I., Kiiveri, K., Kim, J., Kisner, T. S., Kneissl, R., Knoche, J., Knox, L., Krachmalnicoff, N., Kunz, M., Kurki-Suonio, H., Lacasa, F., Lagache, G., Lähteenmäki, A., Lamarre, J. M., Langer, M., Lasenby, A., Lattanzi, M., Lawrence, C. R., Le Jeune, M., Leahy, J. P., Lellouch, E., Leonardi, R., León-Tavares, J., Lesgourgues, J., Levrier, F., Lewis, A., Liguori, M., Lilje, P. B., Lilley, M., Linden-Vørnle, M., Lindholm, V., Liu, H., López-Caniego, M., Lubin, P. M., Ma, Y. Z., Macías-Pérez, J. F., Maggio, G., Maino, D., Mak, D. S. Y., Mandolesi, N., Mangilli, A., Marchini, A., Marcos-Caballero, A., Marinucci, D., Maris, M., Marshall, D. J., Martin, P. G., Martinelli, M., Martínez-González, E., Masi, S., Matarrese, S., Mazzotta, P., McEwen, J. D., McGehee, P., Mei, S., Meinhold, P. R., Melchiorri, A., Melin, J. B., Mendes, L., Mennella, A., Migliaccio, M., Mikkelsen, K., Millea, M., Mitra, S., Miville-Deschênes, M. A., Molinari, D., Moneti, A., Montier, L., Moreno, R., Morgante, G., Mortlock, D., Moss, A., Mottet, S., Münchmeyer, M., Munshi, D., Murphy, J. A., Narimani, A., Naselsky, P., Nastasi, A., Nati, F., Natoli, P., Negrello, M., Netterfield, C. B., Nørgaard-Nielsen, H. U., Noviello, F., Novikov, D., Novikov, I., Olamaie, M., Oppermann, N., Orlando, E., Oxborrow, C. A., Paci, F., Pagano, L., Pajot, F., Paladini, R., Pandolfi, S., Paoletti, D., Partridge, B., Pasian, F., Patanchon, G., Pearson, T. J., Peel, M., Peiris, H. V., Pelkonen, V. M., Perdereau, O., Perotto, L., Perrott, Y. C., Perrotta, F., Pettorino, V., Piacentini, F., Piat, M., Pierpaoli, E., Pietrobon, D., Plaszczynski, S., Pogosyan, D., Pointecouteau, E., Polenta, G., Popa, L., Pratt, G. W., Prézeau, G., Prunet, S., Puget, J. L., Rachen, J. P., Racine, B., Reach, W. T., Rebolo, R., Reinecke, M., Remazeilles, M., Renault, C., Renzi, A., Ristorcelli, I., Rocha, G., Roman, M., Romelli, E., Rosset, C., Rossetti, M., Rotti, A., Roudier, G., Rouillé d'Orfeuil, B., Rowan-Robinson, M., Rubiño-Martín, J. A., Ruiz-Granados, B., Rumsey, C., Rusholme, B., Said, N., Salvatelli, V., Salvati, L., Sandri, M., Sanghera, H. S., Santos, D., Saunders, R. D. E., Sauvé, A., Savelainen, M., Savini, G., Schaefer, B. M., Schammel, M. P., Scott, D., Seiffert, M. D., Serra, P., Shellard, E. P. S., Shimwell, T. W., Shiraishi, M., Smith, K., Souradeep, T., Spencer, L. D., Spinelli, M., Stanford, S. A., Stern, D., Stolyarov, V., Stompor, R., Strong, A. W., Sudiwala, R., Sunyaev, R., Sutter, P., Sutton, D., Suur-Uski, A. S., Sygnet, J. F., Tauber, J. A., Tavagnacco, D., Terenzi, L., Texier, D., Toffolatti, L., Tomasi, M., Tornikoski, M., Tramonte, D., Tristram, M., Troja, A., Trombetti, T., Tucci, M., Tuovinen, J., Türler, M., Umana, G., Valenziano, L., Valiviita, J., Van Tent, F., Vassallo, T., Vibert, L., Vidal, M., Viel, M., Vielva, P., Villa, F., Wade, L. A., Walter, B., Wand elt, B. D., Watson, R., Wehus, I. K., Welikala, N., Weller, J., White, M., White, S. D. M., Wilkinson, A., Yvon, D., Zacchei, A., Zibin, J. P., and Zonca, A. (2016). Planck 2015 results. I. Overview of products and scientific results. A&A, 594:A1.

Planck Collaboration, Ade, P. A. R., Aghanim, N., Armitage-Caplan, C., Arnaud, M., Ashdown, M., Atrio-Barand ela, F., Aumont, J., Baccigalupi, C., Banday, A. J., Barreiro, R. B., Bartlett, J. G., Bartolo, N., Battaner, E., Benabed, K., Benoît, A., Benoit-Lévy, A., Bernard, J. P., Bersanelli, M., Bielewicz, P., Bobin, J., Bock, J. J., Bonaldi, A., Bond, J. R., Borrill, J., Bouchet, F. R., Bridges, M., Bucher, M., Burigana, C., Butler, R. C., Calabrese, E., Cardoso, J. F., Catalano, A., Challinor, A., Chamballu, A., Chiang, H. C., Chiang, L. Y., Christensen, P. R., Church, S., Clements, D. L., Colombi, S., Colombo, L. P. L., Couchot, F., Coulais, A., Crill, B. P., Curto, A., Cuttaia, F., Danese, L., Davies, R. D., Davis, R. J., de Bernardis, P., de Rosa, A., de Zotti, G., Delabrouille, J., Delouis, J. M., Désert, F. X., Dickinson, C., Diego, J. M., Dole, H., Donzelli, S., Doré, O., Douspis, M., Dunkley, J., Dupac, X., Efstathiou, G., Enßlin, T. A., Eriksen, H. K., Finelli, F., Forni, O., Frailis, M., Franceschi, E., Galeotta, S., Ganga, K., Gauthier, C., Giard, M., Giardino, G., Giraud-Héraud, Y., González-Nuevo, J., Górski, K. M., Gratton, S., Gregorio, A., Gruppuso, A., Hamann, J., Hansen, F. K., Hanson, D., Harrison, D., Henrot-Versillé, S., Hernández-Monteagudo, C., Herranz, D., Hildebrand t, S. R., Hivon, E., Hobson, M., Holmes, W. A., Hornstrup, A., Hovest, W., Huffenberger, K. M., Jaffe, A. H., Jaffe, T. R., Jones, W. C., Juvela, M., Keihänen, E., Keskitalo, R., Kisner, T. S., Kneissl, R., Knoche, J., Knox, L., Kunz, M., Kurki-Suonio, H., Lagache, G., Lähteenmäki, A., Lamarre, J. M., Lasenby, A., Laureijs, R. J., Lawrence, C. R., Leach, S., Leahy, J. P., Leonardi, R., Lesgourgues, J., Lewis, A., Liguori, M., Lilje, P. B., Linden-Vørnle, M., López-Caniego, M., Lubin, P. M., Macías-Pérez, J. F., Maffei, B., Maino, D., Mandolesi, N., Maris, M., Marshall, D. J., Martin, P. G., Martínez-González, E., Masi, S., Massardi, M., Matarrese, S., Matthai, F., Mazzotta, P., Meinhold, P. R., Melchiorri, A., Mendes, L., Mennella, A., Migliaccio, M., Mitra, S., Miville-Deschênes, M. A., Moneti, A., Montier, L., Morgante, G., Mortlock, D., Moss, A., Munshi, D., Murphy, J. A., Naselsky, P., Nati, F., Natoli, P., Netterfield, C. B., Nørgaard-Nielsen, H. U., Noviello, F., Novikov, D., Novikov, I., O'Dwyer, I. J., Osborne, S., Oxborrow, C. A., Paci, F., Pagano, L., Pajot, F., Paladini, R., Pand olfi, S., Paoletti, D., Partridge, B., Pasian, F., Patanchon, G., Peiris, H. V., Perdereau, O., Perotto, L., Perrotta, F., Piacentini, F., Piat, M., Pierpaoli, E., Pietrobon, D., Plaszczynski, S., Pointecouteau, E., Polenta, G., Ponthieu, N., Popa, L., Poutanen, T., Pratt, G. W., Prézeau, G., Prunet, S., Puget, J. L., Rachen, J. P., Rebolo, R., Reinecke, M., Remazeilles, M., Renault, C., Ricciardi, S., Riller, T., Ristorcelli, I., Rocha, G., Rosset, C., Roudier, G., Rowan-Robinson, M., Rubiño-Martín, J. A., Rusholme, B., Sandri, M., Santos, D., Savelainen, M., Savini, G., Scott, D., Seiffert, M. D., Shellard, E. P. S., Spencer, L. D., Starck, J. L., Stolyarov, V., Stompor, R., Sudiwala, R., Sunyaev, R., Sureau, F., Sutton, D., Suur-Uski, A. S., Sygnet, J. F., Tauber, J. A., Tavagnacco, D., Terenzi, L., Toffolatti, L., Tomasi, M., Tréguer-Goudineau, J., Tristram, M., Tucci, M., Tuovinen, J., Valenziano, L., Valiviita, J., Van Tent, B., Varis, J., Vielva, P., Villa, F., Vittorio, N., Wade, L. A., Wandelt, B. D., White, M., Wilkinson, A., Yvon, D., Zacchei, A., Zibin, J. P., and Zonca, A. (2014). Planck 2013 results. XXII. Constraints on inflation. A&A, 571:A22.

Plummer, H. C. (1911). On the problem of distribution in globular star clusters. MNRAS, 71:460–470.

Poezd, A., Shukurov, A., and Sokoloff, D. (1993). Global magnetic patterns in the Milky Way and the Andromeda nebula. MNRAS, 264:285–297.

Portegies Zwart, S. F., McMillan, S. L. W., and Gieles, M. (2010). Young Massive Star Clusters. ARA&A, 48:431–493.

Powell, K. G., Roe, P. L., Linde, T. J., Gombosi, T. I., and De Zeeuw, D. L. (1999). A Solution-Adaptive Upwind Scheme for Ideal Magnetohydrodynamics. *Journal of Computational Physics*, 154:284–309.

Press, W. H. and Schechter, P. (1974). Formation of Galaxies and Clusters of Galaxies by Self-Similar Gravitational Condensation. ApJ, 187:425–438.

Price, D. J. (2012). Smoothed particle hydrodynamics and magnetohydrodynamics. *Journal of Computational Physics*, 231(3):759–794.

Price, D. J., Wurster, J., Tricco, T. S., Nixon, C., Toupin, S., Pettitt, A., Chan, C., Mentiplay, D., Laibe, G., Glover, S., Dobbs, C., Nealon, R., Liptai, D., Worpel, H., Bonnerot, C., Dipierro, G., Ballabio, G., Ragusa, E., Federrath, C., Iaconi, R., Reichardt, T., Forgan, D., Hutchison, M., Constantino, T., Ayliffe, B., Hirsh, K., and Lodato, G. (2018). Phantom: A Smoothed Particle Hydrodynamics and Magnetohydrodynamics Code for Astrophysics. PASA, 35:e031.

Pudritz, R. E. and Silk, J. (1989). The Origin of Magnetic Fields and Primordial Stars in Protogalaxies. ApJ, 342:650.

Read, J. I., Hayfield, T., and Agertz, O. (2010). Resolving mixing in smoothed particle hydrodynamics. MNRAS, 405:1513–1530.

Rees, M. J. (1987). The origin and cosmogonic implications of seed magnetic fields. QJRAS, 28:197–206.

Rees, M. J. (1994). Origin of the Seed Magnetic Field for a Galactic Dynamo. In Lynden-Bell, D., editor, *NATO Advanced Science Institutes (ASI) Series C*, volume 422 of *NATO Advanced Science Institutes (ASI) Series C*, page 155.

Rees, M. J. (2005). *Magnetic Fields in the Early Universe*, volume 664, page 1.

Rees, M. J. (2006). Origin of cosmic magnetic fields. *Astronomische Nachrichten*, 327:395.

Rees, M. J. and Ostriker, J. P. (1977). Cooling, dynamics and fragmentation of massive gas clouds: clues to the masses and radii of galaxies and clusters. MNRAS, 179:541–559.

Rees, M. J. and Sciama, D. W. (1968). Large-scale Density Inhomogeneities in the Universe. Nature, 217(5128):511–516.

Reines, F., Sobel, H. W., and Pasierb, E. (1980). Evidence for neutrino instability. Phys. Rev. Lett., 45(16):1307–1311.

Renzo, M., Zapartas, E., de Mink, S. E., Götberg, Y., Justham, S., Farmer, R. J., Izzard, R. G., Toonen, S., and Sana, H. (2019). Massive runaway and walkaway stars. A study of the kinematical imprints of the physical processes governing the evolution and explosion of their binary progenitors. A&A, 624:A66.

Reynolds, R. J., Scherb, F., and Roesler, F. L. (1973). Observations of Diffuse Galactic HA and [n II] Emission. ApJ, 185:869–876.

Reynolds, S. P., Gaensler, B. M., and Bocchino, F. (2012). Magnetic Fields in Supernova Remnants and Pulsar-Wind Nebulae. Space Sci. Rev., 166:231–261.

Richings, A. J., Schaye, J., and Oppenheimer, B. D. (2014). Non-equilibrium chemistry and cooling in the diffuse interstellar medium - II. Shielded gas. MNRAS, 442(3):2780–2796.

Rieder, M. and Teyssier, R. (2016). A small-scale dynamo in feedback-dominated galaxies as the origin of cosmic magnetic fields - I. The kinematic phase. MNRAS, 457:1722–1738.

Rieder, M. and Teyssier, R. (2017a). A small-scale dynamo in feedback-dominated galaxies - II. The saturation phase and the final magnetic configuration. MNRAS, 471(3):2674–2686.

Rieder, M. and Teyssier, R. (2017b). A small-scale dynamo in feedback-dominated galaxies - III. Cosmological simulations. MNRAS, 472(4):4368–4373.

Riess, A. G., Nugent, P. E., Gilliland, R. L., Schmidt, B. P., Tonry, J., Dickinson, M., Thompson, R. I., Budavári, T., Casertano, S., Evans, A. S., Filippenko, A. V., Livio, M., Sanders, D. B., Shapley, A. E., Spinrad, H., Steidel, C. C., Stern, D., Surace, J., and Veilleux, S. (2001). The Farthest Known Supernova: Support for an Accelerating Universe and a Glimpse of the Epoch of Deceleration. ApJ, 560(1):49–71.

Robishaw, T., Quataert, E., and Heiles, C. (2008). Extragalactic Zeeman Detections in OH Megamasers. ApJ, 680:981–998.

Roh, S., Ryu, D., Kang, H., Ha, S., and Jang, H. (2019). Turbulence Dynamo in Galaxy Clusters. *arXiv e-prints*.

Rosswog, S. (2015). SPH Methods in the Modelling of Compact Objects. *Living Reviews in Computational Astrophysics*, 1:1.

Röttgers, B. and Arth, A. (2018). SPH to Grid: a new integral conserving method. *ArXiv e-prints*.

Rubin, V. C. and Ford, W. Kent, J. (1970). Rotation of the Andromeda Nebula from a Spectroscopic Survey of Emission Regions. ApJ, 159:379.

Ruzmaikin, A., Sokolov, D., and Shukurov, A. (1988a). Magnetism of spiral galaxies. Nature, 336:341–347.

Ruzmaikin, A. A., Sokolov, D. D., and Shukurov, A. M., editors (1988b). *Magnetic fields of galaxies*, volume 133 of *Astrophysics and Space Science Library*.

Ruzmaikin, A. A., Turchaninov, V. I., Zeldovich, I. B., and Sokoloff, D. D. (1979). The disk dynamo. Ap&SS, 66:369–384.

Sachs, R. K. and Wolfe, A. M. (1967). Perturbations of a Cosmological Model and Angular Variations of the Microwave Background. ApJ, 147:73.

Saitoh, T. R. and Makino, J. (2009). A Necessary Condition for Individual Time Steps in SPH Simulations. ApJ, 697:L99–L102.

Saitoh, T. R. and Makino, J. (2013). A Density-independent Formulation of Smoothed Particle Hydrodynamics. ApJ, 768:44.

Salpeter, E. E. (1955). The Luminosity Function and Stellar Evolution. ApJ, 121:161.

Sato, H., Matsuda, T., and Takeda, H. (1971). Chapter II. Evolution of the Expanding Hot Universe. *Progress of Theoretical Physics Supplement*, 49:11–82.

Sato, H. and Takahara, F. (1980). Clustering of the Relic Neutrinos in the Expanding Universe. *Progress of Theoretical Physics*, 64(6):2029–2040.

Scalo, J. and Elmegreen, B. G. (2004). Interstellar Turbulence II: Implications and Effects. ARA&A, 42:275–316.

Scannapieco, E. and Oh, S. P. (2004). Quasar Feedback: The Missing Link in Structure Formation. ApJ, 608:62–79.

Schaye, J., Crain, R. A., Bower, R. G., Furlong, M., Schaller, M., Theuns, T., Dalla Vecchia, C., Frenk, C. S., McCarthy, I. G., Helly, J. C., Jenkins, A., Rosas-Guevara, Y. M., White, S. D. M., Baes, M., Booth, C. M., Camps, P., Navarro, J. F., Qu, Y., Rahmati, A., Sawala, T., Thomas, P. A., and Trayford, J. (2015). The EAGLE project: simulating the evolution and assembly of galaxies and their environments. MNRAS, 446(1):521–554.

Schekochihin, A. A., Cowley, S. C., Hammett, G. W., Maron, J. L., and McWilliams, J. C. (2002). A model of nonlinear evolution and saturation of the turbulent MHD dynamo. *New Journal of Physics*, 4:84.

Schekochihin, A. A., Cowley, S. C., Taylor, S. F., Maron, J. L., and McWilliams, J. C. (2004). Simulations of the Small-Scale Turbulent Dynamo. ApJ, 612:276–307.

Schleicher, D. R. G., Banerjee, R., Sur, S., Arshakian, T. G., Klessen, R. S., Beck, R., and Spaans, M. (2010). Small-scale dynamo action during the formation of the first stars and galaxies. I. The ideal MHD limit. A&A, 522:A115.

Schleicher, D. R. G. and Beck, R. (2013). A new interpretation of the far-infrared - radio correlation and the expected breakdown at high redshift. A&A, 556:A142.

Schmidt, M. (1959). The Rate of Star Formation. ApJ, 129:243.

Schmidt, M. (1963). 3C 273 : A Star-Like Object with Large Red-Shift. Nature, 197(4872):1040.

Schnack, D. D. (2009). *Lectures in Magnetohydrodynamics, Springer, ISBN: 978-3-642-00687-6*.

Schober, J., Schleicher, D. R. G., Federrath, C., Bovino, S., and Klessen, R. S. (2015). Saturation of the turbulent dynamo. Phys. Rev. E, 92(2):023010.

Schramm, D. N. and Steigman, G. (1981). Relic Neutrinos and the Density of the Universe. ApJ, 243:1.

Sedov, L. I. (1946). The movement of air in a strong explosion. *Dokl. Akad. Nauk SSSR*, 52:17.

Sedov, L. I. (1959). *Similarity and Dimensional Methods in Mechanics*.

Seifried, D., Walch, S., Haid, S., Girichidis, P., and Naab, T. (2018). Is Molecular Cloud Turbulence Driven by External Supernova Explosions? ApJ, 855:81.

Shakura, N. I. and Sunyaev, R. A. (1973). Reprint of 1973A&A....24..337S. Black holes in binary systems. Observational appearance. A&A, 500:33–51.

Sheffer, Y., Rogers, M., Federman, S. R., Abel, N. P., Gredel, R., Lambert, D. L., and Shaw, G. (2008). Ultraviolet Survey of CO and H_2 in Diffuse Molecular Clouds: The Reflection of Two Photochemistry Regimes in Abundance Relationships. ApJ, 687(2):1075–1106.

Shen, S., Madau, P., Aguirre, A., Guedes, J., Mayer, L., and Wadsley, J. (2012). The Origin of Metals in the Circumgalactic Medium of Massive Galaxies at z = 3. ApJ, 760:50.

Shu, F. H., Adams, F. C., and Lizano, S. (1987). Star formation in molecular clouds: observation and theory. ARA&A, 25:23–81.

Shukurov, A. (2000). Global magnetic structures in spiral galaxies: Evidence for dynamo action. In Berkhuijsen, E. M., Beck, R., and Walterbos, R. A. M., editors, *Proceedings 232. WE-Heraeus Seminar*, pages 191–200.

Shukurov, A., Rodrigues, L. F. S., Bushby, P. J., Hollins, J., and Rachen, J. P. (2019). A physical approach to modelling large-scale galactic magnetic fields. A&A, 623:A113.

Silk, J. (1968). Cosmic Black-Body Radiation and Galaxy Formation. ApJ, 151:459.

Silk, J. (1977). On the fragmentation of cosmic gas clouds. I. The formation of galaxies and the first generation of stars. ApJ, 211:638–648.

Smoot, G. F., Bennett, C. L., Kogut, A., Wright, E. L., Aymon, J., Boggess, N. W., Cheng, E. S., de Amici, G., Gulkis, S., Hauser, M. G., Hinshaw, G., Jackson, P. D., Janssen, M., Kaita, E., Kelsall, T., Keegstra, P., Lineweaver, C., Loewenstein, K., Lubin, P., Mather, J., Meyer, S. S., Moseley, S. H., Murdock, T., Rokke, L., Silverberg, R. F., Tenorio, L., Weiss, R., and Wilkinson, D. T. (1992). Structure in the COBE Differential Microwave Radiometer First-Year Maps. ApJ, 396:L1.

Sobolev, V. V. (1957). The Diffusion of Lα Radiation in Nebulae and Stellar Envelopes. Soviet Ast., 1:678.

Sokoloff, D. D., Bykov, A. A., Shukurov, A., Berkhuijsen, E. M., Beck, R., and Poezd, A. D. (1998). Depolarization and Faraday effects in galaxies. MNRAS, 299(1):189–206.

Somerville, R. S. (2002). Can Photoionization Squelching Resolve the Substructure Crisis? ApJ, 572(1):L23–L26.

Somerville, R. S. and Davé, R. (2015). Physical Models of Galaxy Formation in a Cosmological Framework. ARA&A, 53:51–113.

Spergel, D. N., Bean, R., Doré, O., Nolta, M. R., Bennett, C. L., Dunkley, J., Hinshaw, G., Jarosik, N., Komatsu, E., Page, L., Peiris, H. V., Verde, L., Halpern, M., Hill, R. S., Kogut, A., Limon, M., Meyer, S. S., Odegard, N., Tucker, G. S., Weiland , J. L., Wollack, E., and Wright, E. L. (2007). Three-Year Wilkinson Microwave Anisotropy Probe (WMAP) Observations: Implications for Cosmology. ApJS, 170(2):377–408.

Spitzer, L. (1962). *Physics of Fully Ionized Gases*.

Spitzer, L. (1978). *Physical processes in the interstellar medium*.

Springel, V. (2005). The cosmological simulation code GADGET-2. MNRAS, 364:1105–1134.

Springel, V. (2010). E pur si muove: Galilean-invariant cosmological hydrodynamical simulations on a moving mesh. MNRAS, 401:791–851.

Springel, V., Di Matteo, T., and Hernquist, L. (2005a). Modelling feedback from stars and black holes in galaxy mergers. MNRAS, 361:776–794.

Springel, V. and Hernquist, L. (2002). Cosmological smoothed particle hydrodynamics simulations: the entropy equation. MNRAS, 333:649–664.

Springel, V. and Hernquist, L. (2003). Cosmological smoothed particle hydrodynamics simulations: a hybrid multiphase model for star formation. MNRAS, 339(2):289–311.

Springel, V. and White, S. D. M. (1999). Tidal tails in cold dark matter cosmologies. MNRAS, 307:162–178.

Springel, V., White, S. D. M., Jenkins, A., Frenk, C. S., Yoshida, N., Gao, L., Navarro, J., Thacker, R., Croton, D., Helly, J., Peacock, J. A., Cole, S., Thomas, P., Couchman, H., Evrard, A., Colberg, J., and Pearce, F. (2005b). Simulations of the formation, evolution and clustering of galaxies and quasars. Nature, 435(7042):629–636.

Springel, V., White, S. D. M., Tormen, G., and Kauffmann, G. (2001a). Populating a cluster of galaxies - I. Results at [formmu2]z=0. MNRAS, 328(3):726–750.

Springel, V., Yoshida, N., and White, S. D. M. (2001b). GADGET: a code for collisionless and gasdynamical cosmological simulations. New A, 6(2):79–117.

Spyromilio, J., Meikle, W. P. S., Learner, R. C. M., and Allen, D. A. (1988). Carbon monoxide in supernova 1987A. Nature, 334:327–329.

Squire, J. and Hopkins, P. F. (2018). Resonant Drag Instability of Grains Streaming in Fluids. ApJ, 856(1):L15.

Starobinsky, A. A. (1982). Dynamics of phase transition in the new inflationary universe scenario and generation of perturbations. *Physics Letters B*, 117(3-4):175–178.

Stecher, T. P. and Williams, D. A. (1967). Photodestruction of Hydrogen Molecules in H I Regions. ApJ, 149:L29.

Steenbeck, M., Krause, F., and Rädler, K.-H. (1966). Berechnung der mittleren LORENTZ-Feldstärke für ein elektrisch leitendes Medium in turbulenter, durch CORIOLIS-Kräfte beeinflußter Bewegung. *Zeitschrift Naturforschung Teil A*, 21:369.

Stein, Y., Dettmar, R.-J., Irwin, J., Beck, R., Weżgowiec, M., Miskolczi, A., Krause, M., Heesen, V., Wiegert, T., Heald, G., Walterbos, R. A. M., Li, J.-T., and Soida, M. (2019). CHANG-ES. XIII. Transport processes and the magnetic fields of NGC 4666: indication of a reversing disk magnetic field. A&A, 623:A33.

Steinwandel, U. P., Beck, M. C., Arth, A., Dolag, K., Moster, B. P., and Nielaba, P. (2019). Magnetic buoyancy in simulated galactic discs with a realistic circumgalactic medium. MNRAS, 483:1008–1028.

Steinwandel, U. P., Dolag, K., Lesch, H., Moster, B. P., Burkert, A., and Prieto, A. (2020a). On the origin of magnetic driven winds and the structure of the galactic dynamo in isolated galaxies. MNRAS, 494(3):4393–4412.

Steinwandel, U. P., Moster, B. P., Naab, T., Hu, C.-Y., and Walch, S. (2020b). Hot phase generation by supernovae in ISM simulations: resolution, chemistry, and thermal conduction. MNRAS, 495(1):1035–1060.

Stone, J. M., Tomida, K., White, C. J., and Felker, K. G. (2020). The Athena++ Adaptive Mesh Refinement Framework: Design and Magnetohydrodynamic Solvers. ApJS, 249(1):4.

Su, K.-Y., Hayward, C. C., Hopkins, P. F., Quataert, E., Faucher-Giguère, C.-A., and Kereš, D. (2018). Stellar feedback strongly alters the amplification and morphology of galactic magnetic fields. MNRAS, 473:L111–L115.

Subramanian, K. and Barrow, J. D. (2002). Small-scale microwave background anisotropies arising from tangled primordial magnetic fields. MNRAS, 335(3):L57–L61.

Sun, X. H., Landecker, T. L., Gaensler, B. M., Carretti, E., Reich, W., Leahy, J. P., McClure-Griffiths, N. M., Crocker, R. M., Wolleben, M., Haverkorn, M., Douglas, K. A., and Gray, A. D. (2015). Faraday Tomography of the North Polar Spur: Constraints on the Distance to the Spur and on the Magnetic Field of the Galaxy. ApJ, 811:40.

Sur, S., Shukurov, A., and Subramanian, K. (2007). Galactic dynamos supported by magnetic helicity fluxes. MNRAS, 377:874–882.

Tabatabaei, F. S., Beck, R., Krügel, E., Krause, M., Berkhuijsen, E. M., Gordon, K. D., and Menten, K. M. (2007). High-resolution radio continuum survey of M 33. II. Thermal and nonthermal emission. A&A, 475(1):133–143.

Tabatabaei, F. S., Berkhuijsen, E. M., Frick, P., Beck, R., and Schinnerer, E. (2013). Multi-scale radio-infrared correlations in M 31 and M 33: The role of magnetic fields and star formation. A&A, 557:A129.

Tabatabaei, F. S., Krause, M., Fletcher, A., and Beck, R. (2008). High-resolution radio continuum survey of M 33. III. Magnetic fields. A&A, 490:1005–1017.

Tabatabaei, F. S., Minguez, P., Prieto, M. A., and Fernández-Ontiveros, J. A. (2018). Discovery of massive star formation quenching by non-thermal effects in the centre of NGC 1097. *Nature Astronomy*, 2:83–89.

Tasker, E. J. and Tan, J. C. (2009). Star Formation in Disk Galaxies. I. Formation and Evolution of Giant Molecular Clouds via Gravitational Instability and Cloud Collisions. ApJ, 700(1):358–375.

Taylor, G. (1950). The Formation of a Blast Wave by a Very Intense Explosion. I. Theoretical Discussion. *Proceedings of the Royal Society of London Series A*, 201:159–174.

Tegmark, M., Silk, J., Rees, M. J., Blanchard, A., Abel, T., and Palla, F. (1997). How Small Were the First Cosmological Objects? ApJ, 474:1.

Teklu, A. F., Remus, R.-S., Dolag, K., Arth, A., Burkert, A., Obreja, A., and Schulze, F. (2018). Declining Rotation Curves at z = 2 in ΛCDM Galaxy Formation Simulations. ApJ, 854(2):L28.

Testi, L. and Sargent, A. I. (1998). Star Formation in Clusters: A Survey of Compact Millimeter-Wave Sources in the Serpens Core. ApJ, 508(1):L91–L94.

Teyssier, R. (2002). Cosmological hydrodynamics with adaptive mesh refinement. A new high resolution code called RAMSES. A&A, 385:337–364.

Thornton, K., Gaudlitz, M., Janka, H.-T., and Steinmetz, M. (1998). Energy Input and Mass Redistribution by Supernovae in the Interstellar Medium. ApJ, 500:95–119.

Tobias, S. M., Cattaneo, F., and Boldyrev, S. (2011). MHD Dynamos and Turbulence. *ArXiv e-prints*.

Tomisaka, K. (1984). Coagulation of interstellar clouds in spiral gravitational potential and formation of giant molecular clouds. PASJ, 36(3):457–475.

Tomisaka, K. and Ikeuchi, S. (1986). Evolution of superbubble driven by sequential supernova explosions in a plane-stratified gas distribution. PASJ, 38:697–715.

Toomre, A. and Toomre, J. (1972). Galactic Bridges and Tails. ApJ, 178:623–666.

Toro, E. F., Spruce, M., and Speares, W. (1994). Restoration of the contact surface in the HLL-Riemann solver. *Shock Waves*, 4:25–34.

Tremaine, S. and Gunn, J. E. (1979). Dynamical role of light neutral leptons in cosmology. Phys. Rev. Lett., 42(6):407–410.

van Dishoeck, E. F. (1987). Photodissociation processes of astrophysical molecules. In Vardya, M. S. and Tarafdar, S. P., editors, *Astrochemistry*, volume 120 of *IAU Symposium*, pages 51–65.

Vazza, F., Brunetti, G., Brüggen, M., and Bonafede, A. (2018). Resolved magnetic dynamo action in the simulated intracluster medium. MNRAS, 474:1672–1687.

Veilleux, S., Cecil, G., and Bland-Hawthorn, J. (2005). Galactic Winds. ARA&A, 43:769–826.

Vogelsberger, M., Genel, S., Springel, V., Torrey, P., Sijacki, D., Xu, D., Snyder, G., Nelson, D., and Hernquist, L. (2014). Introducing the Illustris Project: simulating the coevolution of dark and visible matter in the Universe. MNRAS, 444(2):1518–1547.

Walch, S., Girichidis, P., Naab, T., Gatto, A., Glover, S. C. O., Wünsch, R., Klessen, R. S., Clark, P. C., Peters, T., Derigs, D., and Baczynski, C. (2015). The SILCC (SImulating the LifeCycle of molecular Clouds) project - I. Chemical evolution of the supernova-driven ISM. MNRAS, 454:238–268.

Wang, L., Dutton, A. A., Stinson, G. S., Macciò, A. V., Penzo, C., Kang, X., Keller, B. W., and Wadsley, J. (2015). NIHAO project - I. Reproducing the inefficiency of galaxy formation across cosmic time with a large sample of cosmological hydrodynamical simulations. MNRAS, 454:83–94.

Wang, P. and Abel, T. (2009). Magnetohydrodynamic Simulations of Disk Galaxy Formation: The Magnetization of the Cold and Warm Medium. ApJ, 696:96–109.

Wannier, P. G., Lichten, S. M., and Morris, M. (1983). Warm H I halos around molecular clouds. ApJ, 268:727–738.

Weaver, R., McCray, R., Castor, J., Shapiro, P., and Moore, R. (1977). Interstellar bubbles. II - Structure and evolution. ApJ, 218:377–395.

Wechsler, R. H., Somerville, R. S., Bullock, J. S., Kolatt, T. S., Primack, J. R., Blumenthal, G. R., and Dekel, A. (2001). Galaxy Formation at z~3: Constraints from Spatial Clustering. ApJ, 554(1):85–103.

Weinberg, S. (1971). Entropy Generation and the Survival of Protogalaxies in an Expanding Universe. ApJ, 168:175.

Weingartner, J. C. and Draine, B. T. (2001). Dust Grain-Size Distributions and Extinction in the Milky Way, Large Magellanic Cloud, and Small Magellanic Cloud. ApJ, 548(1):296–309.

Westera, P., Lejeune, T., Buser, R., Cuisinier, F., and Bruzual, G. (2002). A standard stellar library for evolutionary synthesis. III. Metallicity calibration. A&A, 381:524–538.

Wetzstein, M., Nelson, A. F., Naab, T., and Burkert, A. (2009). VineA Numerical Code for Simulating Astrophysical Systems Using Particles. I. Description of the Physics and the Numerical Methods. ApJS, 184:298–325.

Weyl, H. (2009). Republication of: On the general relativity theory. *General Relativity and Gravitation*, 41(7):1661–1666.

Wheeler, C., Hopkins, P. F., Pace, A. B., Garrison-Kimmel, S., Boylan-Kolchin, M., Wetzel, A., Bullock, J. S., Kereš, D., Faucher-Giguère, C.-A., and Quataert, E. (2019). Be it therefore resolved: cosmological simulations of dwarf galaxies with 30 solar mass resolution. MNRAS, 490(3):4447–4463.

Whitaker, K. E., Franx, M., Leja, J., van Dokkum, P. G., Henry, A., Skelton, R. E., Fumagalli, M., Momcheva, I. G., Brammer, G. B., Labbé, I., Nelson, E. J., and Rigby, J. R. (2014). Constraining the Low-mass Slope of the Star Formation Sequence at $0.5 < z < 2.5$. ApJ, 795(2):104.

White, S. D. M. (1978). Simulations of merging galaxies. MNRAS, 184:185–203.

White, S. D. M., Davis, M., and Frenk, C. S. (1984). The size of clusters in a neutrino-dominated universe. MNRAS, 209:27P–31P.

White, S. D. M. and Rees, M. J. (1978). Core condensation in heavy halos: a two-stage theory for galaxy formation and clustering. MNRAS, 183:341–358.

Widrow, L. M. (2002). Origin of galactic and extragalactic magnetic fields. *Reviews of Modern Physics*, 74:775–823.

Wielebinski, R. and Krause, F. (1993). Magnetic fields in galaxies. A&A Rev., 4:449–485.

Wiersma, R. P. C., Schaye, J., and Smith, B. D. (2009). The effect of photoionization on the cooling rates of enriched, astrophysical plasmas. MNRAS, 393:99–107.

Wolfire, M. G., Hollenbach, D., and McKee, C. F. (2010). The Dark Molecular Gas. ApJ, 716(2):1191–1207.

Wolfire, M. G., Hollenbach, D., McKee, C. F., Tielens, A. G. G. M., and Bakes, E. L. O. (1995). The Neutral Atomic Phases of the Interstellar Medium. ApJ, 443:152.

Wolfire, M. G., McKee, C. F., Hollenbach, D., and Tielens, A. G. G. M. (2003). Neutral Atomic Phases of the Interstellar Medium in the Galaxy. ApJ, 587(1):278–311.

Woltjer, L. (1972). Supernova Remnants. ARA&A, 10:129.

Wurster, J., Bate, M. R., and Price, D. J. (2019). There is no magnetic braking catastrophe: low-mass star cluster and protostellar disc formation with non-ideal magnetohydrodynamics. MNRAS, 489(2):1719–1741.

Xu, H., Li, H., Collins, D. C., Li, S., and Norman, M. L. (2009). Turbulence and Dynamo in Galaxy Cluster Medium: Implications on the Origin of Cluster Magnetic Fields. ApJ, 698:L14–L17.

Yuen, K. H., Hu, Y., Lazarian, A., and Pogosyan, D. (2019). Comment on Clark et al. (2019) "The Physical Nature of Neutral Hydrogen Intensity Structure". *arXiv e-prints*, page arXiv:1904.03173.

Yuen, K. H. and Lazarian, A. (2017). Tracing Interstellar Magnetic Field Using Velocity Gradient Technique: Application to Atomic Hydrogen Data. ApJ, 837(2):L24.

Yusef-Zadeh, F., Roberts, D. A., Goss, W. M., Frail, D. A., and Green, A. J. (1996). Detection of 1720 MHz Hydroxl Masers at the Galactic Center: Evidence for Shock-excited Gas and Milligauss Fields. ApJ, 466:L25.

Zeeman, P. (1897). The Effect of Magnetisation on the Nature of Light Emitted by a Substance. Nature, 55(1424):347.

Zeldovich, I. B., Ruzmaikin, A. A., and Sokolov, D. D., editors (1983). *Magnetic fields in astrophysics*, volume 3.

Zel'Dovich, Y. B. (1970). Reprint of 1970A&A.....5...84Z. Gravitational instability: an approximate theory for large density perturbations. A&A, 500:13–18.

Zeldovich, Y. B. (1972). A hypothesis, unifying the structure and the entropy of the Universe. MNRAS, 160:1P.

Zwicky, F. (1933). Die Rotverschiebung von extragalaktischen Nebeln. *Helvetica Physica Acta*, 6:110–127.

Danksagung

Finally, I would like the thank the following people, who I consider had a significant impact not only on my academic growth but also on my personal growth over the past three years.

- First, I would like to thank my supervisor Dr. Benjamin P. Moster, who provided me with the opportunity to work on the forefront of galaxy formation and evolution simulations and never restricted me in following my own ideas.

- Second, I would like to thank PD Dr. Klaus Dolag, who I consider had the biggest impact on me as a scientist and without whom I would probably not doing this job today. I cannot thank you enough for the support over the past three years! I would also

- Third, I would like to thank Dr. Thorsten Naab, who co supervised my thesis. We did not always agree on how to exactly we should move forward but we always found a way to move forward. I am very grateful for your guidance over the last three years.

- I would like to than Prof. Dr. Harald Lesch, not only for co-evaluating this thesis but also for all the discussion about the dynamo from which I greatly benefit.

- I would like to thank my parents Astrid and Jürgen, my sister Sigrun and my Grandma Emma, who always encouraged me to go forward in doing this job and who constantly supported me. Also a shout out to my cat Tomi, who provided moral support as well.

- I would like to thank Eirini Batziou, who supported me not only by reading all my papers and providing valuable comments to every single draft, which always improved my work, but also for her support in writing this thesis. I am also very grateful for all the adventures we have been through together alongside this journey and I hope for many more to come. I could not have done this without you over the last months and I will be ever grateful for your support during this difficult times.

- I want to thank the members of the CAST group at USM. Specifically, I would like to thank Joseph O'Leary as I think it is fair to say I could not have wished for a better working buddy. Further, I would like to thank him for providing food, all the fun work trips and comments for this thesis. I would like to thank Ludwig Böss who provided me with comments for this thesis and who I enjoy to work on magnetic fields with. I would like to thank my office mates Felix, Marcel, Kristina and Rafael for the valuable discussions. I would like to thank Stefan Heigl for the valuable discussions on the ISM, which I was definitely not an expert on when I started my PhD and for taking the lead the daily coffee-endeavours of our group.

- I would like to thank the galaxy formation group at MPA.

- Last but not least I would like to mention that the importance of coffee for the work presented in this thesis cannot be underestimated and I would like to close with a statement from one of the first mentors in the physical sciences I had, Prof. Dr. Peter Nielaba: It is possible to do physics without coffee, but it is also pointless.